ERA-40 Project Report Series

19. ERA-40 Atlas

Per Kållberg, Paul Berrisford, Brian Hoskins, Adrian Simmons,
Sakari Uppala, Sylvie Lamy-Thépaut and Rob Hine

Series: ECMWF ERA-40 Project Report Series

A full list of ECMWF Publications can be found on our web site under:
http://www.ecmwf.int/publications/

Contact: library@ecmwf.int

ERA-40 Project Report Series No. 19

ERA-40 Atlas

Per Kållberg, Paul Berrisford[1], Brian Hoskins[1],
Adrian Simmons, Sakari Uppala,
Sylvie Lamy-Thépaut and Rob Hine

June 2005

[1] Department of Meteorology, University of Reading, UK

Personal Foreword by Brian Hoskins

This atlas is the latest in a sequence that was originally inspired by the diagnostics of the general circulation of the atmosphere produced by Mike Wallace, Maurice Blackmon, Gabriel Lau and collaborators. In the middle and late 1970s they had taken advantage of the availability on magnetic tape of 10 years of routine analyses produced by the US National Meteorological Center for the region 20–90N. The advent and archiving of routine global analyses by the recently established European Centre for Medium-Range Forecasts (ECMWF) in Reading provided the opportunity to diagnose the global circulation. This opportunity was exploited in a Joint Diagnostics project involving the University of Reading, ECMWF and the UK Met Office. The diagnostics of ECMWF data were a crucial part of our activity in the UK Universities Modelling Group. Atlases were produced for the individual years 1980–81, 1981–82 and the FGGE year, 1979–80, and also for the 10-year period 1979–89.

It was realised that a significant reservation over the diagnostics based on the routine analyses produced by ECMWF and other NWP centres was the evolution over the period of interest of the observational system and of the data analysis system. The former is inevitable but the latter has been overcome by the extremely welcome move to the occasional performance of reanalyses of all the available data with state-of-the-art analysis systems. The first of these at ECMWF, ERA-15, was for the years 1979–94. ERA-15 was diagnosed in some detail by ECMWF and by us at the University of Reading, but no atlas was produced partly because of some technical difficulties and also because we could not decide what to leave out!

The ECMWF reanalysis for the period 1957–2002, ERA-40, has given a new opportunity to produce an unprecedented view of the global circulation of the atmosphere. The excellent work done by ECMWF alone and in collaboration with its partners in this venture led to the overcoming of almost all technical difficulties. The advent of fast internet access and massive data storage at ECMWF means that all the diagnostics produced can be accessed very widely, so that this published atlas is just the shop window indicating the range of goods available. Because of the non-uniform observational system issue, the decision has been made to show here the diagnostics based on the satellite era, 1979 onwards, to give a uniform view with more credibility in the Southern Hemisphere. However diagnostics for the whole period are available at ECMWF.

I should like to express my personal thanks to ECMWF, and particularly the ERA-40 team, for both their superb professionalism and their friendly attitude to those eager to use their data. For this atlas the main ECMWF player has been Per Kållberg, and from our side Paul Berrisford of the NCAS Centre for Global Atmospheric Modelling: I should also like to thank them both for their excellent work.

As retiring vice-chair of the Joint Scientific Committee of the World Climate Research Programmme I can say how much the Committee appreciates the reanalysis efforts at ECMWF and elsewere. We are pleased to acknowledge the funds towards publication and distribution of this Atlas provided by WCRP.

Index

1. The ERA-40 Reanalysis

1.1 The project

The objectives of ERA-40 were:

- to create high-quality global analyses of atmosphere, land and ocean-wave conditions for the past four decades or more using an up-to-date data assimilation system and exploiting, at any time, the maximum information from the available observational sources;
- to make the results available to a wide scientific community to be used in studies of the general circulation, global change, predictability and the evolution of the observing system.

Production of analyses for the 45-year period from September 1957 to August 2002 was completed in April 2003. The analyses were produced by ECMWF, working in partnership with a number of institutions. Observational data in addition to ECMWF's own holdings were provided largely by the US National Center for Atmospheric Research (NCAR) and National Centers for Environmental Prediction (NCEP) and supplemented by data from other organisations. The principal validation partners were the national weather services of France (Météo-France), the Netherlands (Koninklijk Nederlands Meteorologisch Instituut) and the United Kingdom (the Met Office), meteorological research institutes from Germany (Max-Planck-Institut für Meteorologie) and the USA (NCAR), and the Meteorology Department of the University of Reading, UK. The ERA-40 data assimilation system has benefited from the work of very many individuals at ECMWF and elsewhere. The production phase of ERA-40 was partially funded by the European Commission through contract EVK2-CT-1999-00027. Fujitsu Ltd supported the project by supplying computer resources beyond their original contractual obligation. The Institute of Atmospheric Physics, China, the Japan Meteorological Agency and the Program for Climate Model Diagnosis and Intercomparison, USA, seconded staff to work on the project. Support for planning and progress meetings with members of the wider user community was provided by the World Climate Research Programme and the Global Climate Observing System.

A general account of ERA-40, with extensive references to further documentation of the project, is given by Uppala *et al*. (2005).

1.2 The observations

The global observing system changed considerably between 1957 and 2002. The ever-present observation types are the synoptic surface observations from land stations and ships, and the soundings from radiosonde and pilot balloons. The quality of the radiosonde measurements improved over the period, but geographical and temporal coverage declined. Other types of observation introduced over the period, shown schematically in the following table, more than compensated for the decline in radiosonde coverage. 1973 was a key year that saw a significant increase in the number of available aircraft observations, the first few buoy observations, and radiances available from the first of the VTPR instruments flown on the early NOAA series of operational polar-orbiting satellites. A major enhancement of the observing system was in place by the beginning of 1979 for the Global Weather Experiment (or FGGE, the First Global Experiment of the Global Atmospheric Research Programme.) VTPR data were replaced by data from the three (MSU/HIRS/SSU) TOVS instruments on new NOAA platforms, winds first became available in significant numbers from geostationary satellites and there were substantial increases in buoy and aircraft data. Ozone data become available from the TOMS and SBUV instruments at about the same time. Observation counts declined for a while after FGGE, but recovered during the 1980s. ERA-40 benefited also in this period from the additional satellite winds derived for it by EUMETSAT's reprocessing of the data from Meteosat-2 (1982–1988). The density of wind and temperature measurements from aircraft and winds from geostationary satellites increased substantially in the 1990s. Newer satellite instruments from which data were assimilated in ERA-40 are SSM/I from 1987 onwards, the ERS altimeter (for the ocean-wave analysis) from 1991, the ERS scatterometer from 1993 and AMSU-A (the MSU/SSU replacement) from 1998.

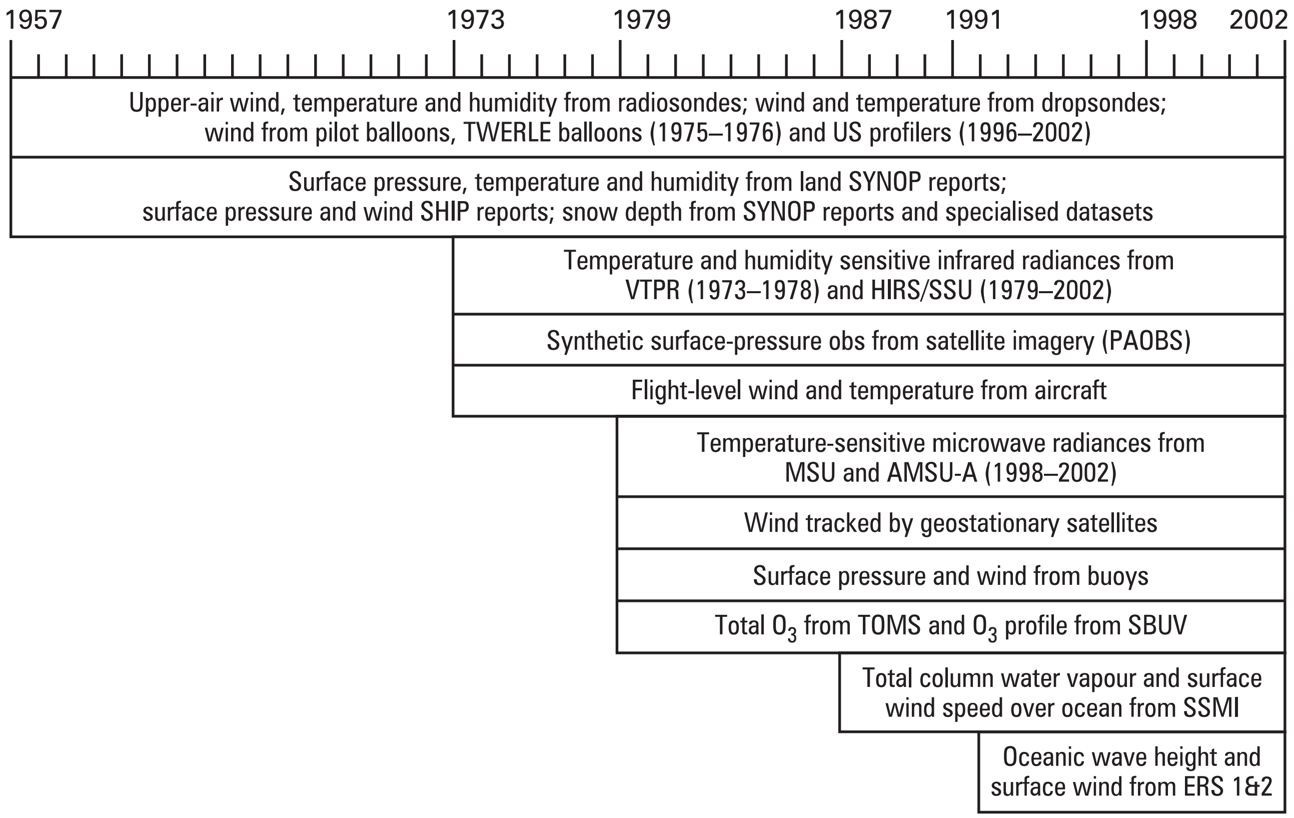

1.3 The ERA-40 data assimilation system

The ERA-40 atmospheric analysis was produced by three-dimensional variational data assimilation using six-hourly cycling. The assimilating atmospheric model had T159 spectral truncation in the horizontal, with corresponding ~125 km grid spacing, and a 60-level resolution in the vertical, with variables represented up to a pressure of 0.1 hPa. The version of ECMWF's "Integrated Forecasting System" software that was operational from June 2001 to January 2002 was used, though with some modifications either introduced in later operational versions or specifically developed for the configuration of the system used for ERA-40. The directly analysed variables were horizontal wind components, temperature, specific humidity and ozone at the sixty model levels, and surface pressure. Particular features of the assimilation system especially relevant to ERA-40 include the direct variational use of radiances from the VTPR, TOVS and ATOVS instruments, the background and variational quality control applied to observations in general, and the bias correction applied to satellite radiances and (from 1980 onwards) radiosonde data.

A separate analysis of temperature and humidity at two-metre height was made using optimal interpolation (OI) of measurements of dry-bulb temperature and dew point from land stations and ships. These analyses were used as input to an OI analysis of soil temperature and moisture for use in the background model. In-situ measurements of snow depth were analysed using Cressman interpolation to correct background values, with an adjustment applied that relaxed the analysis towards climatology in the absence of measurements. The assimilating atmospheric model was coupled with an ocean-wave model, with wave height analysed from 1991 onwards.

Sea-surface temperatures and sea-ice distributions were taken from two main sources. The HADISST1 dataset of monthly values produced by the Met Office was used up to November 1981, and the NCEP 2D-Var dataset of weekly values was used for most of the remaining period. Both sources used the same sea-ice analysis, which was developed collaboratively for use in ERA-40. Trends in the amounts of specified, radiatively-active gases were based on values given in the 1995 scientific assessment of the International Panel on Climate

Change. A trend in chlorine loading was used in the parametrization of ozone loss due to heterogeneous chemistry. The model did not include any aerosol trend or interaction between the model's radiation scheme and variable ozone fields, using instead a fixed geographical distribution of aerosol and a climatological ozone distribution for its radiation calculation.

1.4 The products

Comprehensive sets of products have been derived and archived in addition to the basic analysed variables. Analysed and derived upper-air variables (such as geopotential, vertical velocity and potential vorticity (PV), depending on context) have been interpolated to constant pressure and isentropic levels and to the |PV|=2 surface. A large set of single-level fields in addition to the basic analysed and model surface variables has been produced either from the analysed fields (boundary-layer height, for example) or from the six-hour background forecasts of the data assimilation (precipitation, for example). This includes vertical integrals of constituents and energy components, and their fluxes. Forecast data out to 36-hour range from 00 UTC and 12 UTC, and out to 6-hour range from 06 and 18 UTC have also been archived. Parameters to support chemical transport modelling, tendencies from cloudy and clear-sky radiation and net tendencies from parametrized processes have been accumulated as integrals over the six-hour background forecasts. Monthly means, variances and covariances have also been produced for selected variables.

The products of ERA-40 are available through:

- public internet access to a set of 2.5° resolution products held online at ECMWF (http://data.ecmwf.int/data);
- direct access to ECMWF's Meteorological Archival and Retrieval System by users from authorised institutions in the ECMWF Member and Co-operating States;
- ECMWF Data Services (http://www.ecmwf.int/products/data);
- several data centres in Europe that have built up data holdings for supply to national users (e.g. http://www.mad.zmaw.de/, http://climserv.lmd.polytechnique.fr, http://badc.nerc.ac.uk/data/);
- NCAR for supply of data to members of UCAR and other research and educational institutions in the USA (http://dss.ucar.edu/pub/era40/);
- an ECMWF ISLSCP-II initiative funded by NASA that has developed a near-surface dataset (http://islscp2.sesda.com).

1.5 The quality of the products

The quality of reanalysis products depends both on the quality of the observing system and on the quality of the assimilating numerical model and analysis system. Some assessments of ERA-40 products are summarized below. More information on these and other aspects of product quality is provided in journal articles, project reports and on the project website.

- The general quality of the analyses improves over time.
- Quality is most uniform in time for the northern hemisphere troposphere and lower stratosphere. Quality for the southern hemisphere is substantially better after 1978 and approaches that of the northern hemisphere later in the period.
- Trends and interannual variability in global-mean temperature from the surface to the lower stratosphere are in reasonable agreement with a number of specialised data studies from the 1970s onwards.
- Long-term temperature time series for particular regions, and for the upper stratosphere in general, require careful interpretation due to model biases and variations in observational coverage.
- Stratospheric sudden warmings and the quasi-biennial oscillation of stratospheric winds are well captured. The Brewer Dobson circulation is too strong.
- Total-column water vapour validates quite well against independent data for the satellite era. Tropical analyses are much drier in the pre-satellite period.

- Precipitation in short-range forecasts for the satellite era is too high over tropical oceans, but in much more reasonable agreement with verifying data elsewhere.
- The clear-sky outgoing long-wave radiation is of quite high quality, but there are some evident deficiencies in the all-sky radiation budget.
- Total-column ozone agrees well with independent data for most regions and much of the period. There are some problems with vertical structures, particularly at higher latitudes.
- Ocean-wave products are of generally good quality. High wave heights are underestimated, but can be corrected statistically.

2. Methodology and content of this atlas

The visual content of this Atlas is presented in 7 chapters from Chapter A through to Chapter G. These chapters contain the following information: A invariant fields, B surface or 2 dimensional fields, C column integrated fields, D pressure level fields, E isentropic level fields, F potential vorticity level fields and G time series data. For Chapters B through to F climatological information for each field is presented for the 4 seasons and for the annual average together with its interannual variability.

Most maps and cross sections in this Atlas have been prepared directly from the archived 23-year ERA-40 climatology. The climatology contains monthly/diurnal averages from 1979 to 2001. Analyses and 6 hour forecast fields are used in this Atlas. Fields on pressure levels, on isentropic levels and on the 2 pvu potential vorticity level were post-processed from the model's hybrid levels by the standard IFS post-processing package. The column climatology in Chapter C was integrated vertically directly using the 60 model levels.

The climatology is archived in the original spectral T159 resolution or on the corresponding 'N80' reduced Gaussian grid. For the actual plotting by the ECMWF 'Magics' graphics package, the fields were interpolated to a regular 1.125º×1.125º latitude/longitude grid.

The Atlas also contains various other diagnostics whose derivation from the basic climatology is described below.

2.1 The mean meridional circulation

The mean meridional mass transport is depicted in both pressure and isentropic co-ordinates using the mean meridional streamfunction, ψ. The mathematical problem for ψ can be formulated in both co-ordinate frameworks in the following manner. On taking the temporal (denoted by an overbar) and longitudinal (denoted by square brackets) averages in the continuity equations, and ignoring the contributions from local time derivatives, which should be small, the motion becomes purely non-divergent and we get the following relationships for the mean meridional streamfunction:

$$2\pi a \cos\phi \left[\overline{\sigma v}\right] = -\frac{\partial\psi}{\partial Z}\ ,\ 2\pi a^2 \cos\phi \left[\overline{\sigma w}\right] = \frac{\partial\psi}{\partial\phi}$$

where a is the radius of the earth, ϕ is latitude, Z is the vertical co-ordinate (which above ground is equal to pressure, p , or potential temperature, ϕ), σ, the mass density, is given by $-1/g\ \partial p/\partial Z$, v is the meridional wind and w is the vertical motion, equal to $\omega = Dp/Dt$ or the cross isentropic flow, $\dot{\theta} = D\theta/Dt$. In principle the meridional streamfunction could be derived from either equation or a combination of them. Here, after much testing, we use the equation involving v, partly because it is an analysed variable and so should give the most reliable results. This is particularly true in isentropic co-ordinates where the vertical motion is obtained from the parameterized processes in the model forecasts. Using the methodology of *Juckes et al*. (1994) the mass weighted vertical integration of v is performed in model level space where we have the best resolution, from $p = 0$ where $\psi = 0$, and the results are interpolated to the output levels where the temporal and longitudinal averages are computed. There is no constraint on the meridional streamfunction returning to zero at the ground, a fact which gives rise to vertical contours in so called underground regions. The amplitude of these is a measure of the error in the calculation.

It should be noted that given the meridional streamfunction is computed in model level space, the dramatic differences between the pressure and isentropic forms have a physical origin associated with the spatial and temporal averaging being performed on the different co-ordinate surfaces, see *Karoly et al*. 1997.

2.2 Heating and cross isentropic flow

Diagnostics of pressure layer heating, H_l, pressure level zonal mean heating, $[H]$, and cross isentropic flow, $\dot{\theta}$, in both zonal mean and latitude/longitude form, are exhibited in this Atlas. The fields are computed from the forecast net temperature tendencies, $\dot{T}$, output from the model's parameterizations. Following *Juckes et al.* (1994) and *Boer* (1982), the variables are computed as:

$$H_l = -\frac{C_p}{g}\overline{\int_{p_l}^{p_u}\dot{T}dp}\ ,\ [H] = \frac{\left[\overline{\int_{p-}^{p+}\dot{T}dp}\right]}{\left[\overline{\int_{p-}^{p+}dp}\right]}\ ,\ \dot{\theta} = \frac{\overline{\int_{\theta-}^{\theta+}\dot{T}\theta/Tdp}}{\overline{\int_{\theta-}^{\theta+}dp}}\ ,\ \left[\dot{\theta}\right] = \frac{\left[\overline{\int_{\theta-}^{\theta+}\dot{T}\theta/Tdp}\right]}{\left[\overline{\int_{\theta-}^{\theta+}dp}\right]}$$

where C_p is the specific heat of air at constant pressure. Again the vertical integration is carried out on model levels whereupon the values are interpolated to the intermediate levels of the output space and the relevant averaging is performed. The limits of the integration for the layer heating, indicated by the subscripts *u* and *l*, refer to the upper and lower limits of the layer whereas for level variables the limits + and - correspond to the intermediate levels located above and below the full output level respectively. Here, all positional terms such as upper and above refer to physical locations.

It should be noted that the cross isentropic flow exhibits spurious negative values near the ground in some tropical regions. This occurs over certain land masses, such as Africa, where nocturnal cooling at low potential temperatures is captured when the 6 hour analysis and forecast time occurs in the 3 hours after the local midnight.

2.3 Masks

The denominators in the equations given in section 2.2 indicate the mass associated with a particular level. If the mass happens to be zero, i.e. the level in question does not exist at that location, then the heating and cross isentropic flow are masked out and are not plotted at that point. The same masks are applied to the zonal means of all fields.

2.4 Spatial smoothing

Spatial smoothing is performed on some of the fields in this Atlas using a spectral filter, S, of the form

$$S_n = e^{-K(n(n+1))^2} \quad \text{for } n \le 159$$

$$S_n = 0 \quad \text{for } n > 159$$

where n is the total wave number on the sphere and with K chosen so that $S_{159} = 0.1$. In addition to eliminating possibly spurious small-scale noise this filter has other attractive properties, see *Sardeshmukh and Hoskins* (1984).

2.5 Isotachs

Isotachs are computed from the climatological wind components as the speed of the mean wind. Note, this is not the same quantity as the mean wind speed.

2.6 Interannual variability

The interannual variability of a field is in general calculated as the standard deviation of the annual mean about its 23-year climatology. The only exception to this is for isotachs in which case the quantity plotted is computed as the square root of the sum of the interannual variance of the wind components. For all vectors, only the magnitude of the interannual variability is presented.

2.7 Temporal filtering

Temporal filtering is performed on certain fields using Lanczos filters, *Duchon* (1979). The 6-hourly data for the required fields are filtered into 4 bands: low pass to 90 days; band pass from 90 to 30 days; band pass from 30 to 6 days and band pass from 6 to 2 days. Filter lengths of 721 are used and the responses are shown in Figure 1. For the QBO indices in Chapter G, monthly mean data are filtered into the 48–9 month band using a filter length of 73 months, the response being shown in Figure 2.

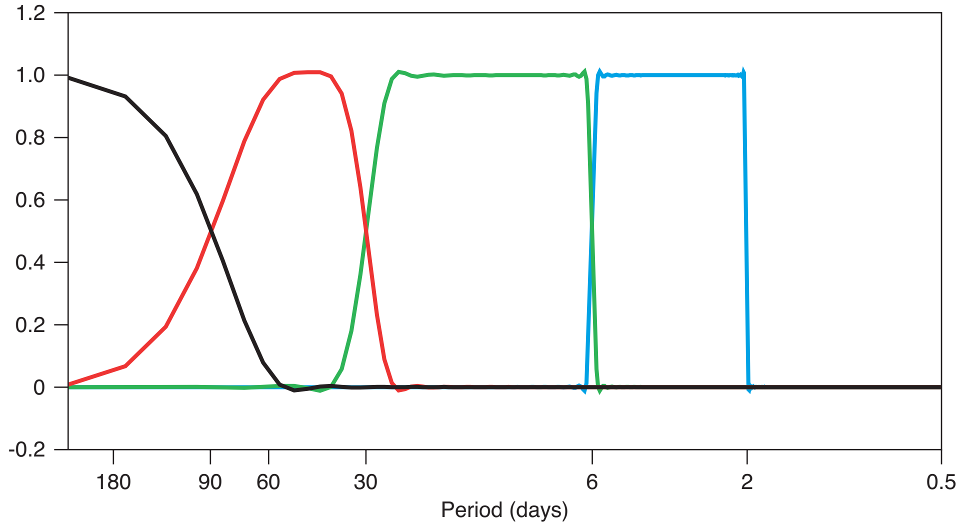

Figure 1 Response curves for the 721 point, 6-hourly Lanczos filters: low pass to 90 days (black line), band pass from 90 to 30 days (red line), band pass from 30 to 6 days (green line) and band pass from 6 to 2 days (blue line).

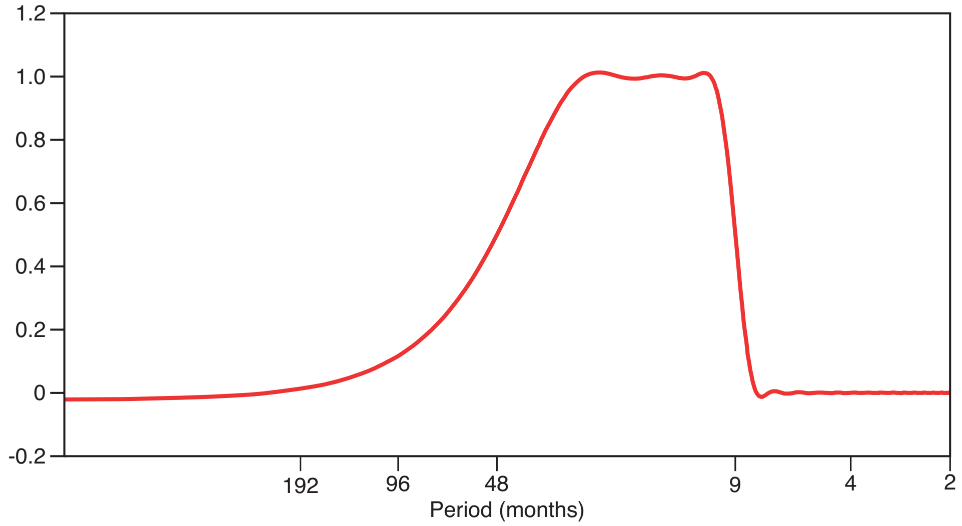

Figure 2 Response curve for the 73 point, monthly Lanczos filter: band pass from 48 to 9 months.

2.8 Time series

Chapter G contains several time series. The semi-annual oscillation (SAO) and quasi-biennial oscillation (QBO) are computed according to *Pascoe et al.* (2005), the Madden-Julian Oscillation (MJO) index follows Slingo et al. (1999) and the Pacific North American (PNA) index follows *Wallace and Gutzler* (1981).

3. Acknowledgements

The authors would like to express their thanks to various people whose efforts have helped in the completion of this Atlas. Dr. Jeff Cole has provided, and upgraded where necessary, the data format conversion tool XCONV. Dr Mike Blackburn, Professor Lesley Gray and Professor Julia Slingo have provided invaluable advice on diagnostics.

4. References

Boer, G.J., 1982. Diagnostic equations in isobaric coordinates. *Mon. Weather Rev.*, **110**, 1801-1820.

Duchon, C.E., 1979. Lanczos filtering in one and two dimensions. *J. Appl. Met.*, **18**, 1016-1022.

Juckes, M.N., James, I.N. and Blackburn, M., 1994. The influence of Antarctica on the momentum budget of the southern extratropics. *Q.J.R. Meteorol. Soc.*, **120**, 1017-1044.

Karoly, D.J., McIntosh, P.C., Berrisford, P., McDougall, T.J. and Hirst, A.C., 1997. Similarities of the Deacon cell in the southern ocean and Ferrel cells in the atmosphere. *Q.J.R. Meteorol. Soc.*, **123**, 519-526.

Pascoe, C.L., Gray, L.J., Crooks, S.A., Juckes, M.N., and Baldwin, M.P., 2005. The quasi-biennial oscillation: analysis using ERA-40 data. *J. Geophys. Res.*, **110**, D08105.

Sardeshmukh, P.D. and Hoskins, B.J., 1984. Spatial smoothing on the sphere. *Mon. Wea. Rev.*, **112**, 2524-2529.

Slingo, J.M., Rowell, D.P., Sperber, K.R. and Nortley, F., 1999. On the predictability of the interannual behaviour of the Madden-Julian Oscillation and its relationship with El Niño. *Q.J.R. Meteorol. Soc.*, **125**, 583-609.

Uppala, S.M., Kållberg, P.W., Simmons, A.J., Andrae, U., da Costa Bechtold, V., Fiorino, M., Gibson, J.K., Haseler, J., Hernandez, A., Kelly, G.A., Li, X., Onogi, K., Saarinen, S., Sokka, N., Allan, R.P., Andersson, E., Arpe, K., Balmaseda, M.A., Beljaars, A.C.M., van de Berg, L., Bidlot, J., Bormann, N., Caires, S., Chevallier, F., Dethof, A., Dragosavac, M., Fisher, M., Fuentes, M., Hagemann, S., Hólm, E., Hoskins, B.J., Isaksen, L., Janssen, P.A.E.M., Jenne, R., McNally, A.P., Mahfouf, J.-F., Morcrette, J.-J., Rayner, N.A., Saunders, R.W., Simon, P., Sterl, A., Trenberth, K.E., Untch, A., Vasiljevic, D., Viterbo, P., and Woollen, J. 2005: The ERA-40 Reanalysis. *Q.J.R. Meteorol. Soc.*, in press.

Wallace, J.M. and Gutzler, D.S., 1981. Teleconnections in the geopotential height field during the Northern Hemisphere winter. *Mon. Wea. Rev.*, **109**, 784-812.

Section A

Surface orography and land/sea mask

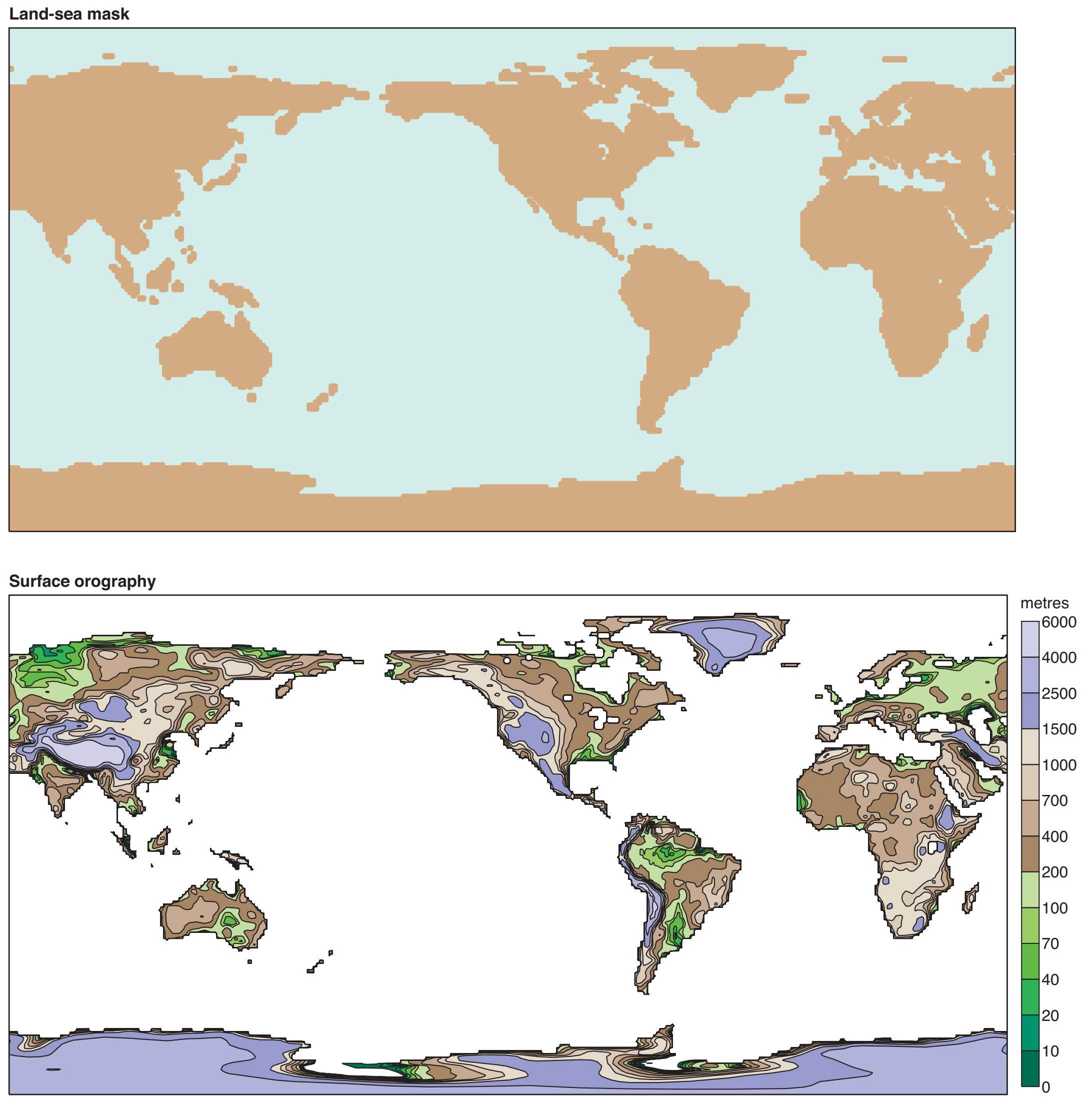

A1 Land-sea mask and surface orography (m).

Section B

Surface climatologies

Mean sea level pressure — Annual mean

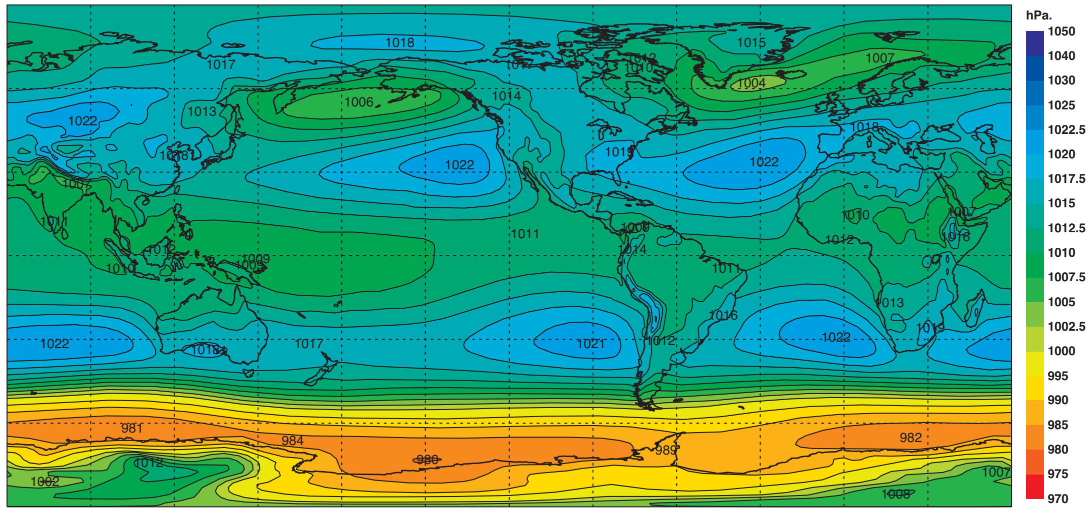

Mean sea level pressure — December-February

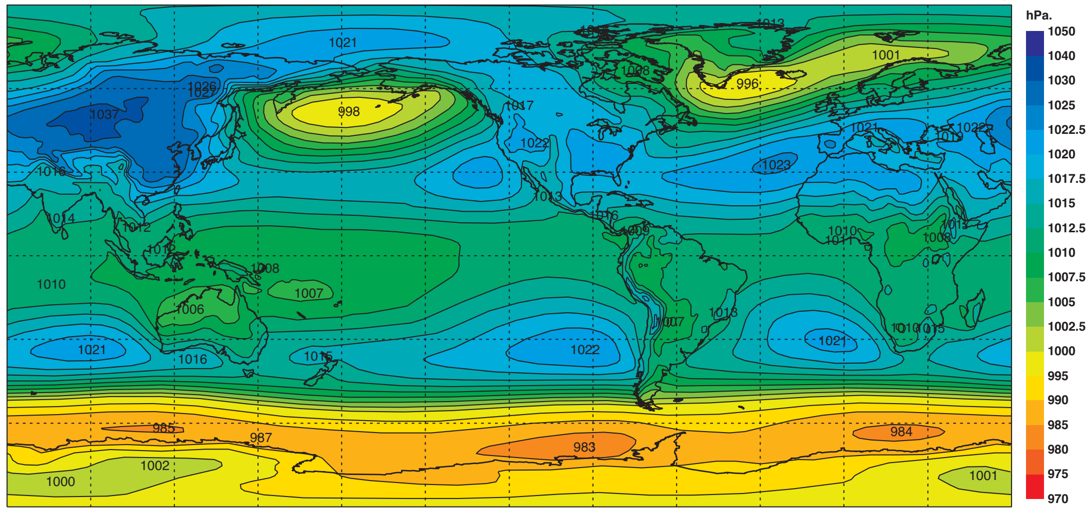

Mean sea level pressure — June-August

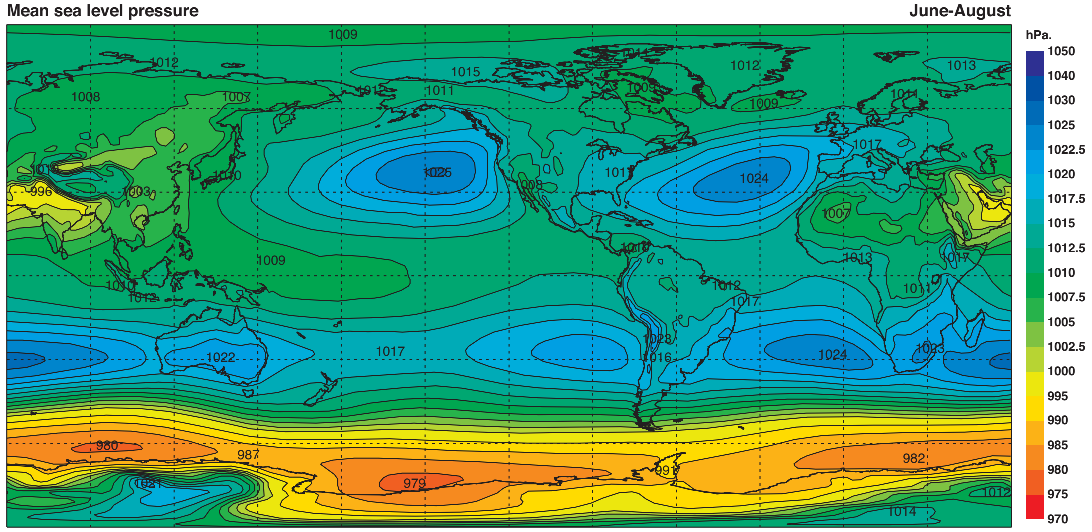

Mean sea level pressure — Interannual variability

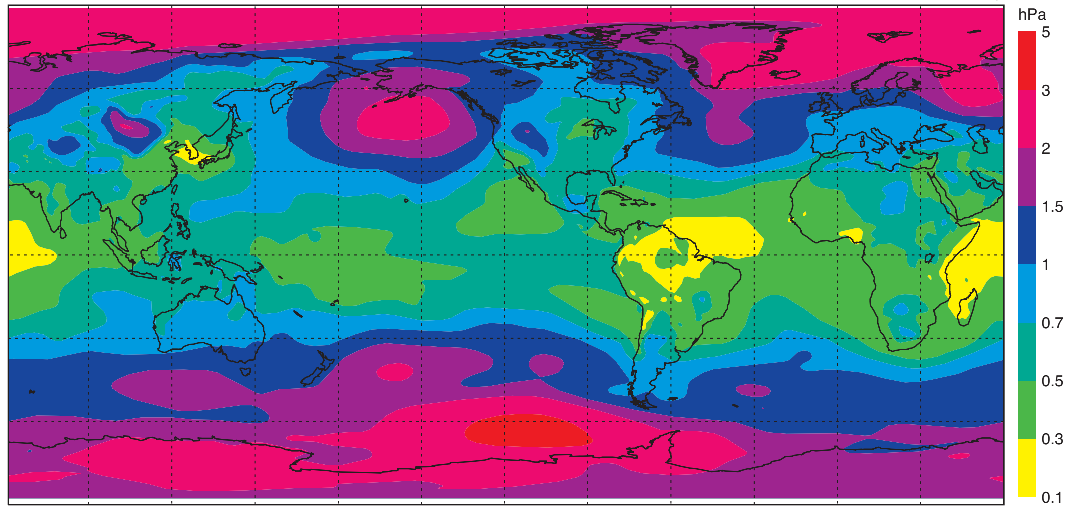

Mean sea level pressure — March-May

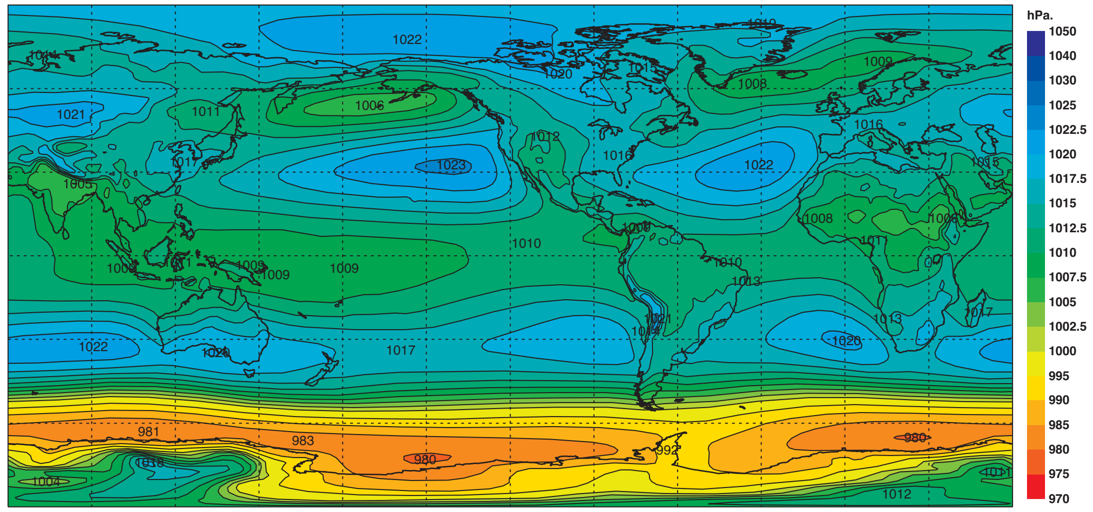

Mean sea level pressure — September-November

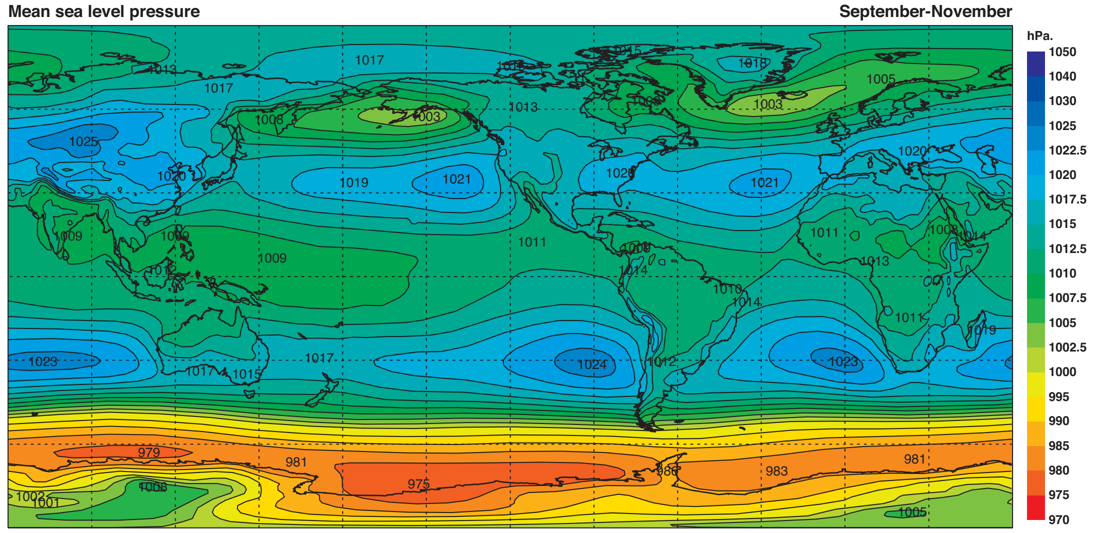

B1 Mean sea level pressure (hPa).

10 metre wind — Annual mean

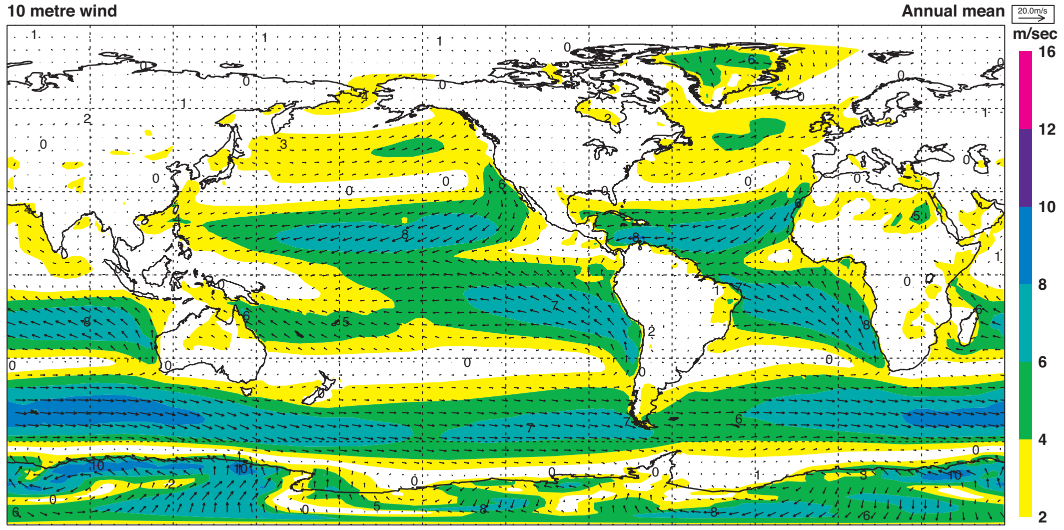

10 metre wind — December-February

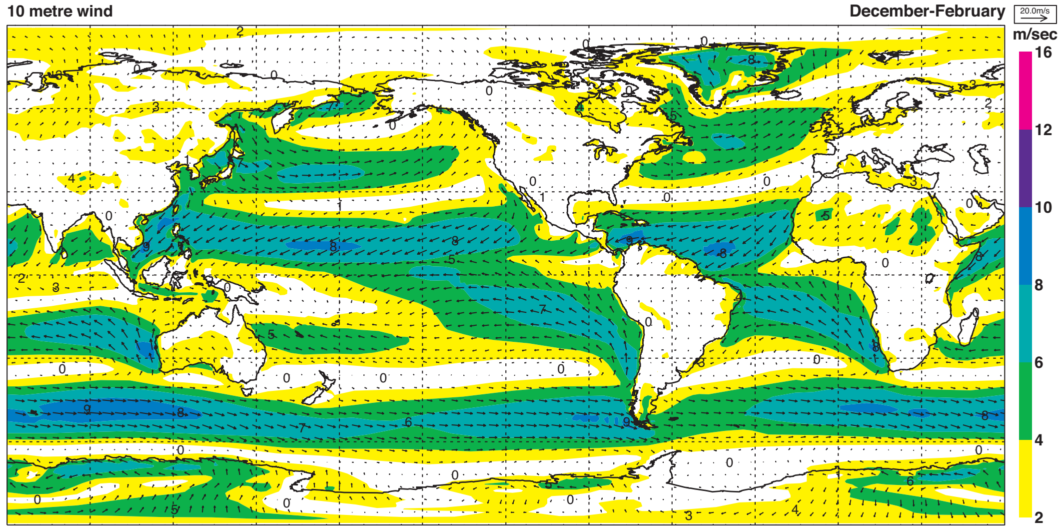

10 metre wind — June-August

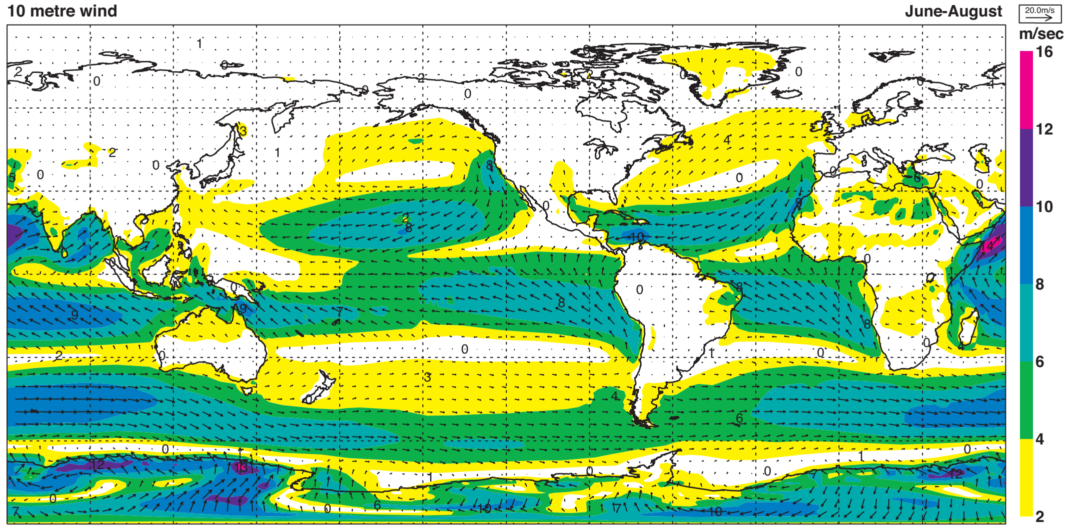

10 metre wind — Interannual variability

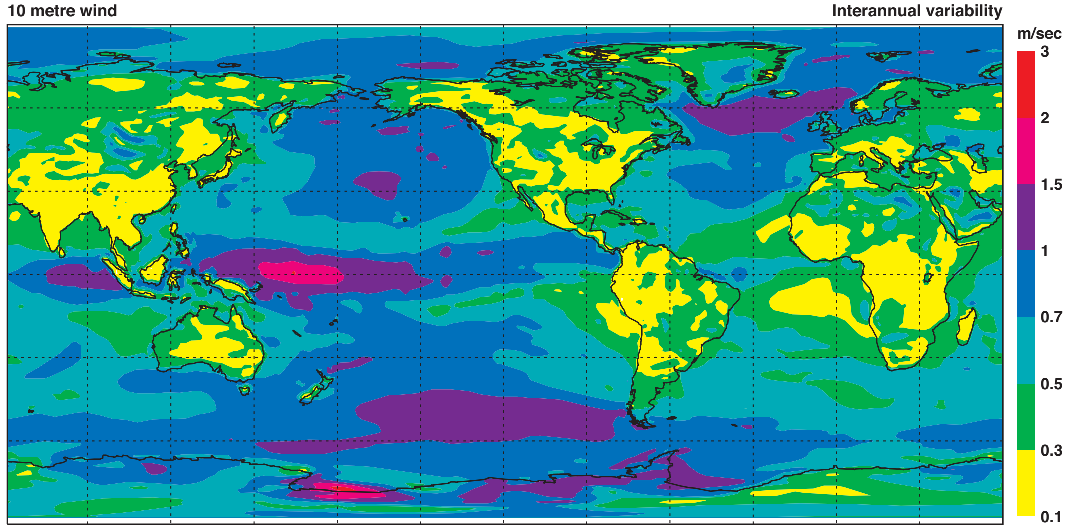

10 metre wind — March-May

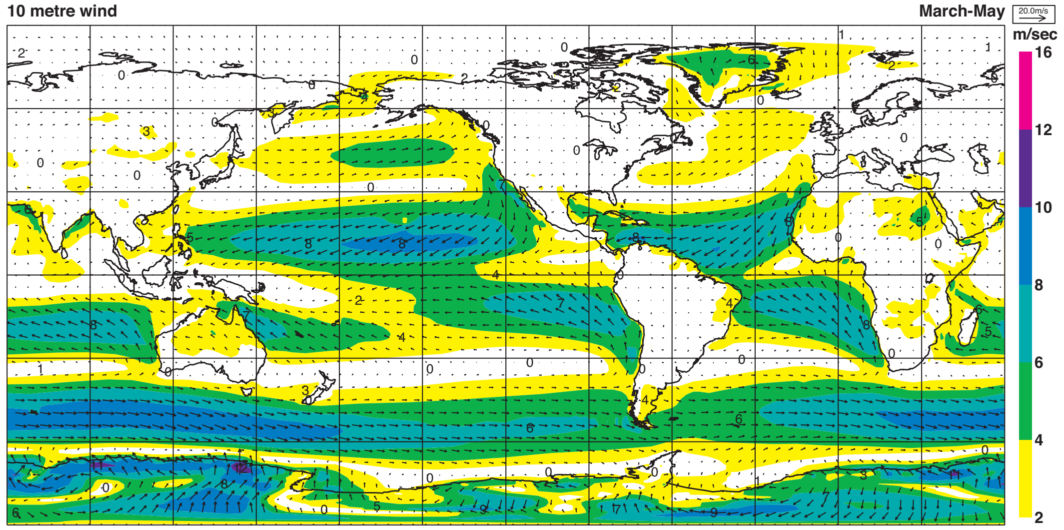

10 metre wind — September-November

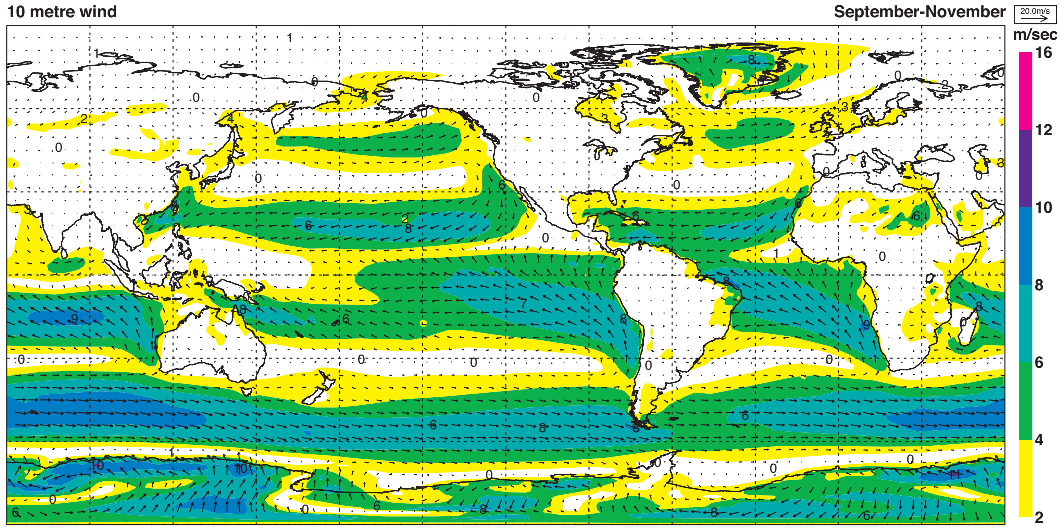

B2 10m vector wind (ms^{-1}) with isotachs (ms^{-1}). For the interannual variability, the vectors are omitted.

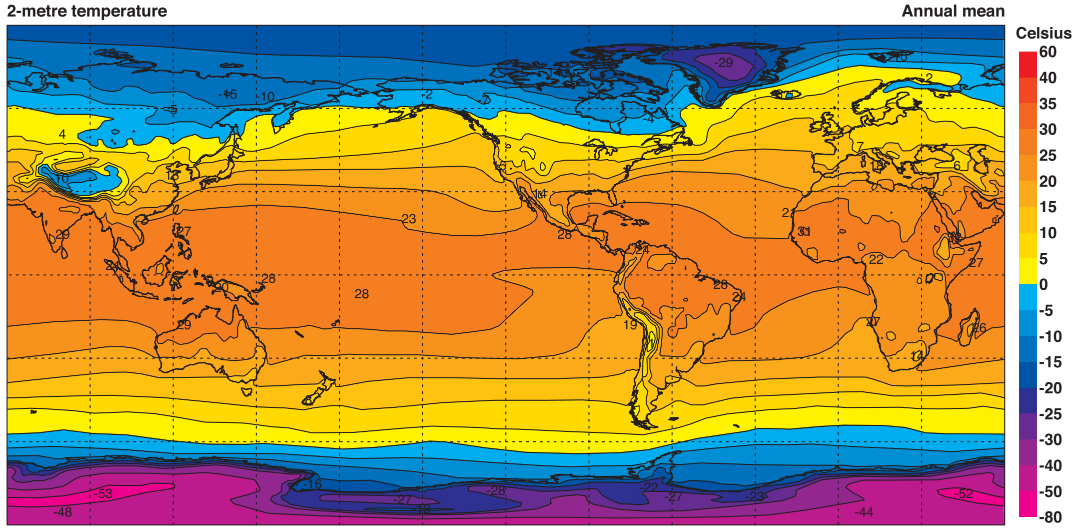

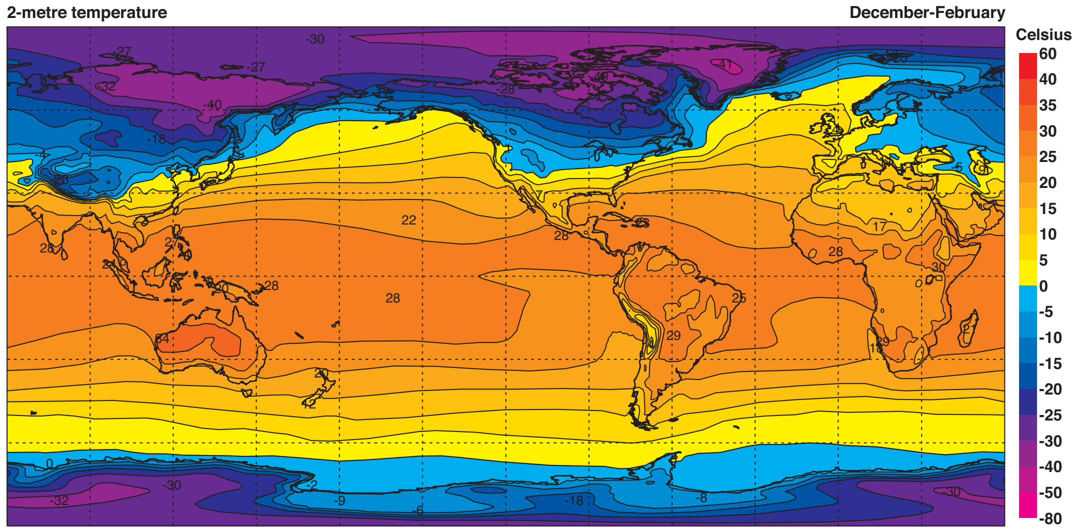

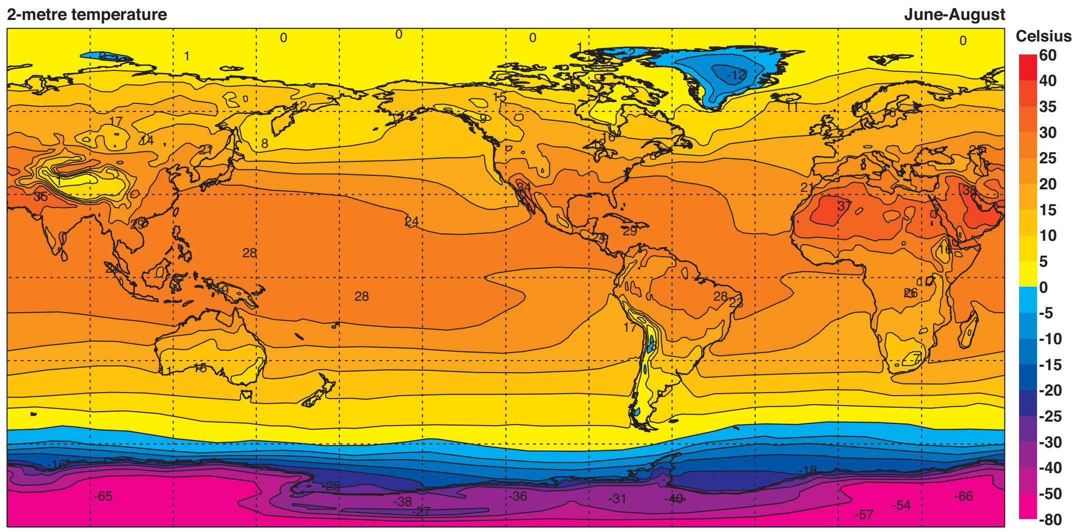

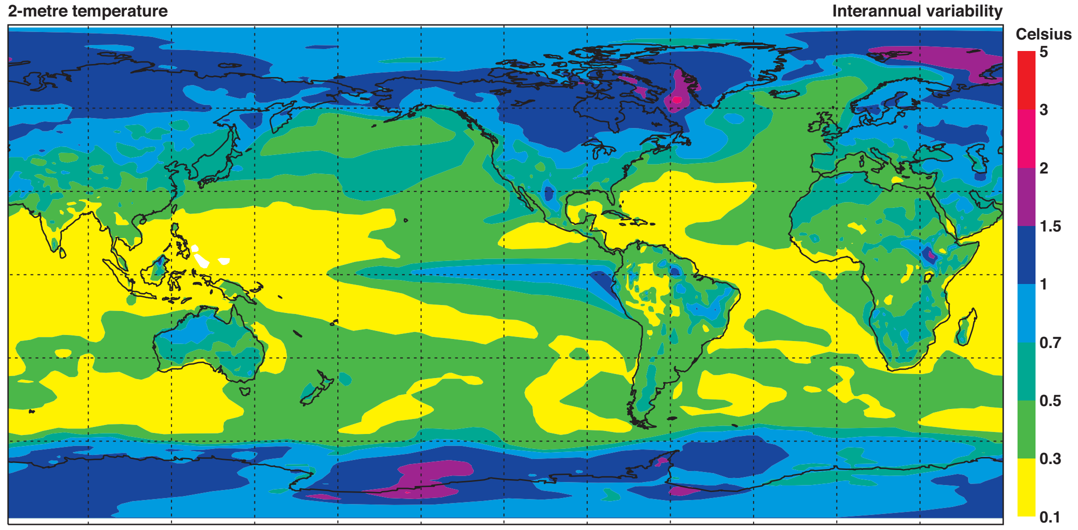

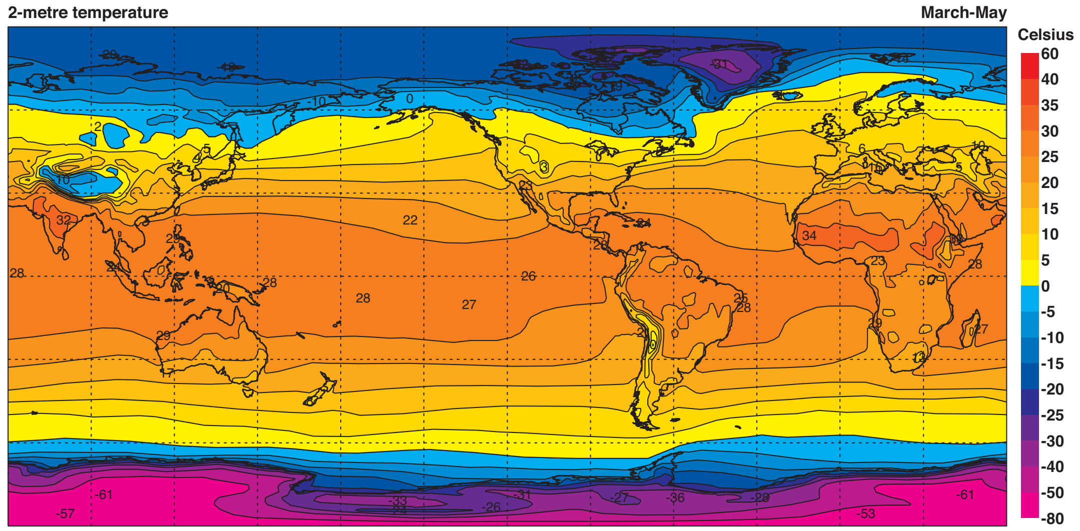

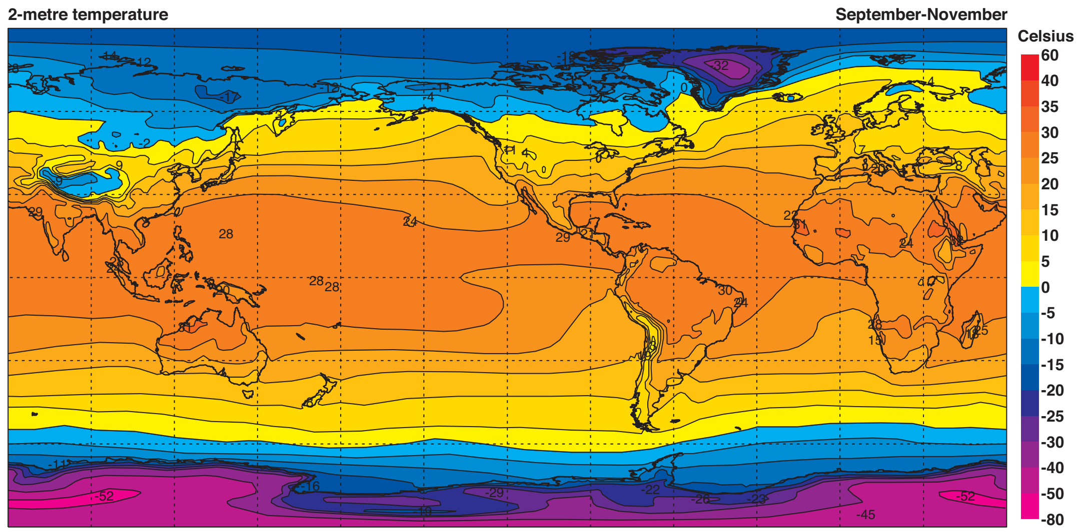

B3 2m temperature (°C).

Net surface heat exchange Annual mean

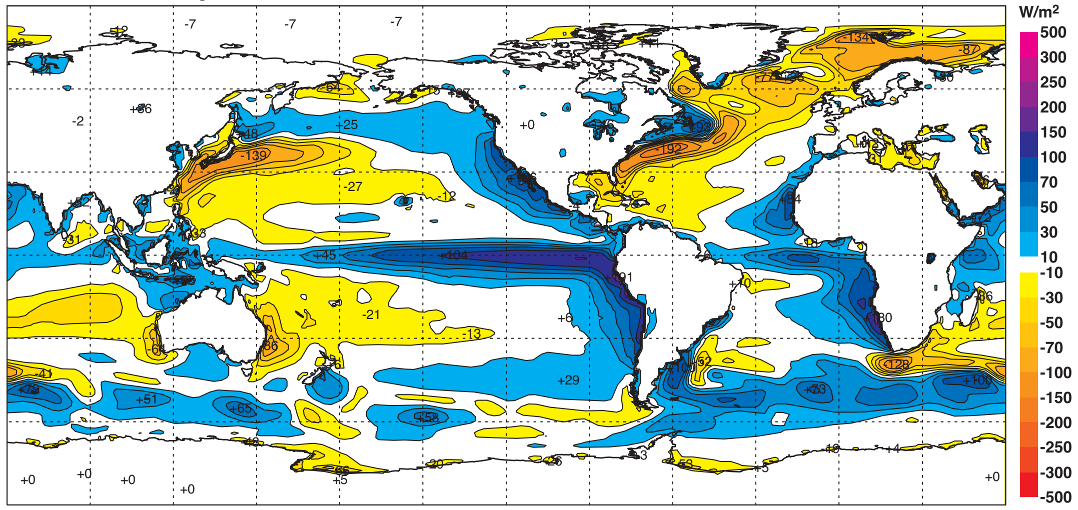

Net surface heat exchange December-February

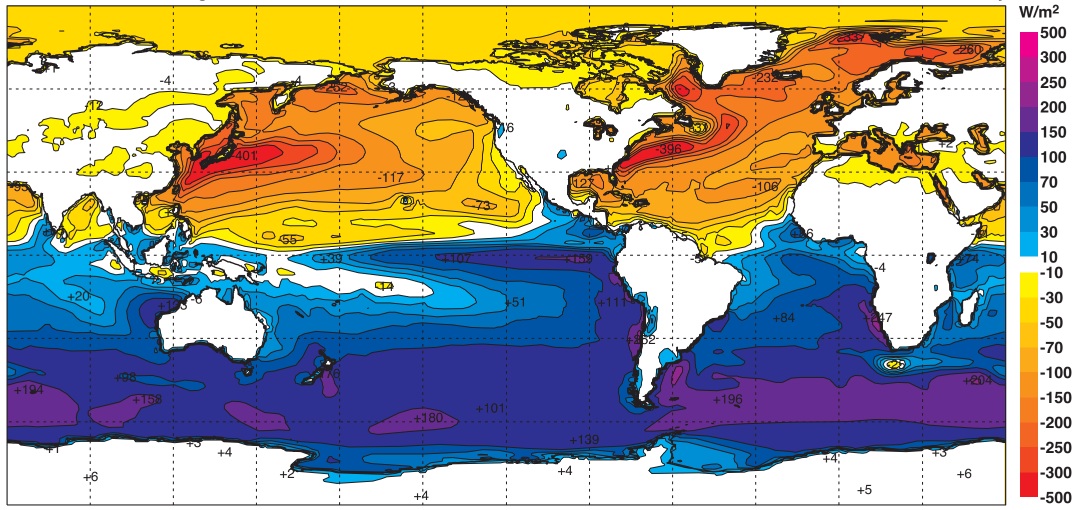

Net surface heat exchange June-August

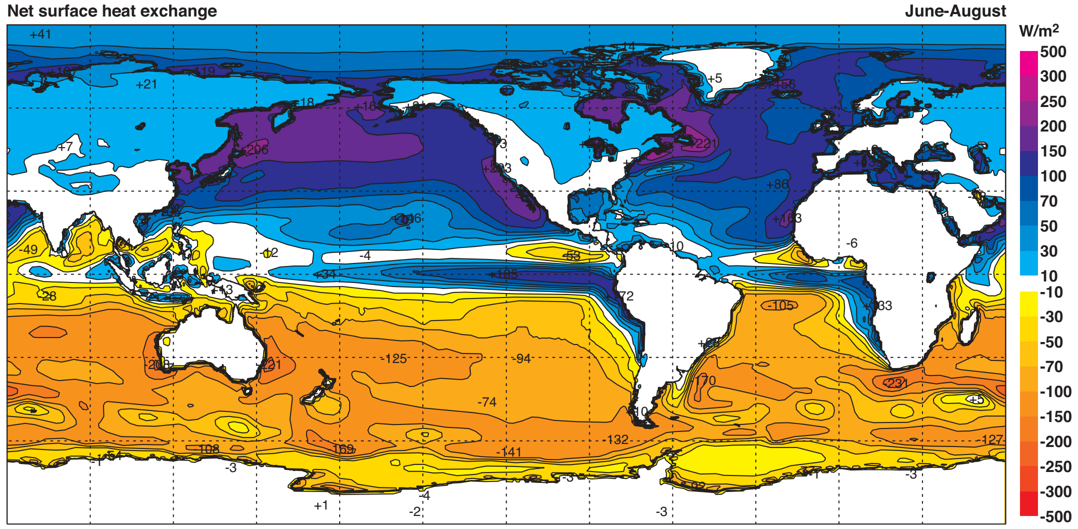

Net surface heat exchange Interannual variability

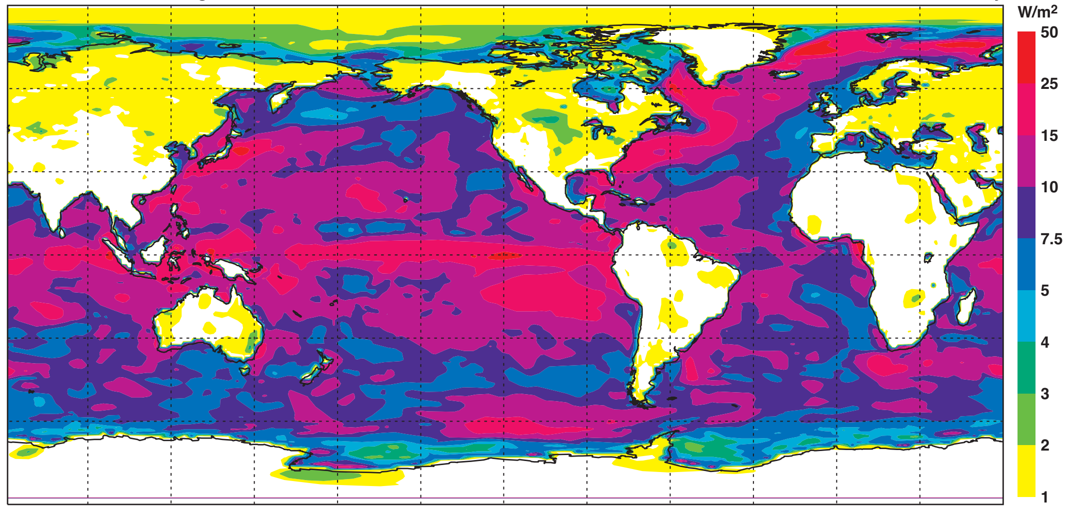

Net surface heat exchange March-May

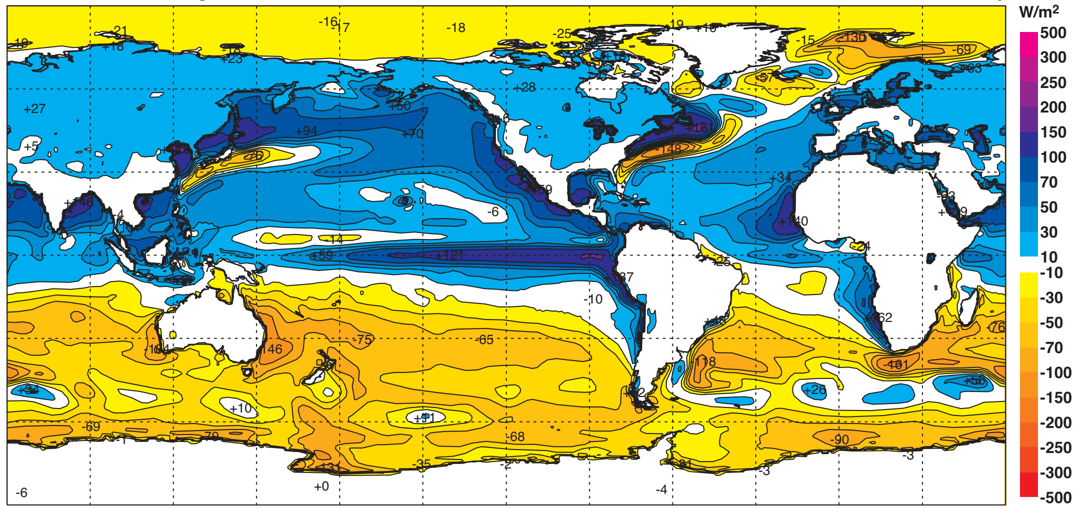

Net surface heat exchange September-November

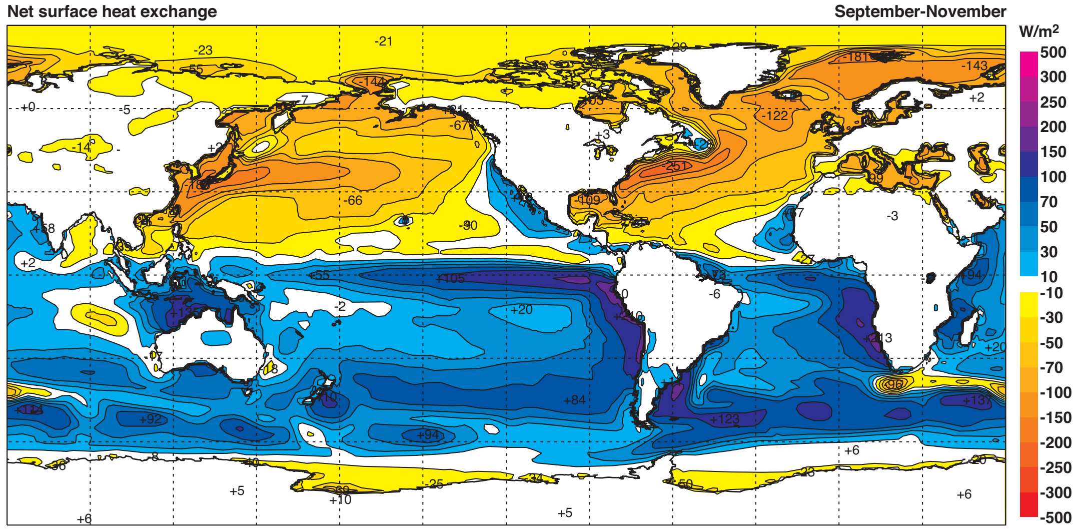

B4 Net surface fluxes of heat (Wm^{-2}), positive downwards.

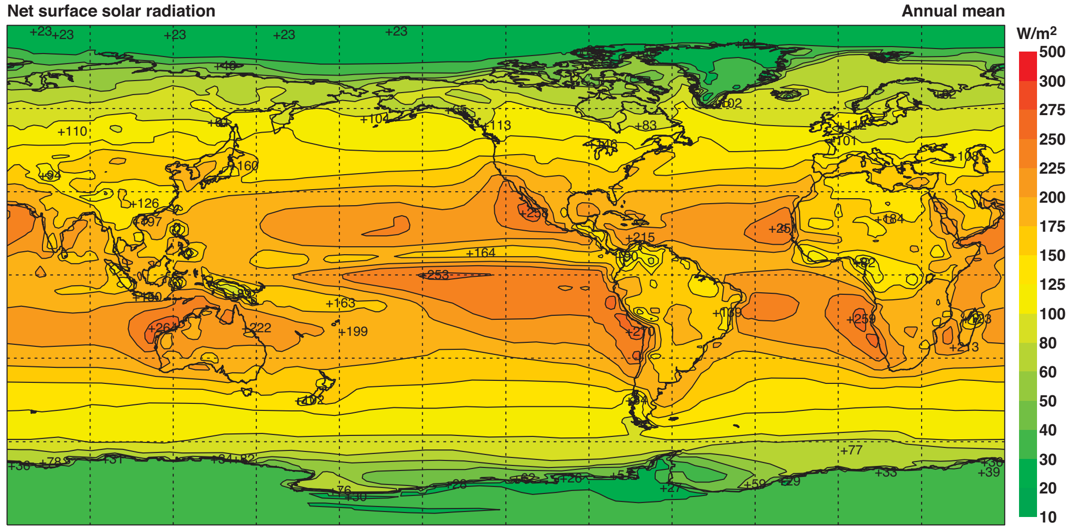

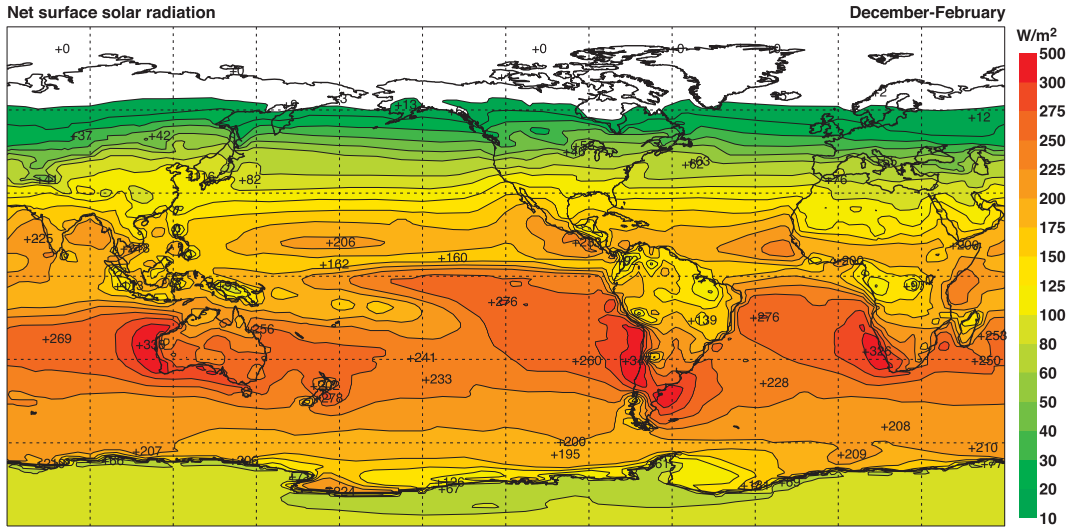

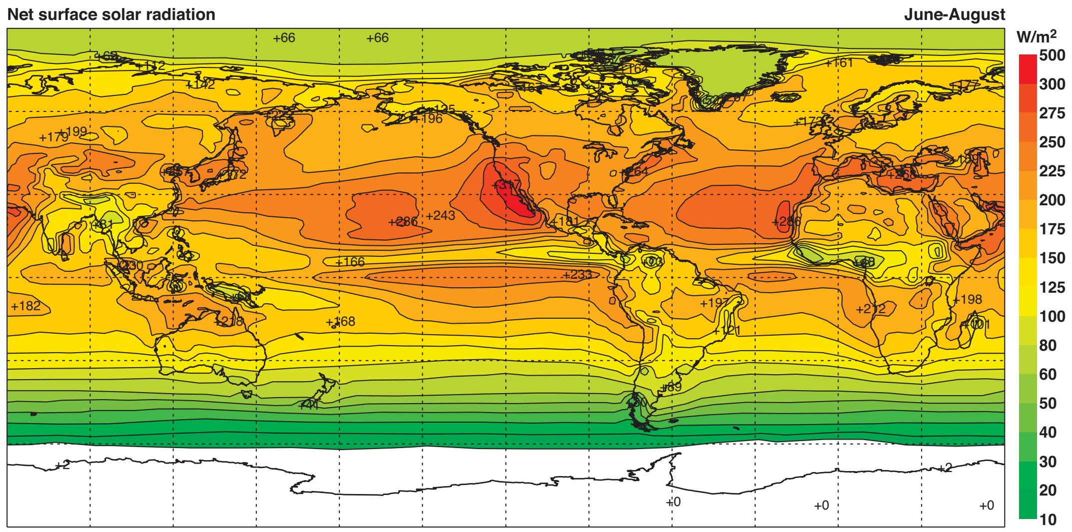

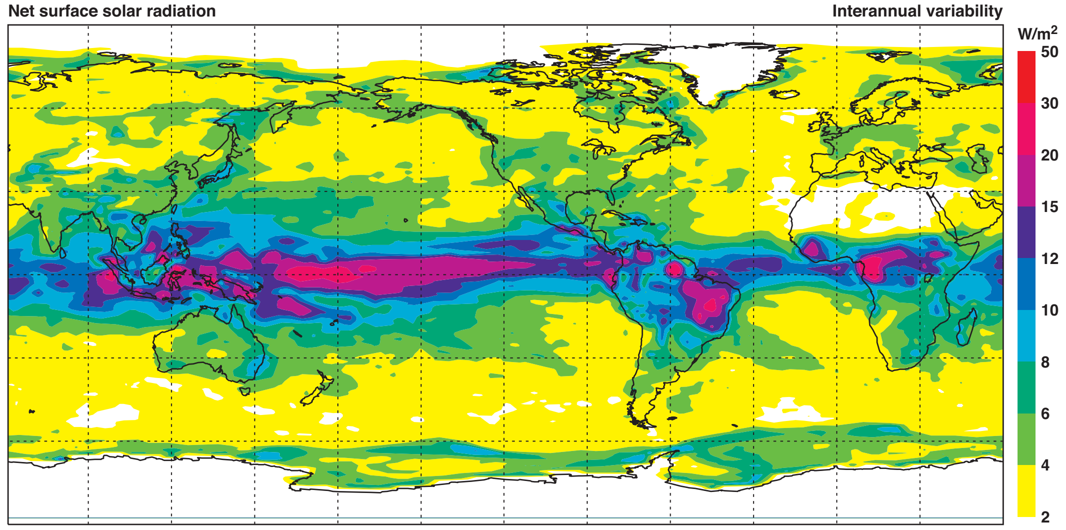

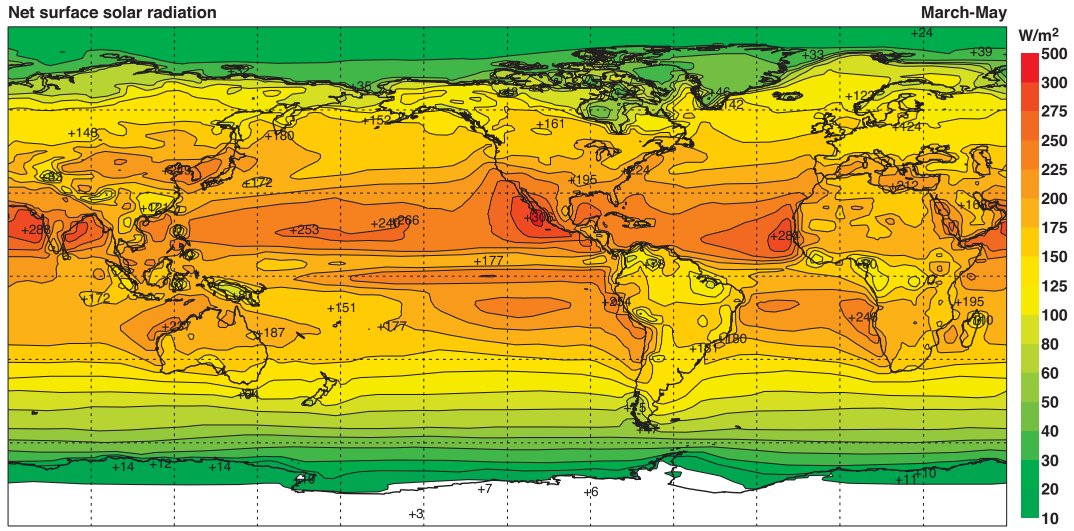

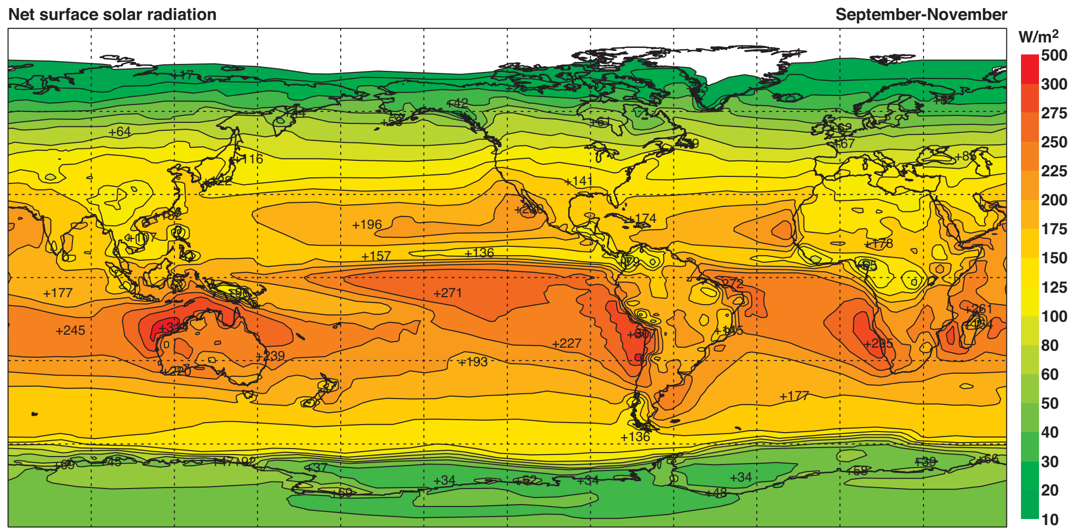

B5 Net surface fluxes of solar radiation (Wm^{-2}), positive downwards.

Net surface thermal radiation — Annual mean

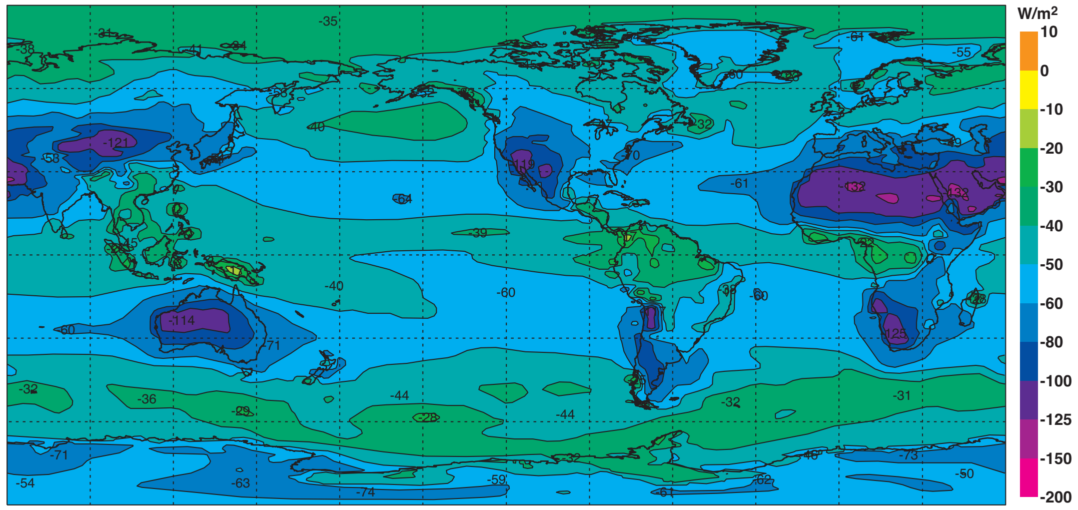

Net surface thermal radiation — December-February

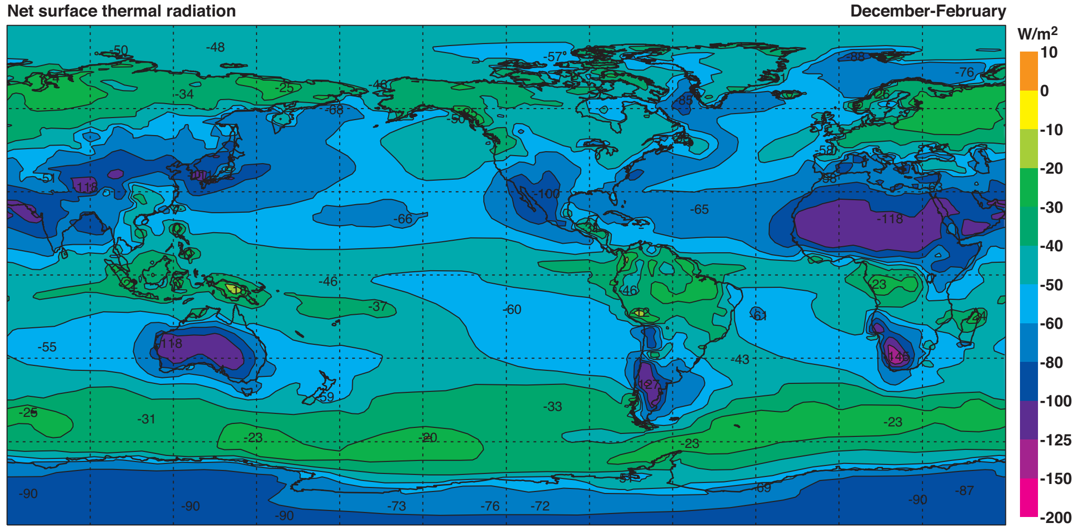

Net surface thermal radiation — June-August

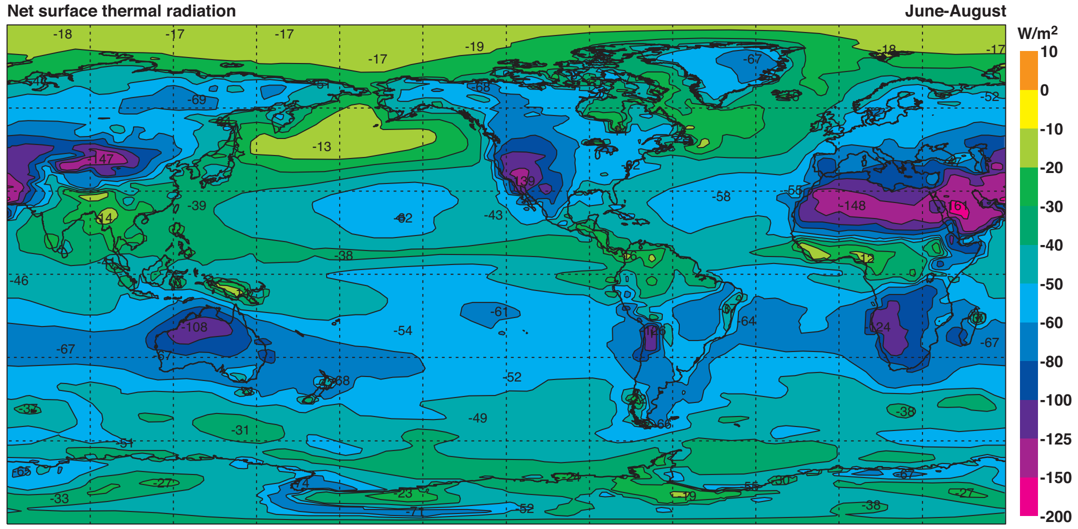

Net surface thermal radiation — Interannual variability

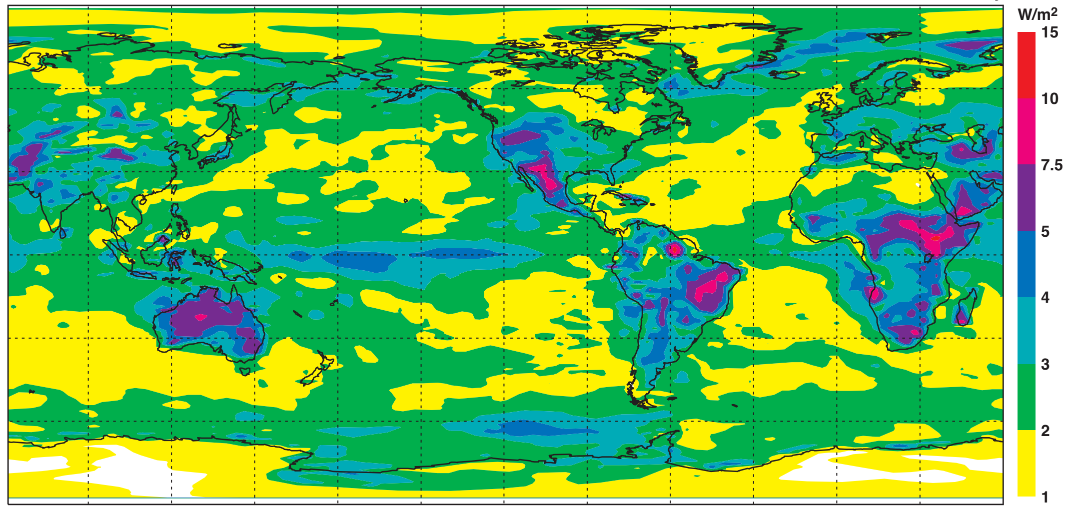

Net surface thermal radiation — March-May

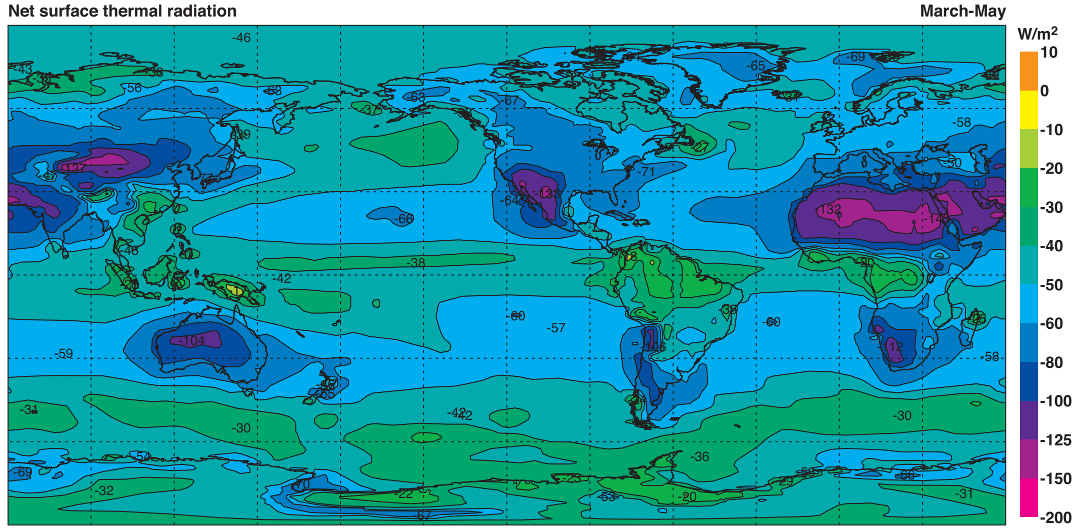

Net surface thermal radiation — September-November

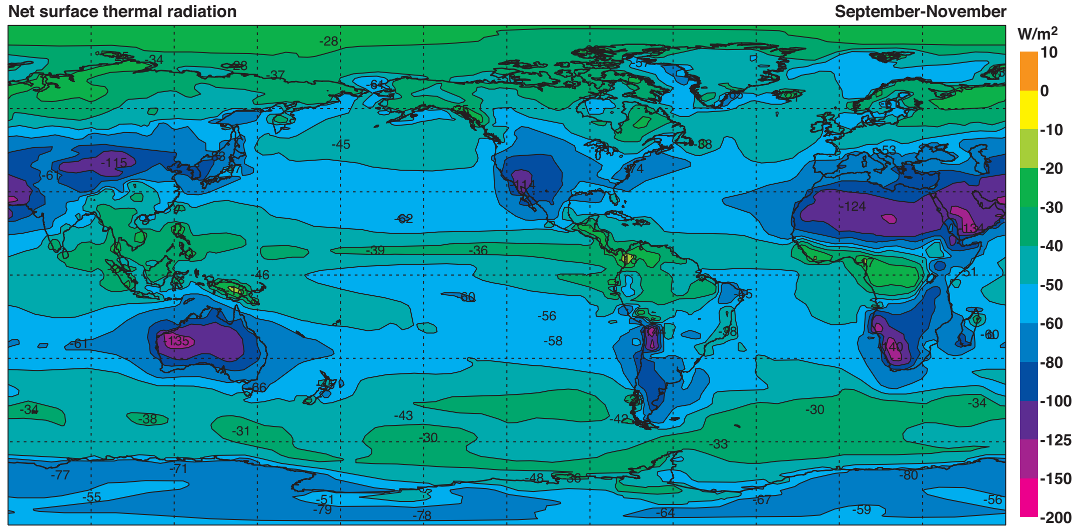

B6 Net surface fluxes of thermal radiation (Wm^{-2}), positive downwards.

Surface sensible heat flux — Annual mean

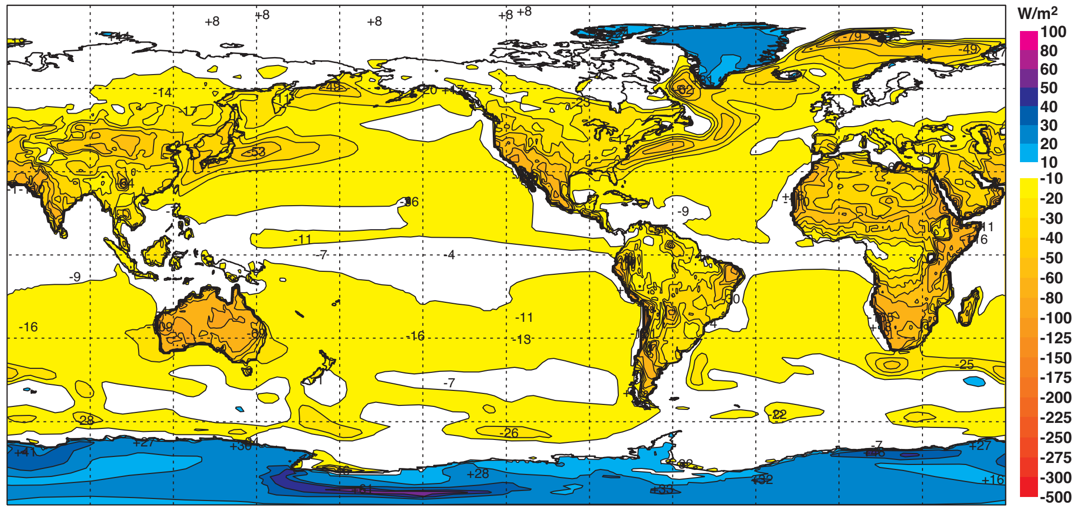

Surface sensible heat flux — December-February

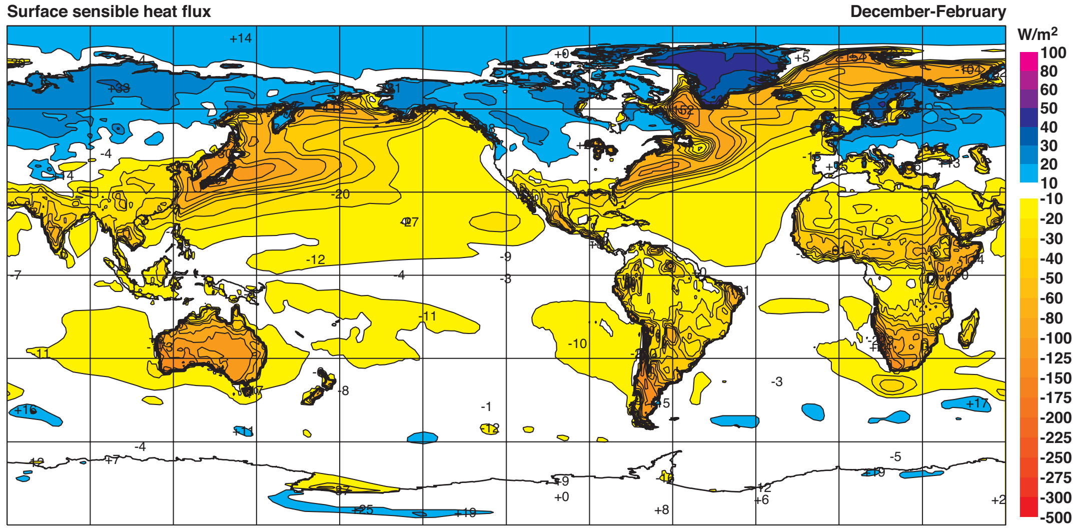

Surface sensible heat flux — June-August

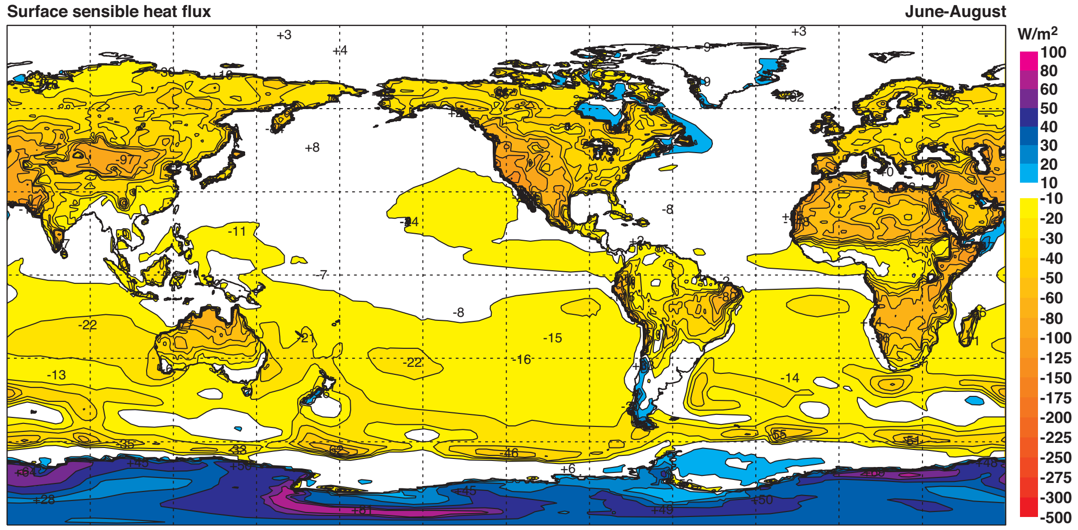

Surface sensible heat flux — Interannual variability

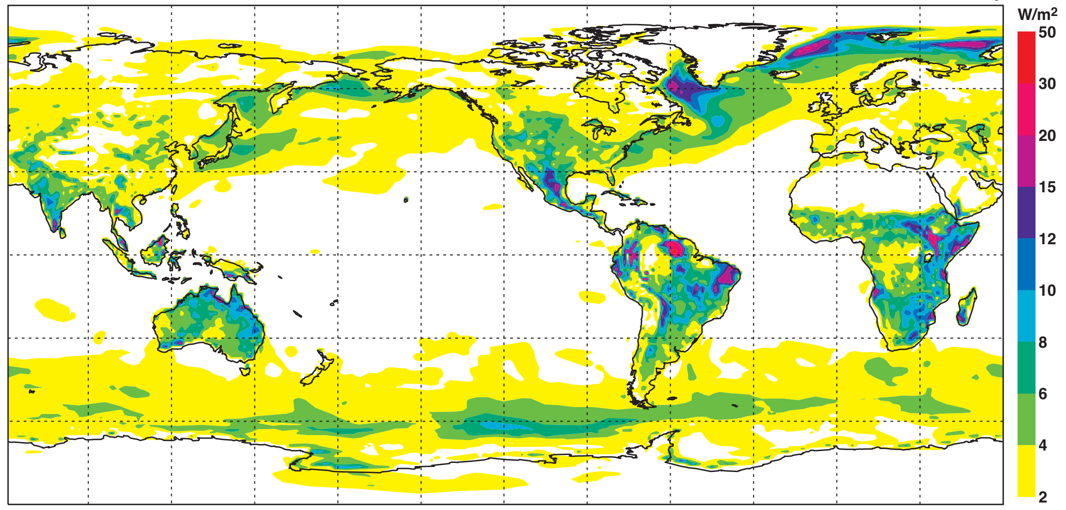

Surface sensible heat flux — March-May

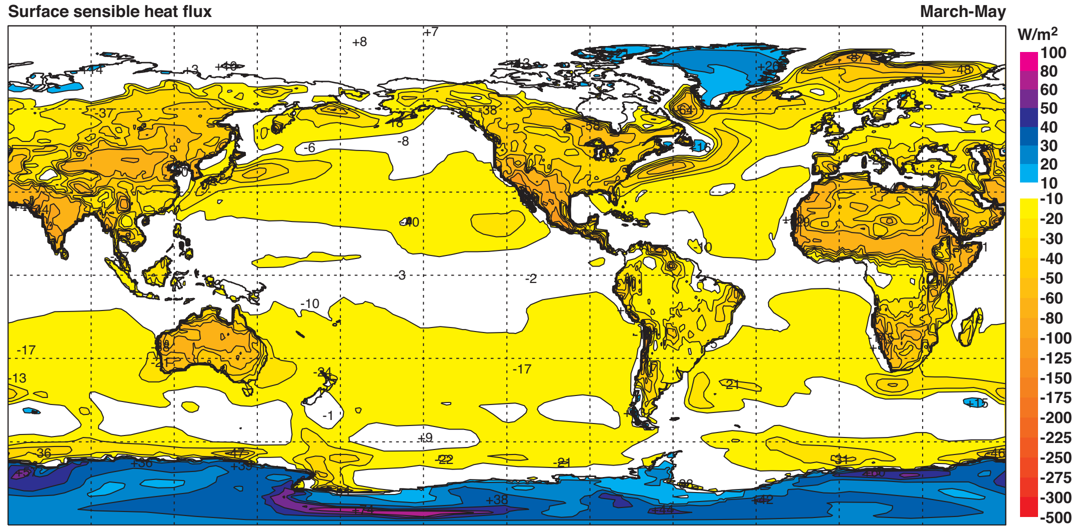

Surface sensible heat flux — September-November

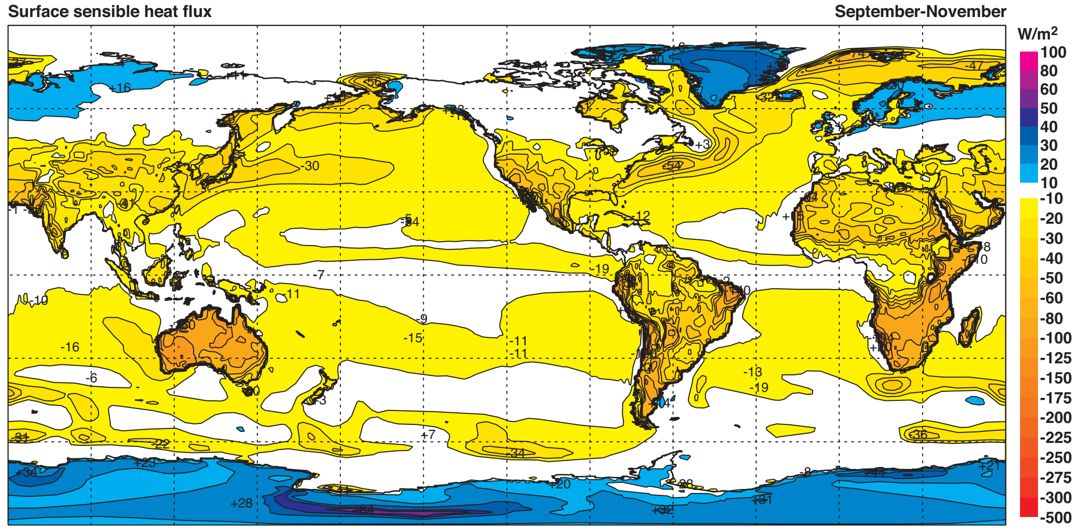

B7 Surface fluxes of sensible heat (Wm^{-2}), positive downwards.

Surface latent heat flux — Annual mean

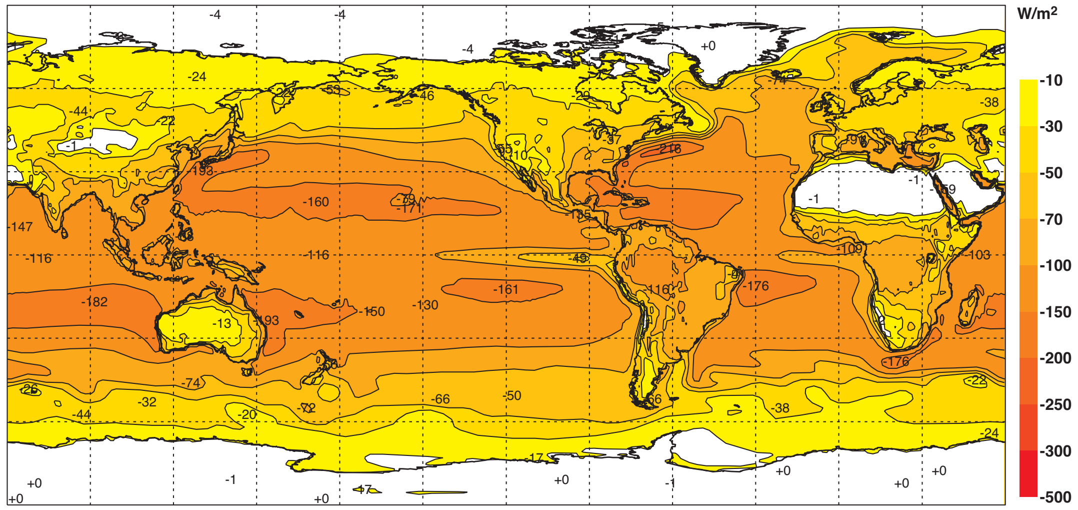

Surface latent heat flux — December-February

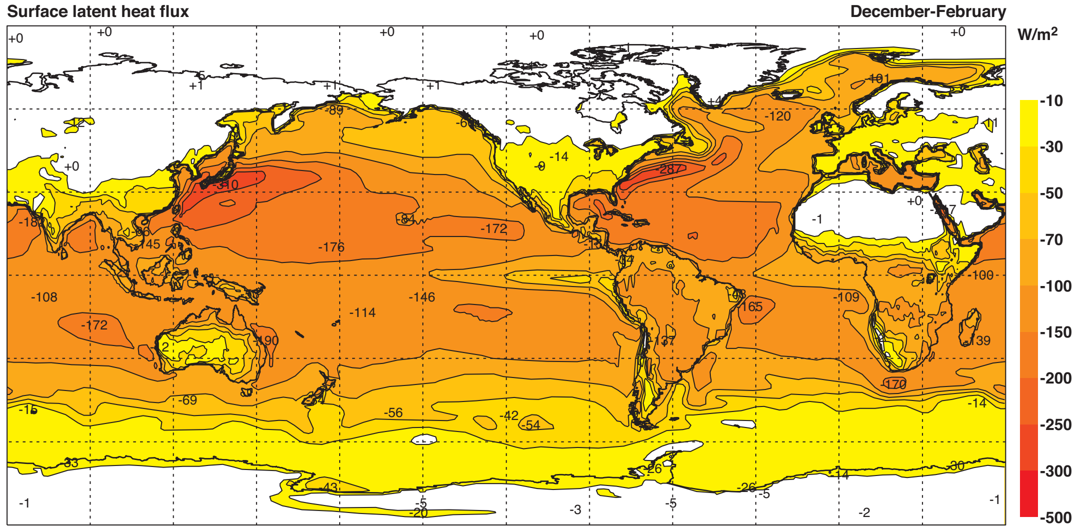

Surface latent heat flux — June-August

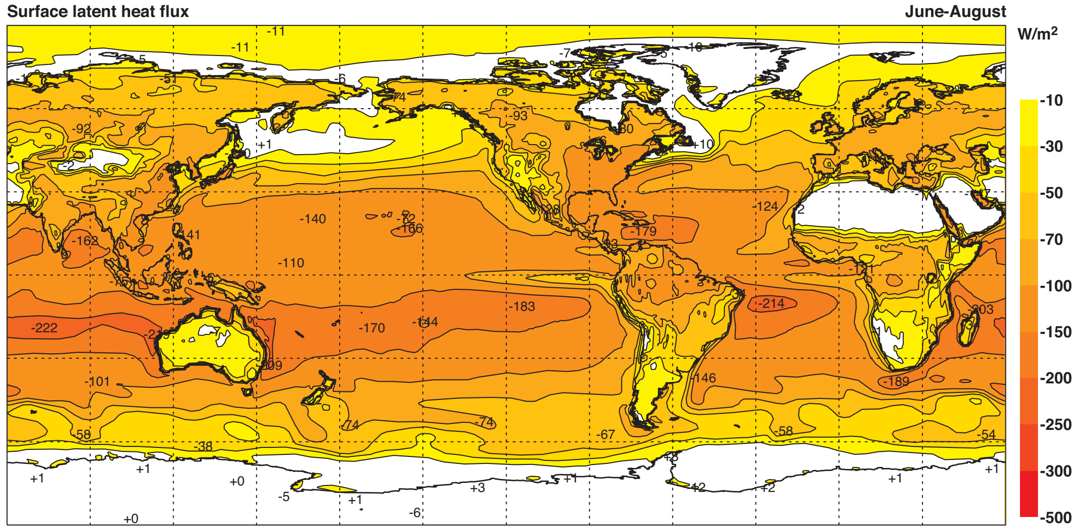

Surface latent heat flux — Interannual variability

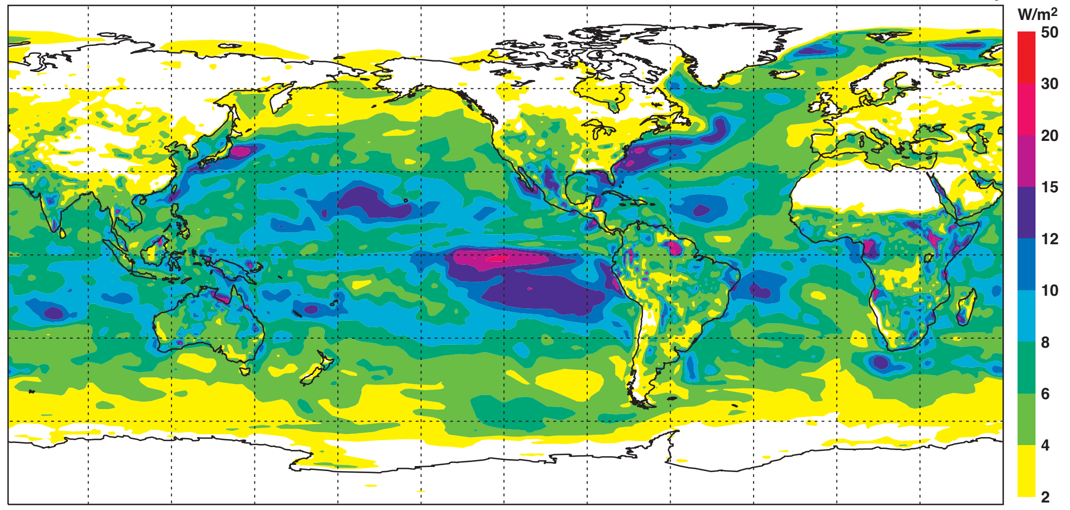

Surface latent heat flux — March-May

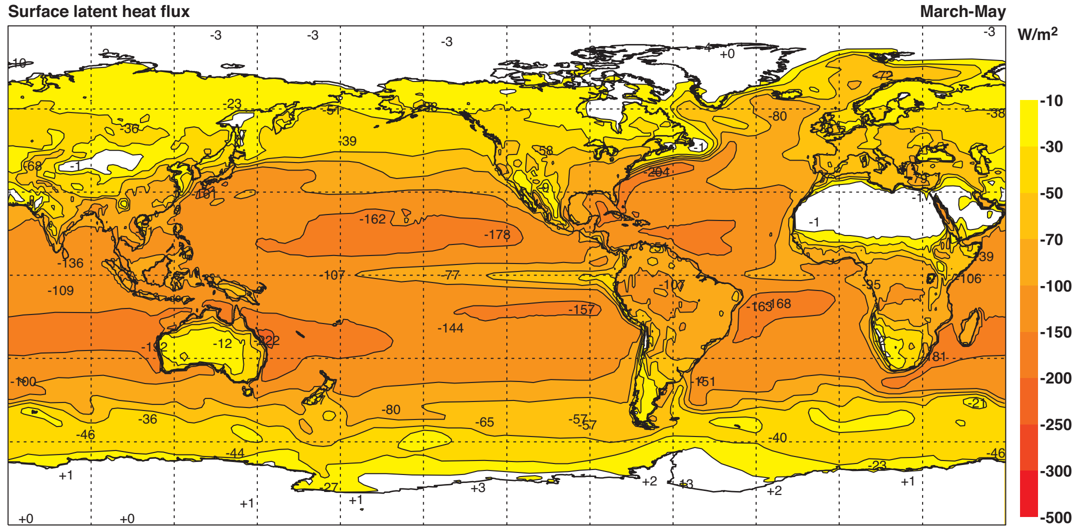

Surface latent heat flux — September-November

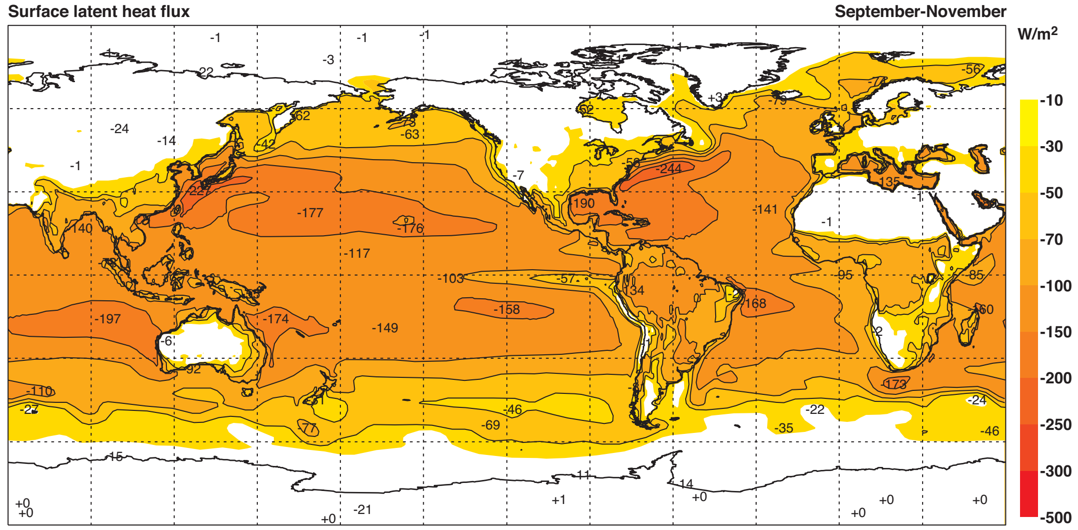

B8 Surface fluxes of latent heat (Wm^{-2}), positive downwards.

Top of atmosphere net solar radiation. Annual mean

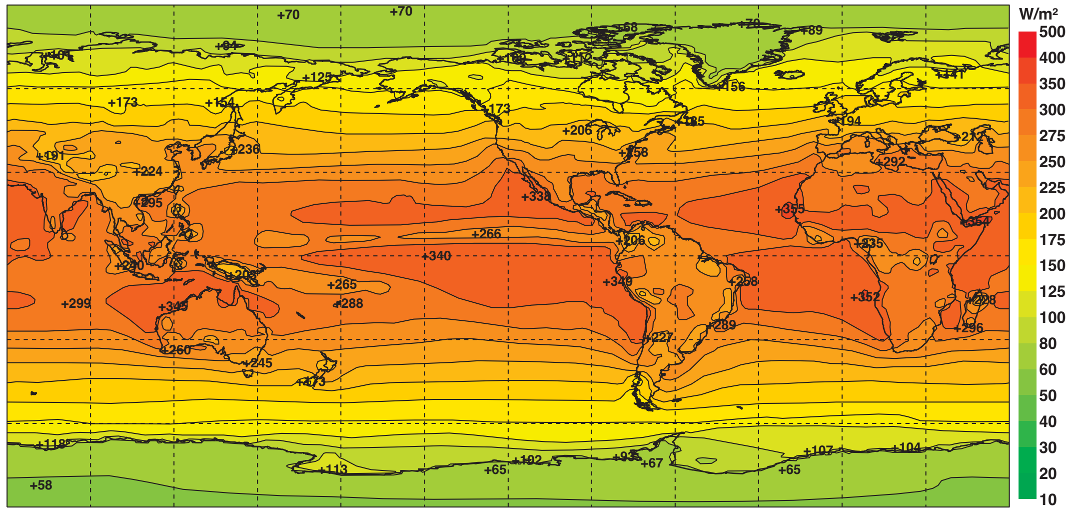

Top of atmosphere net solar radiation. December-February

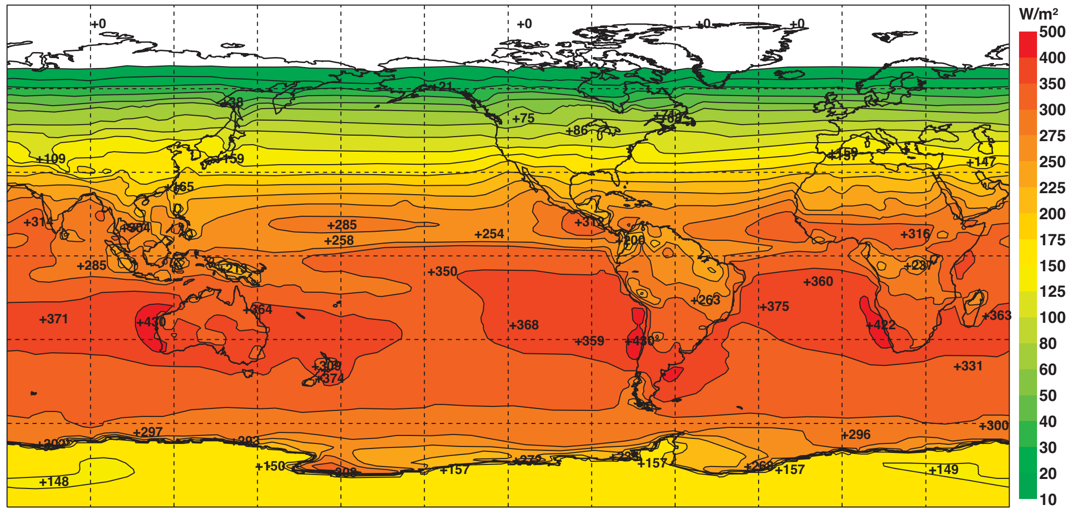

Top of atmosphere net solar radiation. June-August

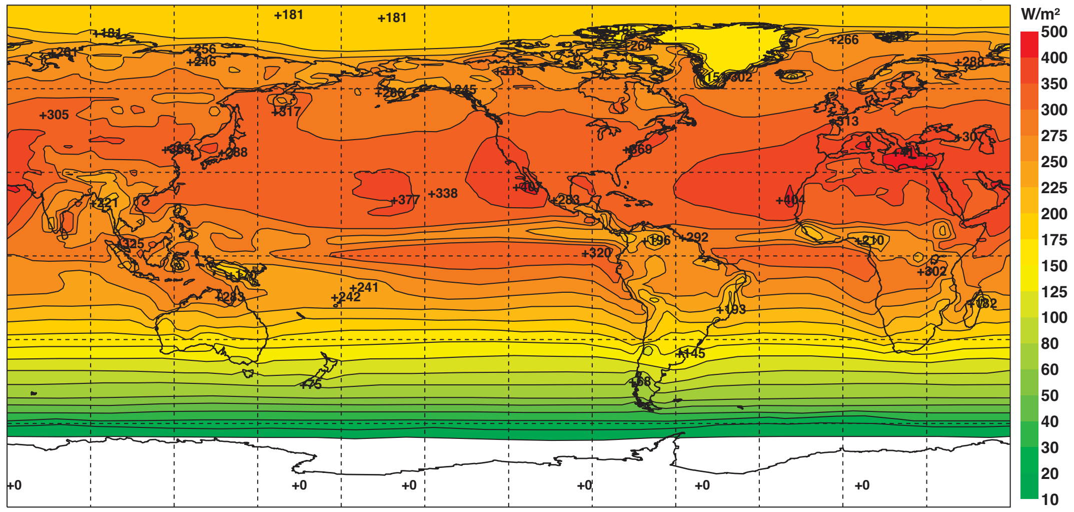

Top of atmosphere net solar radiation Interannual variability

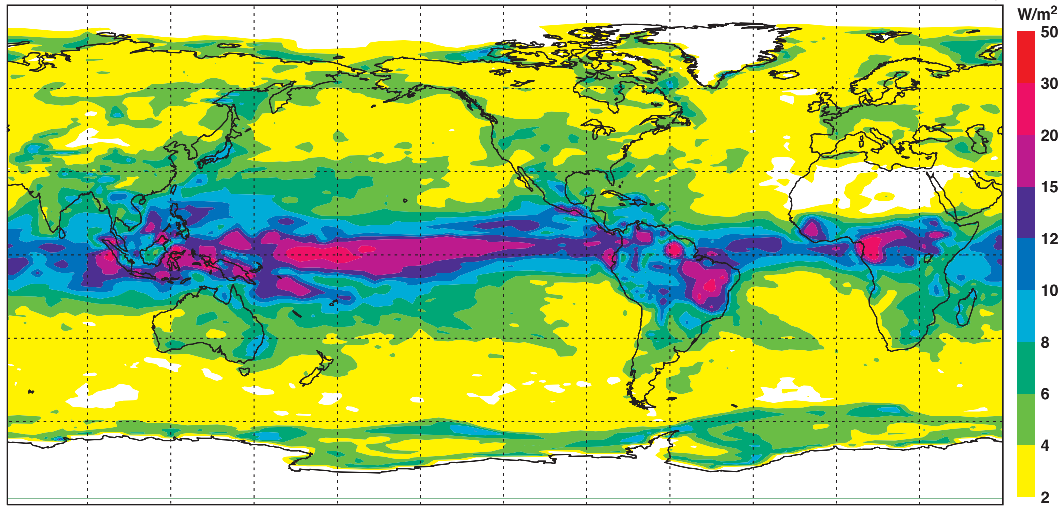

Top of atmosphere net solar radiation. March-May

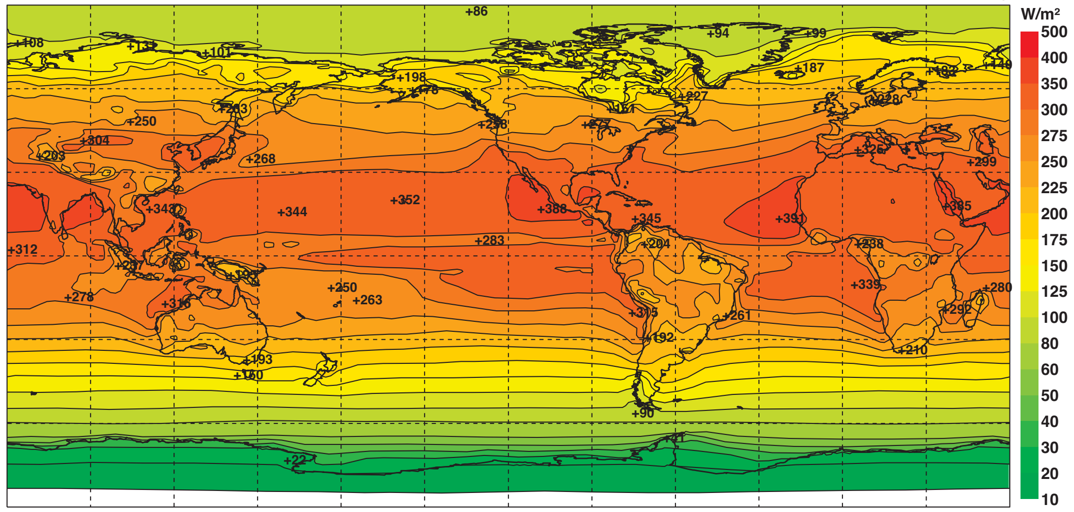

Top of atmosphere net solar radiation. September-November

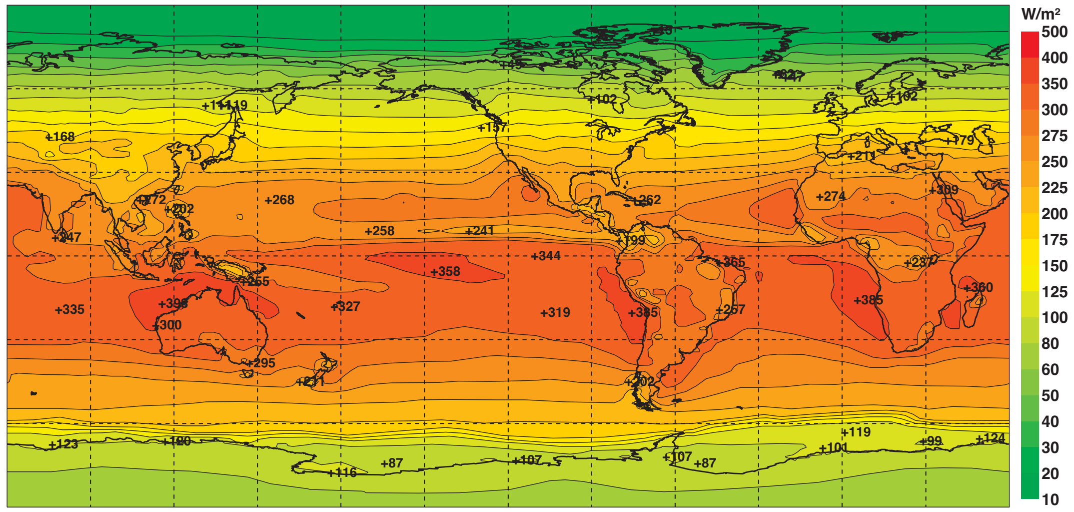

B9 Net top of the atmosphere fluxes of solar radiation (Wm^{-2}), positive downwards.

Top of atmosphere net thermal radiation — Annual mean

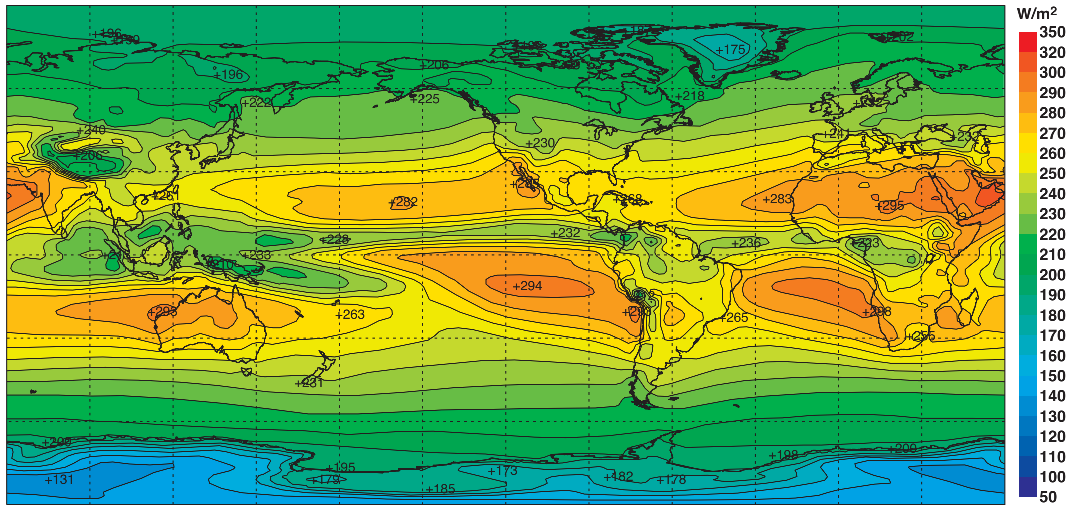

Top of atmosphere net thermal radiation — December-February

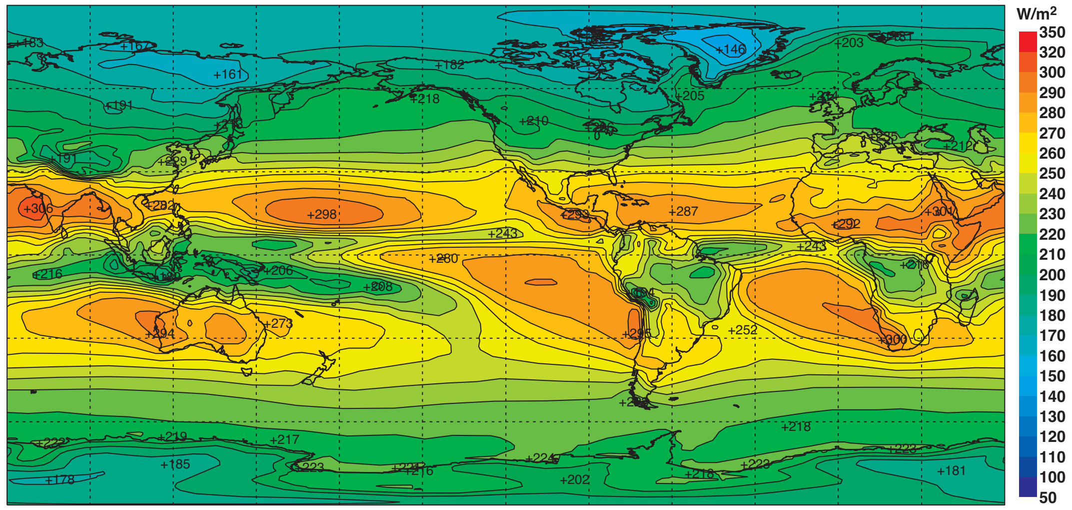

Top of atmosphere net thermal radiation — June-August

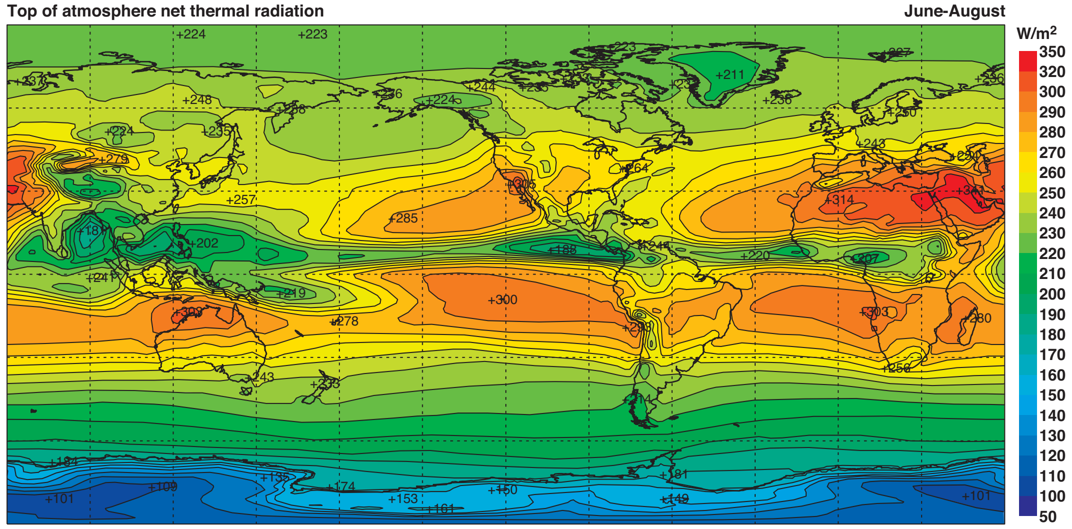

Top of atmosphere net thermal radiation — Interannual variability

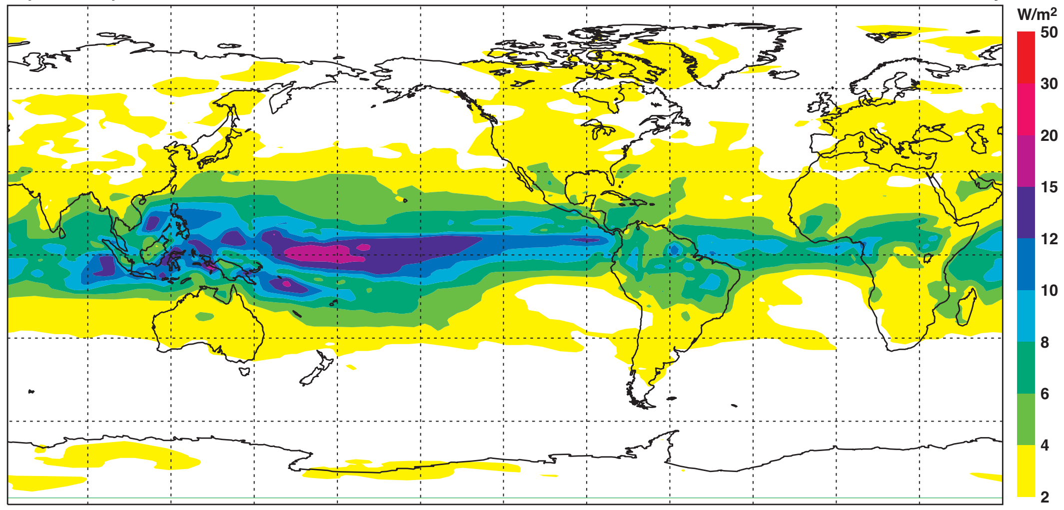

Top of atmosphere net thermal radiation — March-May

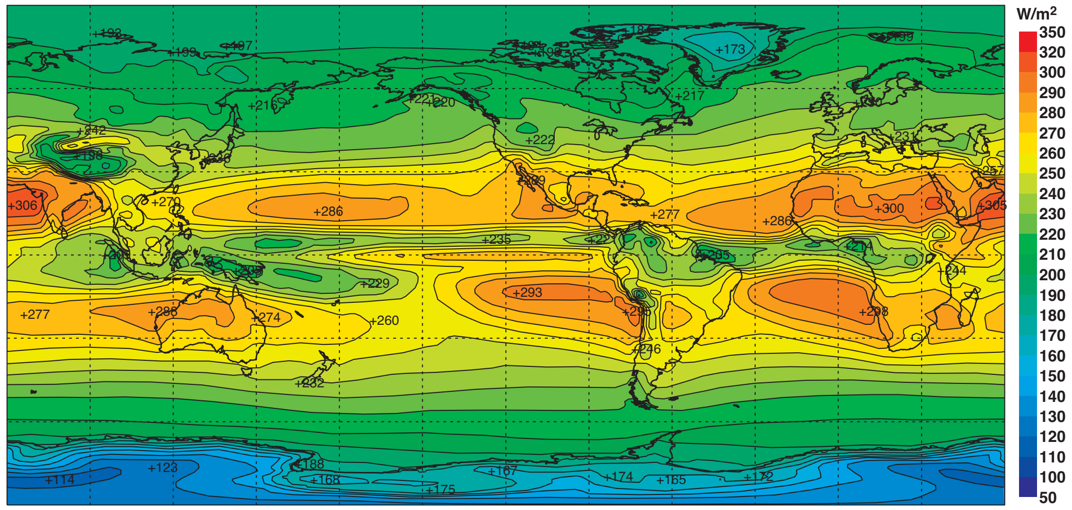

Top of atmosphere net thermal radiation — September-November

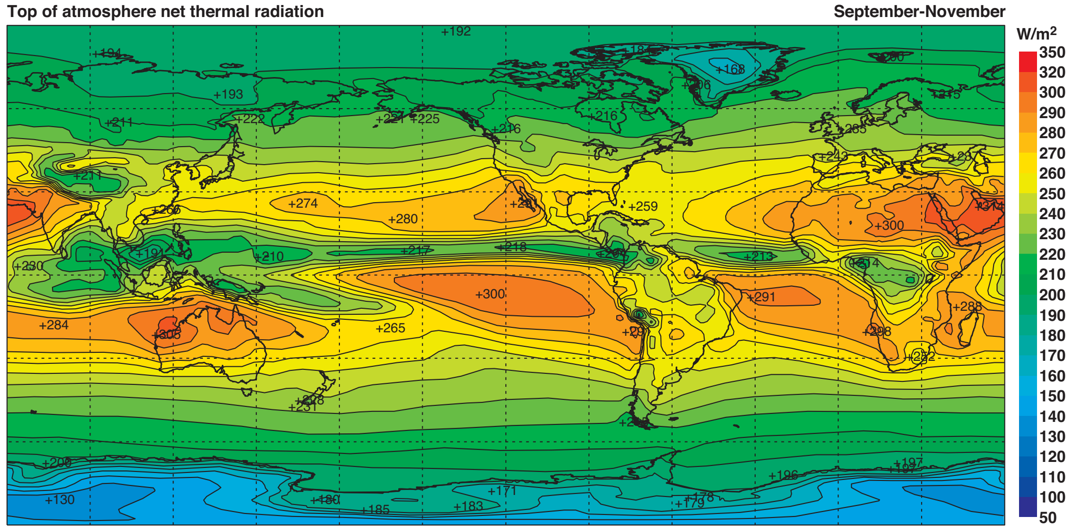

B10 Net top of the atmosphere fluxes of thermal radiation (Wm^{-2}), positive upwards.

Total precipitation Annual mean

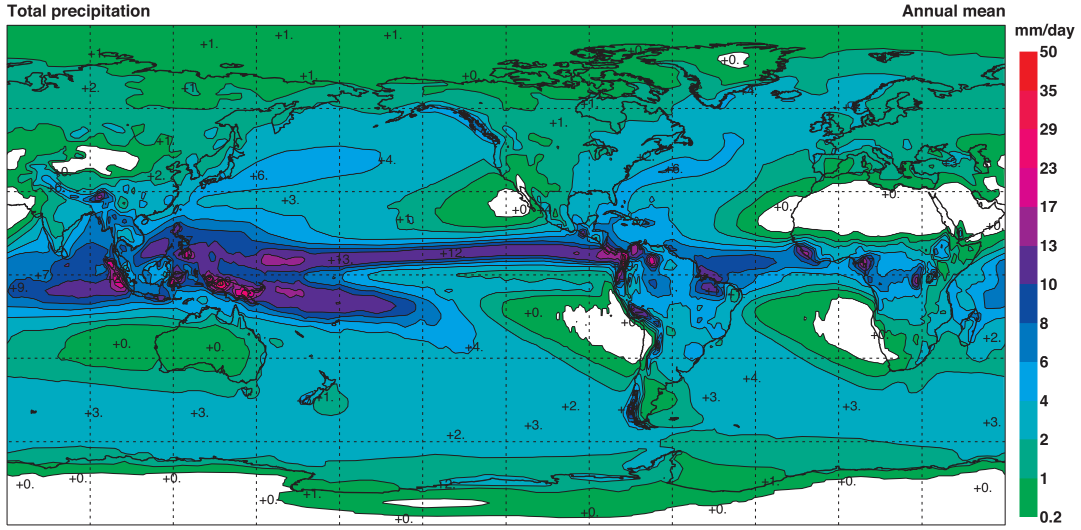

Total precipitation December-February

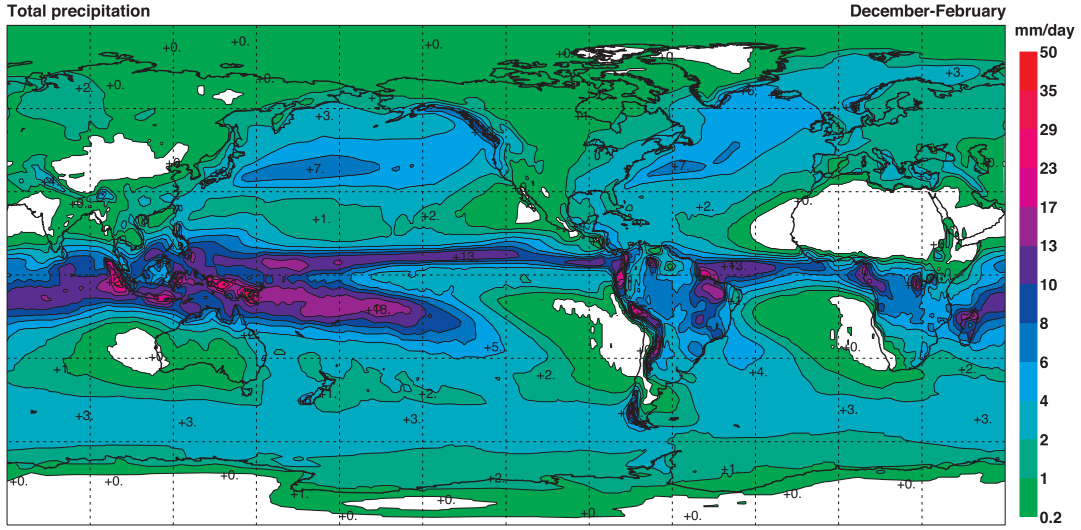

Total precipitation June-August

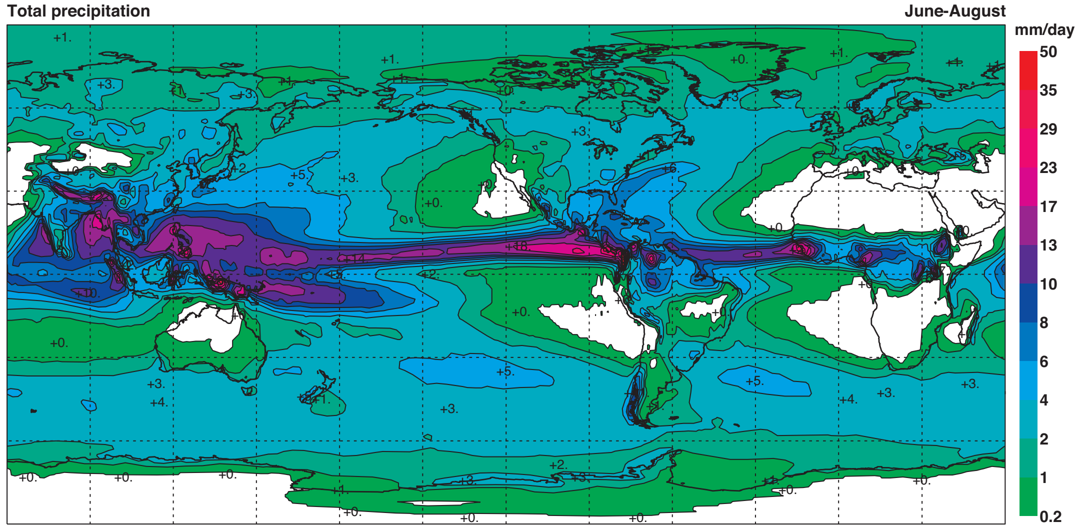

Total precipitation Interannual variability

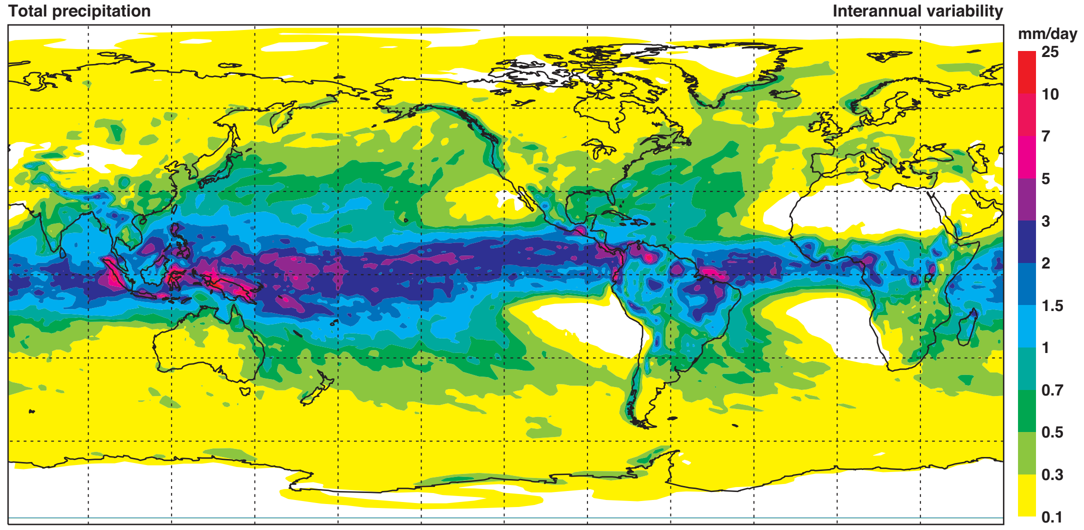

Total precipitation March-May

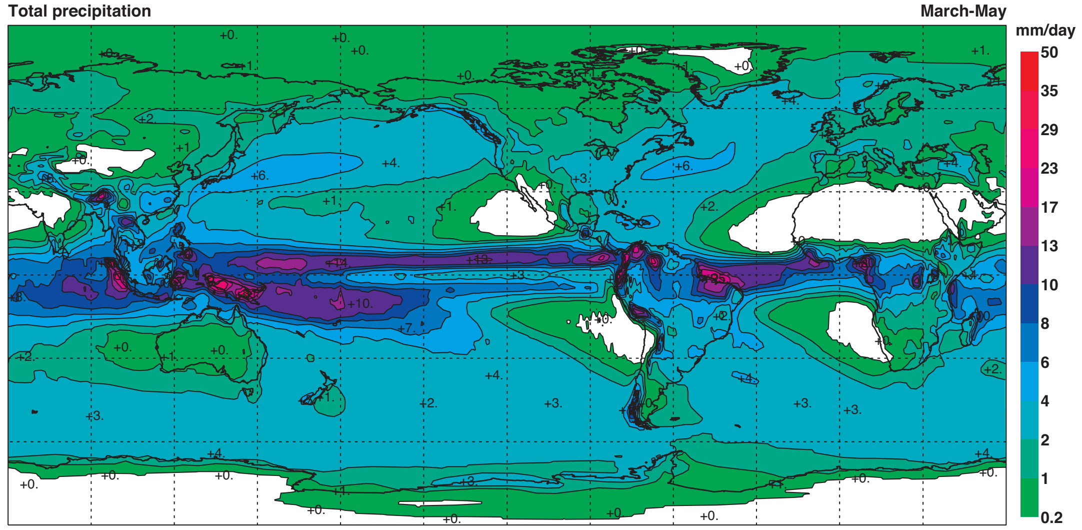

Total precipitation September-November

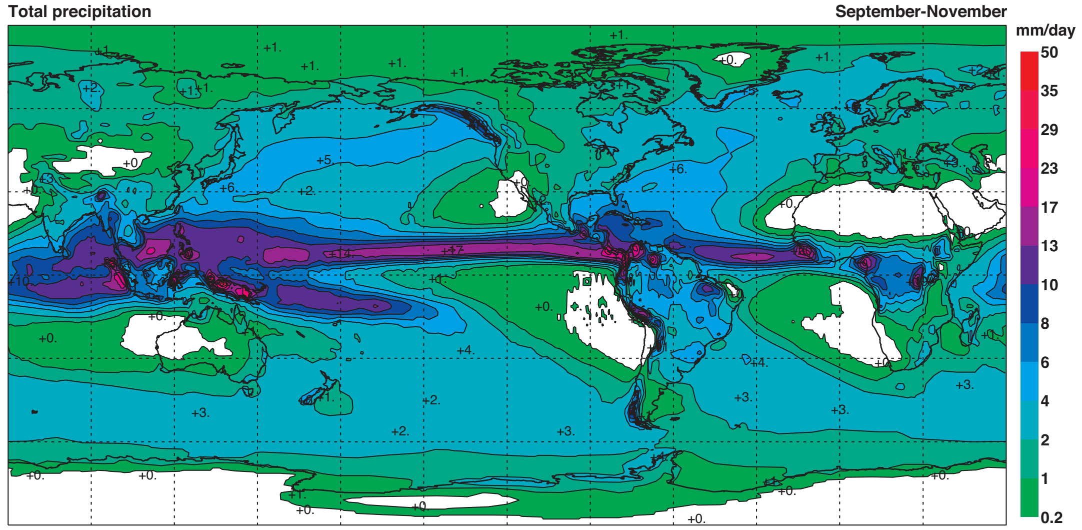

B11 Total precipitation (mm day^{-1}).

Evaporation minus precipitation — Annual mean

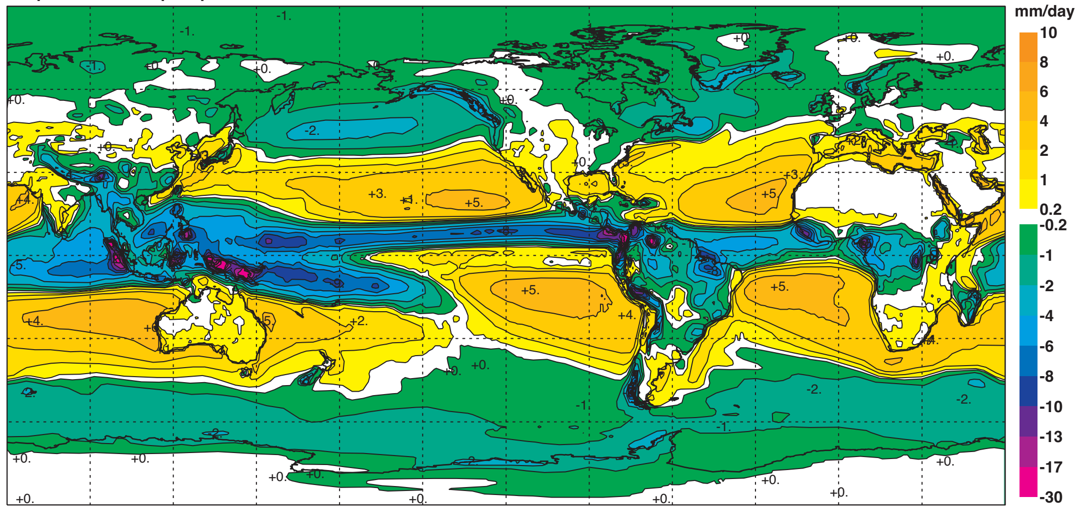

Evaporation minus precipitation — December-February

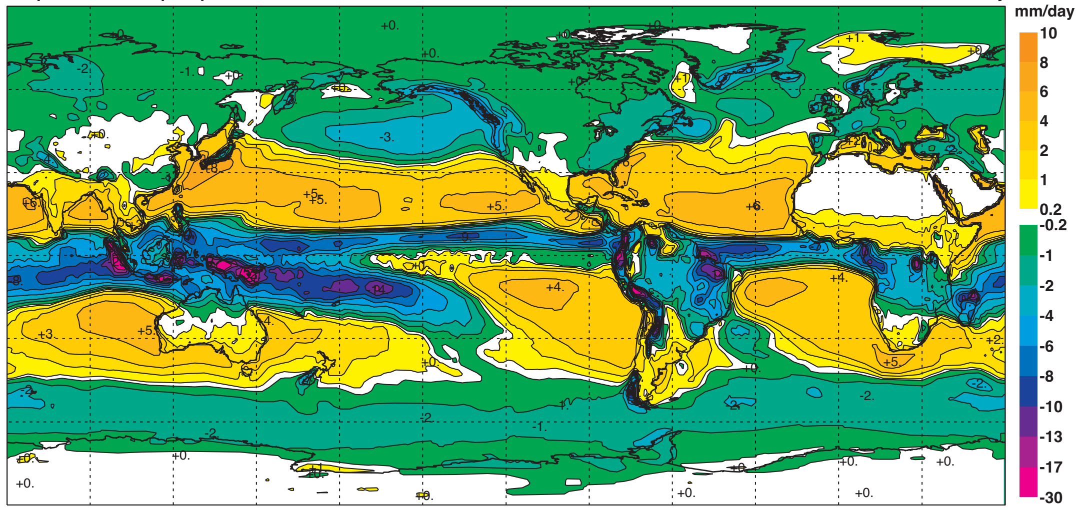

Evaporation minus precipitation — June-August

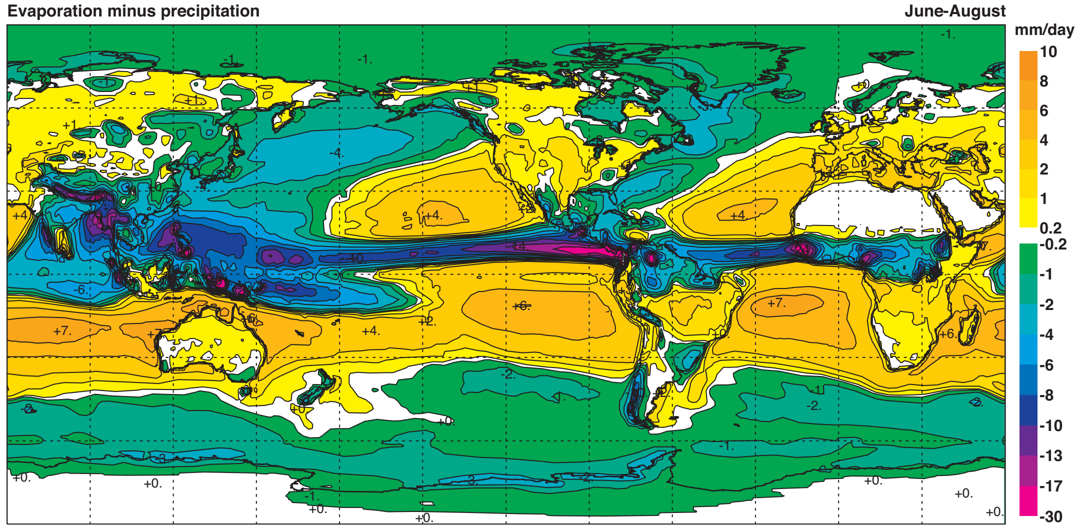

Evaporation minus precipitation — Interannual variability

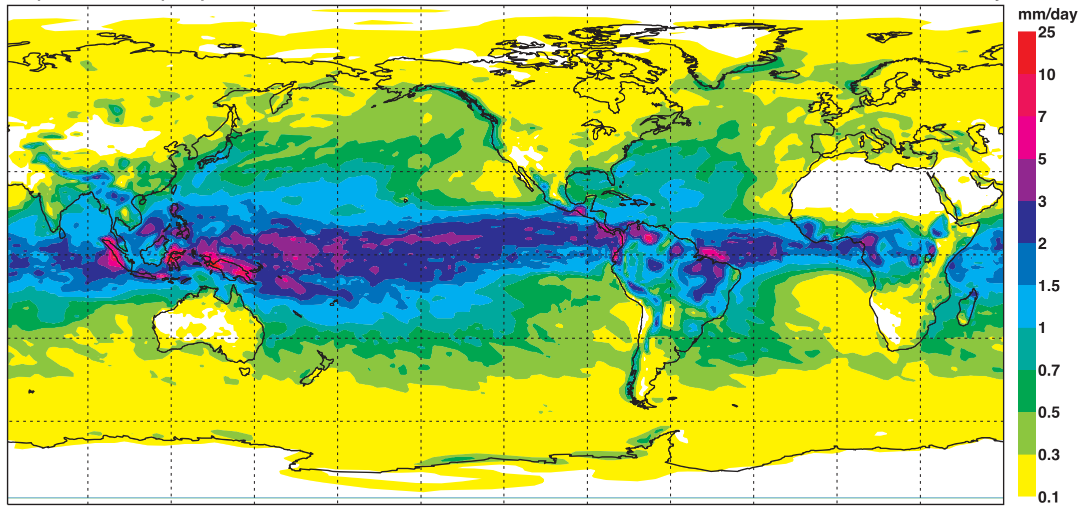

Evaporation minus precipitation — March-May

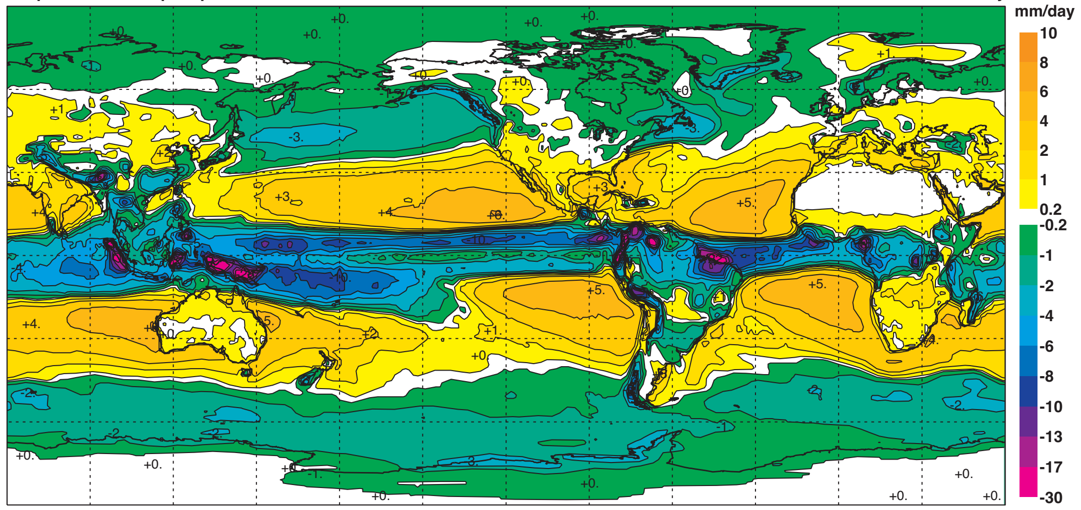

Evaporation minus precipitation — September-November

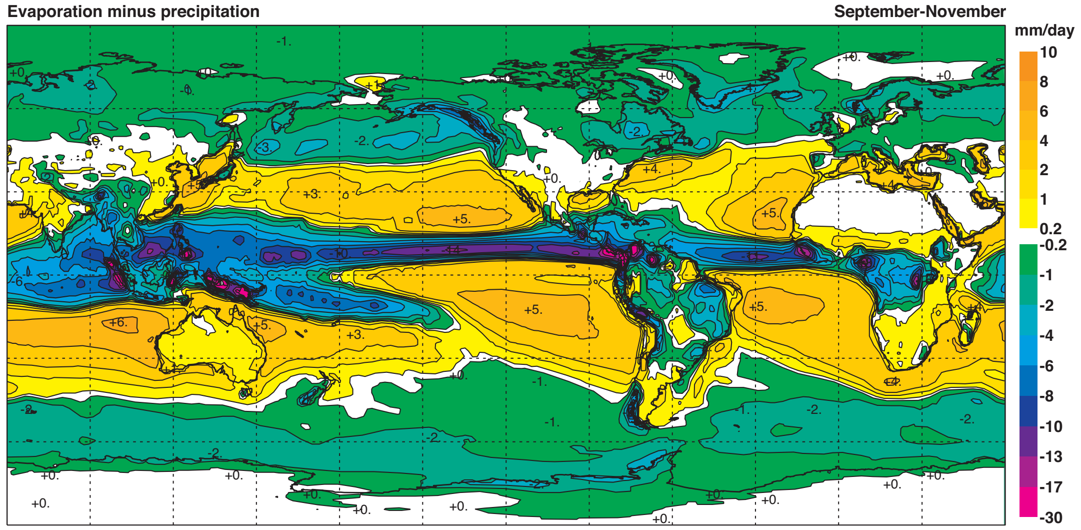

B12 Evaporation minus precipitation (mm day^{-1}).

Section C

Column climatologies

Column integrated heating — Annual mean

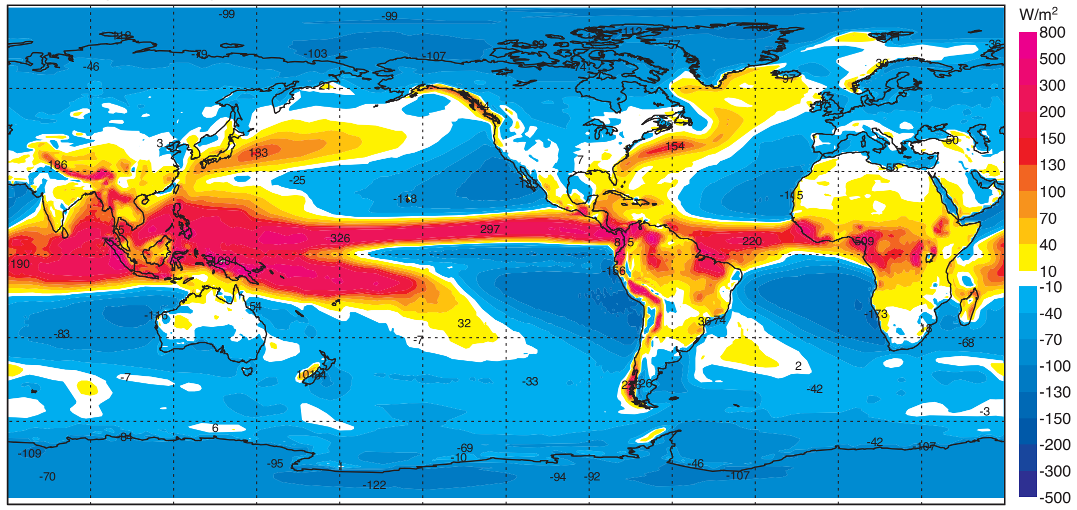

Column integrated heating — December-February

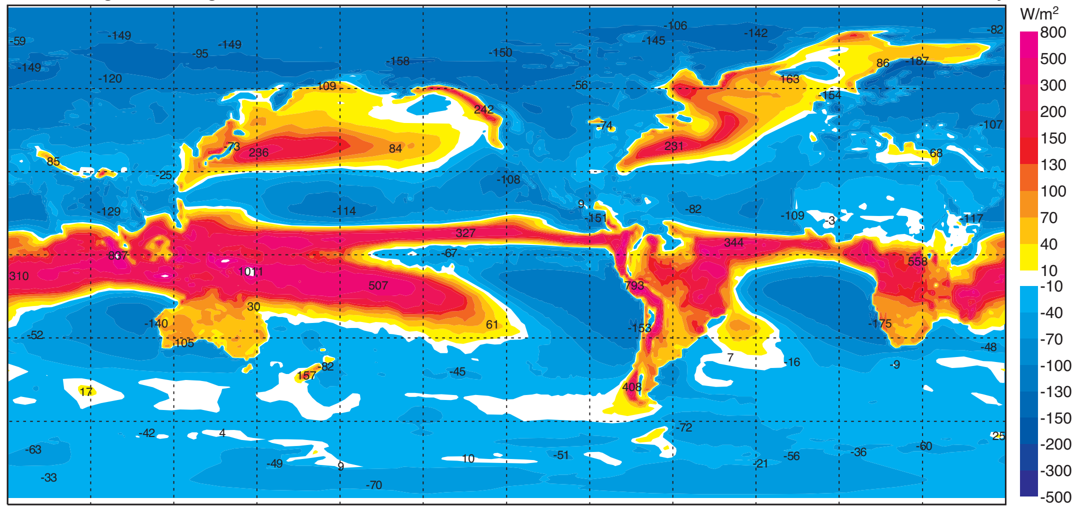

Column integrated heating — June-August

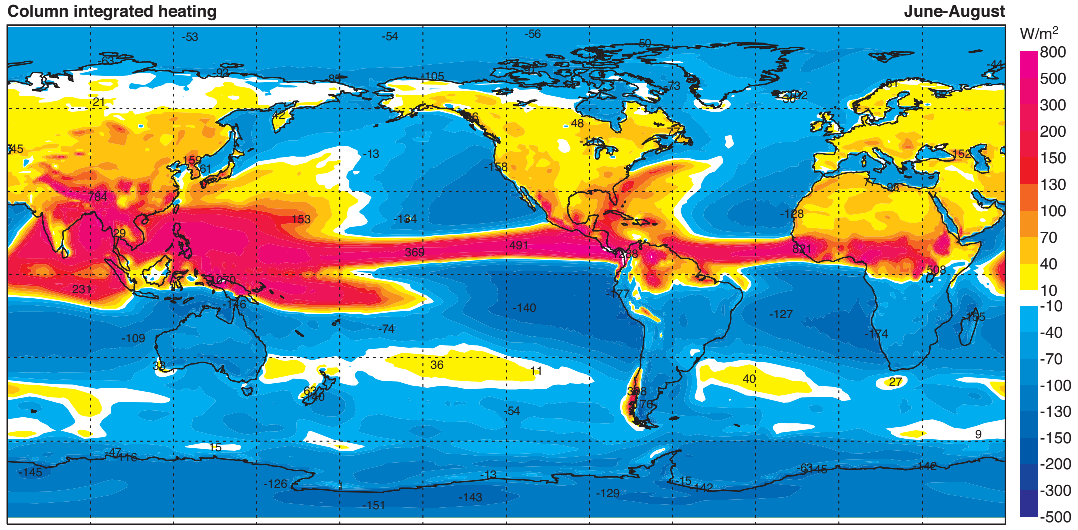

Column integrated heating — Interannual variability

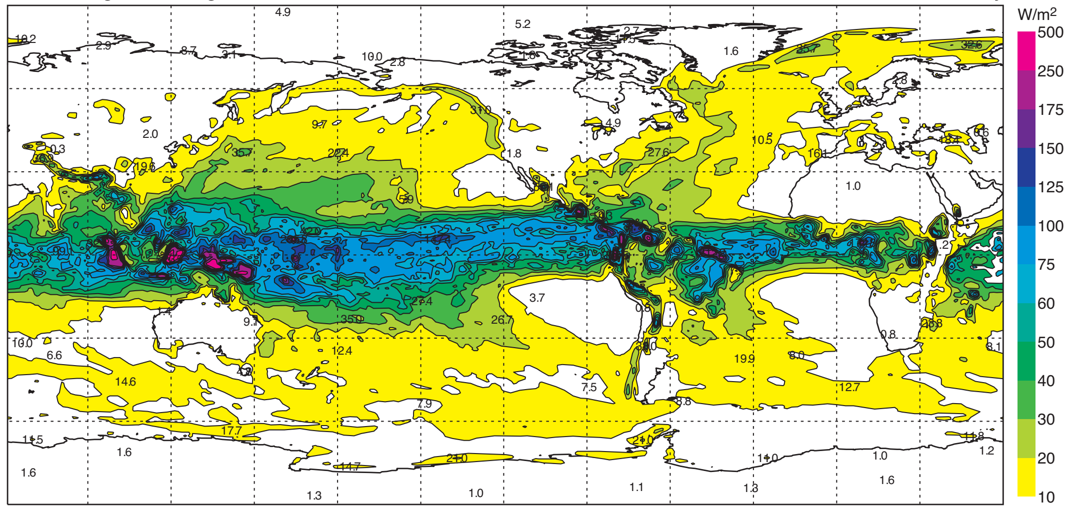

Column integrated heating — March–May

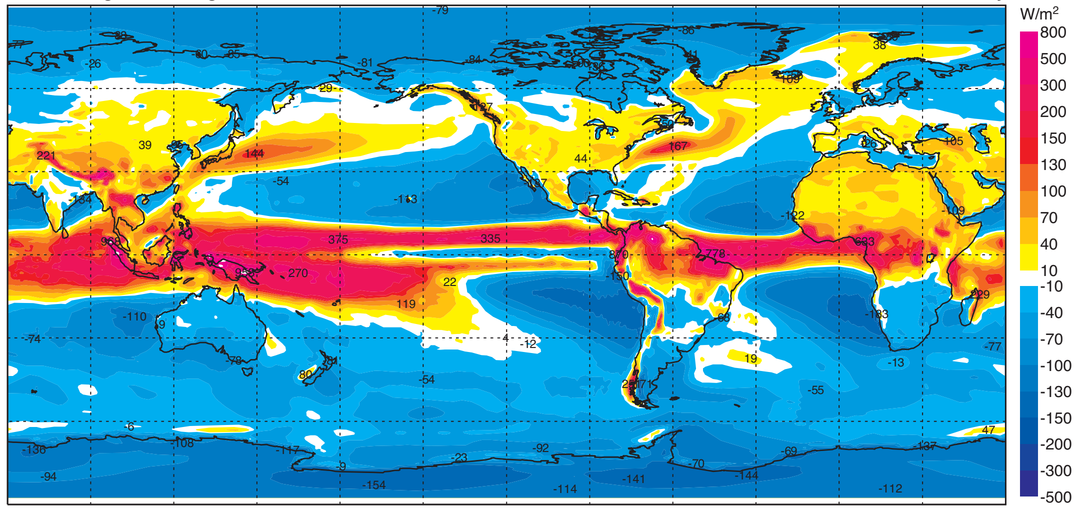

Column integrated heating — September–November

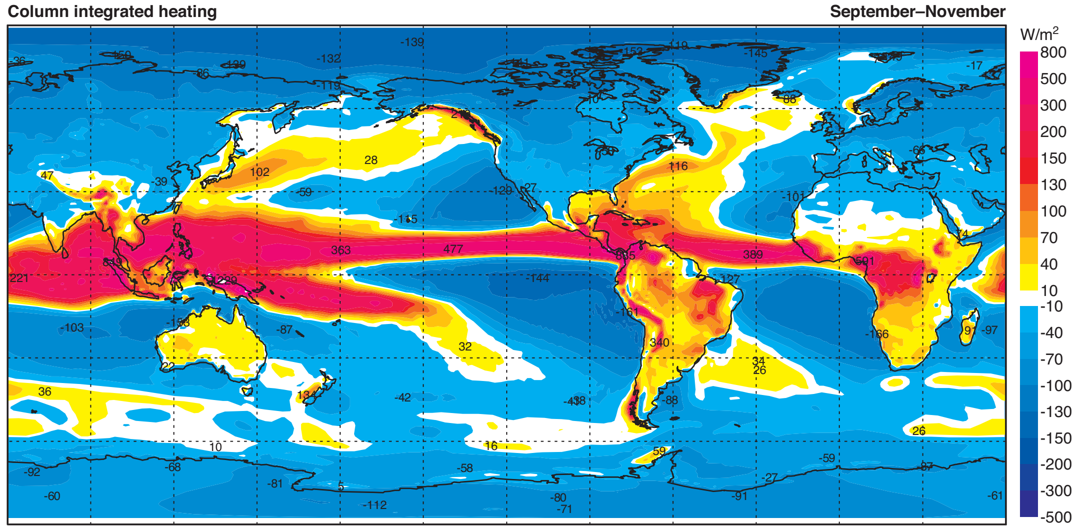

C1 Column integrated heating (Wm^{-2}).

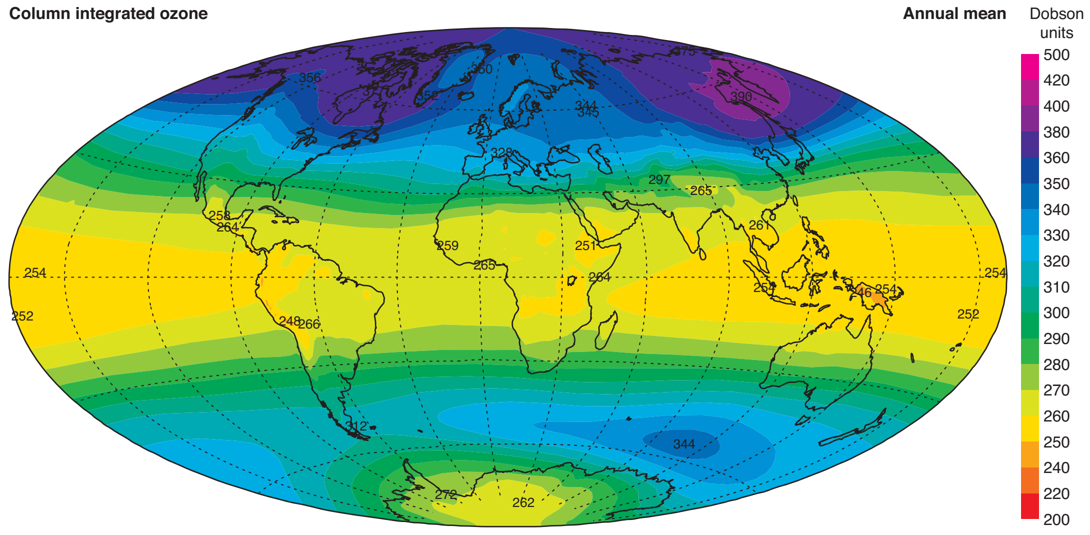

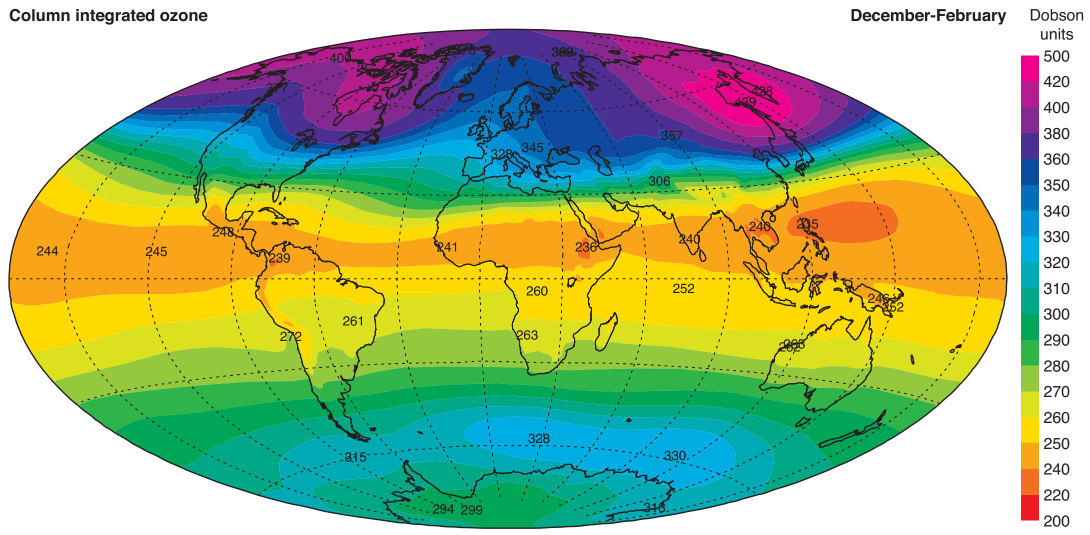

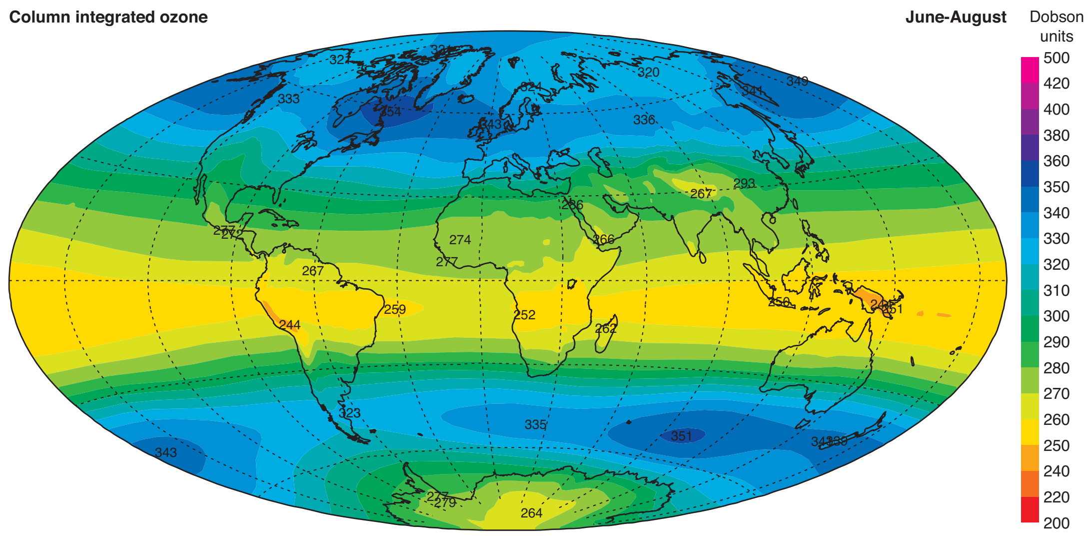

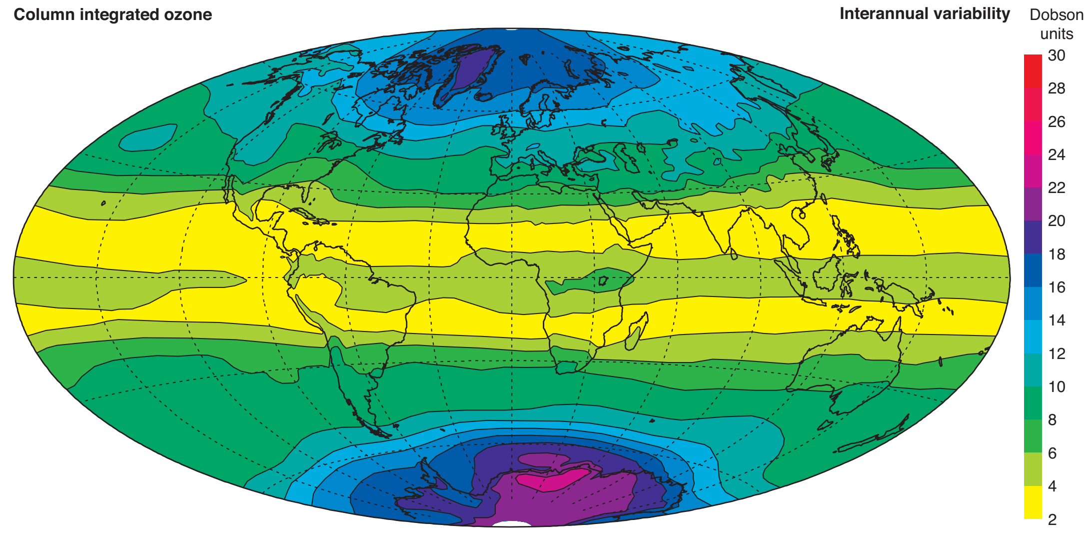

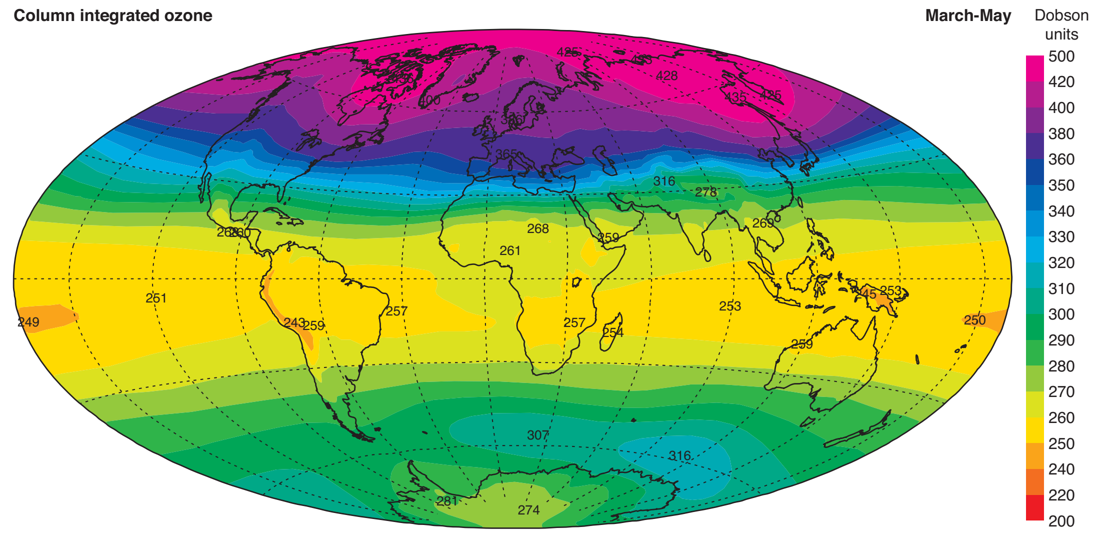

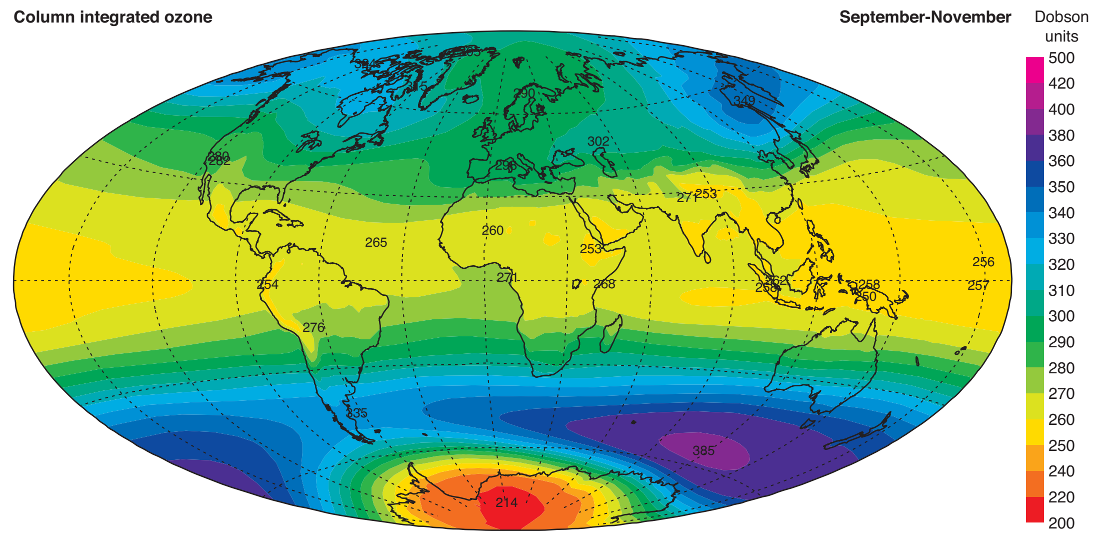

C2 Column integrated ozone (Dobson units).

Column integrated fluxes of water vapour with their convergence. Annual mean

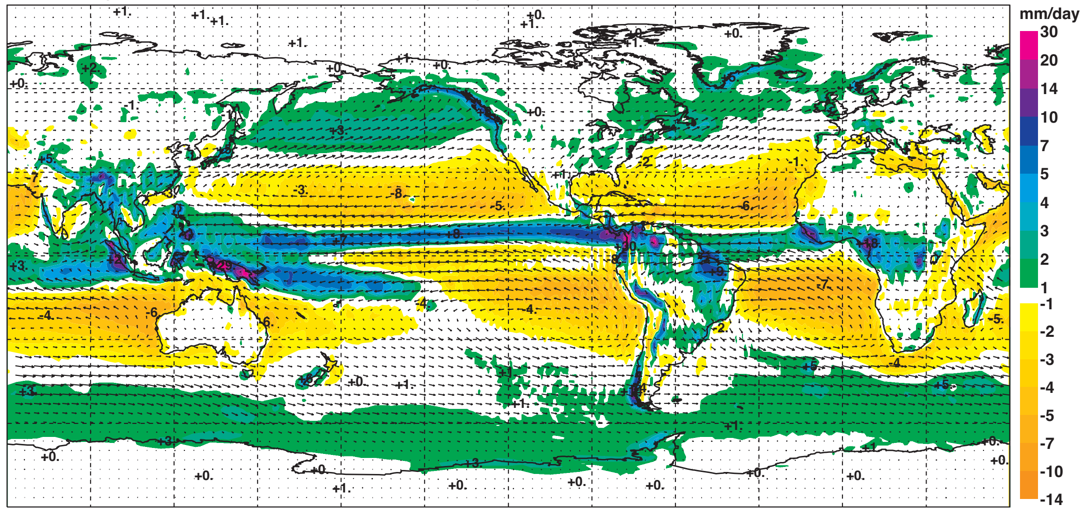

Column integrated fluxes of water vapour with their convergence. December-February

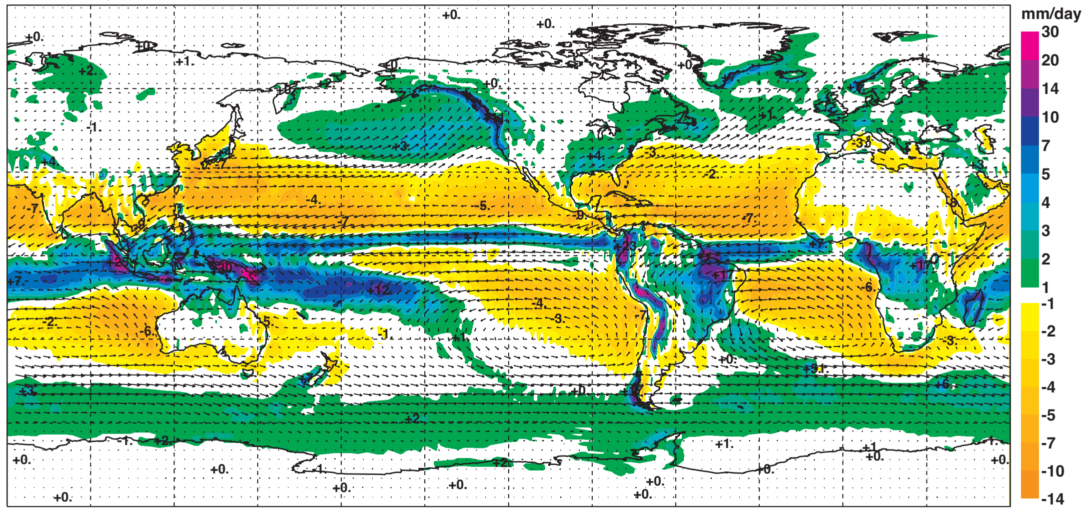

Column integrated fluxes of water vapour with their convergence. June-August

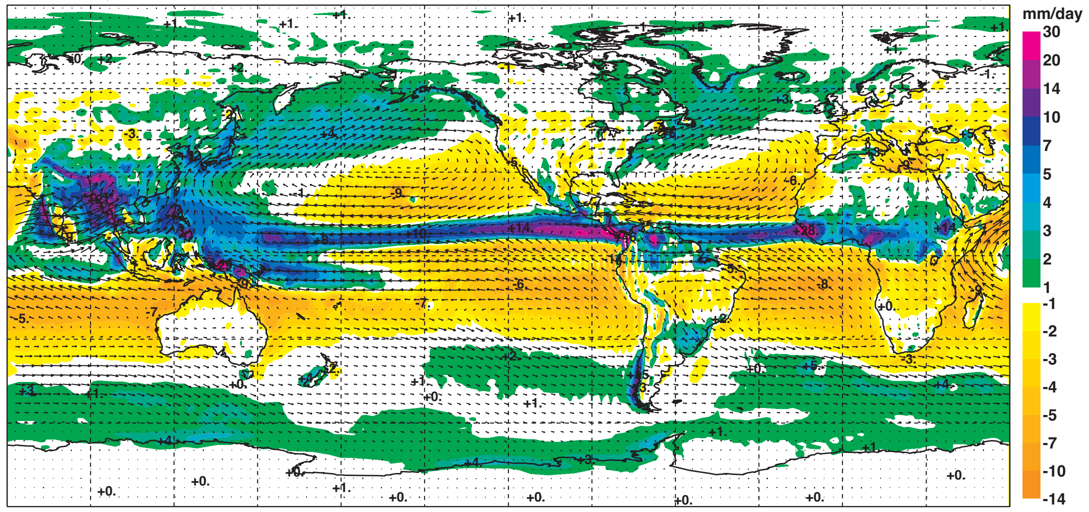

Column integrated fluxes of water vapour (kgm^{-1}s^{-1}) (contours) with their convergence Interannual variability

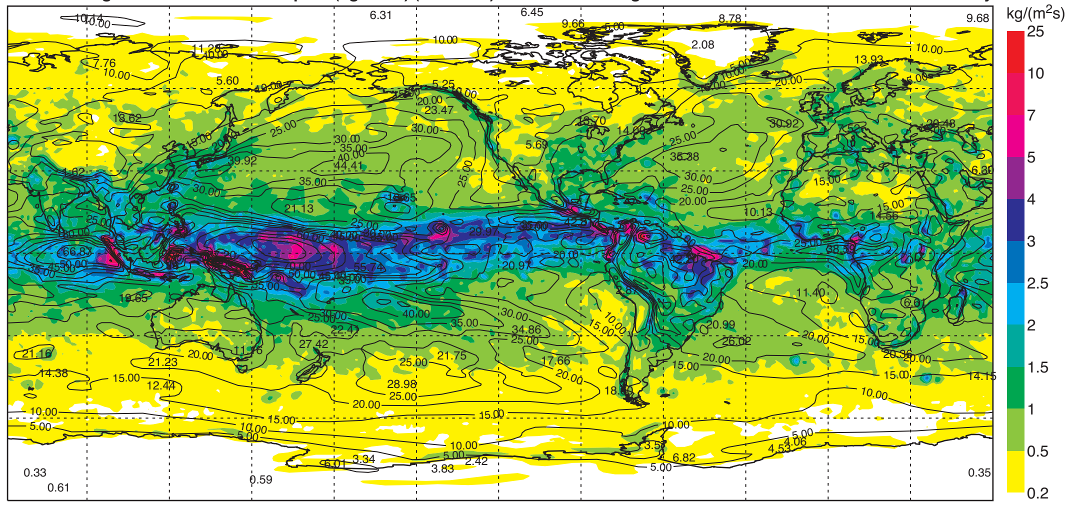

Column integrated fluxes of water vapour with their convergence. March-May

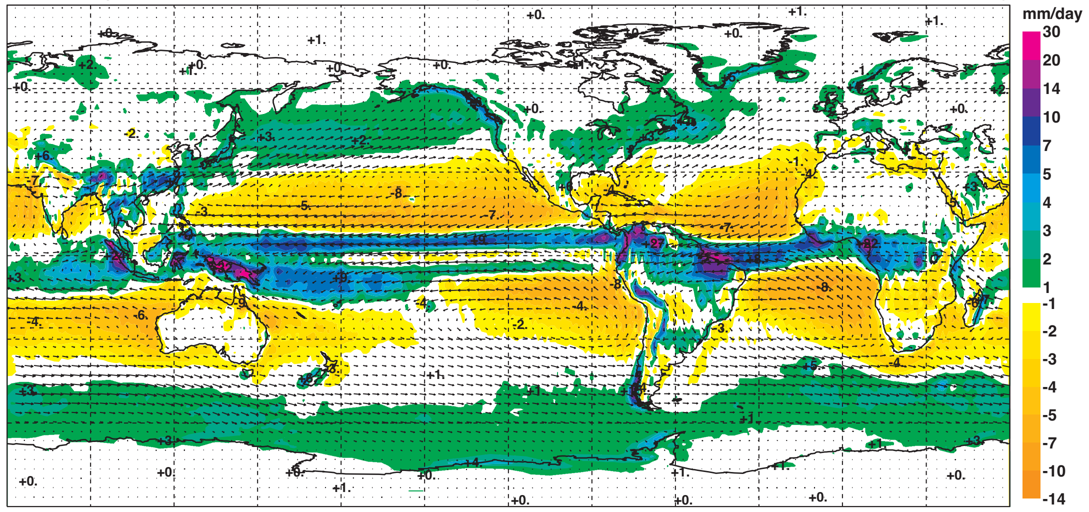

Column integrated fluxes of water vapour with their convergence. September-November

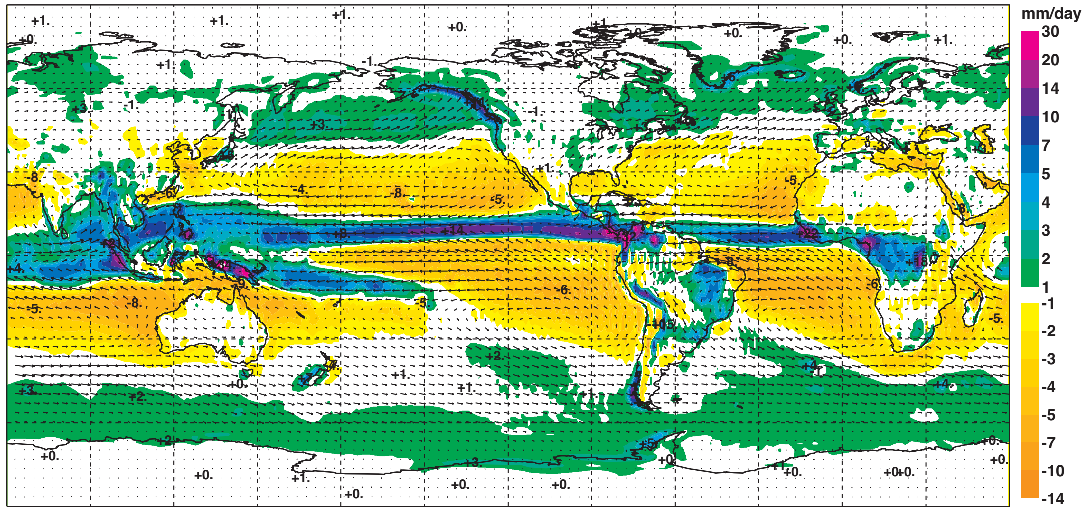

C3 Column integrated vector fluxes of water vapour (kgm^{-1}s^{-1}) with their convergence (kgm^{-2}s^{-1}) (colour shading). For the interannual variability, the magnitude of the fluxes is plotted (contours) instead of the vector.

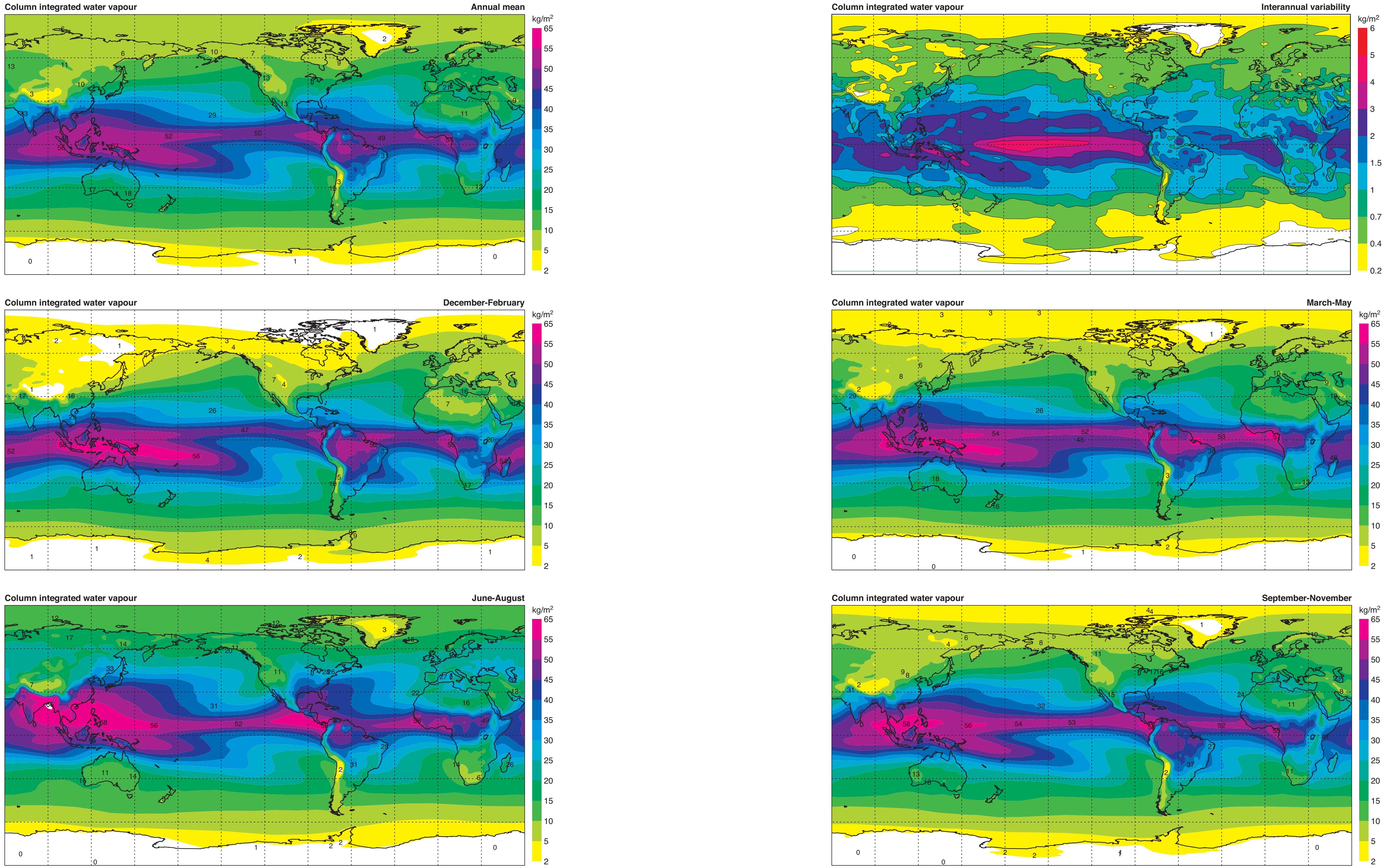

C4 Column integrated water vapour (kgm^{-2}).

Section D

Pressure level climatologies

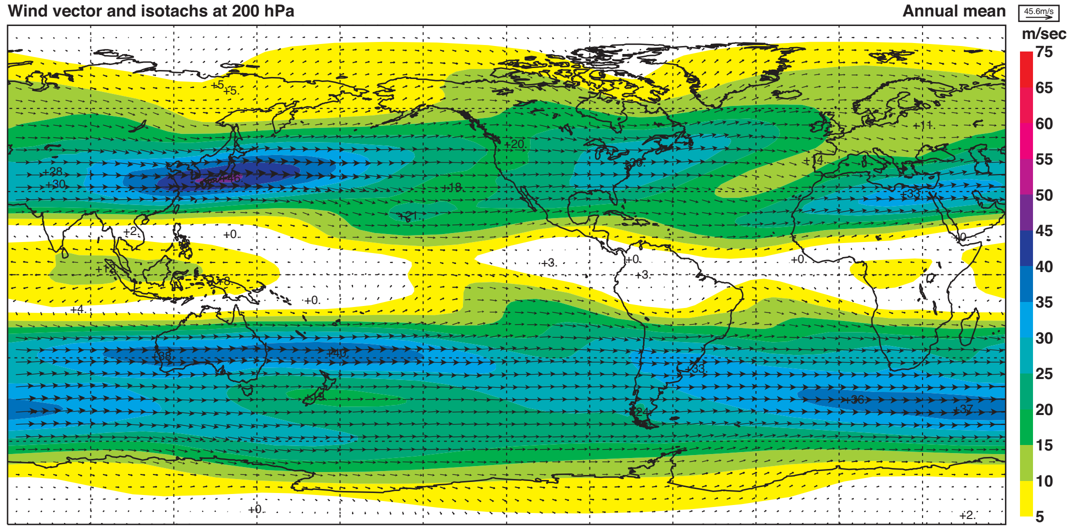

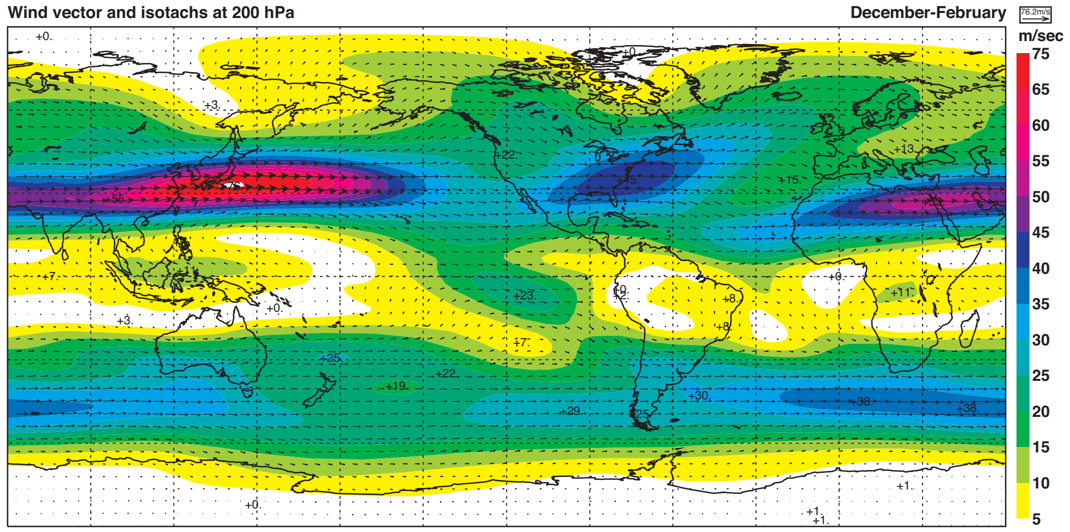

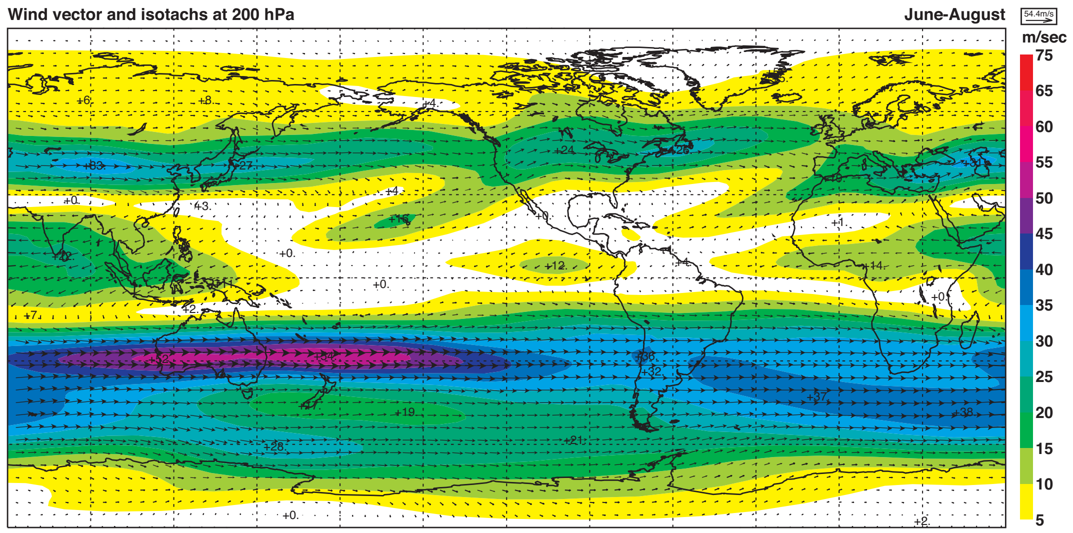

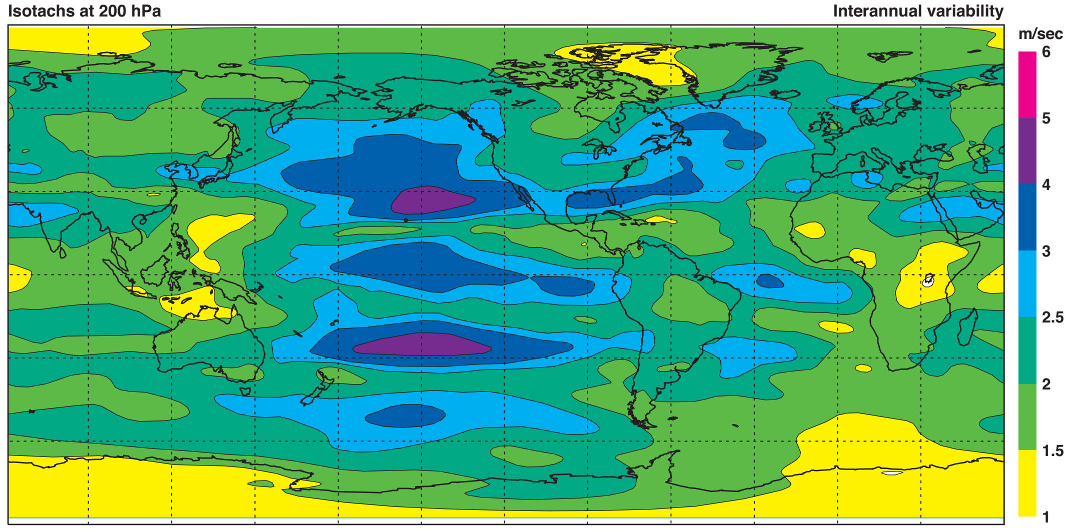

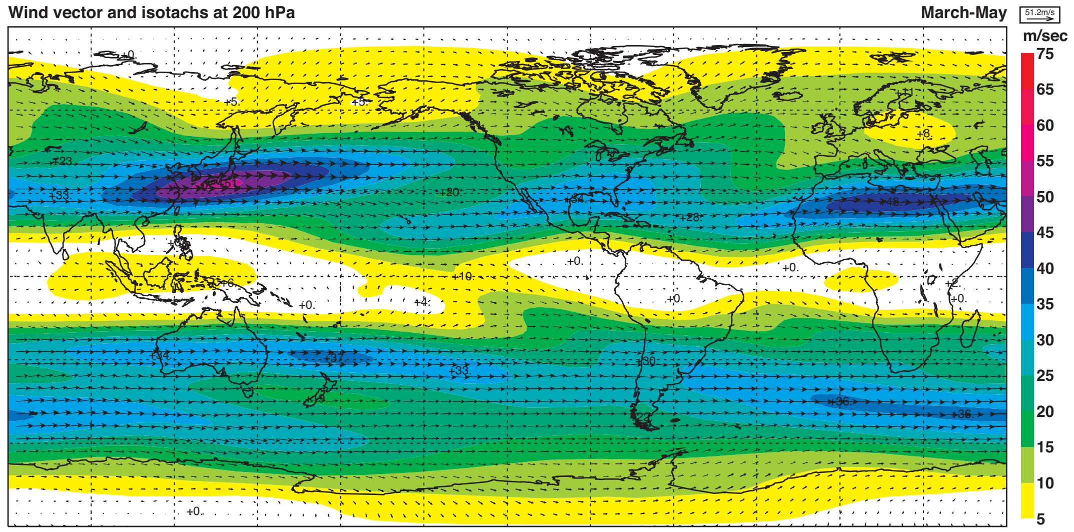

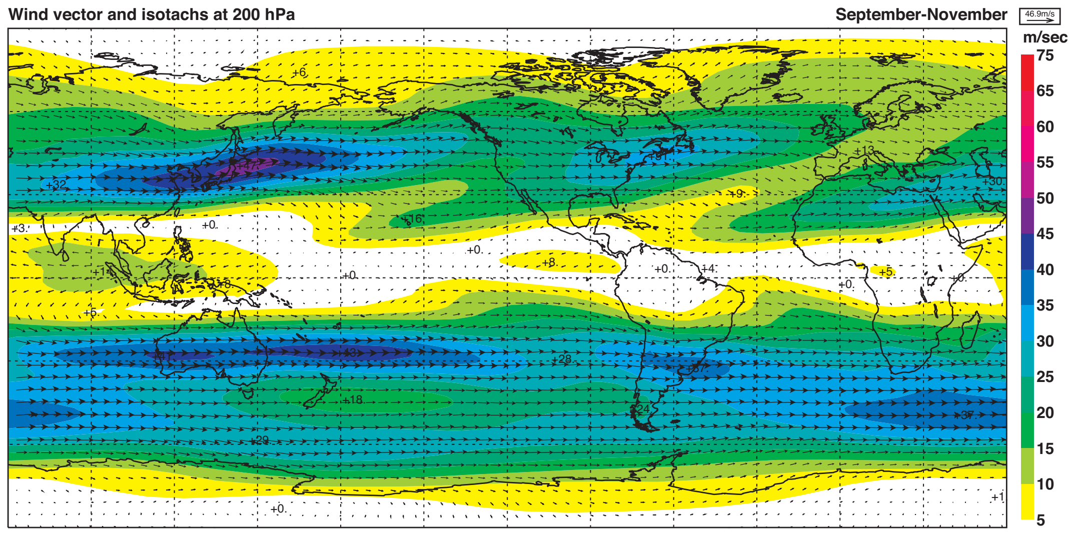

D1 Vector wind (ms^{-1}) with isotachs (ms^{-1}) at 200 hPa. For the interannual variability, the vectors are omitted.

Wind vector and isotachs at 300 hPa — Annual mean

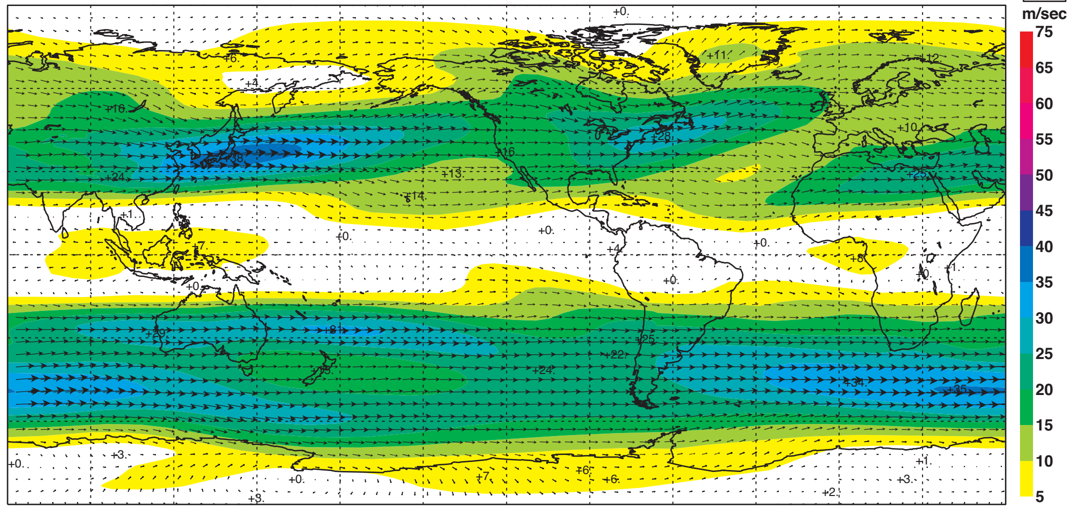

Wind vector and isotachs at 300 hPa — December-February

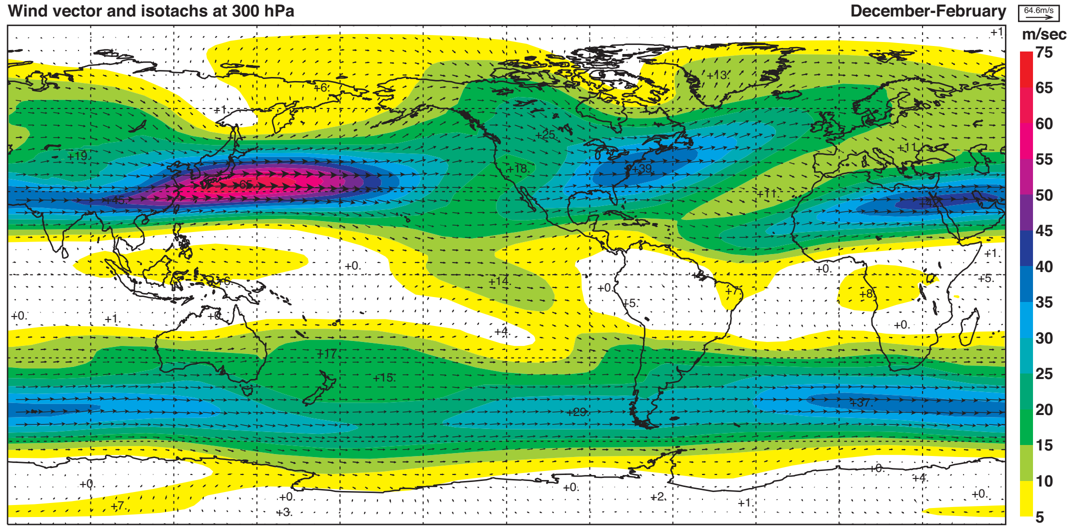

Wind vector and isotachs at 300 hPa — June-August

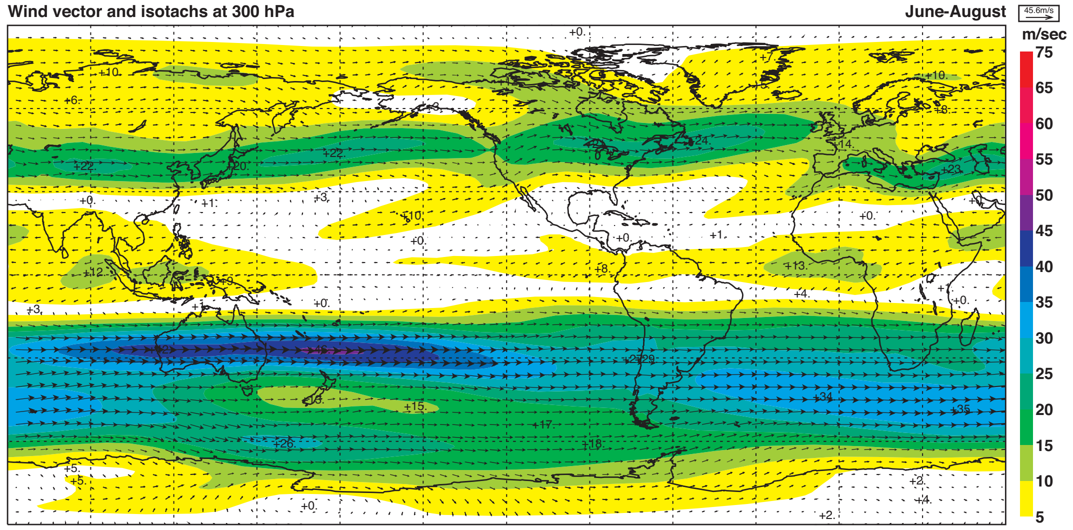

Isotachs at 300 hPa — Interannual variability

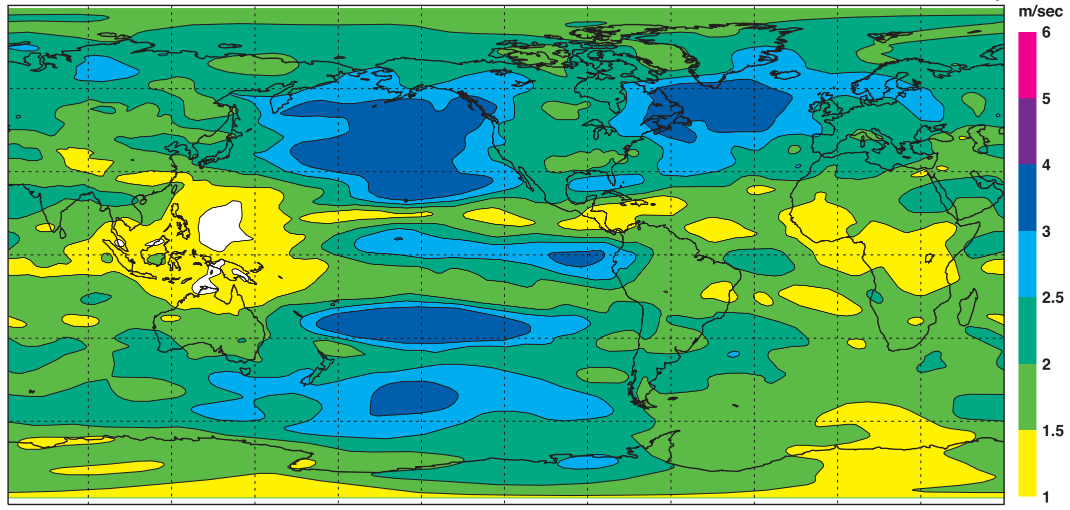

Wind vector and isotachs at 300 hPa — March-May

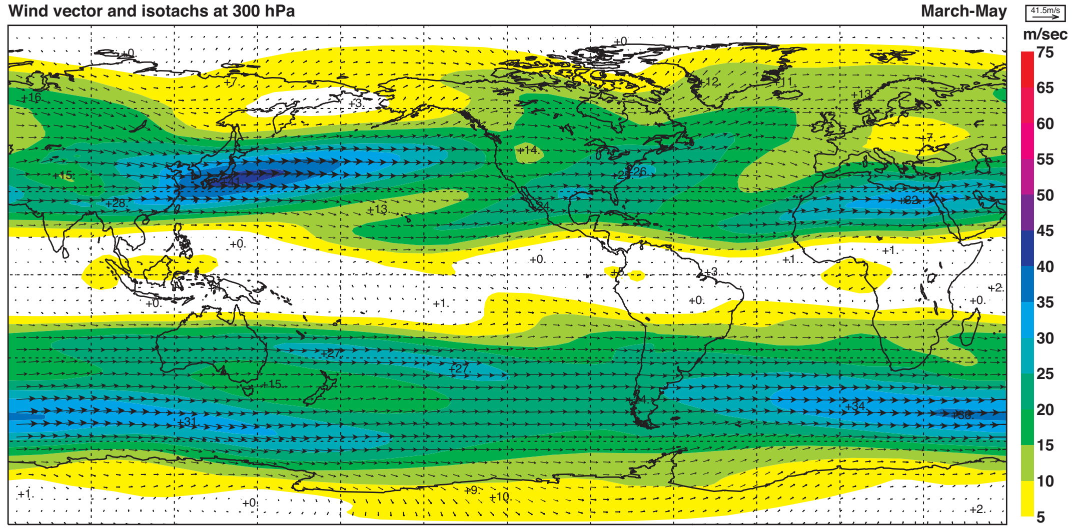

Wind vector and isotachs at 300 hPa — September-November

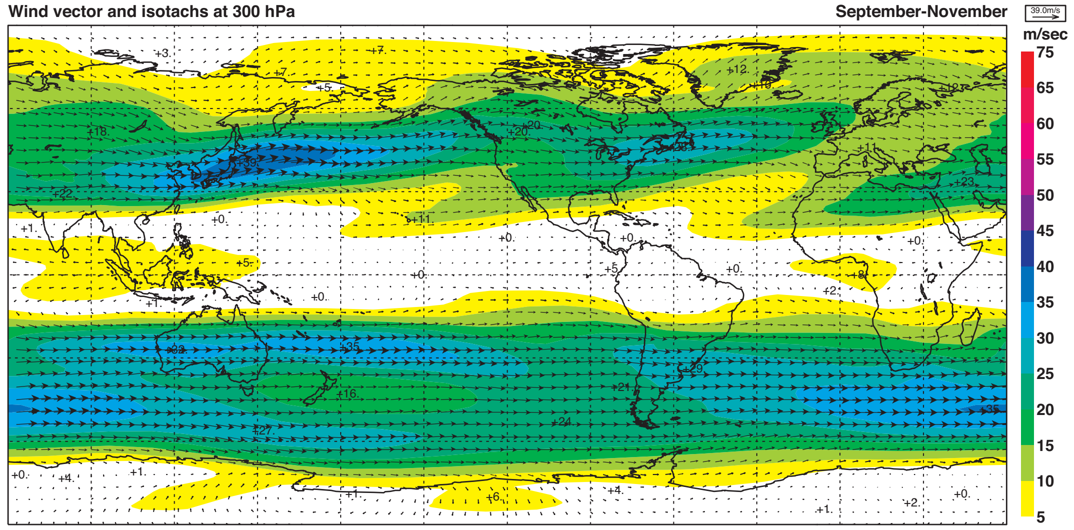

D2 Vector wind (ms^{-1}) with isotachs (ms^{-1}) at 300 hPa. For the interannual variability, the vectors are omitted.

Wind vector and isotachs at 500 hPa — Annual mean

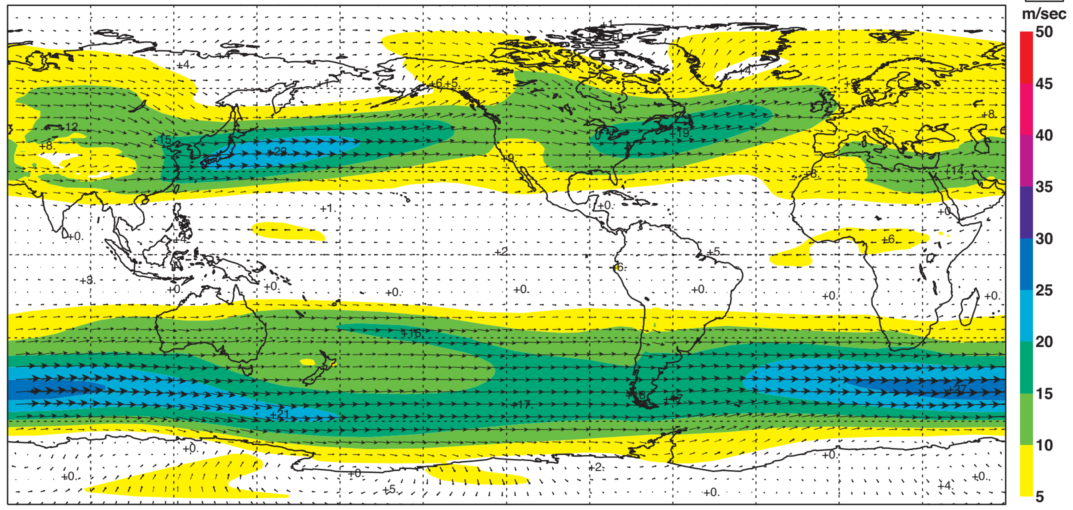

Wind vector and isotachs at 500 hPa — December-February

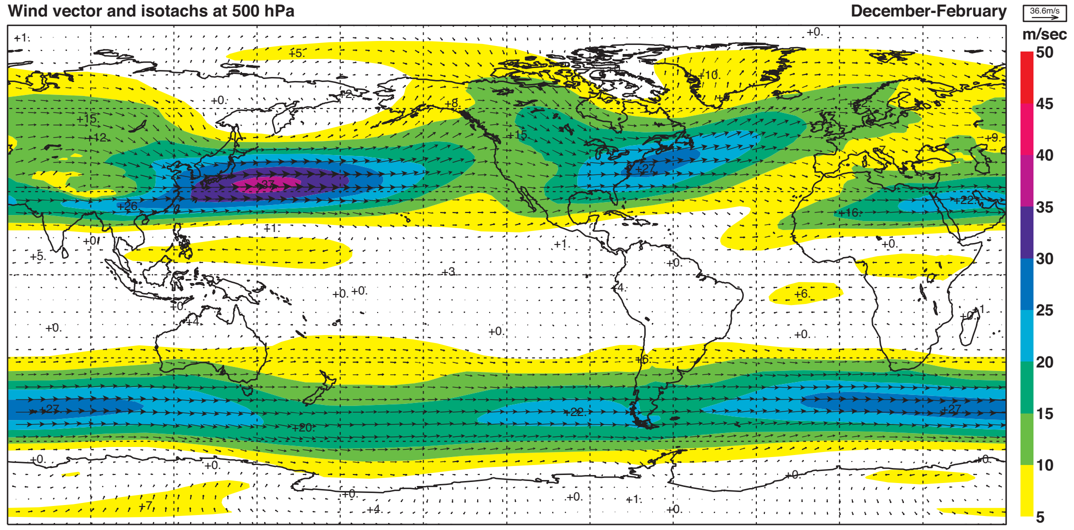

Wind vector and isotachs at 500 hPa — June-August

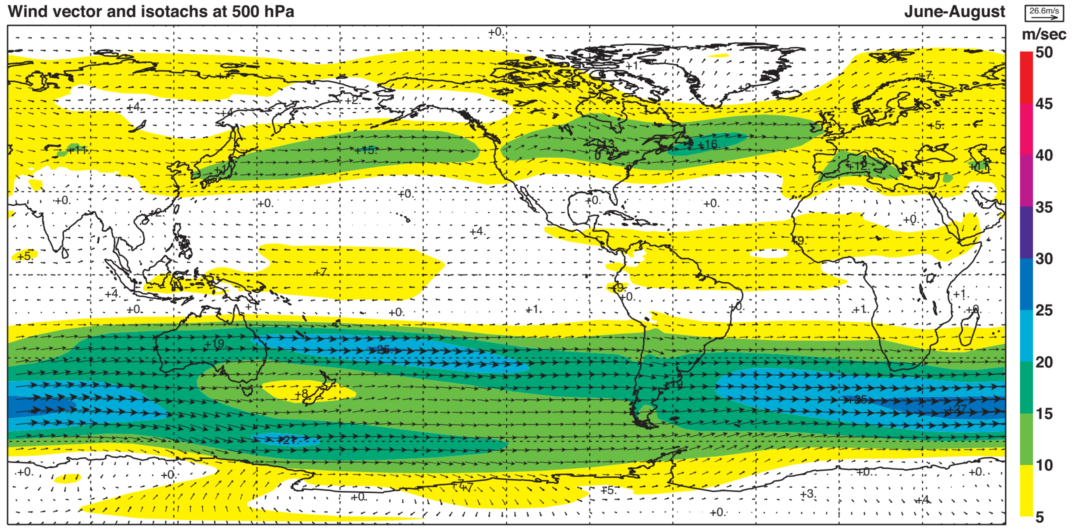

Isotachs at 500 hPa — Interannual variability

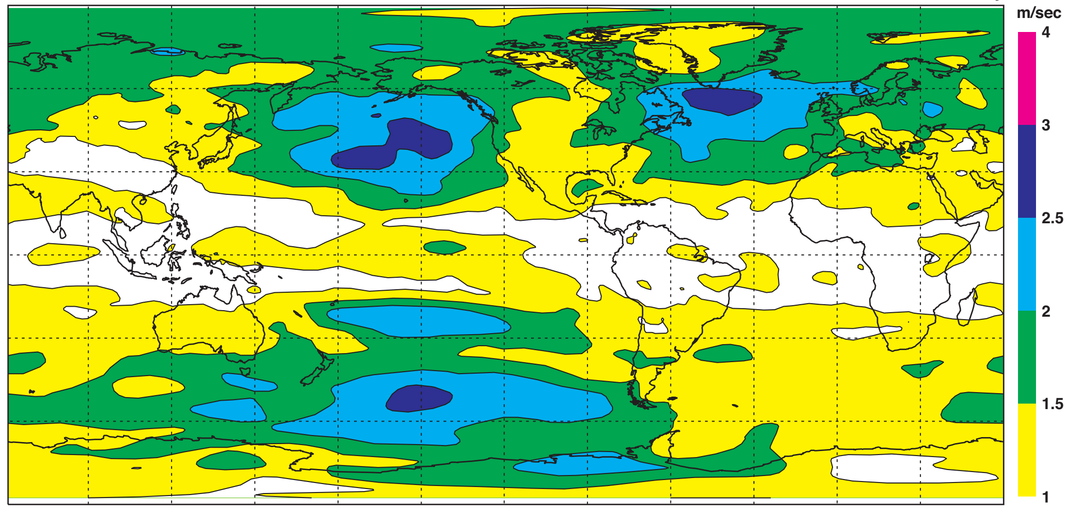

Wind vector and isotachs at 500 hPa — March-May

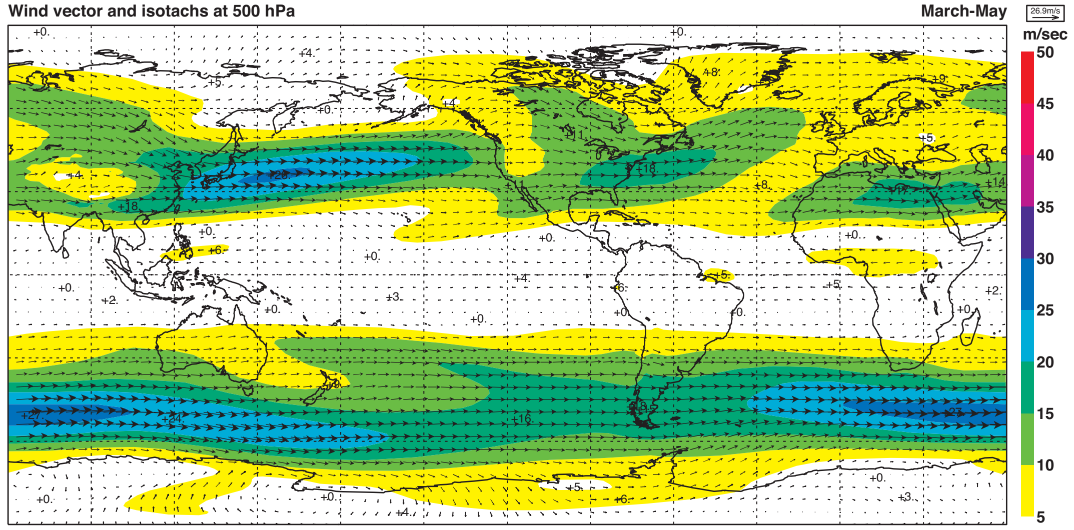

Wind vector and isotachs at 500 hPa — September-November

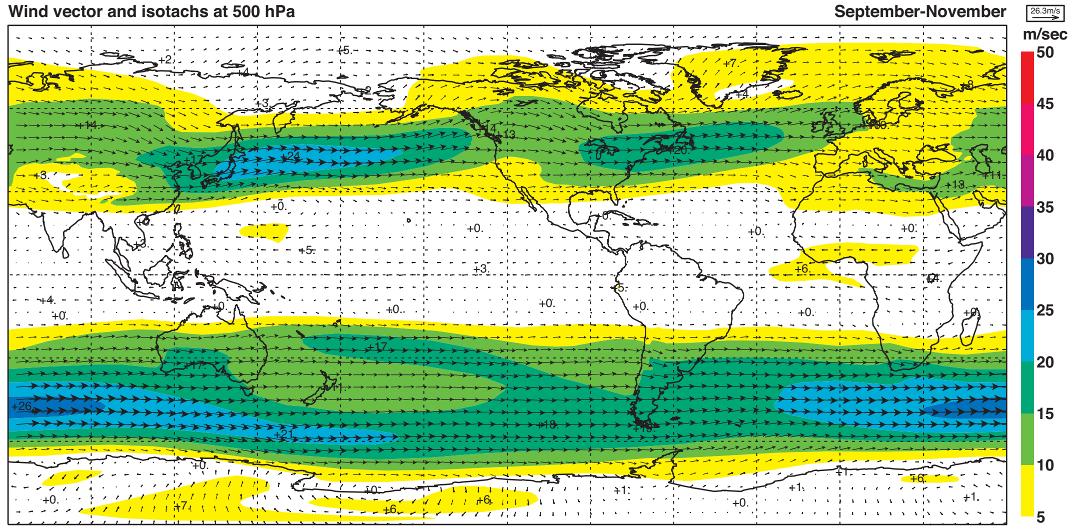

D3 Vector wind (ms^{-1}) with isotachs (ms^{-1}) at 500hPa. For the interannual variability, the vectors are omitted.

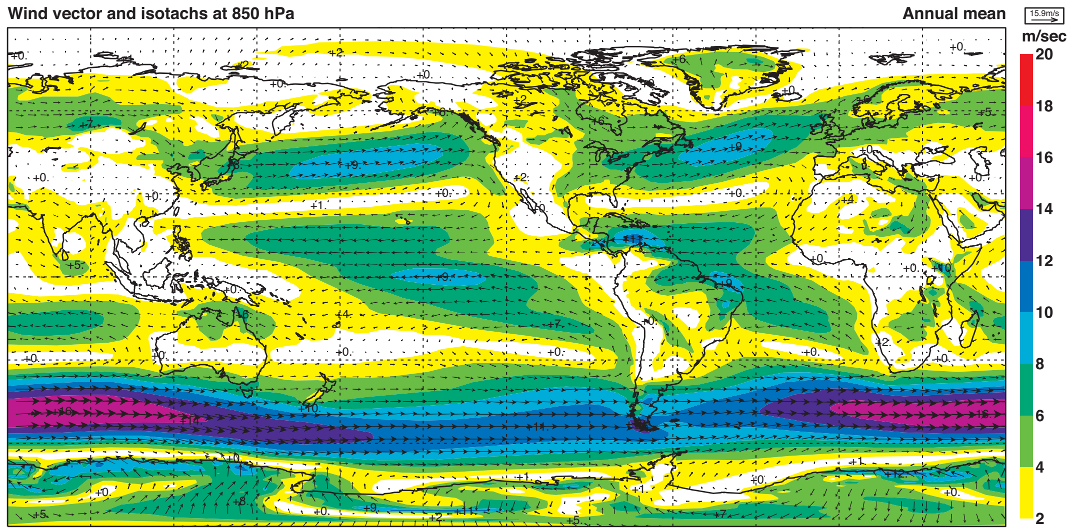

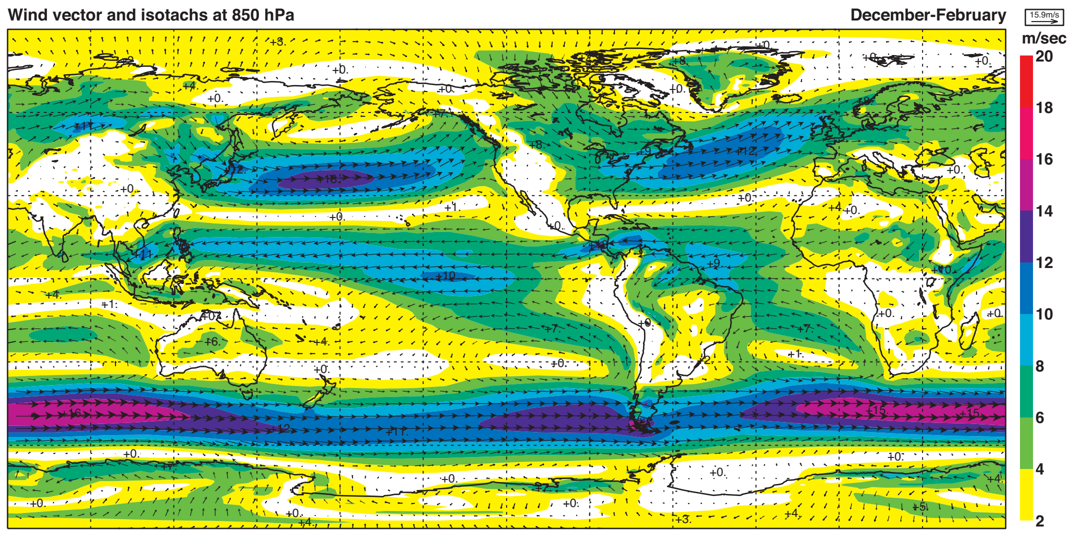

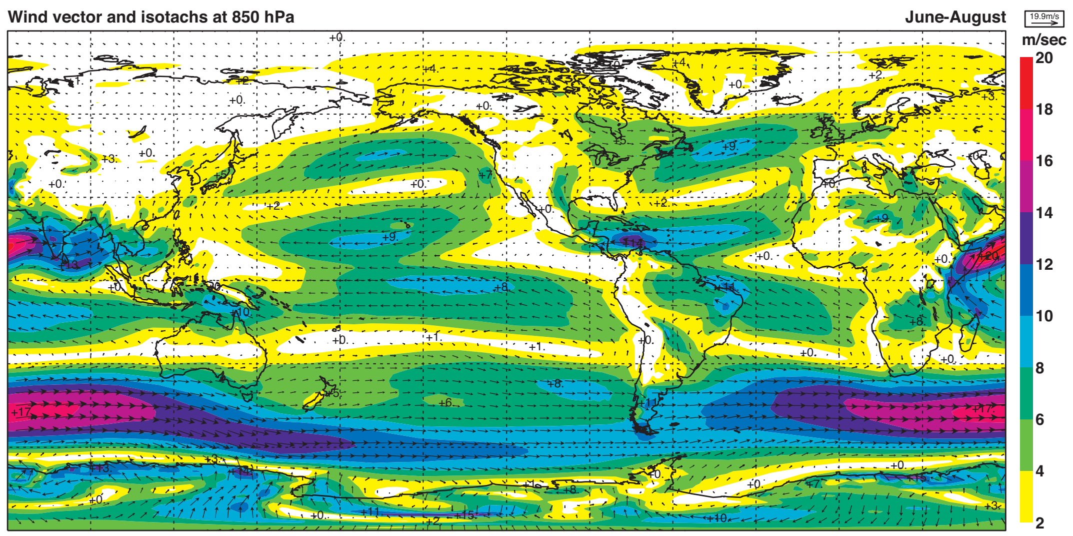

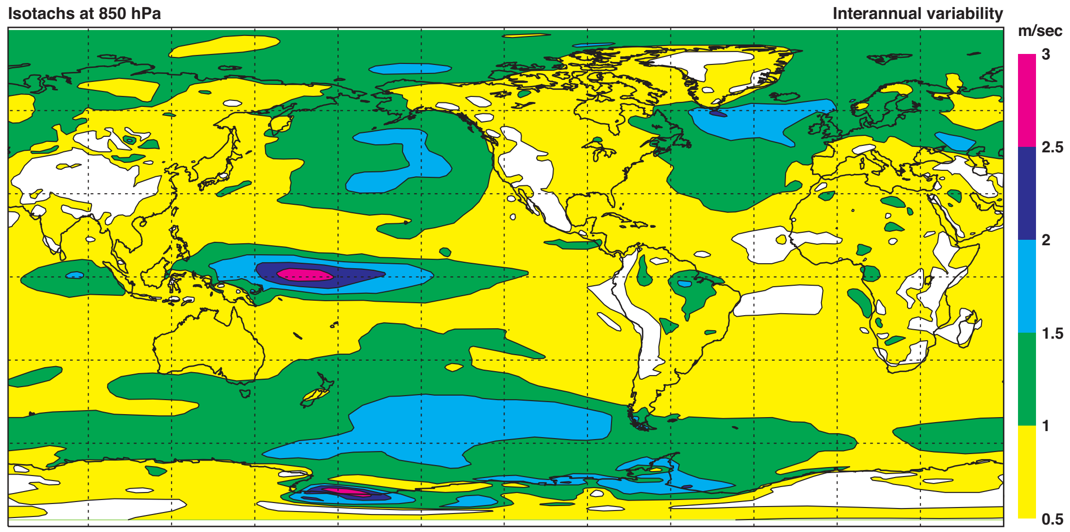

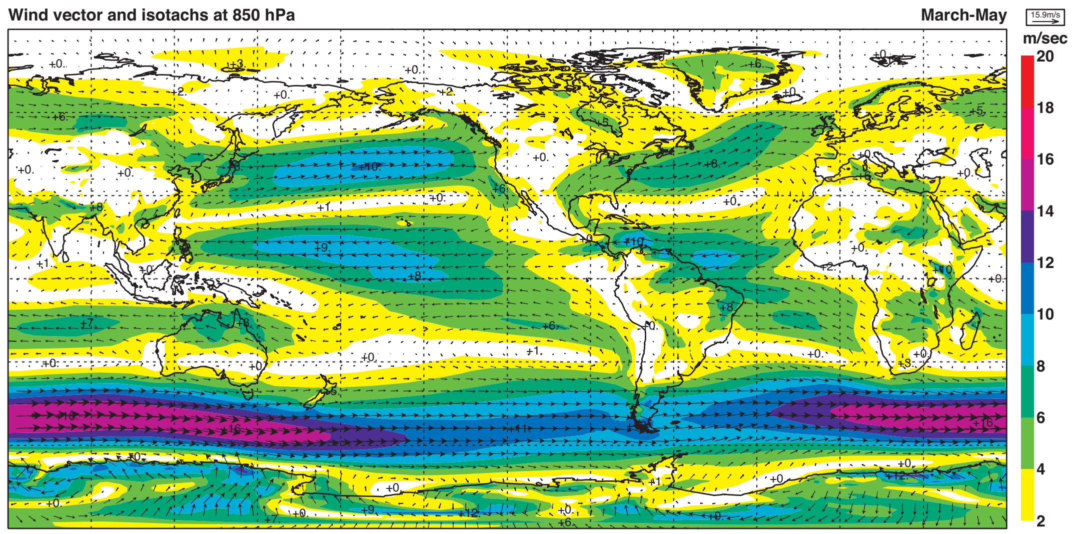

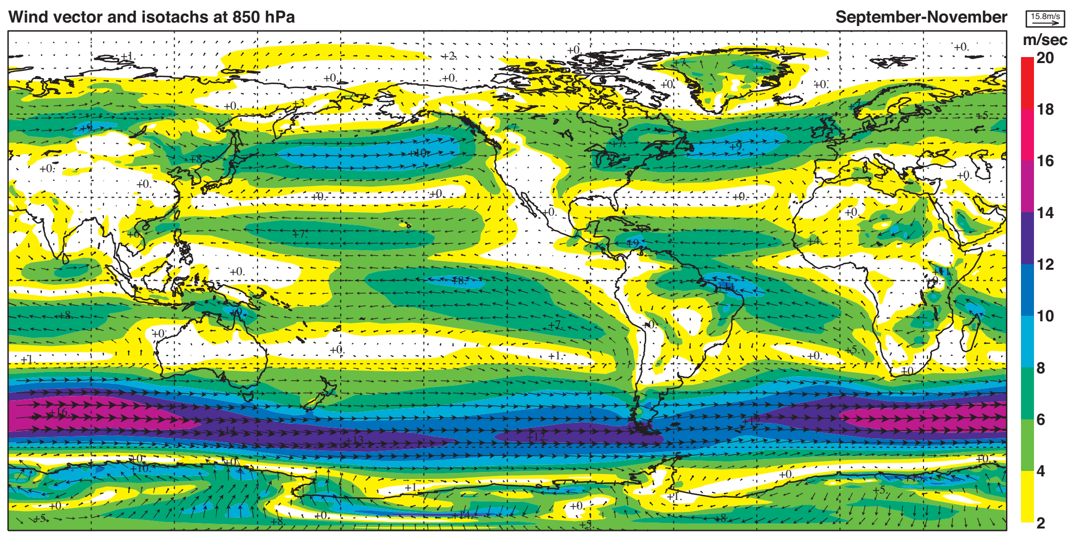

D4 Vector wind (ms^{-1}) with isotachs (ms^{-1}) at 850 hPa. For the interannual variability, the vectors are omitted.

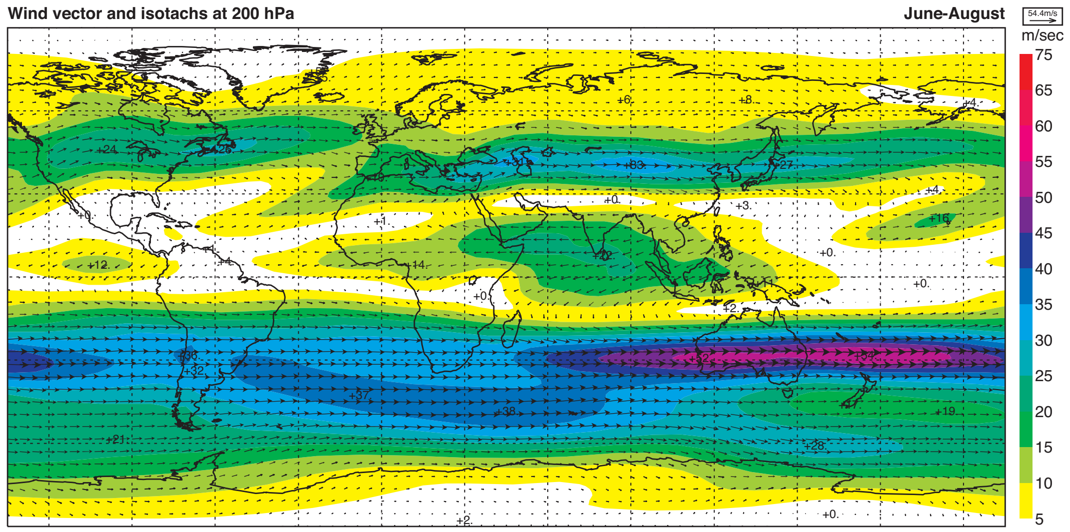

D1b Vector wind (ms^{-1}) with isotachs (ms^{-1}) at 200 hPa (plot centred on 60E for the Asian summer monsoon and only shown for JJA).

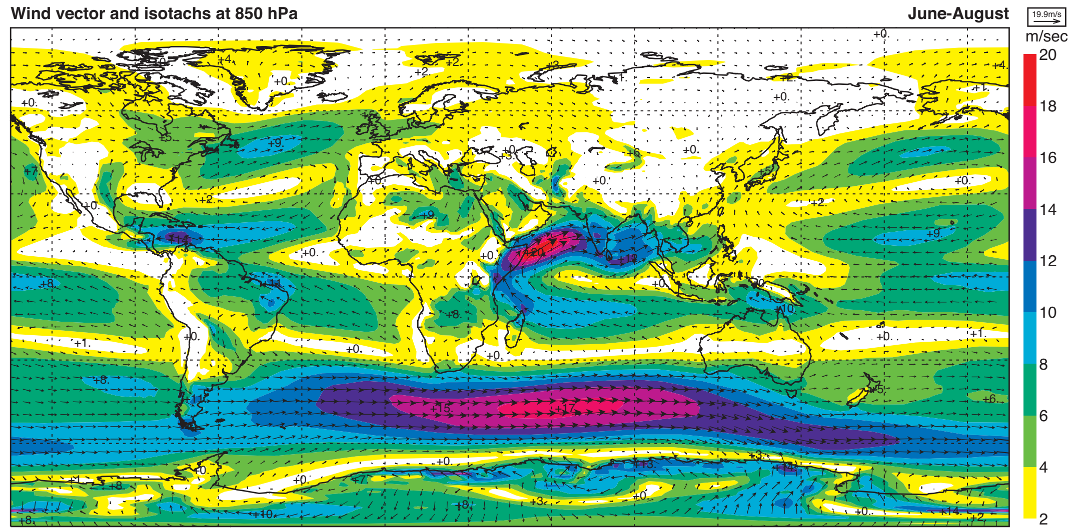

D4b Vector wind (ms^{-1}) with isotachs (ms^{-1}) at 850hPa (plot centred on 60E for the Asian summer monsoon and only shown for JJA).

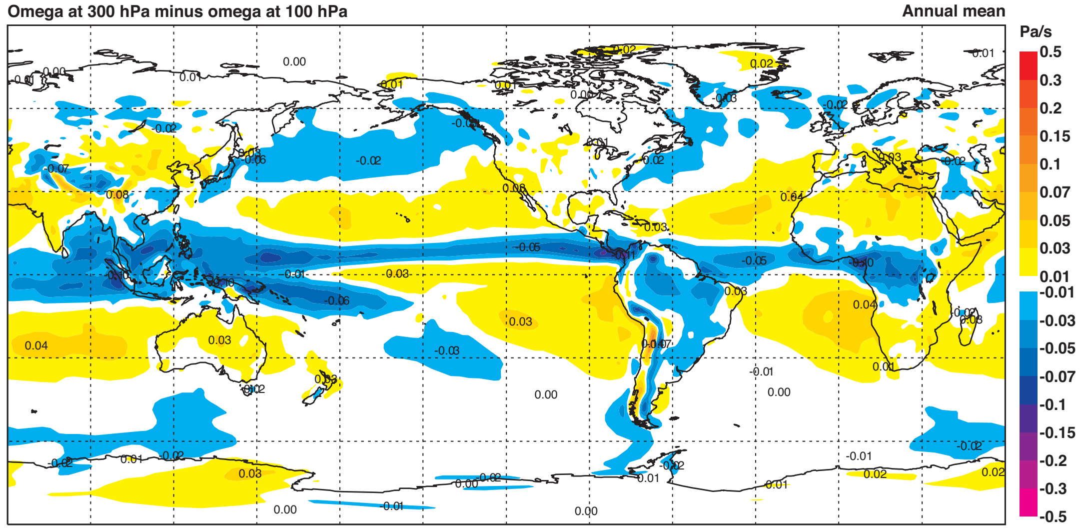

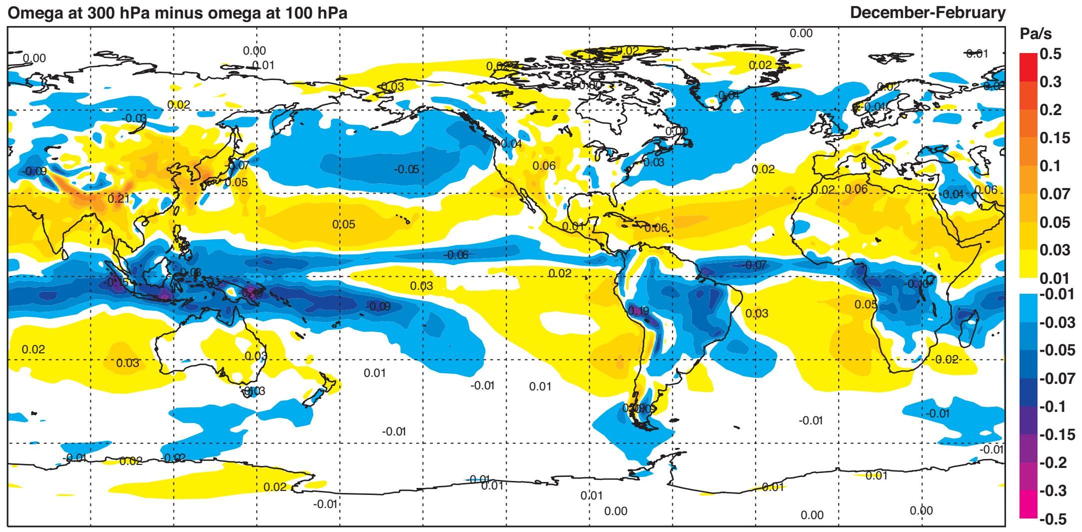

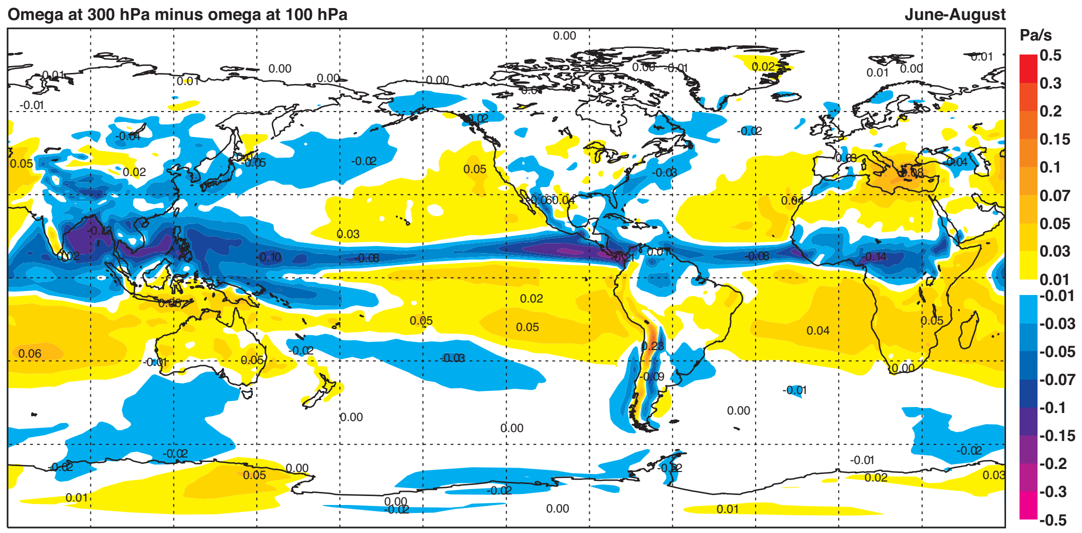

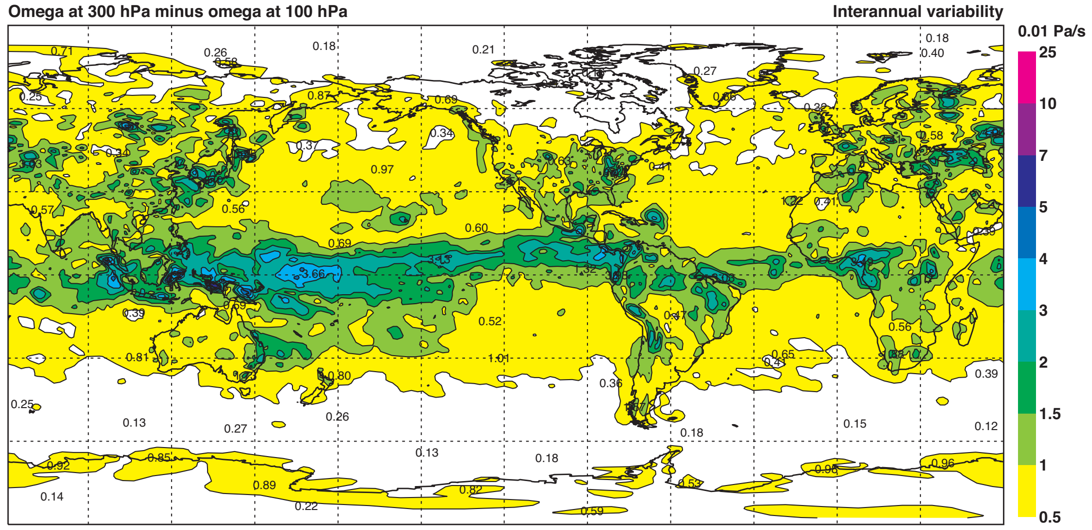

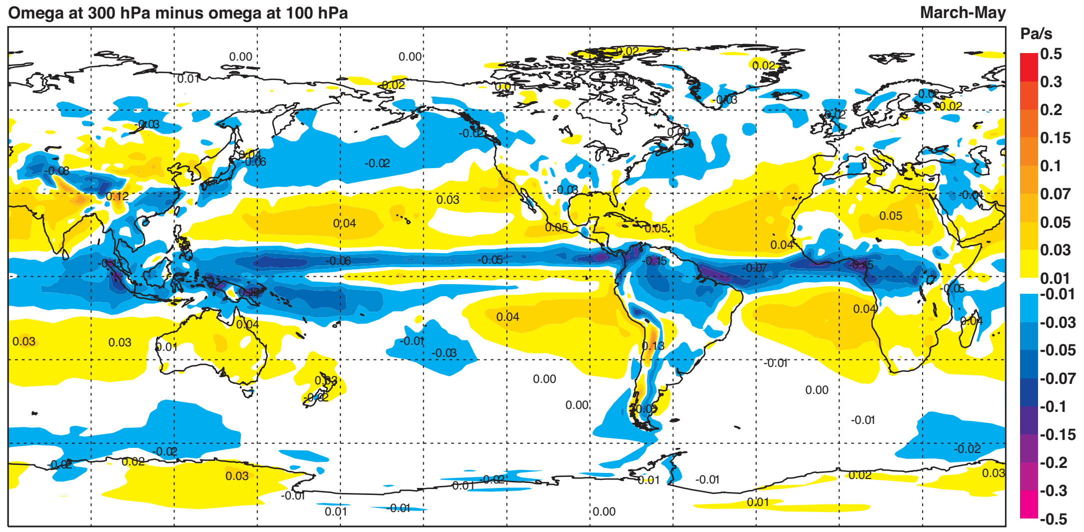

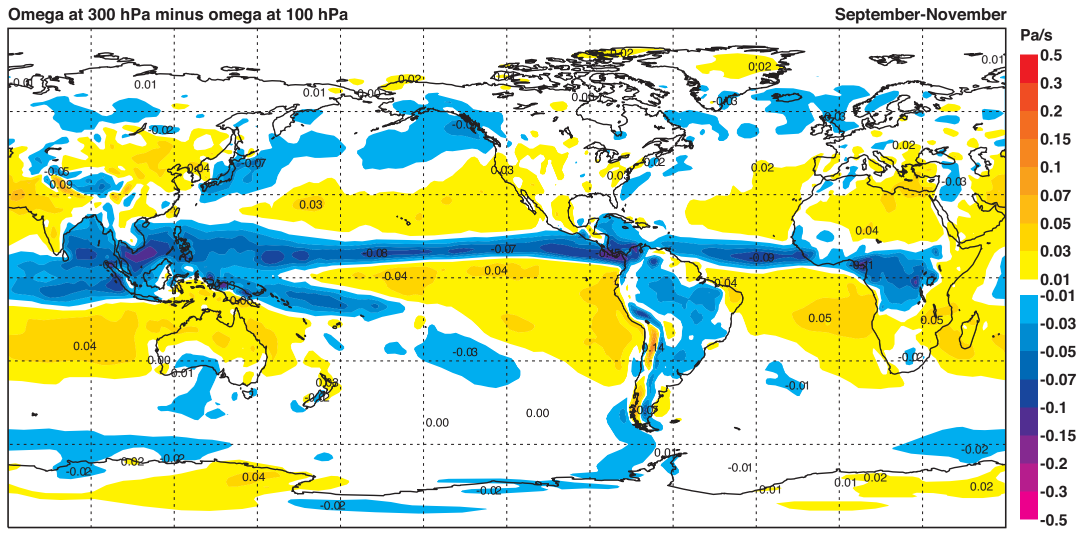

D5 Omega at 300hPa minus omega at 100 hPa (Pas^{-1}). Except for the interannual variability, the fields have been spatially smoothed (*see Section 2.4*).

Omega at 500 hPa — Annual mean

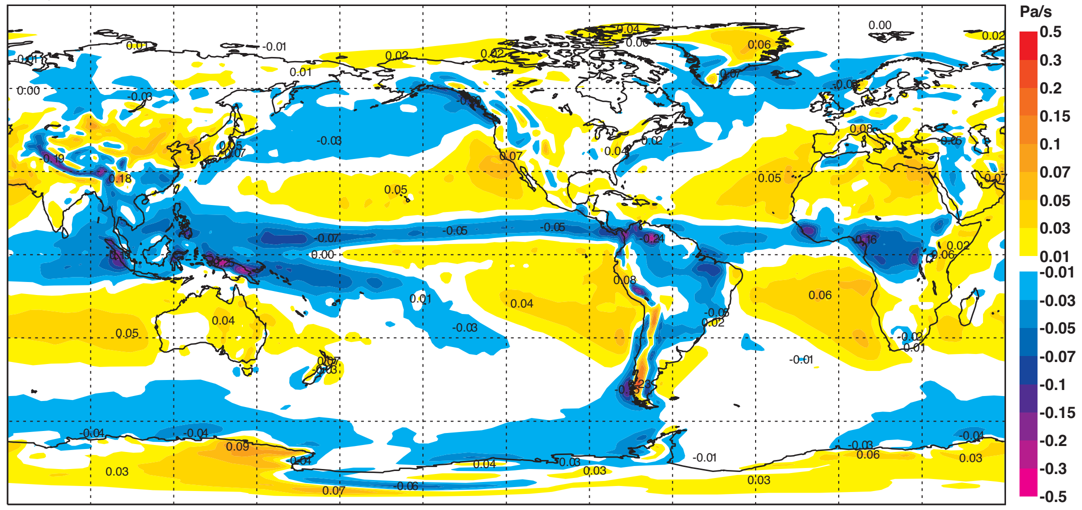

Omega at 500 hPa — December-February

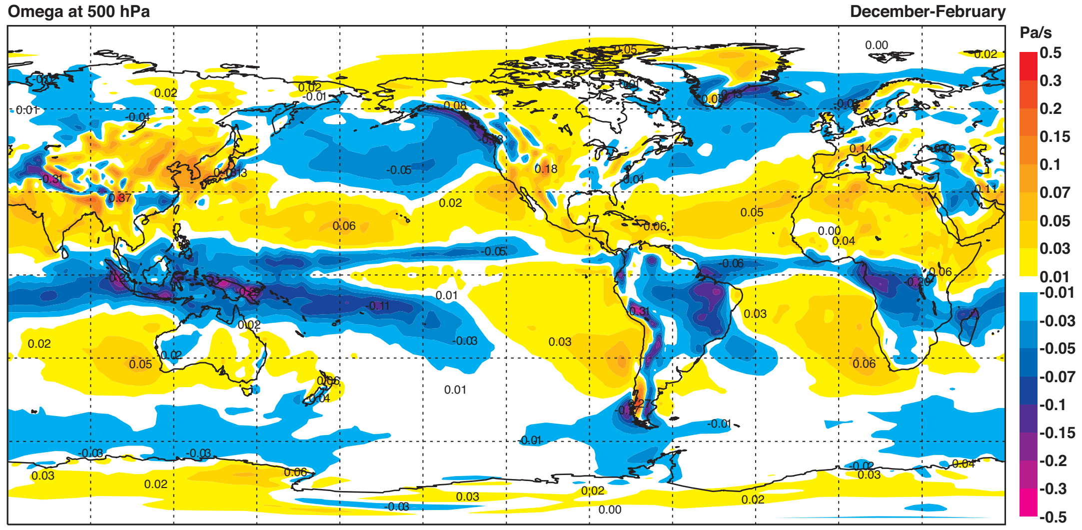

Omega at 500 hPa — June-August

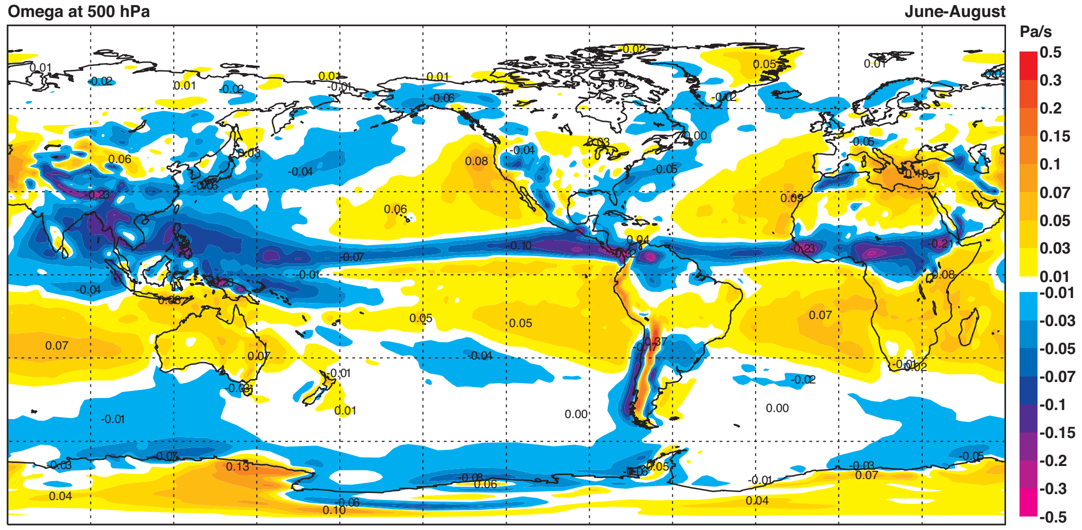

Omega at 500hPa — Interannual variability

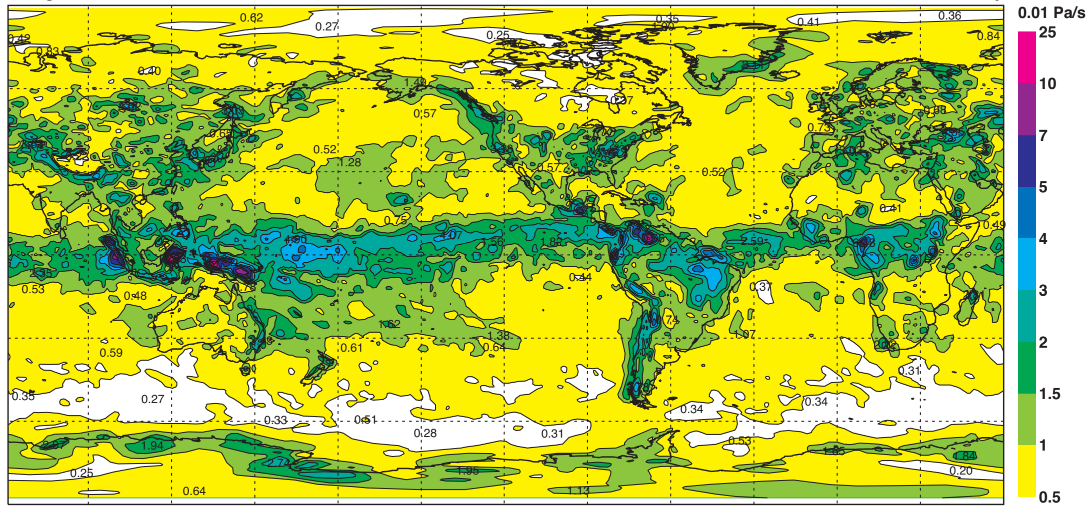

Omega at 500 hPa — March-May

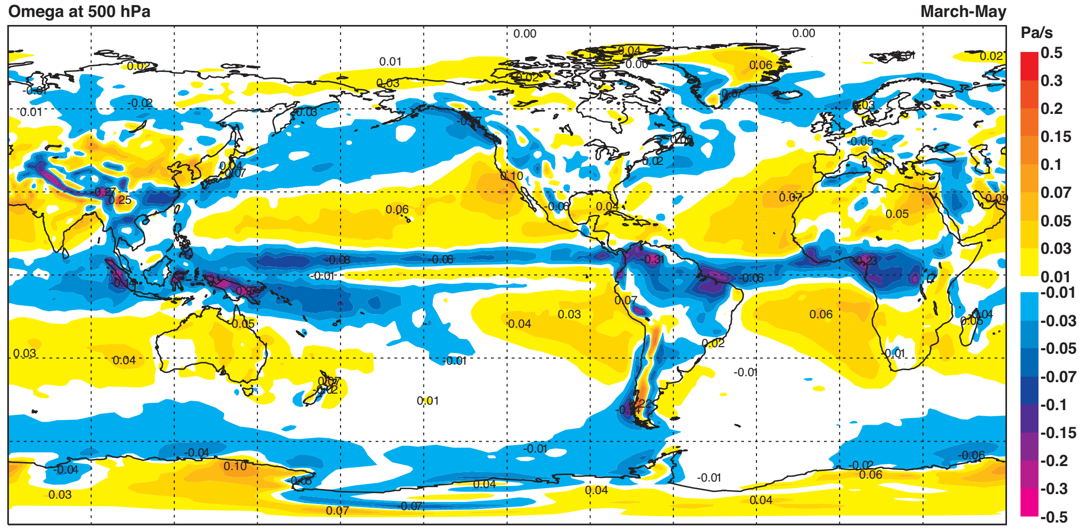

Omega at 500 hPa — September-November

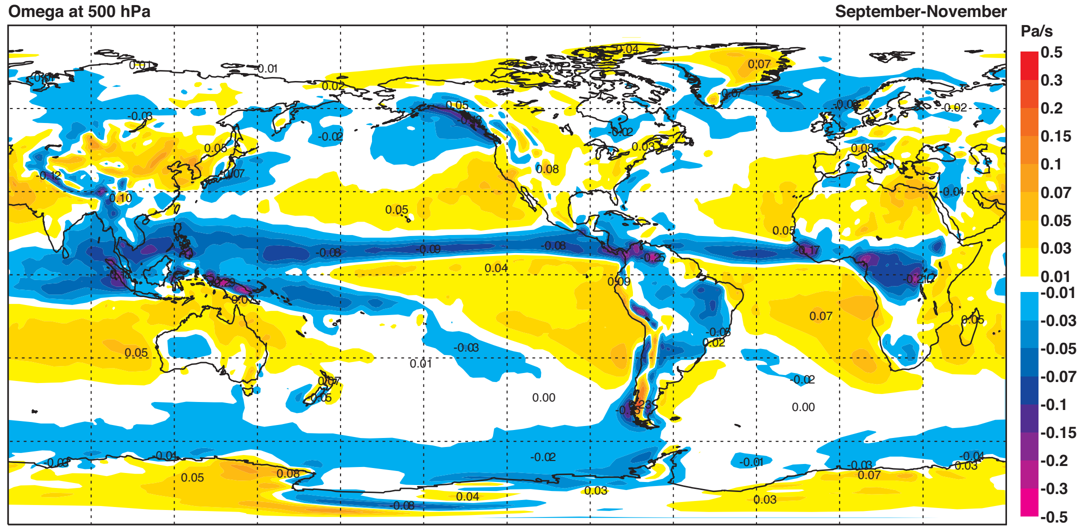

D6 Omega (Pas^{-1}) at 500 hPa. Except for the interannual variability, the fields have been spatially smoothed (*see Section 2.4*).

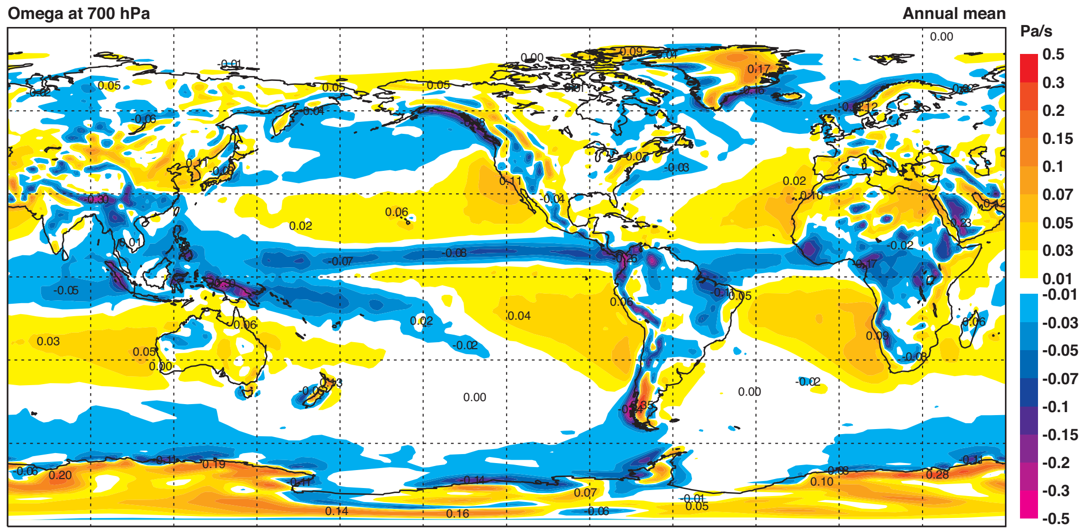

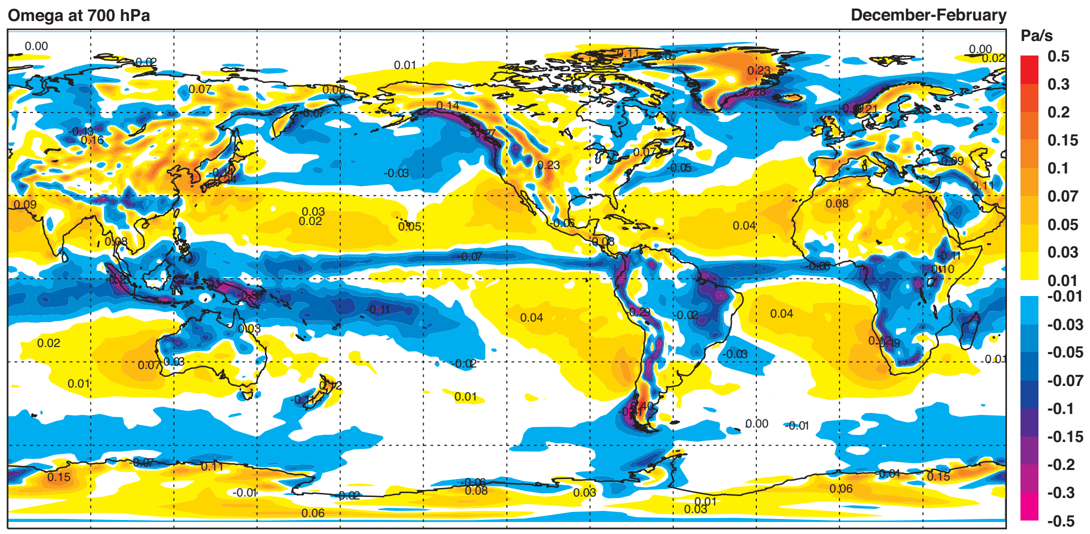

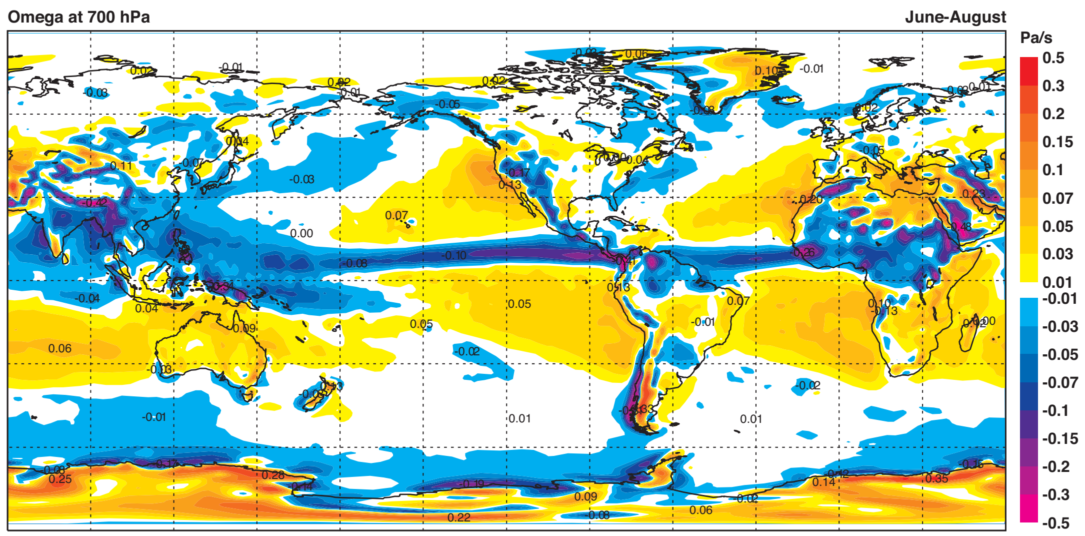

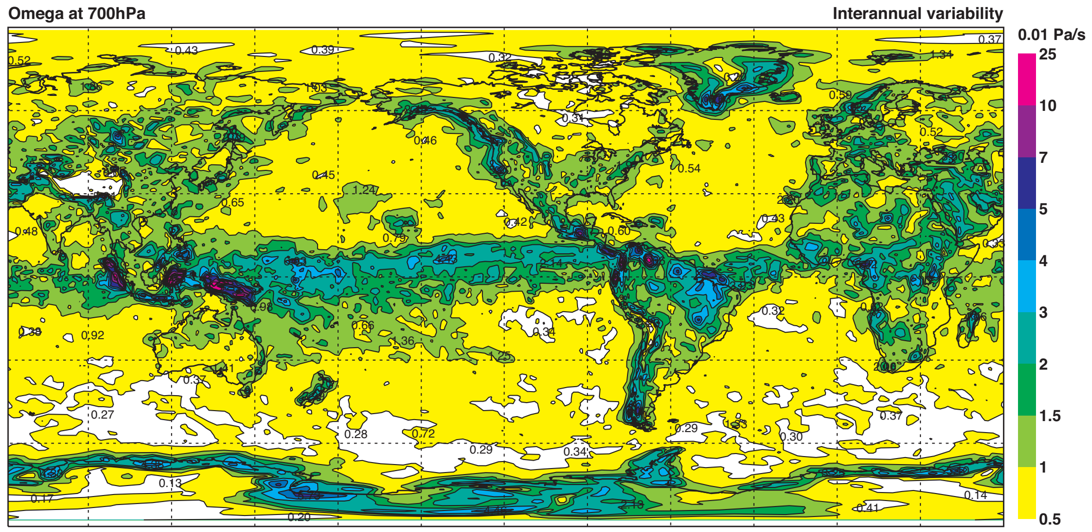

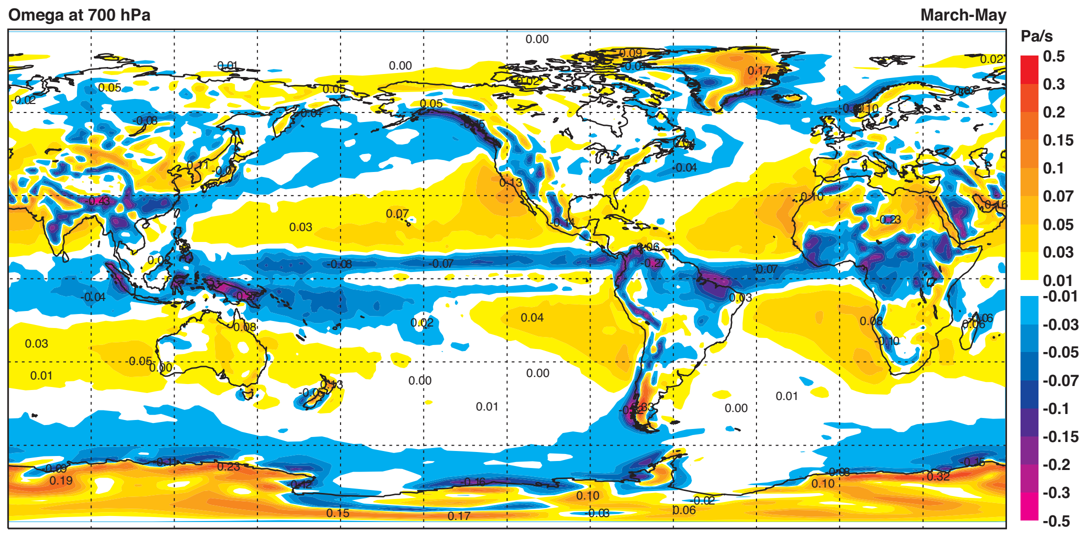

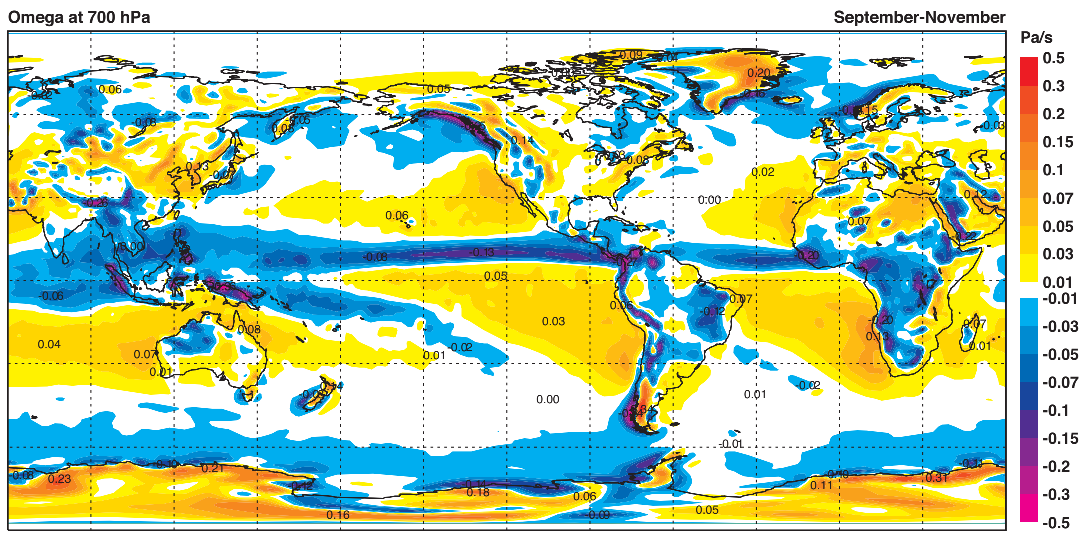

D7 Omega ($Pa s^{-1}$) at 700 hPa. Except for the interannual variability, the fields have been spatially smoothed (*see Section 2.4*).

Layer heating from 0.1 – 250 hPa — Annual mean

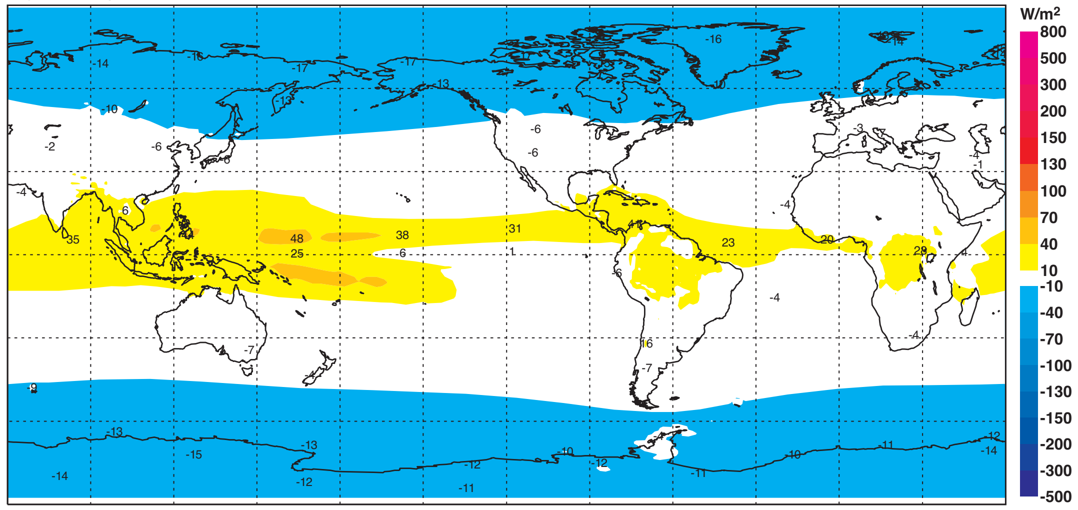

Layer heating from 0.1 – 250 hPa — December-February

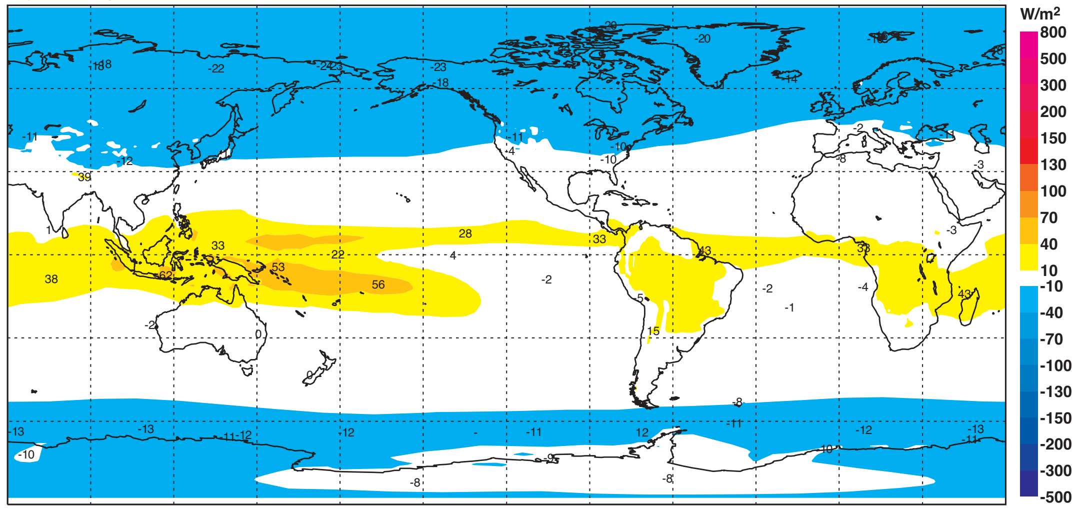

Layer heating from 0.1 – 250 hPa — June-August

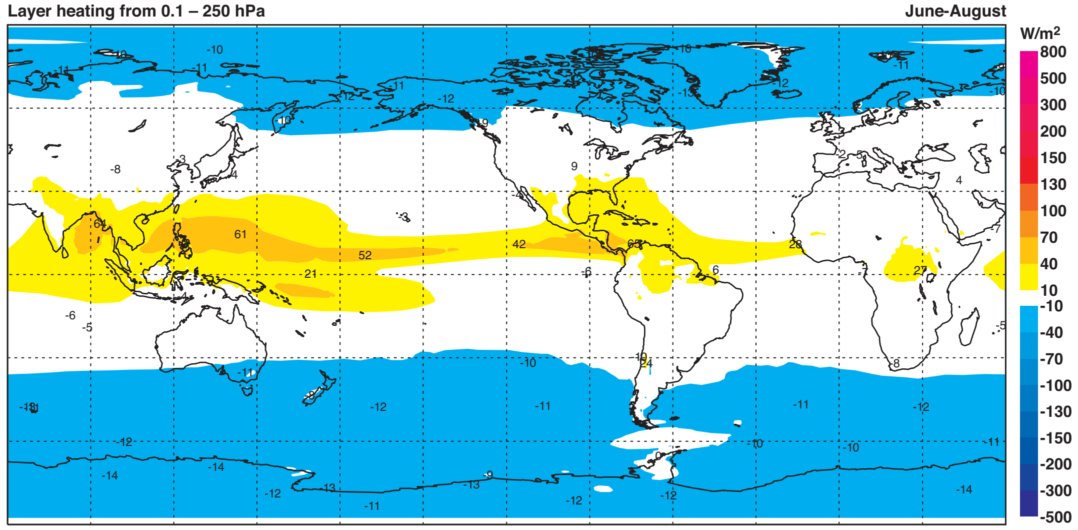

Layer heating from 0.1 – 250 hPa — Interannual variability

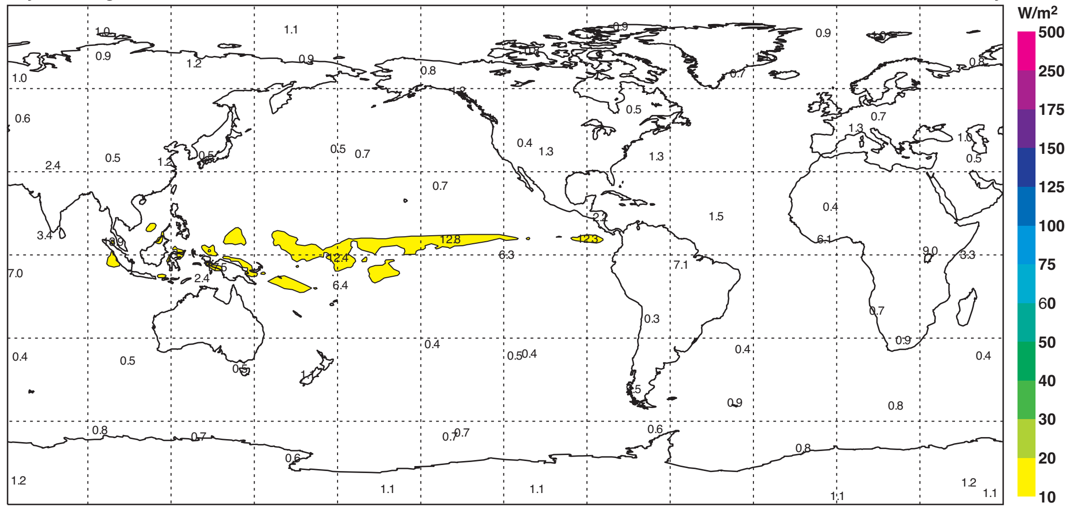

Layer heating from 0.1 – 250 hPa — March-May

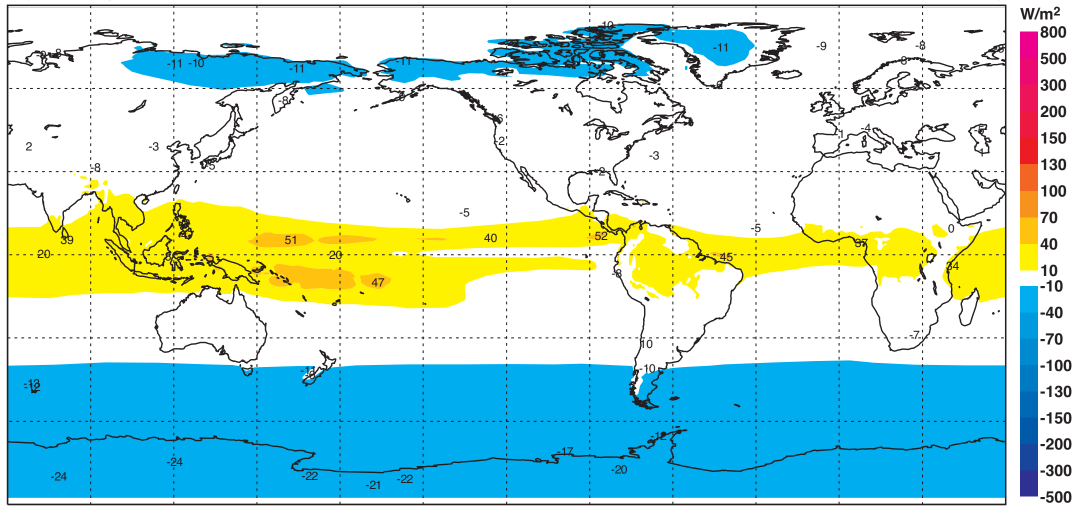

Layer heating from 0.1 – 250 hPa — September-November

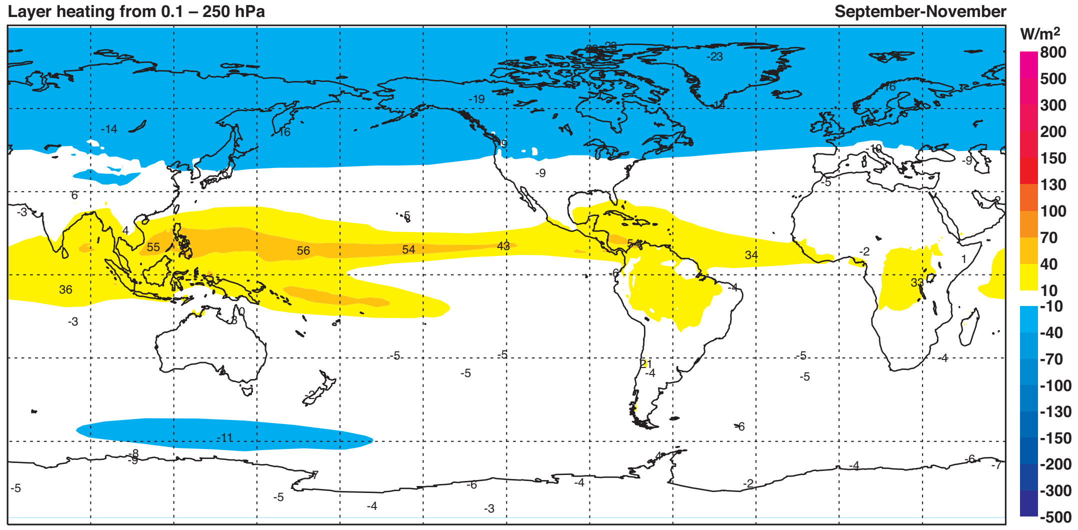

D8 Layer heating (Wm^{-2}) from 0.1 to 250 hPa.

Layer heating from 250 – 500 hPa — Annual mean

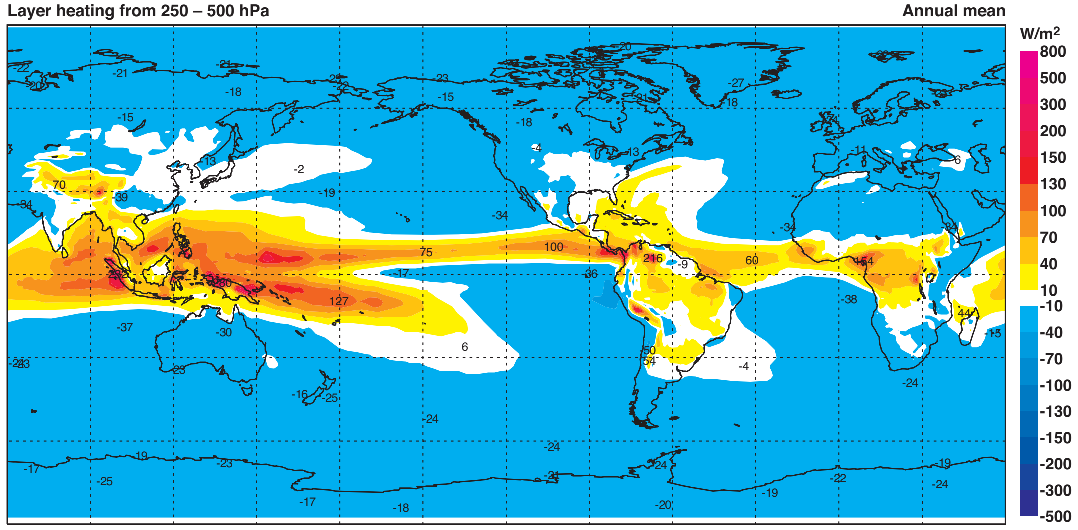

Layer heating from 250 – 500 hPa — December-February

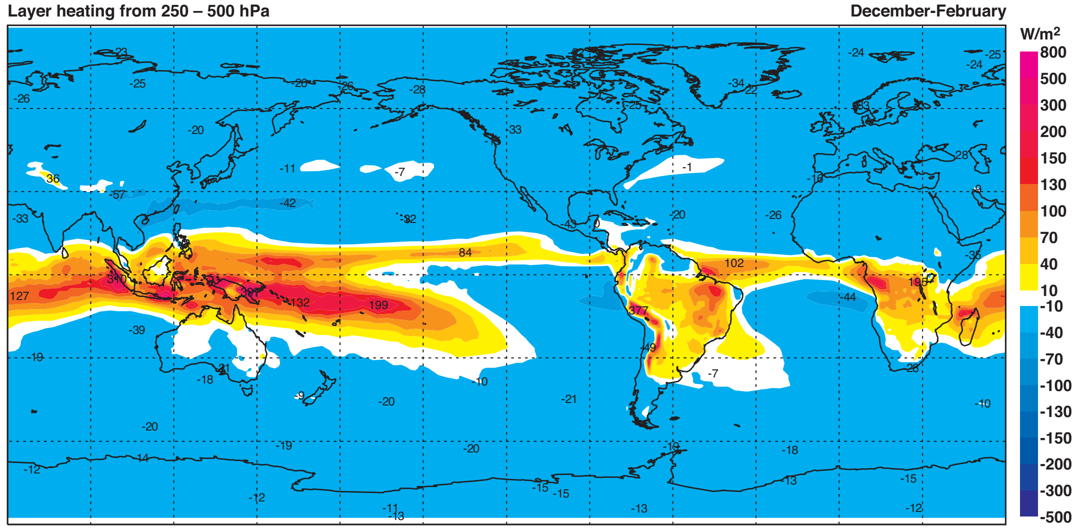

Layer heating from 250 – 500 hPa — June-August

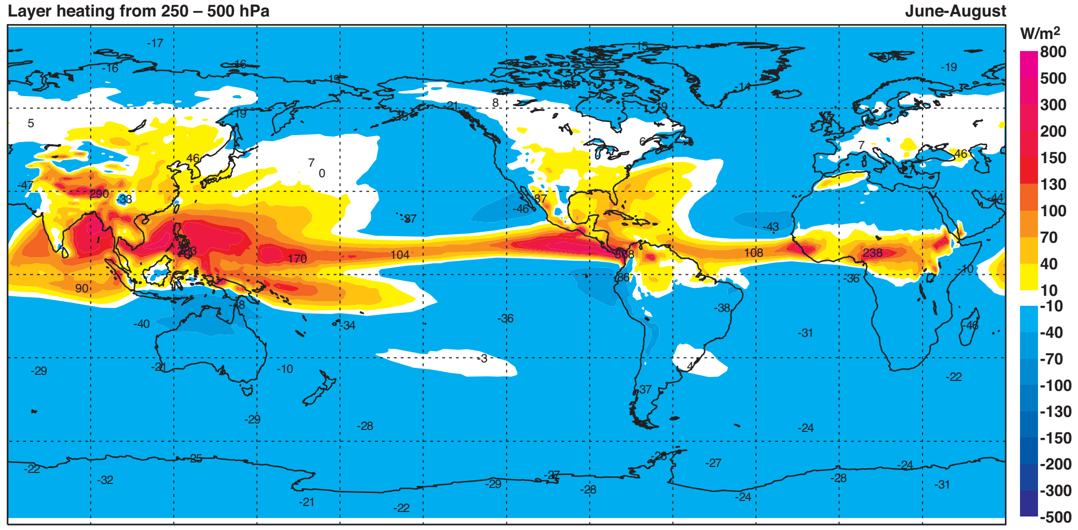

Layer heating from 250 – 500 hPa — Interannual variability

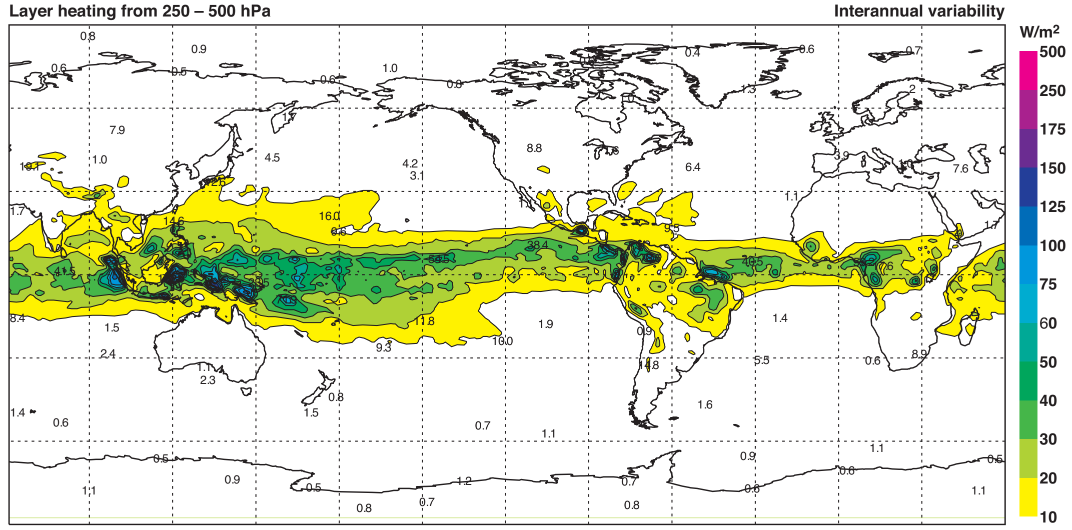

Layer heating from 250 – 500 hPa — March-May

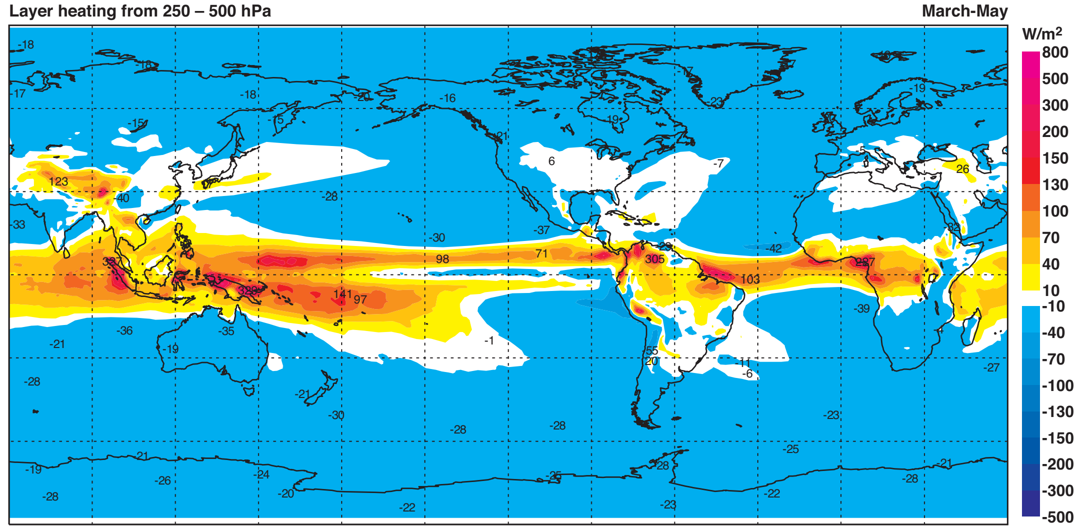

Layer heating from 250 – 500 hPa — September-November

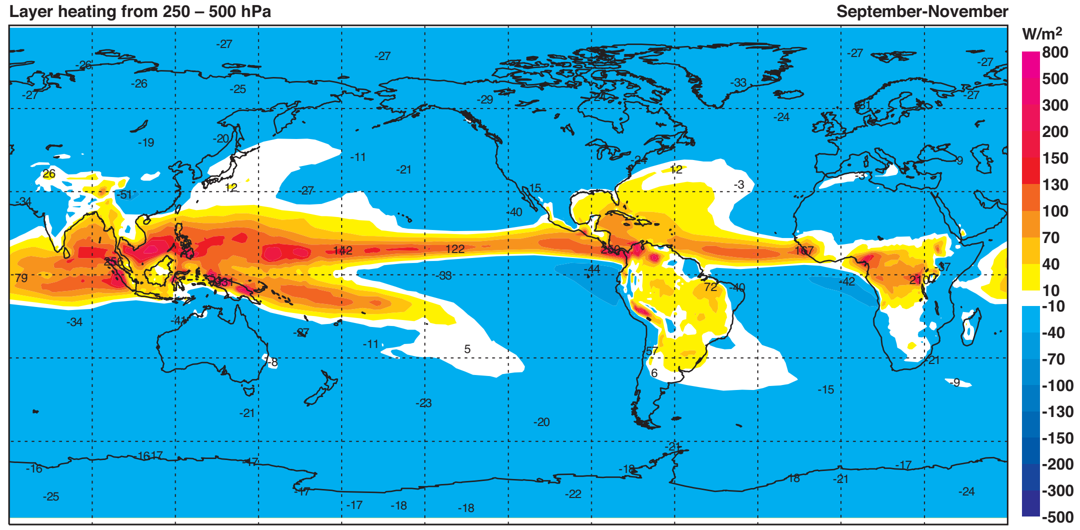

D9 Layer heating (Wm^{-2}) from 250 to 500 hPa.

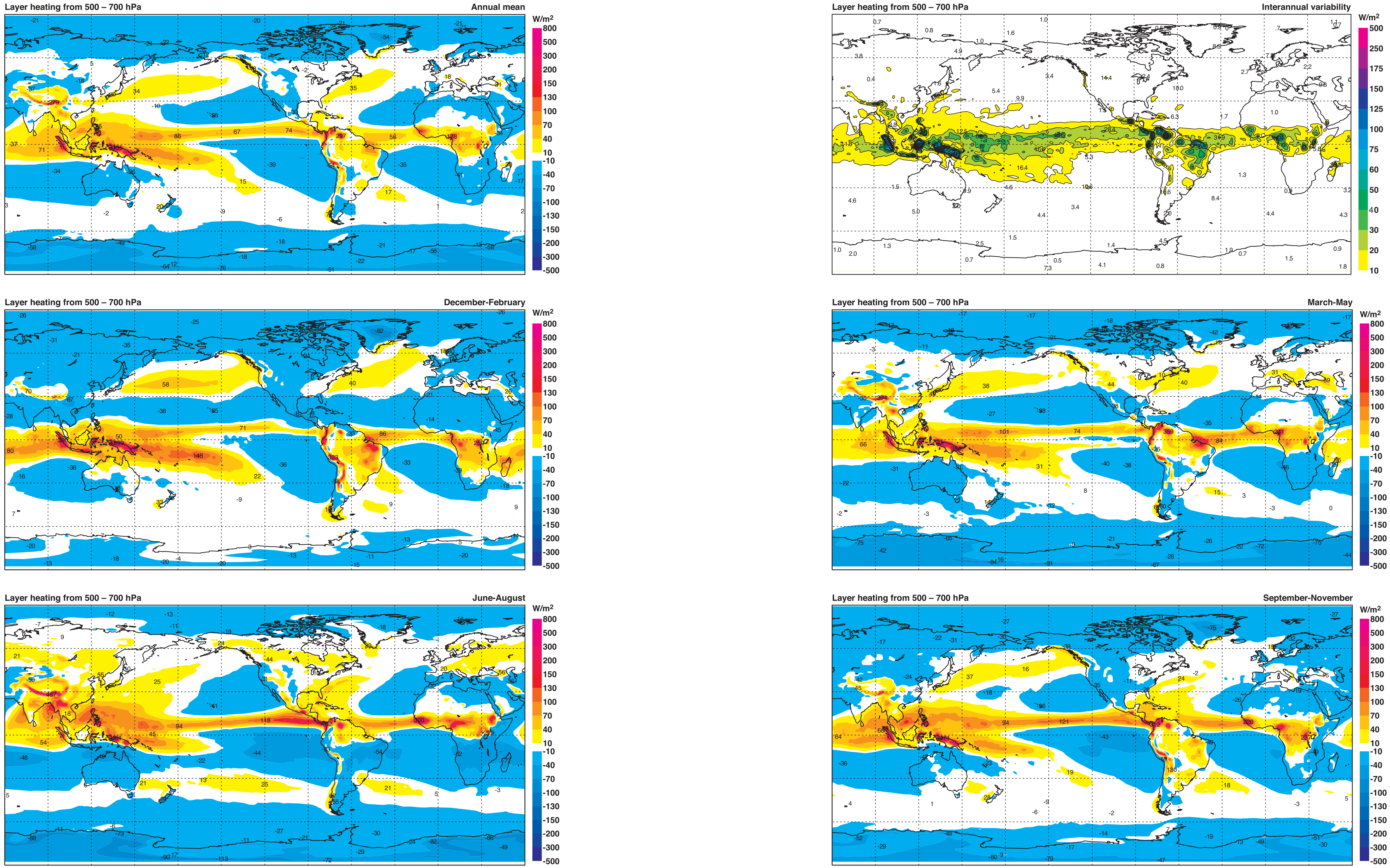

D10 Layer heating (Wm^{-2}) from 500 to 700 hPa.

Layer heating from 700 hPa to the ground — Annual mean

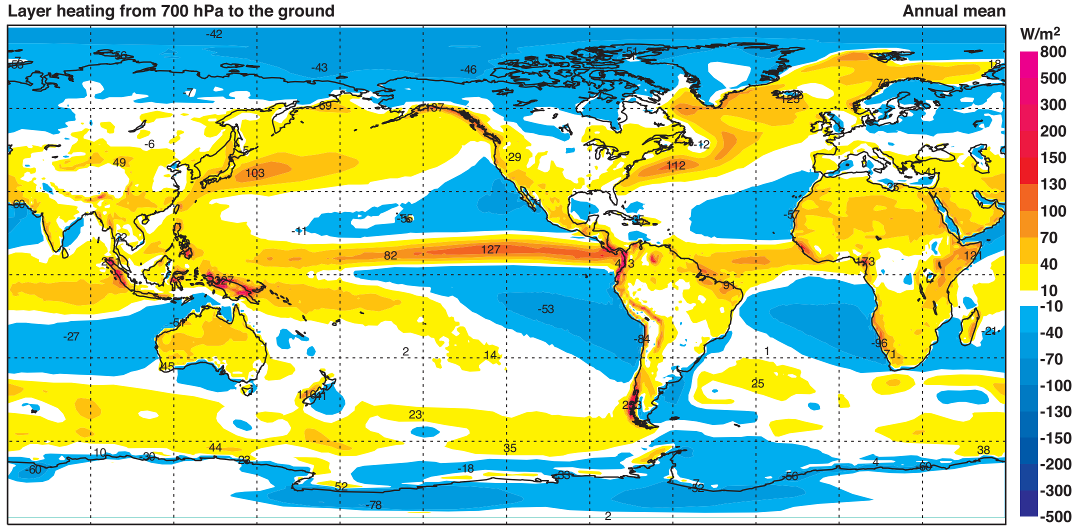

Layer heating from 700 hPa to the ground — December-February

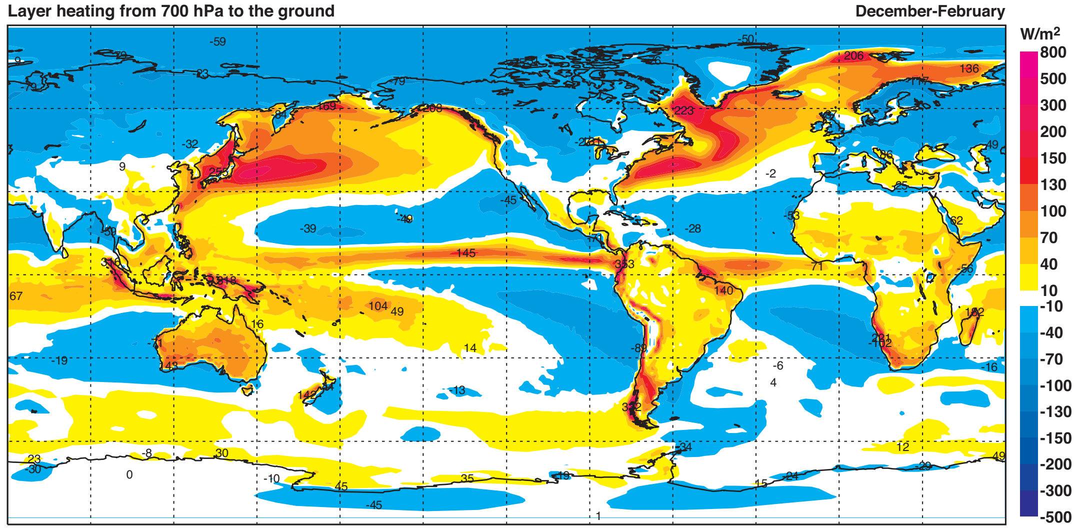

Layer heating from 700 hPa to the ground — June-August

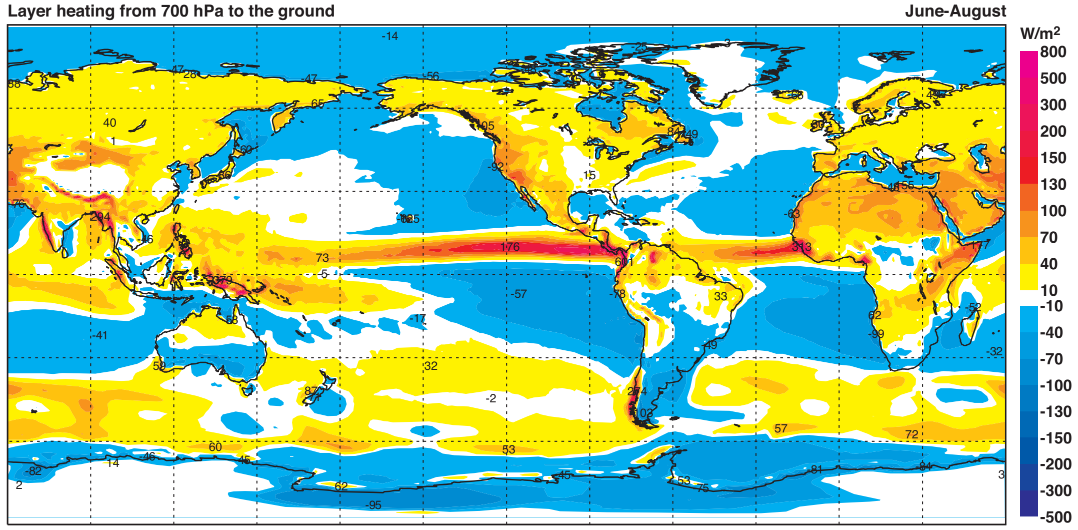

Layer heating from 700 hPa to the ground — Interannual variability

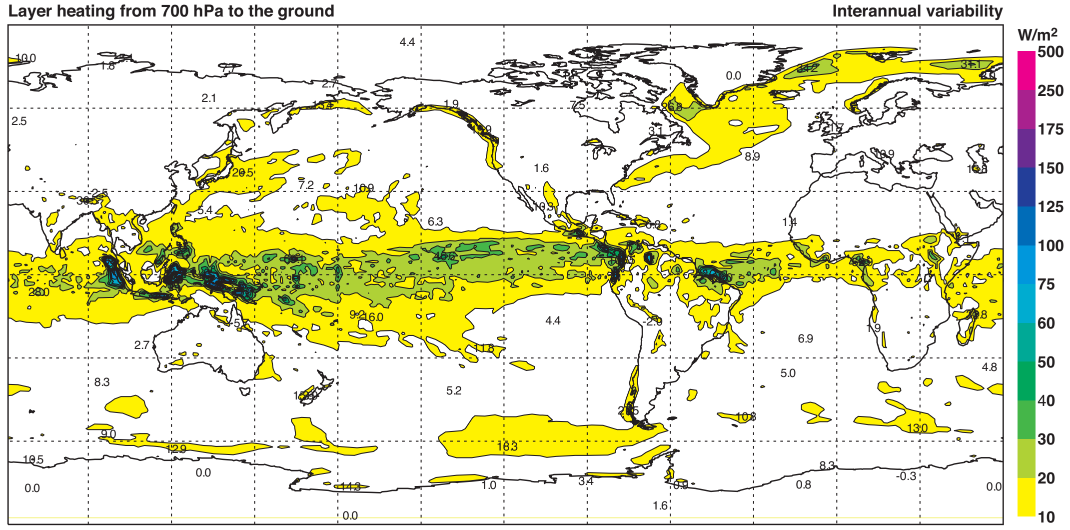

Layer heating from 700 hPa to the ground — March-May

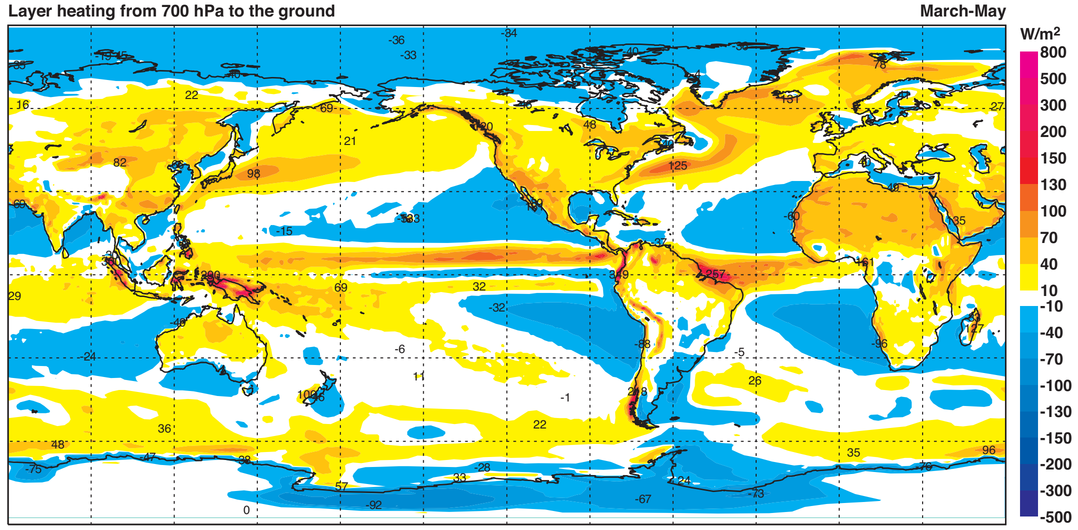

Layer heating from 700 hPa to the ground — September-November

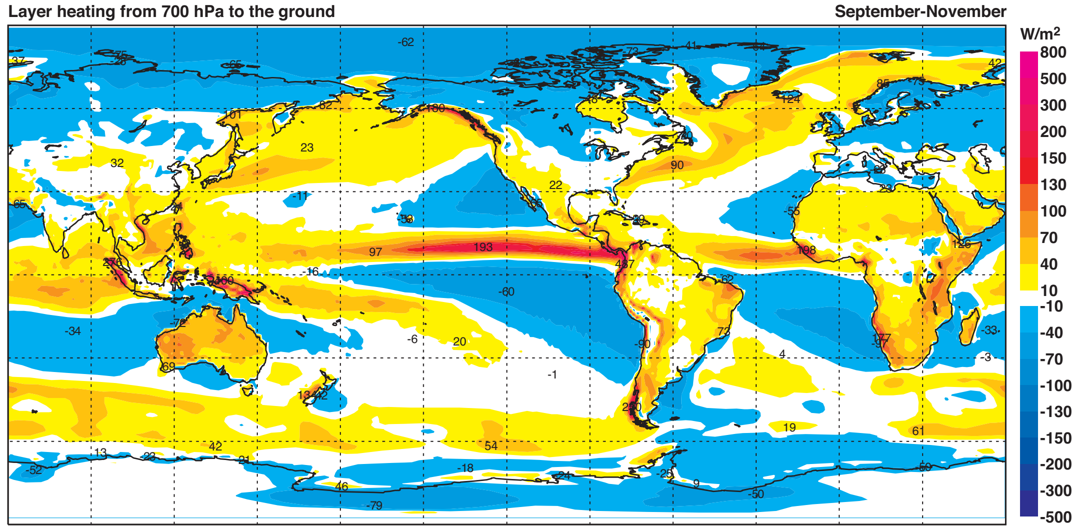

D11 Layer heating (Wm^{-2}) from 700 hPa to the ground.

Absolute vorticity ($10^{-5}s^{-1}$) with the vector divergent wind at 200 hPa — Annual mean

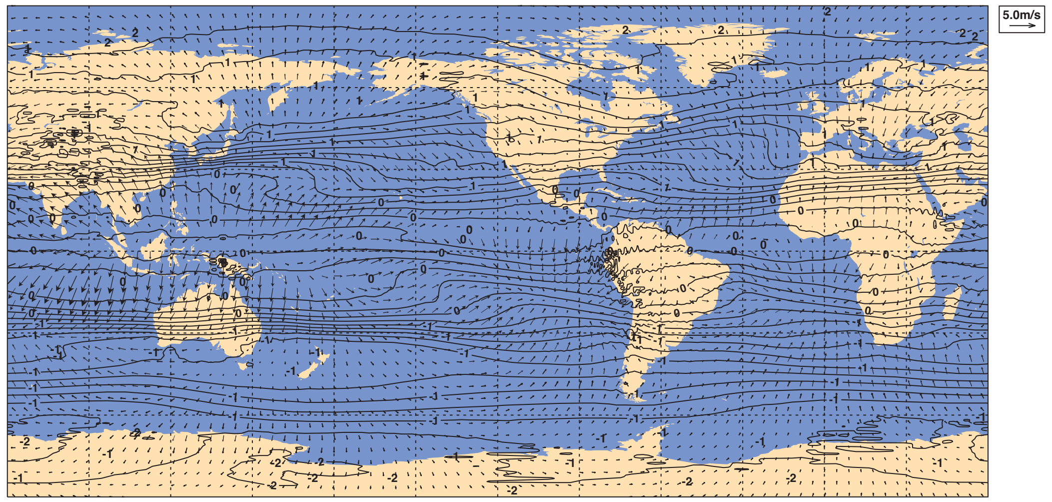

Absolute vorticity ($10^{-5}s^{-1}$) with the vector divergent wind at 200 hPa — December-February

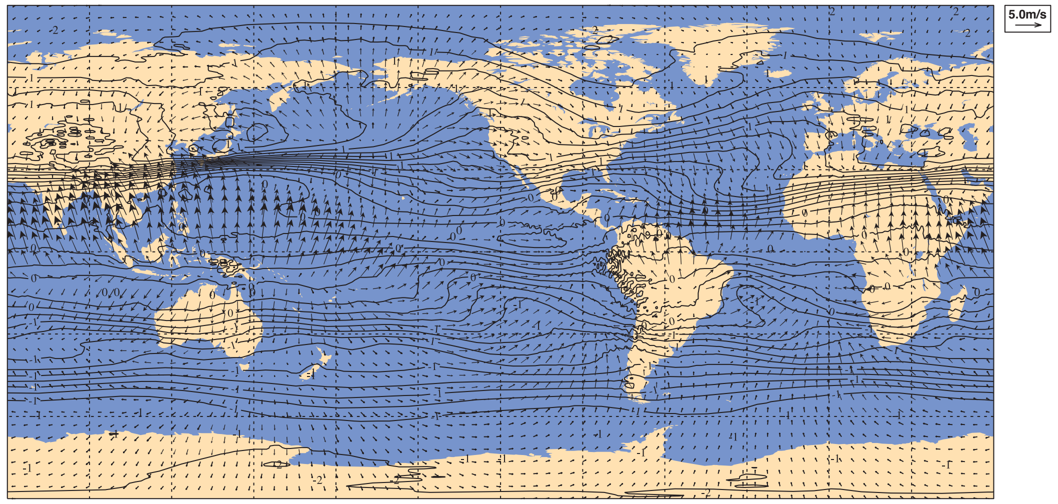

Absolute vorticity ($10^{-5}s^{-1}$) with the vector divergent wind at 200 hPa — June-August

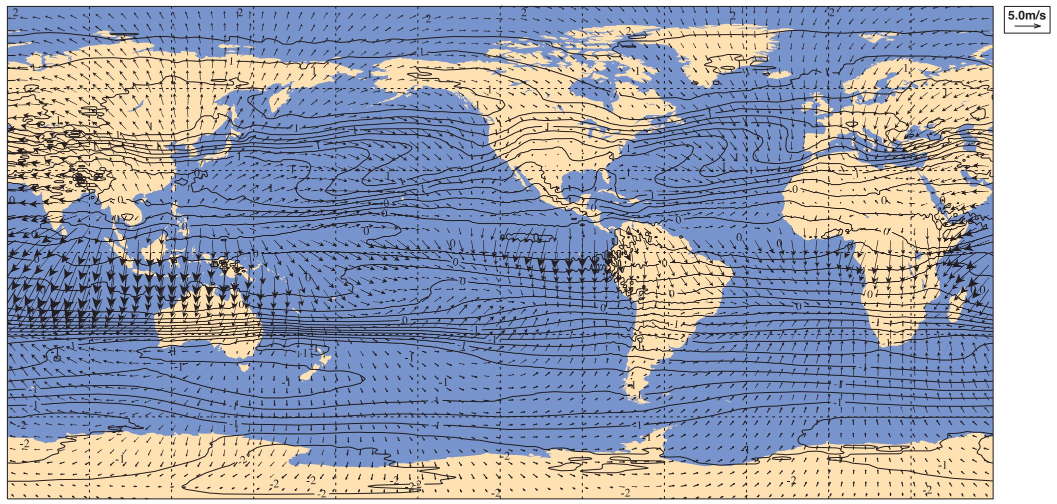

Absolute vorticity ($10^{-6}s^{-1}$) (contours) with the magnitude of the vector divergent wind (ms^{-1}) at 200 hPa — Interannual variability

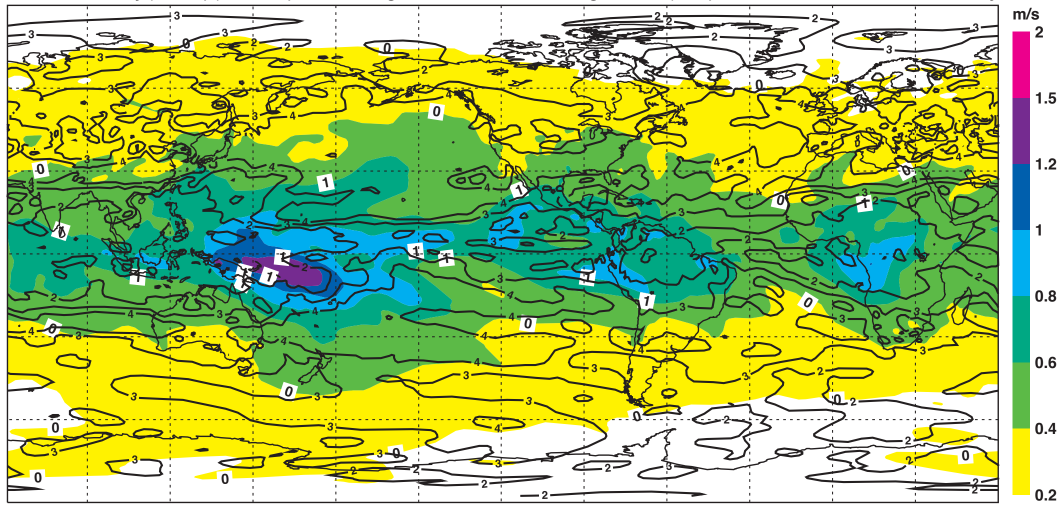

Absolute vorticity ($10^{-5}s^{-1}$) with the vector divergent wind at 200 hPa — March-May

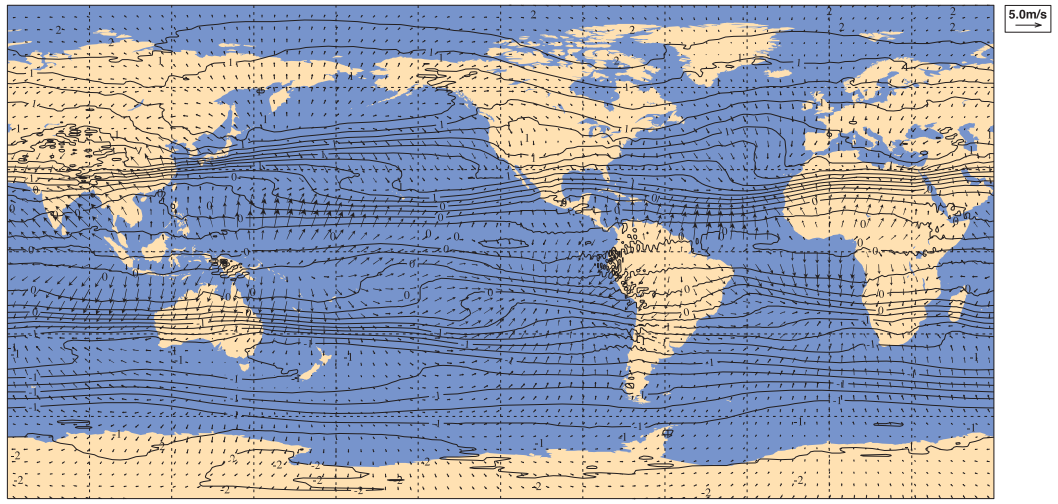

Absolute vorticity ($10^{-5}s^{-1}$) with the vector divergent wind at 200 hPa — September-November

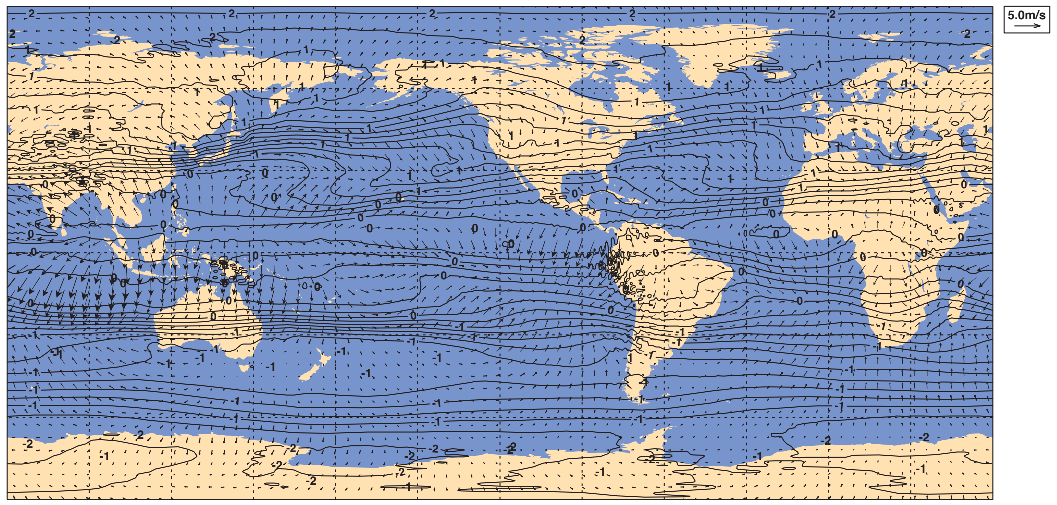

D12 Absolute vorticity ($10^{-5}s^{-1}$) (contours) with the vector divergent wind (ms^{-1}) at 200 hPa. For the interannual variability, the isotachs are plotted (colour shading) instead of the vector wind.

Streamfunction ($10^6 m^2 s^{-1}$) with velocity potential ($10^6 m^2 s^{-1}$) at 200 hPa — Annual mean

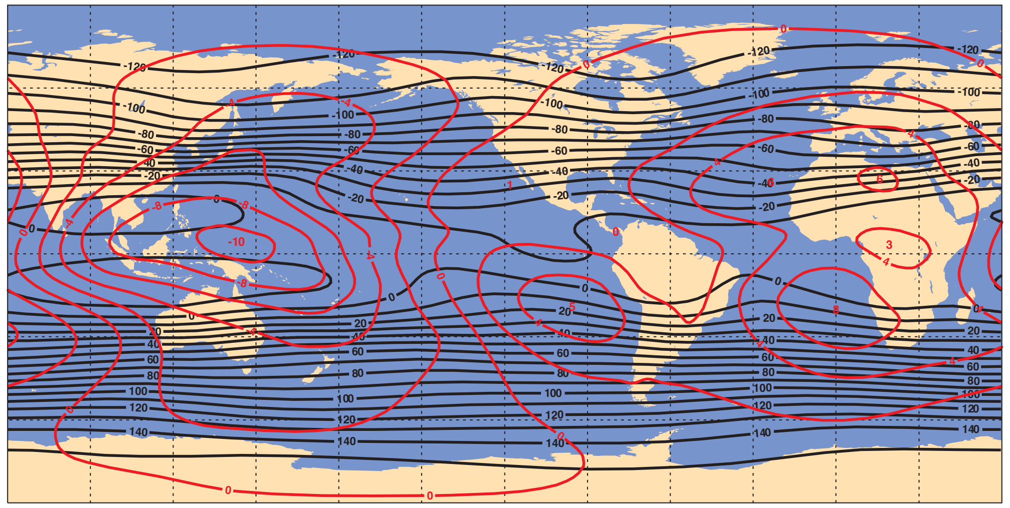

Streamfunction ($10^6 m^2 s^{-1}$) with velocity potential ($10^6 m^2 s^{-1}$) at 200 hPa — December-February

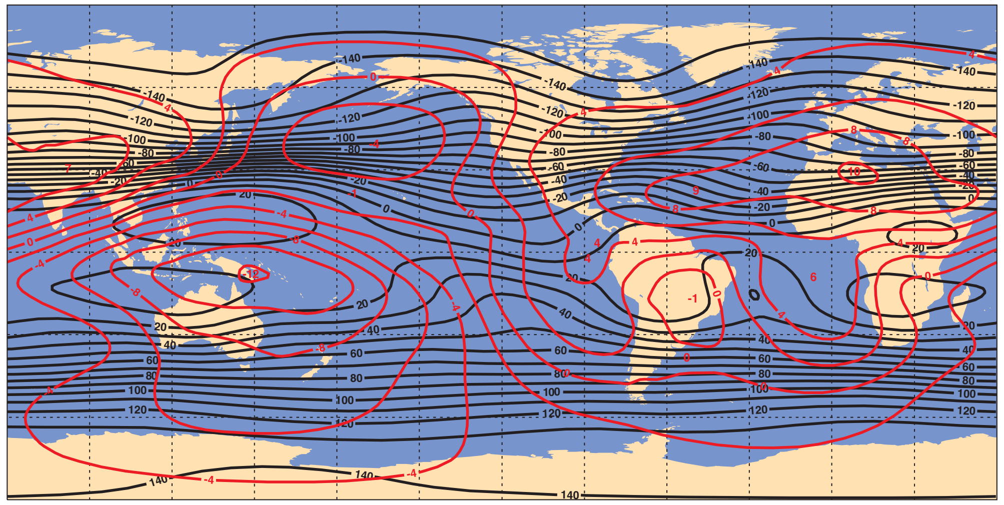

Streamfunction ($10^6 m^2 s^{-1}$) with velocity potential ($10^6 m^2 s^{-1}$) at 200 hPa — June-August

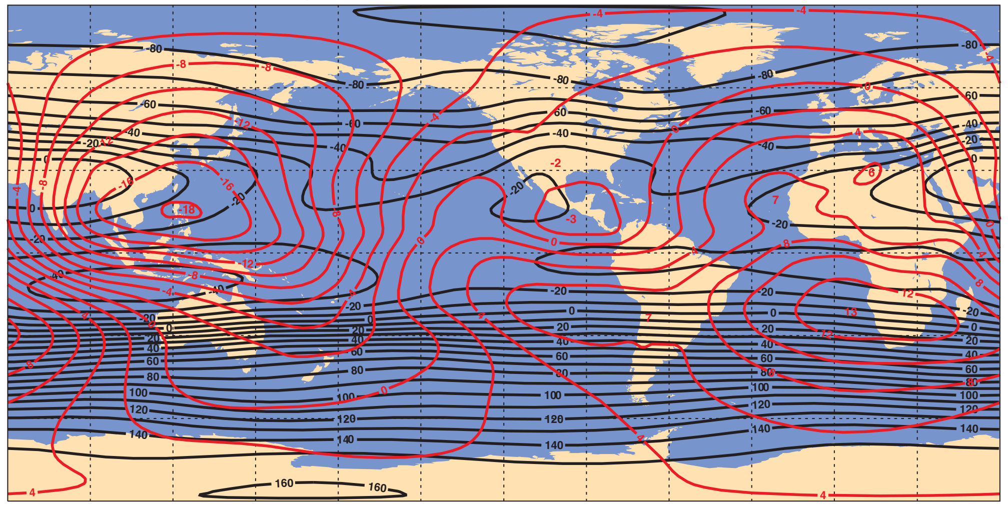

Streamfunction ($10^6 m^2 s^{-1}$) with velocity potential ($10^6 m^2 s^{-1}$) at 200 hPa — Interannual variability

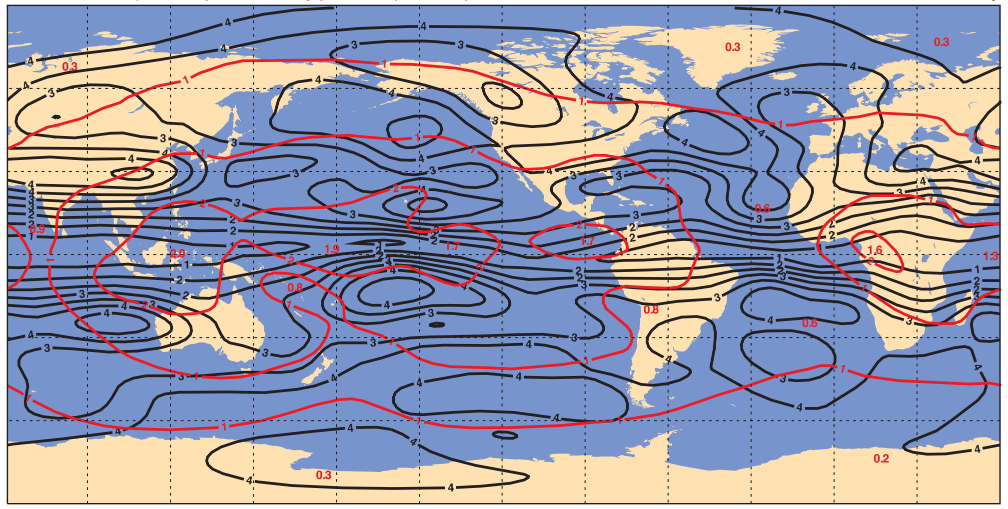

Streamfunction ($10^6 m^2 s^{-1}$) with velocity potential ($10^6 m^2 s^{-1}$) at 200 hPa — March-May

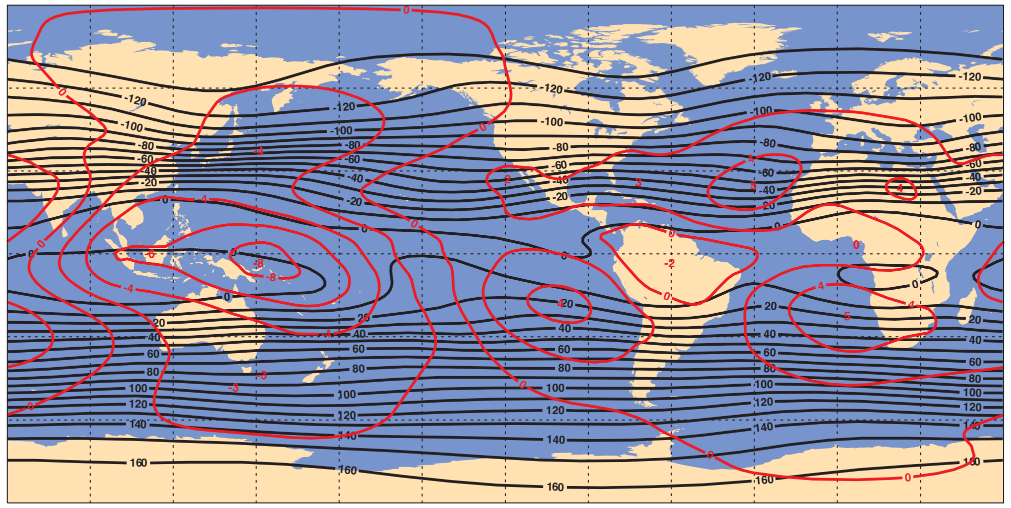

Streamfunction ($10^6 m^2 s^{-1}$) with velocity potential ($10^6 m^2 s^{-1}$) at 200 hPa — September-November

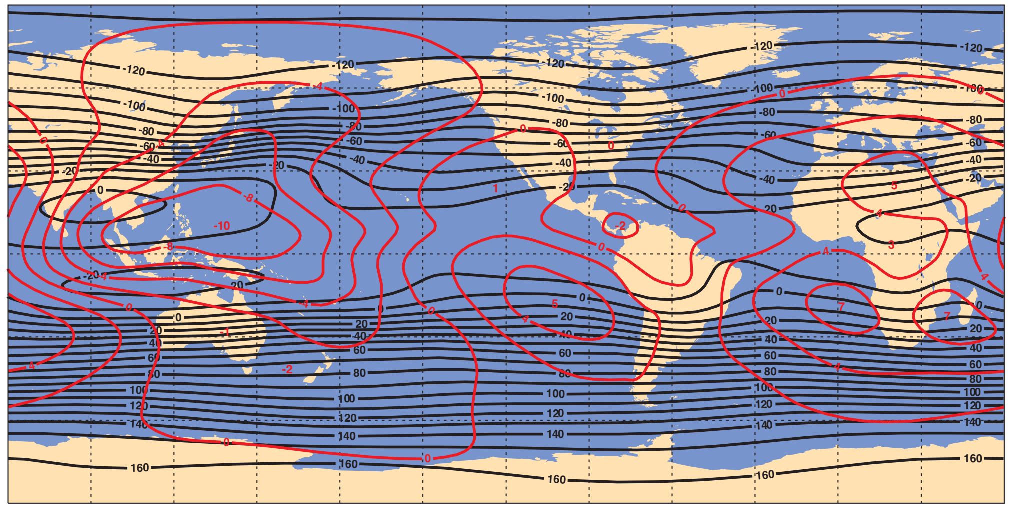

D13 Streamfunction ($10^6 m^2 s^{-1}$) (black contours) with velocity potential ($10^6 m^2 s^{-1}$) (red contours) at 200 hPa.

Streamfunction ($10^6 m^2 s^{-1}$) with velocity potential ($10^6 m^2 s^{-1}$) at 850 hPa — Annual mean

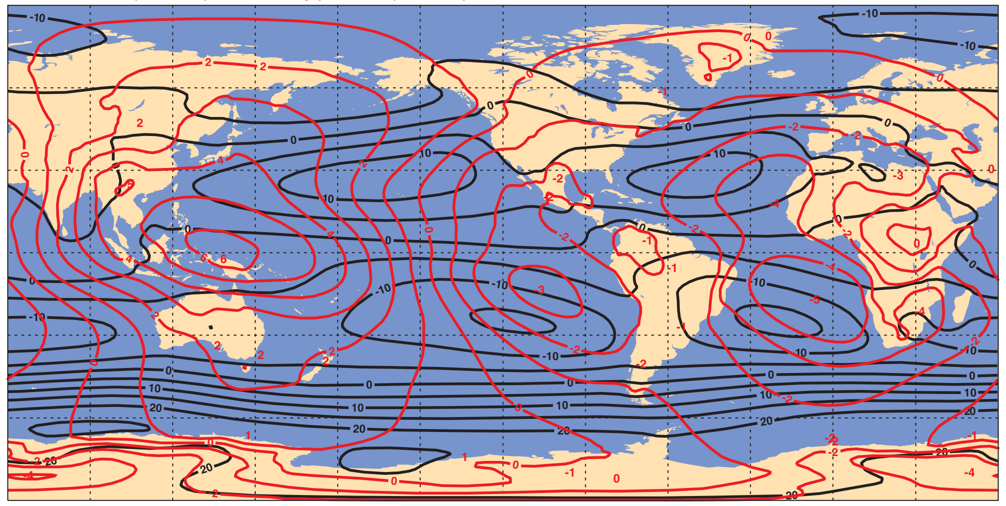

Streamfunction ($10^6 m^2 s^{-1}$) with velocity potential ($10^6 m^2 s^{-1}$) at 850 hPa — December-February

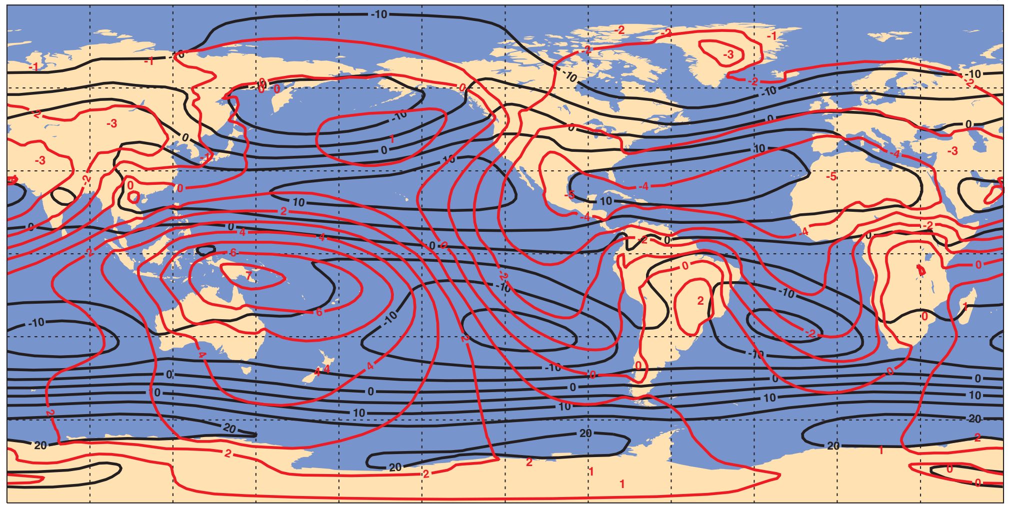

Streamfunction ($10^6 m^2 s^{-1}$) with velocity potential ($10^6 m^2 s^{-1}$) at 850 hPa — June-August

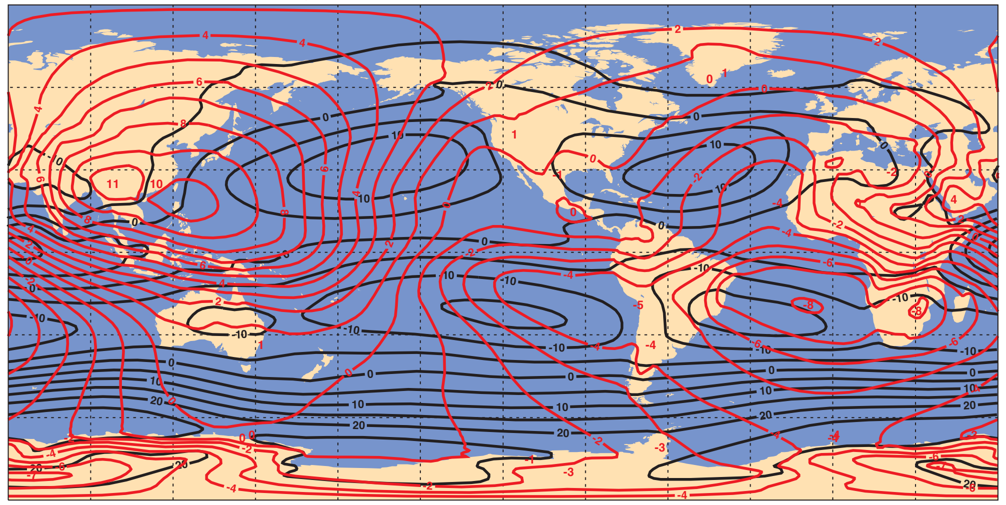

Streamfunction ($10^6 m^2 s^{-1}$) with velocity potential ($10^6 m^2 s^{-1}$) at 850 hPa — Interannual variability

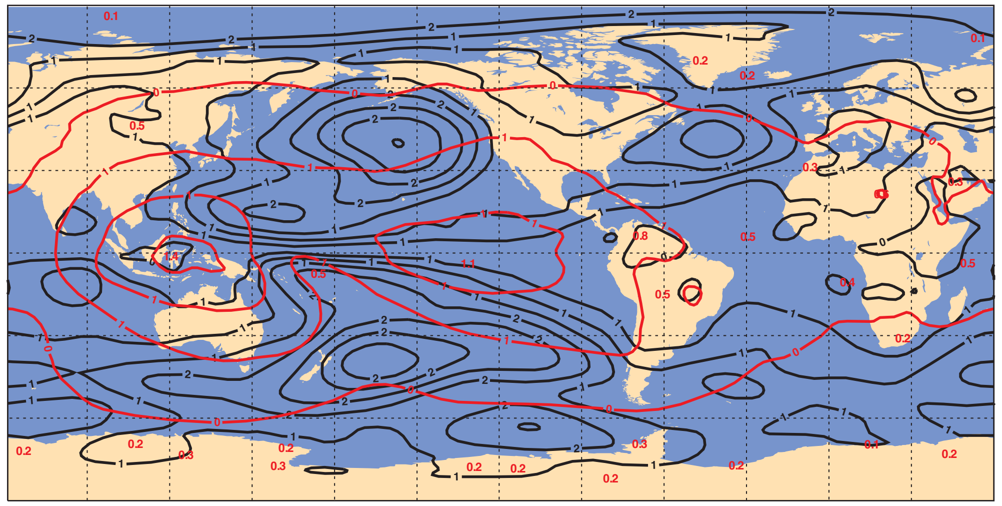

Streamfunction ($10^6 m^2 s^{-1}$) with velocity potential ($10^6 m^2 s^{-1}$) at 850 hPa — March-May

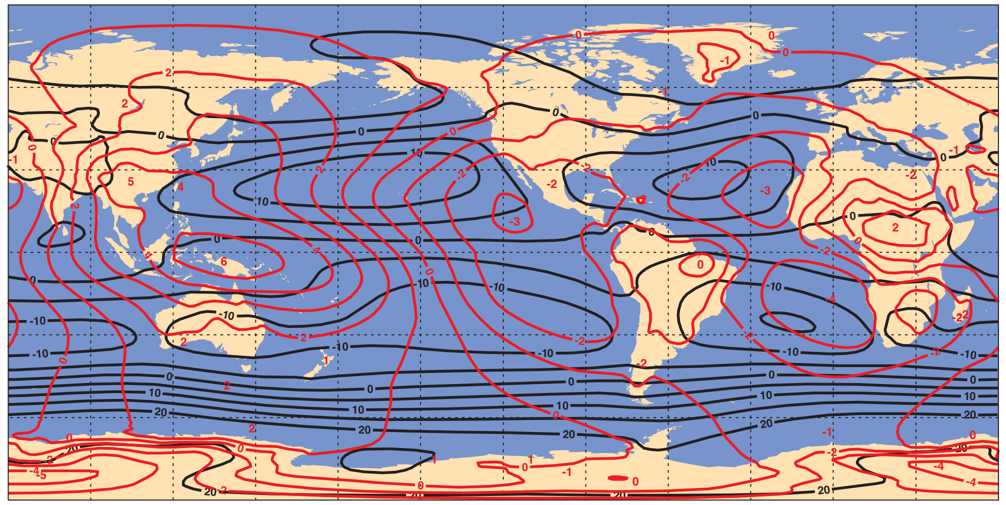

Streamfunction ($10^6 m^2 s^{-1}$) with velocity potential ($10^6 m^2 s^{-1}$) at 850 hPa — September-November

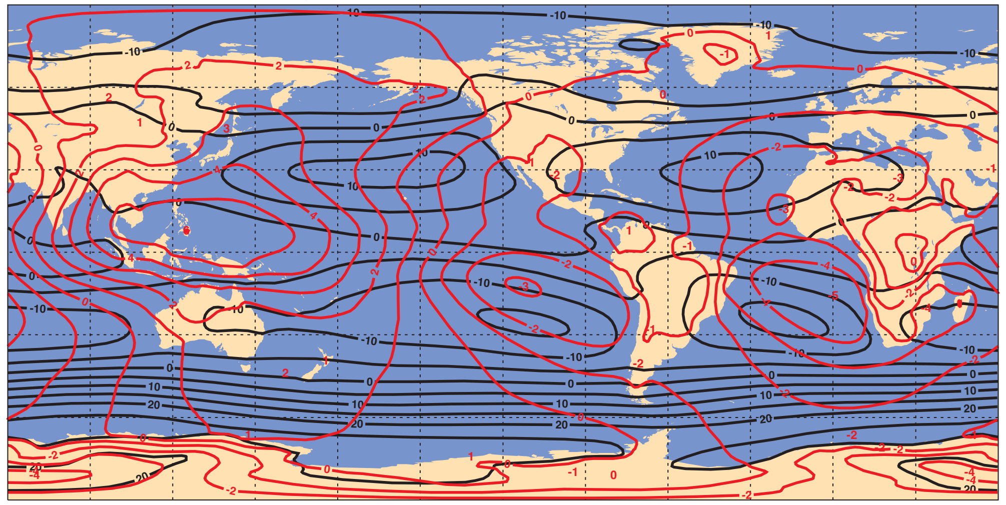

D14 Streamfunction ($10^6 m^2 s^{-1}$) (black contours) with velocity potential ($10^6 m^2 s^{-1}$) (red contours) at 850 hPa.

Geopotential height (m) (contours) and isotachs at 250 hPa — Annual mean

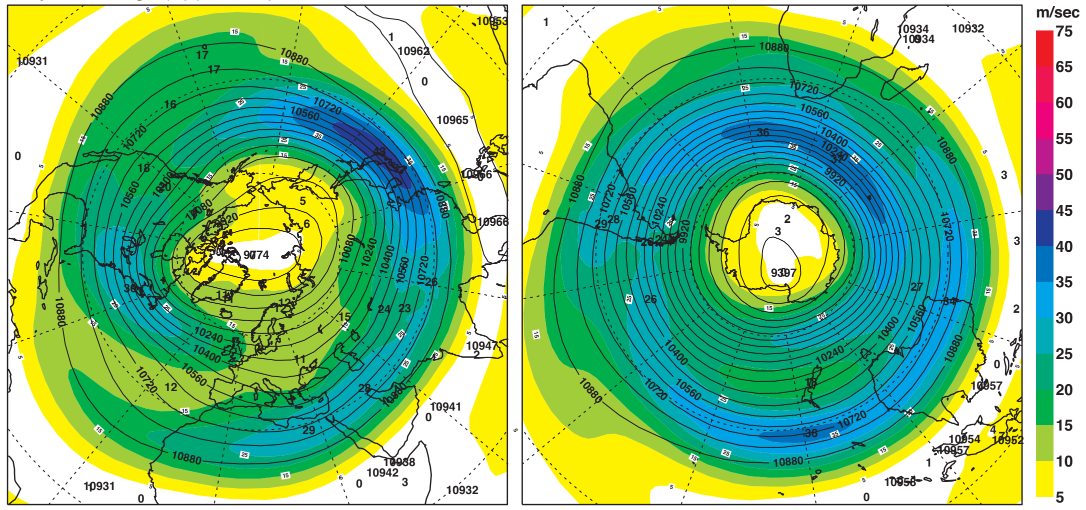

Geopotential height (m) (contours) and isotachs at 250 hPa — December-February

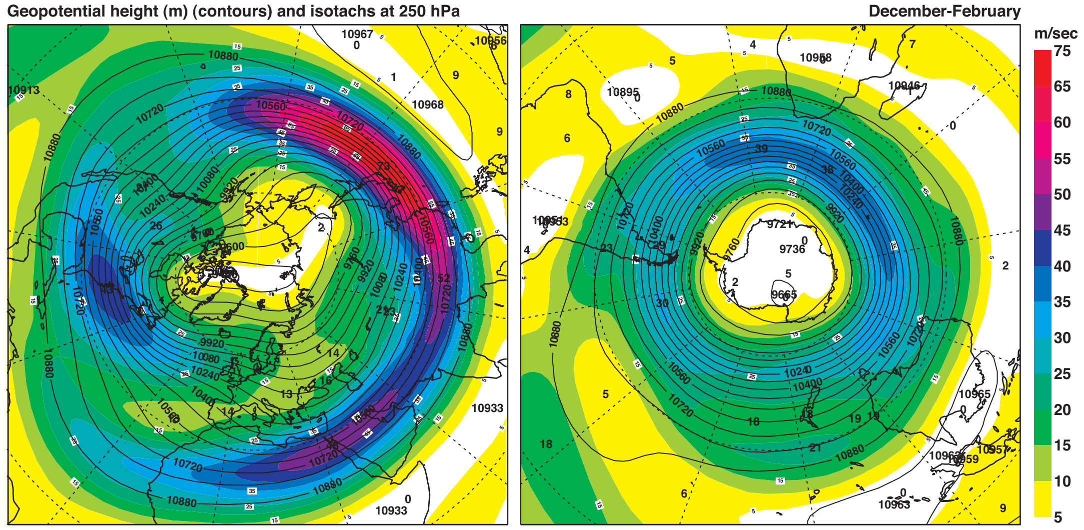

Geopotential height (m) (contours) and isotachs at 250 hPa — June-August

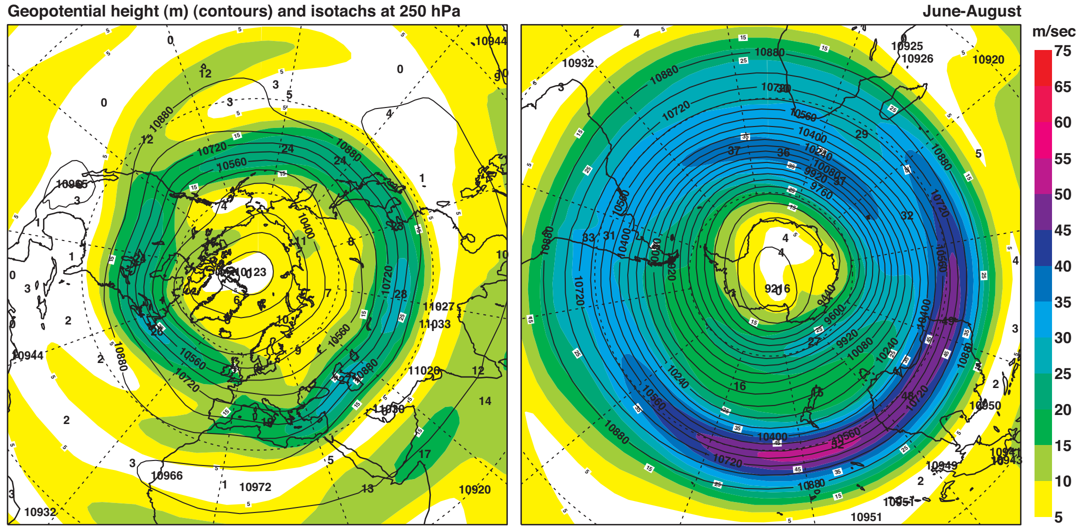

Geopotential height (m) (contours) and isotachs at 250 hPa — Interannual variability

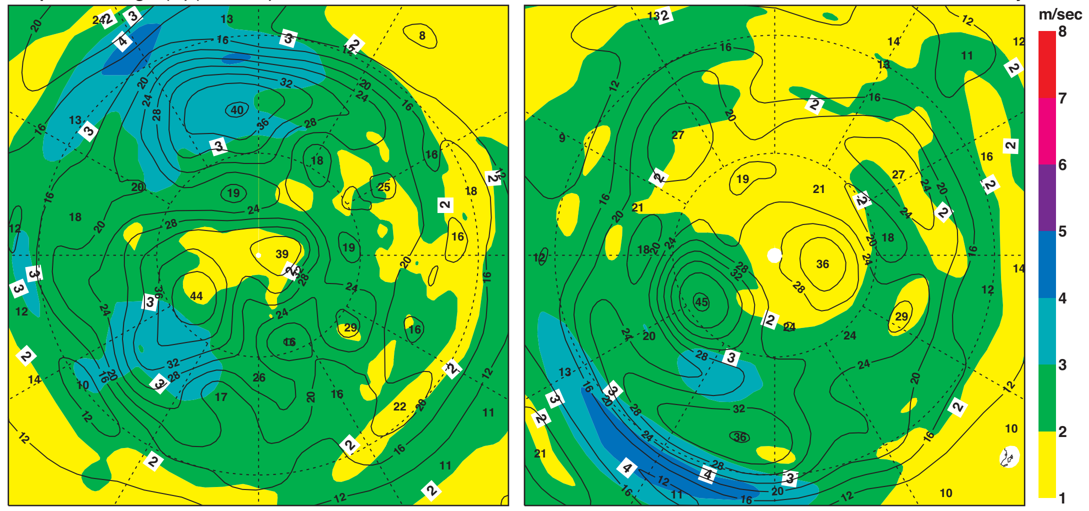

Geopotential height (m) (contours) and isotachs at 250 hPa — March-May

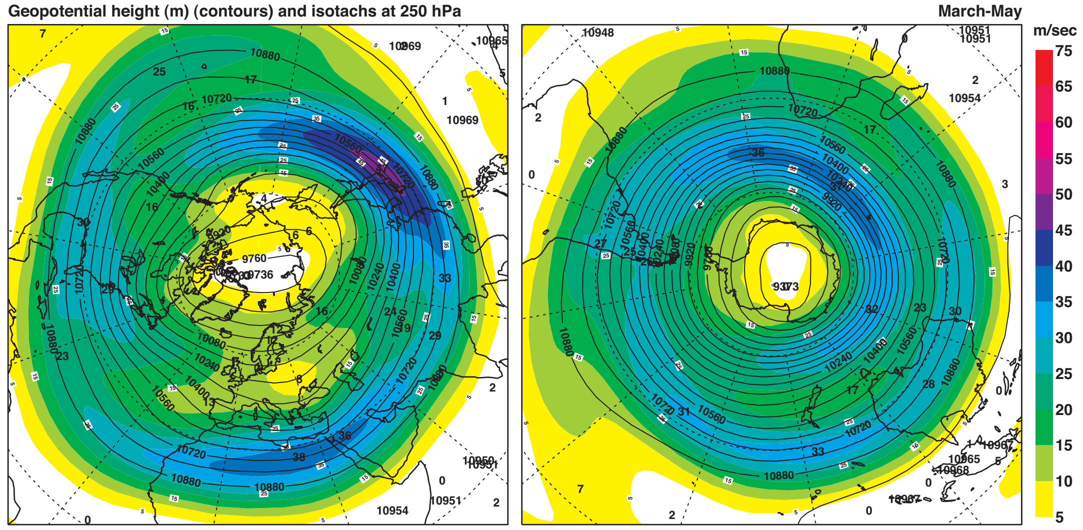

Geopotential height (m) (contours) and isotachs at 250 hPa — September-November

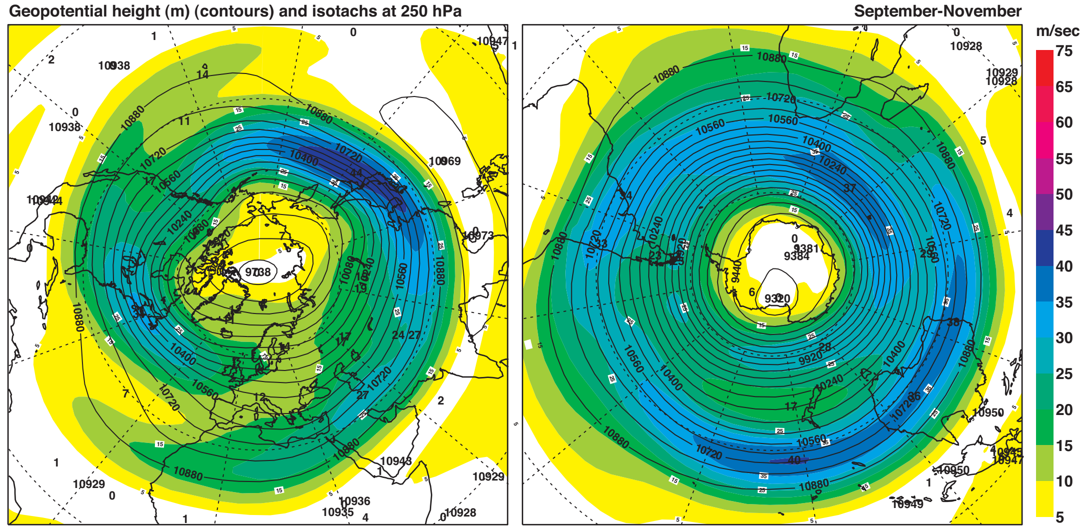

D15 Isotachs (ms^{-1}) (colour shading) and geopotential height (m) (contours) at 250 hPa.

Geopotential height (m) (contours) and isotachs at 1000 hPa — Annual mean

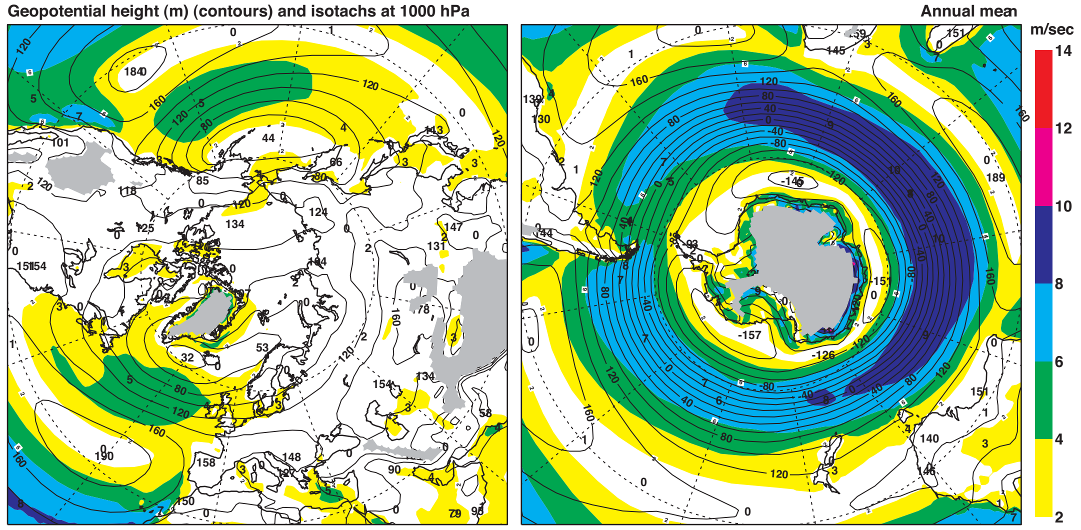

Geopotential height (m) (contours) and isotachs at 1000 hPa — December-February

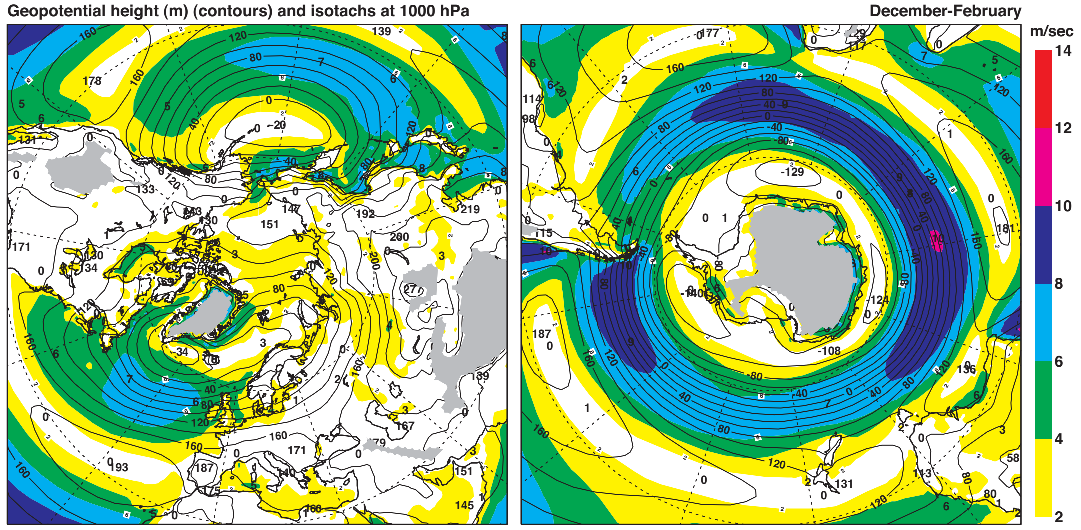

Geopotential height (m) (contours) and isotachs at 1000 hPa — June-August

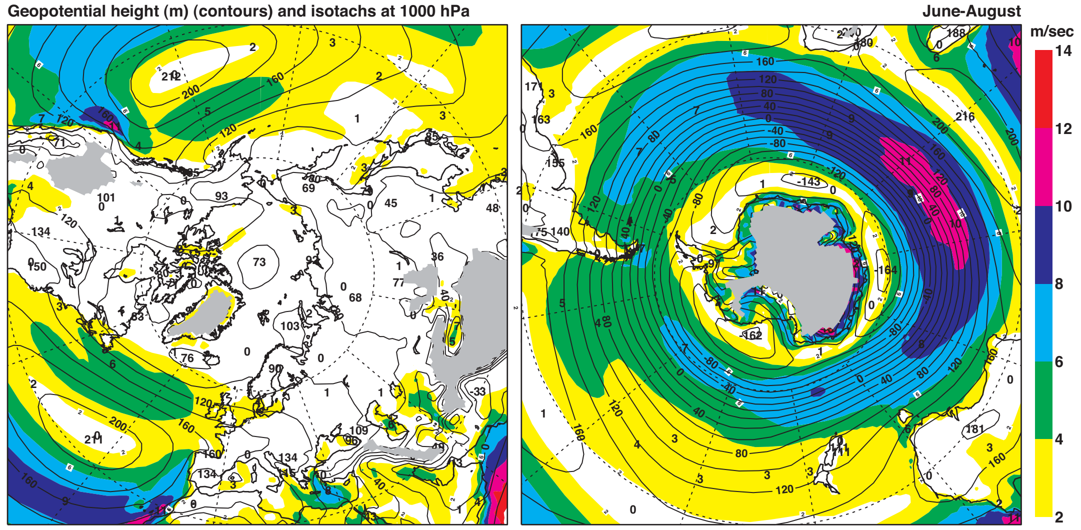

Geopotential height (m) (contours) and isotachs at 1000 hPa — Interannual variability

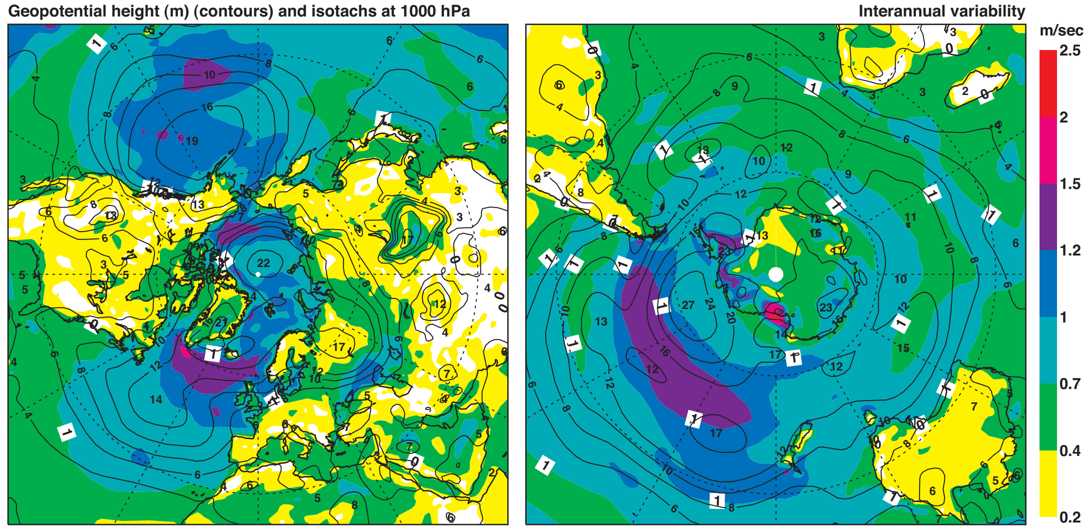

Geopotential height (m) (contours) and isotachs at 1000 hPa — March-May

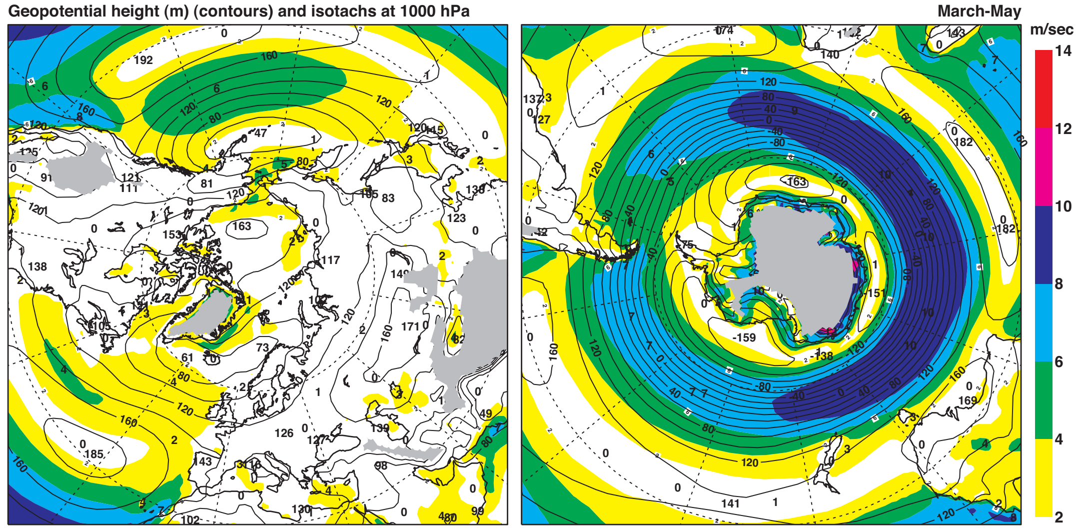

Geopotential height (m) (contours) and isotachs at 1000 hPa — September-November

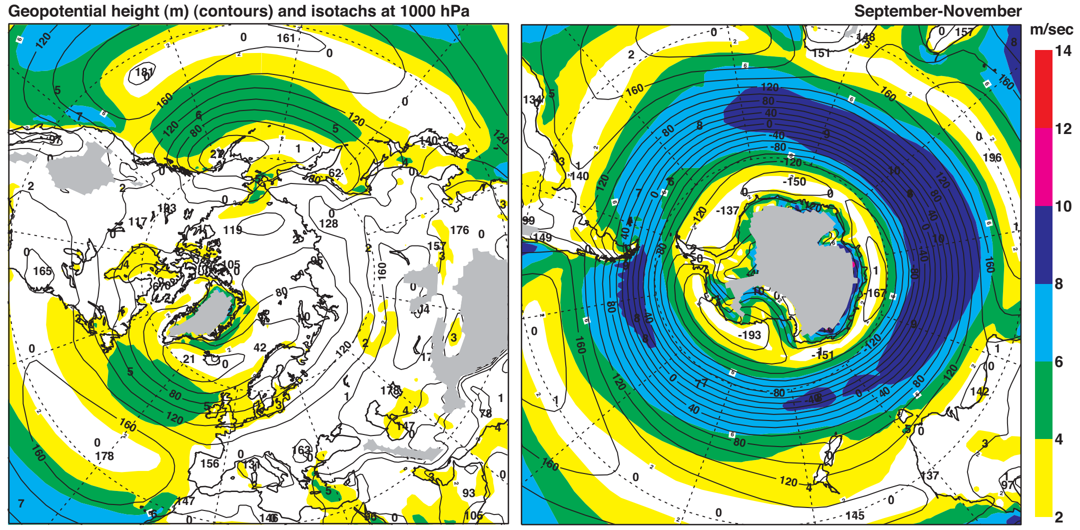

D16 Isotachs (ms^{-1}) (colour shading) and geopotential height (m) (contours) at 1000 hPa.

Mean zonal wind and E-vectors for 6 – 2 days at 250 hPa — Annual mean

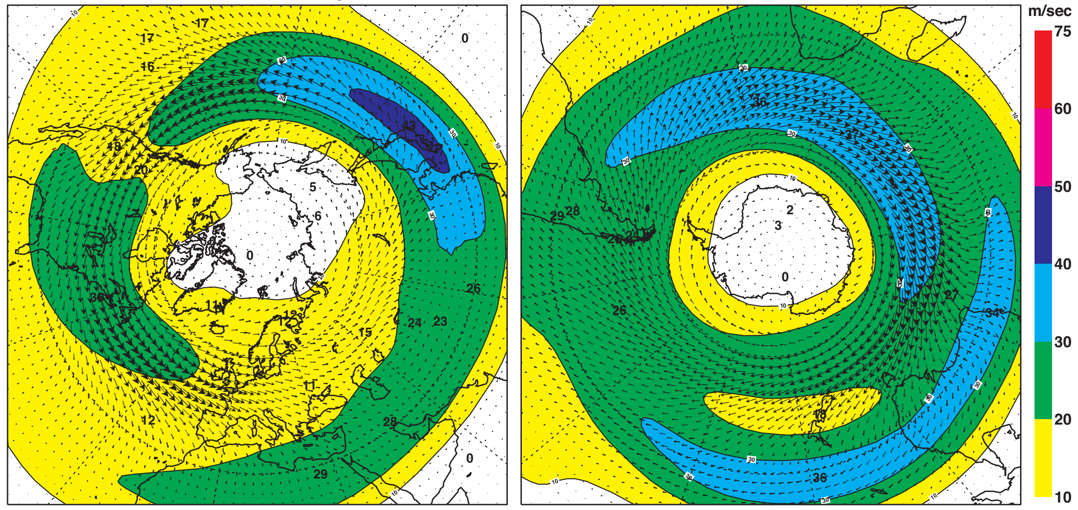

Mean zonal wind and E-vectors for 6 – 2 days at 250 hPa — December-February

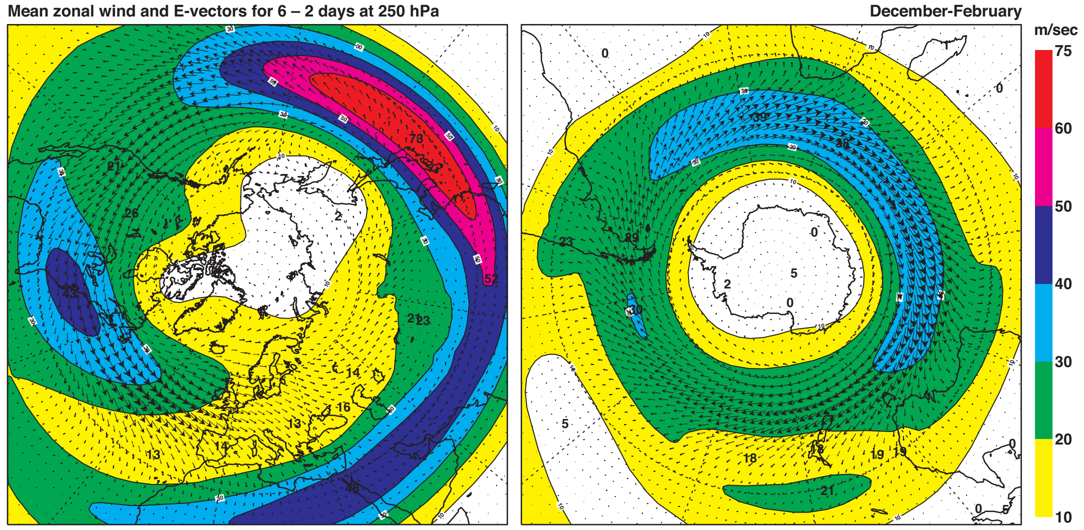

Mean zonal wind and E-vectors for 6 – 2 days at 250 hPa — June-August

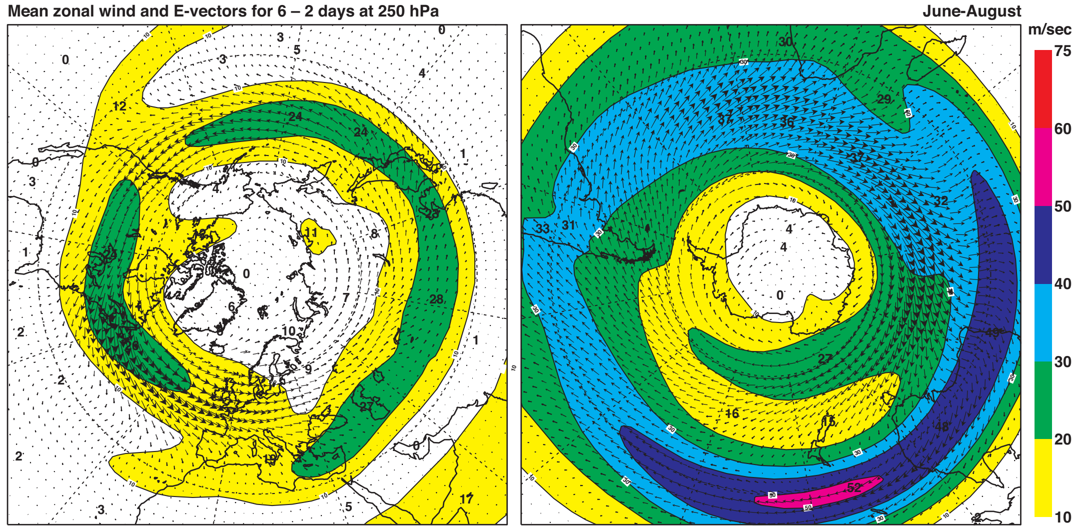

Mean zonal wind and the magnitude of the E-vectors (m^{2}s^2) (contours) for 6 – 2 days at 250 hPa — Interannual variability

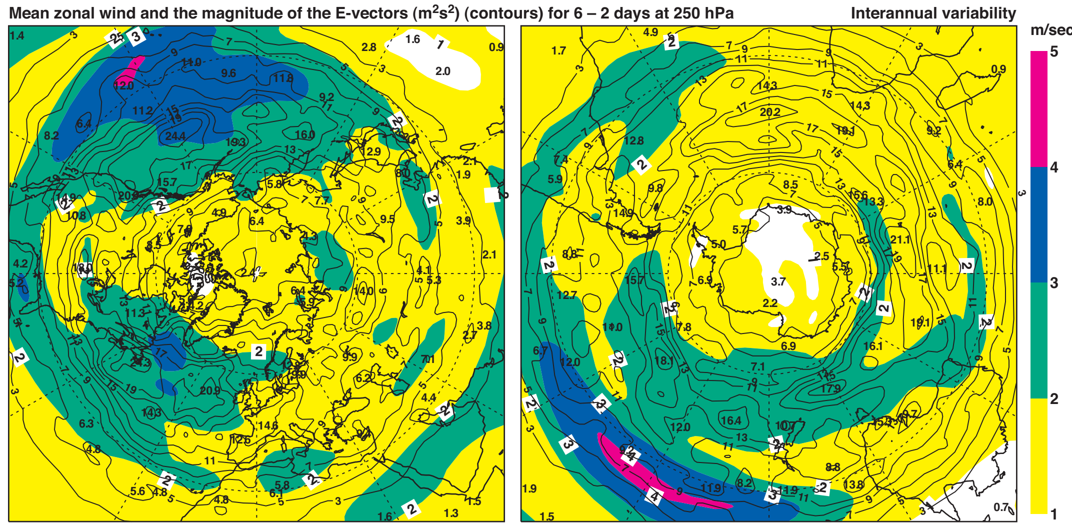

Mean zonal wind and E-vectors for 6 – 2 days at 250 hPa — March-May

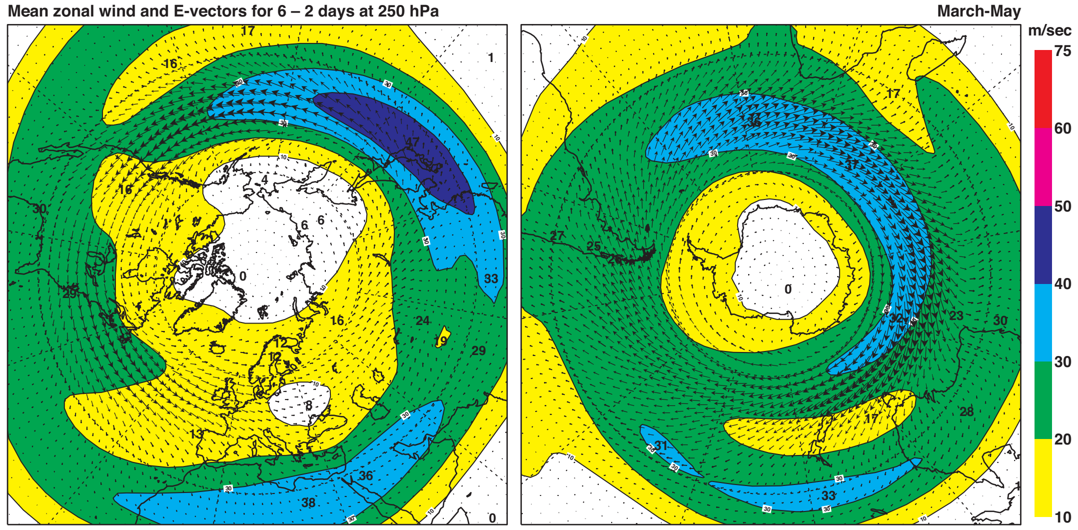

Mean zonal wind and E-vectors for 6 – 2 days at 250 hPa — September-November

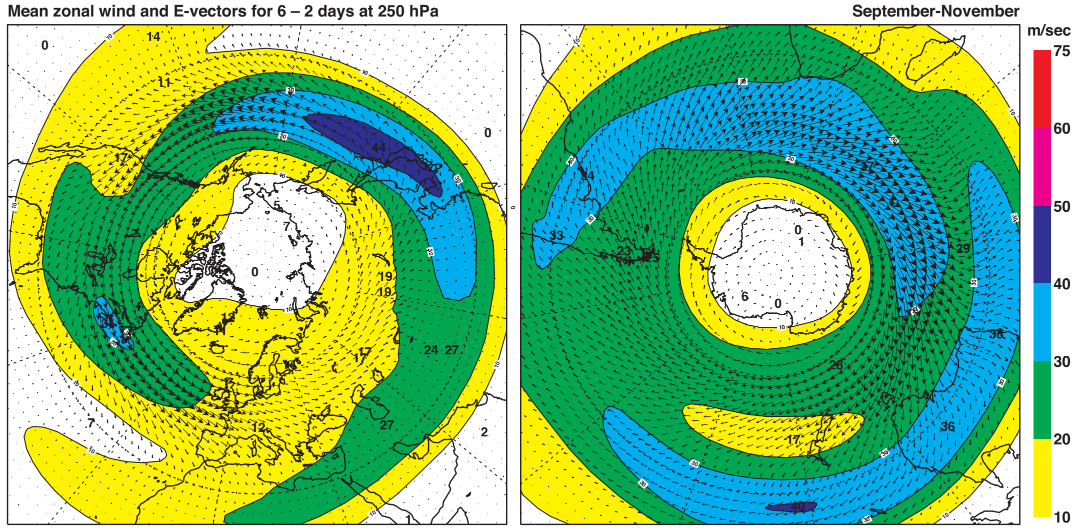

D17 Zonal wind (ms^{-1}) (colour shading) with the E-vector $(\overline{v'^2-u'^2}, -\overline{u'v'})$ (m^{2}s^{-2}) for 6–2 day band pass filtered winds at 250 hPa. For the interannual variability, the magnitude of the E-vector is plotted (contours) instead of the vector.

Geopotential height at 500 hPa — Annual mean

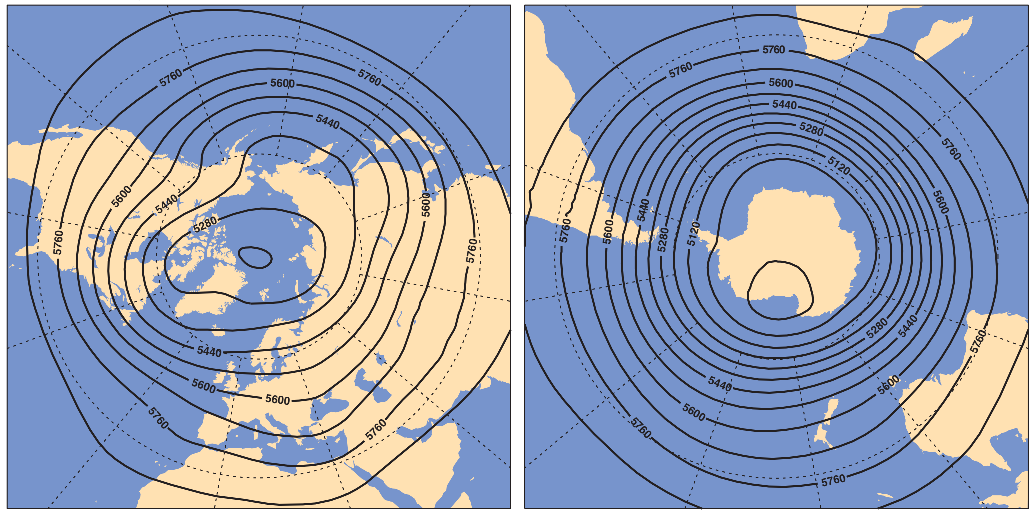

Geopotential height at 500 hPa — December-February

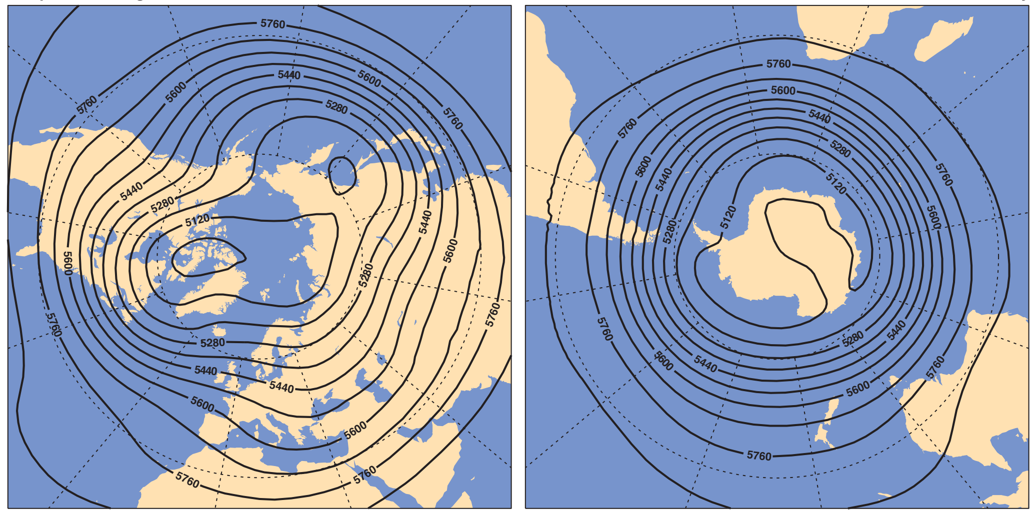

Geopotential height at 500 hPa — June-August

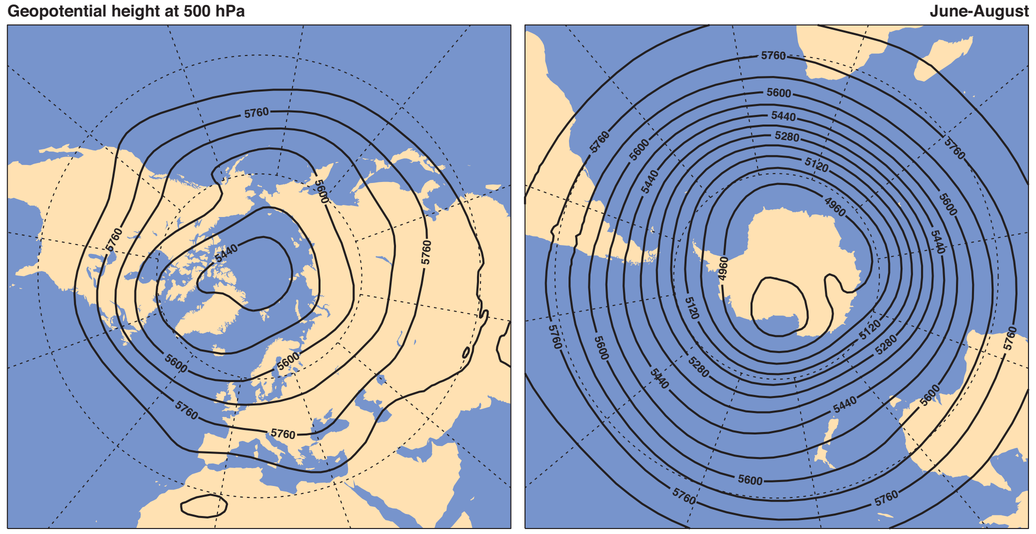

Geopotential height at 500 hPa — Interannual variability

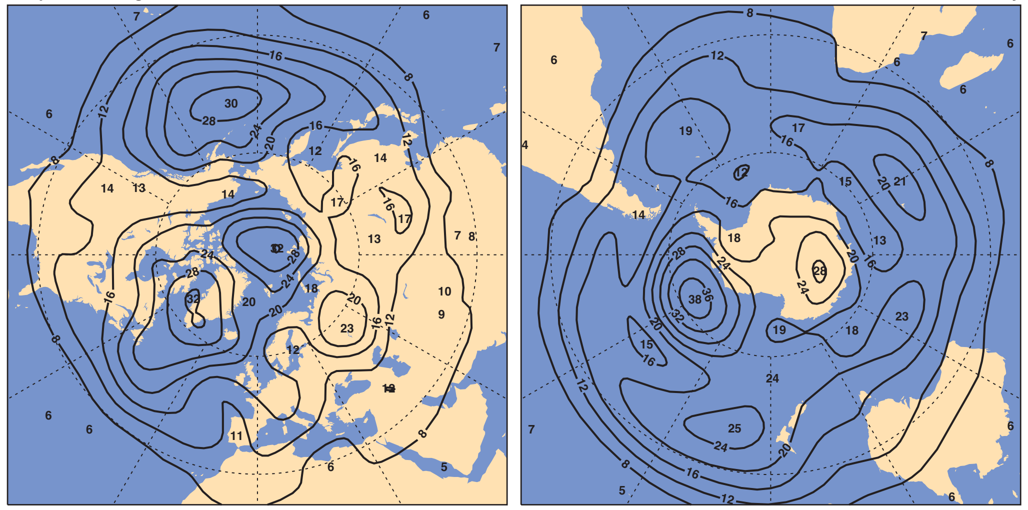

Geopotential height at 500 hPa — March-May

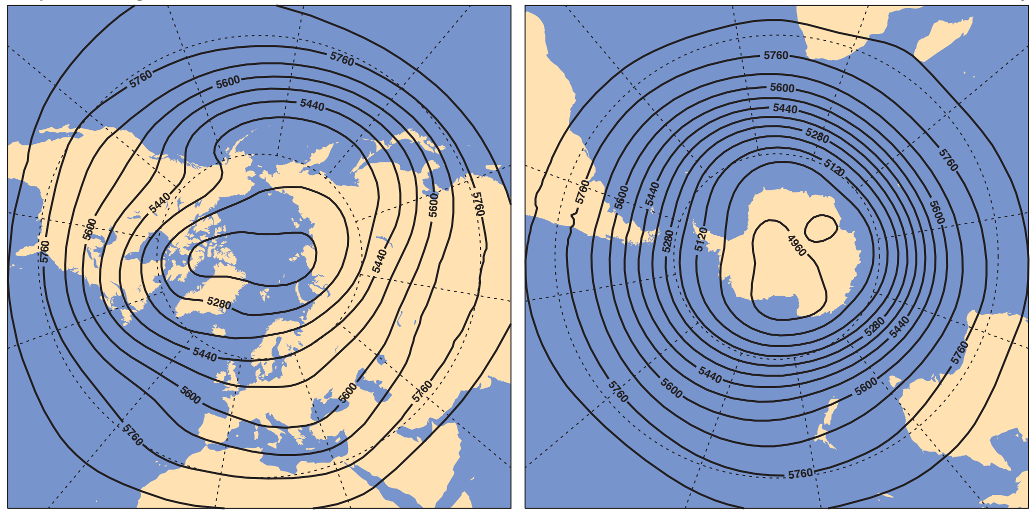

Geopotential height at 500 hPa — September-November

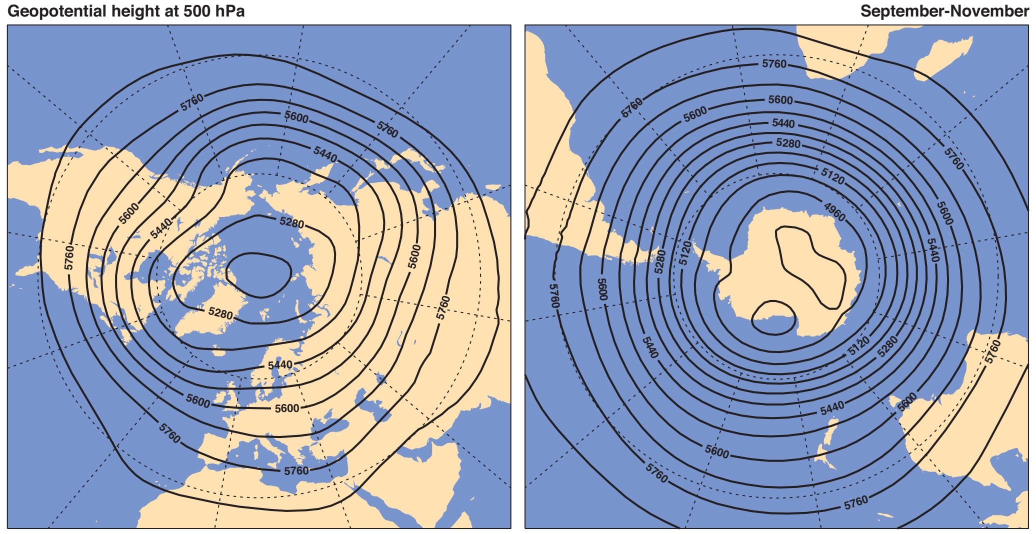

D18 Geopotential height (m) at 500 hPa.

Temperature with the 6-2 day transient horizontal fluxes of temperature at 700 hPa — Annual mean

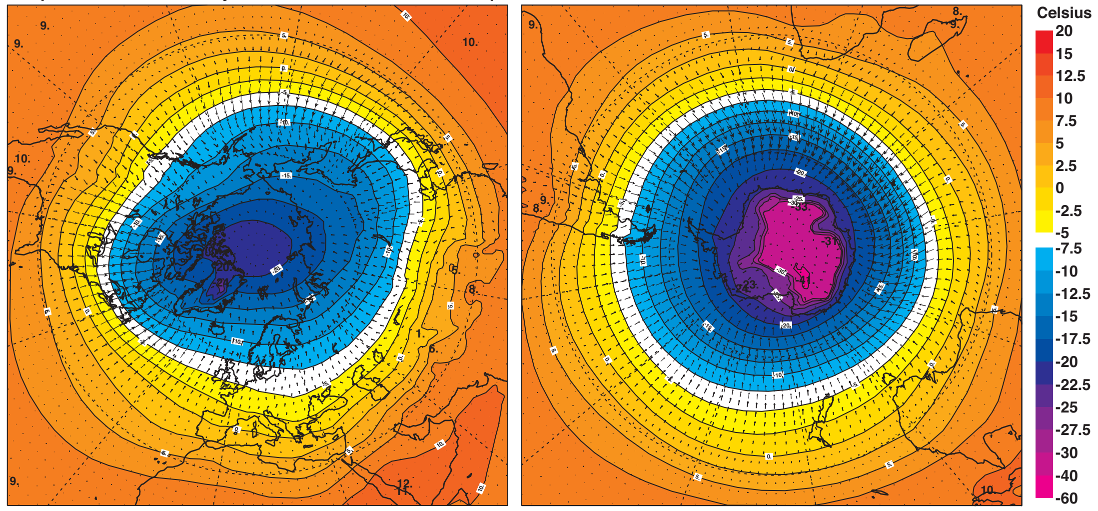

Temperature with the 6-2 day transient horizontal fluxes of temperature at 700 hPa — December-February

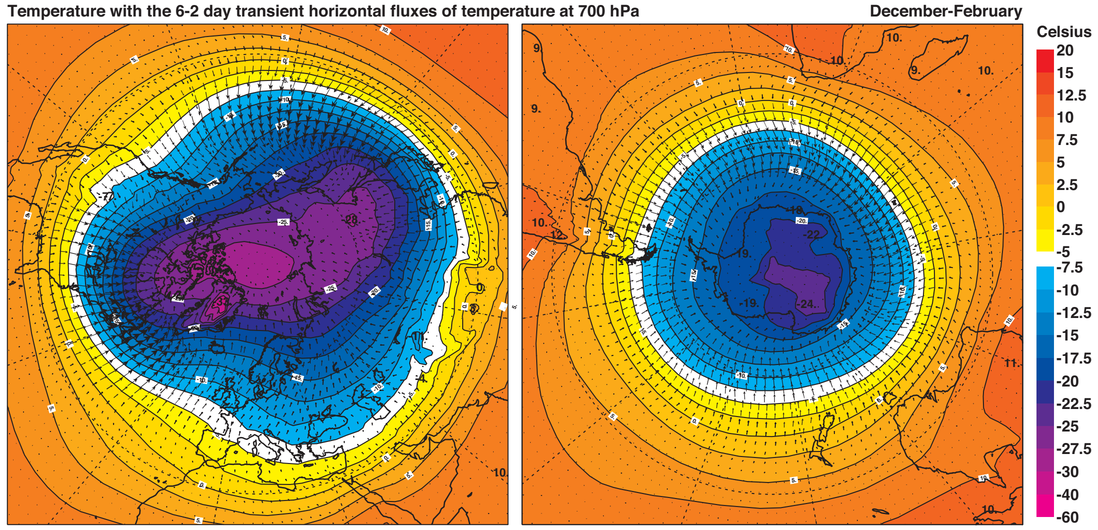

Temperature with the 6-2 day transient horizontal fluxes of temperature at 700 hPa — June-August

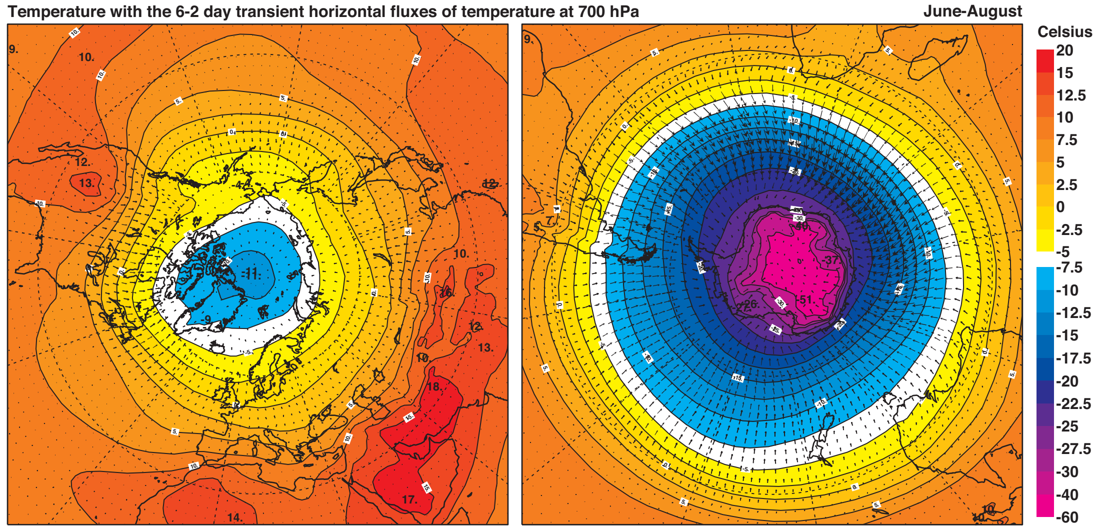

Temperature with the 6-2 day transient horizontal fluxes of temperature (Kms^{-1}) (contours) at 700 hPa — Interannual variability

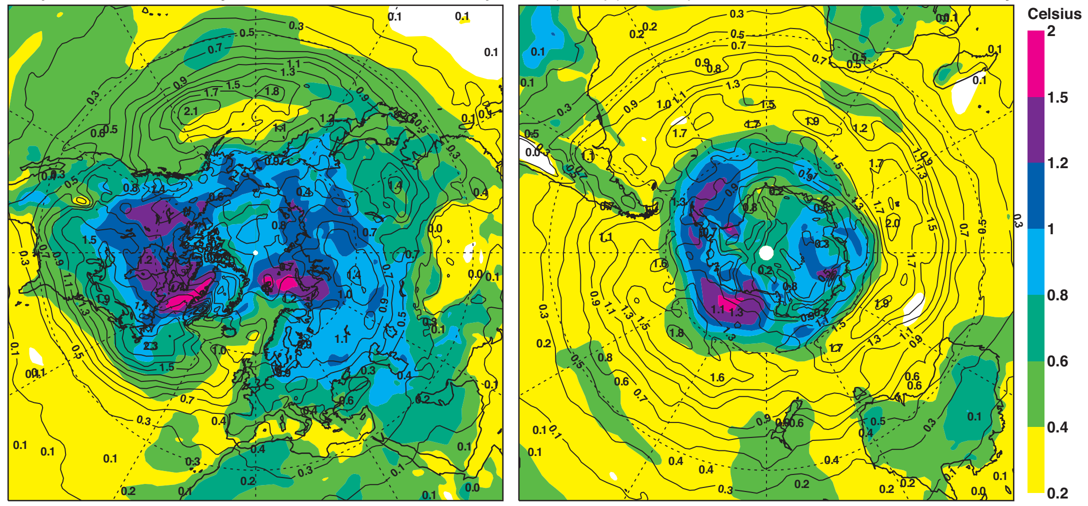

Temperature with the 6-2 day transient horizontal fluxes of temperature at 700 hPa — March-May

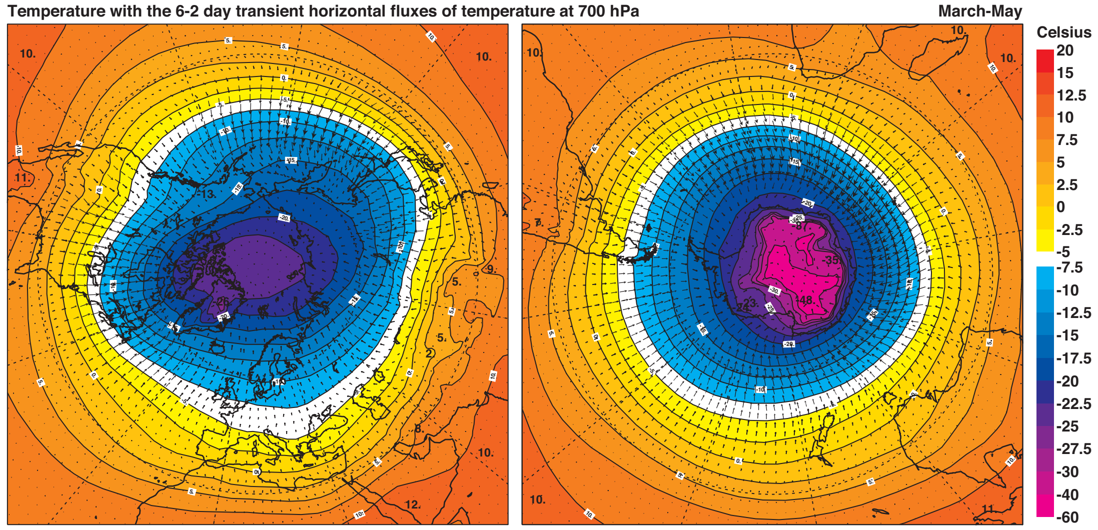

Temperature with the 6-2 day transient horizontal fluxes of temperature at 700 hPa — September-November

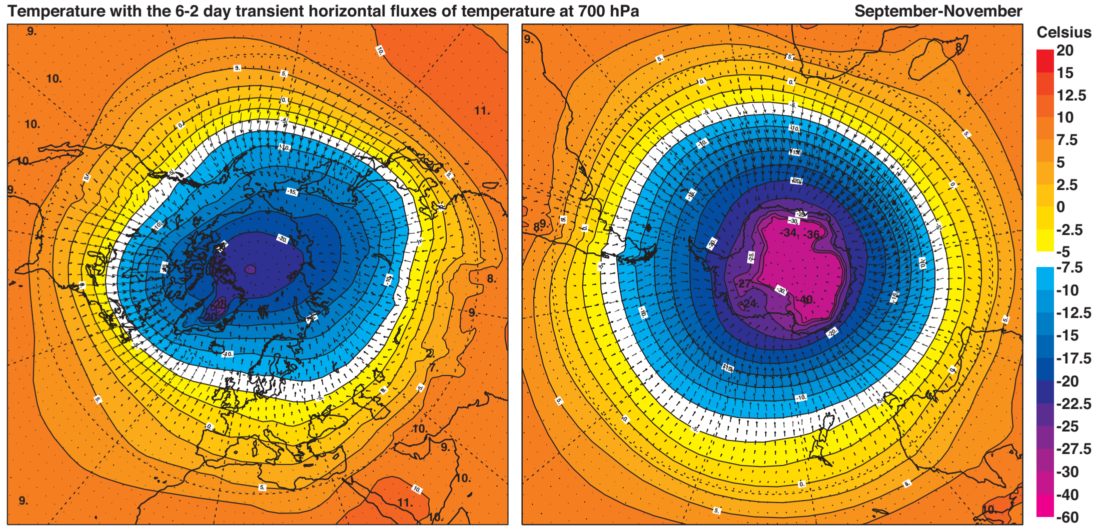

D19 Temperature (C) (colour shading) with the transient horizontal vector fluxes of temperature (Kms^{-1}) for 6–2 day band pass filtered data at 700 hPa. For the interannual variability, the magnitude of the fluxes is plotted (contours) instead of the vector.

Vertical (upward) transient fluxes of temperature at 700 hPa. Band-pass 6 – 2 days — Annual mean

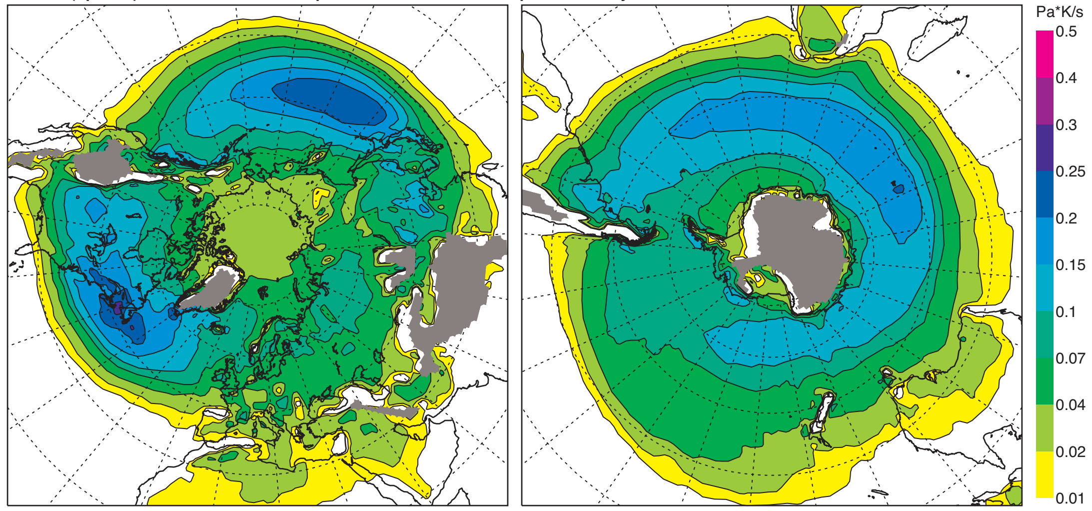

Vertical (upward) transient fluxes of temperature at 700 hPa. Band-pass 6 – 2 days — December-February

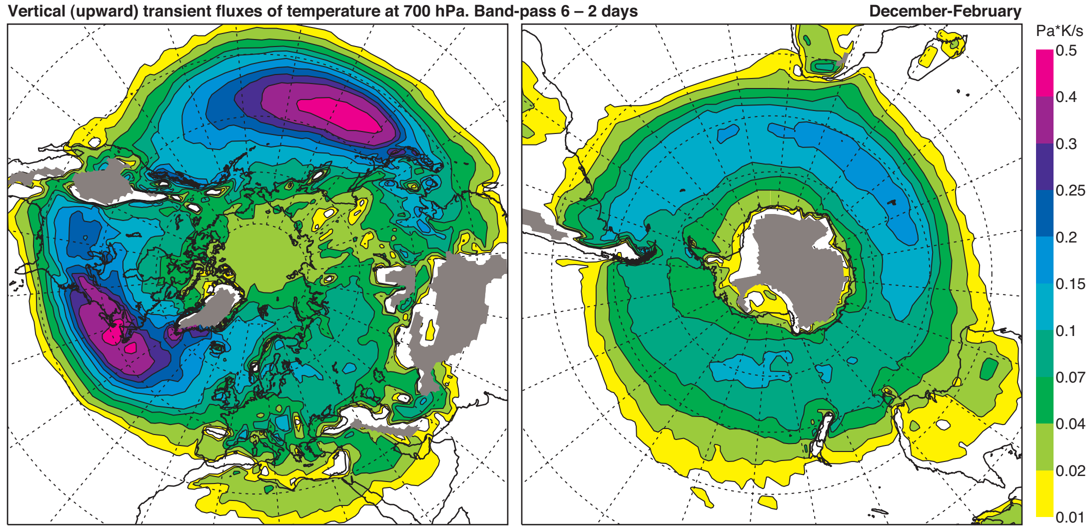

Vertical (upward) transient fluxes of temperature at 700 hPa. Band-pass 6 – 2 days — June-August

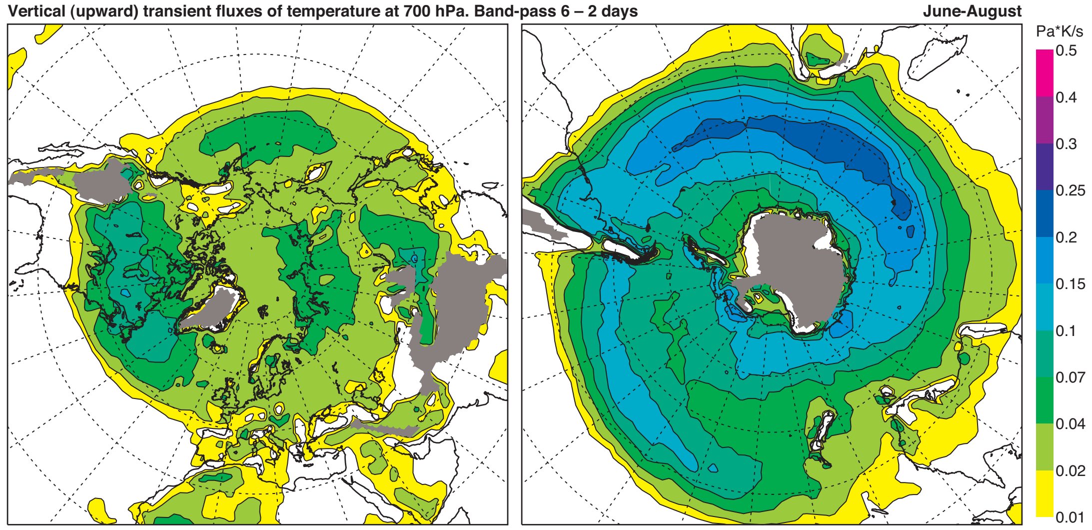

Vertical (upward) transient fluxes of temperature at 700 hPa. Band-pass 6 – 2 days — Interannual variability

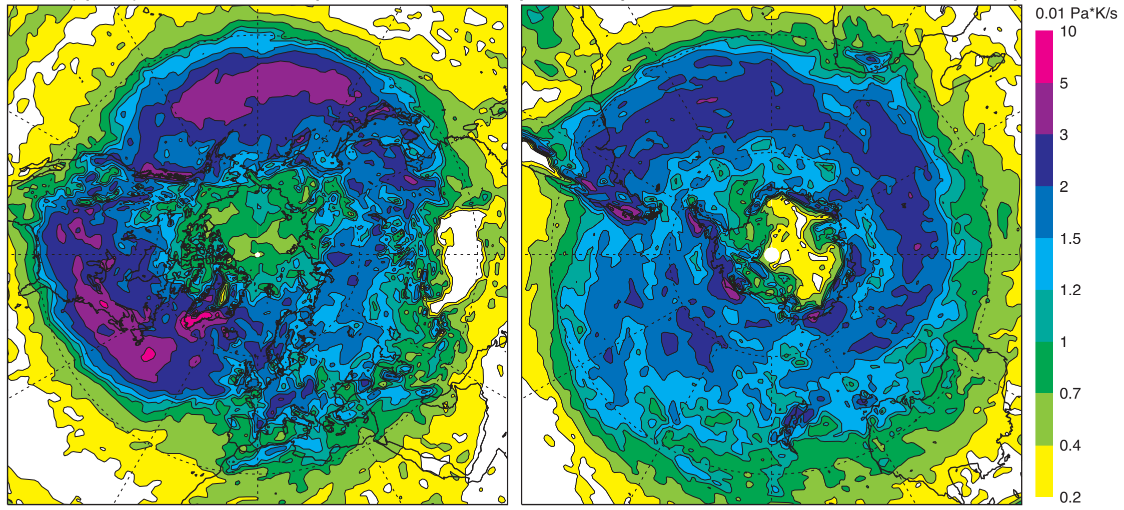

Vertical (upward) transient fluxes of temperature at 700 hPa. Band-pass 6 – 2 days — March-May

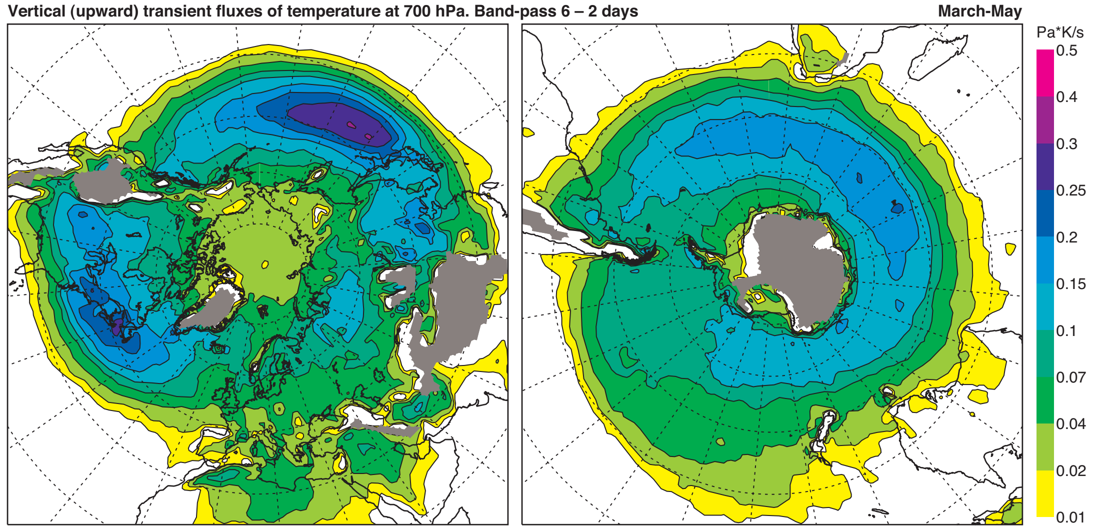

Vertical (upward) transient fluxes of temperature at 700 hPa. Band-pass 6 – 2 days — September-November

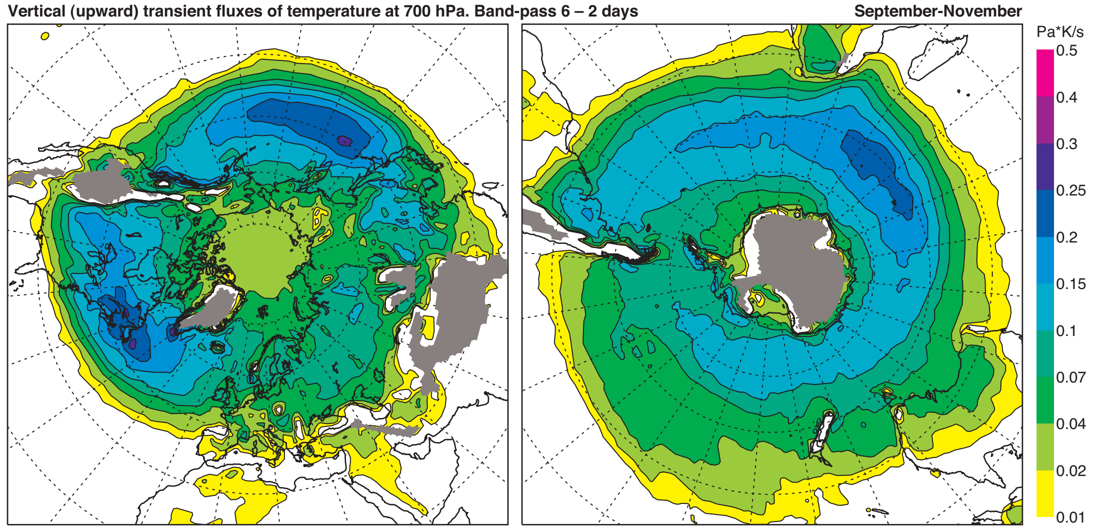

D20 Vertical (upward) transient fluxes of temperature (KPas^{-1}) for 6–2 day band pass filtered data at 700 hPa.

Transient eddy kinetic energy at 250 hPa. Filtered 90-day low pass — Annual mean

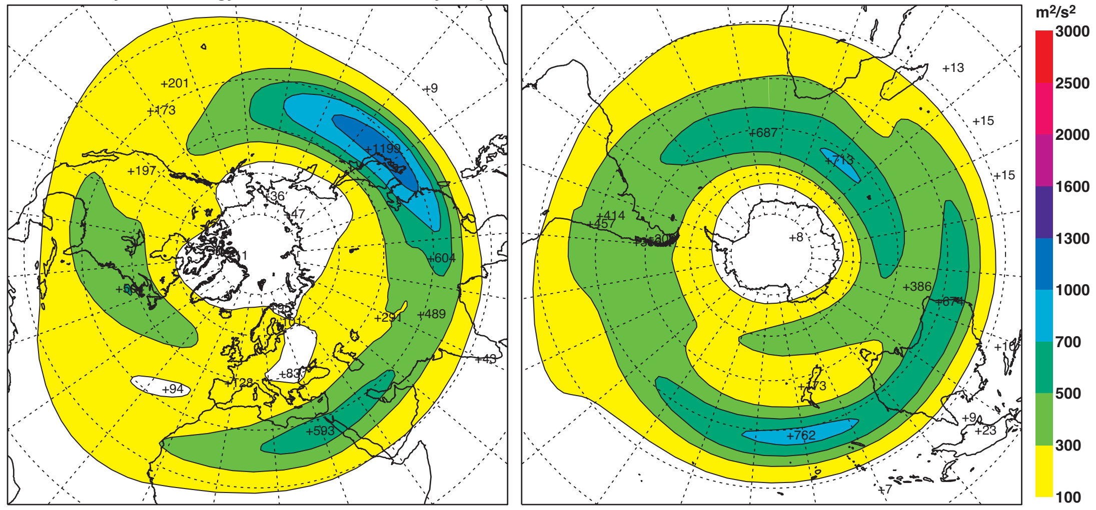

Transient eddy kinetic energy at 250 hPa. Filtered 90-day low pass — December-February

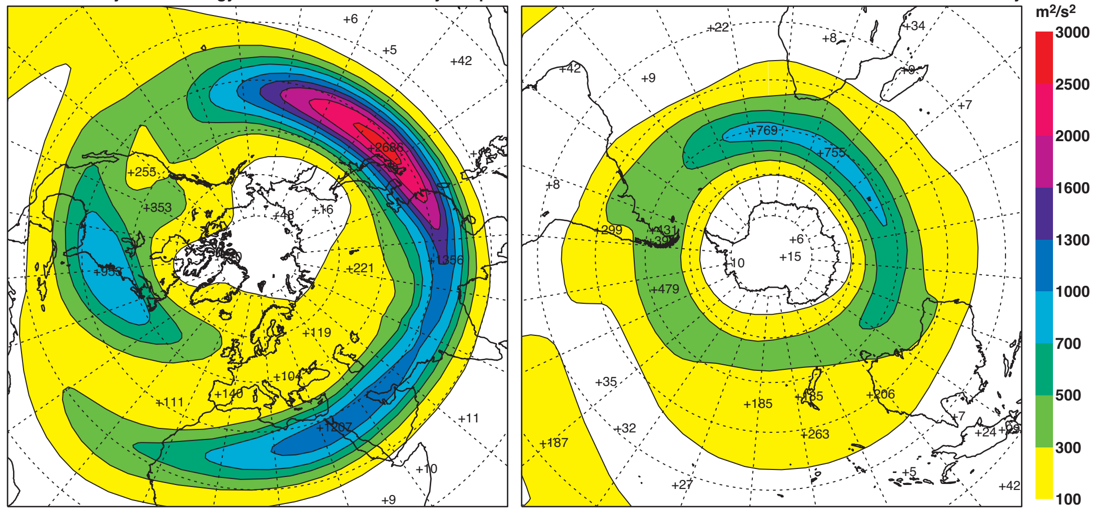

Transient eddy kinetic energy at 250 hPa. Filtered 90-day low pass — June-August

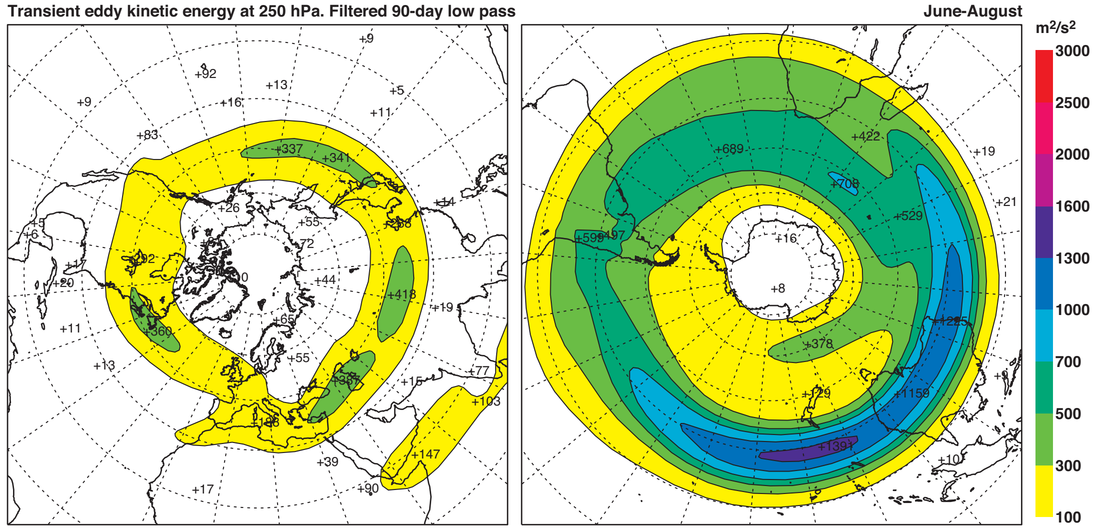

Transient eddy kinetic energy at 250 hPa. Filtered 90-day low pass — Interannual variability

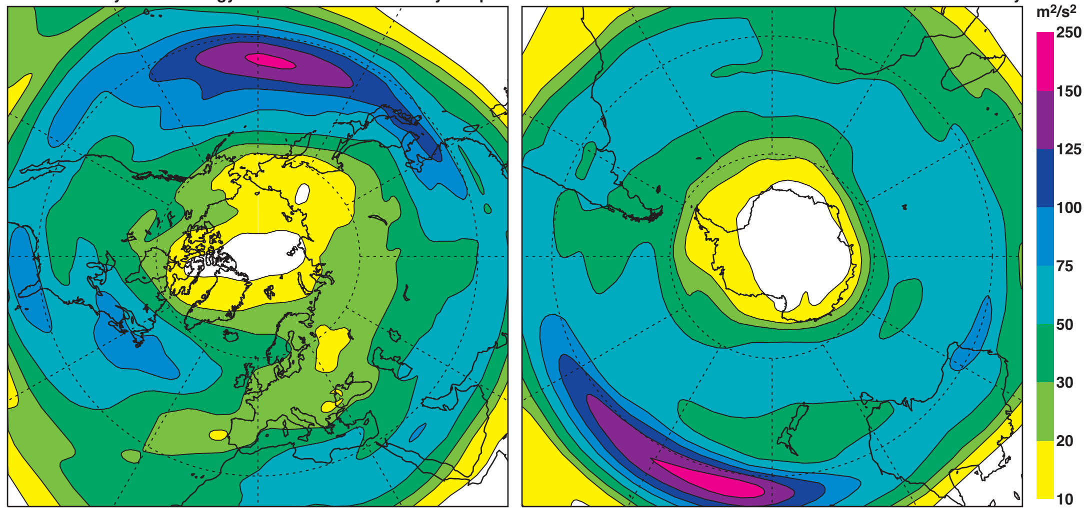

Transient eddy kinetic energy at 250 hPa. Filtered 90-day low pass — March-May

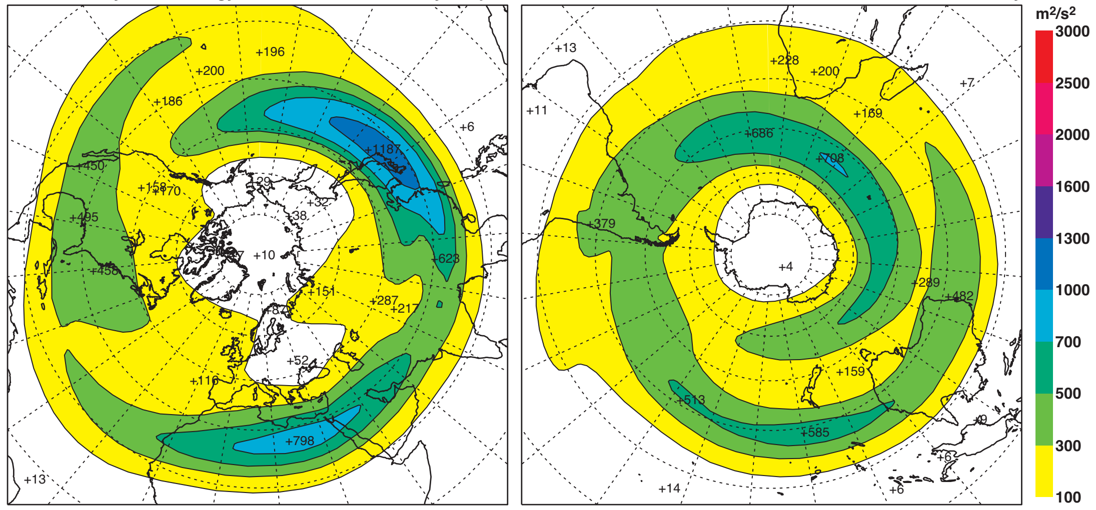

Transient eddy kinetic energy at 250 hPa. Filtered 90-day low pass — September-November

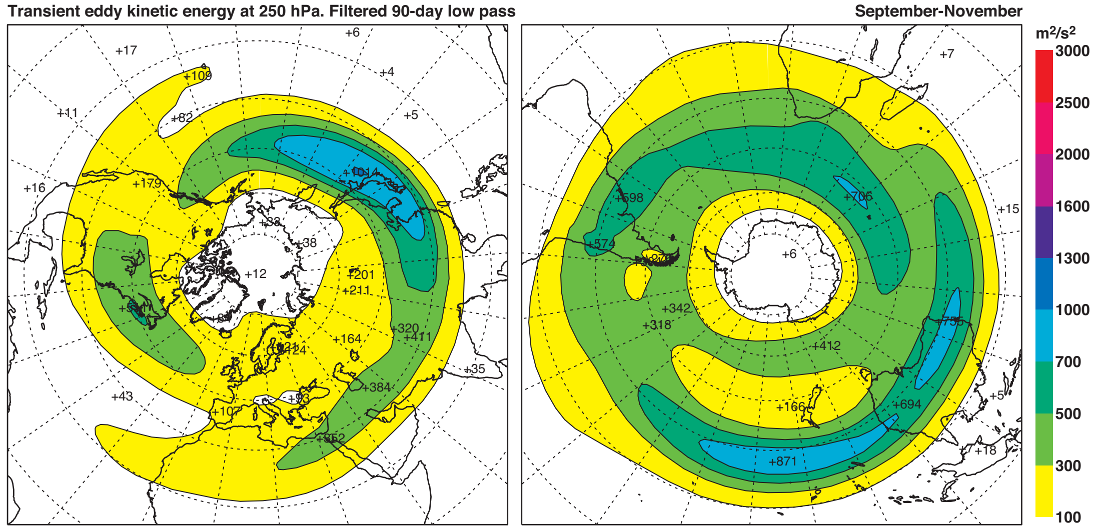

D21 Transient eddy kinetic energy (m^2s^{-2}) for 90-day low pass filtered winds at 250 hPa.

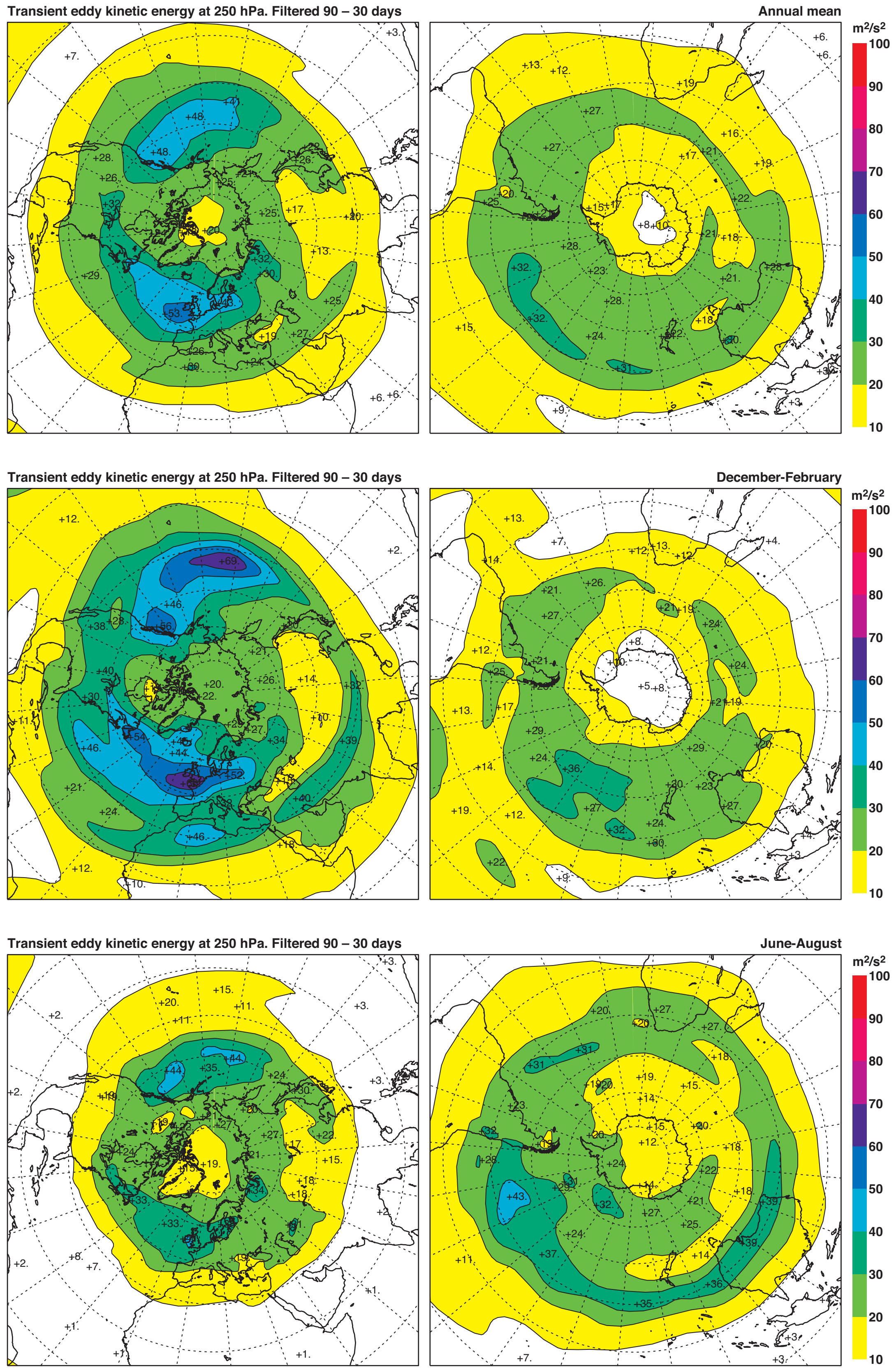

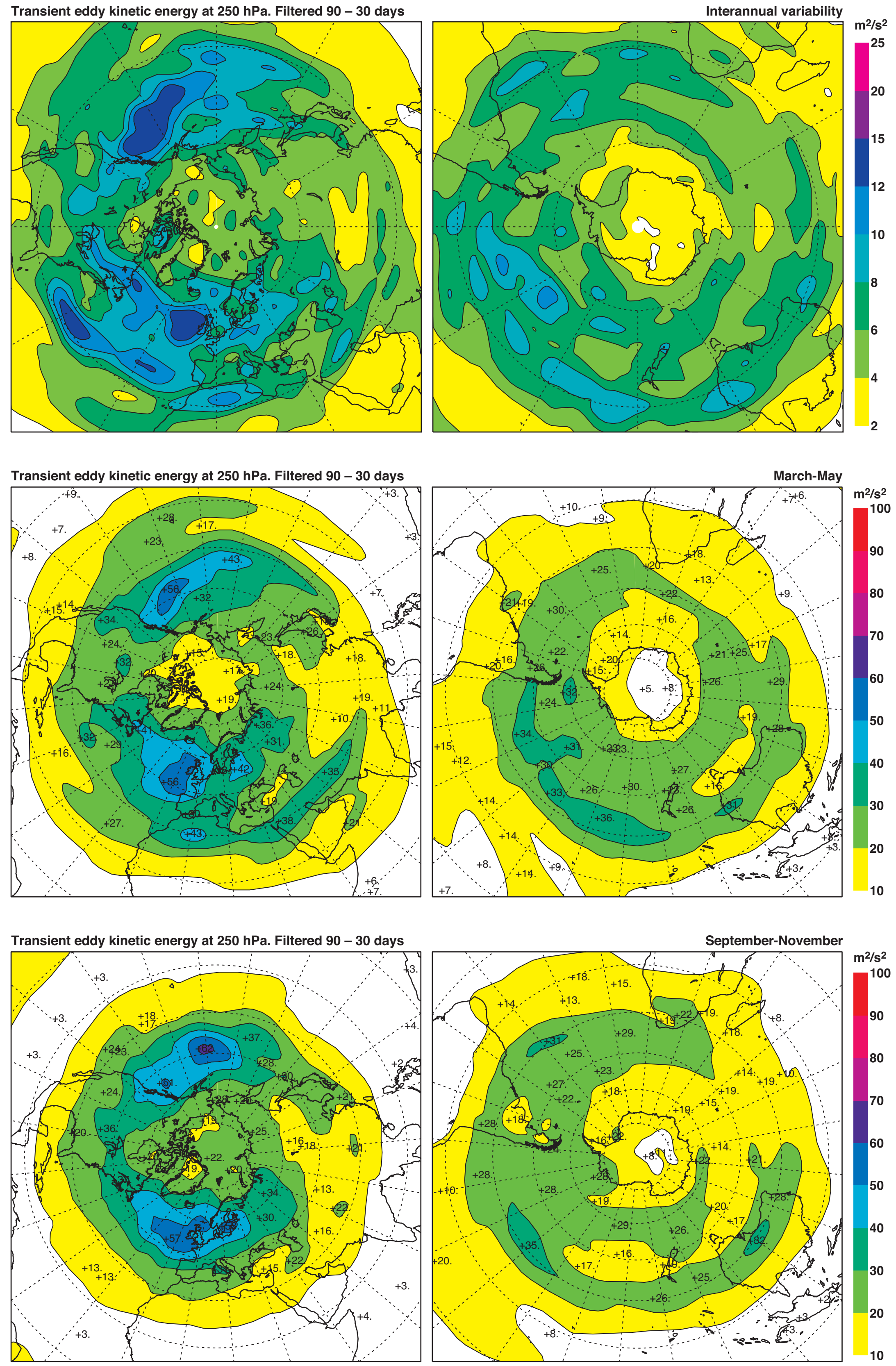

D22 Transient eddy kinetic energy (m^2s^{-2}) for 90–30 day band pass filtered winds at 250 hPa.

Transient eddy kinetic energy at 250 hPa. Filtered 30 – 6 days — Annual mean

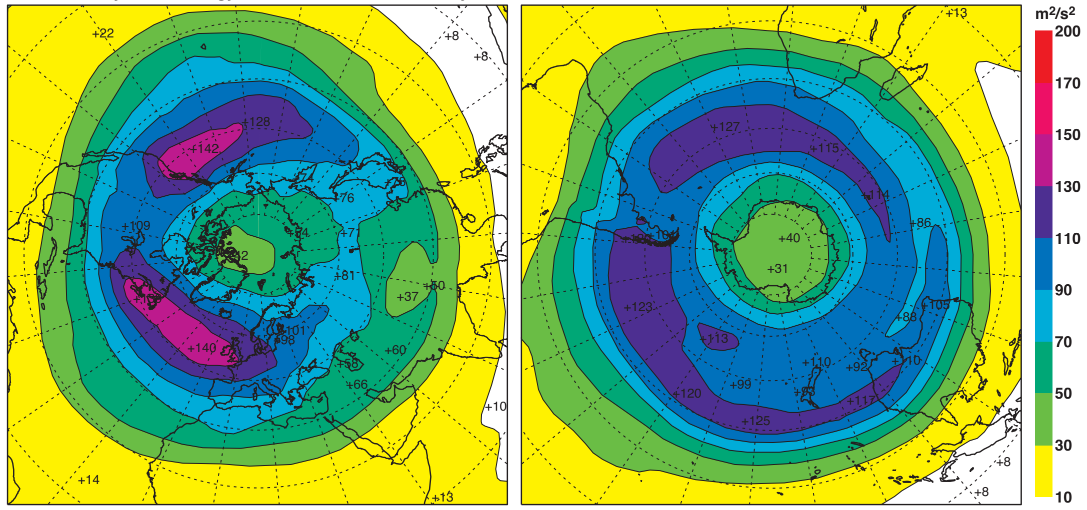

Transient eddy kinetic energy at 250 hPa. Filtered 30 – 6 days — December-February

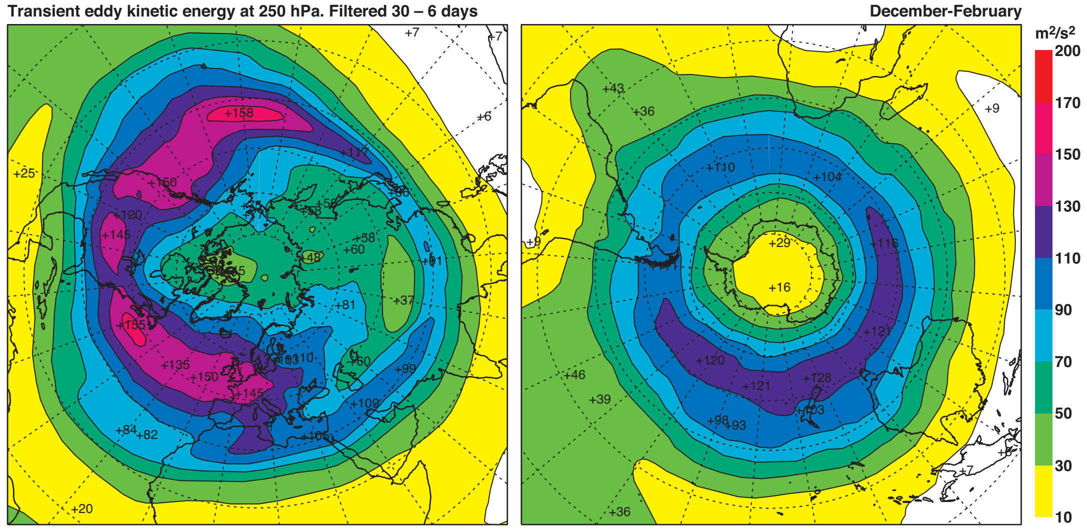

Transient eddy kinetic energy at 250 hPa. Filtered 30 – 6 days — June-August

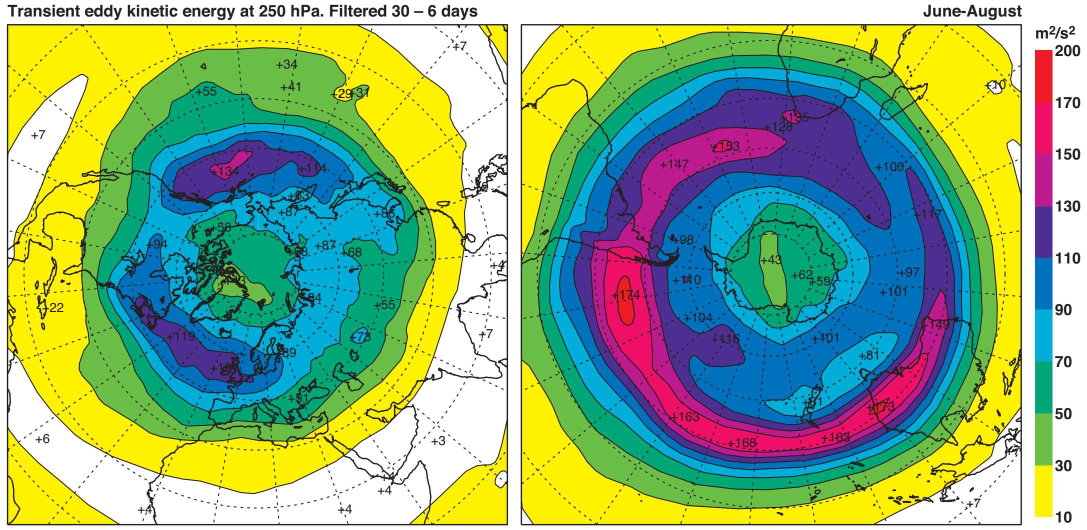

Transient eddy kinetic energy at 250 hPa. Filtered 30 – 6 days — Interannual variability

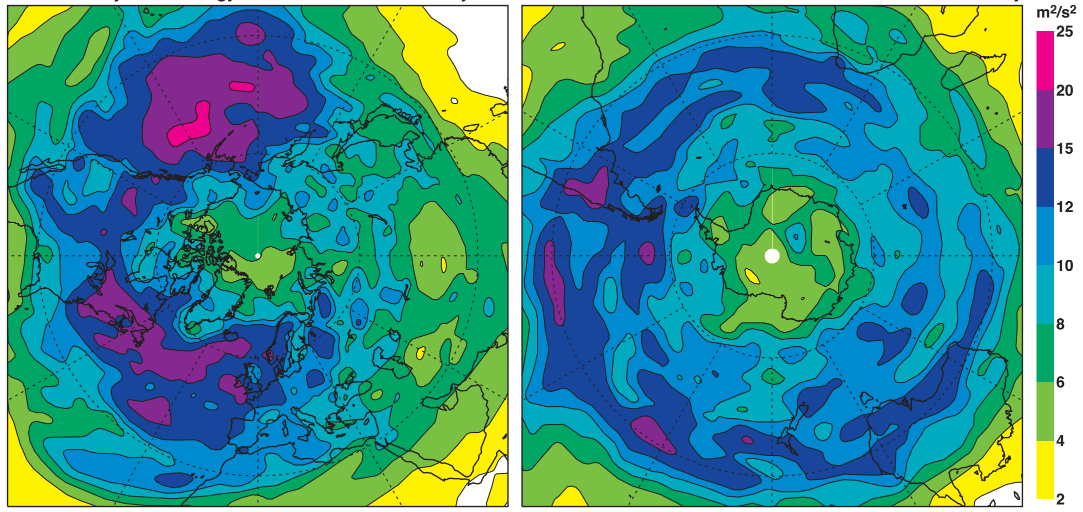

Transient eddy kinetic energy at 250 hPa. Filtered 30 – 6 days — March-May

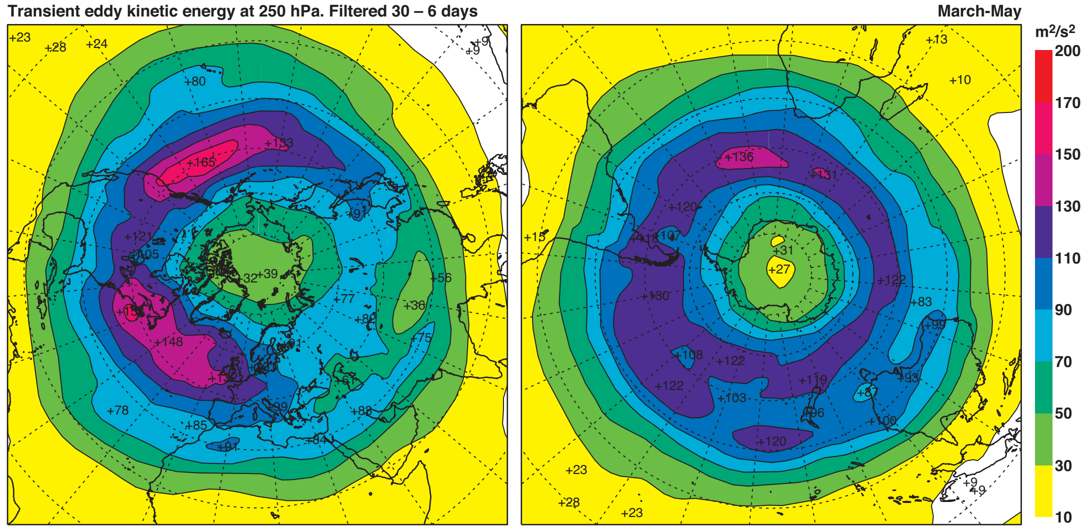

Transient eddy kinetic energy at 250 hPa. Filtered 30 – 6 days — September-November

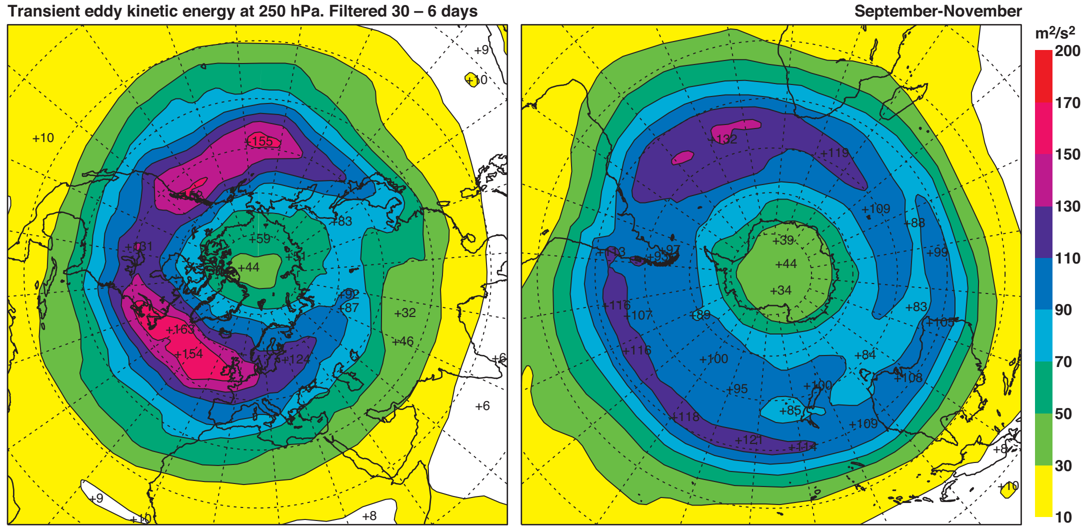

D23 Transient eddy kinetic energy (m^2s^{-2}) for 30–6 day band pass filtered winds at 250 hPa.

Transient eddy kinetic energy at 250 hPa. Filtered 6 – 2 days | Annual mean

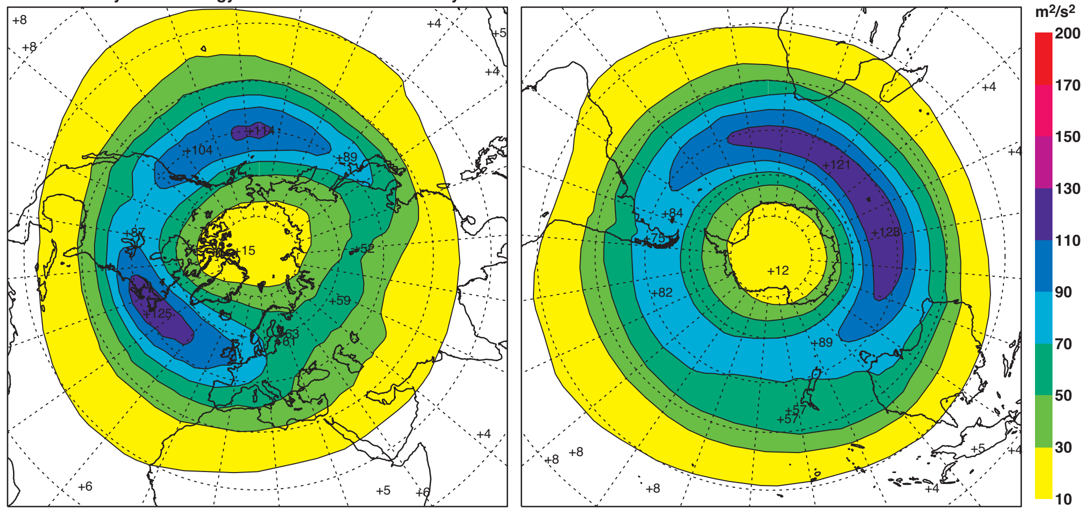

Transient eddy kinetic energy at 250 hPa. Filtered 6 – 2 days | December-February

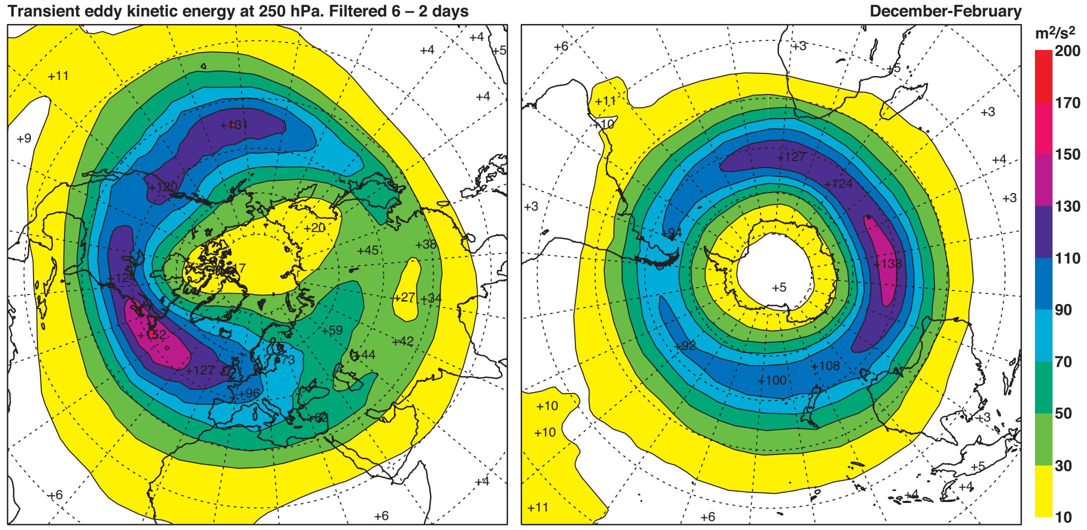

Transient eddy kinetic energy at 250 hPa. Filtered 6 – 2 days | June-August

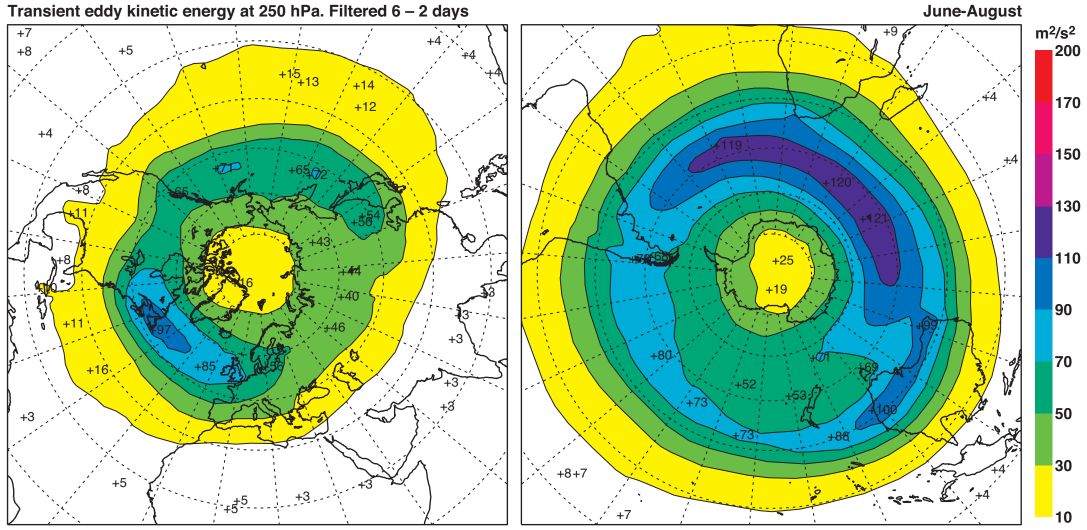

Transient eddy kinetic energy at 250 hPa. Filtered 6 – 2 days | Interannual variability

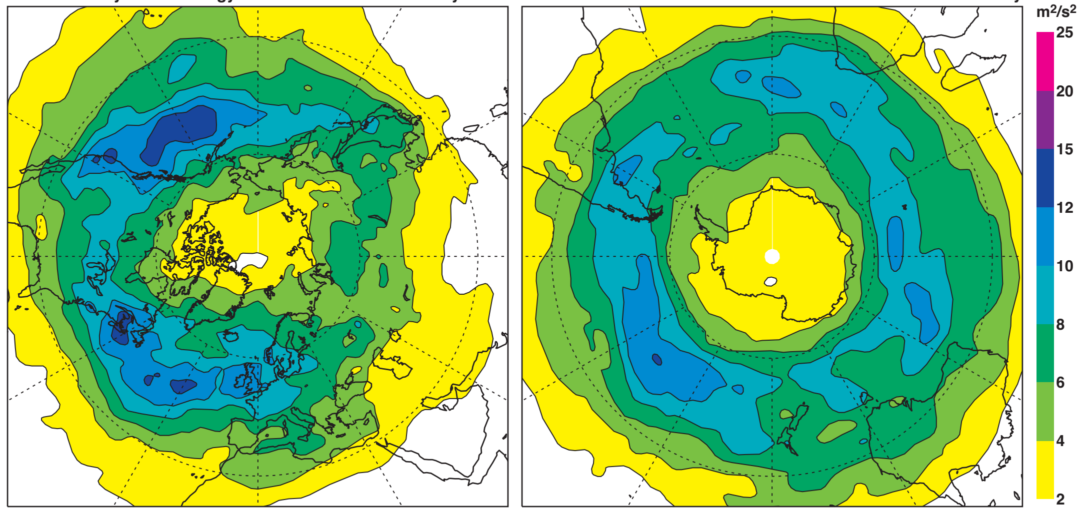

Transient eddy kinetic energy at 250 hPa. Filtered 6 – 2 days | March-May

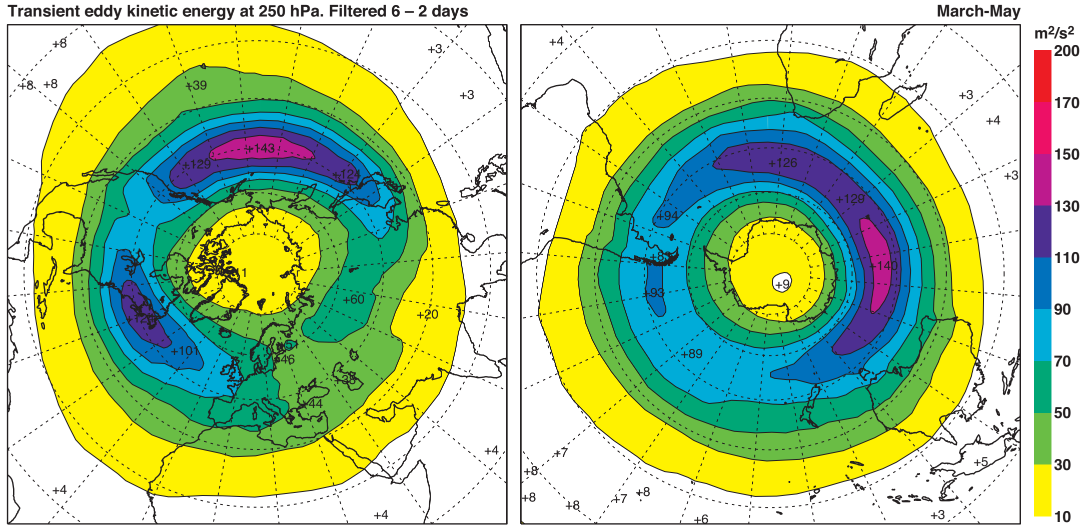

Transient eddy kinetic energy at 250 hPa. Filtered 6 – 2 days | September-November

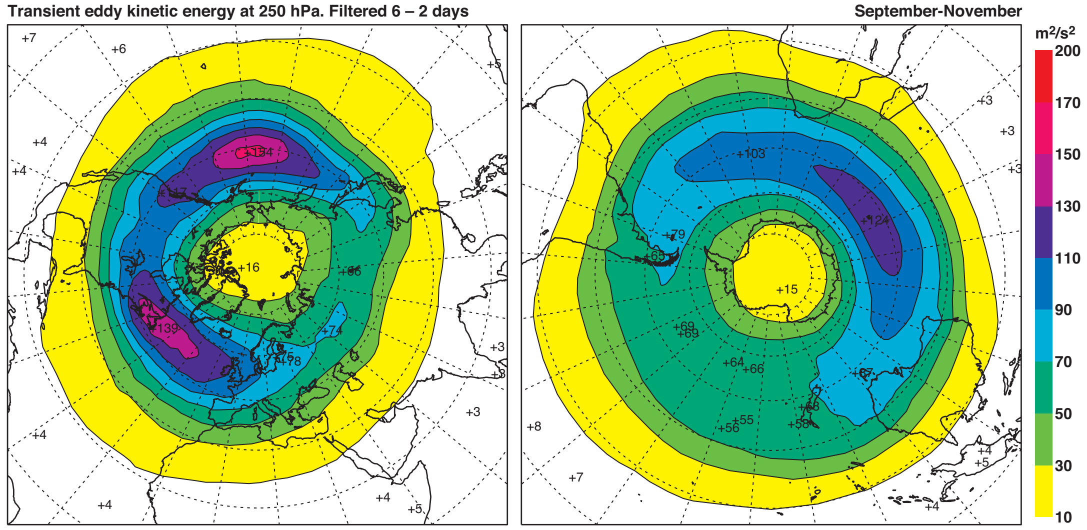

D24 Transient eddy kinetic energy (m^2s^{-2}) for 6–2 day band pass filtered winds at 250 hPa.

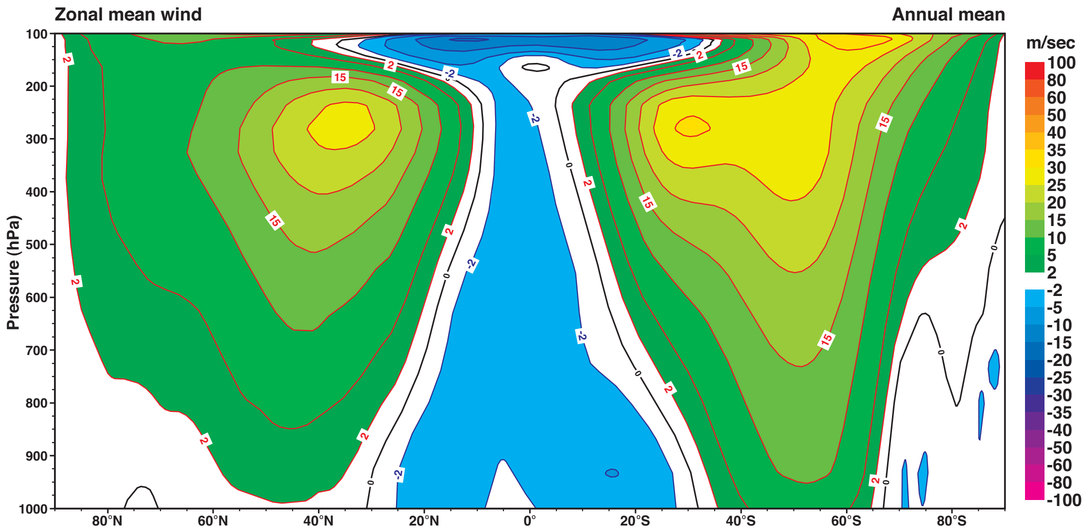

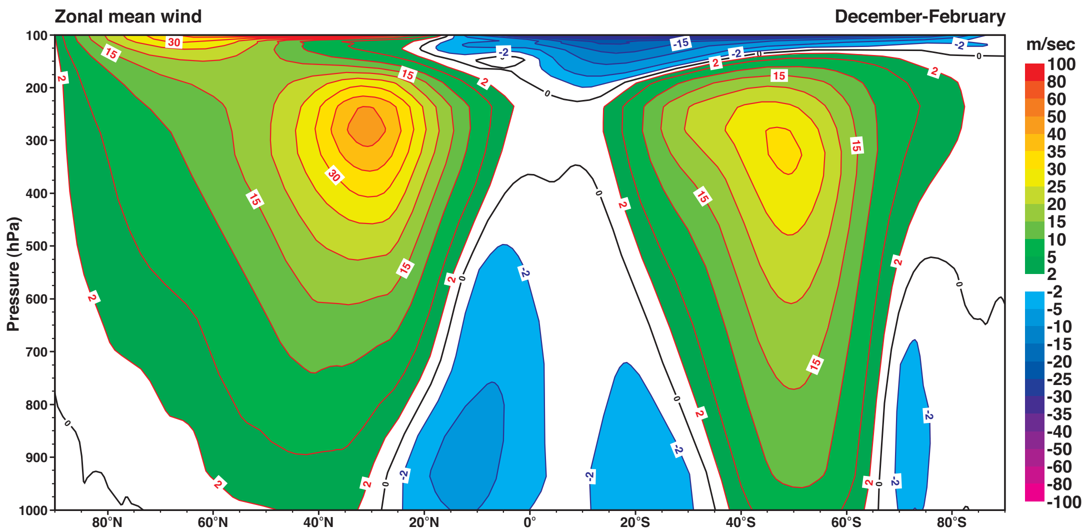

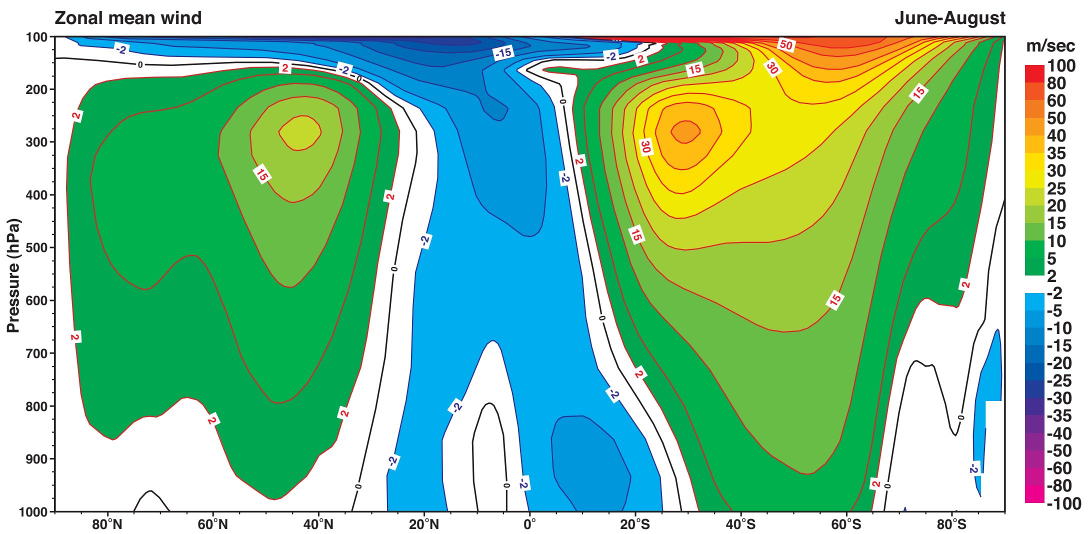

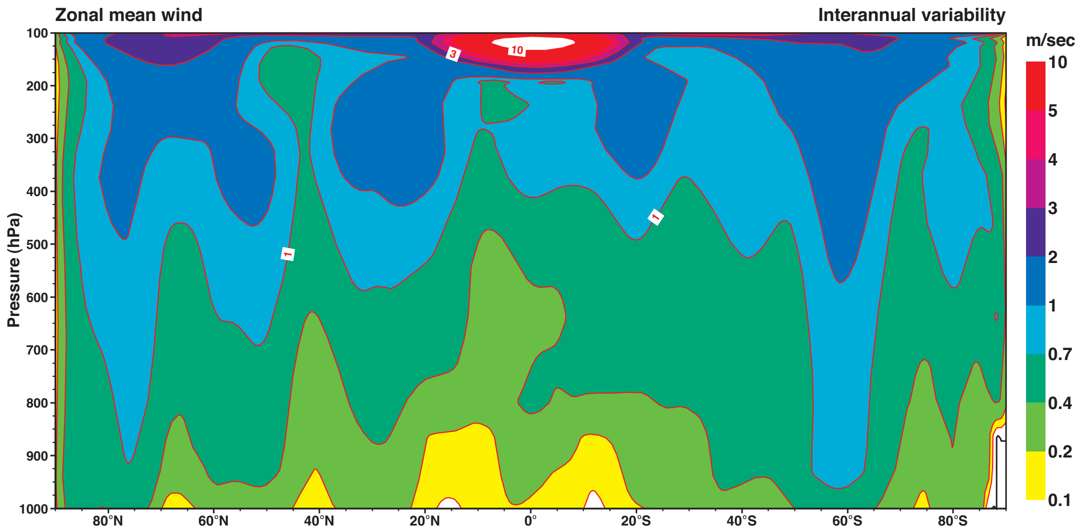

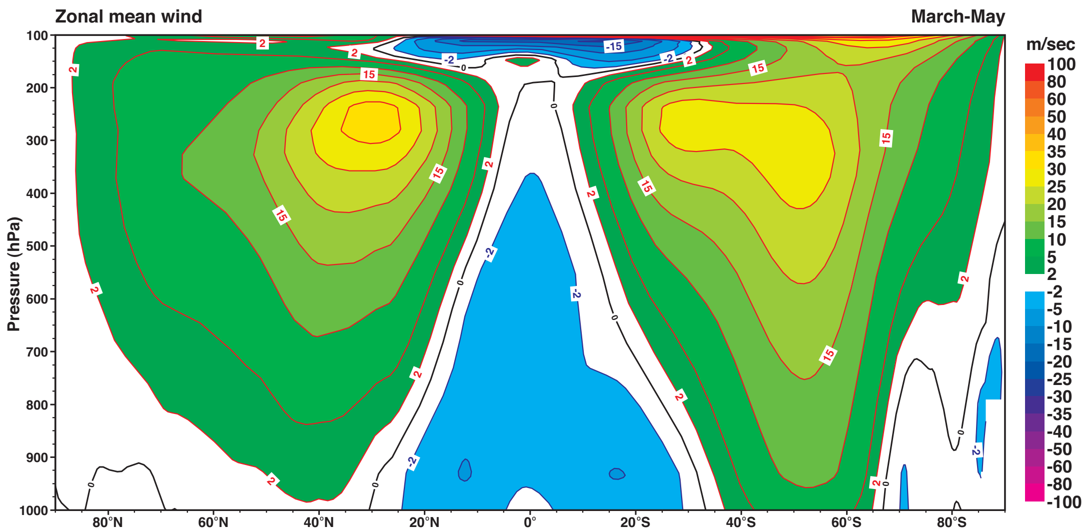

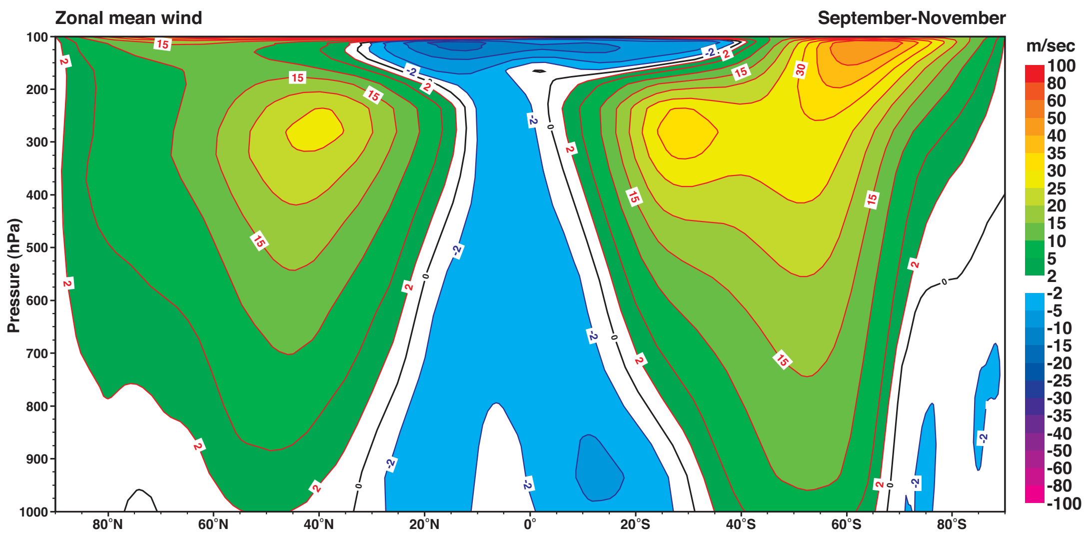

D25 A pressure based tropospheric perspective of zonal mean zonal wind (ms^{-1}).

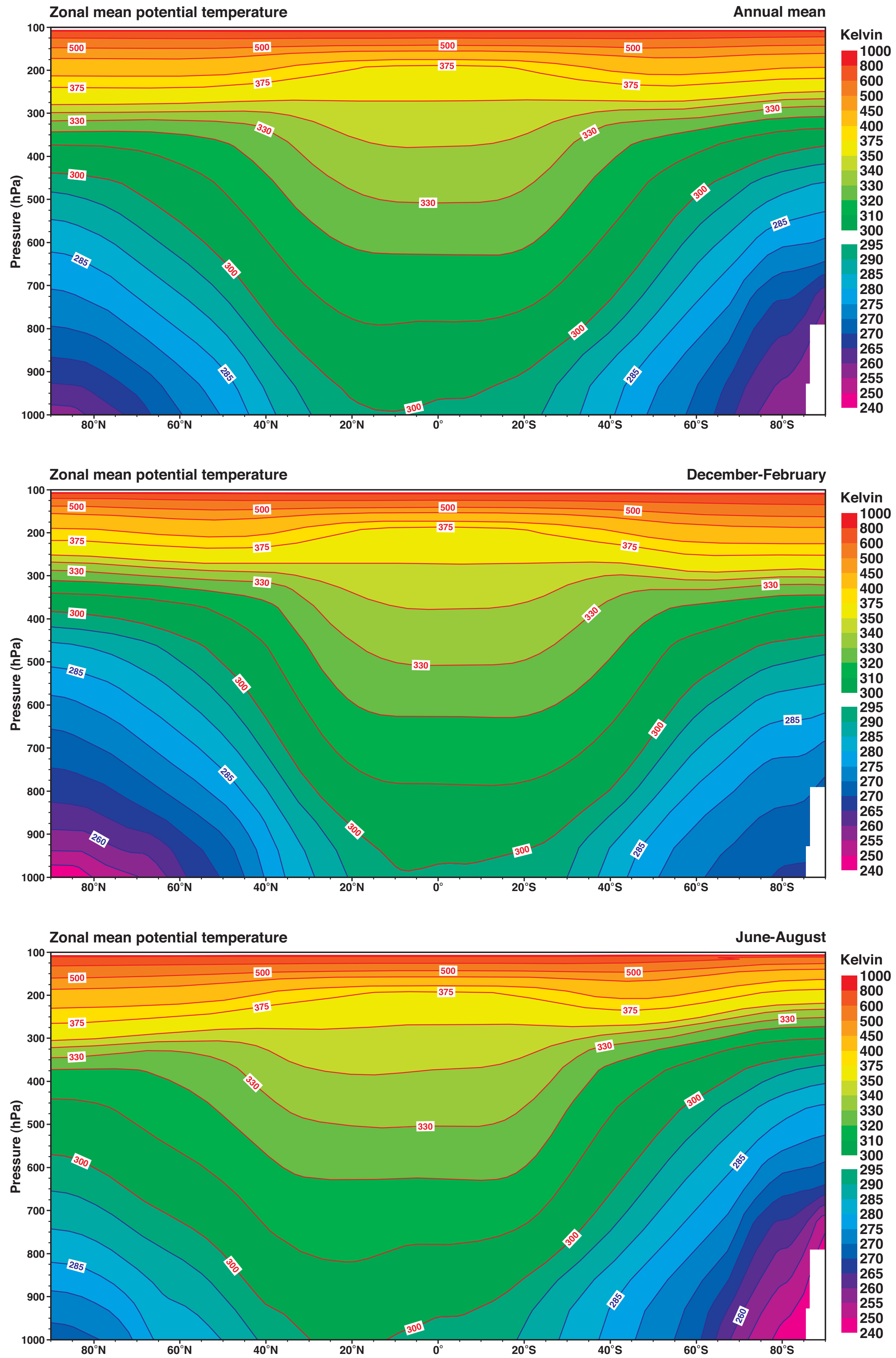

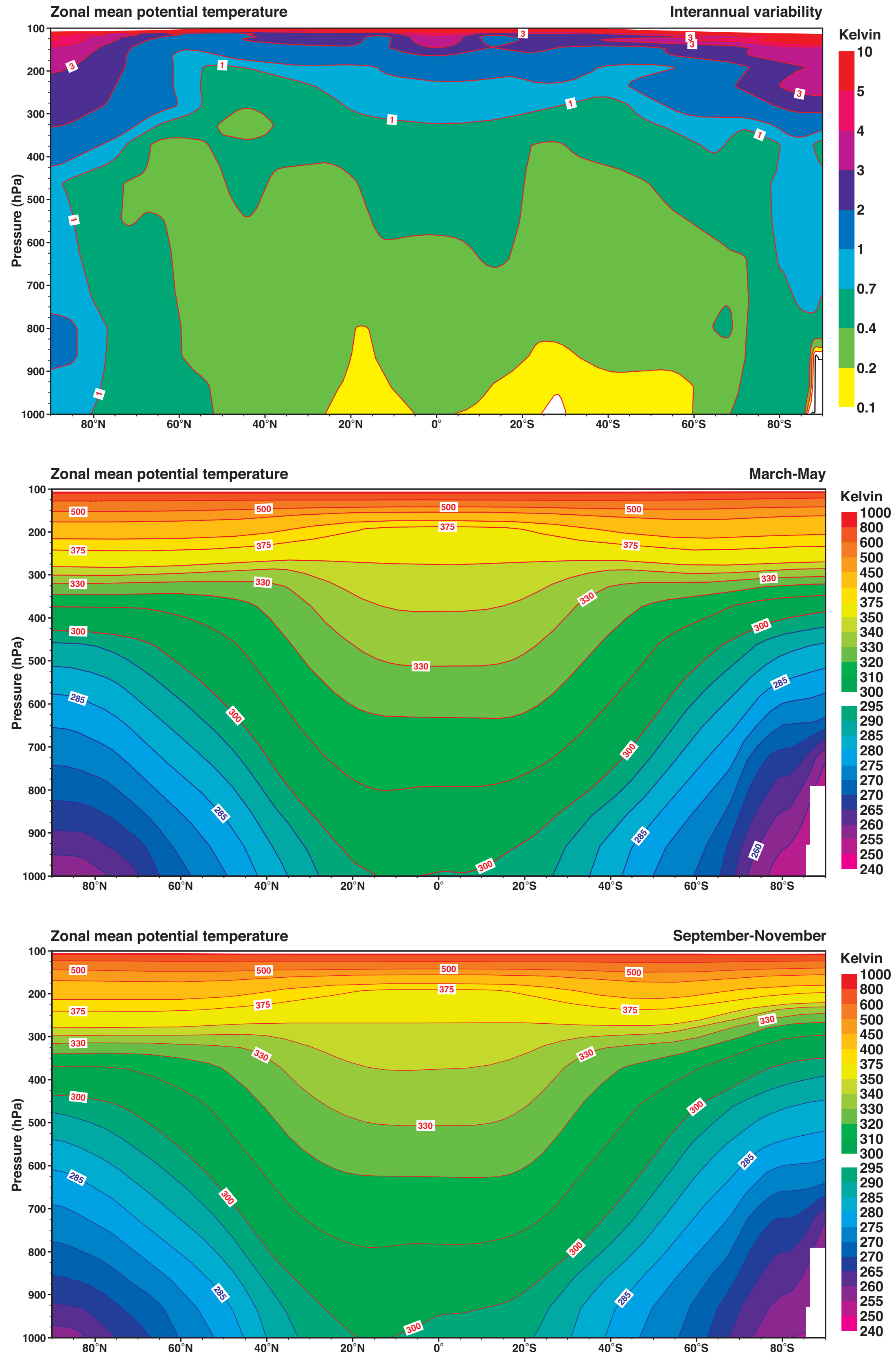

D26 A pressure based tropospheric perspective of zonal mean potential temperature (K).

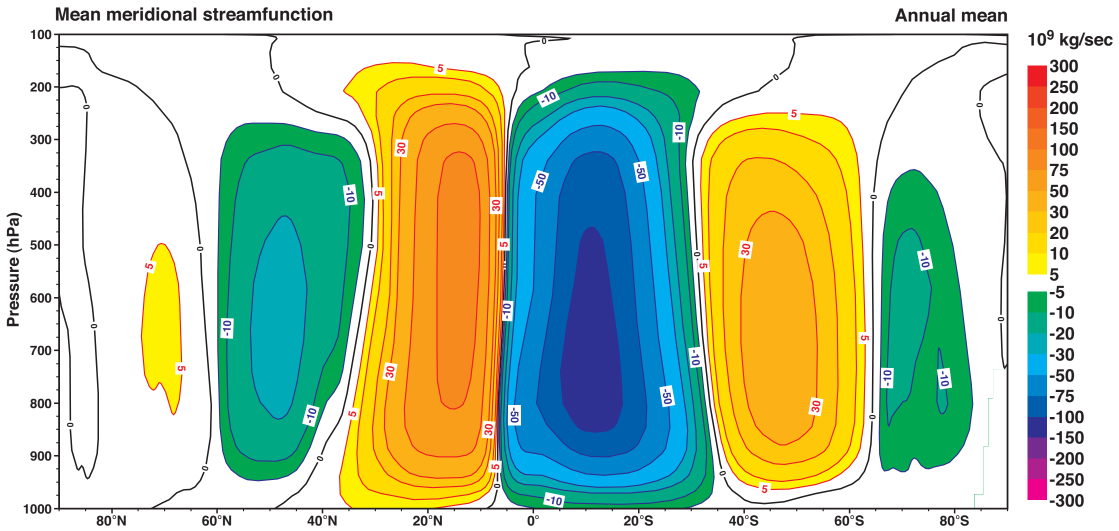

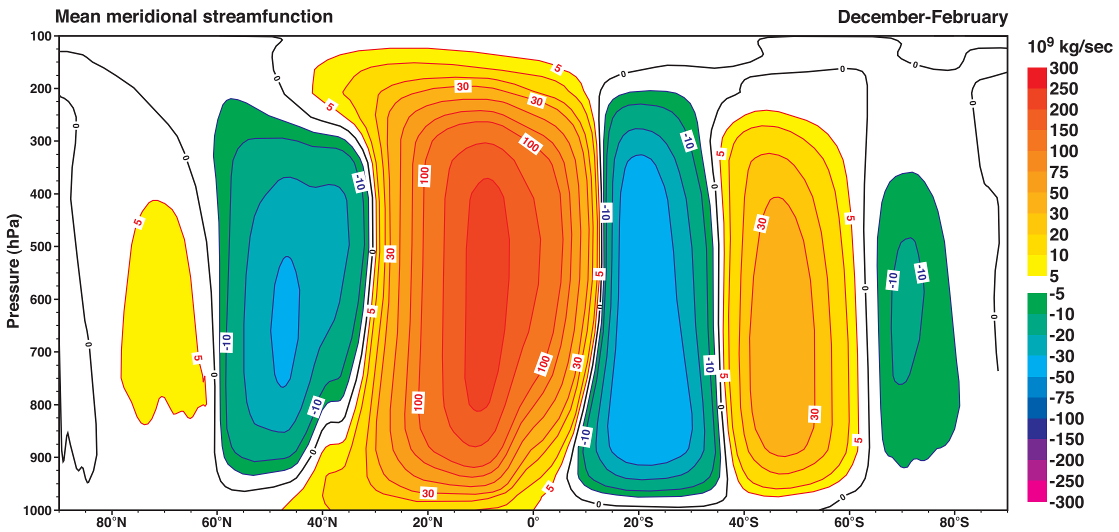

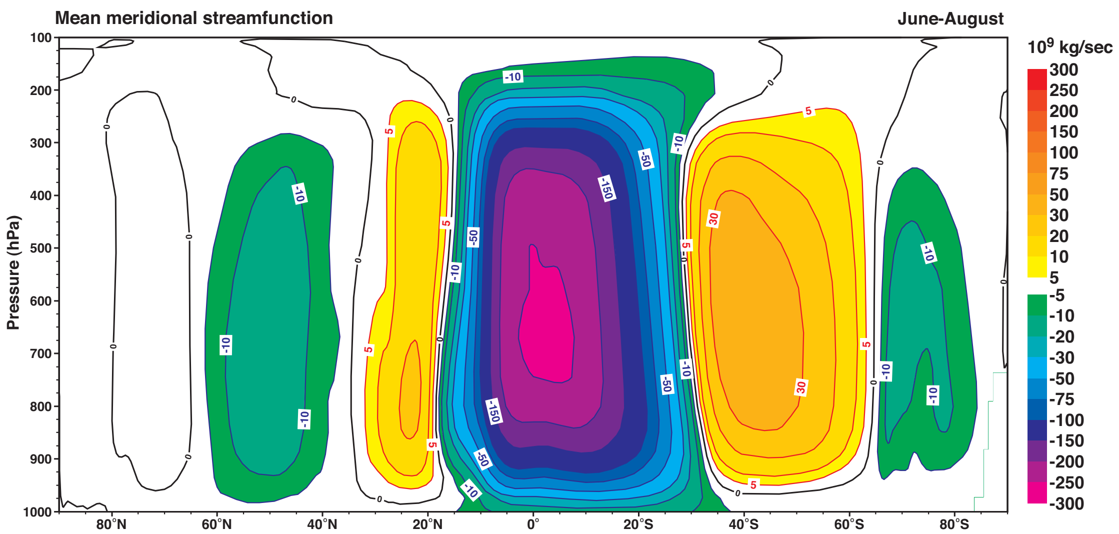

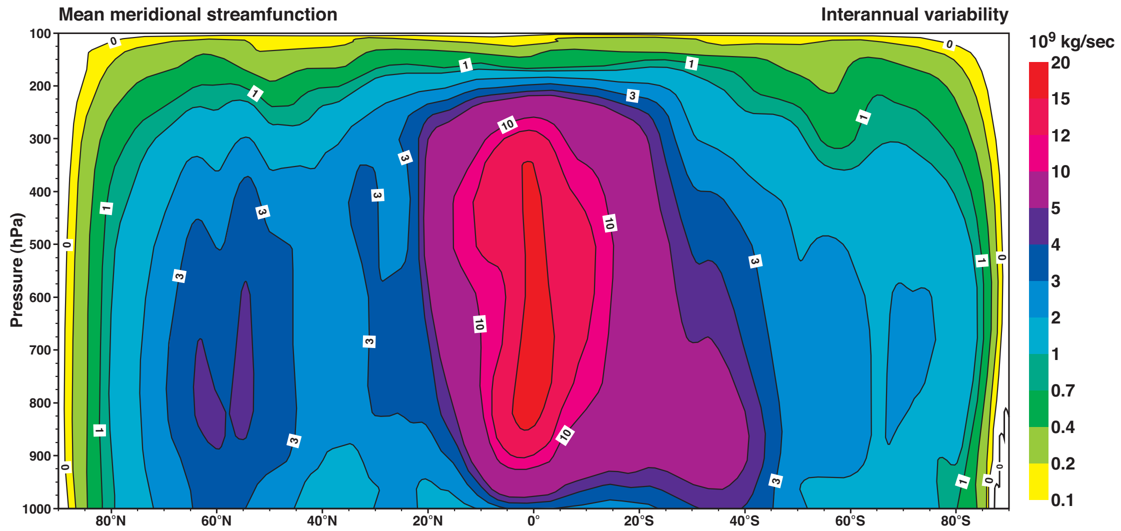

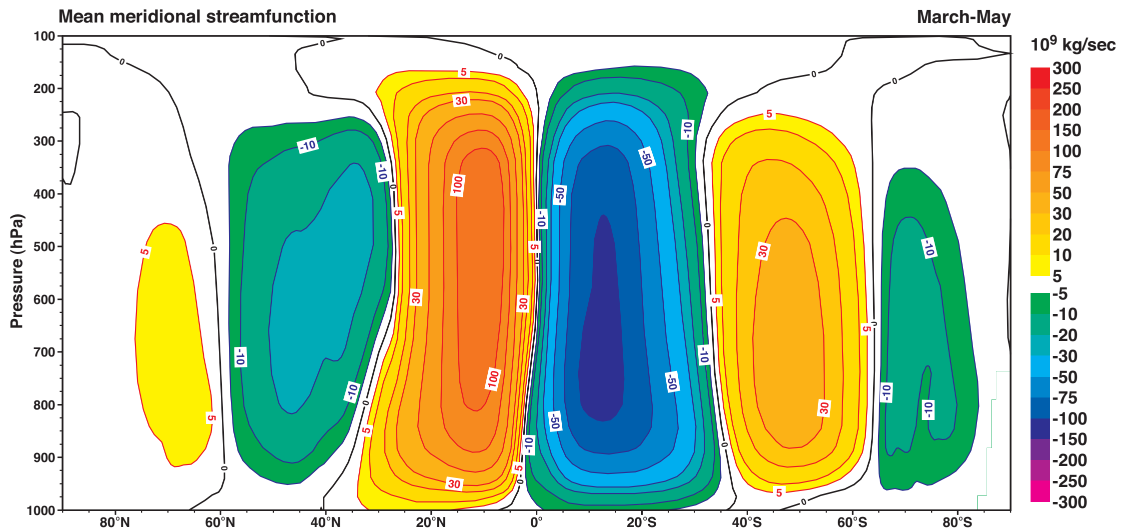

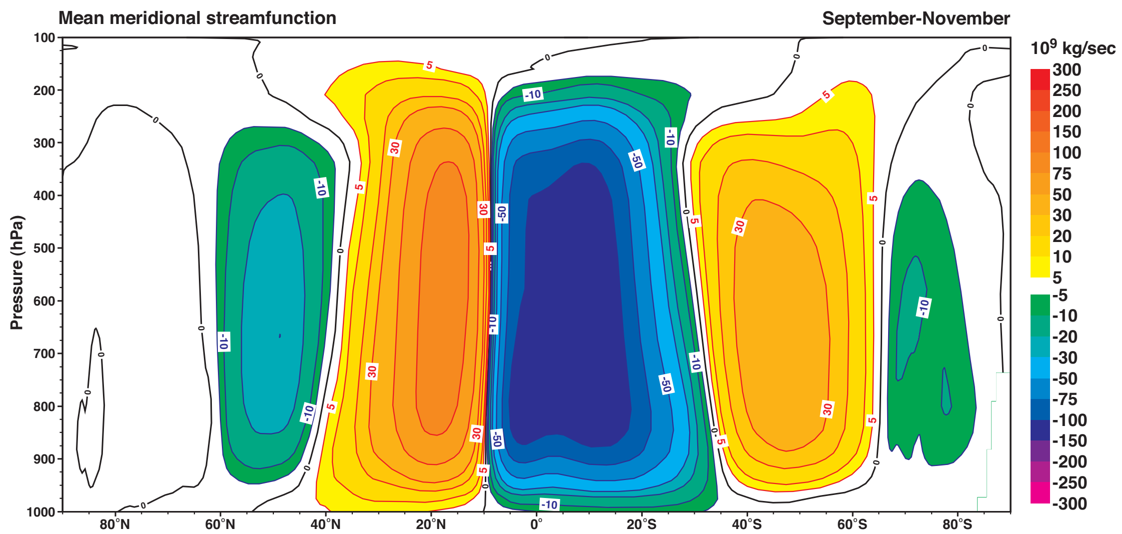

D27 A pressure based tropospheric perspective of mean meridional streamfunction (kgs^{-1}).

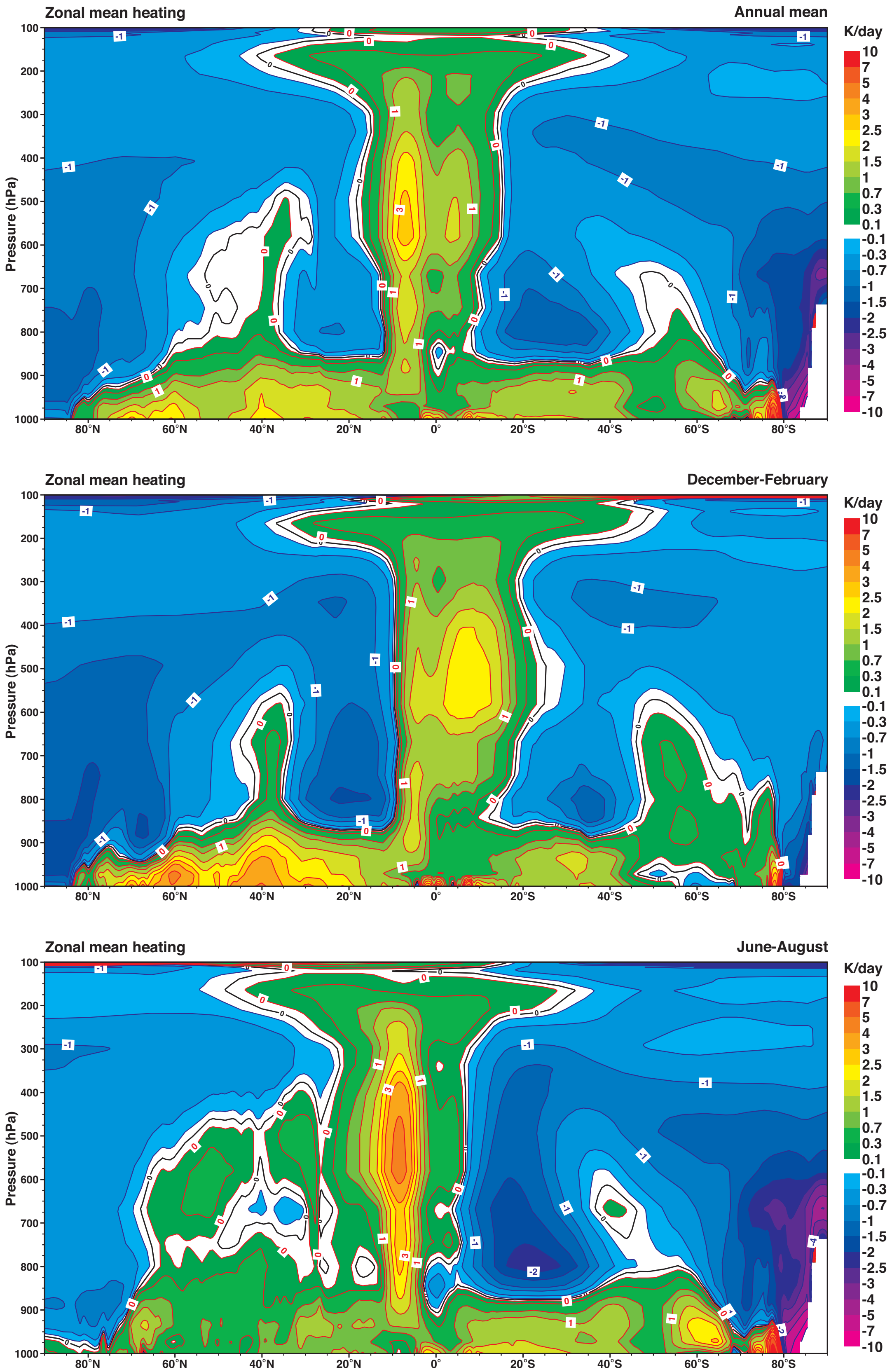

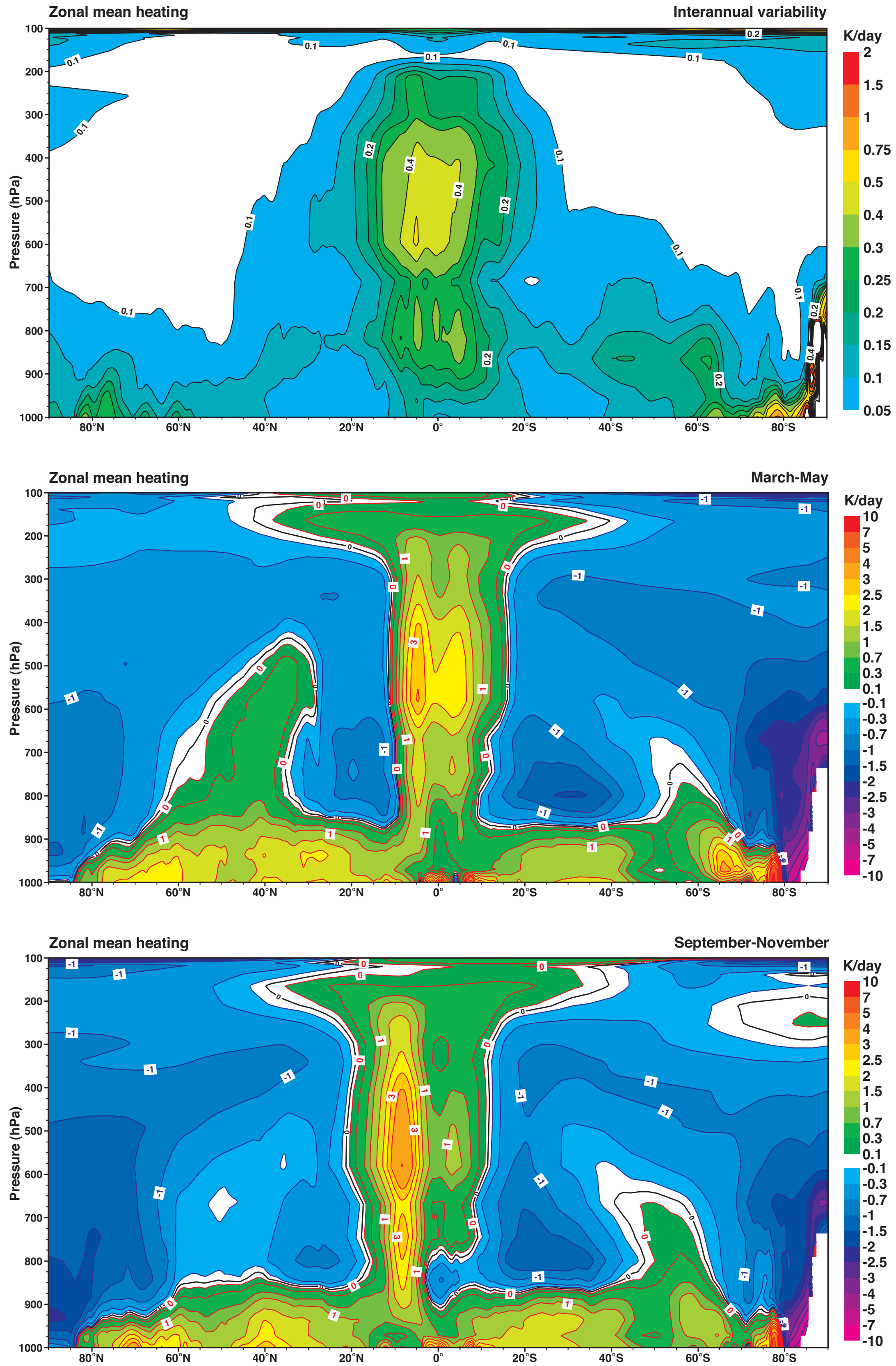

D28 A pressure based tropospheric perspective of zonal mean heating (Kday^{-1}).

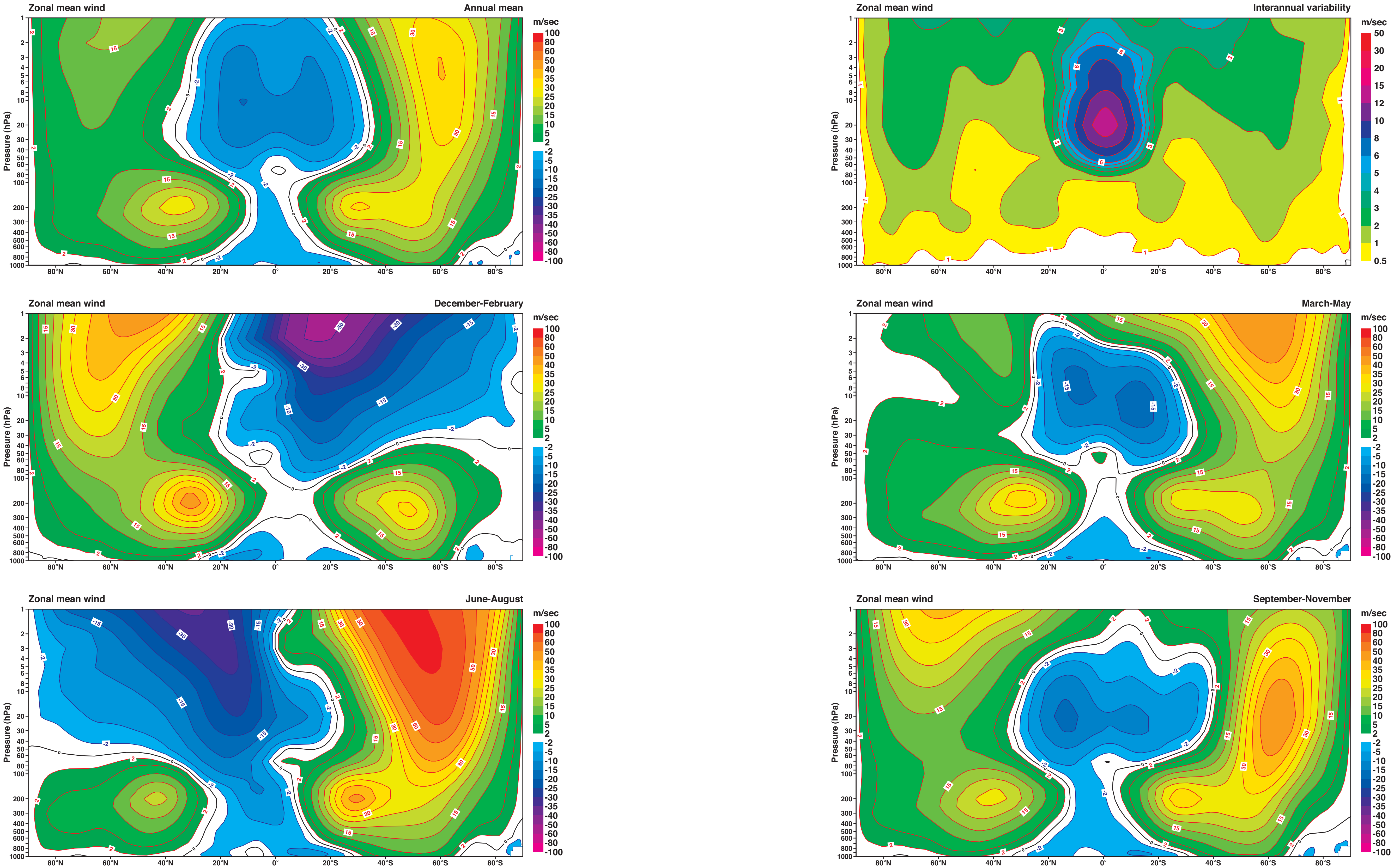

D29 A pressure based stratospheric perspective of zonal mean zonal wind (ms^{-1}).

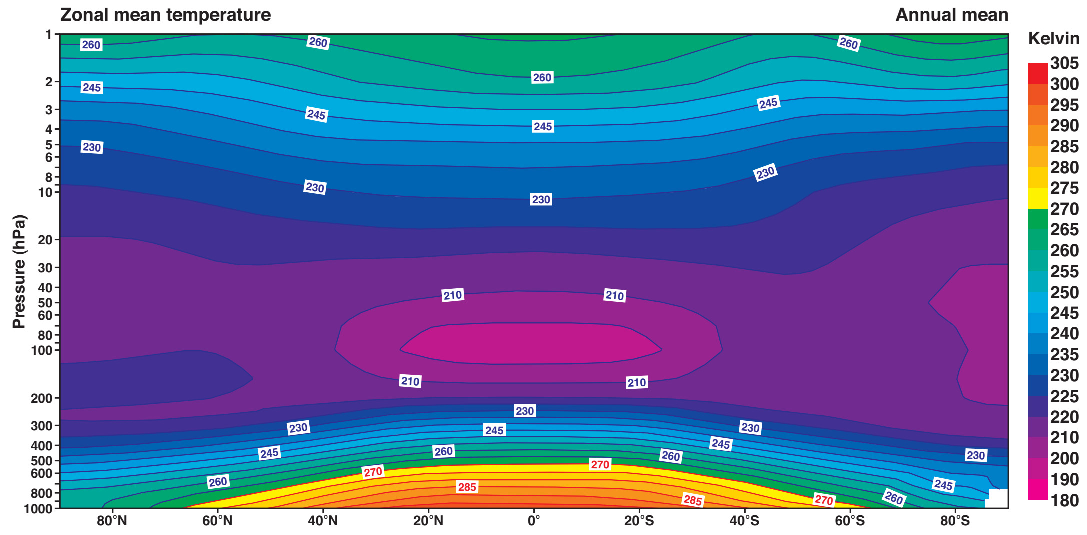

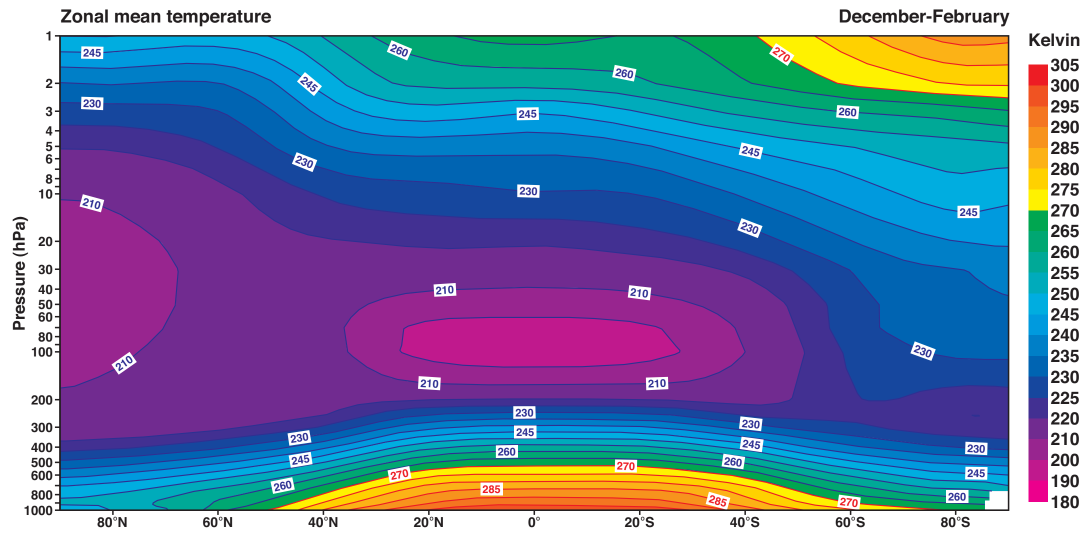

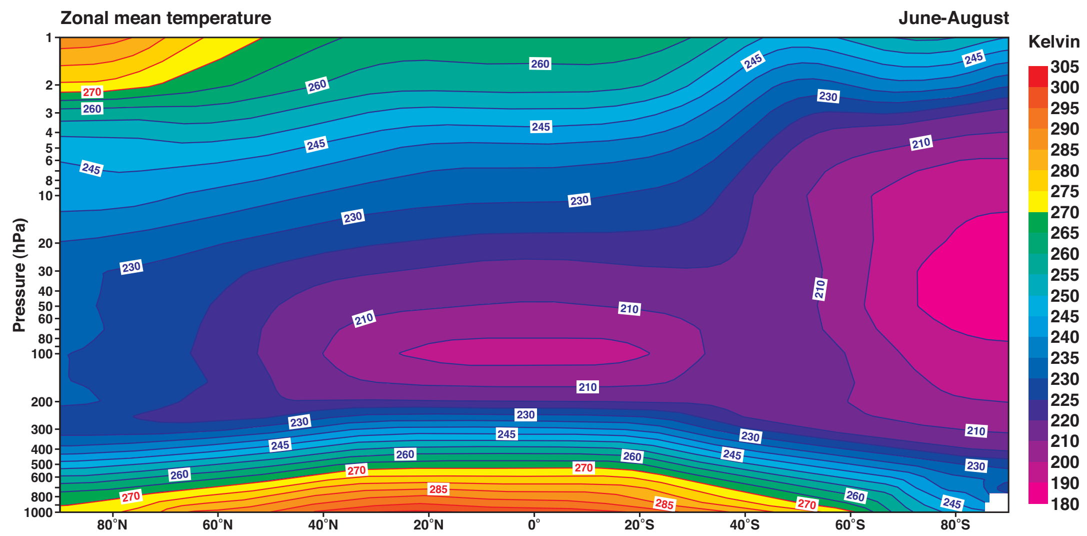

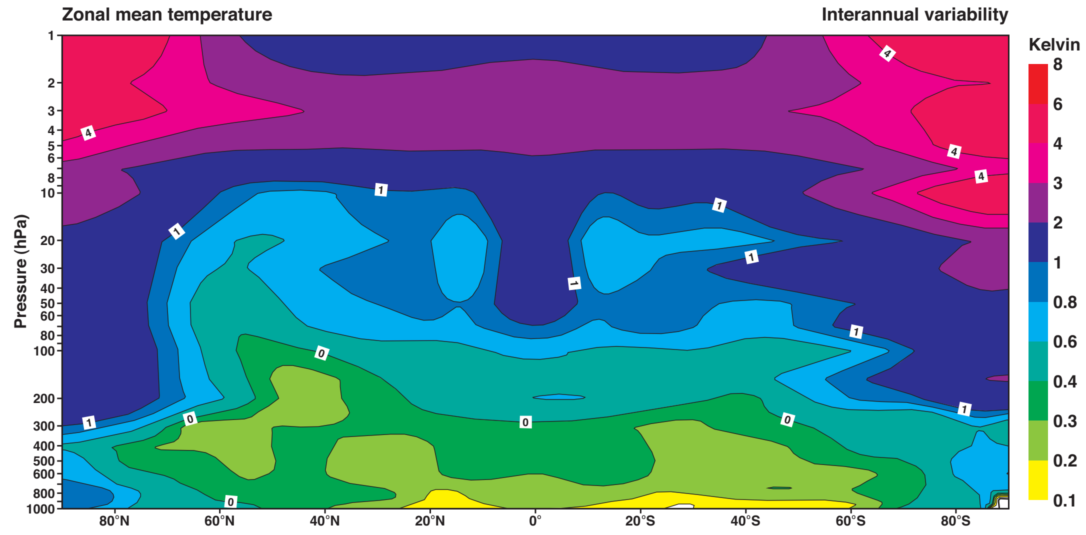

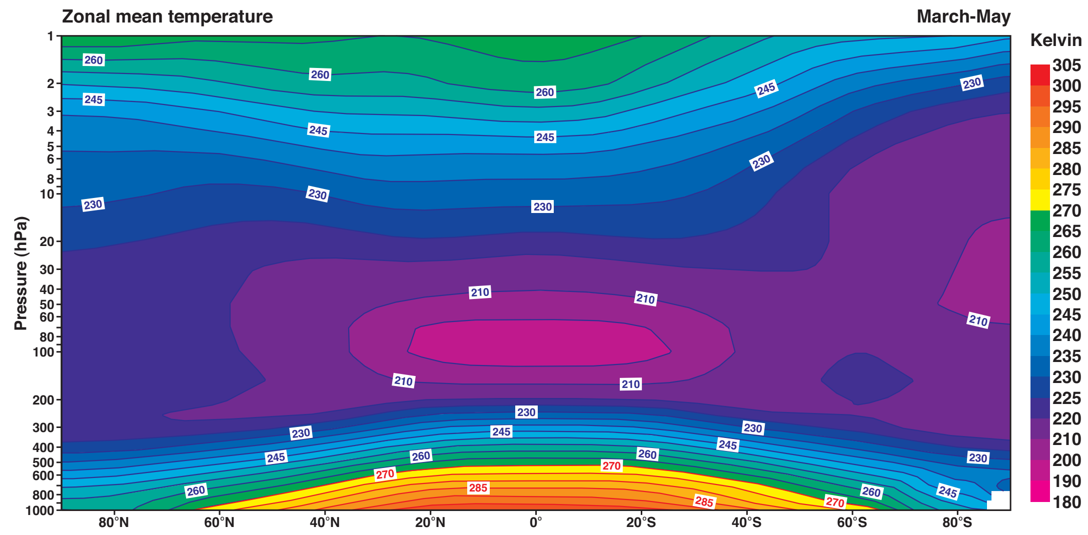

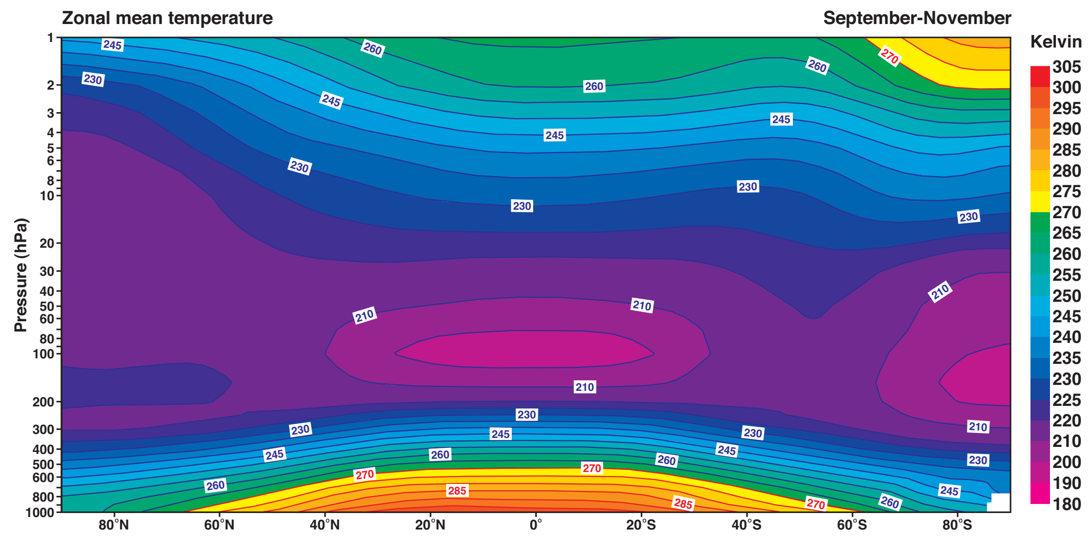

D30 A pressure based stratospheric perspective of zonal mean temperature (K).

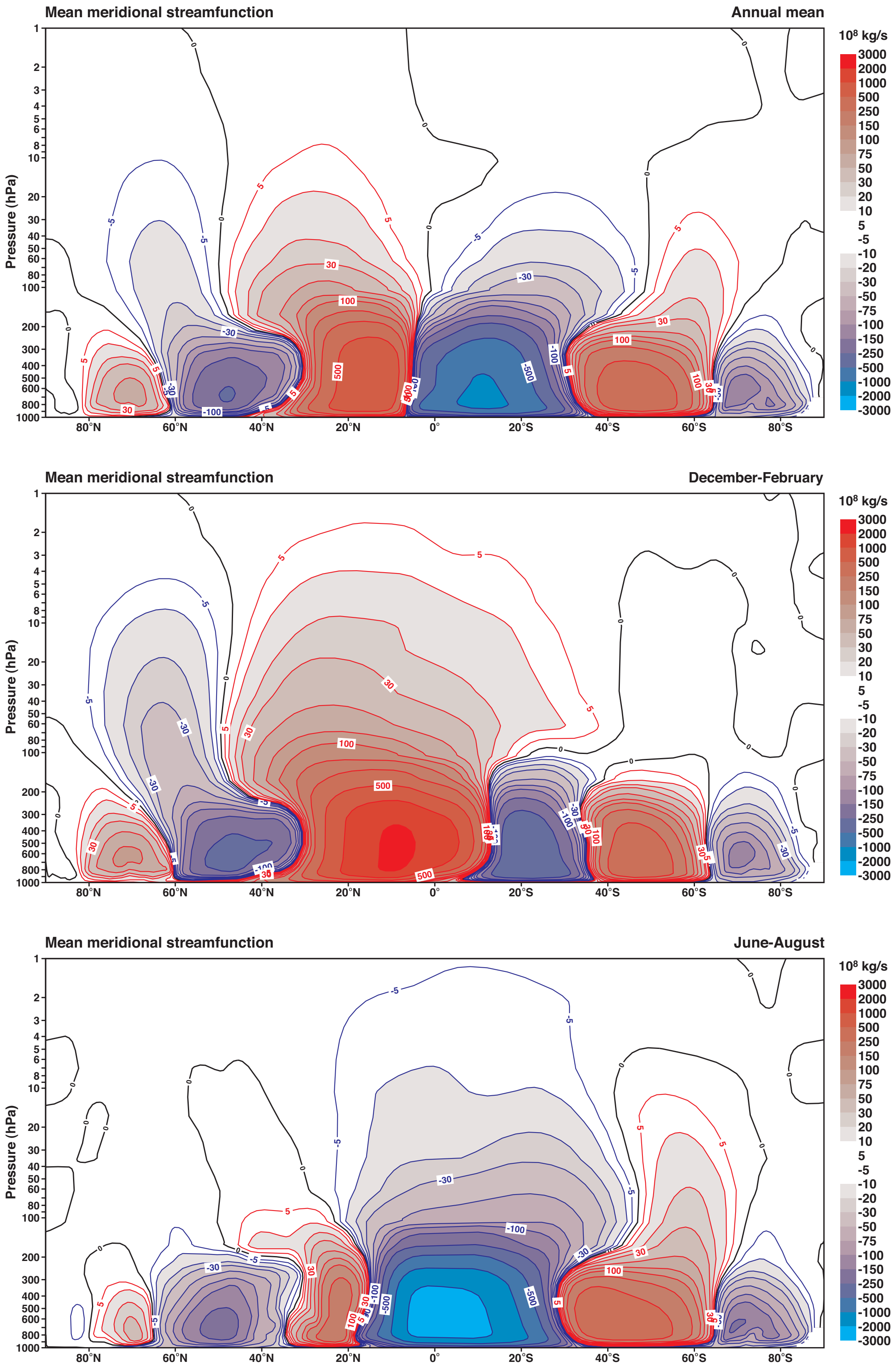

ERA-40 Atlas

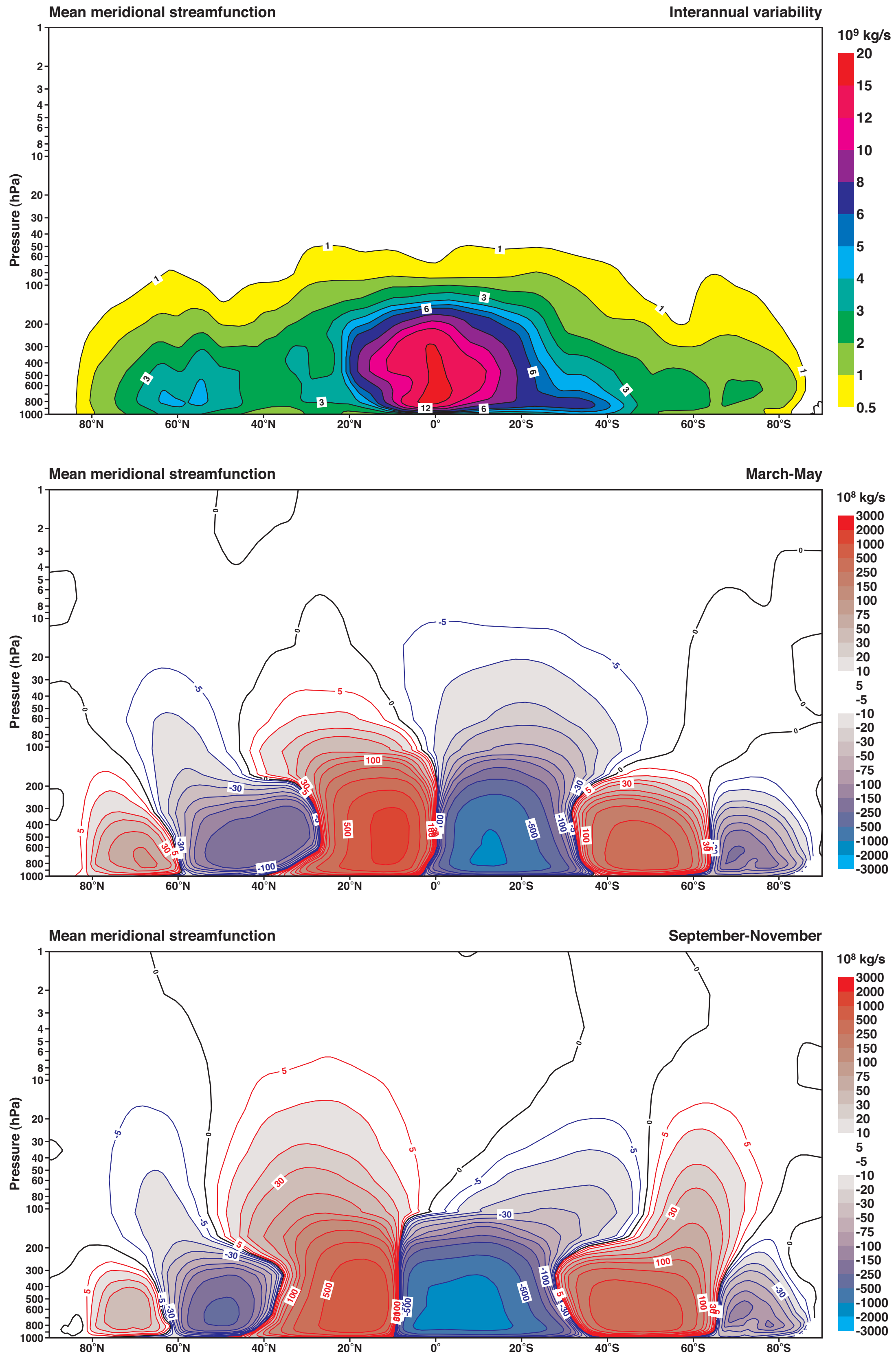

D31 A pressure based stratospheric perspective of mean meridional streamfunction (kgs^{-1}).

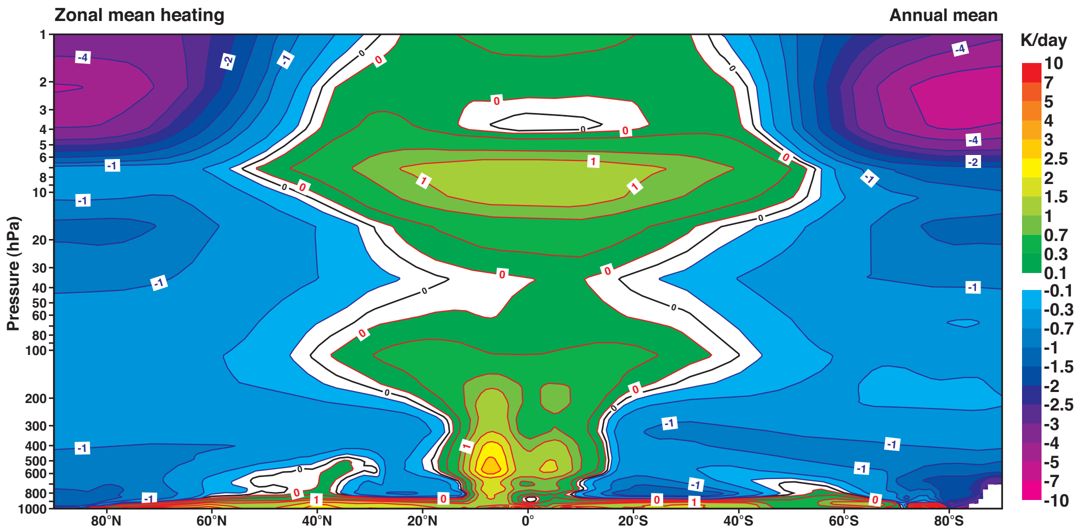

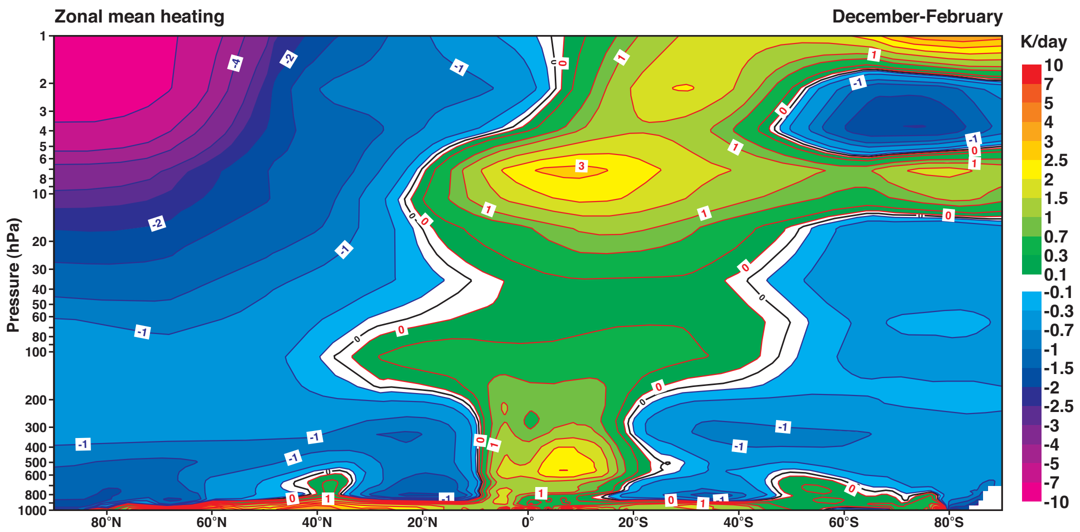

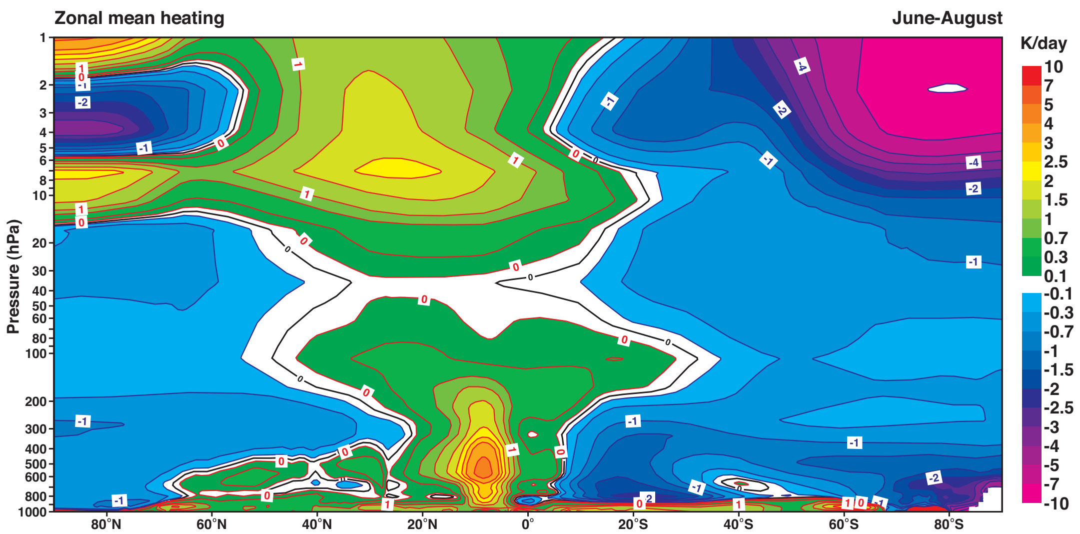

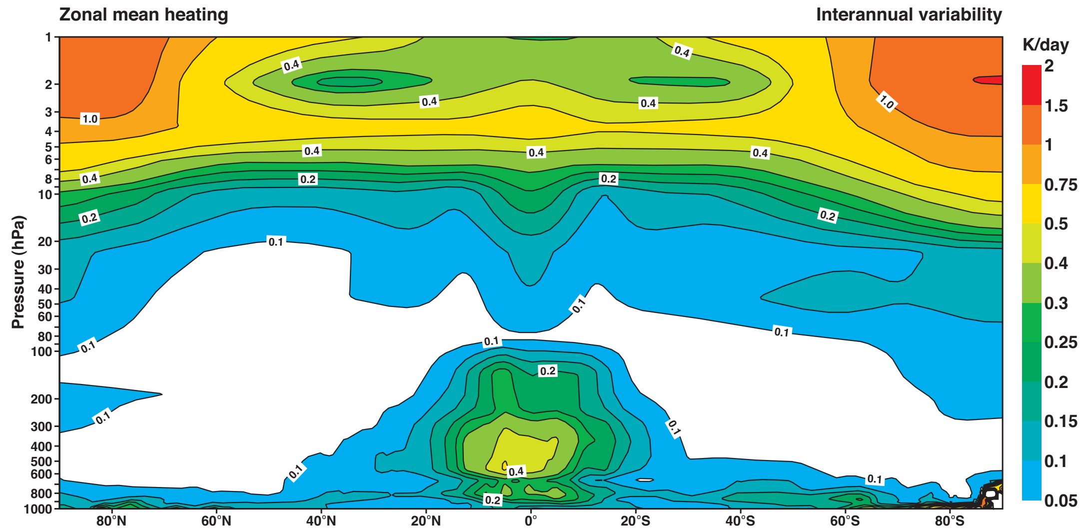

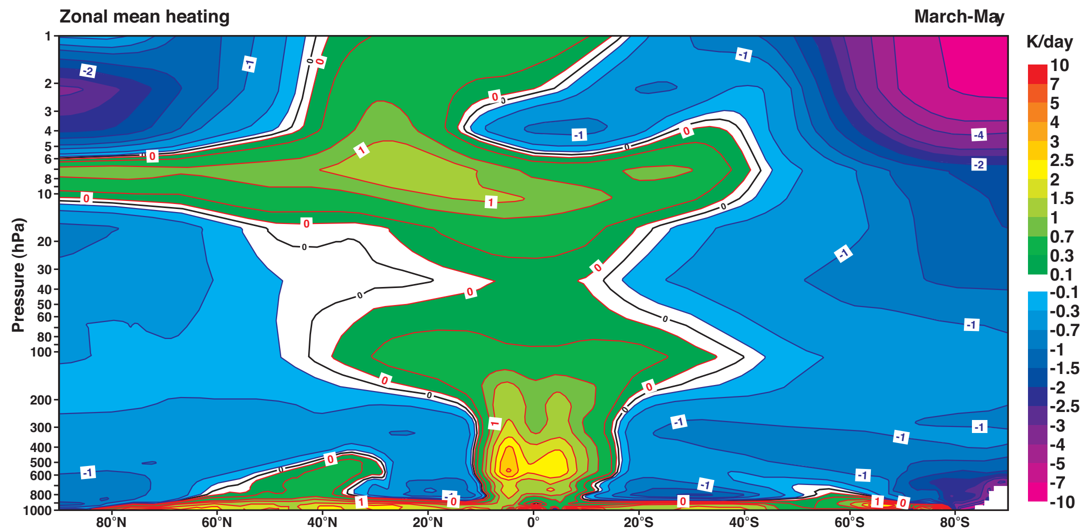

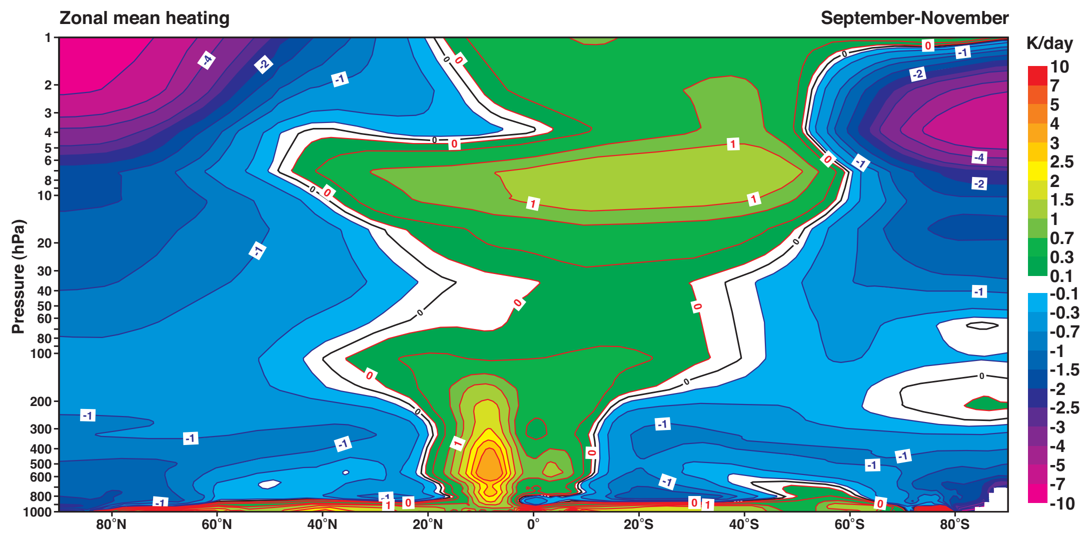

D32 A pressure based stratospheric perspective of zonal mean heating (Kday^{-1}).

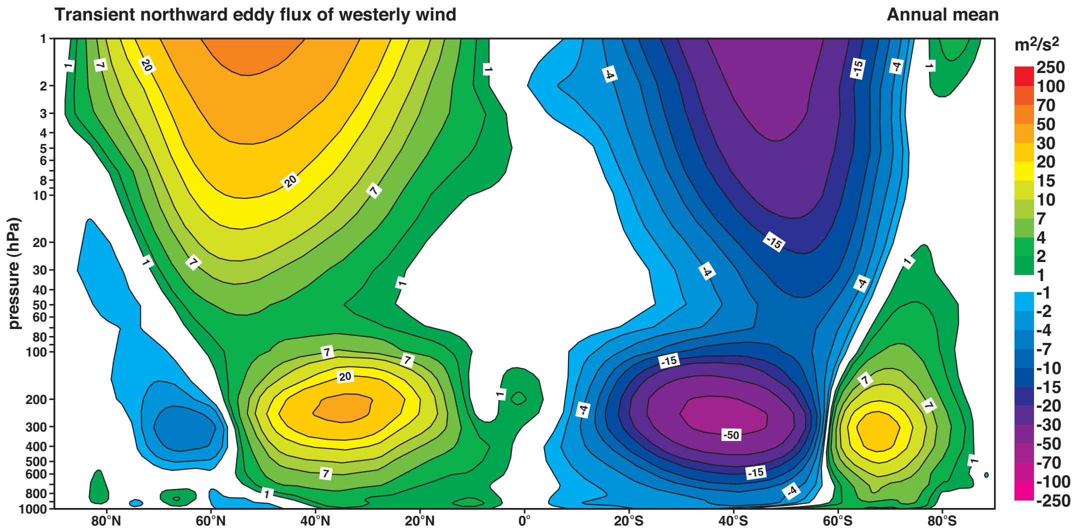

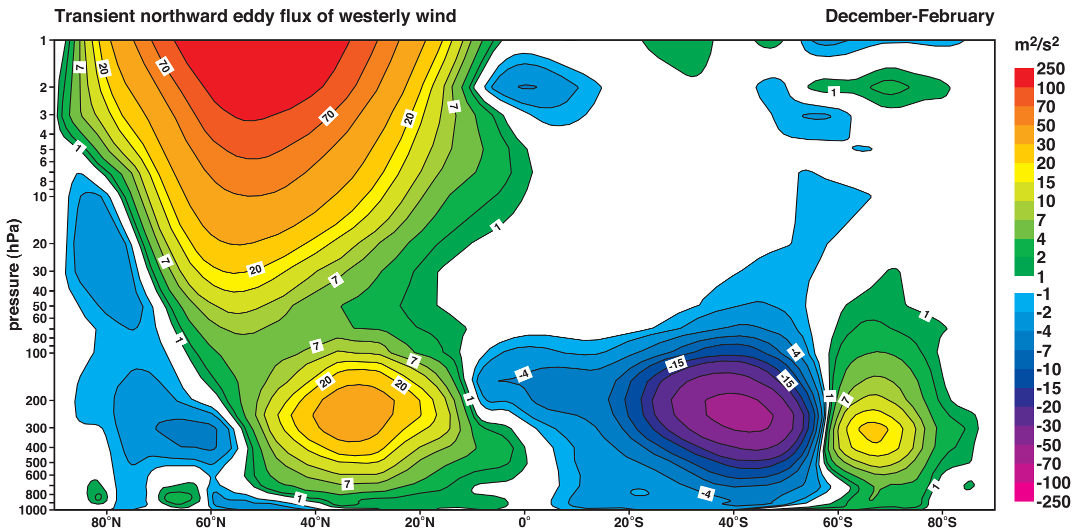

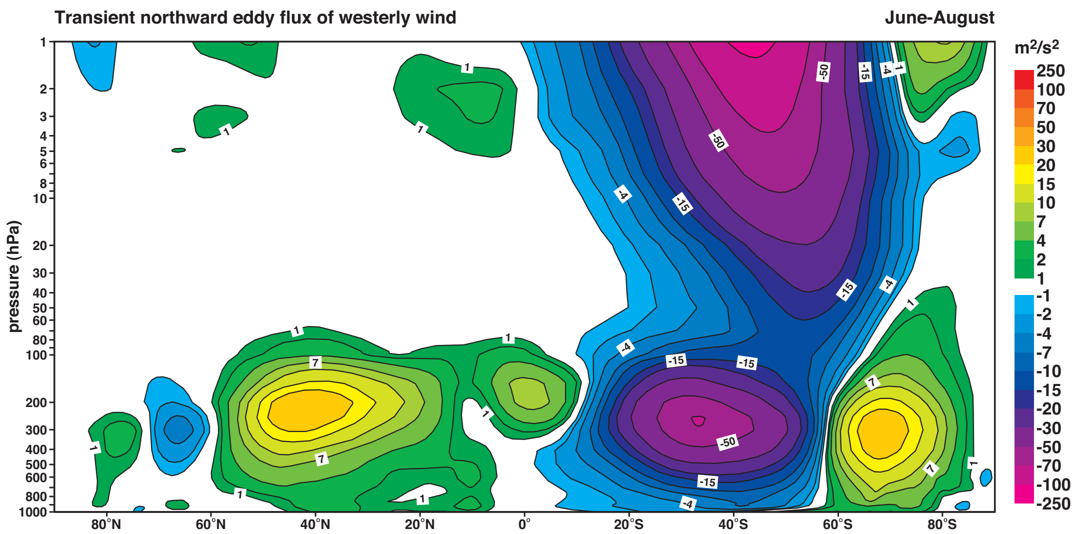

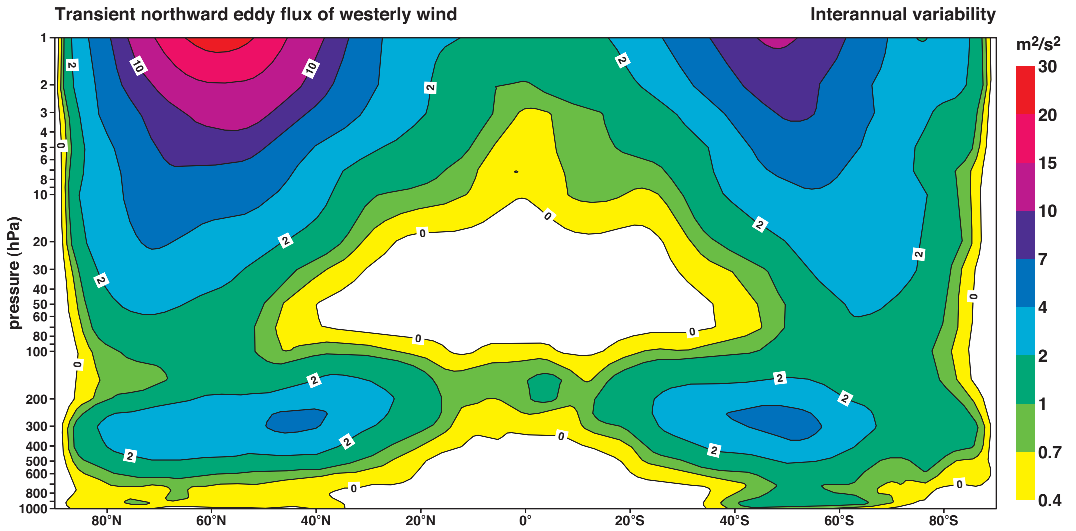

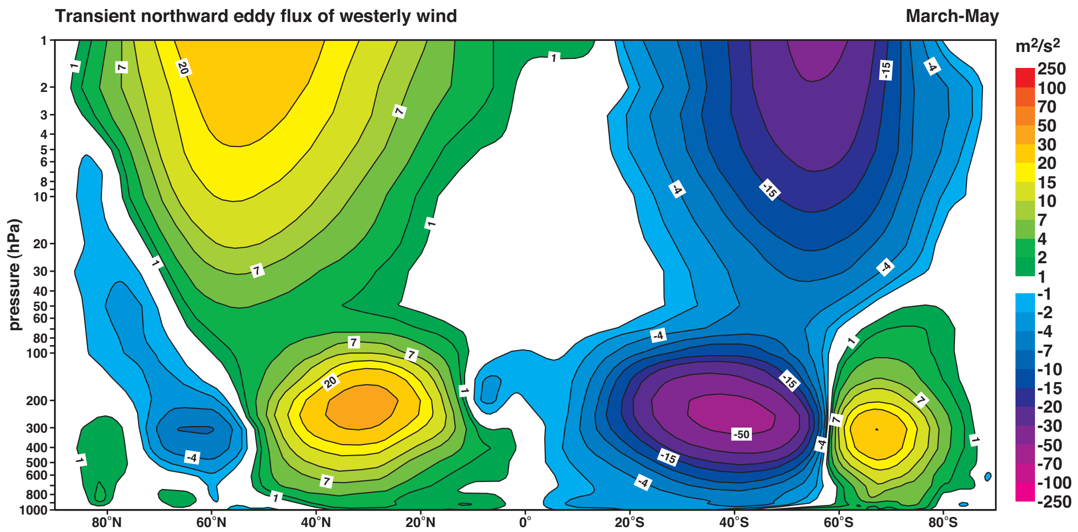

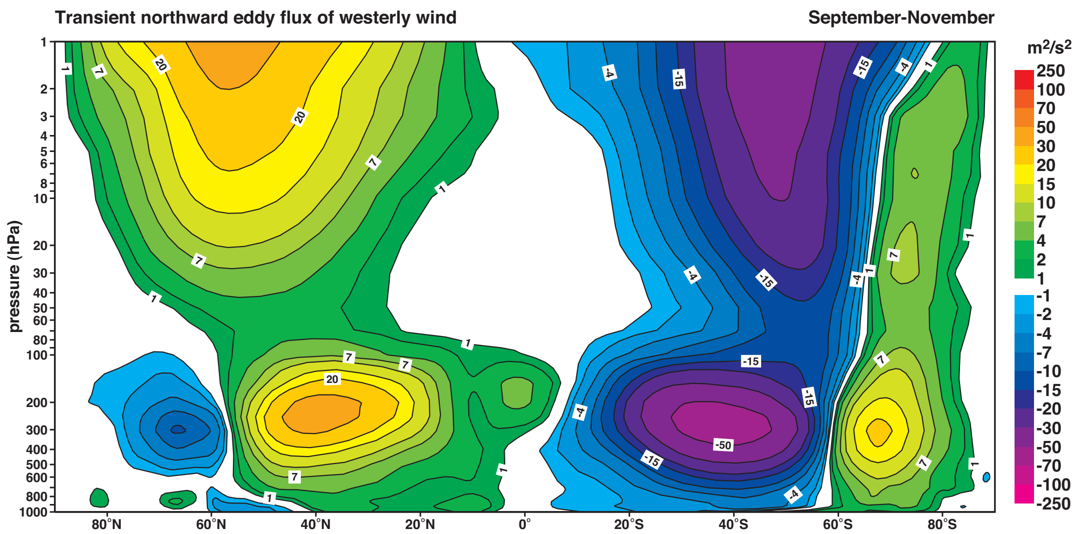

D33 The zonal mean total transient of the northward flux of westerly wind (m^2s^{-2}).

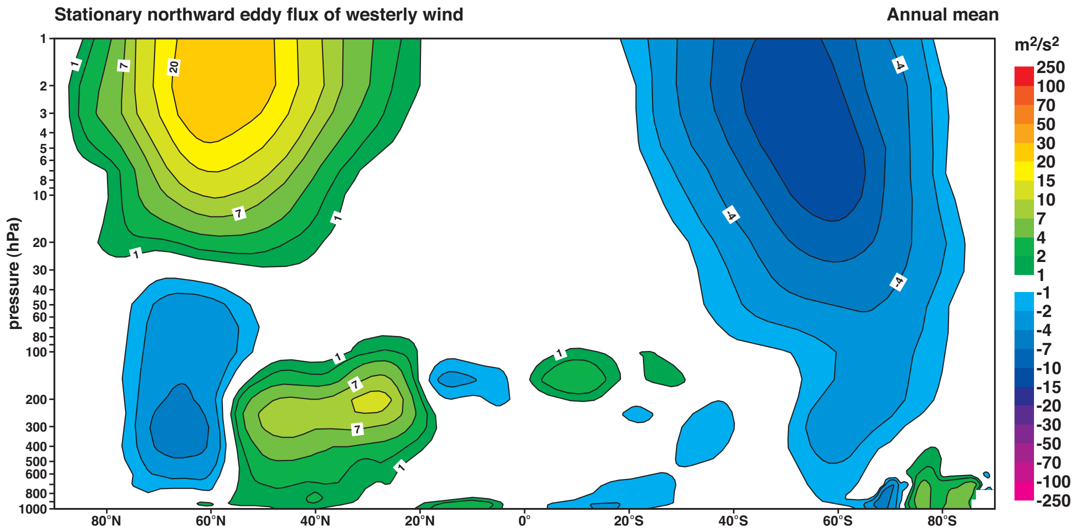

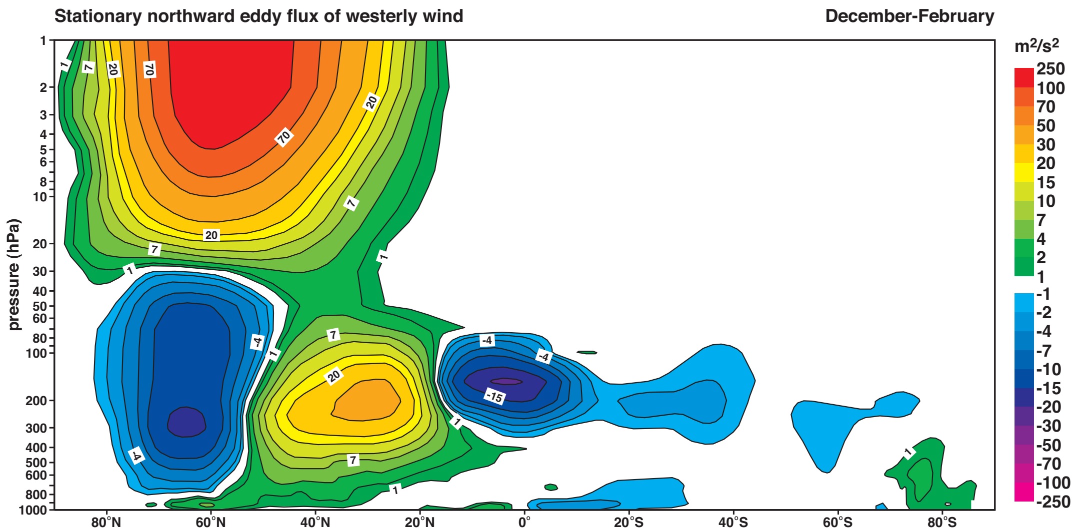

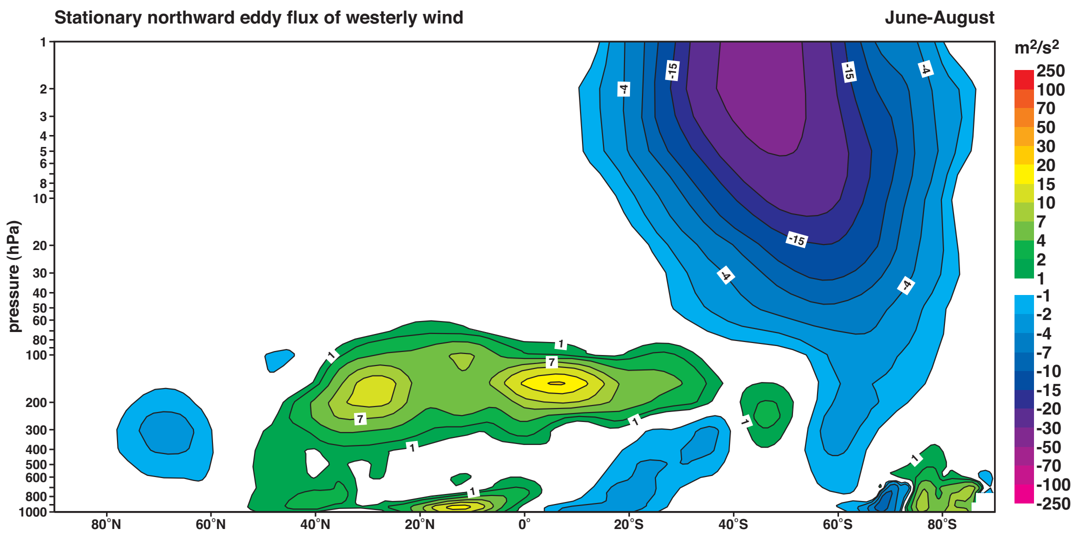

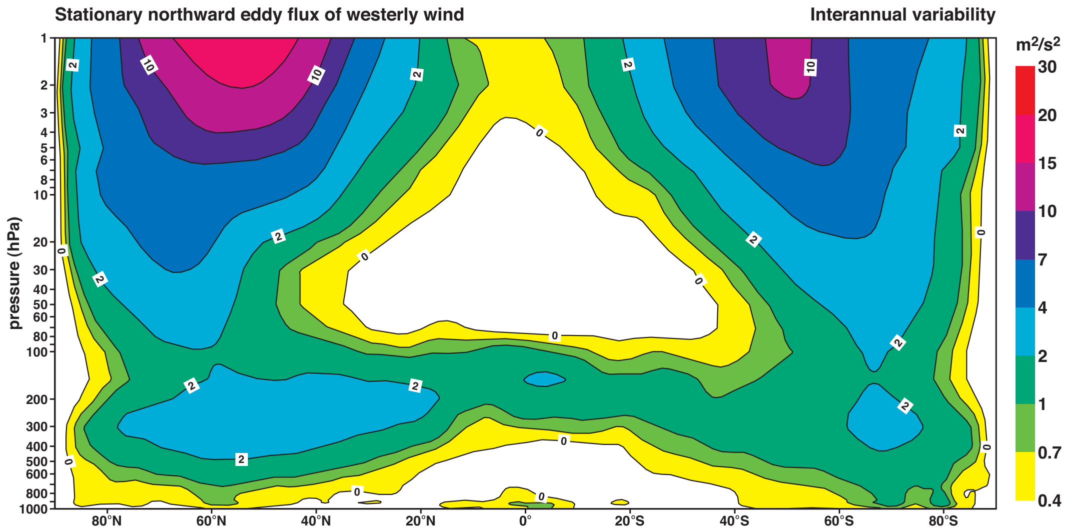

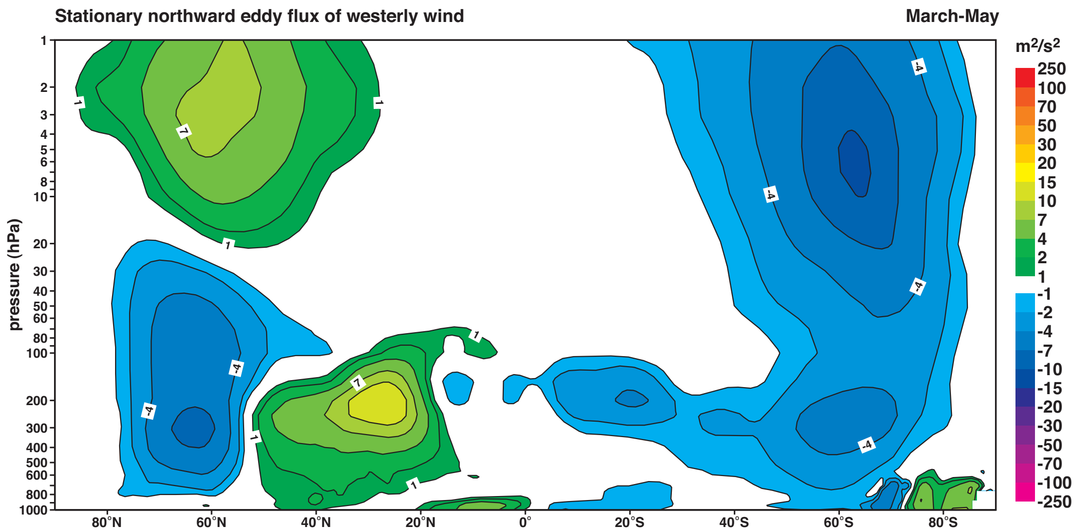

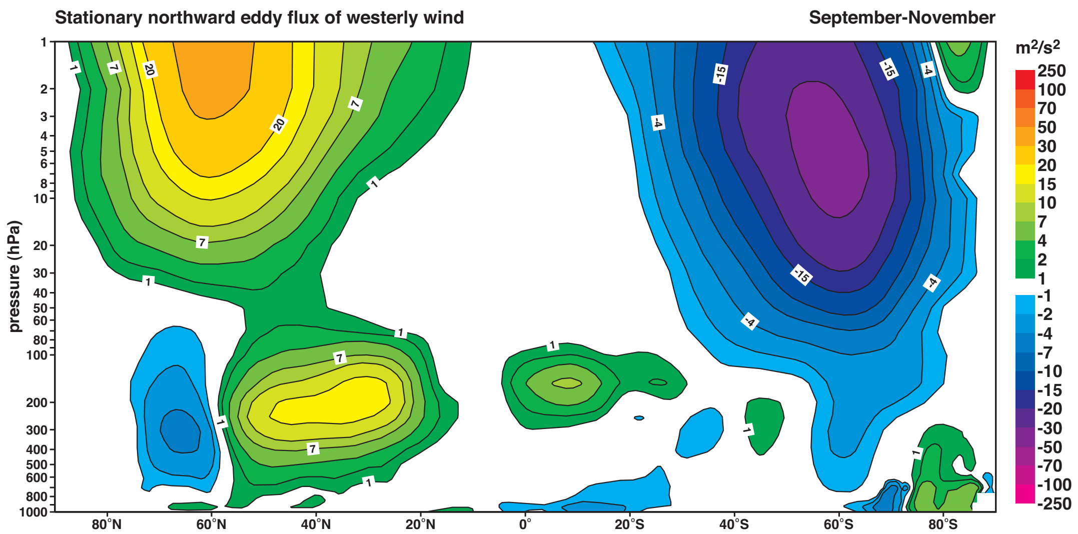

D34 The zonal mean stationary eddy of the northward flux of westerly wind (m^2s^{-2}).

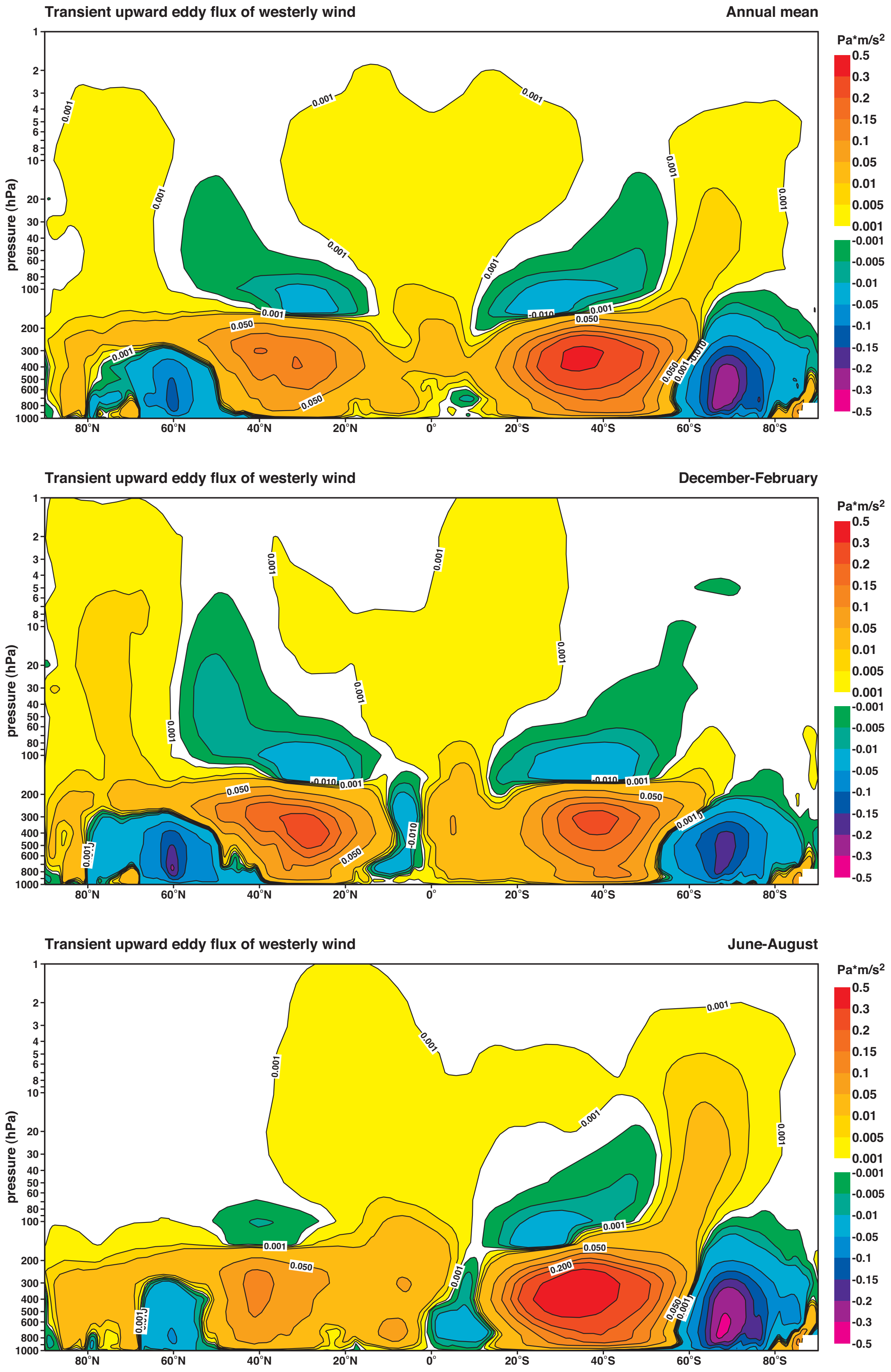

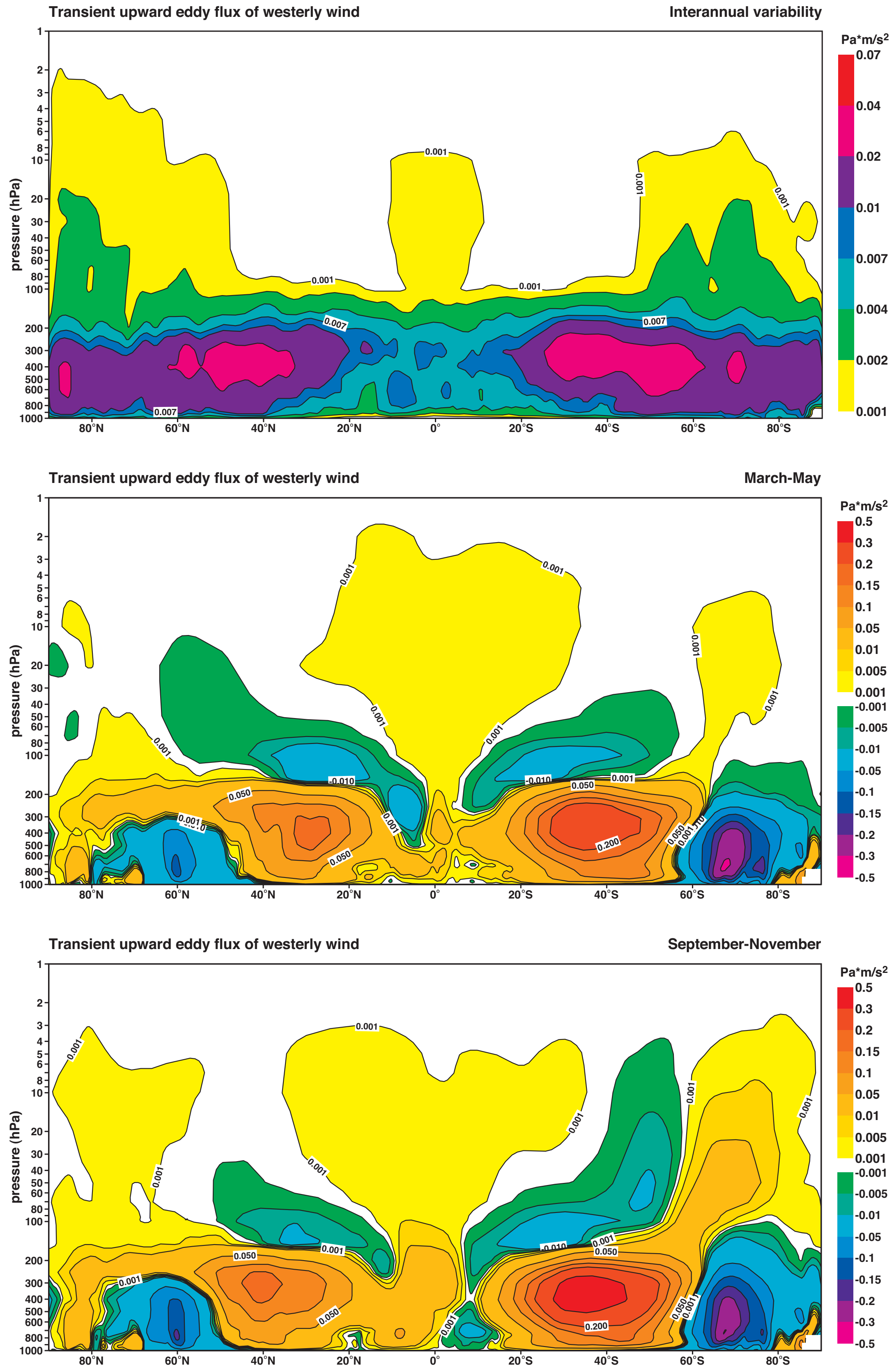

D35 The zonal mean total transient of the upward flux of westerly wind (mPas-2).

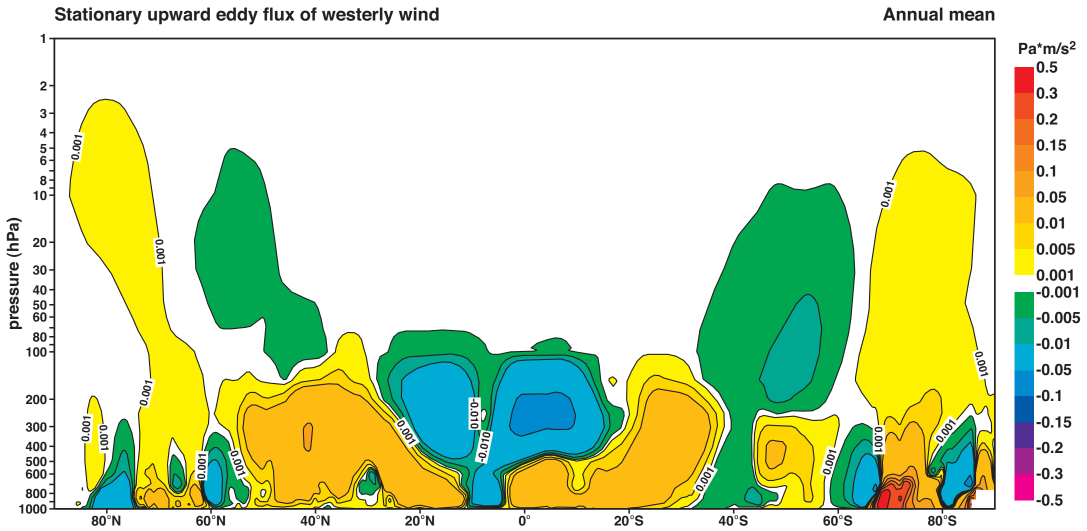

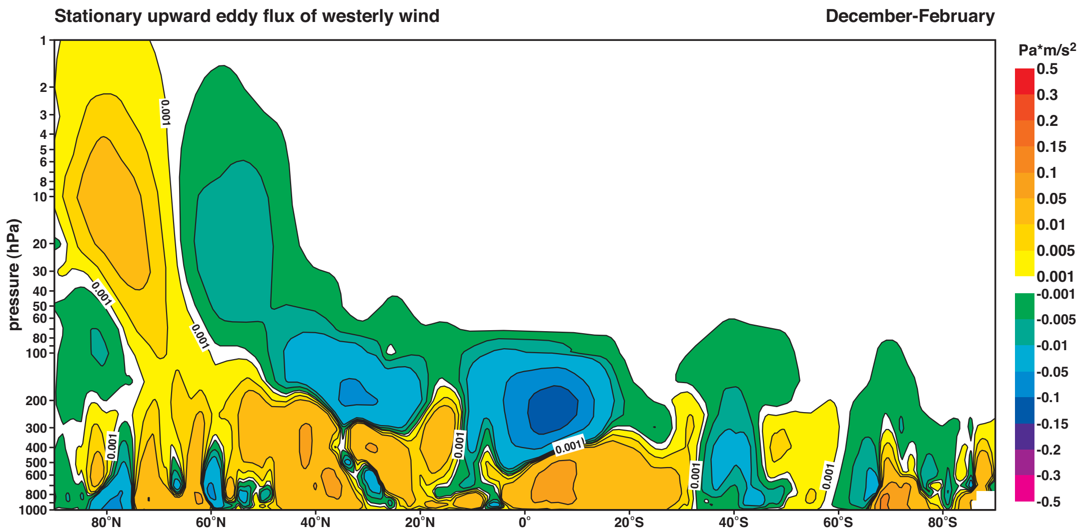

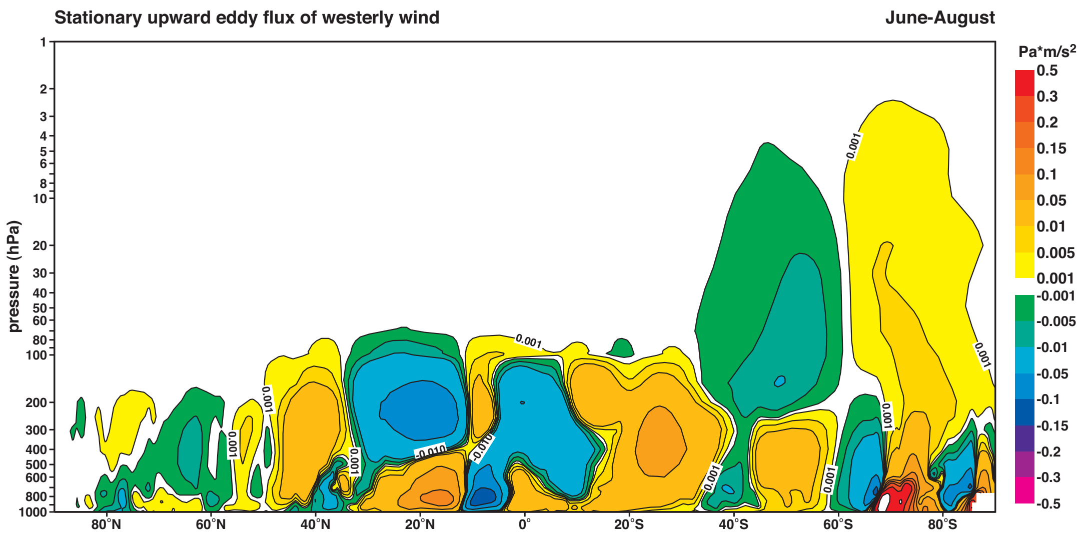

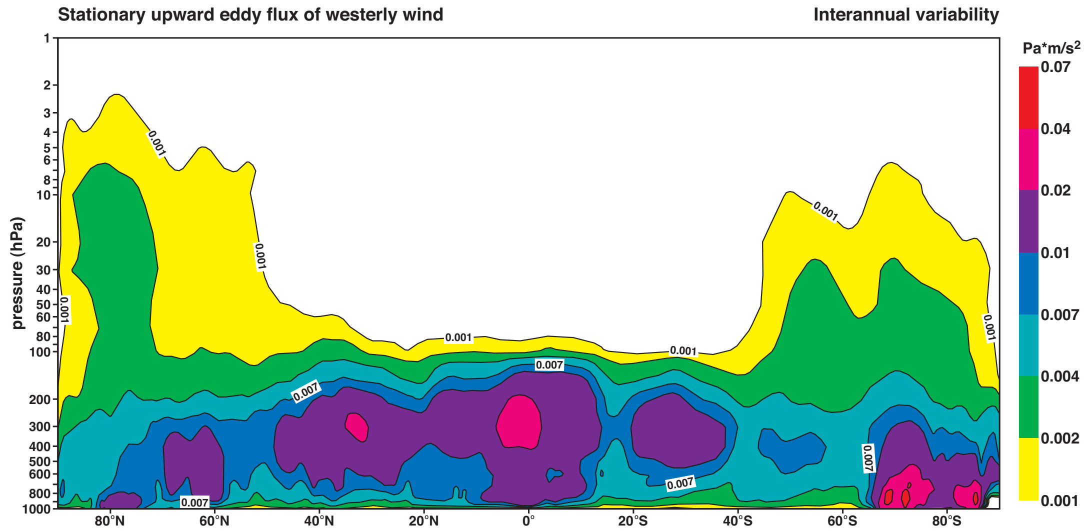

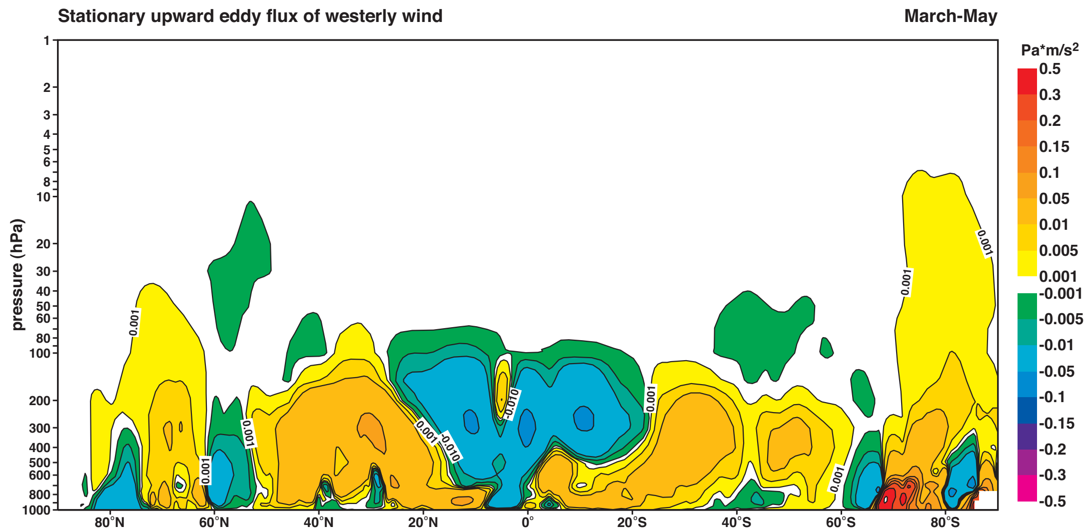

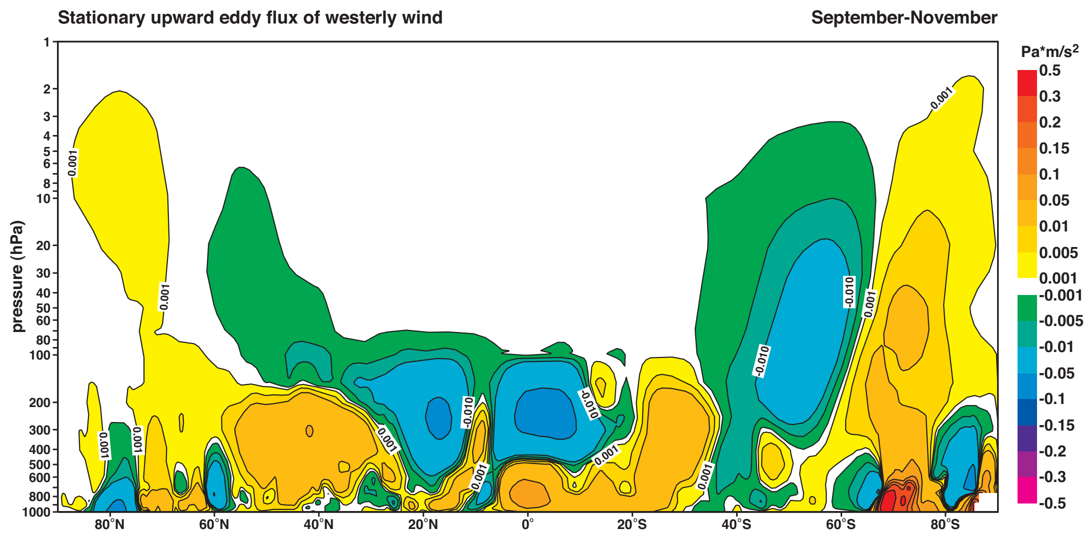

D36 The zonal mean stationary eddy of the upward flux of westerly wind (mPas^{-2}).

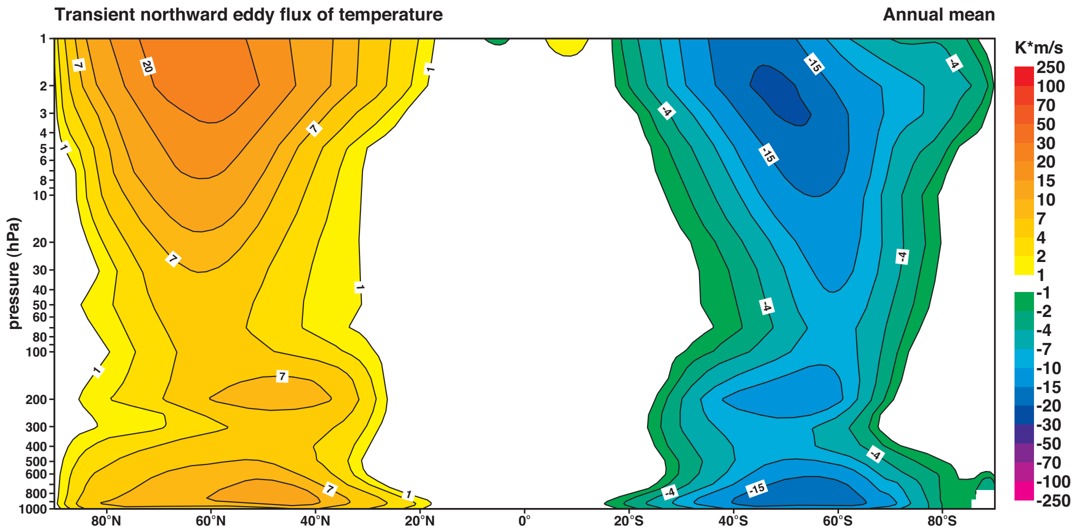

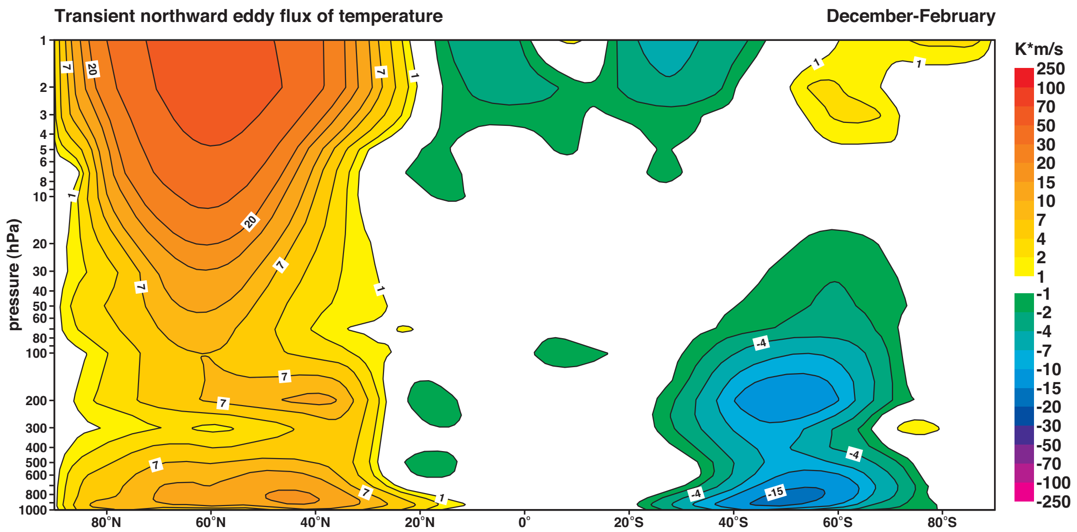

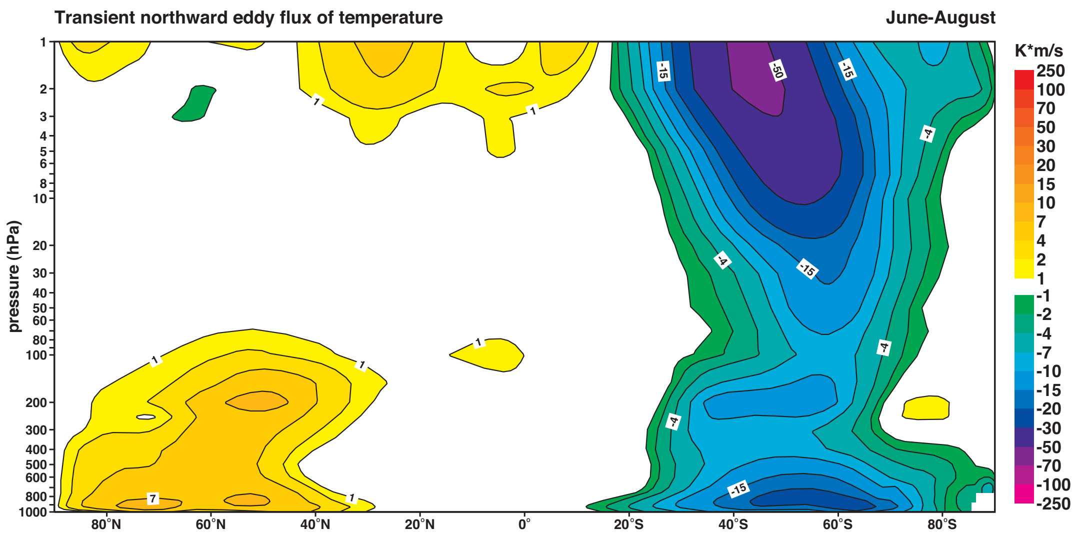

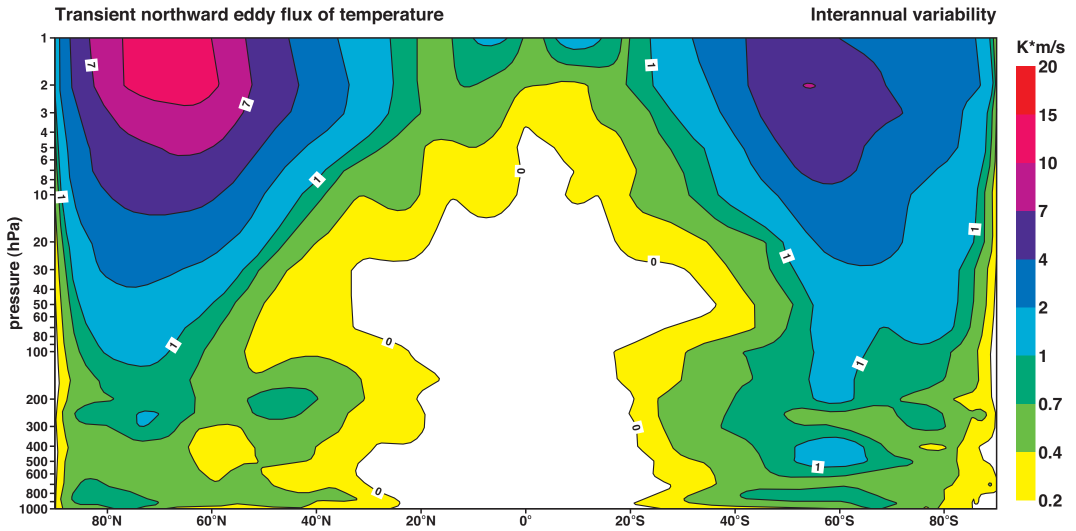

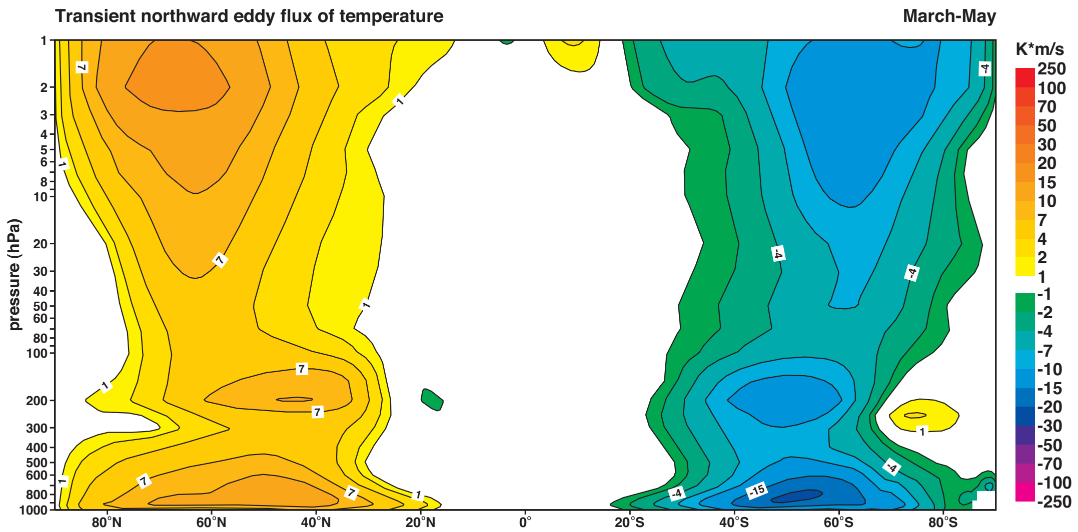

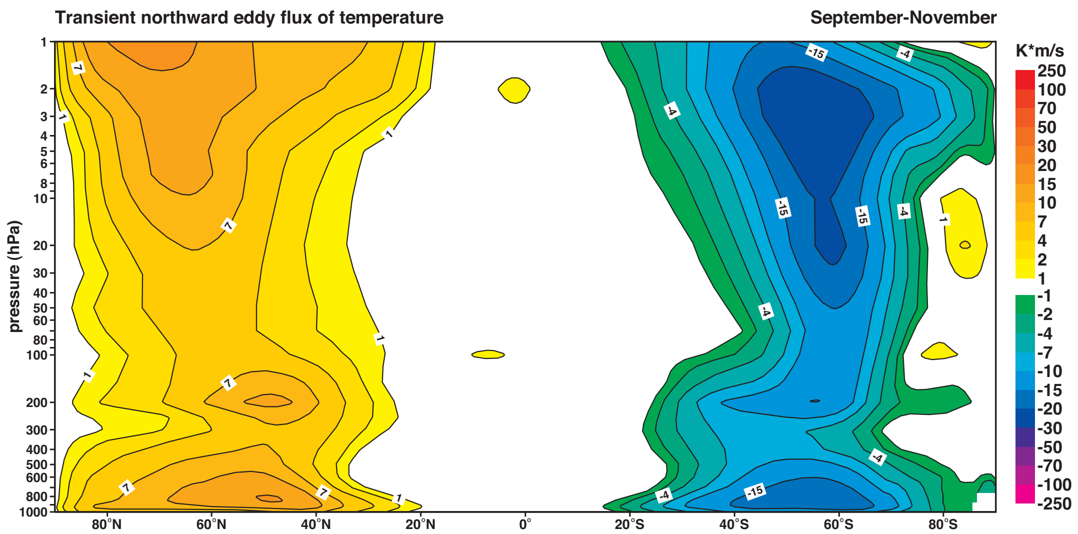

D37 The zonal mean total transient of the northward flux of temperature (Kms^{-1}).

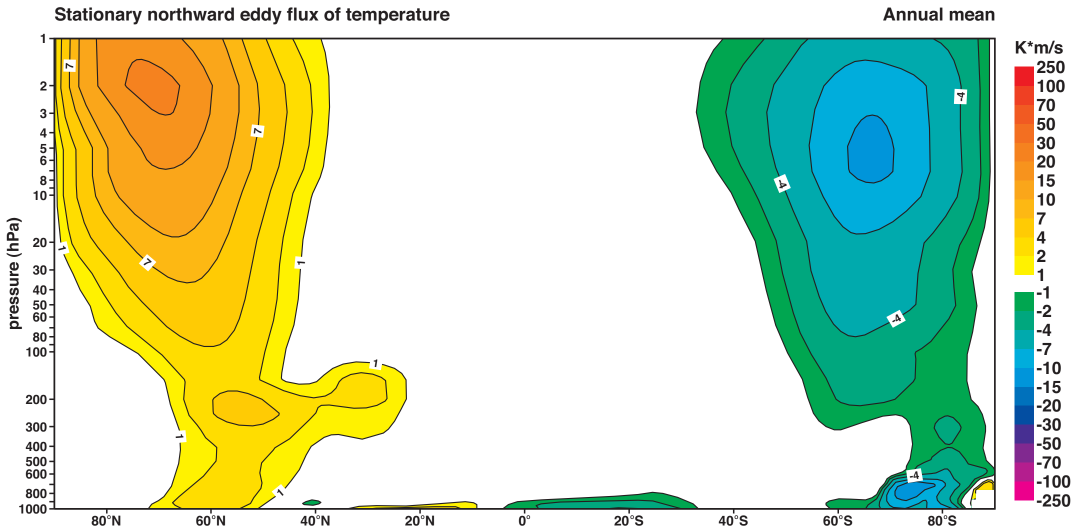

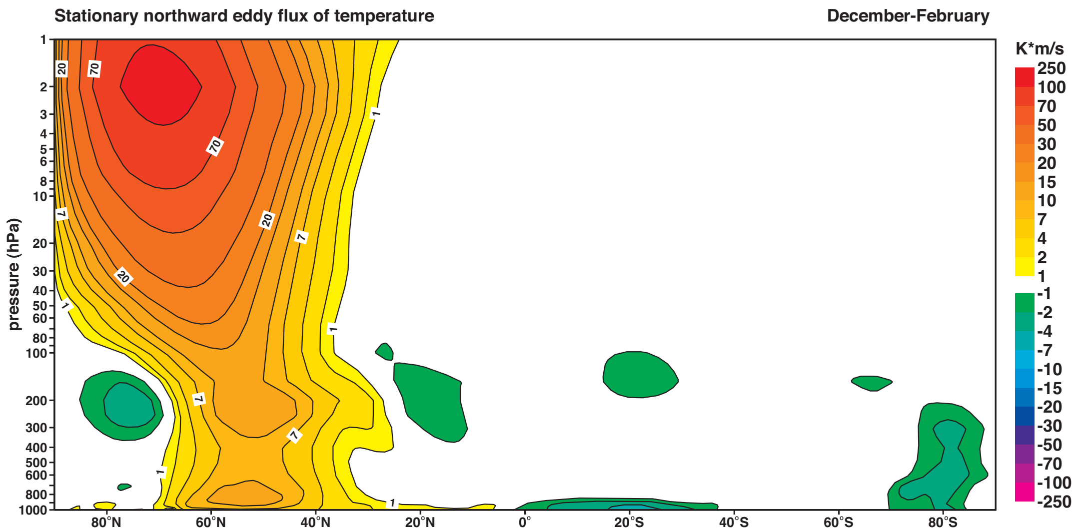

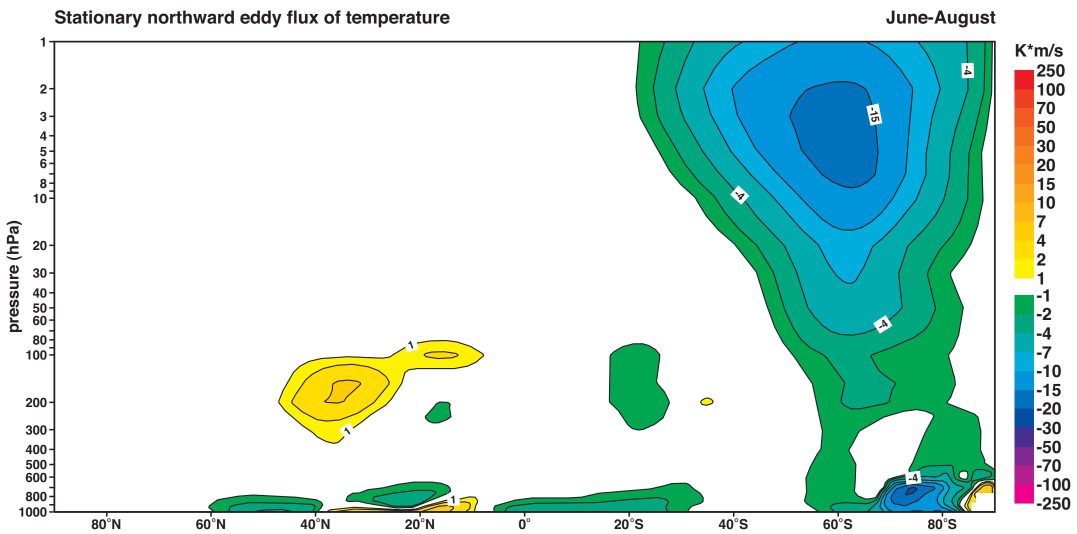

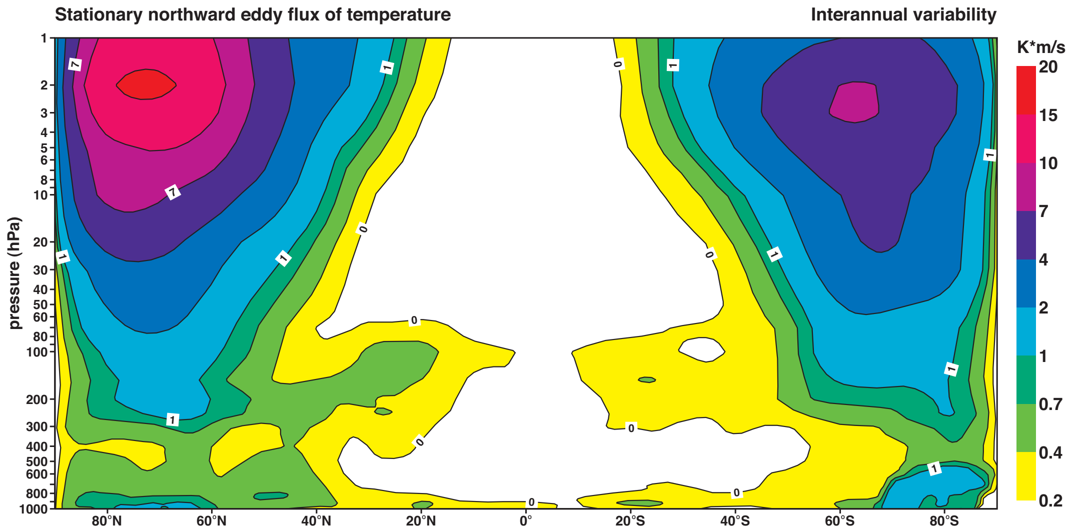

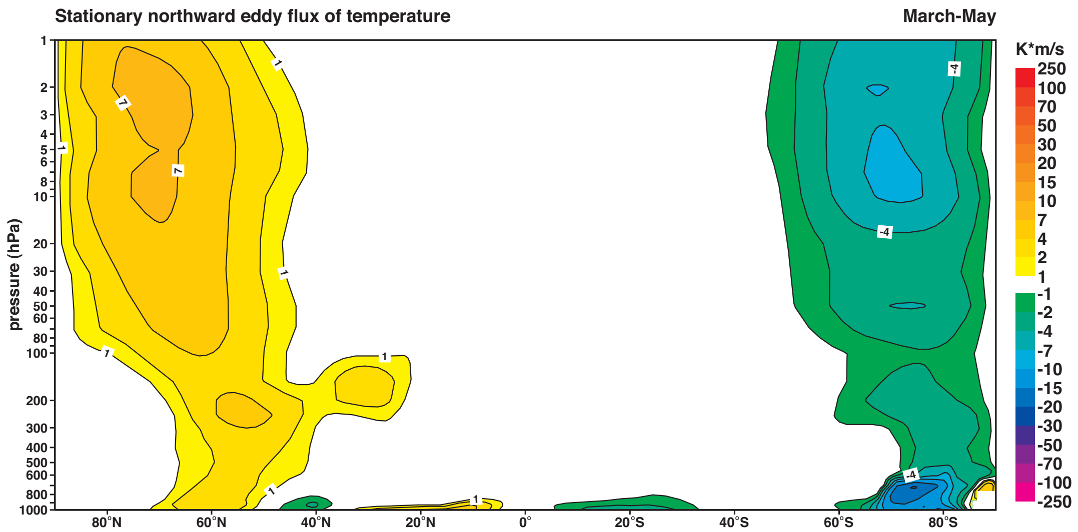

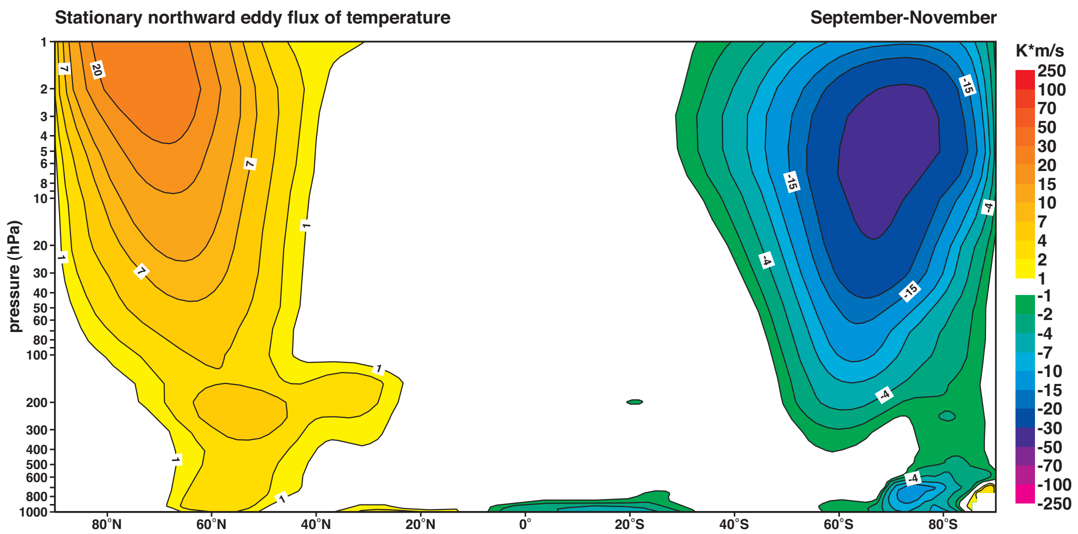

D38 The zonal mean stationary eddy of the northward flux of temperature (Kms^{-1}).

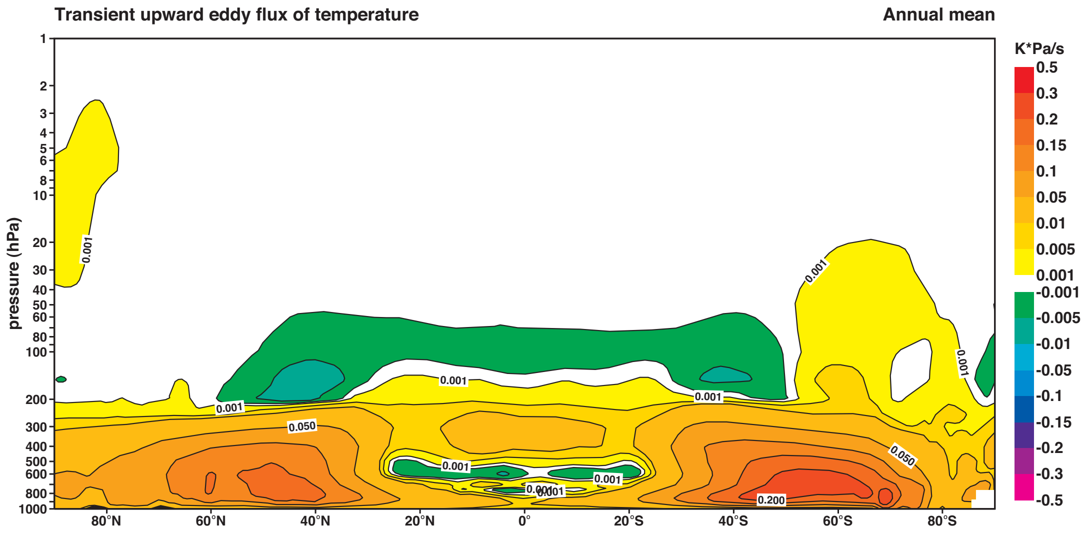

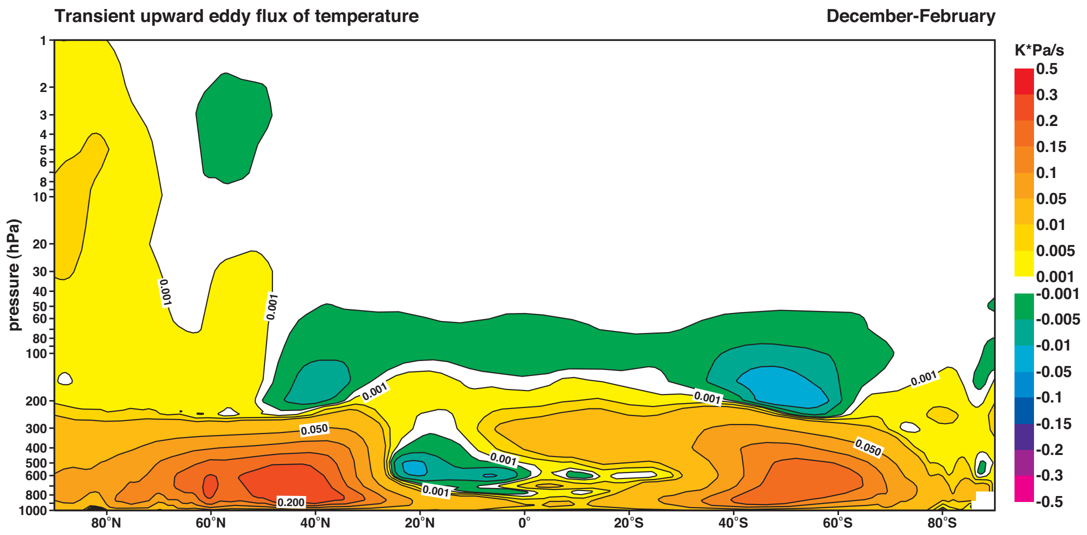

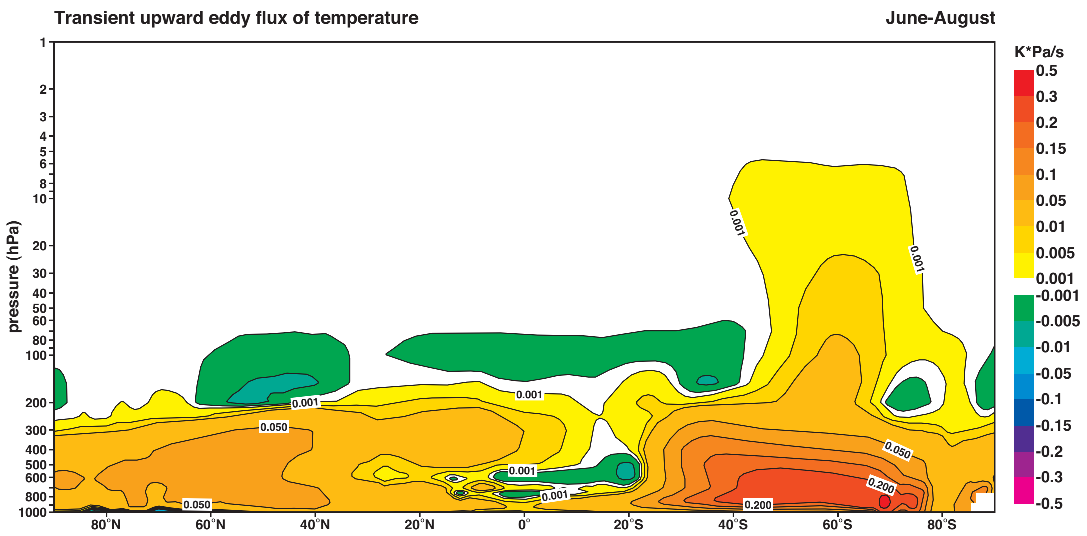

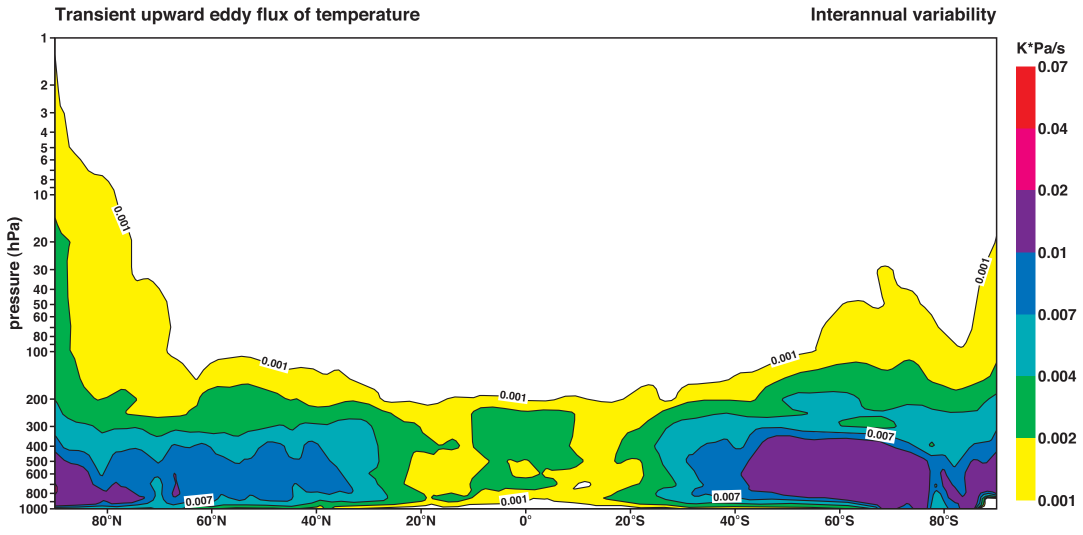

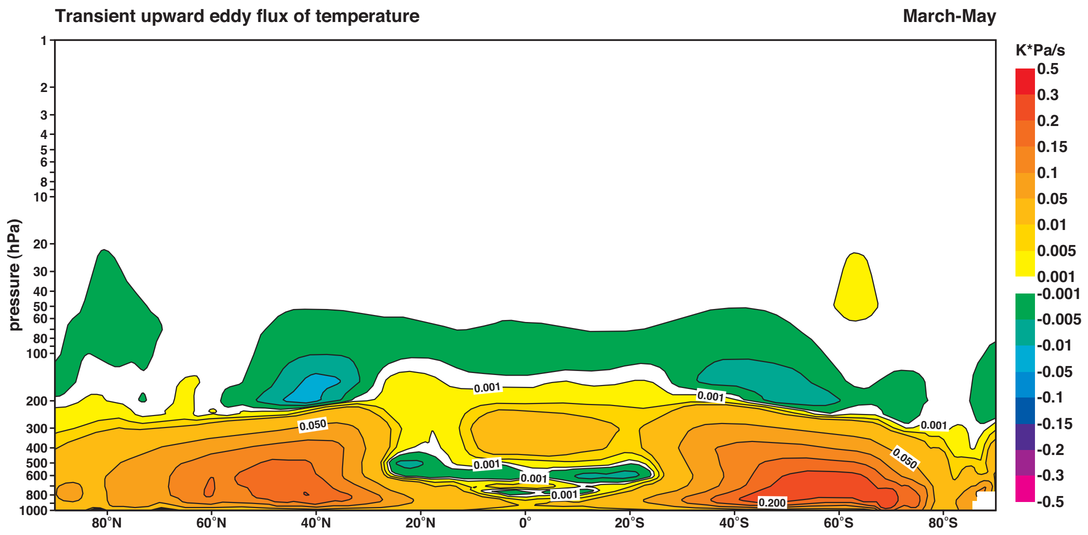

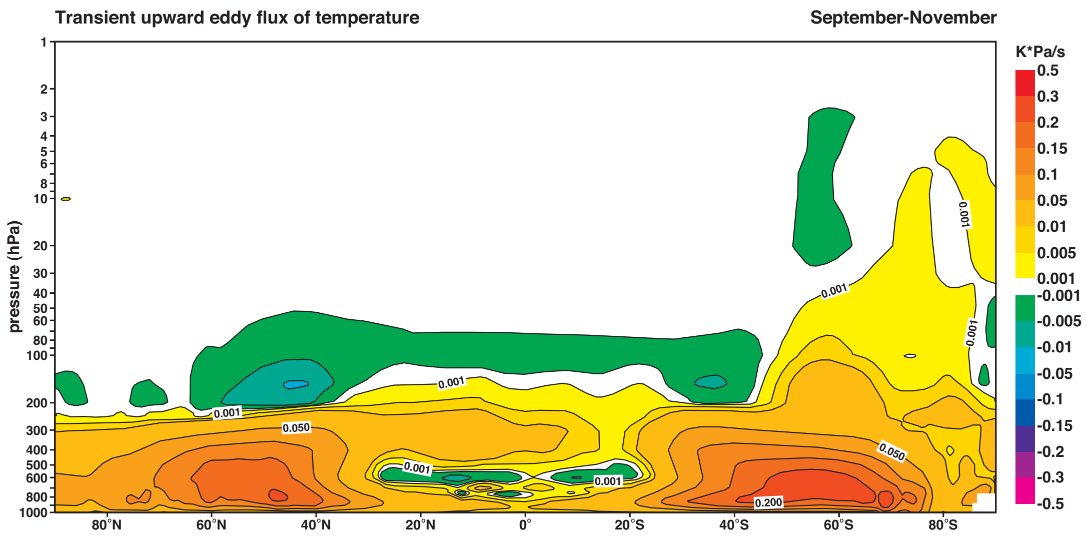

D39 The zonal mean total transient of the upward flux of temperature (KPas^{-1}).

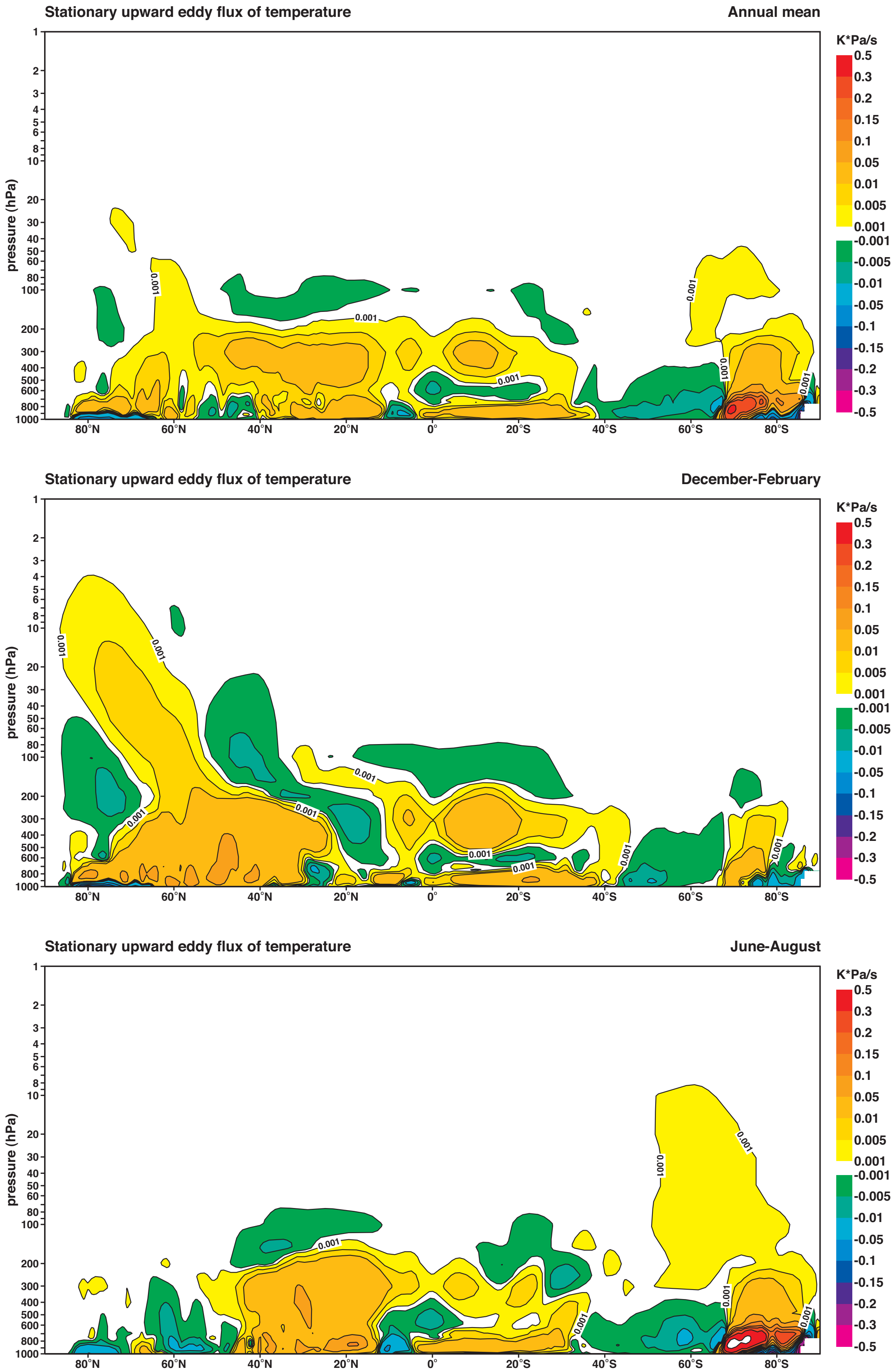

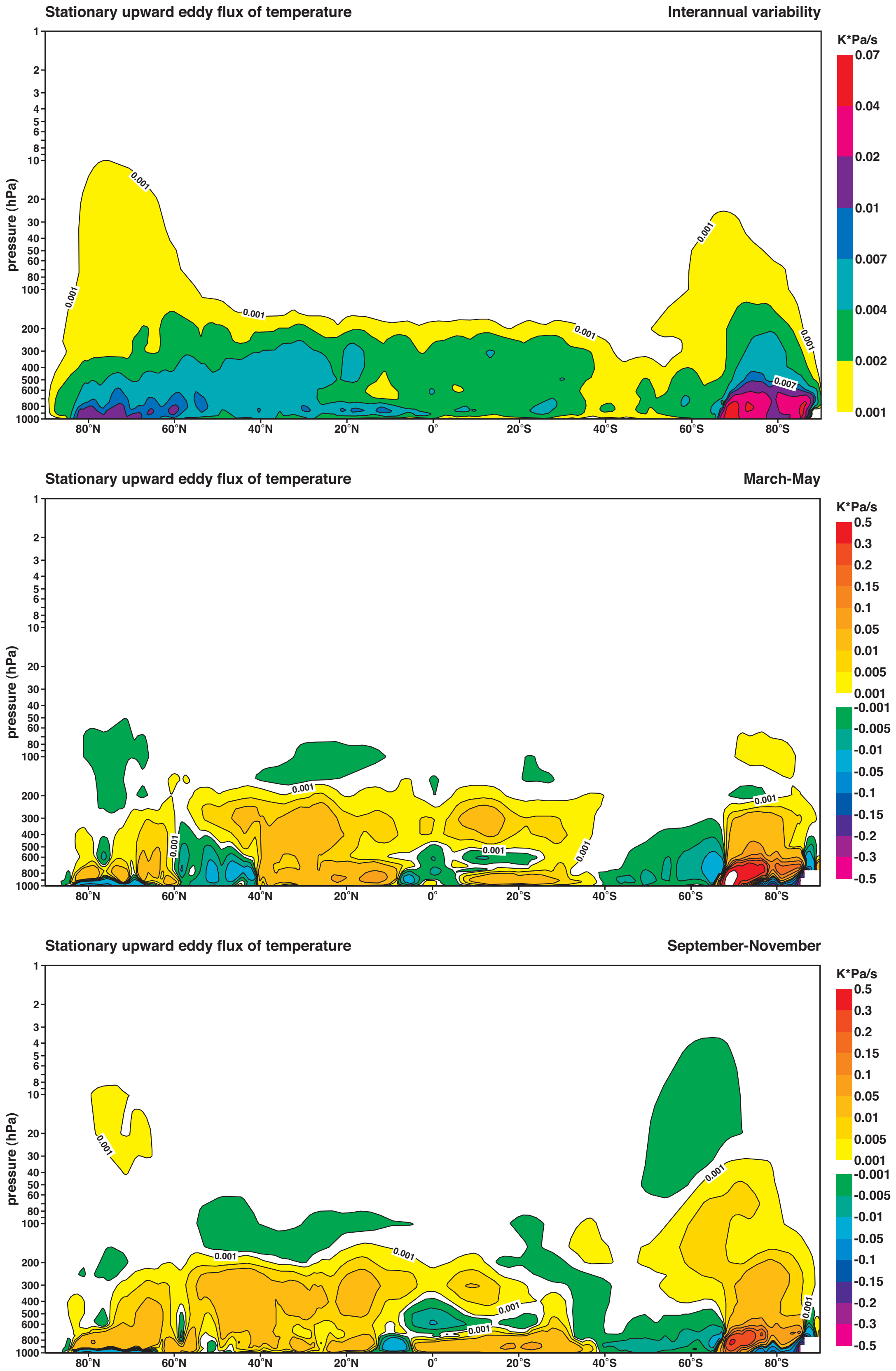

D40 The zonal mean stationary eddy of the upward flux of temperature (KPas[-1]).

Section E

Isentropic level climatologies

Wind and pressure (hPa) at 350 K — **Annual mean**

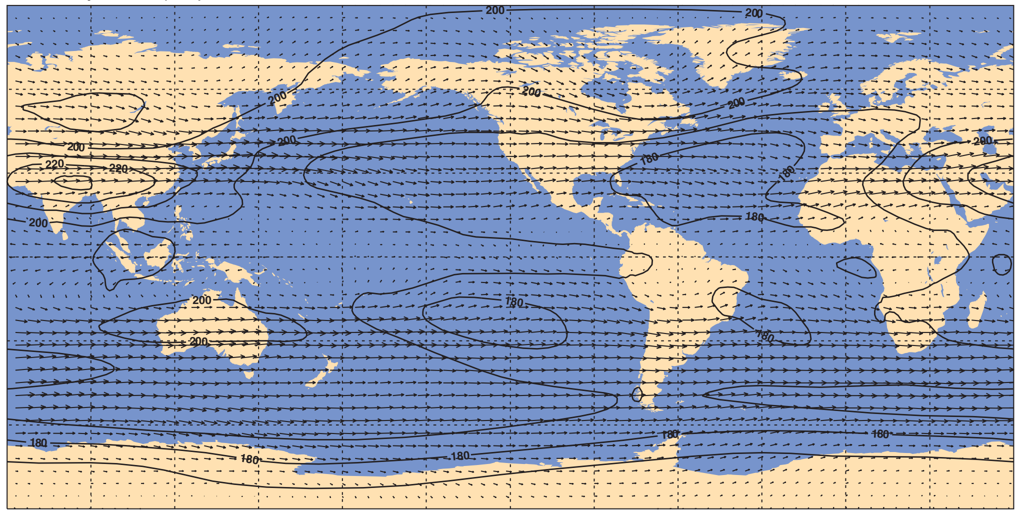

Wind and pressure (hPa) at 350 K — **December-February**

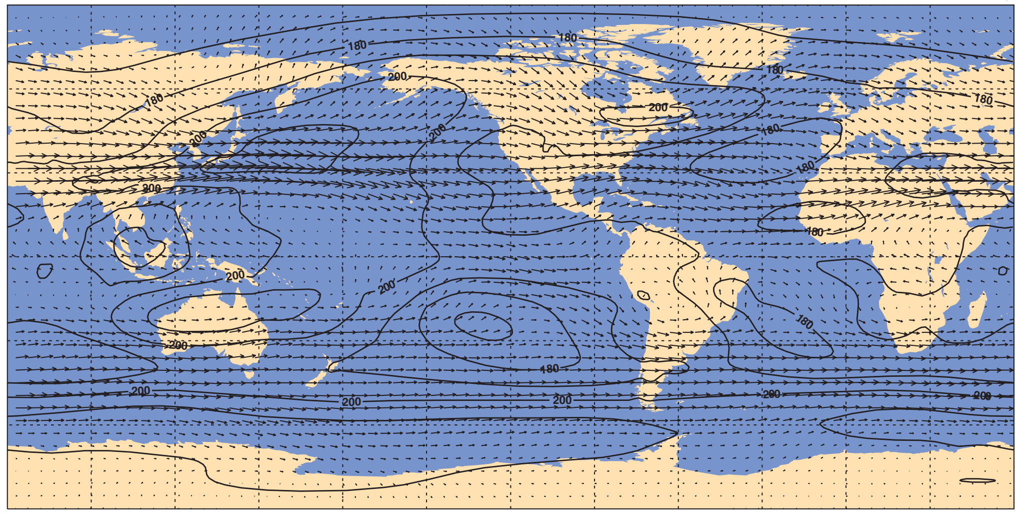

Wind and pressure (hPa) at 350 K — **June-August**

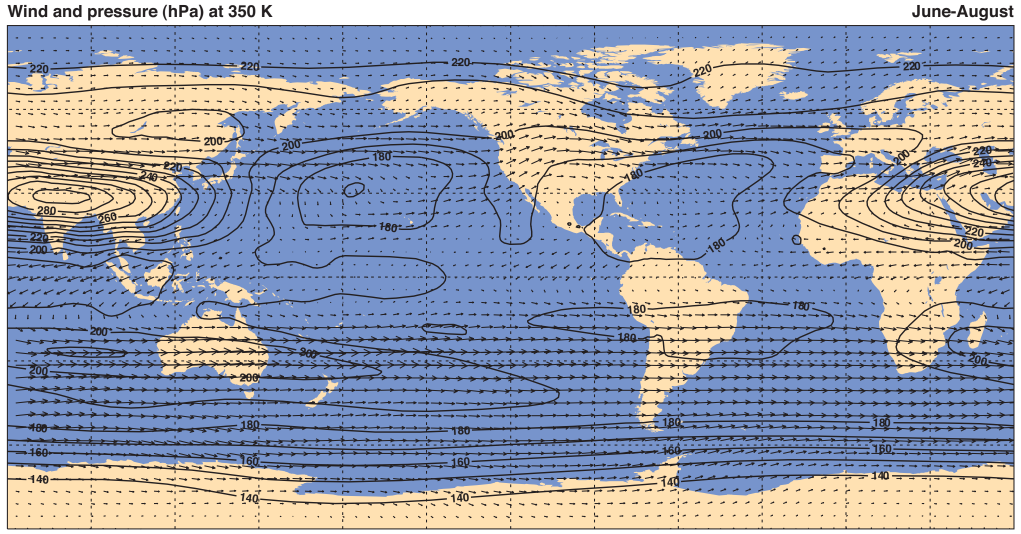

Isotachs and pressure (hPa) (contours) at 350 K — **Interannual variability**

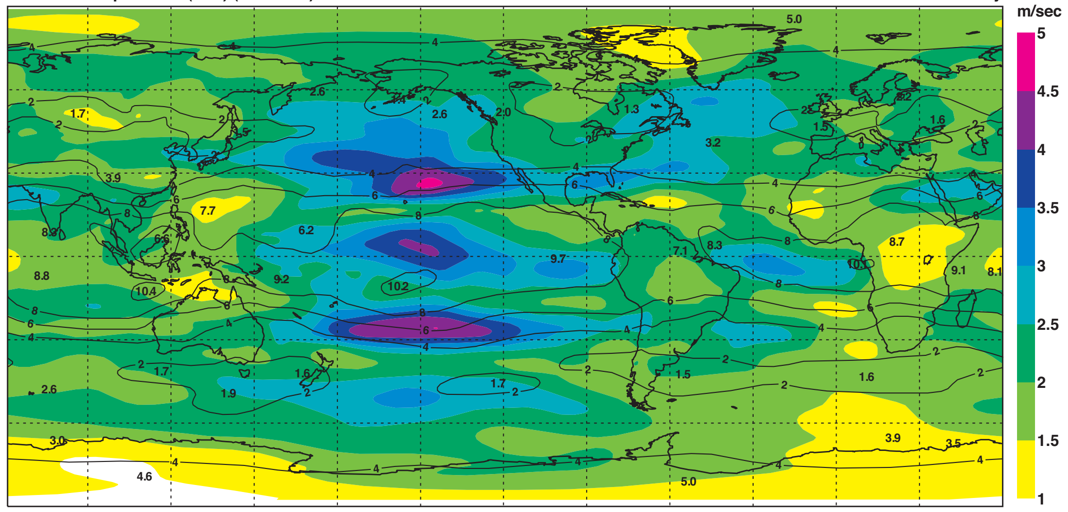

Wind and pressure (hPa) at 350 K — **March-May**

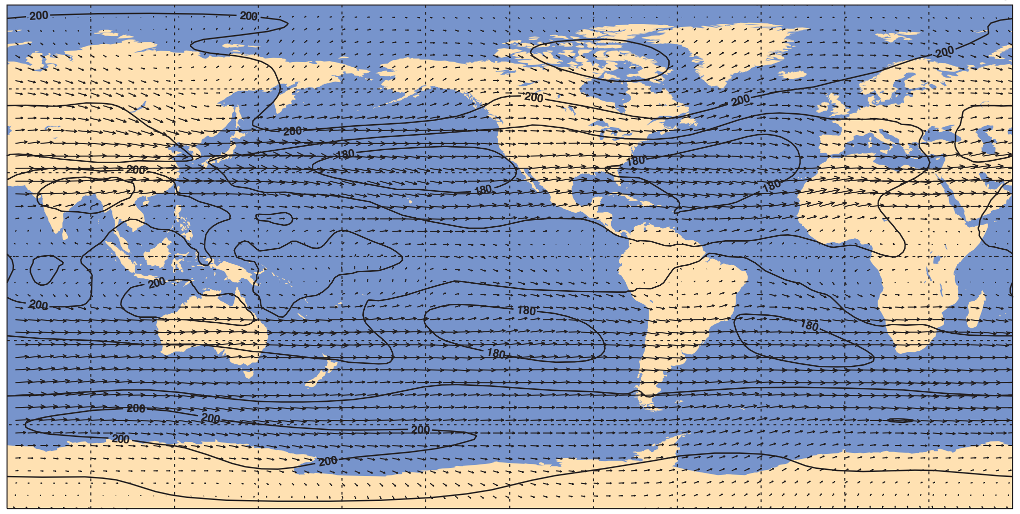

Wind and pressure (hPa) at 350 K — **September-November**

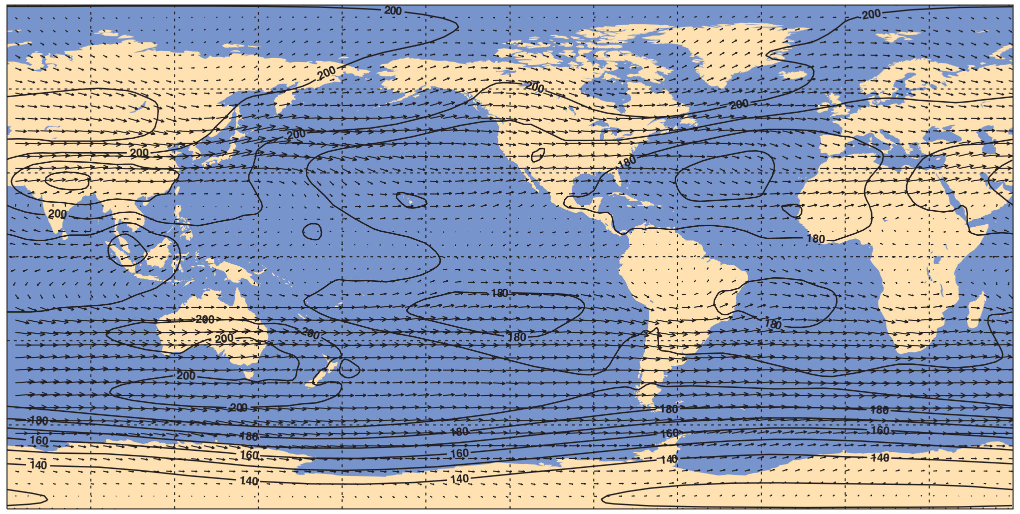

E1 Pressure (hPa) (contours) with vector wind (ms^{-1}) at 350 K. For the interannual variability, the isotachs are plotted (colour shading) instead of the vector wind.

Wind and pressure (hPa) at 330 K — Annual mean

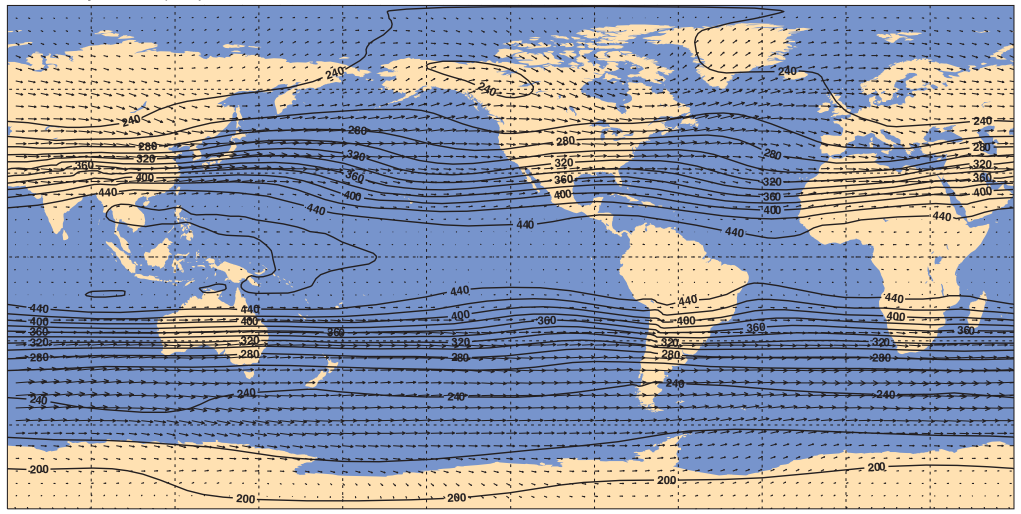

Wind and pressure (hPa) at 330 K — December-February

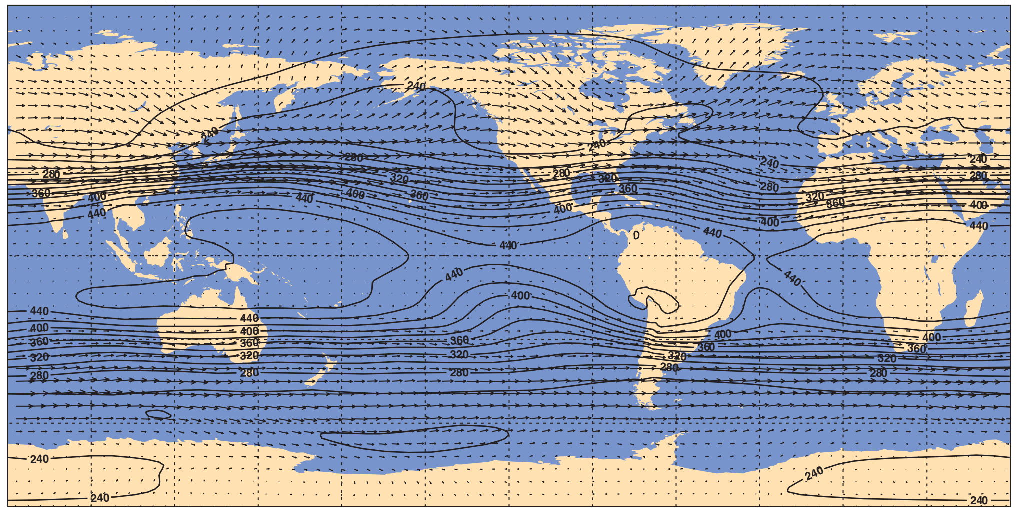

Wind and pressure (hPa) at 330 K — June-August

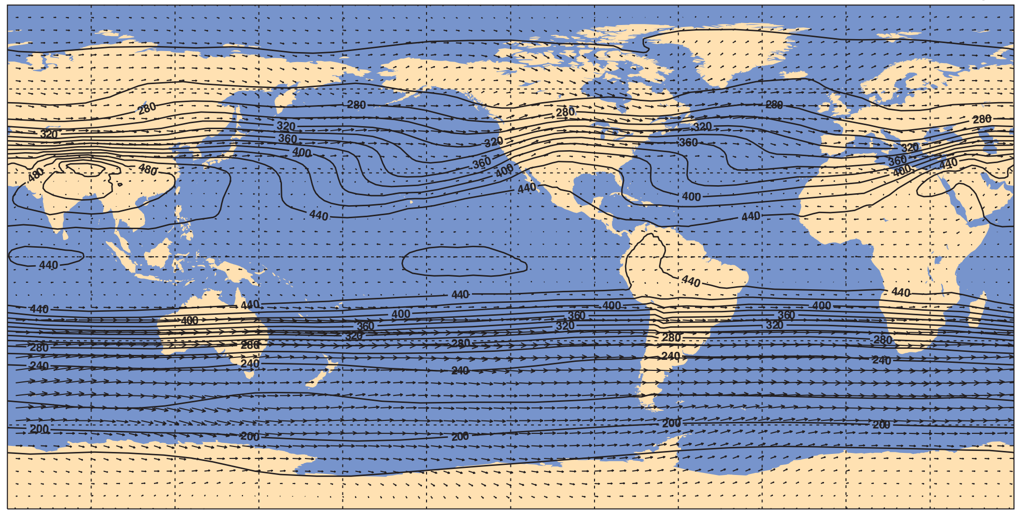

Isotachs and pressure (hPa) (contours) at 330 K — Interannual variability

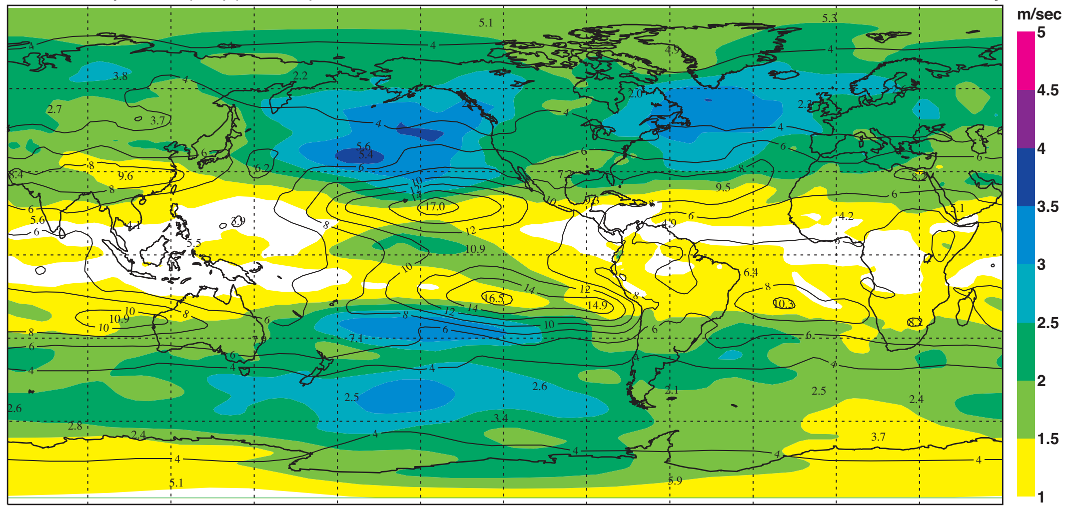

Wind and pressure (hPa) at 330 K — March-May

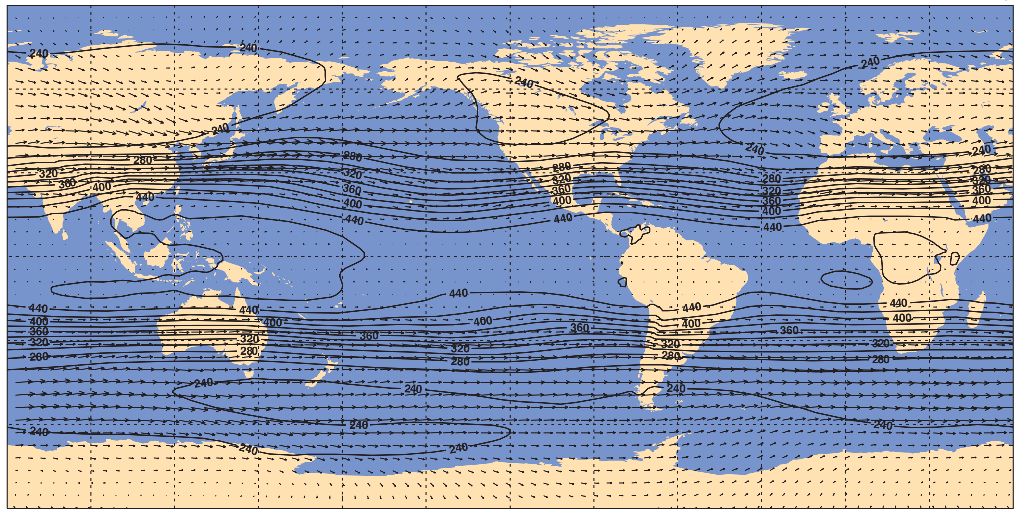

Wind and pressure (hPa) at 330 K — September-November

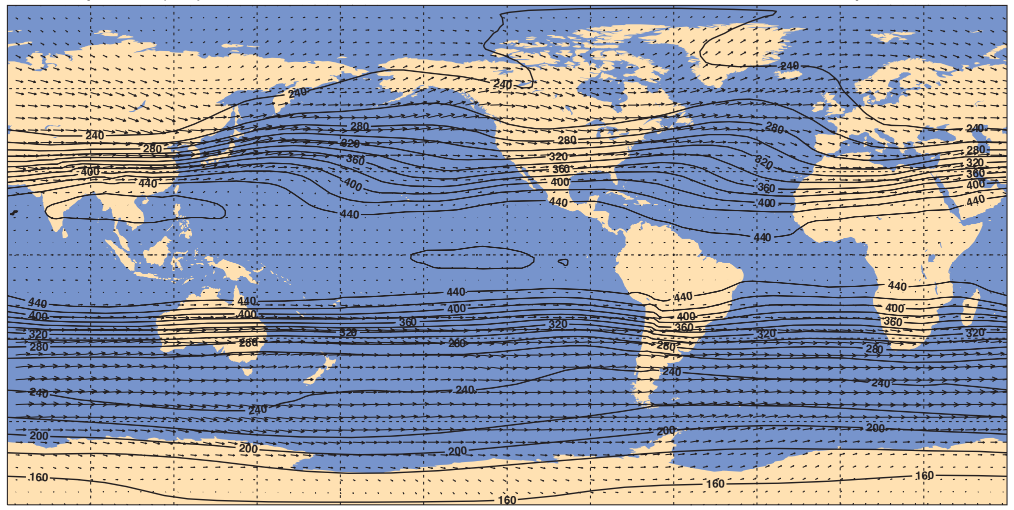

E2 Pressure (hPa) (contours) with vector wind (ms^{-1}) at 330 K. For the interannual variability, the isotachs are plotted (colour shading) instead of the vector wind.

Wind and pressure (hPa) at 315 K — Annual mean

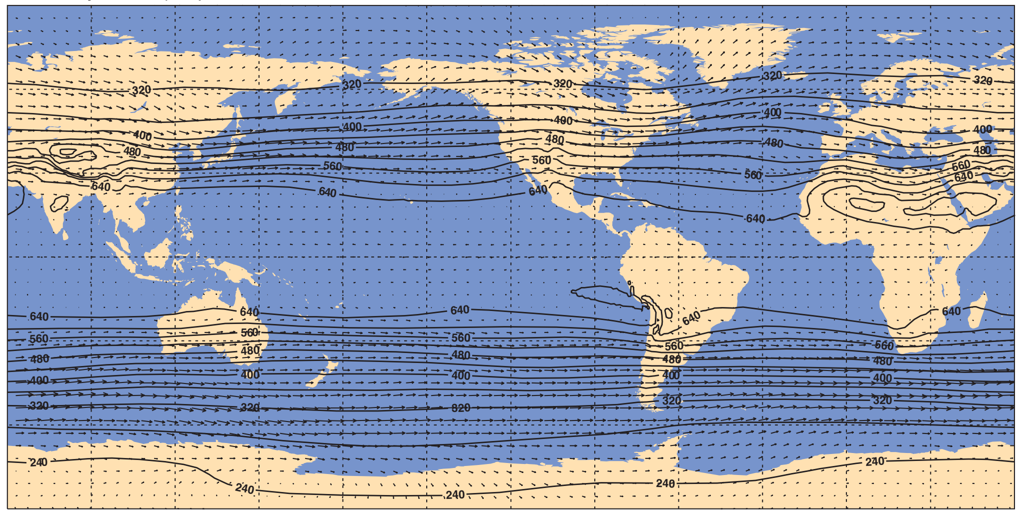

Wind and pressure (hPa) at 315 K — December-February

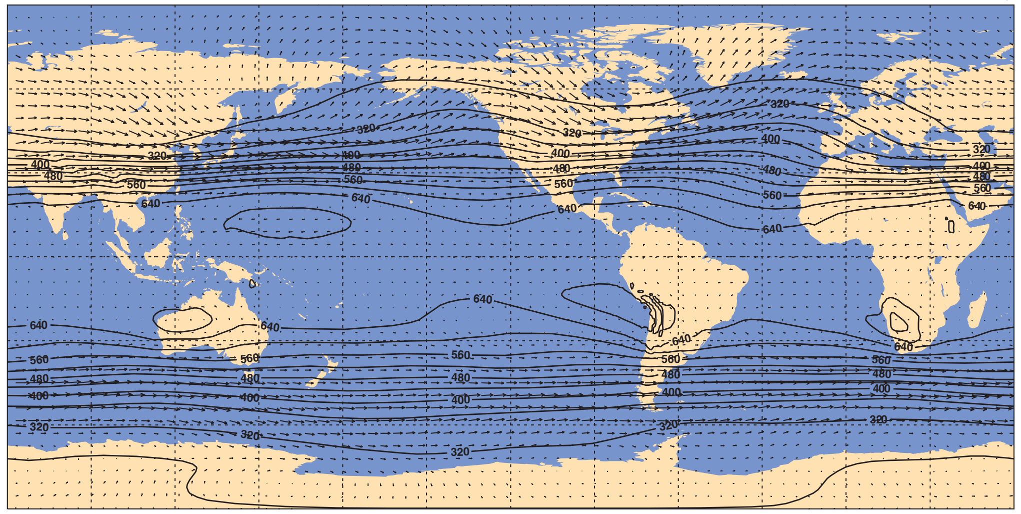

Wind and pressure (hPa) at 315 K — June-August

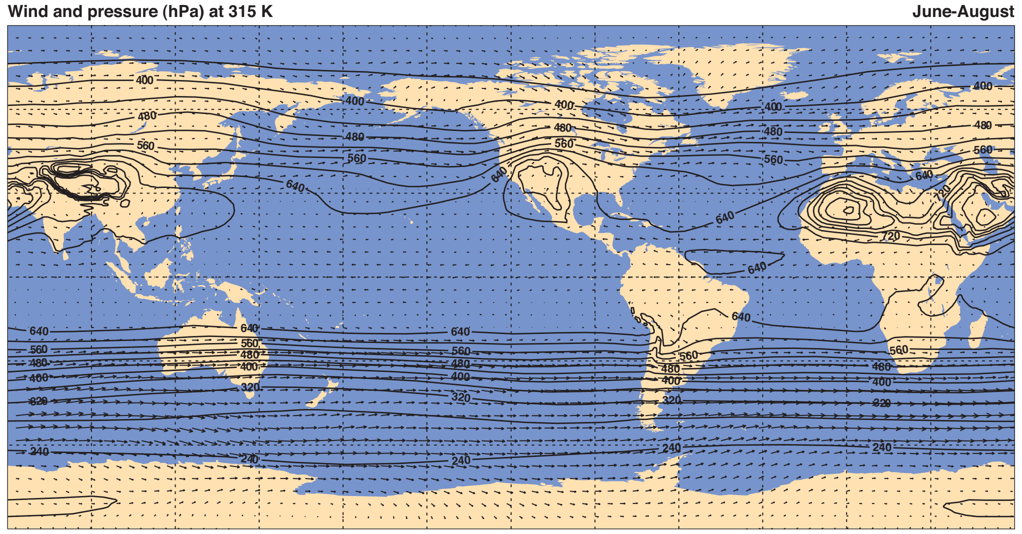

Isotachs and pressure (hPa) (contours) at 315 K — Interannual variability

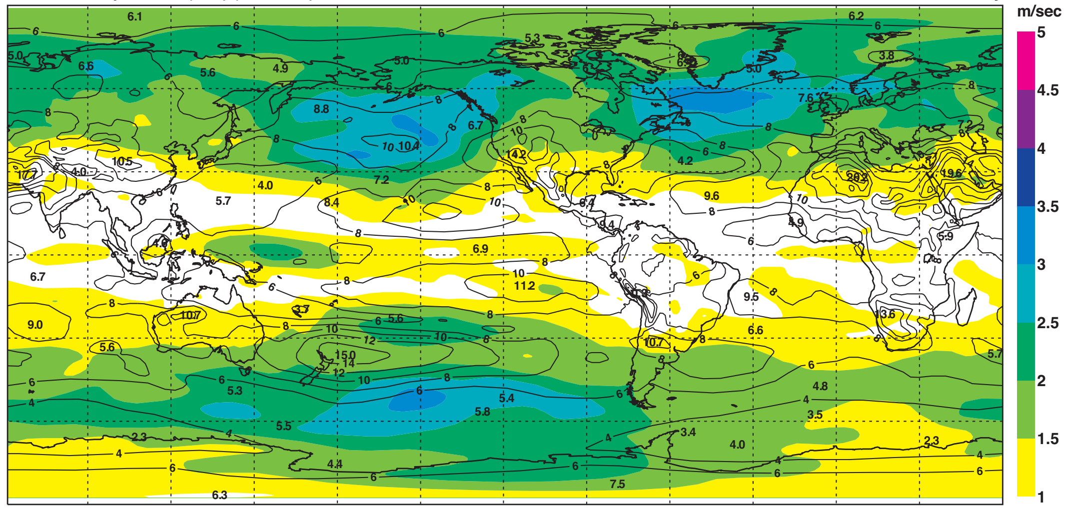

Wind and pressure (hPa) at 315 K — March-May

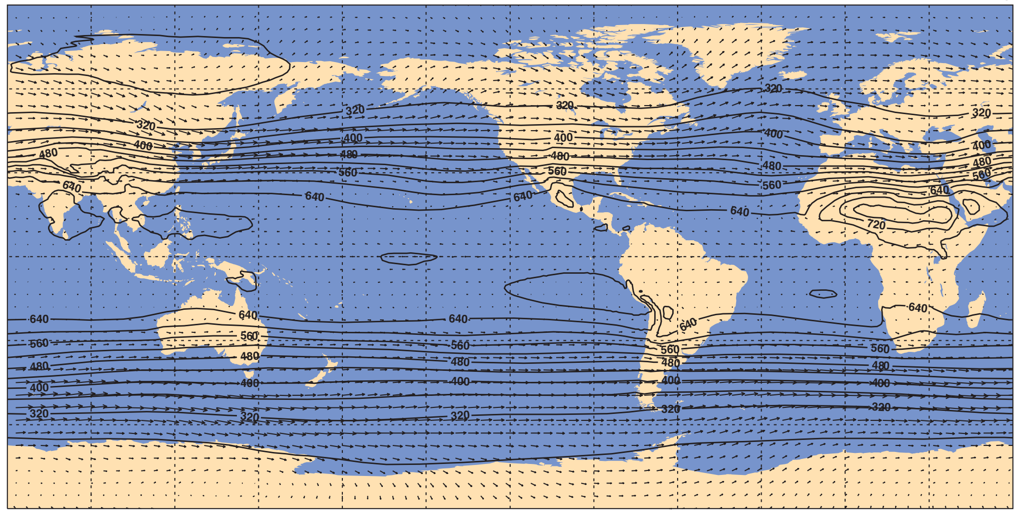

Wind and pressure (hPa) at 315 K — September-November

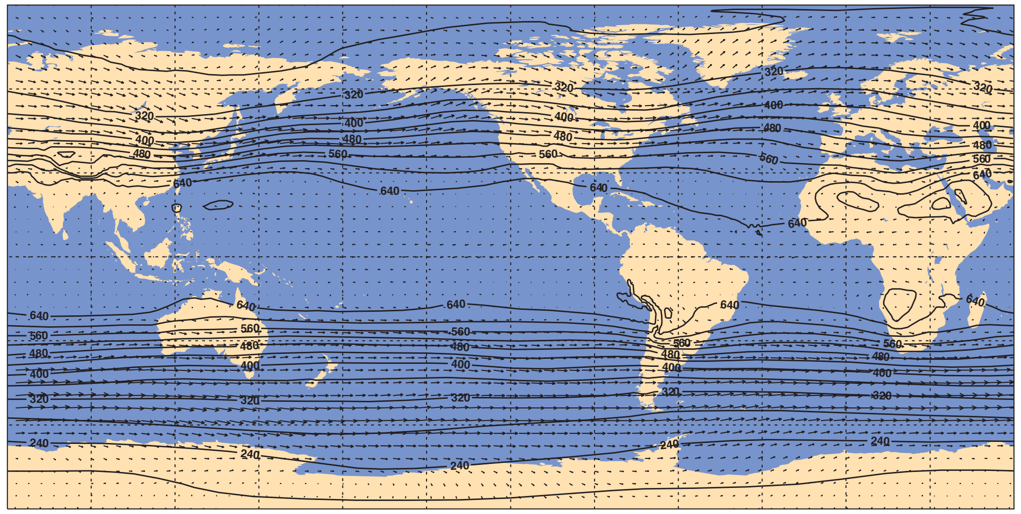

E3 Pressure (hPa) (contours) with vector wind (ms^{-1}) at 315 K. For the interannual variability, the isotachs are plotted (colour shading) instead of the vector wind.

Wind and pressure (hPa) at 300 K — Annual mean

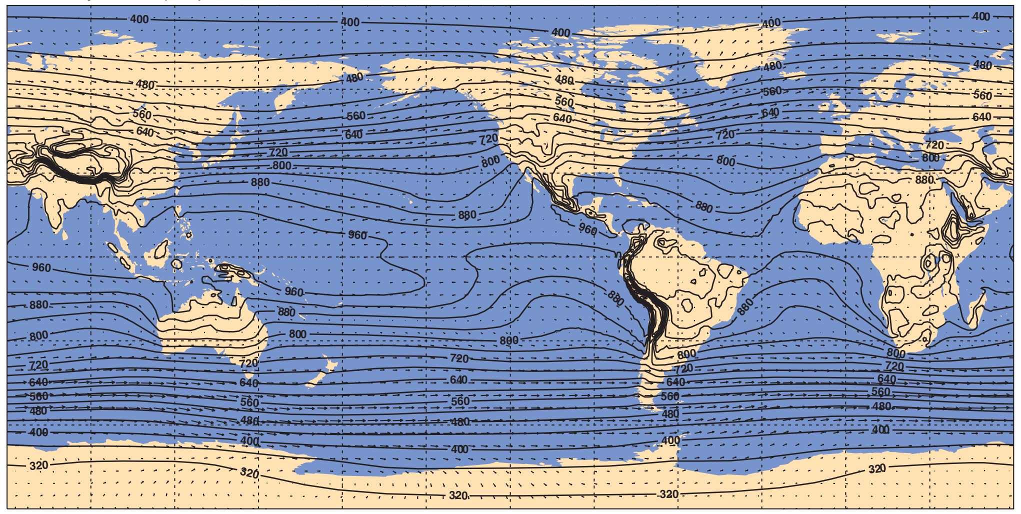

Wind and pressure (hPa) at 300 K — December-February

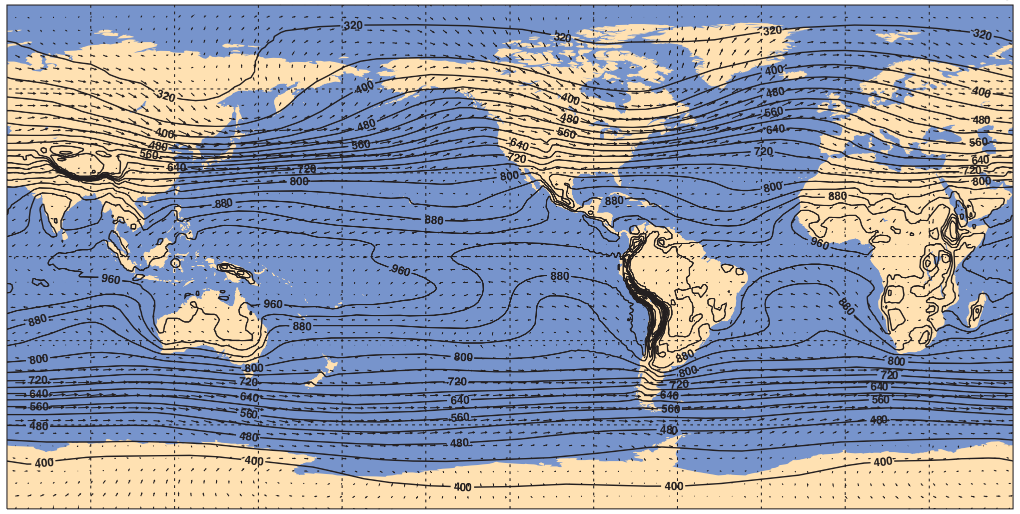

Wind and pressure (hPa) at 300 K — June-August

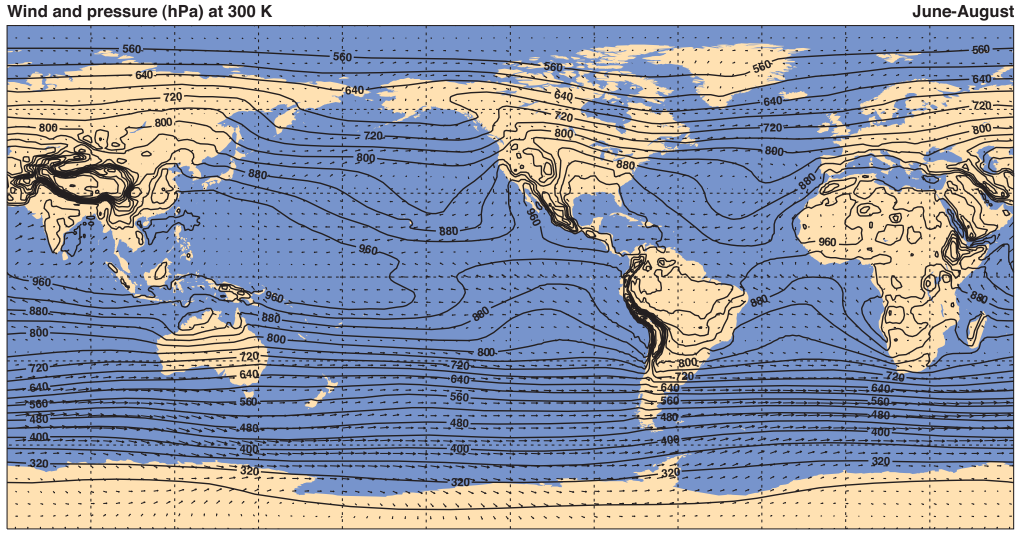

Isotachs and pressure (hPa) (contours) at 300 K — Interannual variability

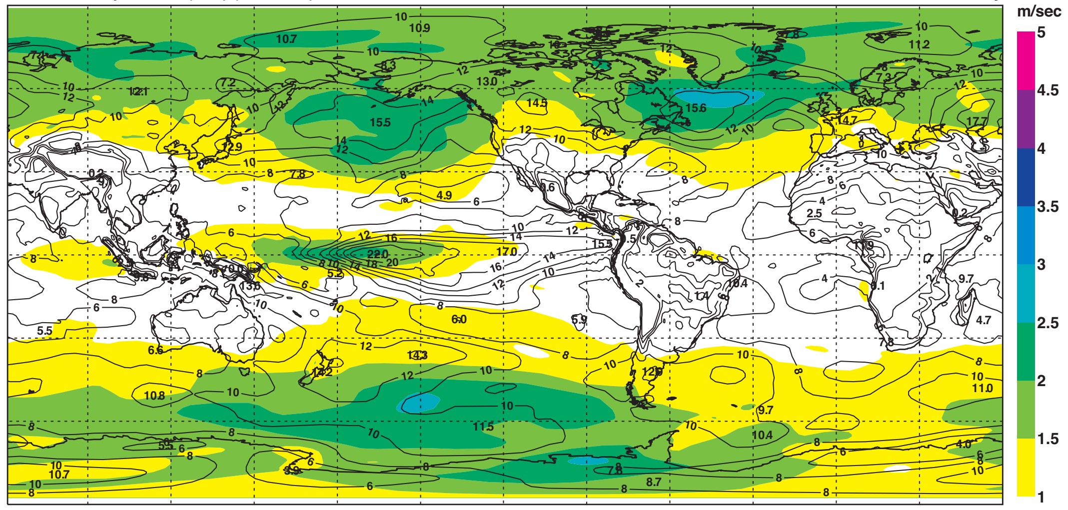

Wind and pressure (hPa) at 300 K — March-May

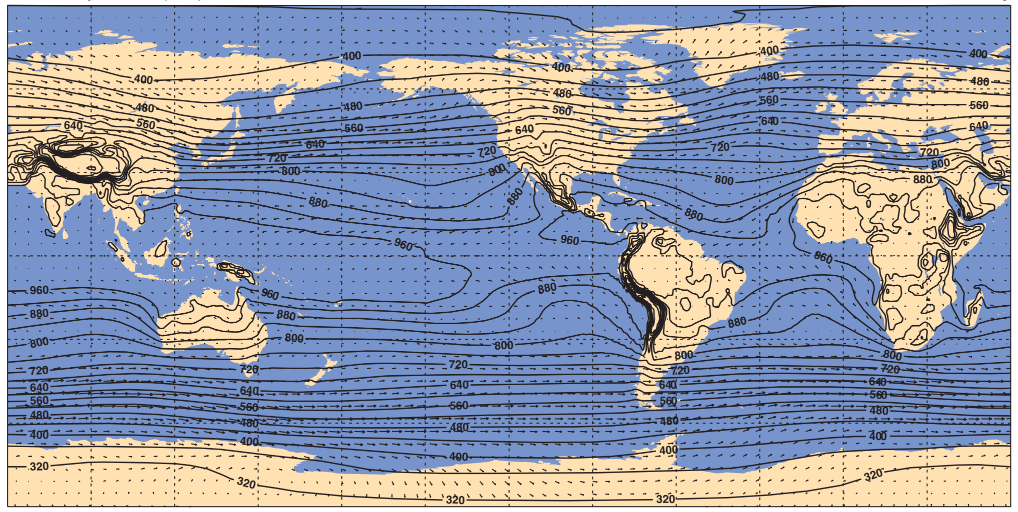

Wind and pressure (hPa) at 300 K — September-November

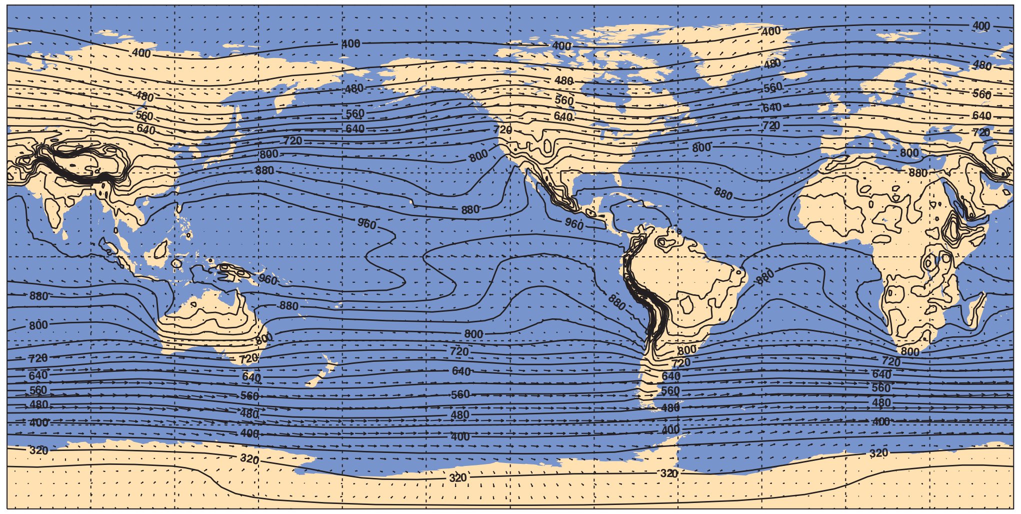

E4 Pressure (hPa) (contours) with vector wind (ms^{-1}) at 300 K. For the interannual variability, the isotachs are plotted (colour shading) instead of the vector wind.

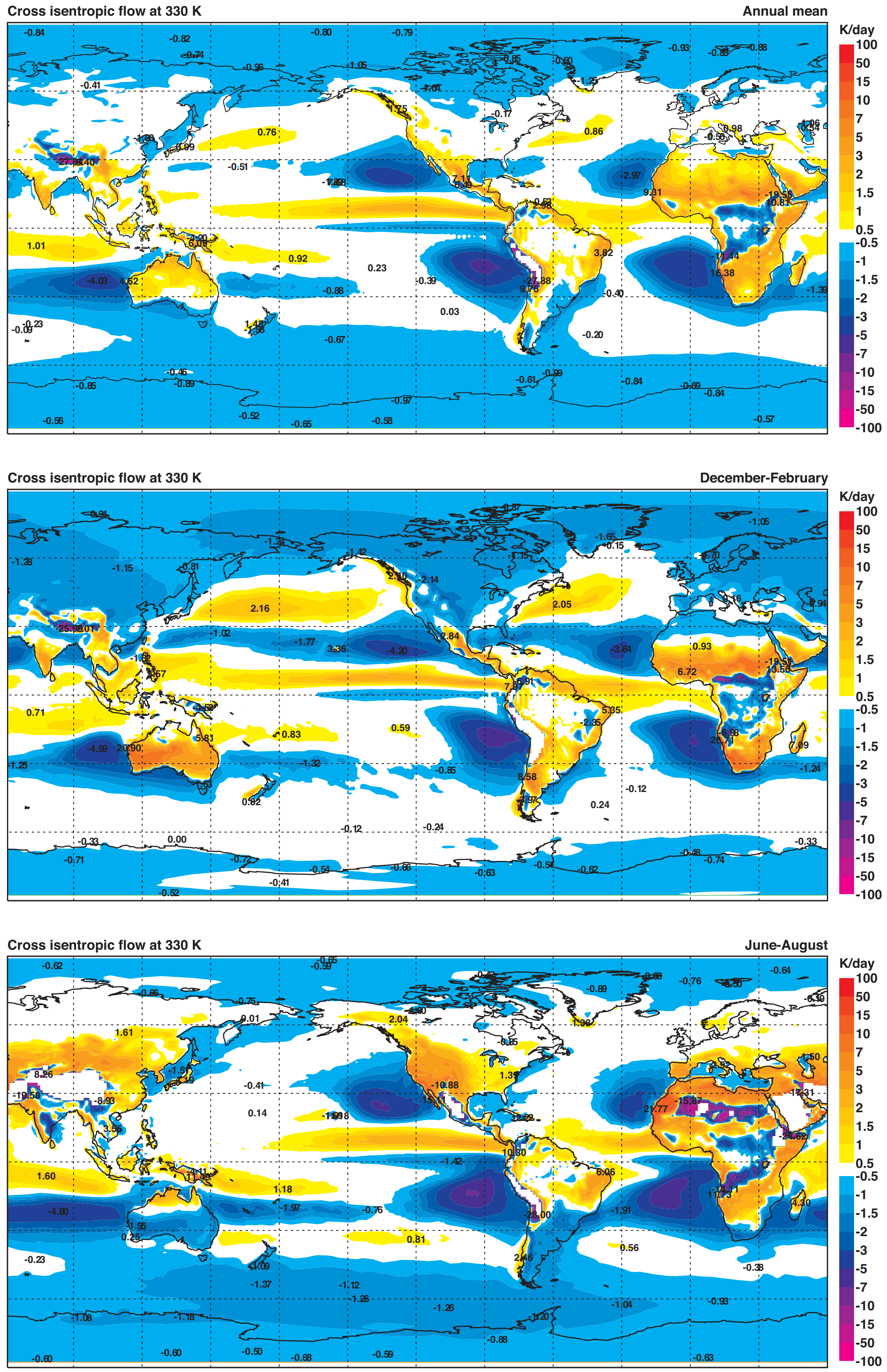

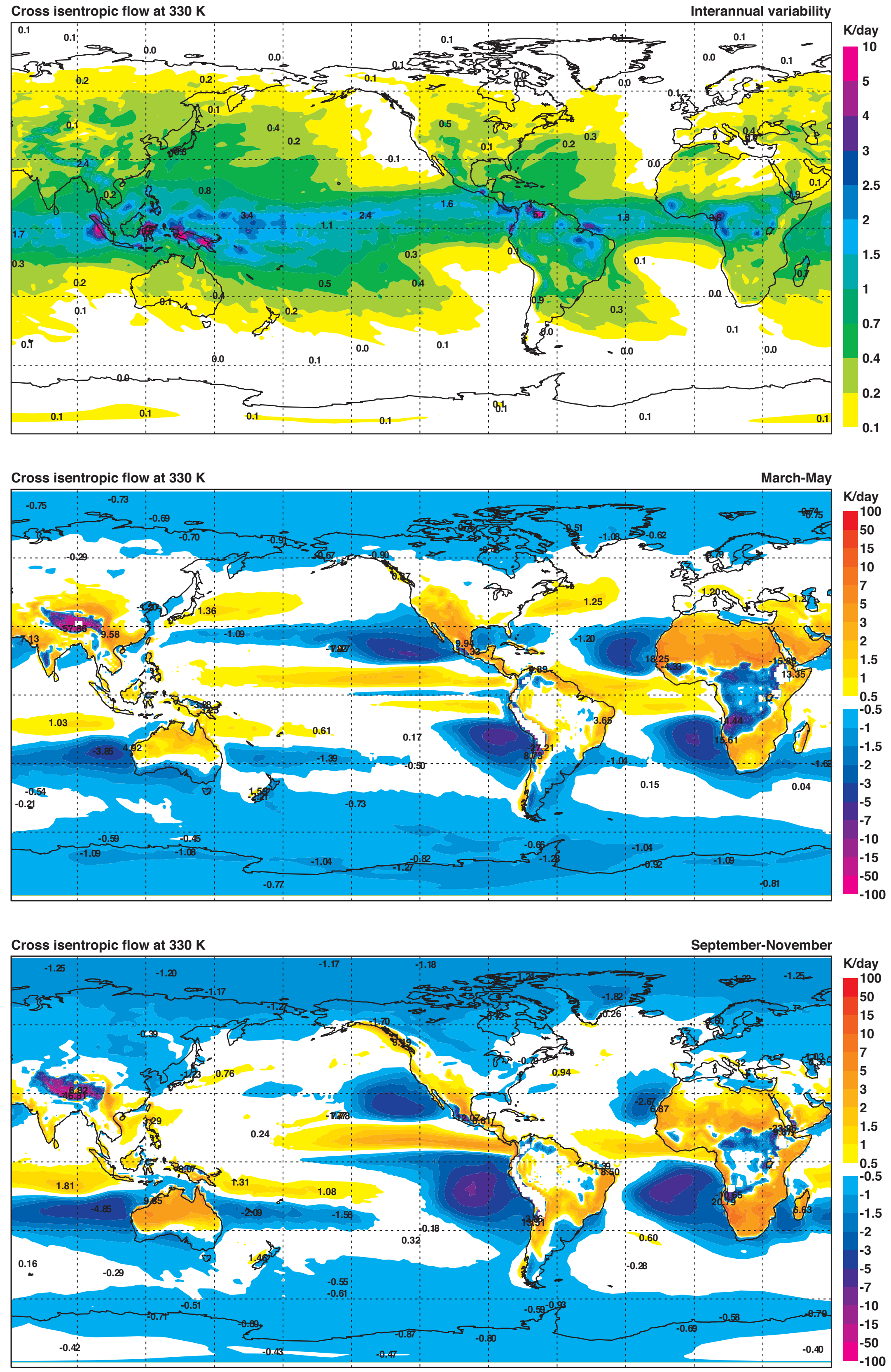

E5 Cross isentropic flow ($Kday^{-1}$) at 330 K.

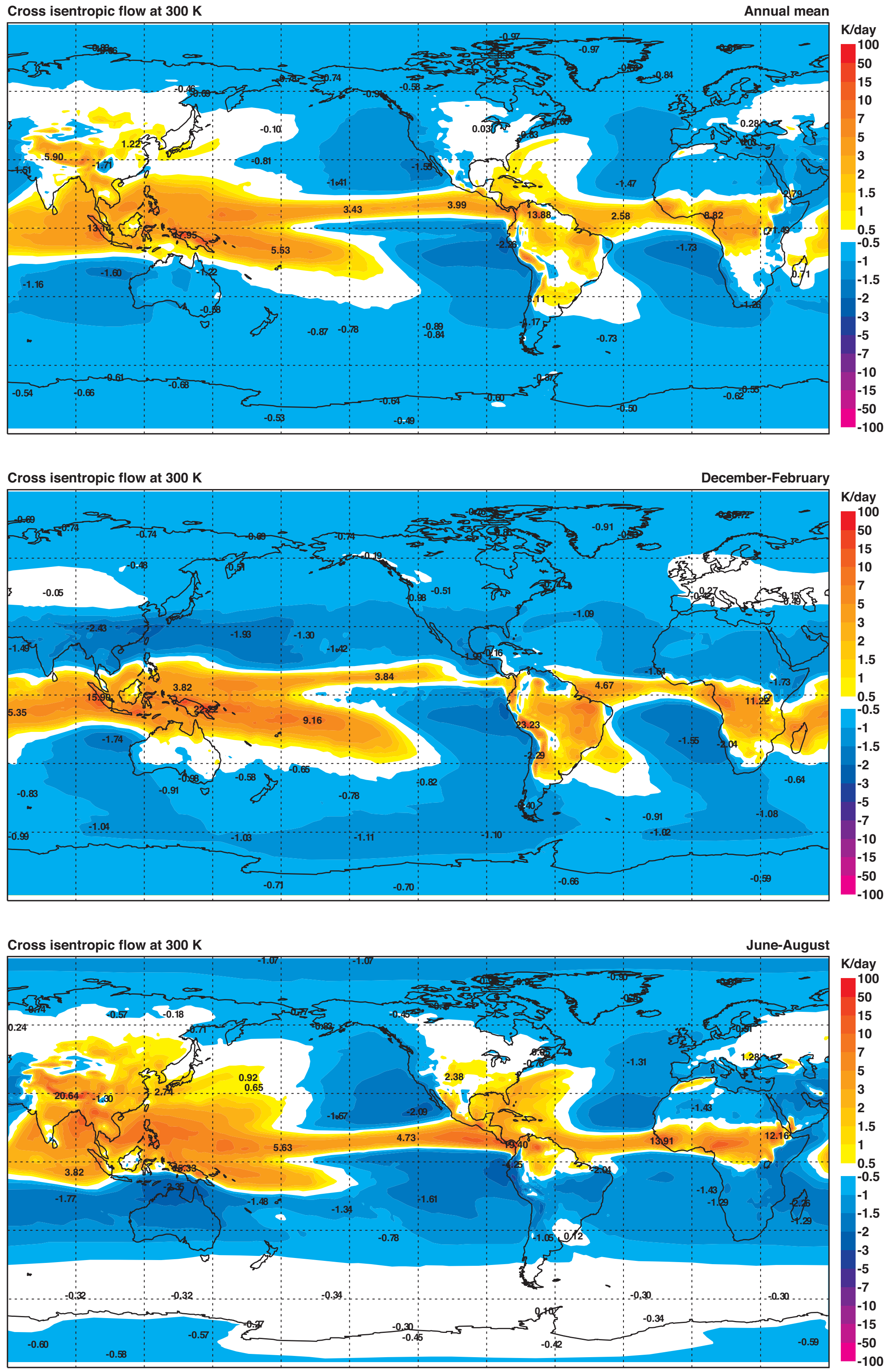

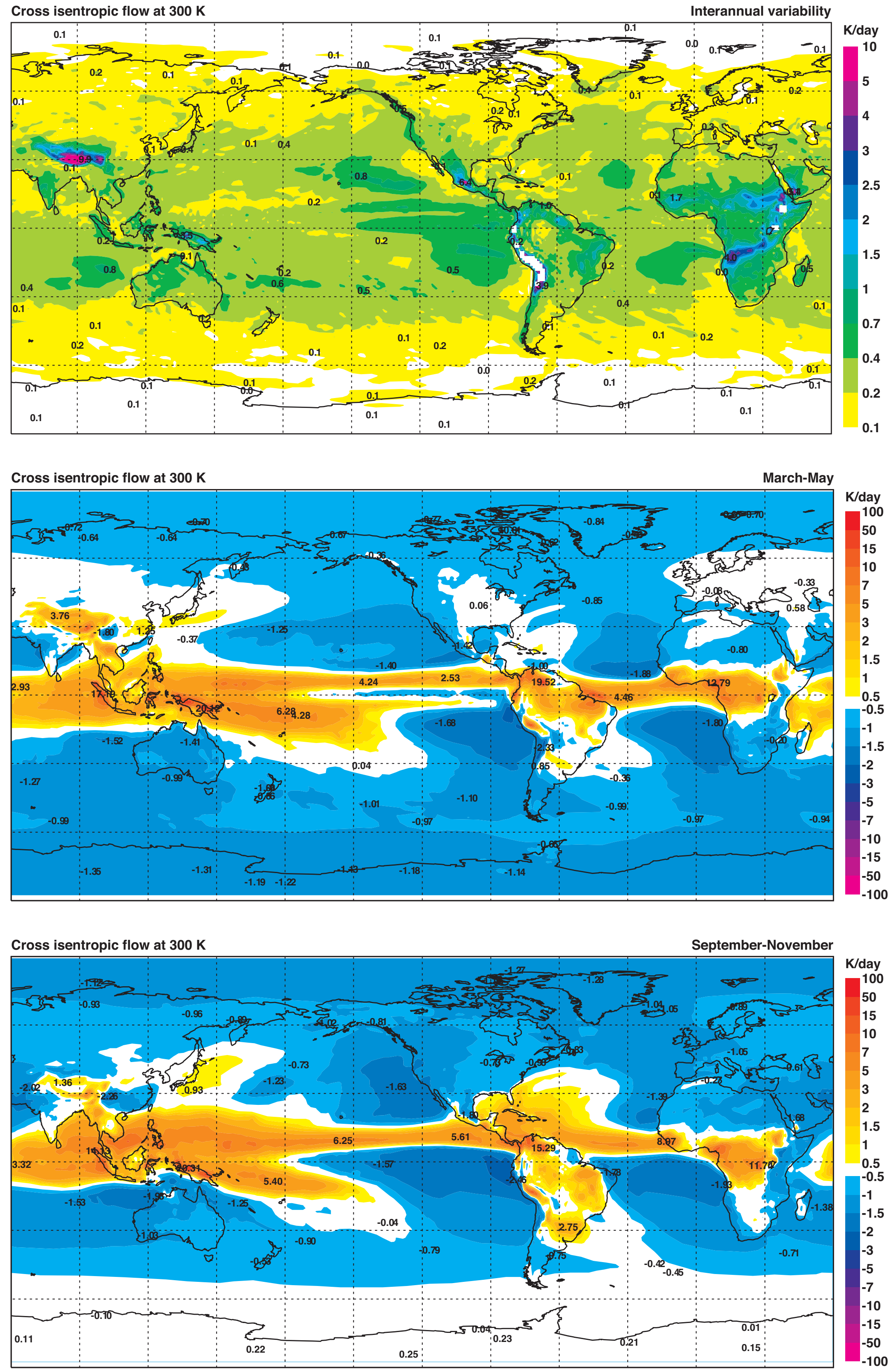

E6 Cross isentropic flow (Kday^{-1}) at 300 K.

Stream function ($10^6 m^2 s^{-1}$) with velocity potential ($10^6 m^2 s^{-1}$) at 350 K — Annual mean

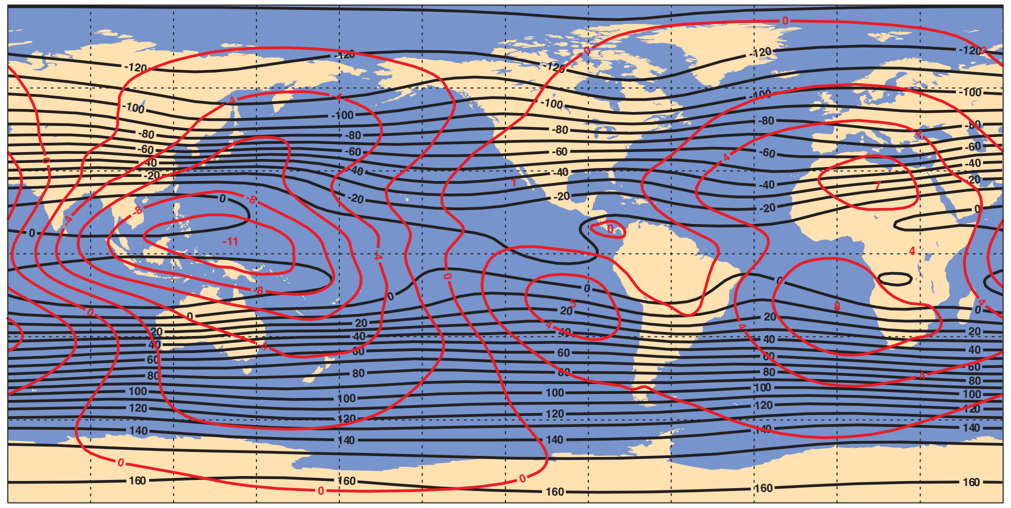

Stream function ($10^6 m^2 s^{-1}$) with velocity potential ($10^6 m^2 s^{-1}$) at 350 K — December-February

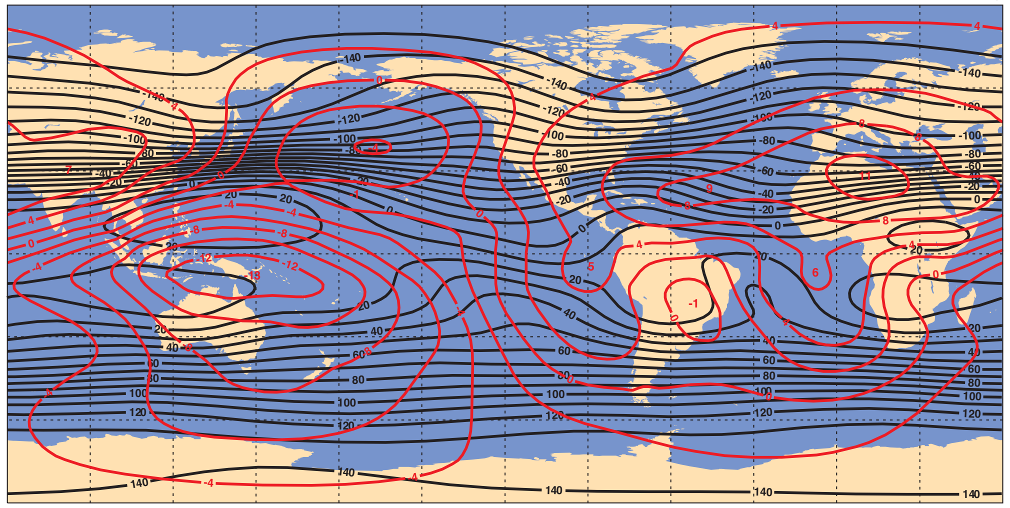

Stream function ($10^6 m^2 s^{-1}$) with velocity potential ($10^6 m^2 s^{-1}$) at 350 K — June-August

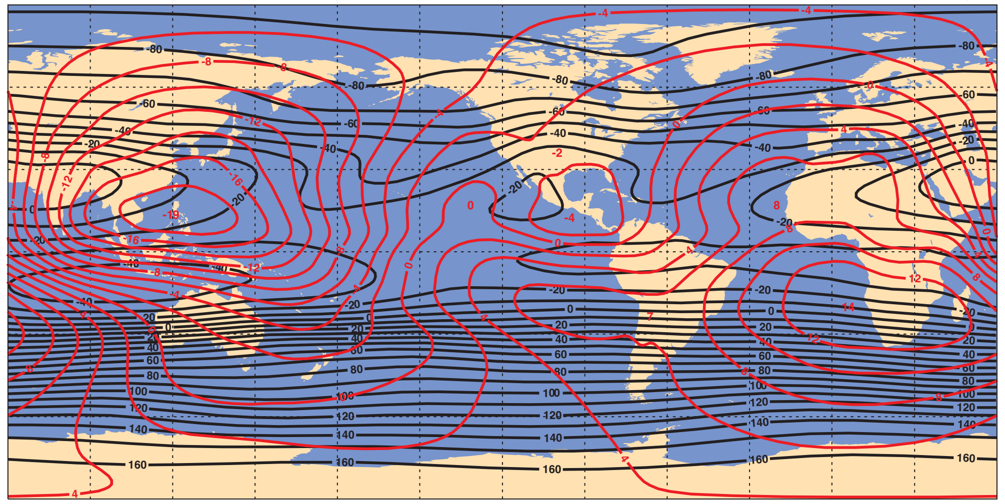

Stream function ($10^5 m^2 s^{-1}$) with velocity potential ($10^5 m^2 s^{-1}$) at 350 K — Interannual variability

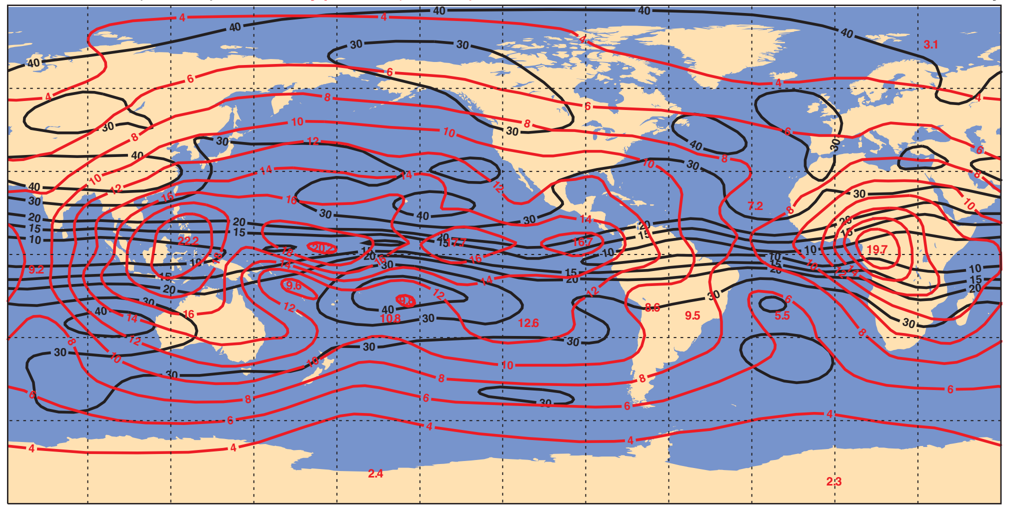

Stream function ($10^6 m^2 s^{-1}$) with velocity potential ($10^6 m^2 s^{-1}$) at 350 K — March-May

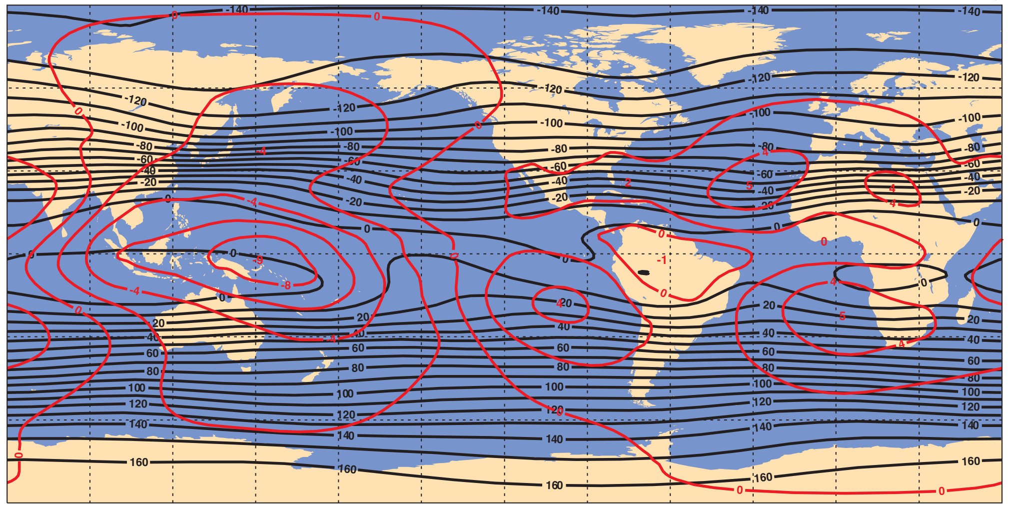

Stream function ($10^6 m^2 s^{-1}$) with velocity potential ($10^6 m^2 s^{-1}$) at 350 K — September-November

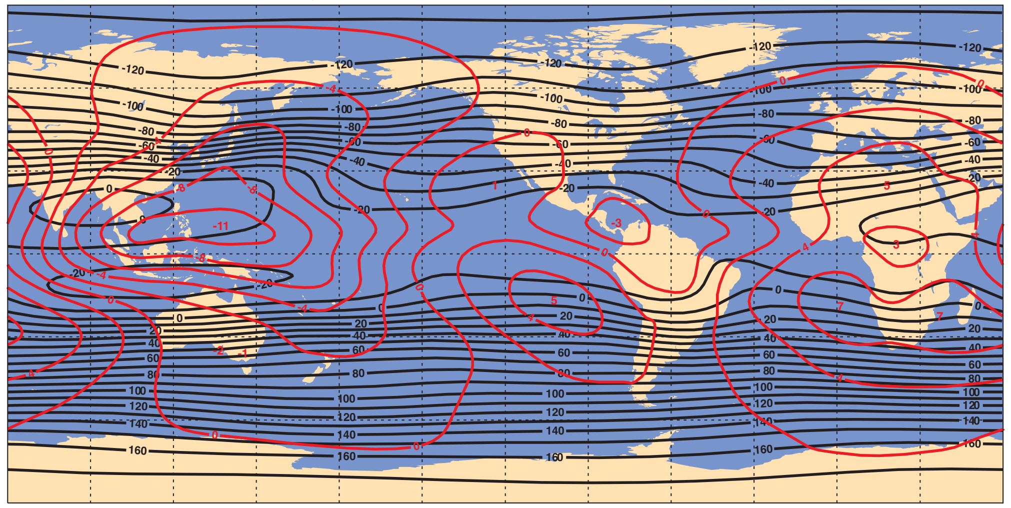

E7 Streamfunction ($m^2 s^{-1}$) (black contours) with velocity potential ($m^2 s^{-1}$) (red contours) at 350 K.

Stream function ($10^6 m^2 s^{-1}$) with velocity potential ($10^6 m^2 s^{-1}$) at 300 K — Annual mean

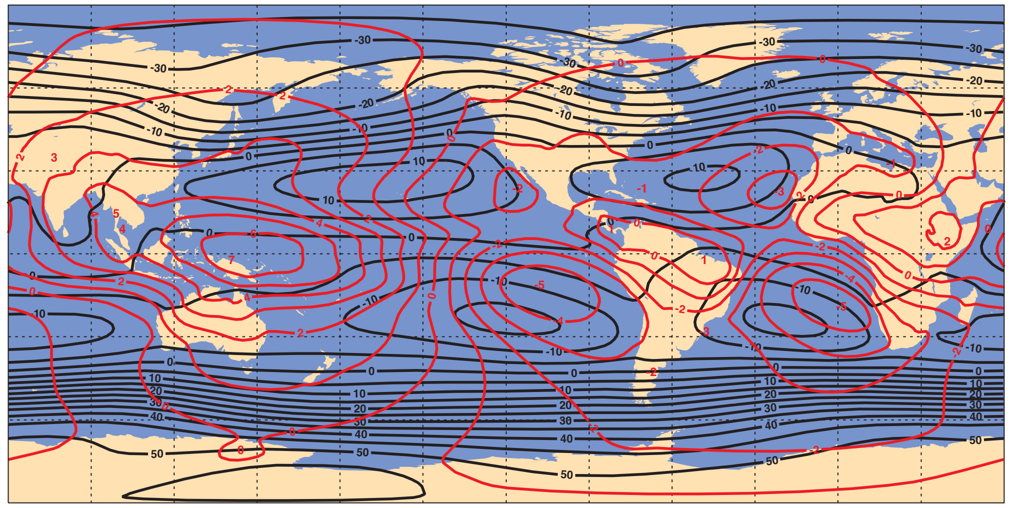

Stream function ($10^6 m^2 s^{-1}$) with velocity potential ($10^6 m^2 s^{-1}$) at 300 K — December-February

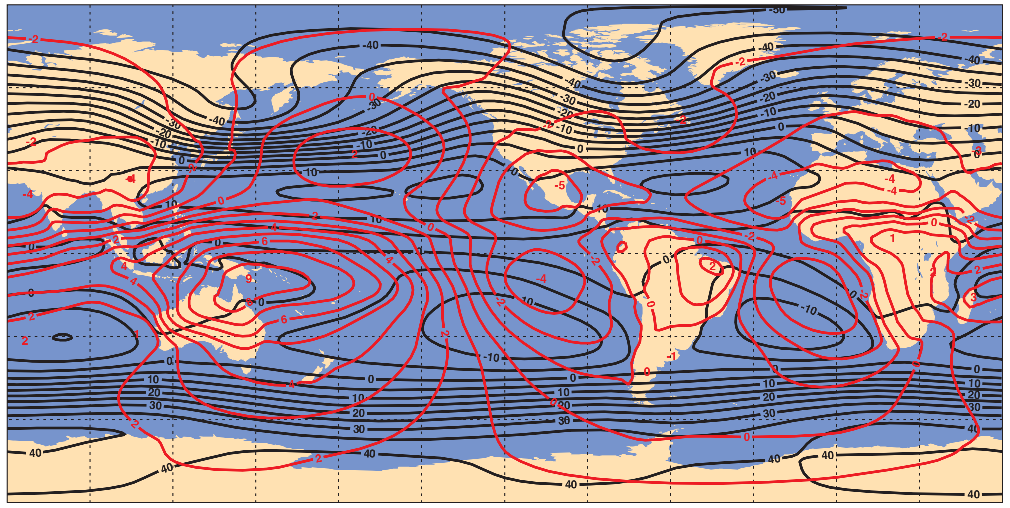

Stream function ($10^6 m^2 s^{-1}$) with velocity potential ($10^6 m^2 s^{-1}$) at 300 K — June-August

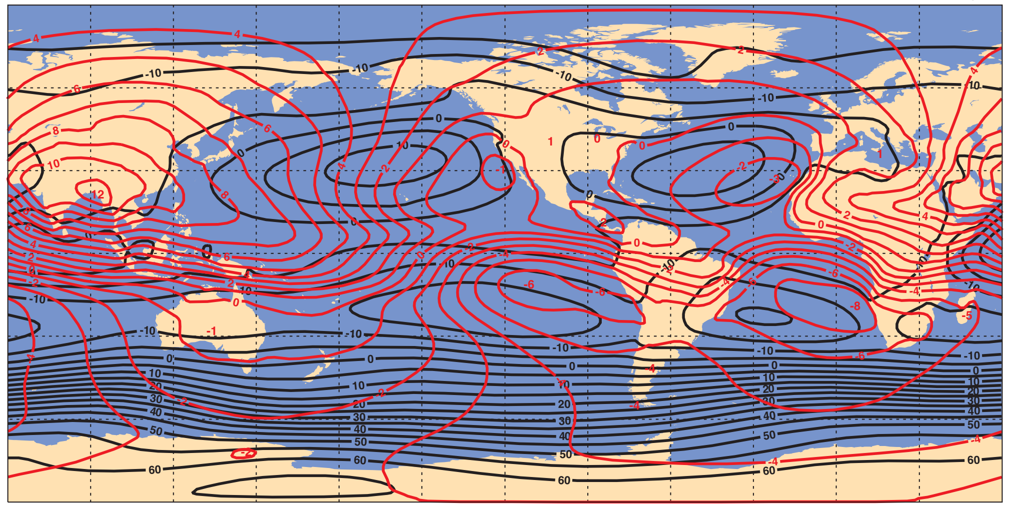

Stream function ($10^5 m^2 s^{-1}$) with velocity potential ($10^5 m^2 s^{-1}$) at 300 K — Interannual variability

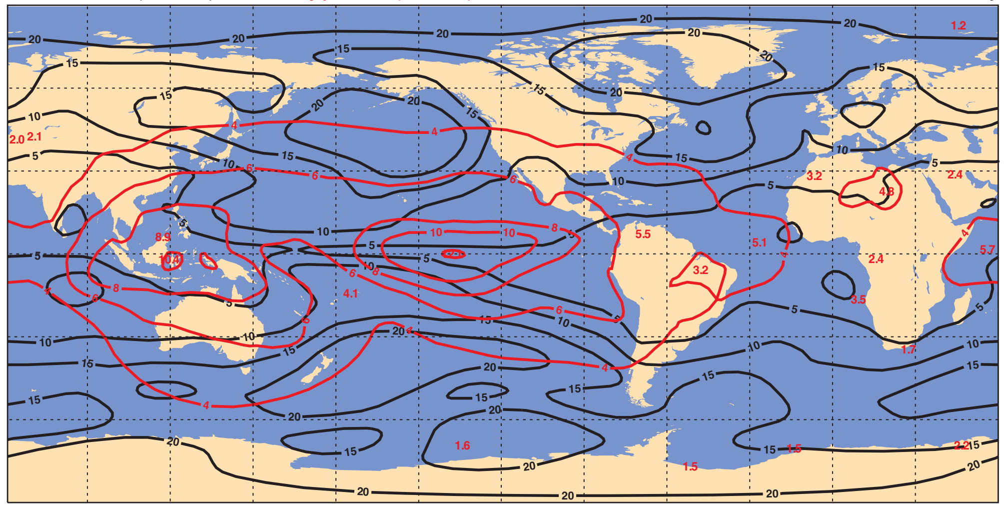

Stream function ($10^6 m^2 s^{-1}$) with velocity potential ($10^6 m^2 s^{-1}$) at 300 K — March-May

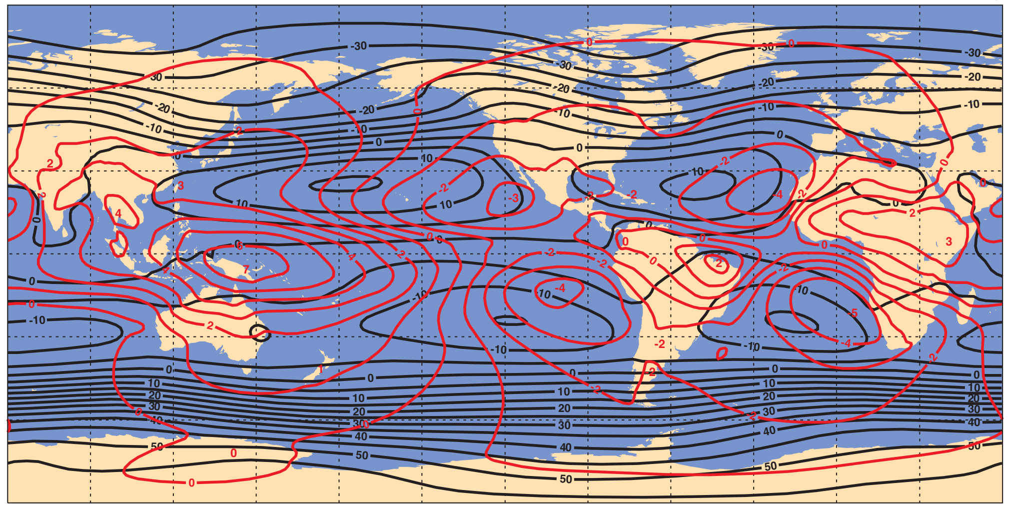

Stream function ($10^6 m^2 s^{-1}$) with velocity potential ($10^6 m^2 s^{-1}$) at 300 K — September-November

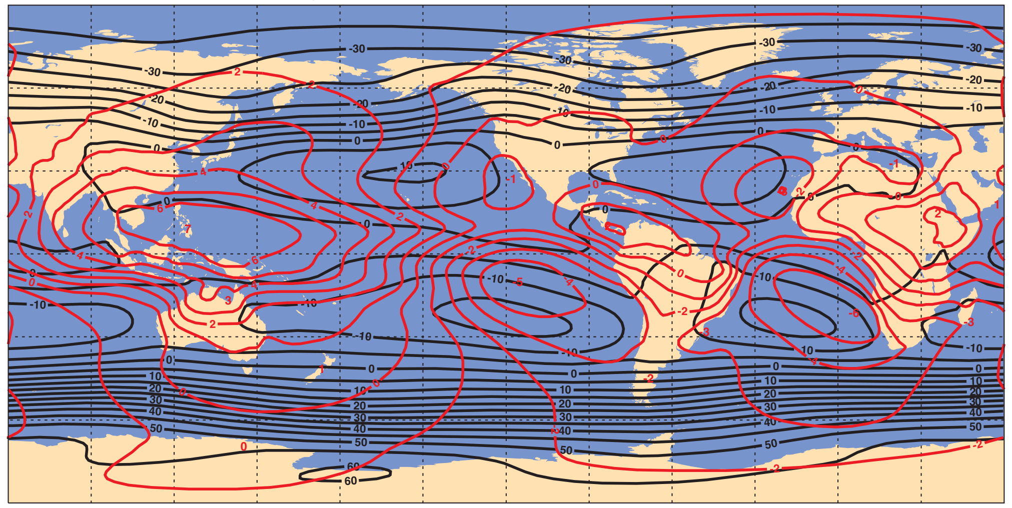

E8 Streamfunction ($m^2 s^{-1}$) (black contours) with velocity potential ($m^2 s^{-1}$) (red contours) at 300 K.

Isotachs and Montgomery potential (1000 m^2s^{-2}) (contours) at 330 K — Annual mean

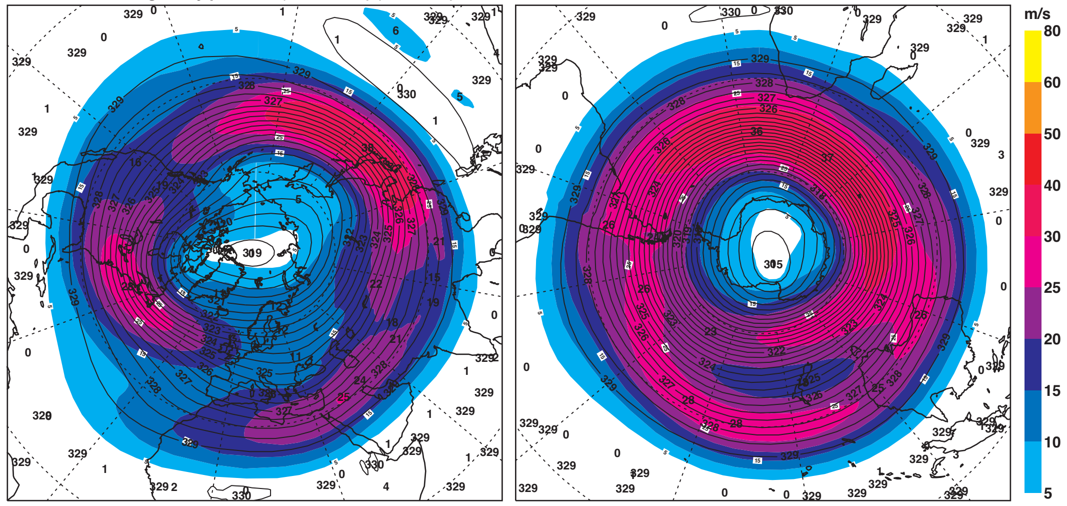

Isotachs and Montgomery potential (1000 m^2s^{-2}) (contours) at 330 K — December-February

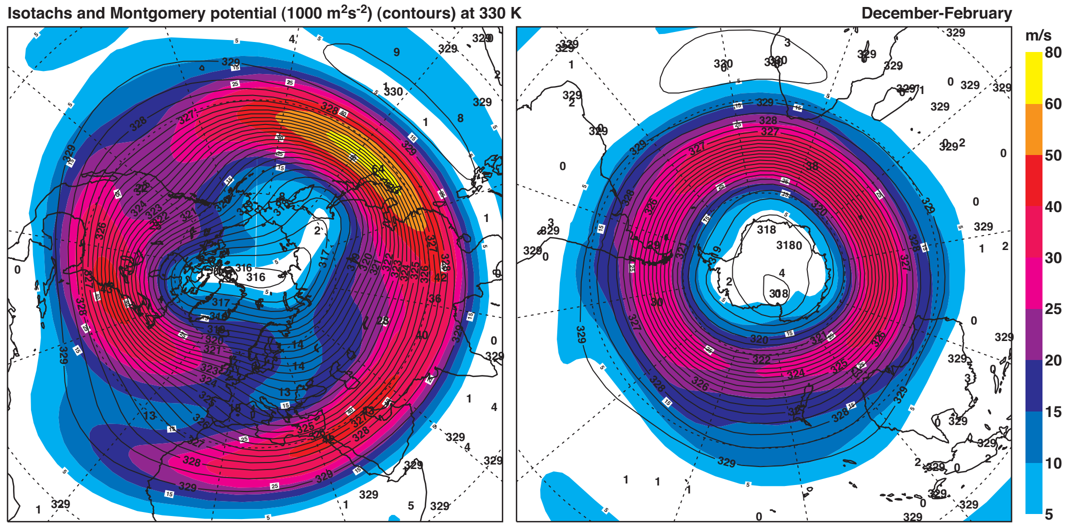

Isotachs and Montgomery potential (1000 m^2s^{-2}) (contours) at 330 K — June-August

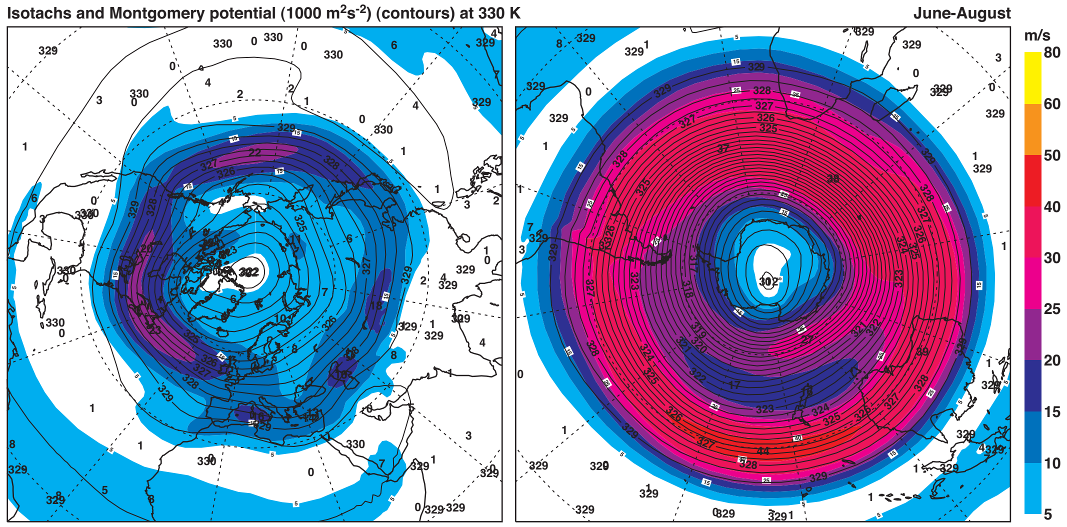

Isotachs and Montgomery potential (m^2s^{-2}) (contours) at 330 K — Interannual variability

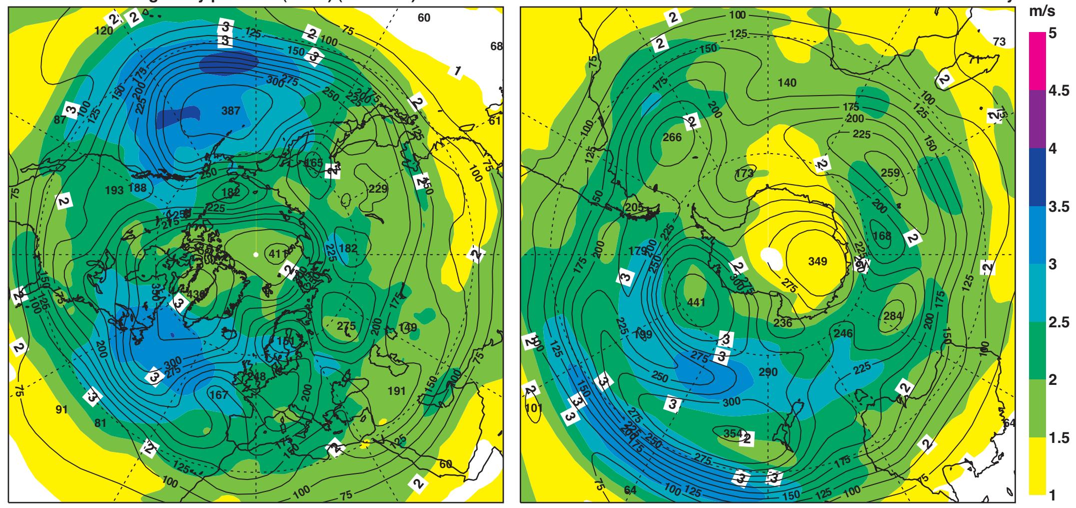

Isotachs and Montgomery potential (1000 m^2s^{-2}) (contours) at 330 K — March-May

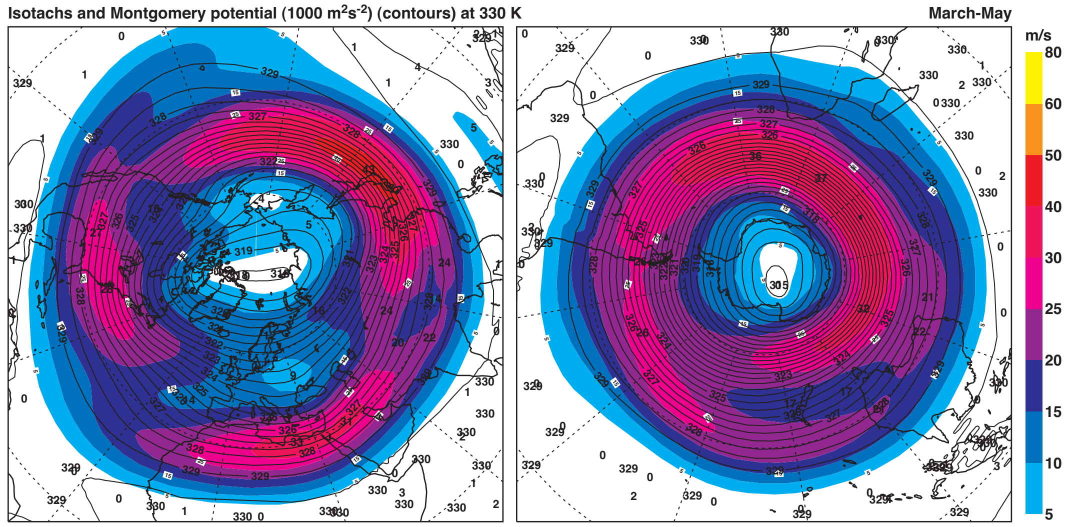

Isotachs and Montgomery potential (1000 m^2s^{-2}) (contours) at 330 K — September-November

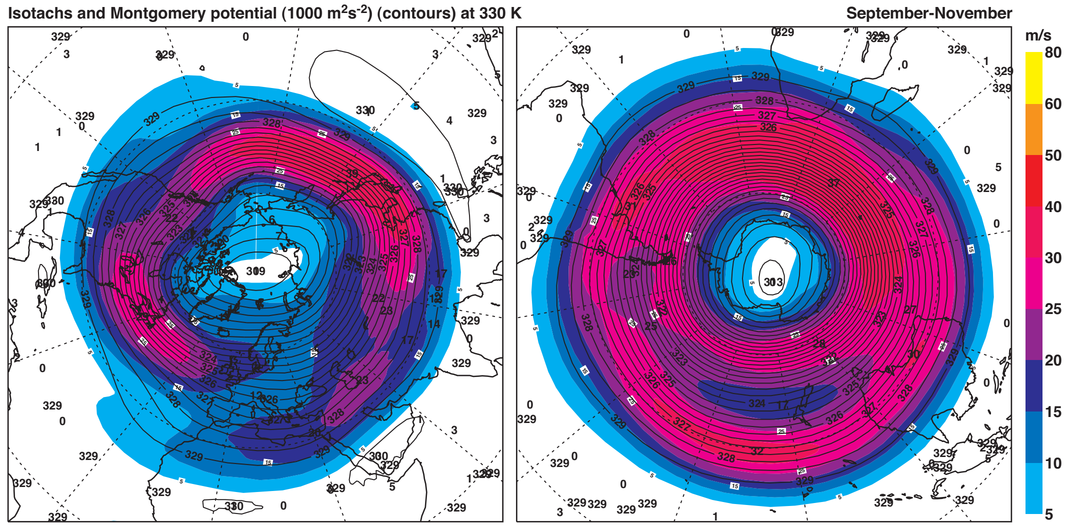

E9 Montgomery Potential (m^2s^{-2}) (contours) with isotachs (ms^{-1}) (colour shading) at 330 K.

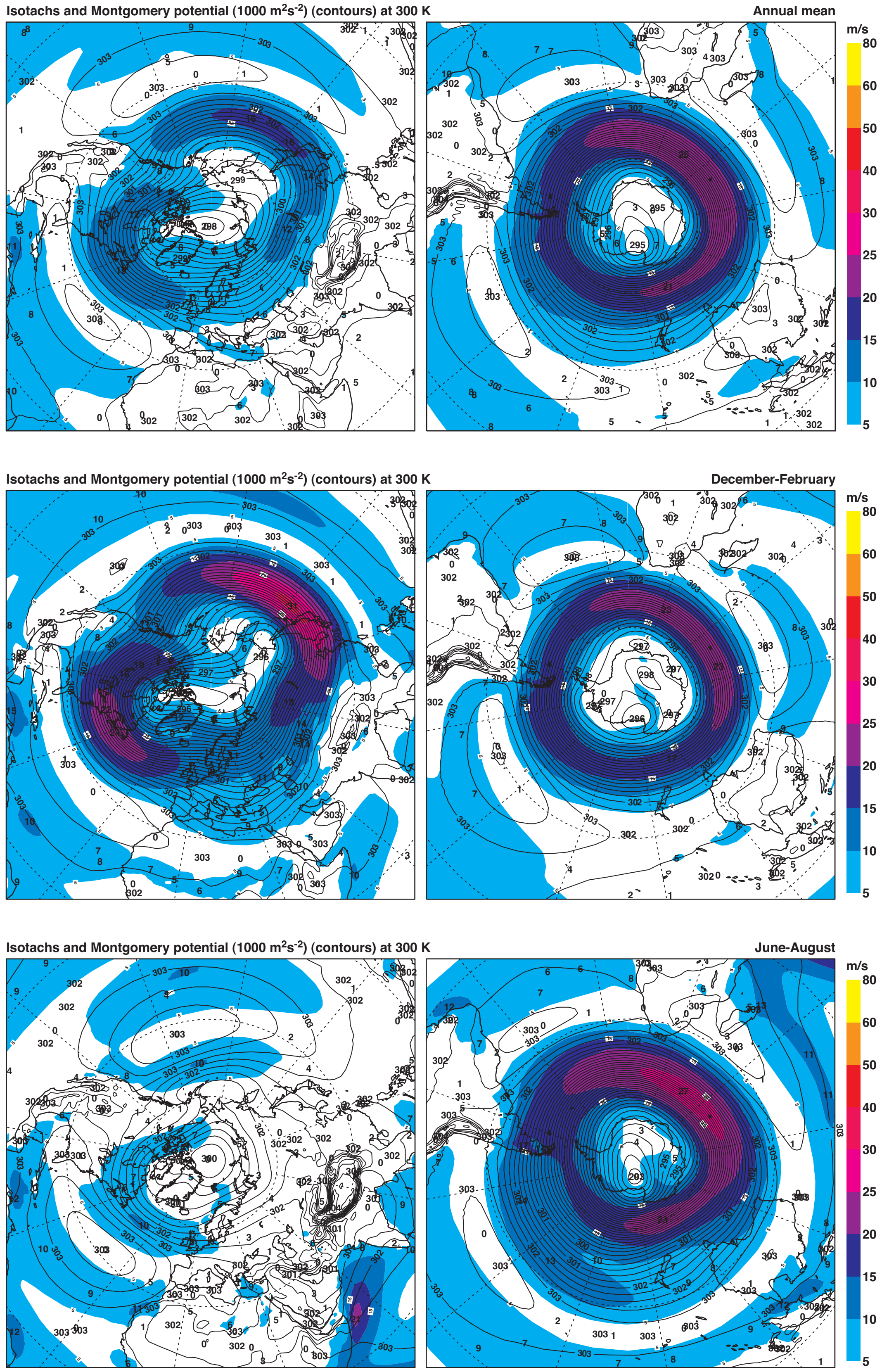

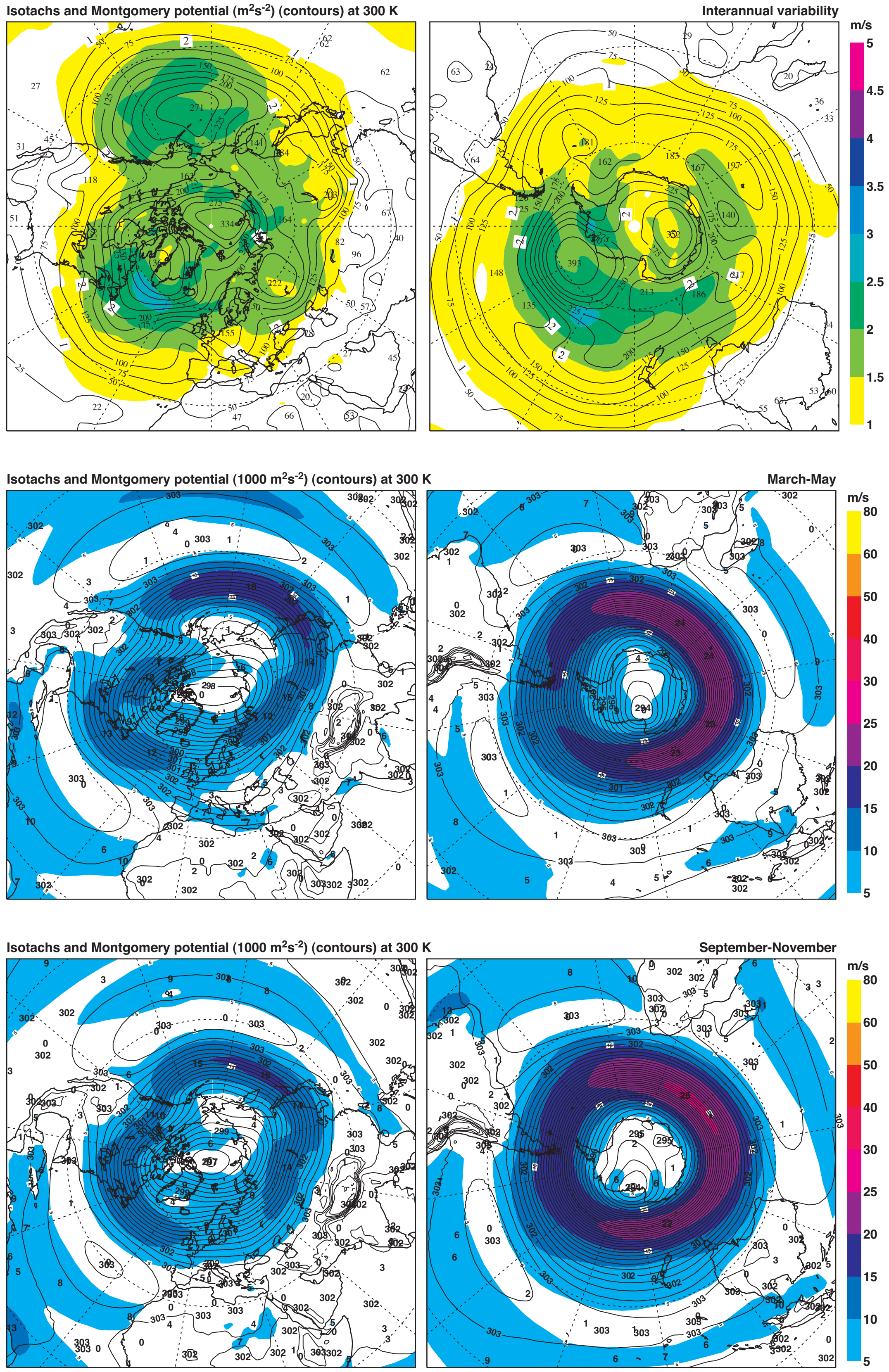

E10 Montgomery Potential (m^2s^{-2}) (contours) with isotachs (ms^{-1}) (colour shading) at 300 K.

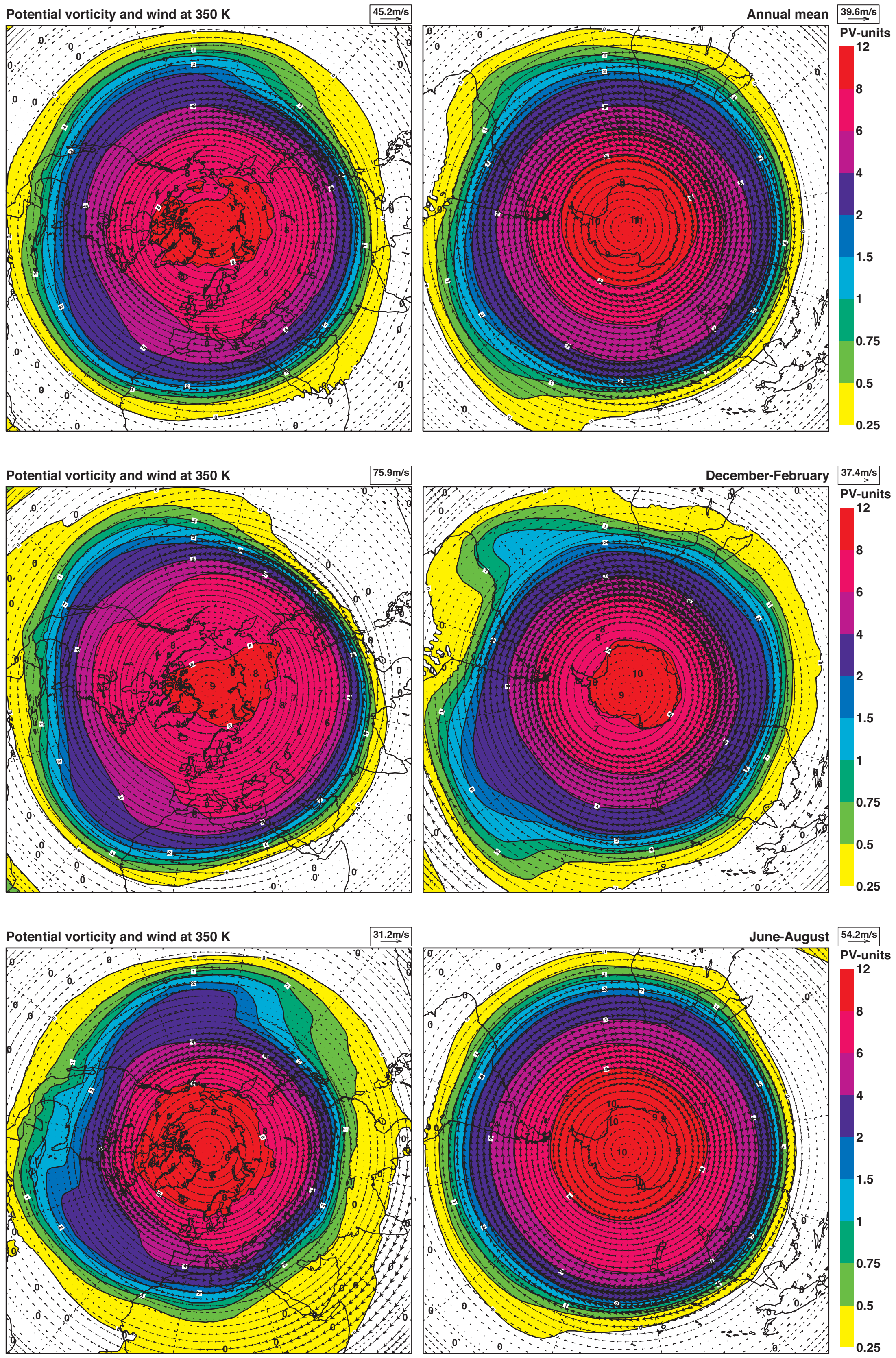

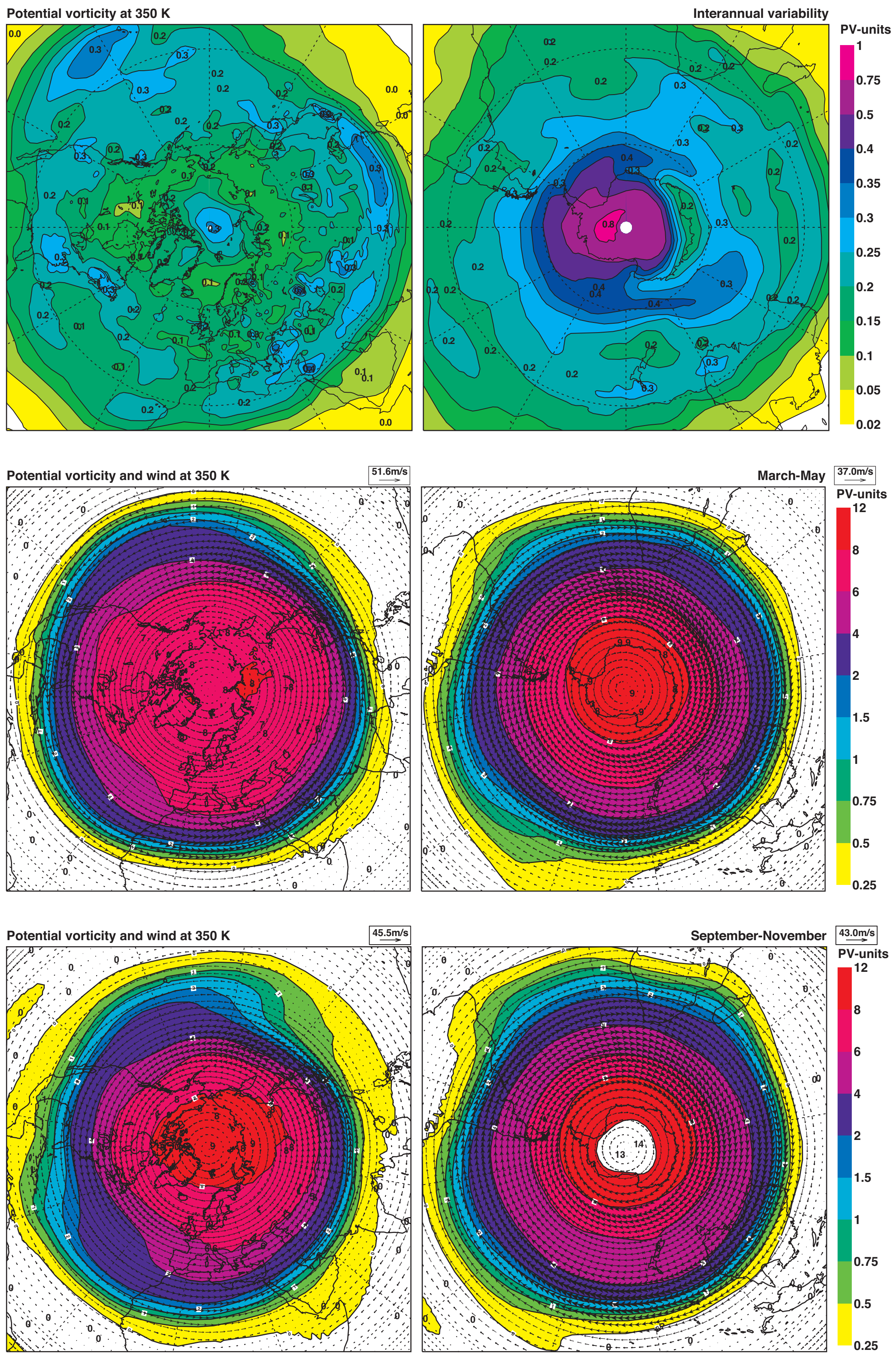

E11 Potential vorticity (pvu) with vector wind (ms^{-1}) at 350 K. For the interannual variability, the winds are omitted.

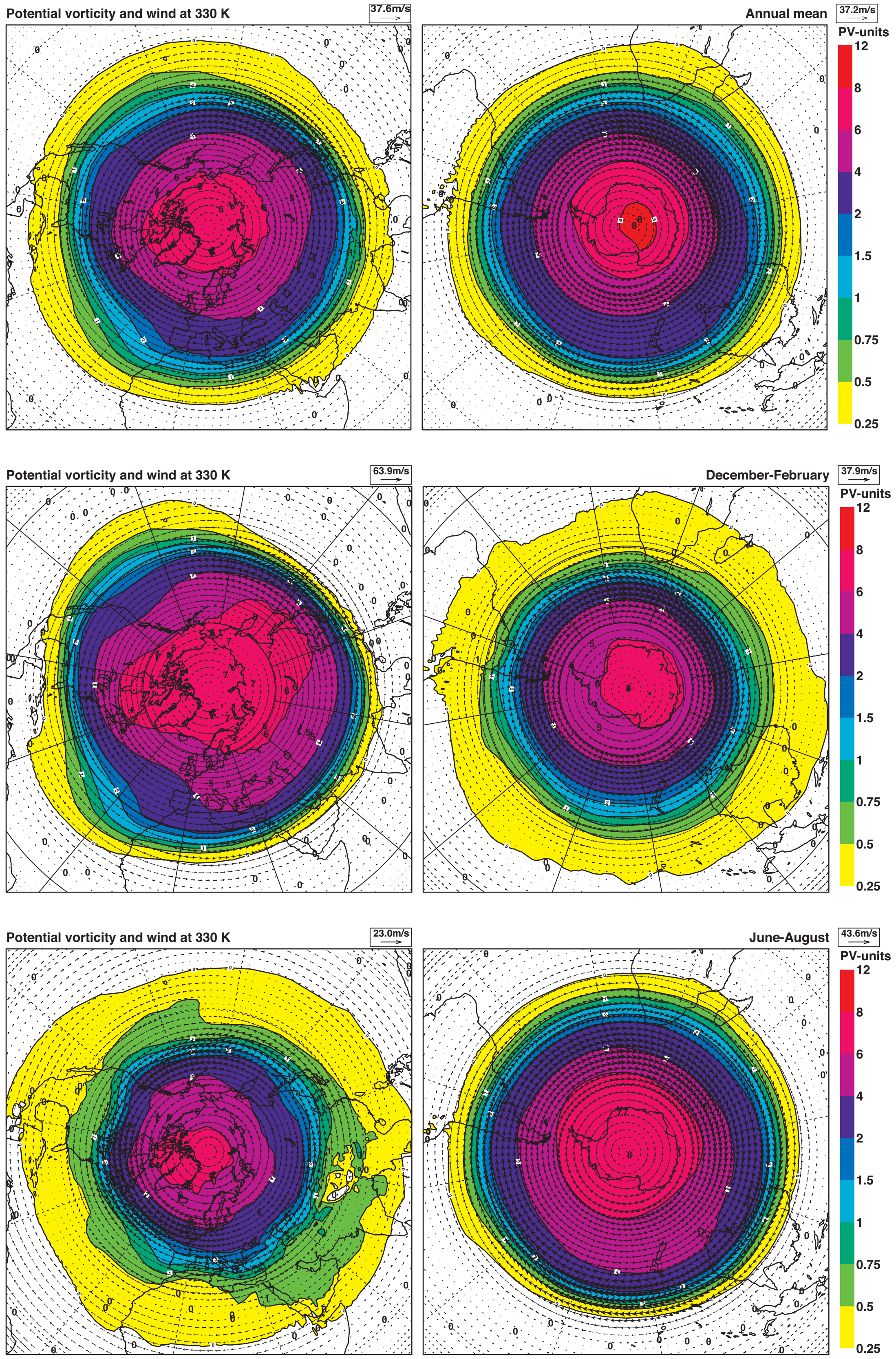

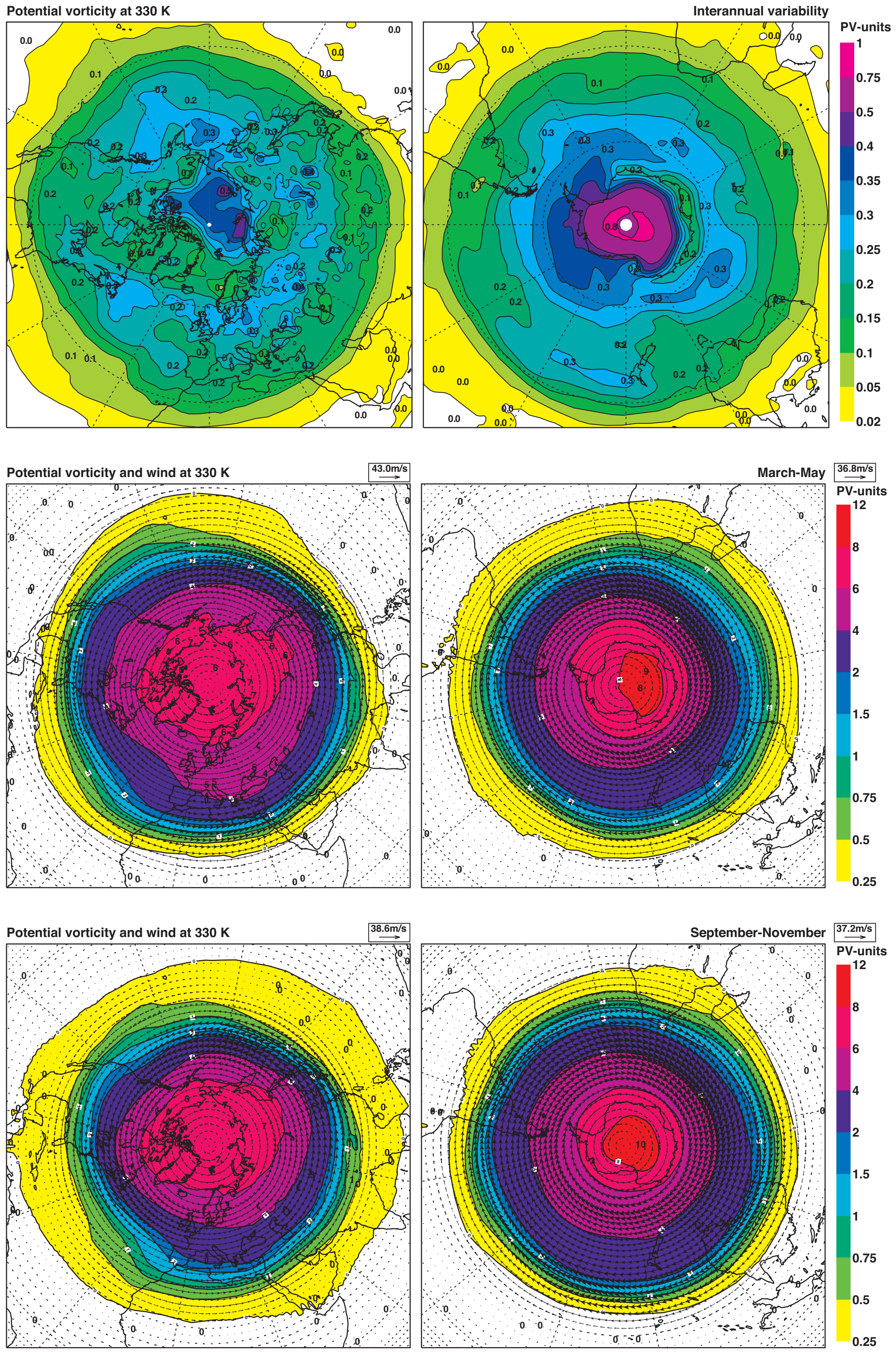

E12 Potential vorticity (pvu) with vector wind (ms^{-1}) at 330 K. For the interannual variability, the winds are omitted.

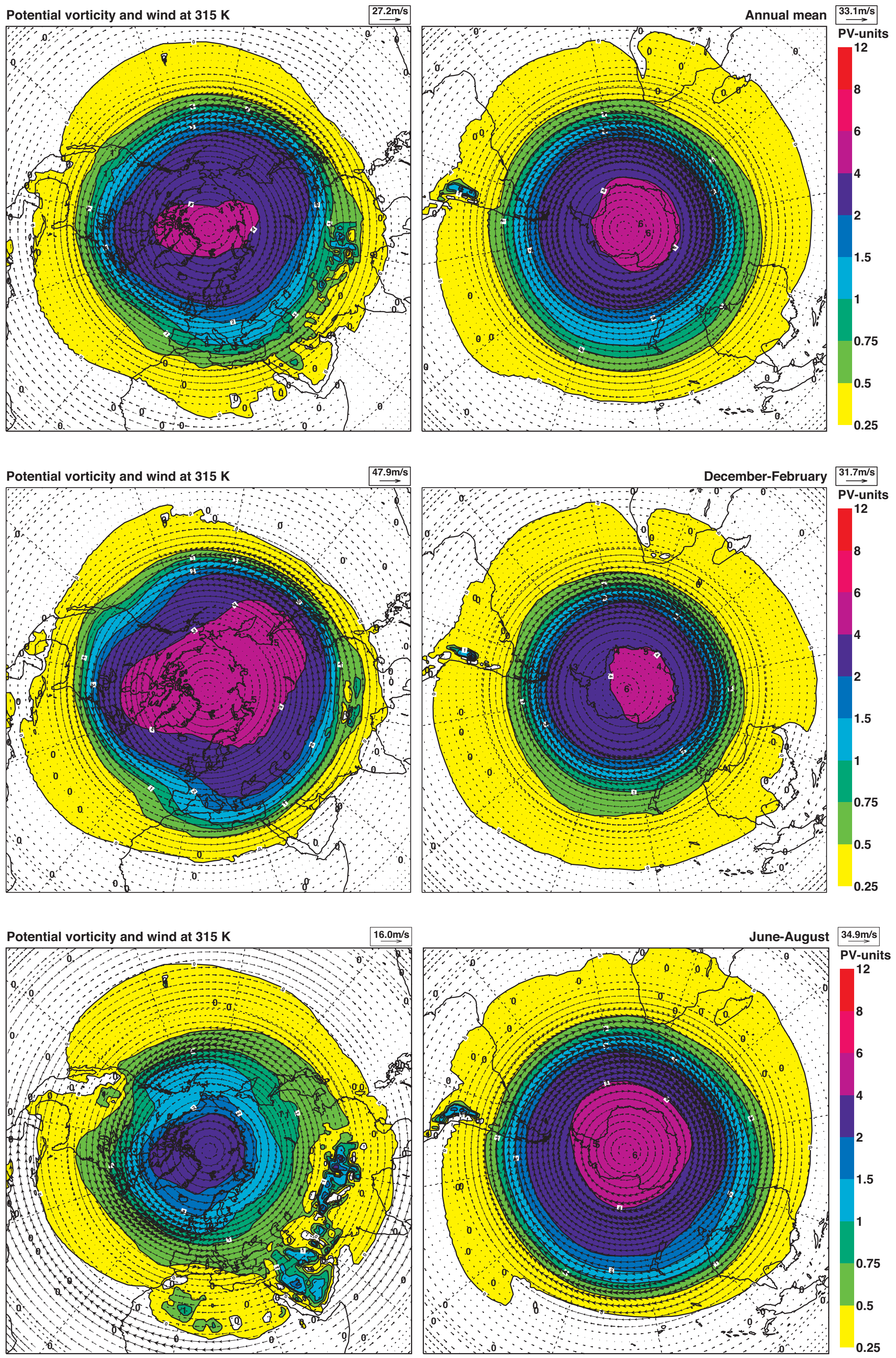

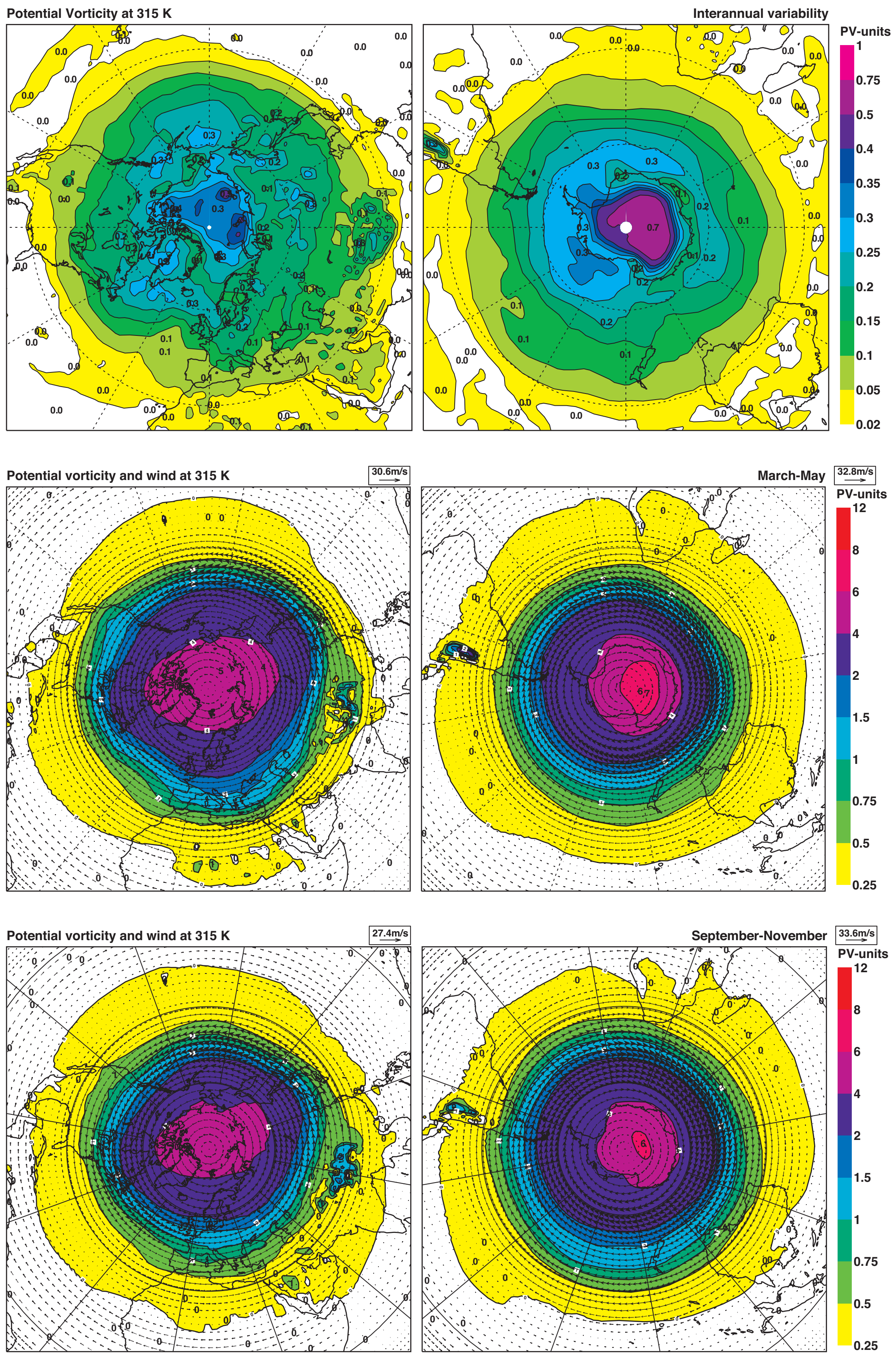

E13 Potential vorticity (pvu) with vector wind (ms^{-1}) at 315 K. For the interannual variability, the winds are omitted.

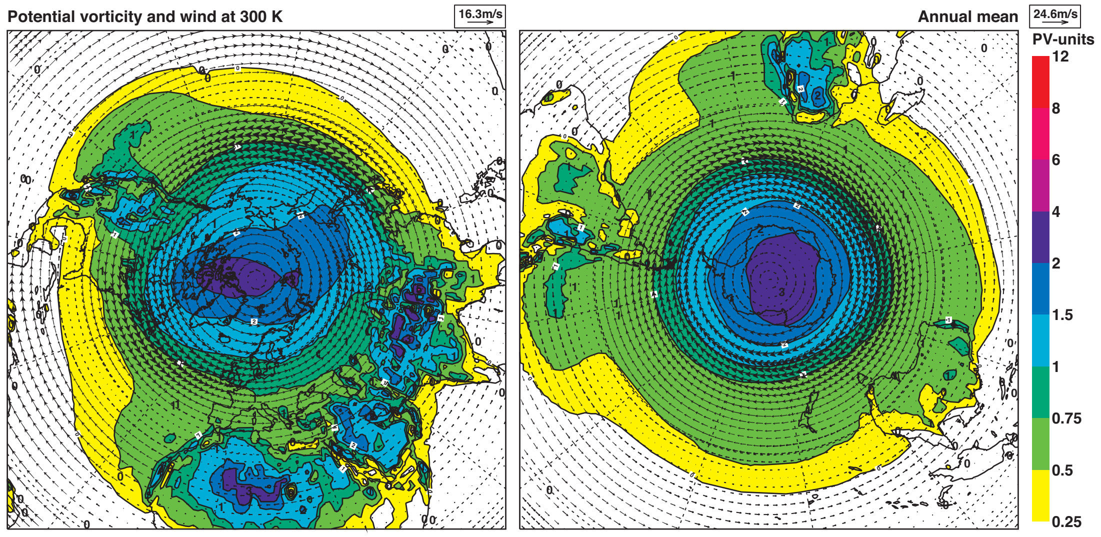

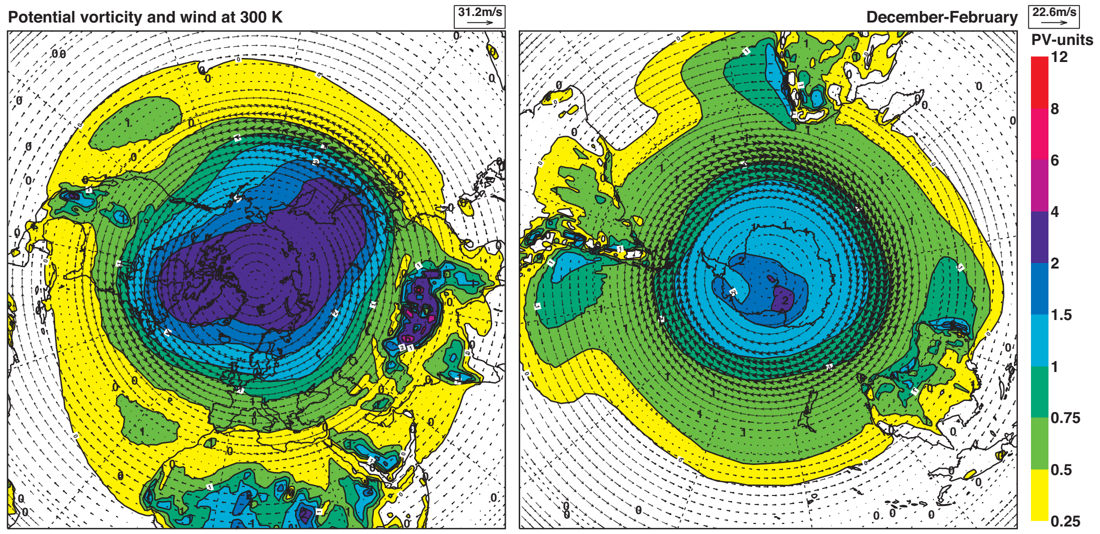

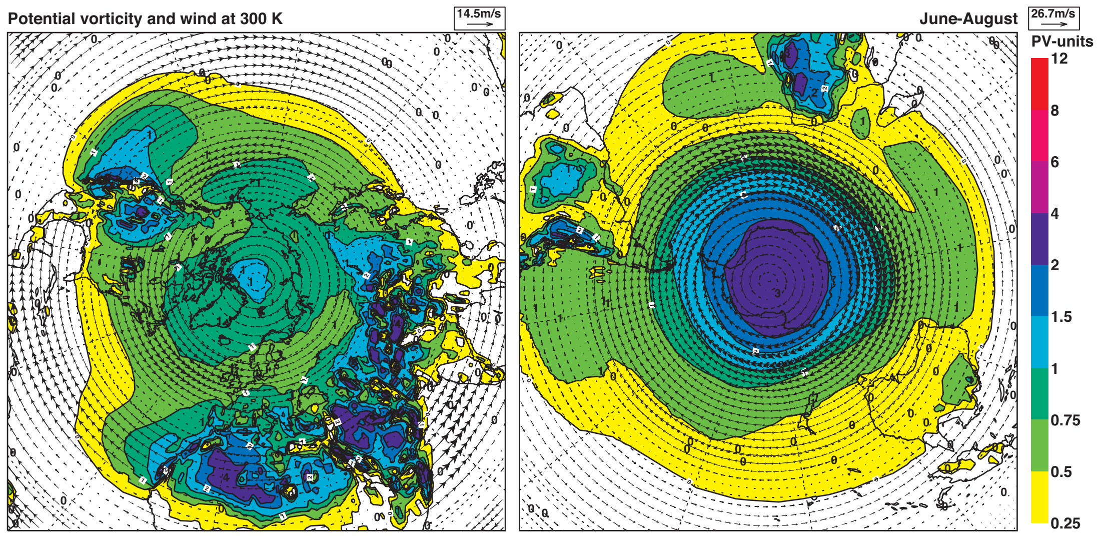

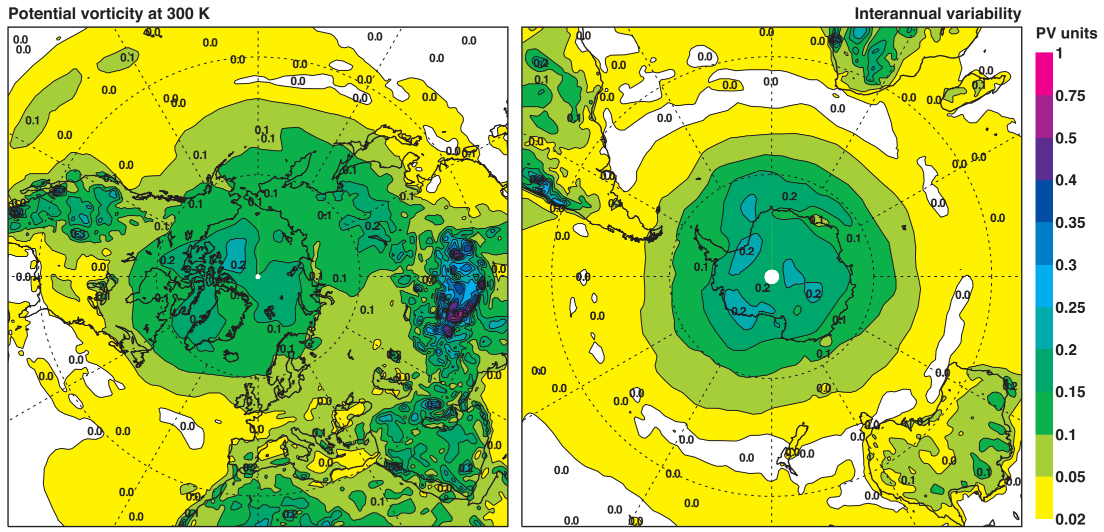

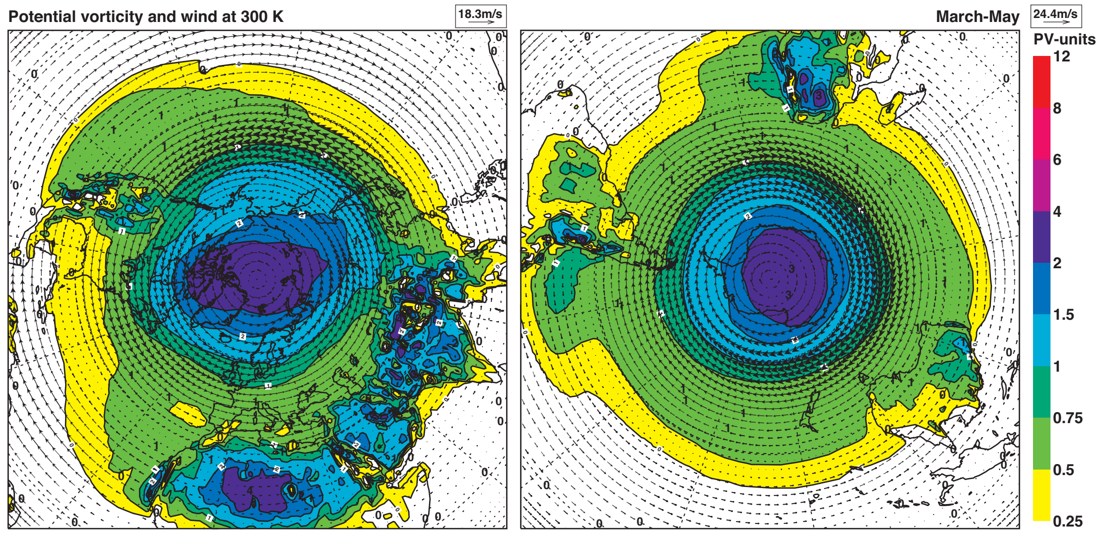

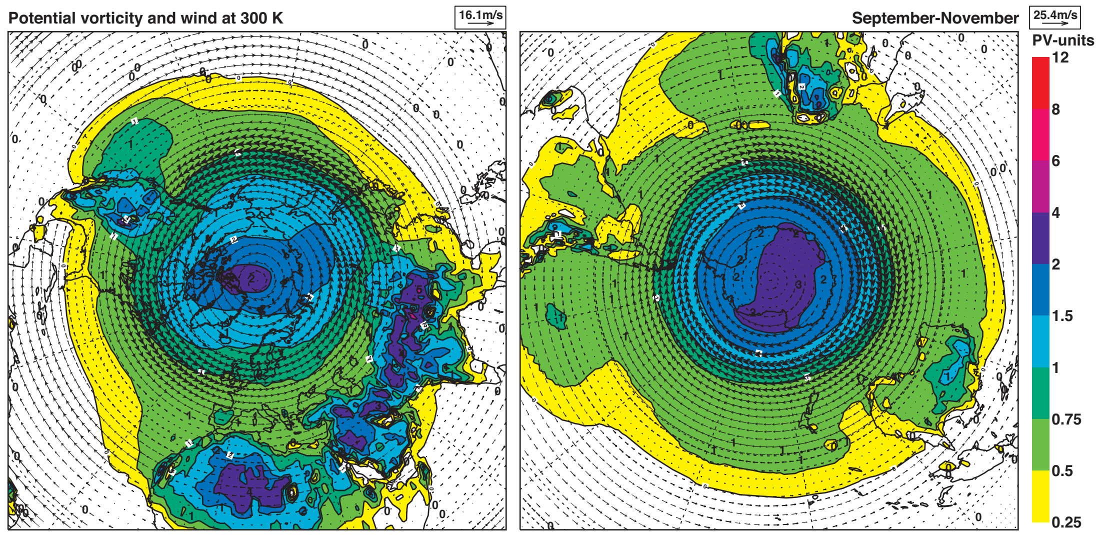

E14 Potential vorticity (pvu) with vector wind (ms^{-1}) at 300 K. For the interannual variability, the winds are omitted.

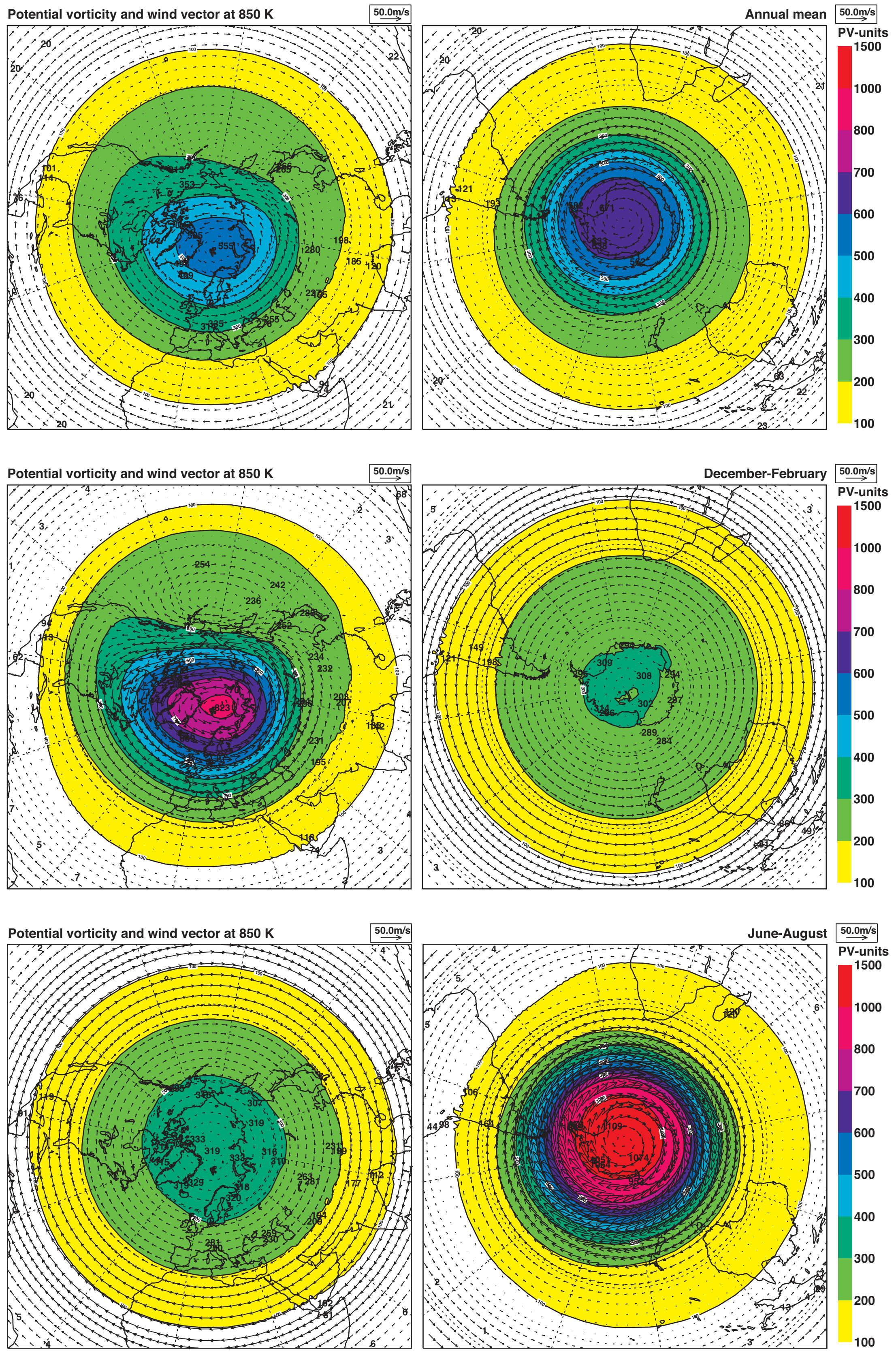

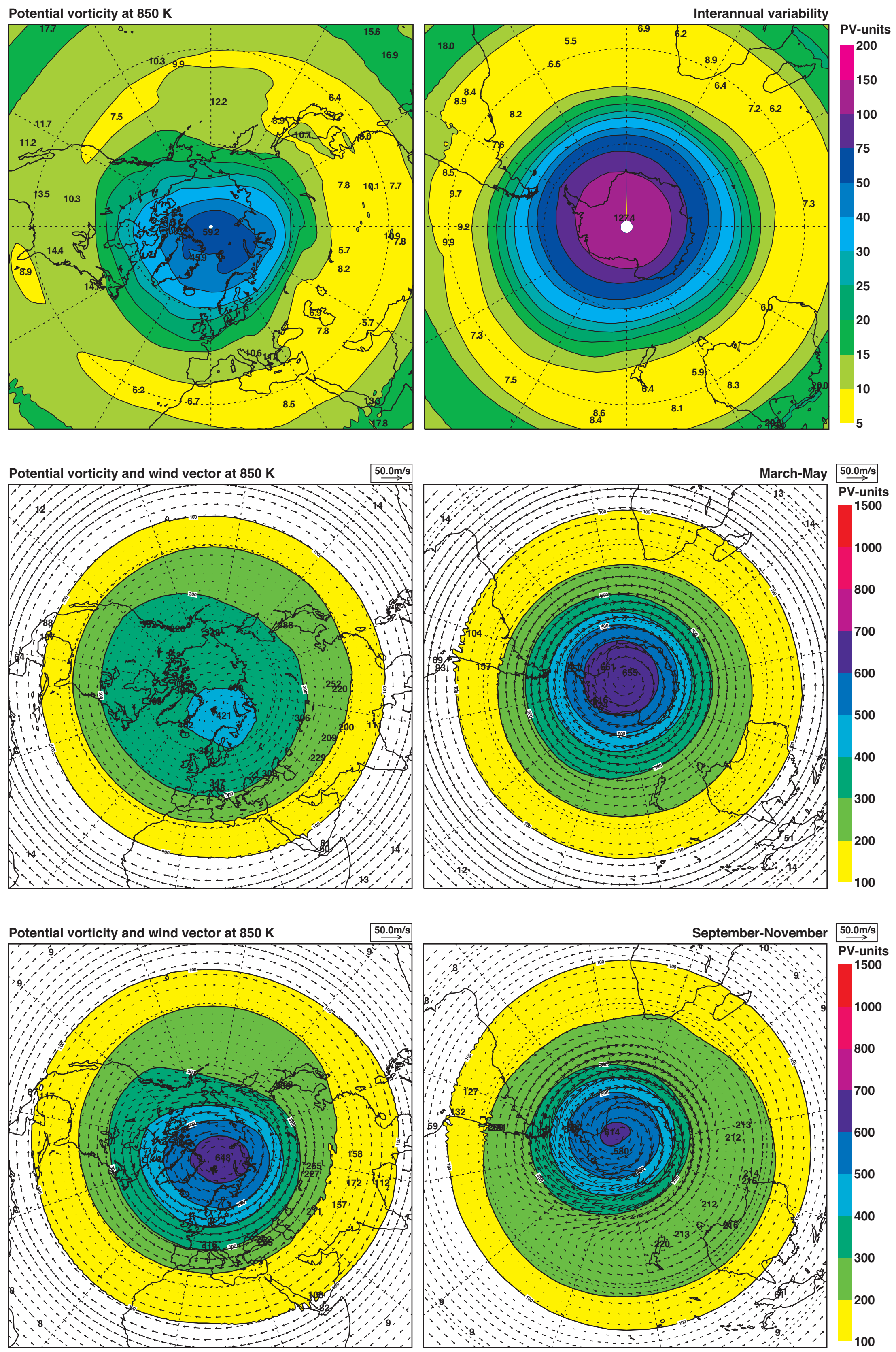

E15 Potential vorticity (pvu) with vector wind (ms^{-1}) at 850 K. For the interannual variability, the winds are omitted.

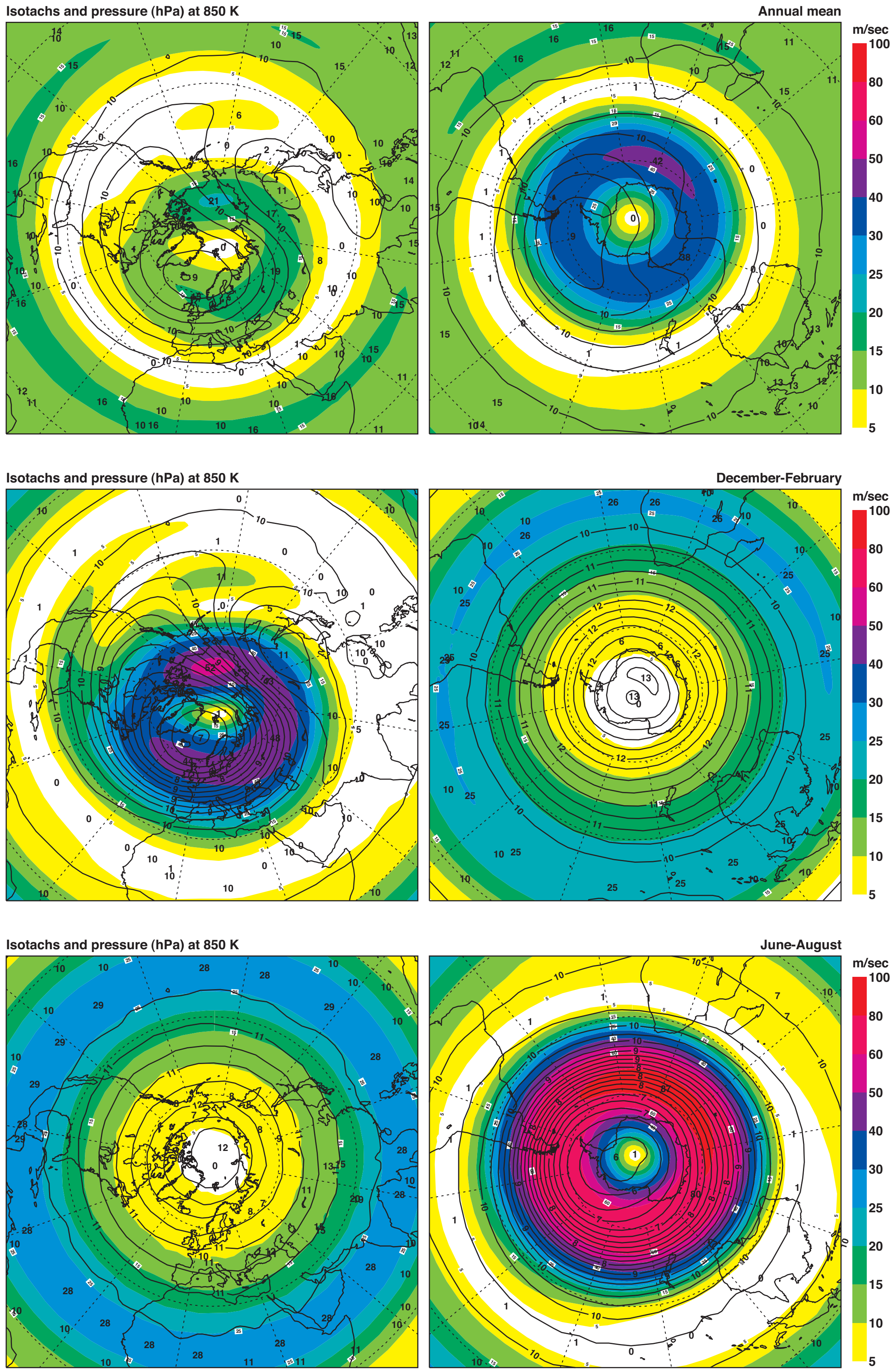

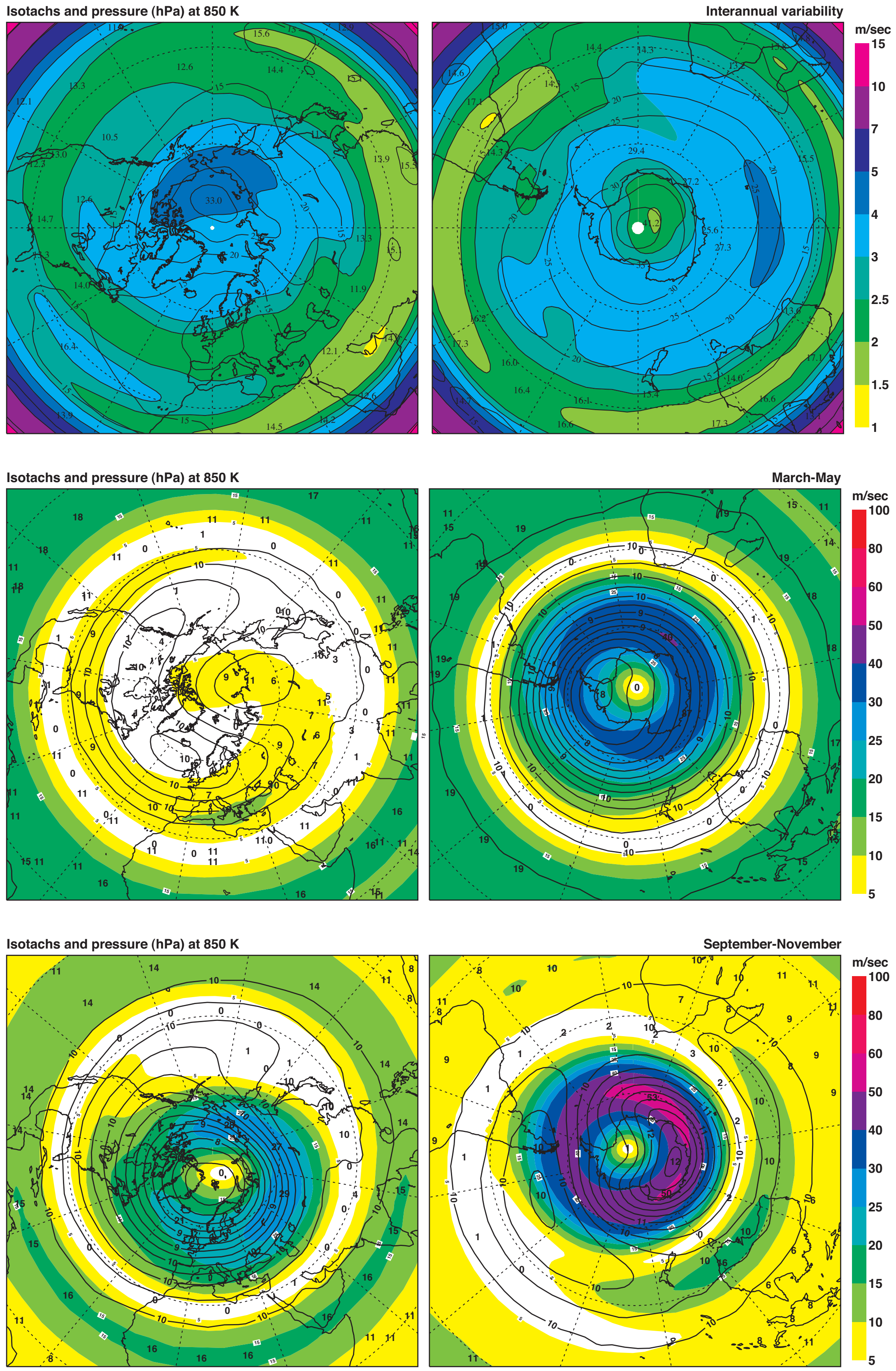

E16 Pressure (hPa) (contours) with isotachs (ms^{-1}) (colour shading) at 850 K.

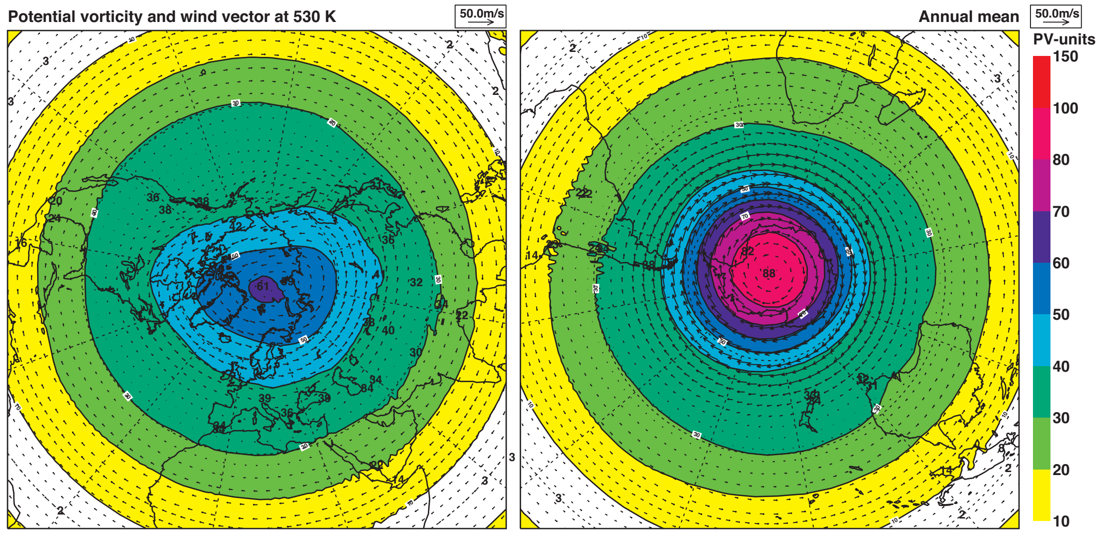

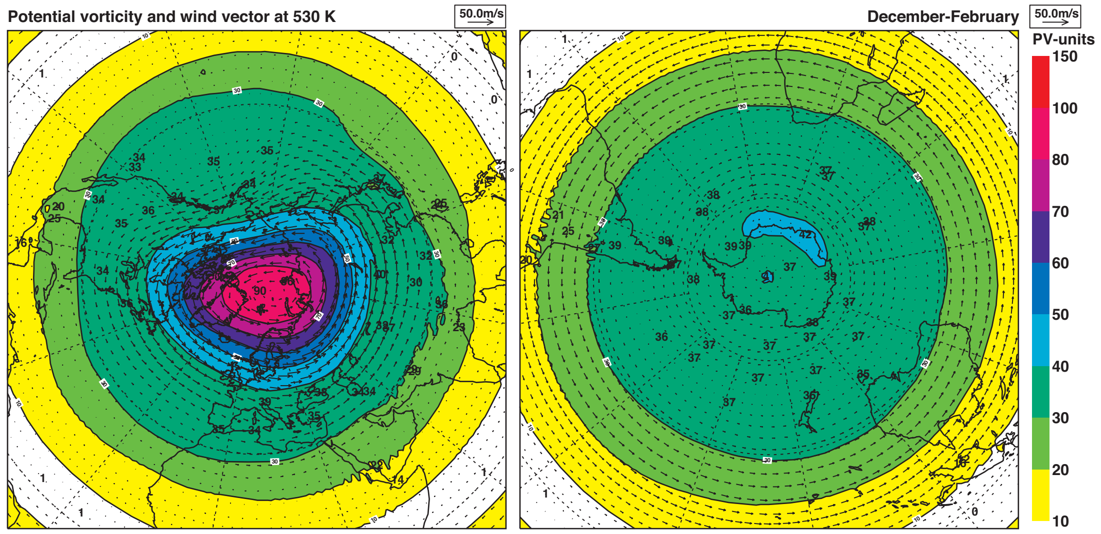

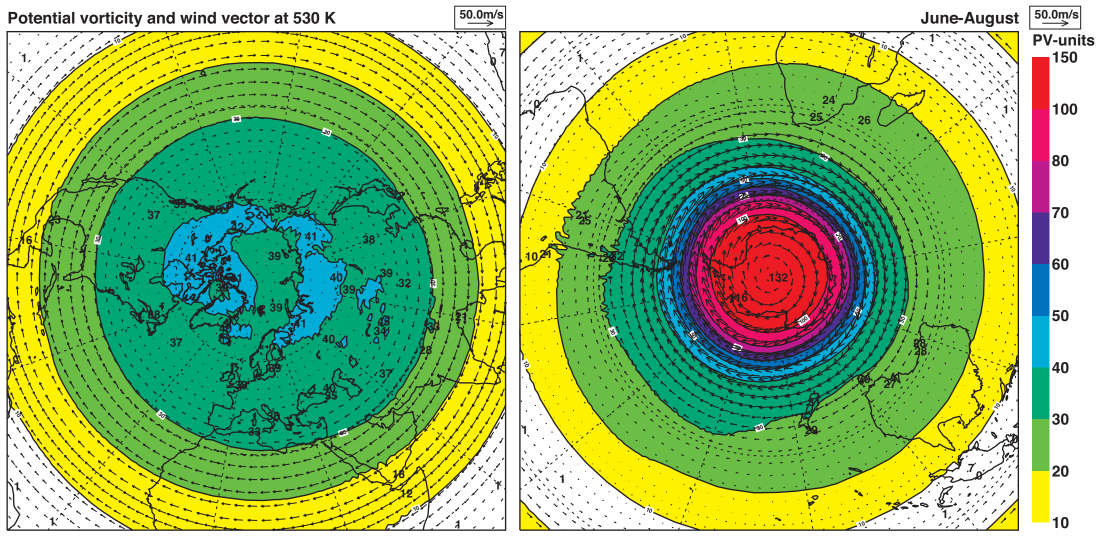

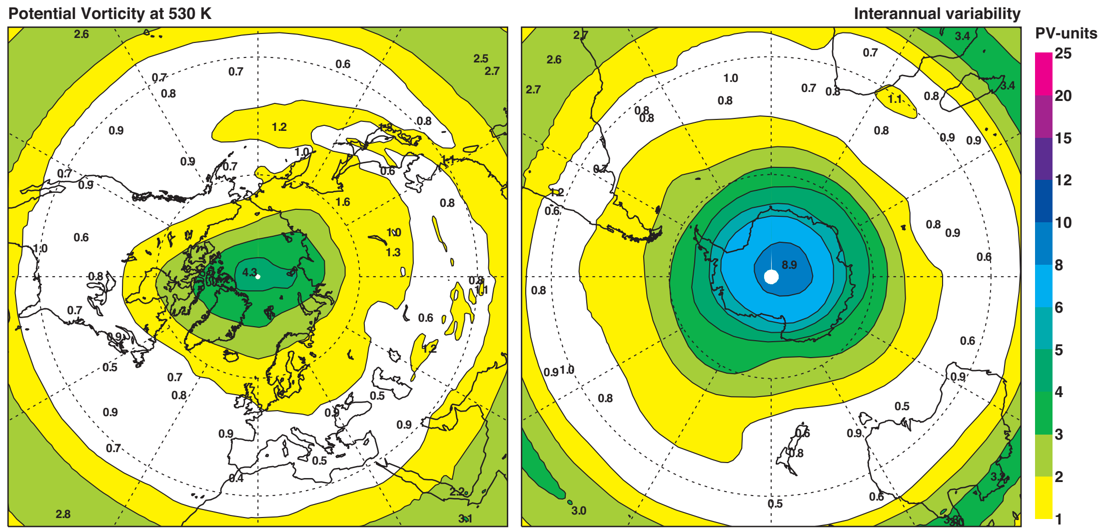

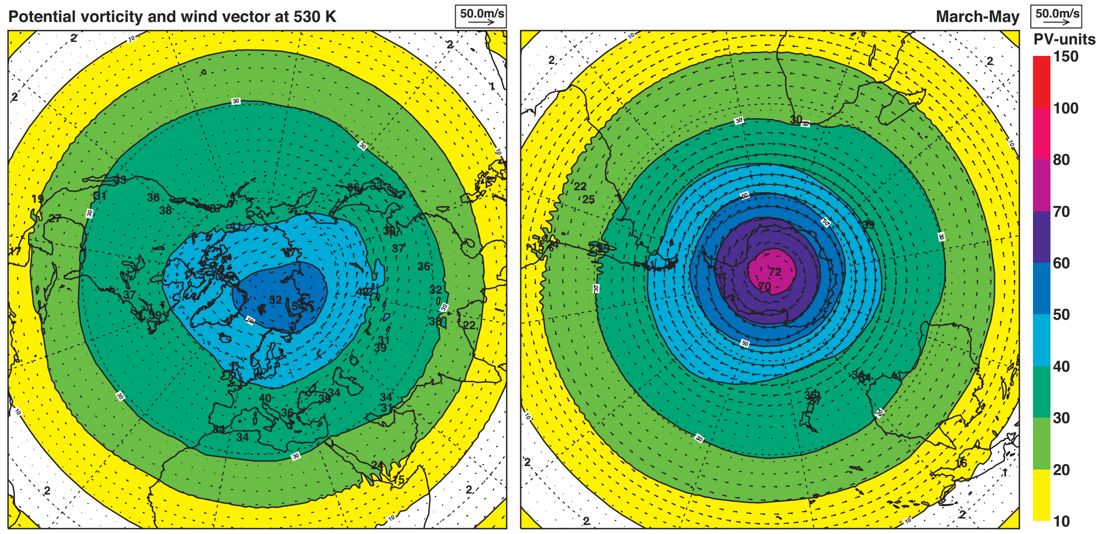

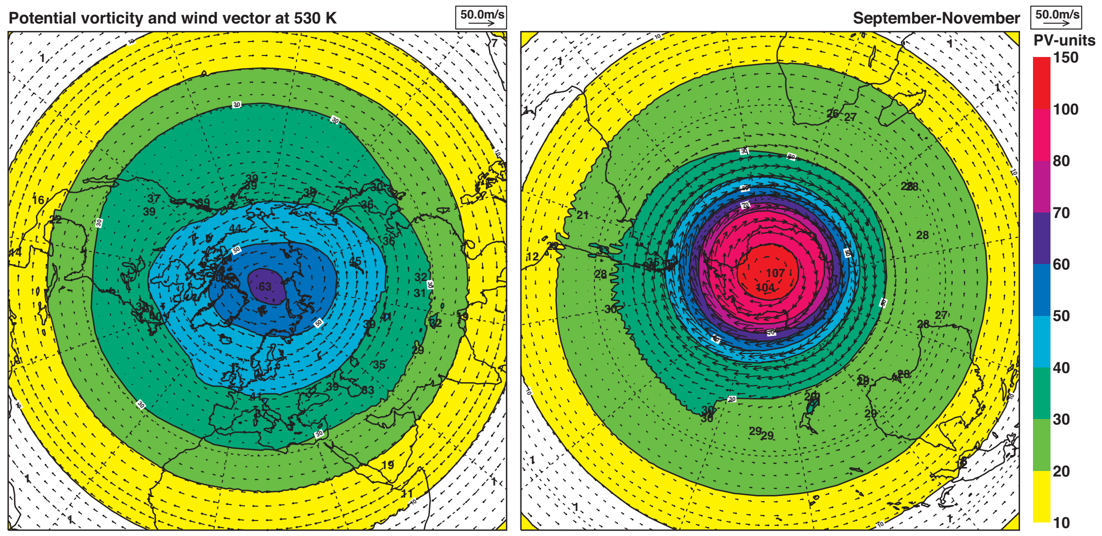

E17 Potential vorticity (pvu) with vector wind (ms^{-1}) at 530 K. For the interannual variability, the winds are omitted.

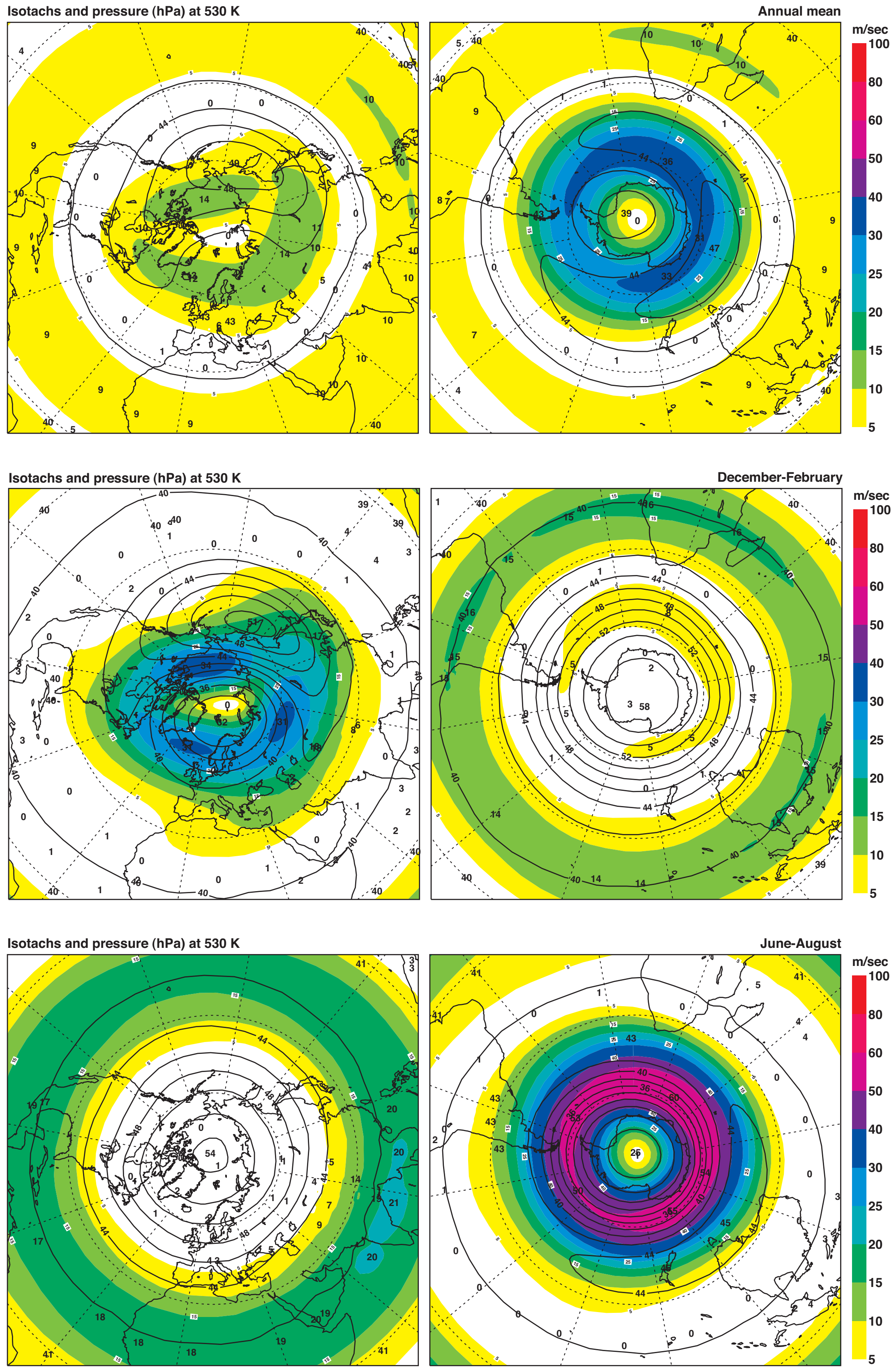

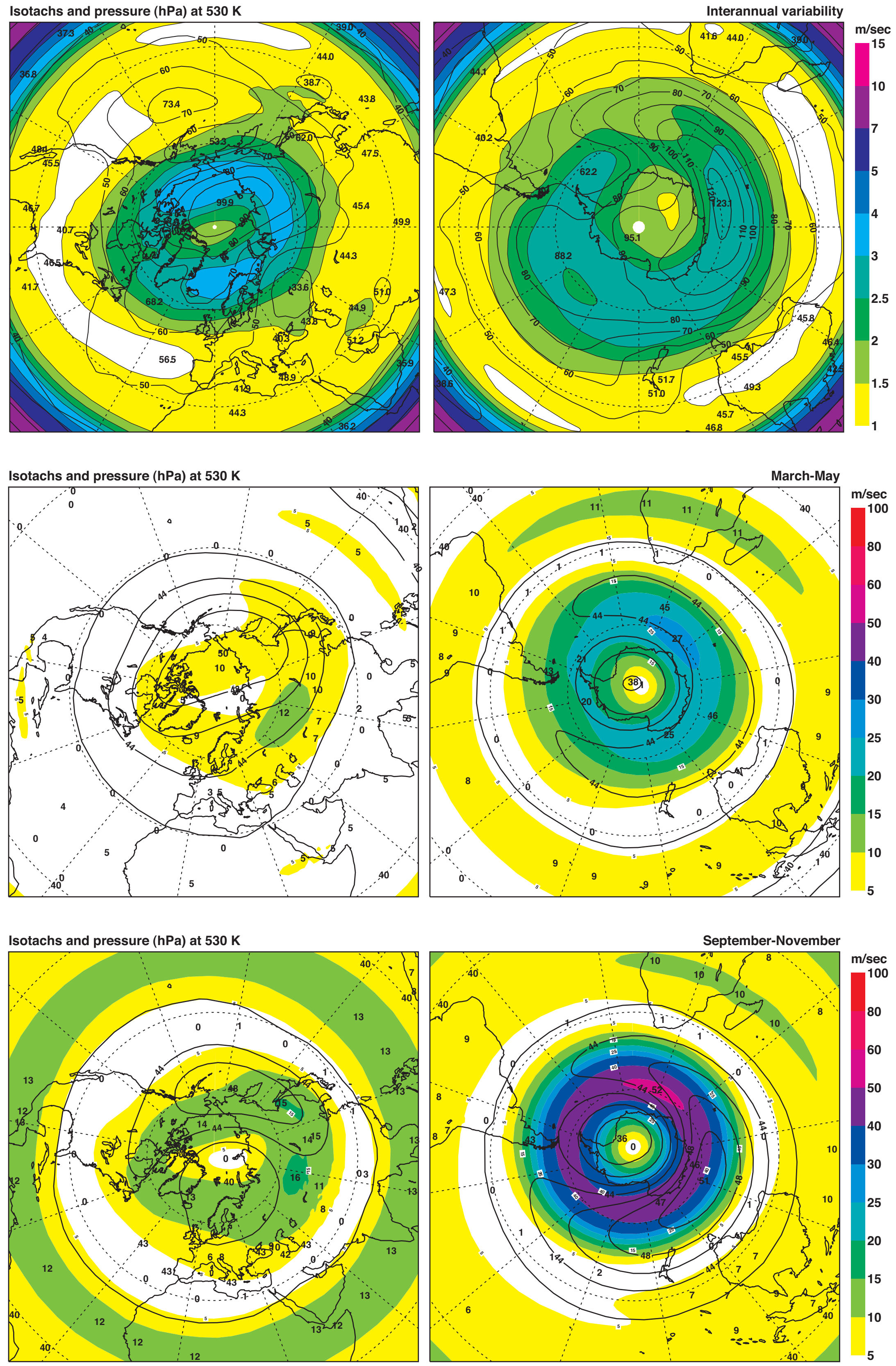

E18 Pressure (hPa) (contours) with isotachs (ms^{-1}) (colour shading) at 530 K.

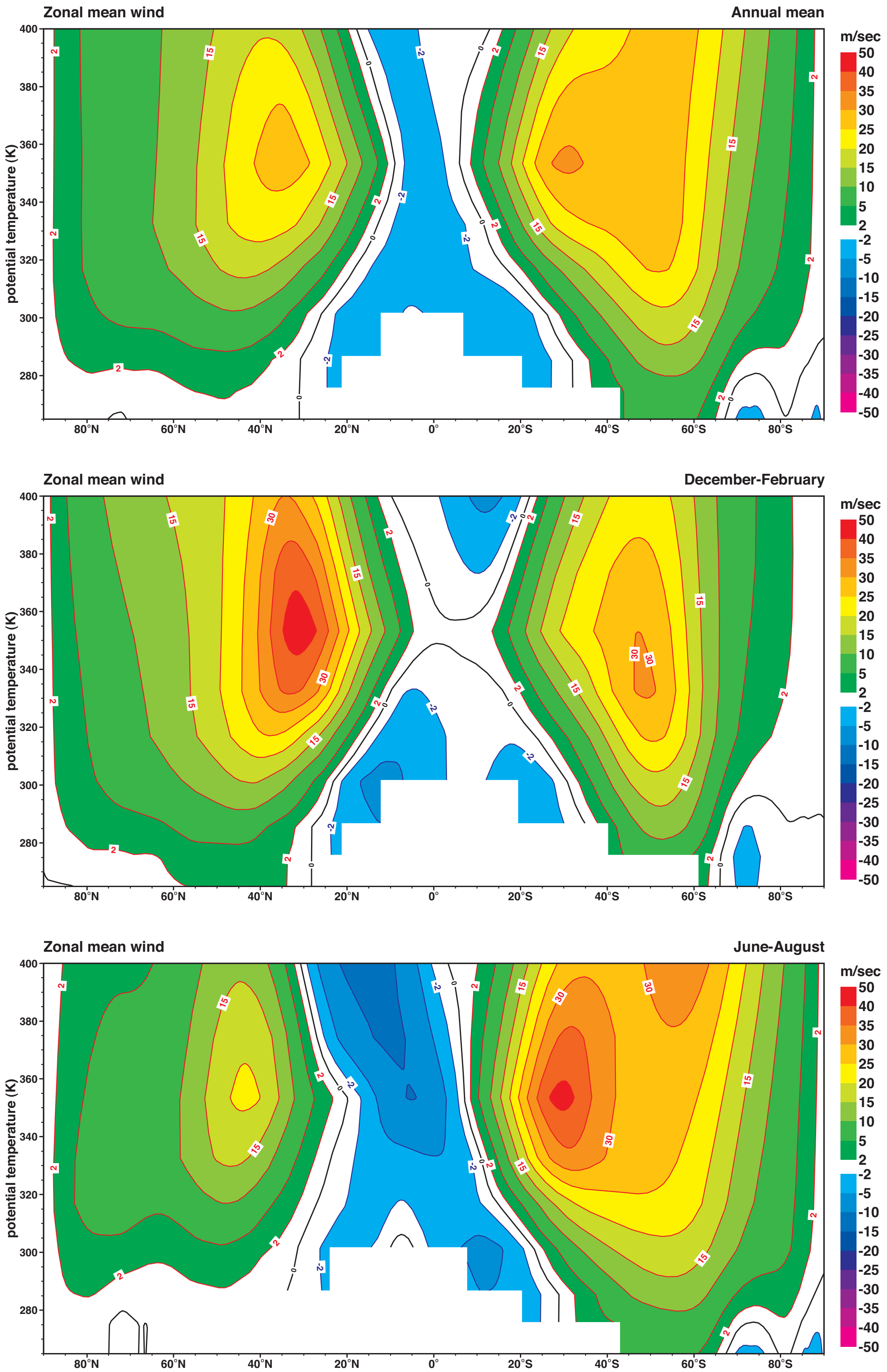

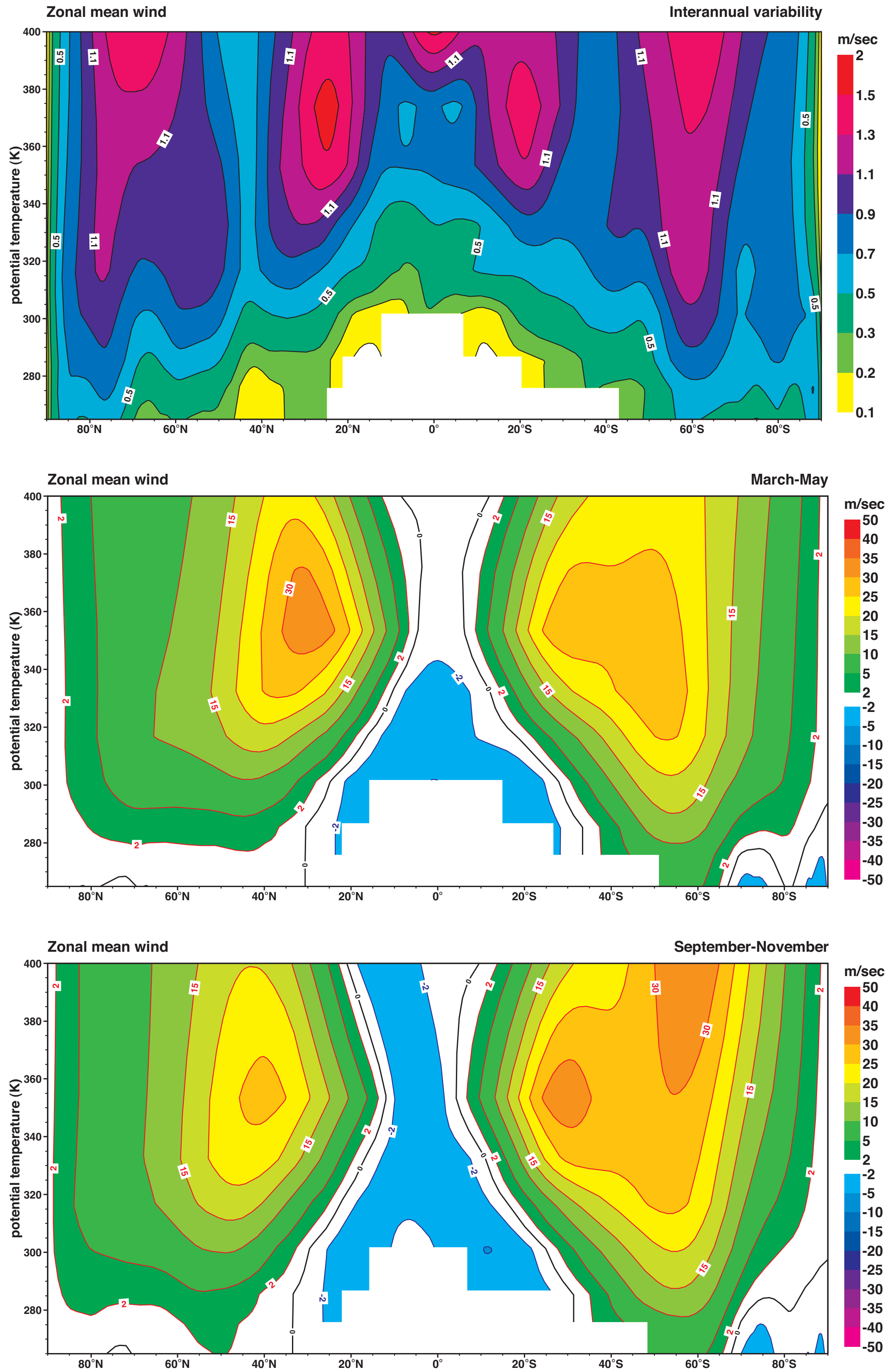

E19 An isentropic tropospheric perspective of zonal mean zonal wind (ms^{-1}).

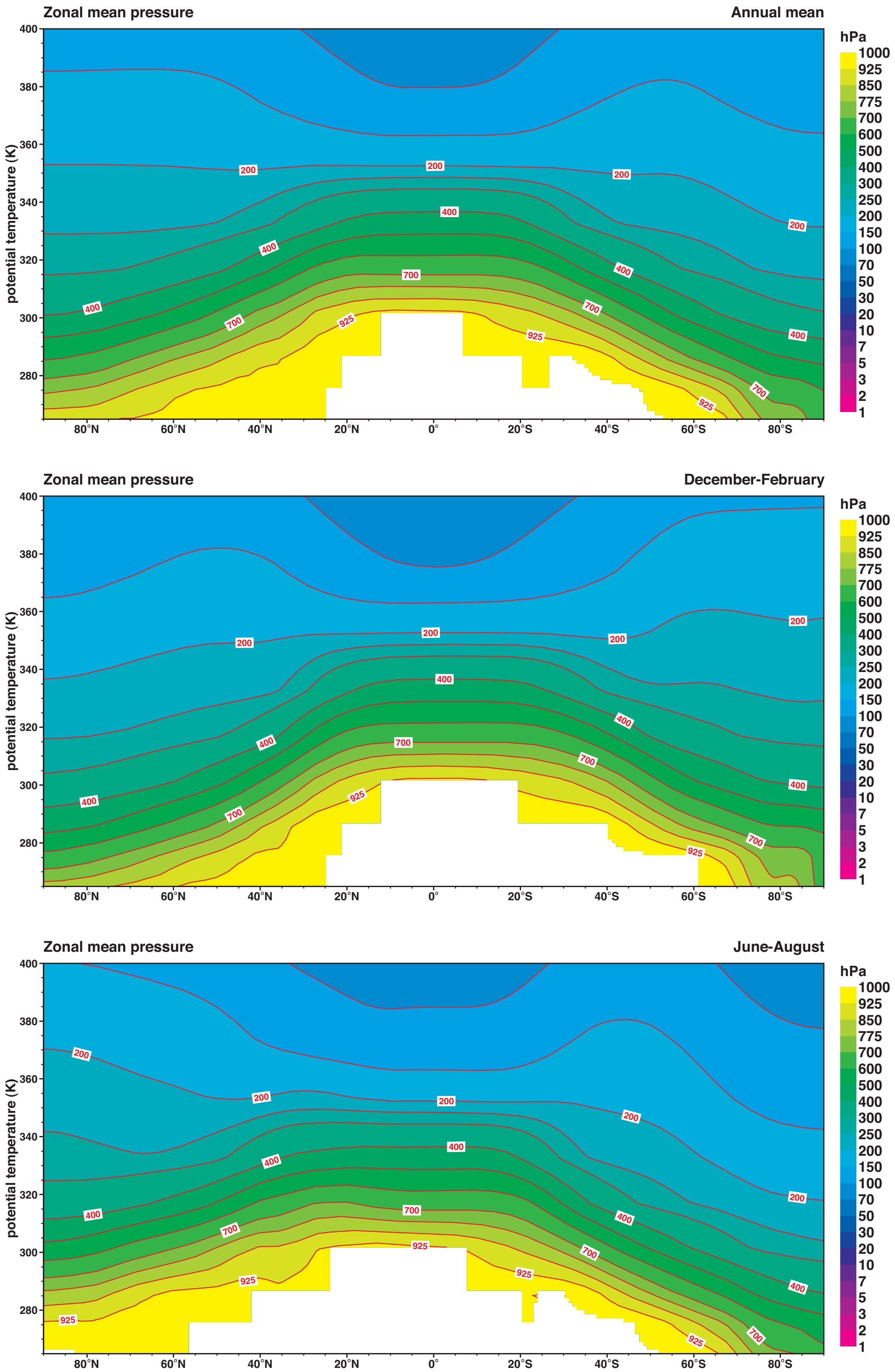

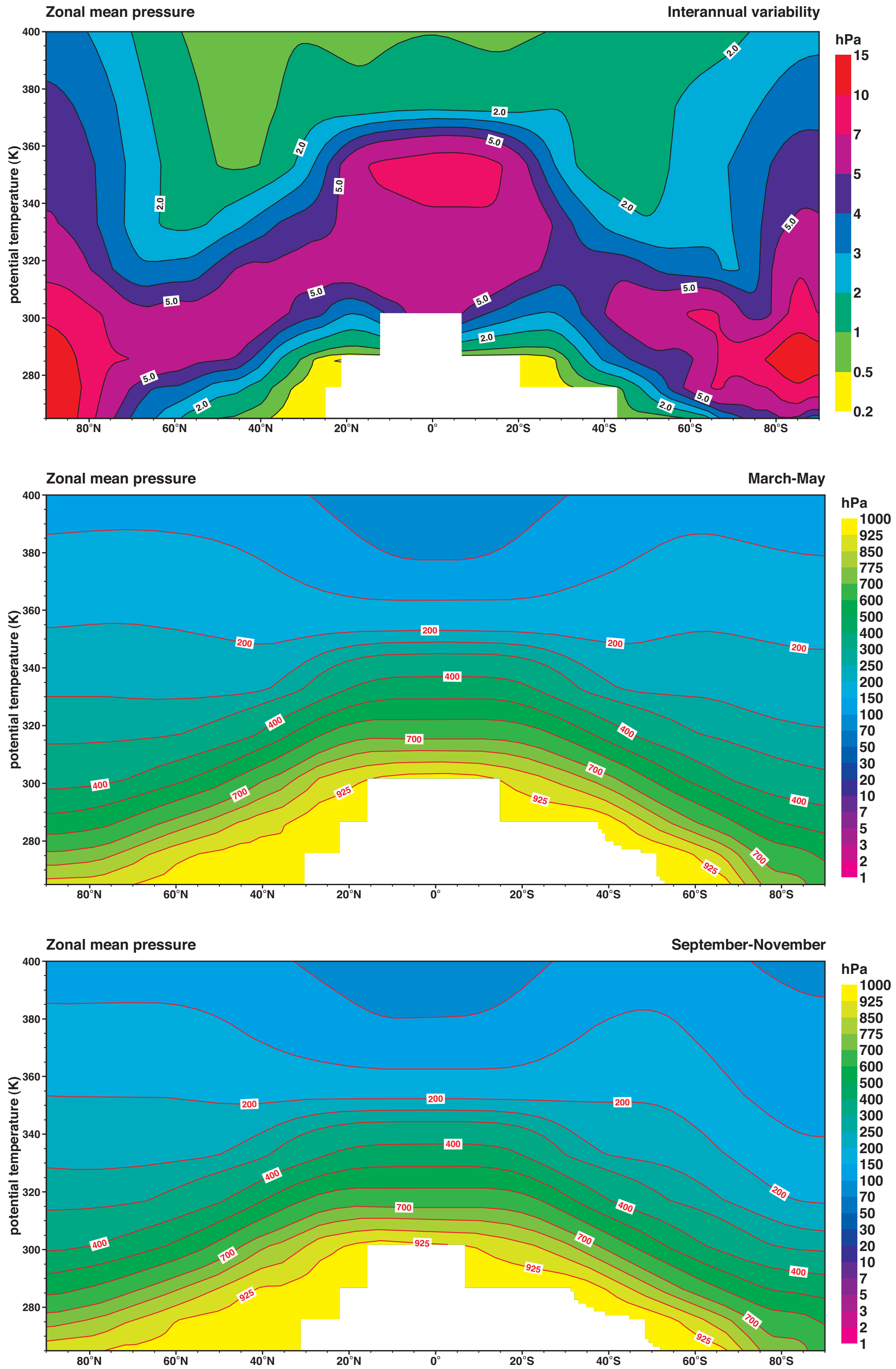

E20 An isentropic tropospheric perspective of zonal mean pressure (hPa).

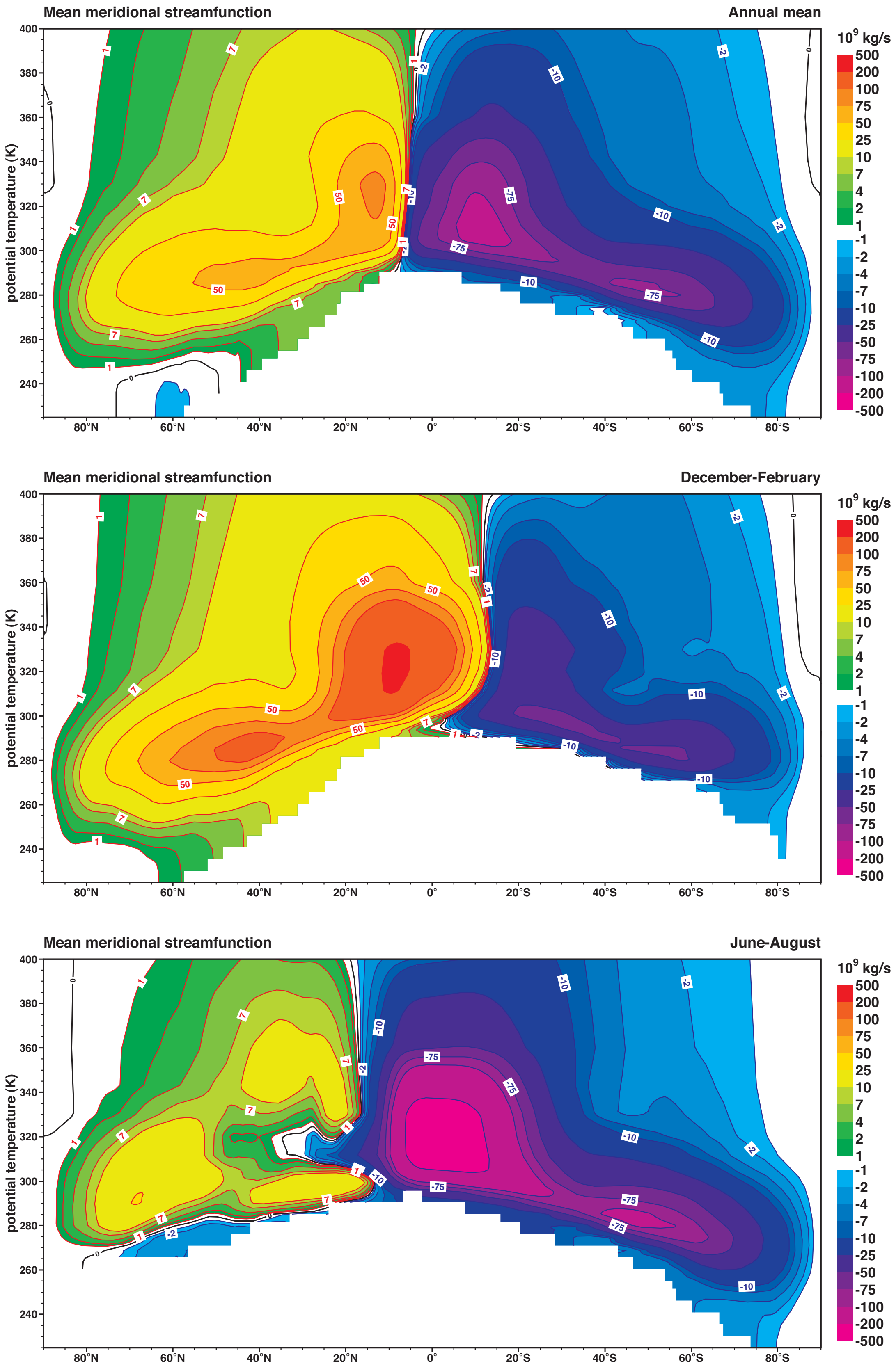

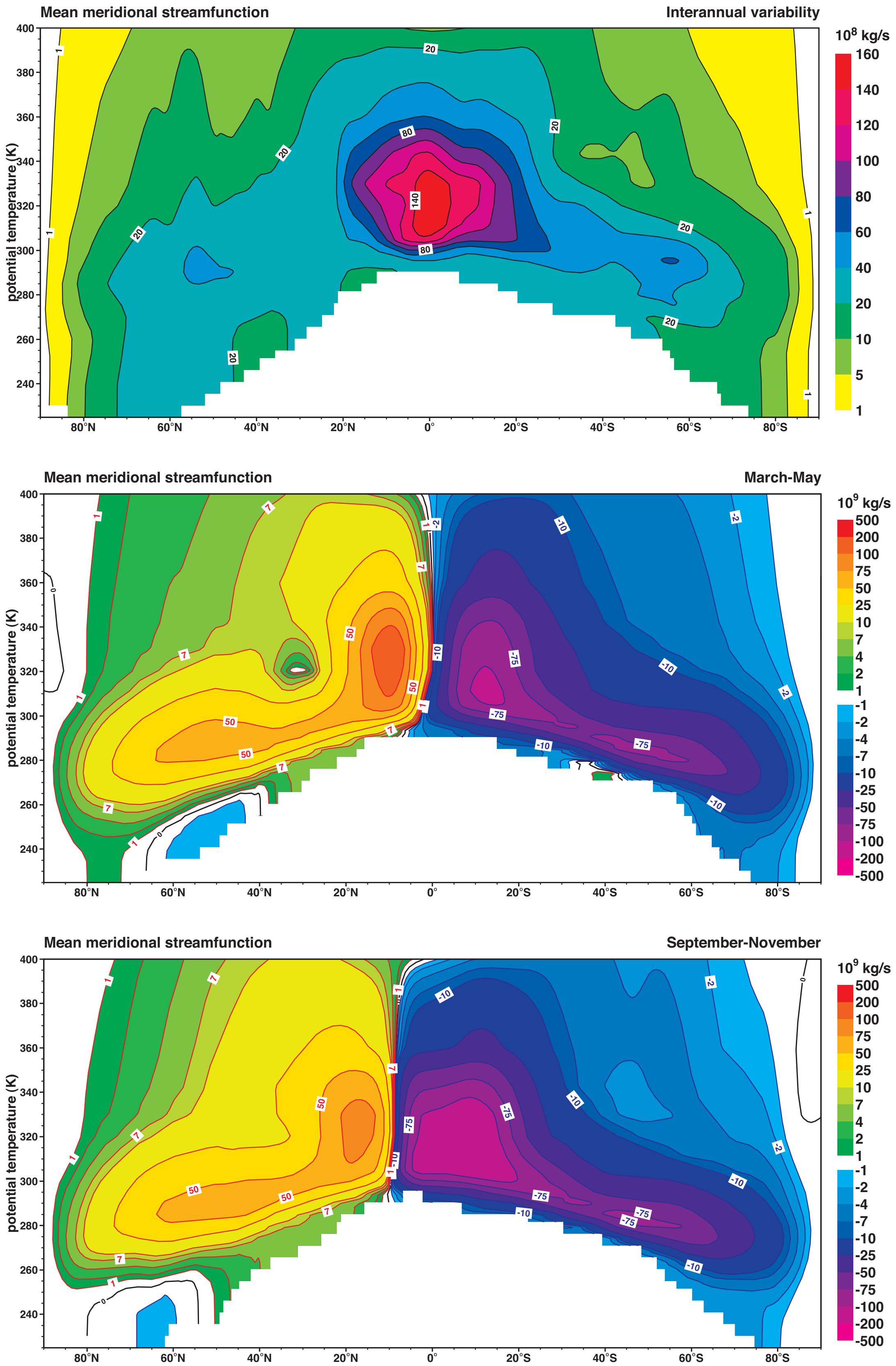

E21 An isentropic tropospheric perspective of mean meridional streamfunction (kgs^{-1}).

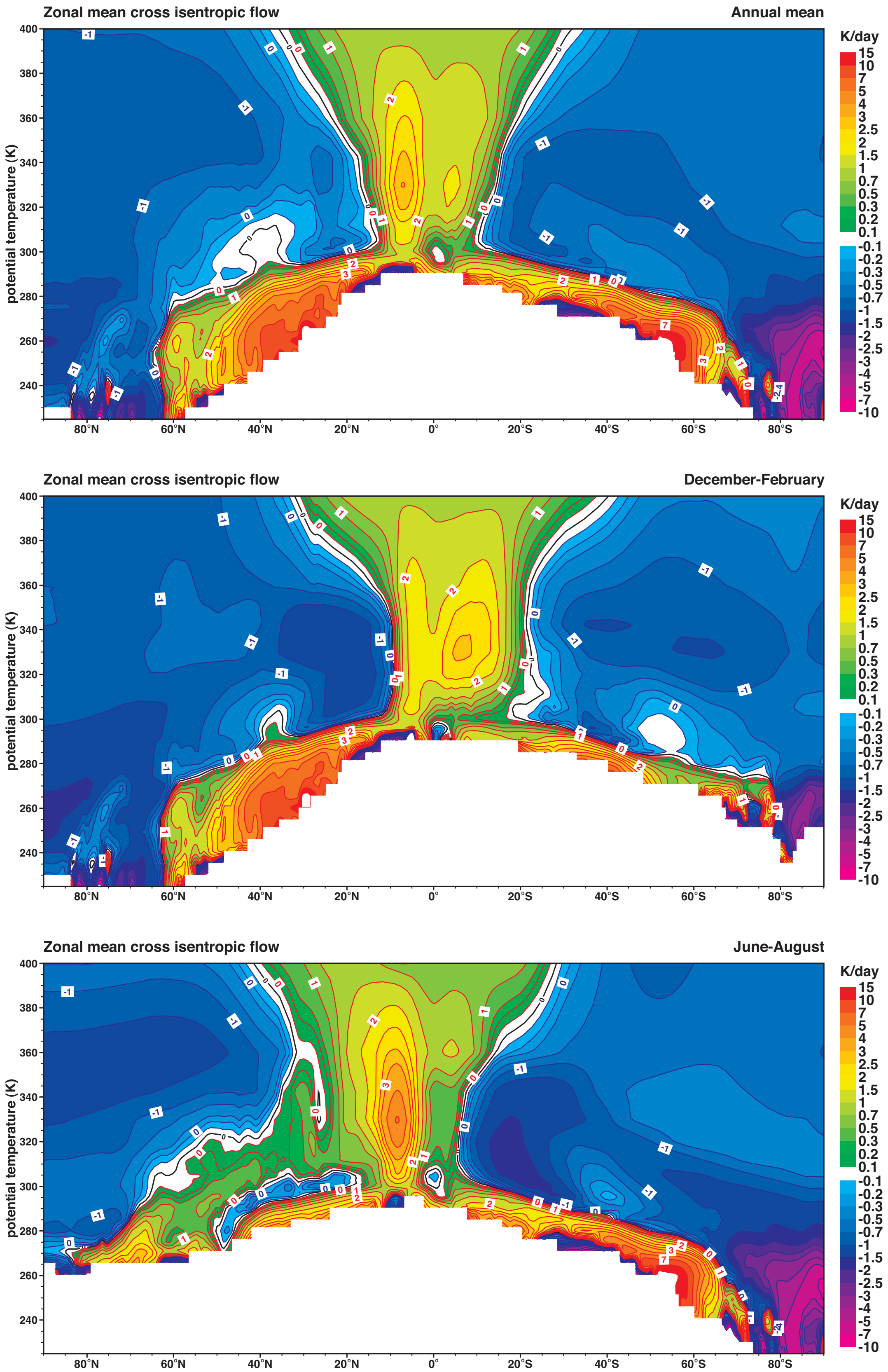

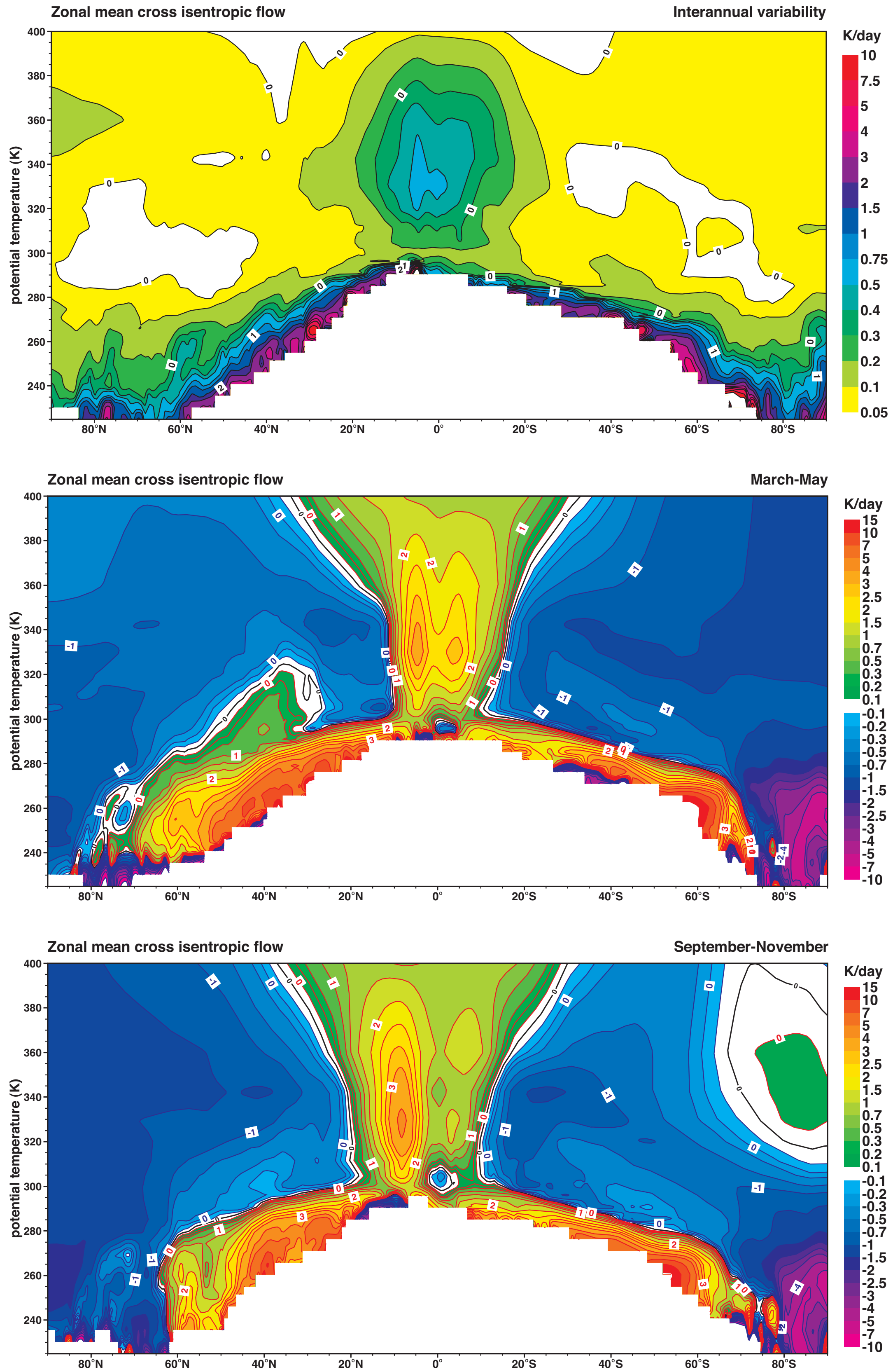

E22 An isentropic tropospheric perspective of zonal mean cross isentropic flow (Kday^{-1}).

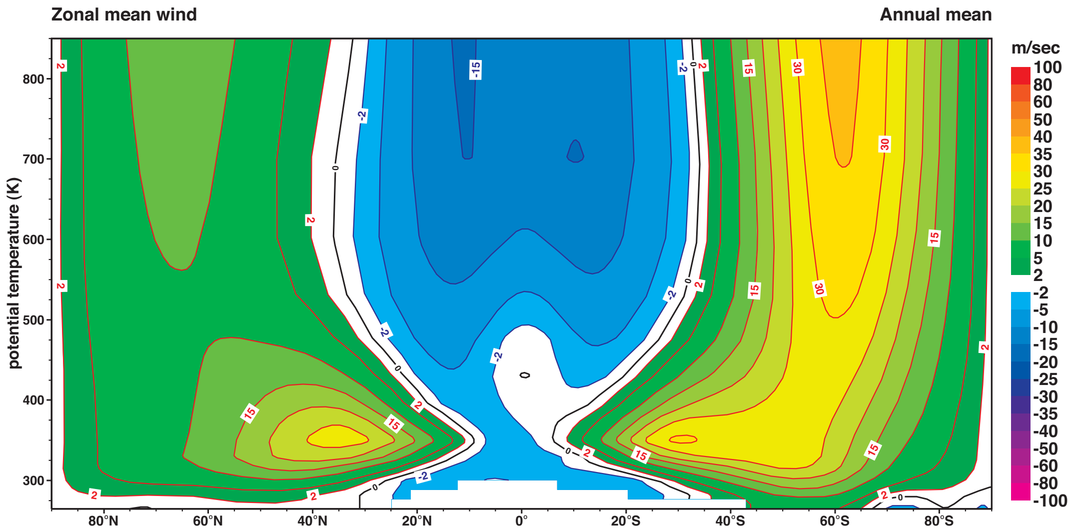

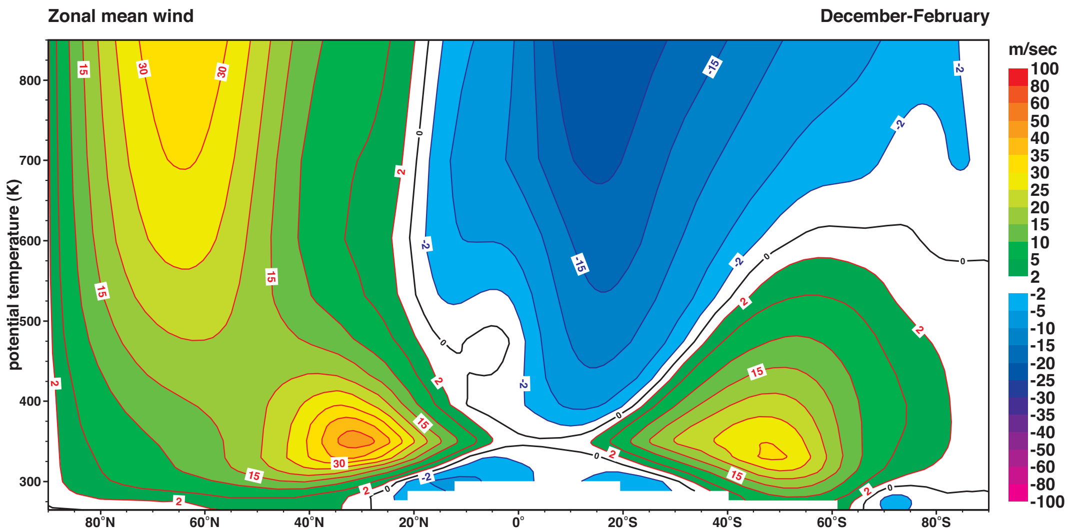

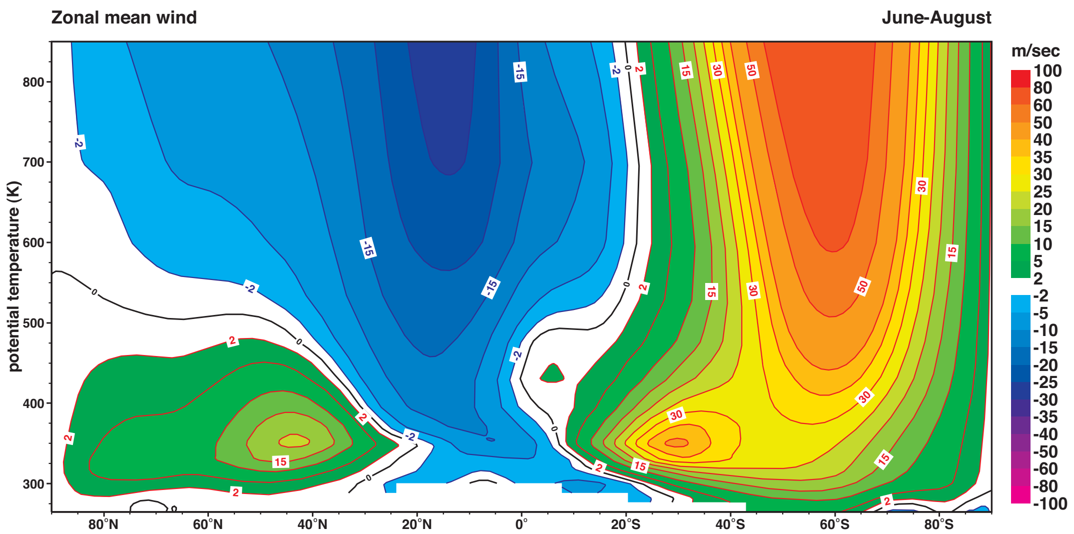

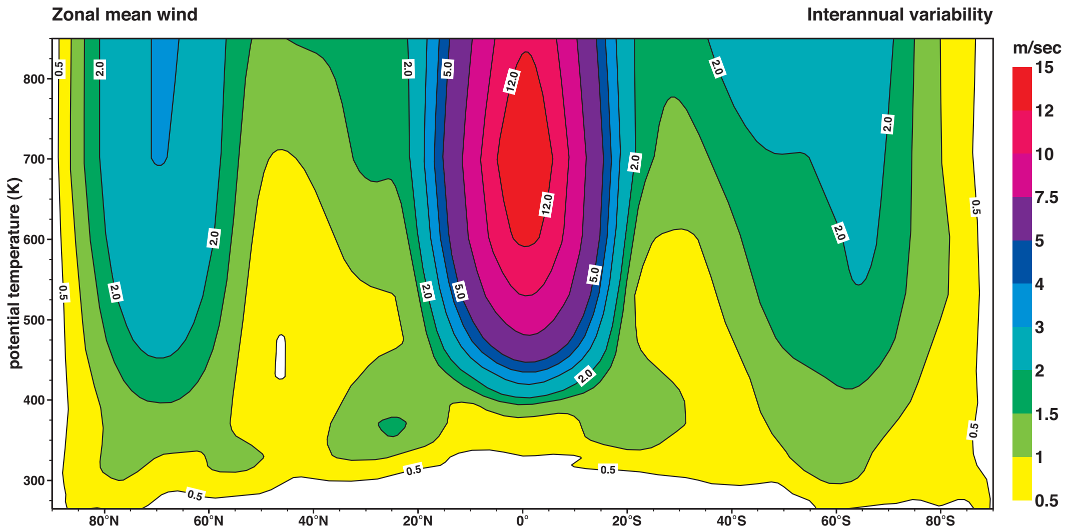

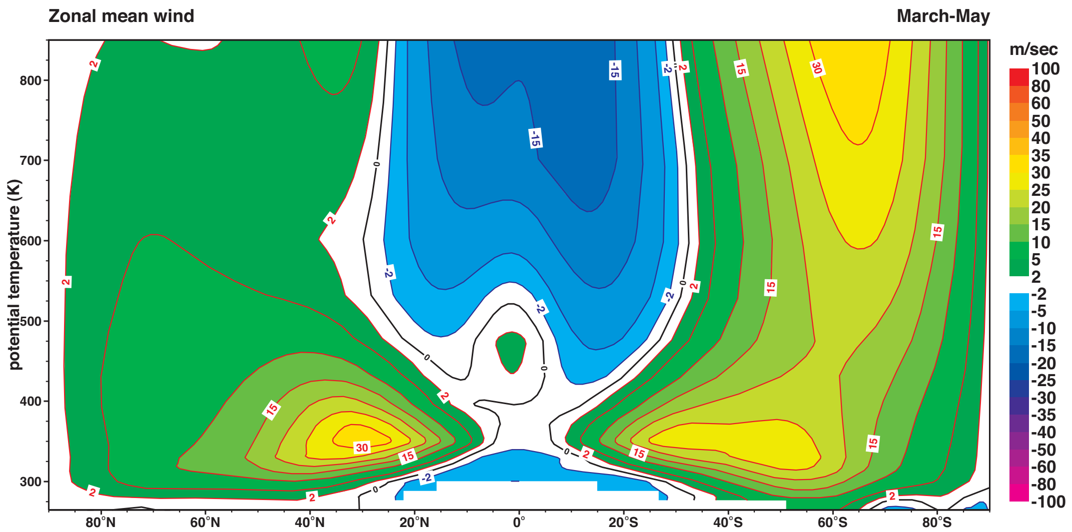

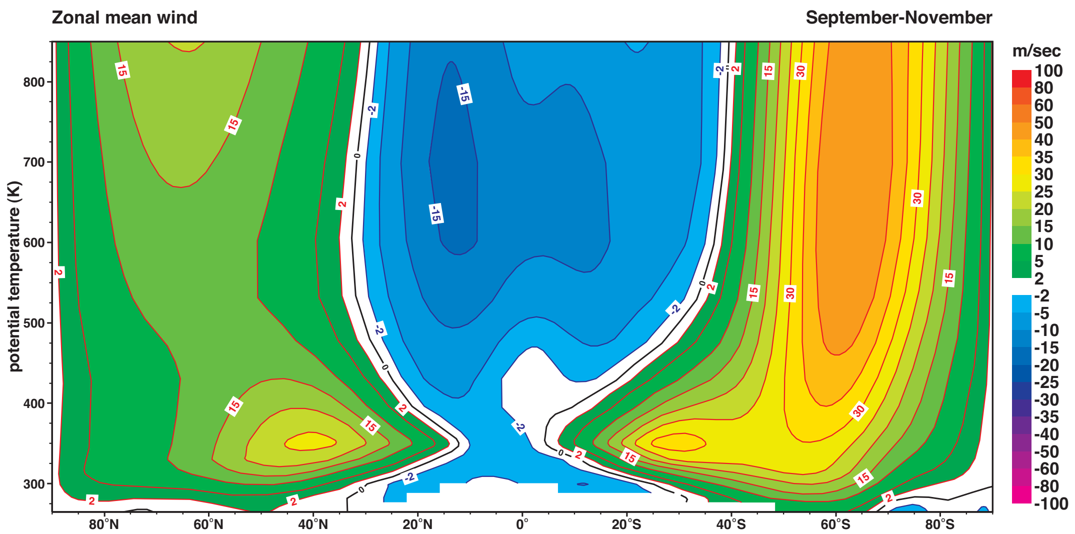

E23 An isentropic stratospheric perspective of zonal mean zonal wind (ms^{-1}).

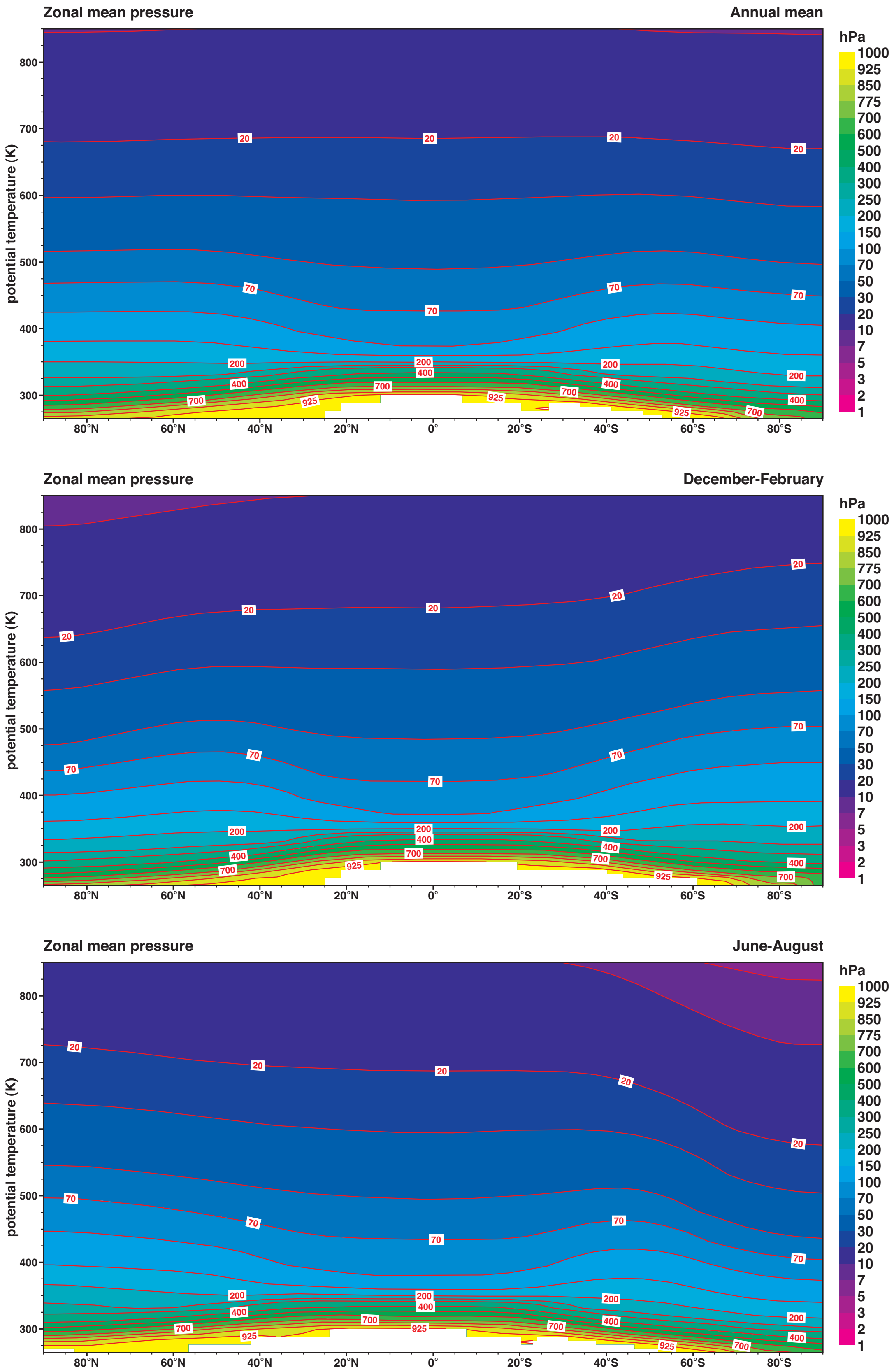

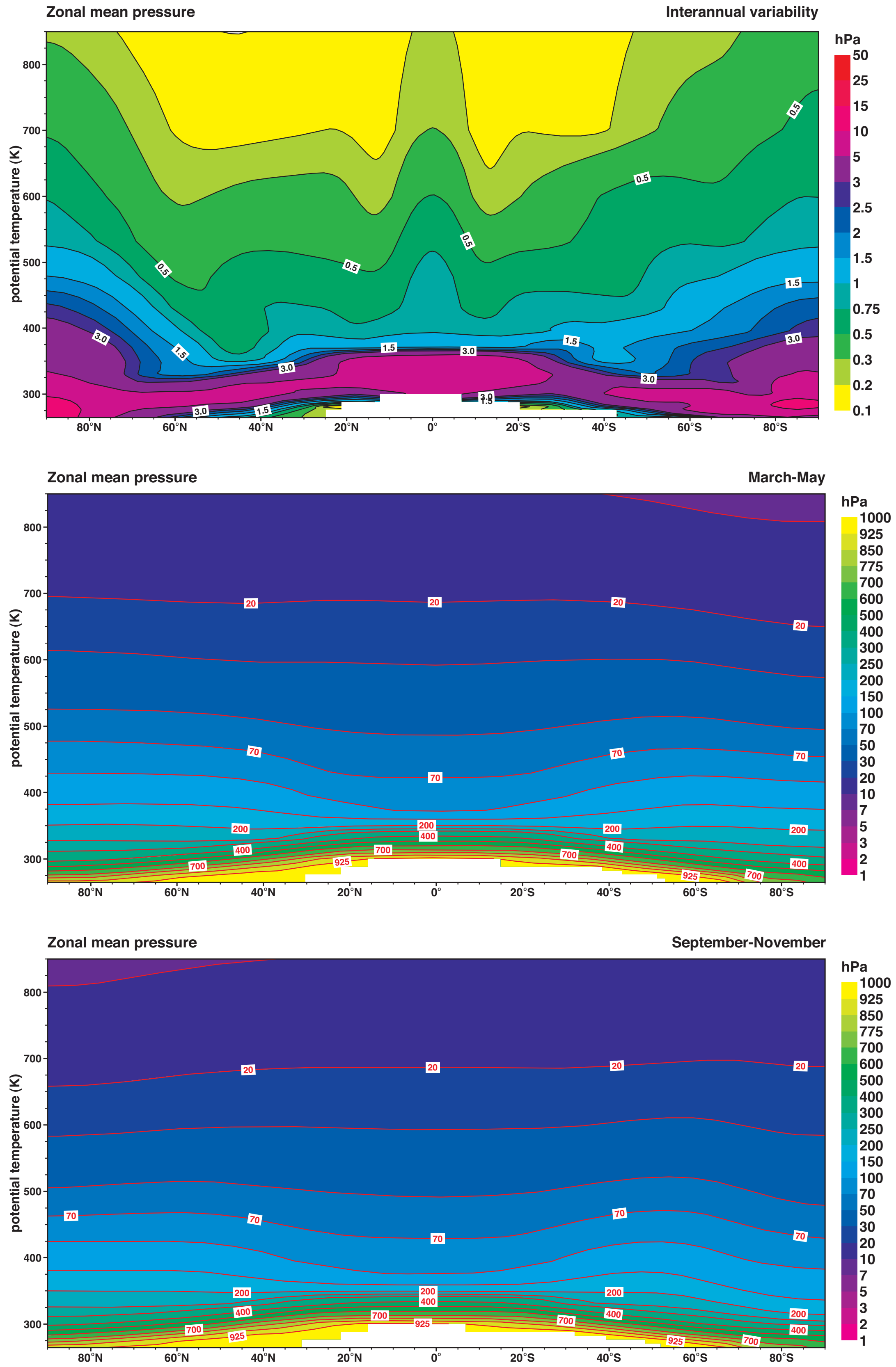

E24 An isentropic stratospheric perspective of zonal mean pressure (hPa).

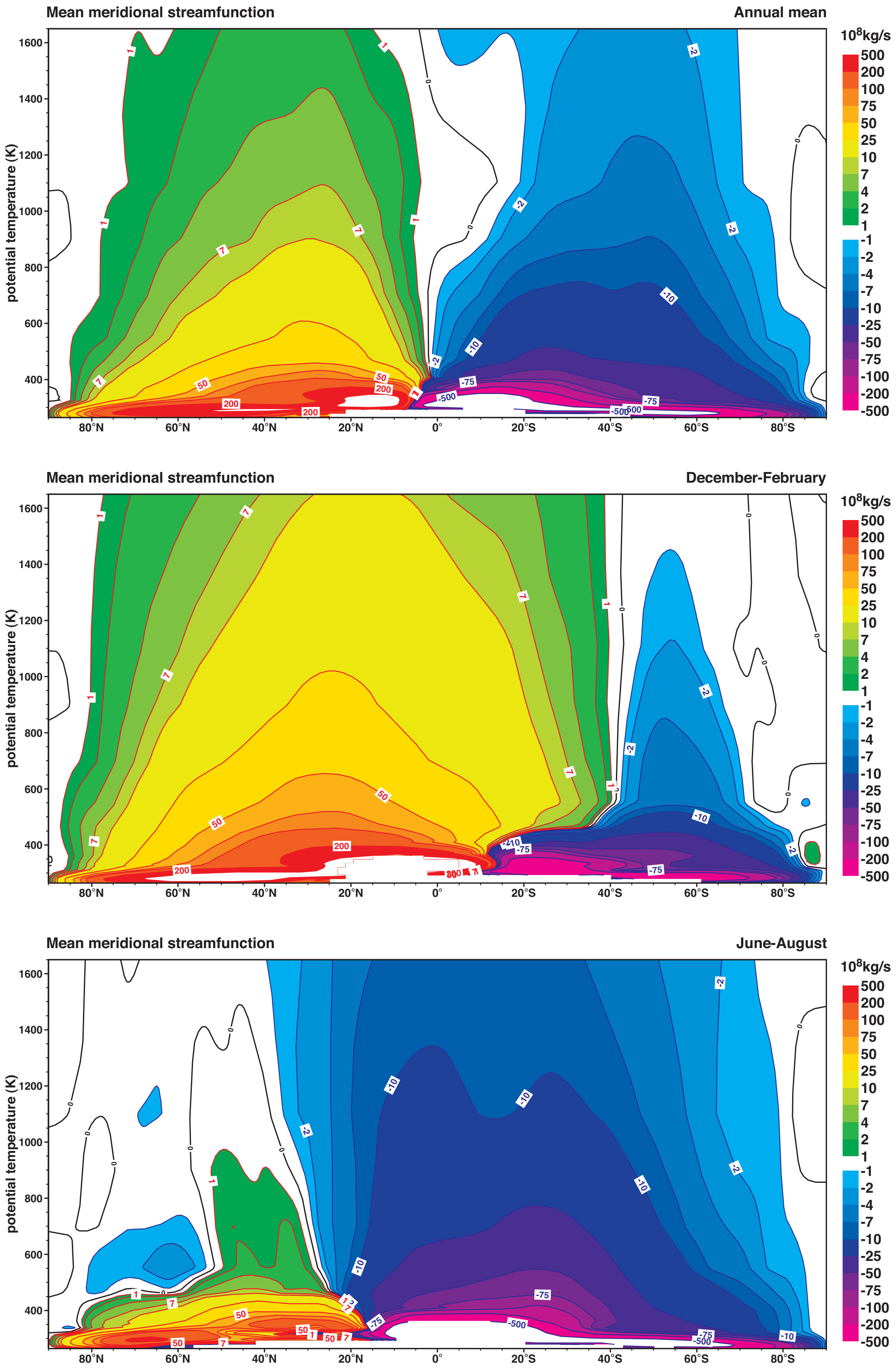

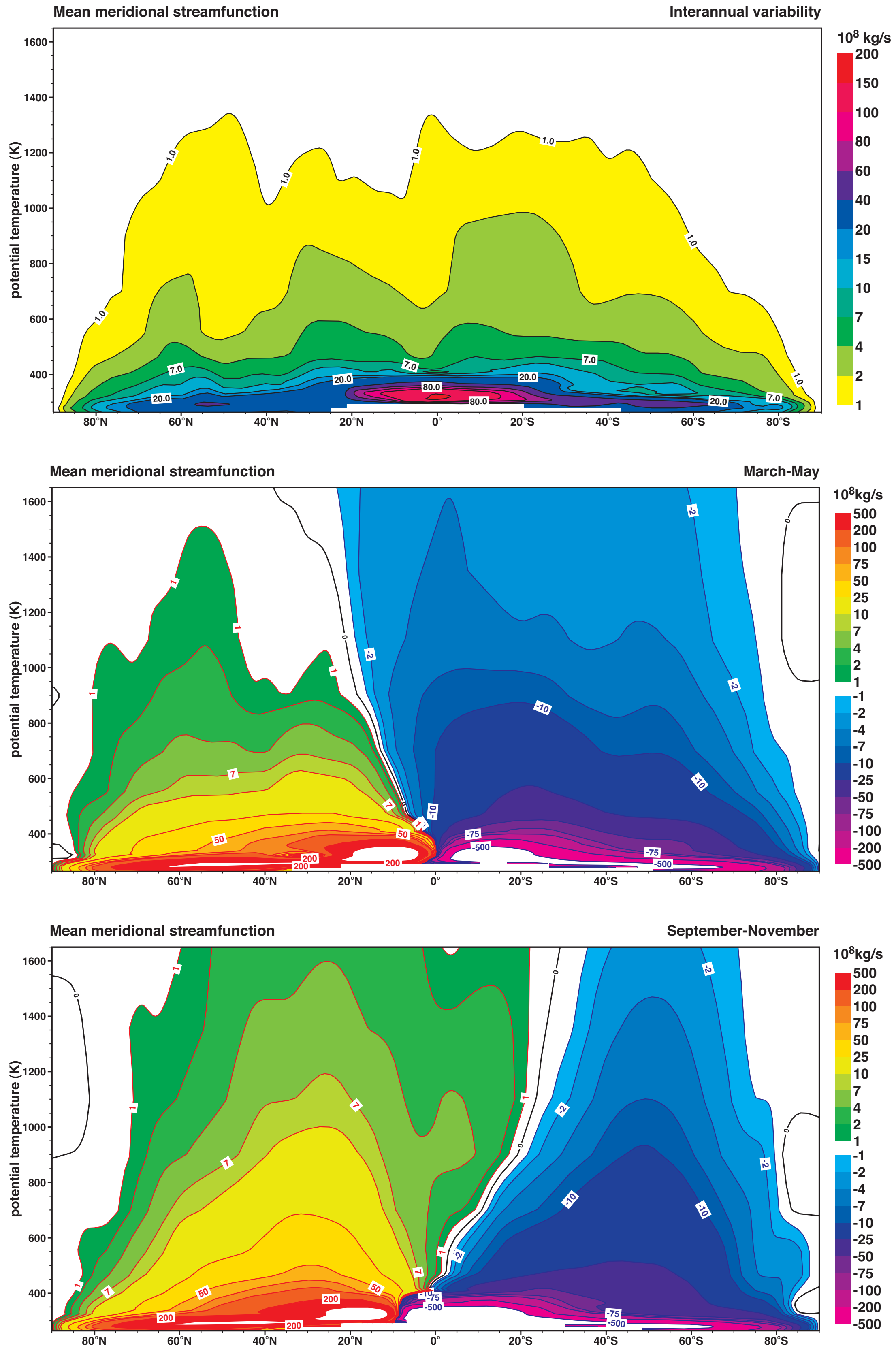

E25 An isentropic stratospheric perspective of mean meridional streamfunction (kgs^{-1}).

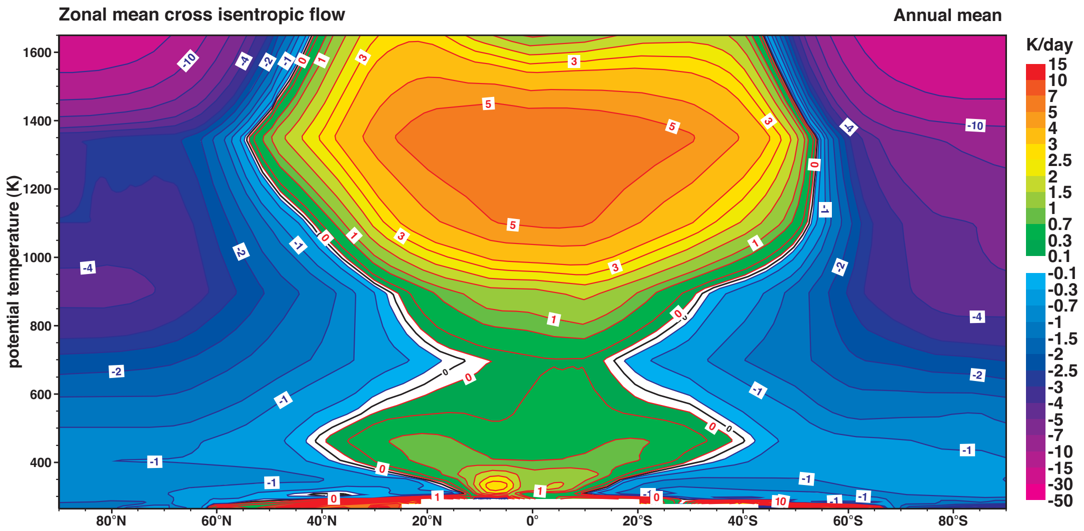

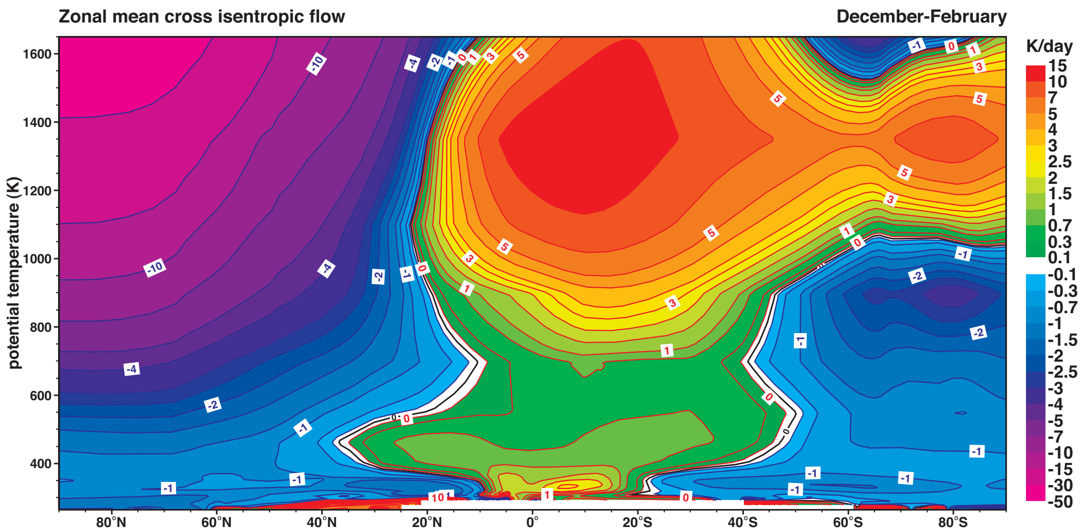

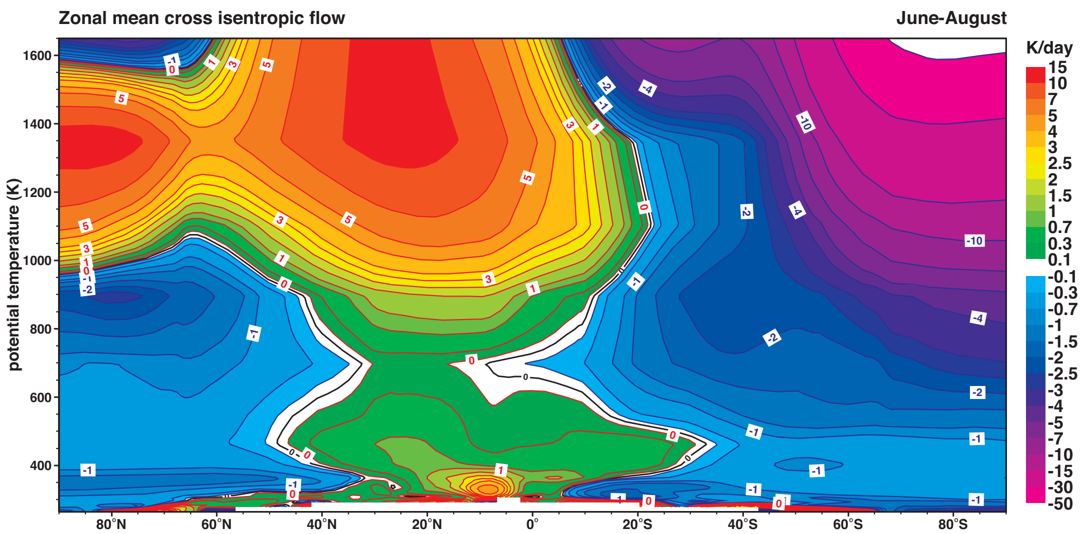

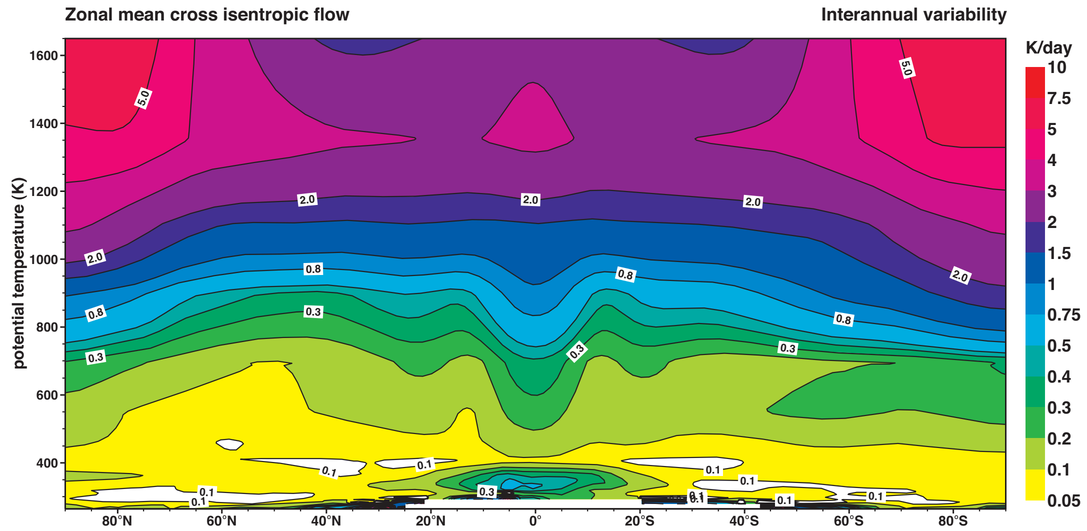

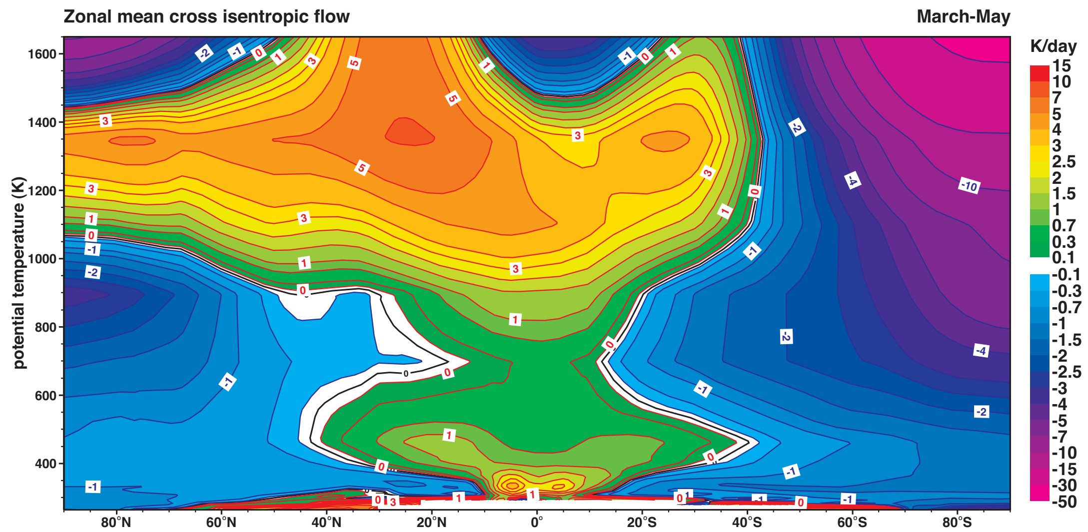

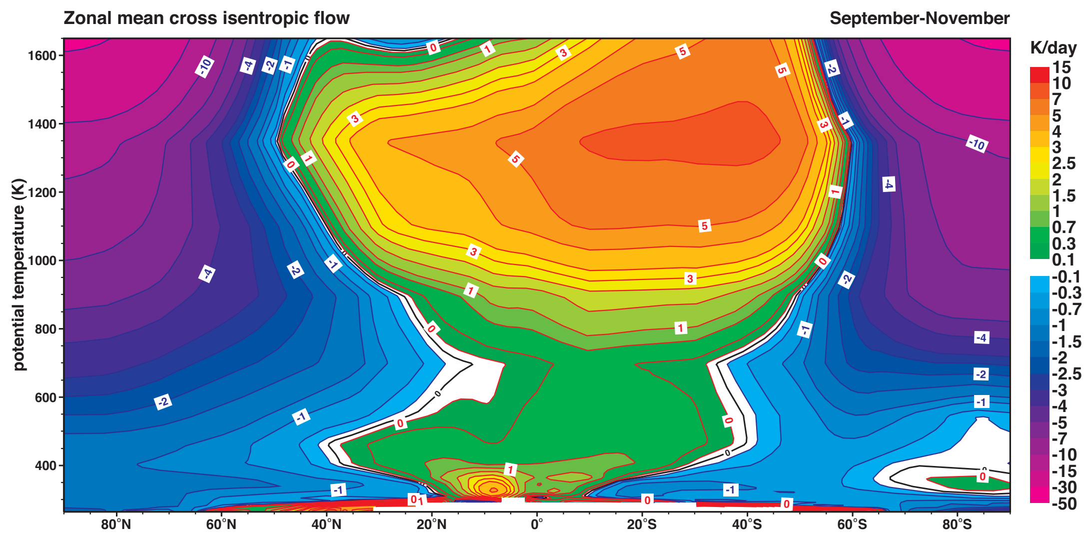

E26 An isentropic stratospheric perspective of zonal mean cross isentropic flow (Kday^{-1}).

Section F

PV=2 climatologies

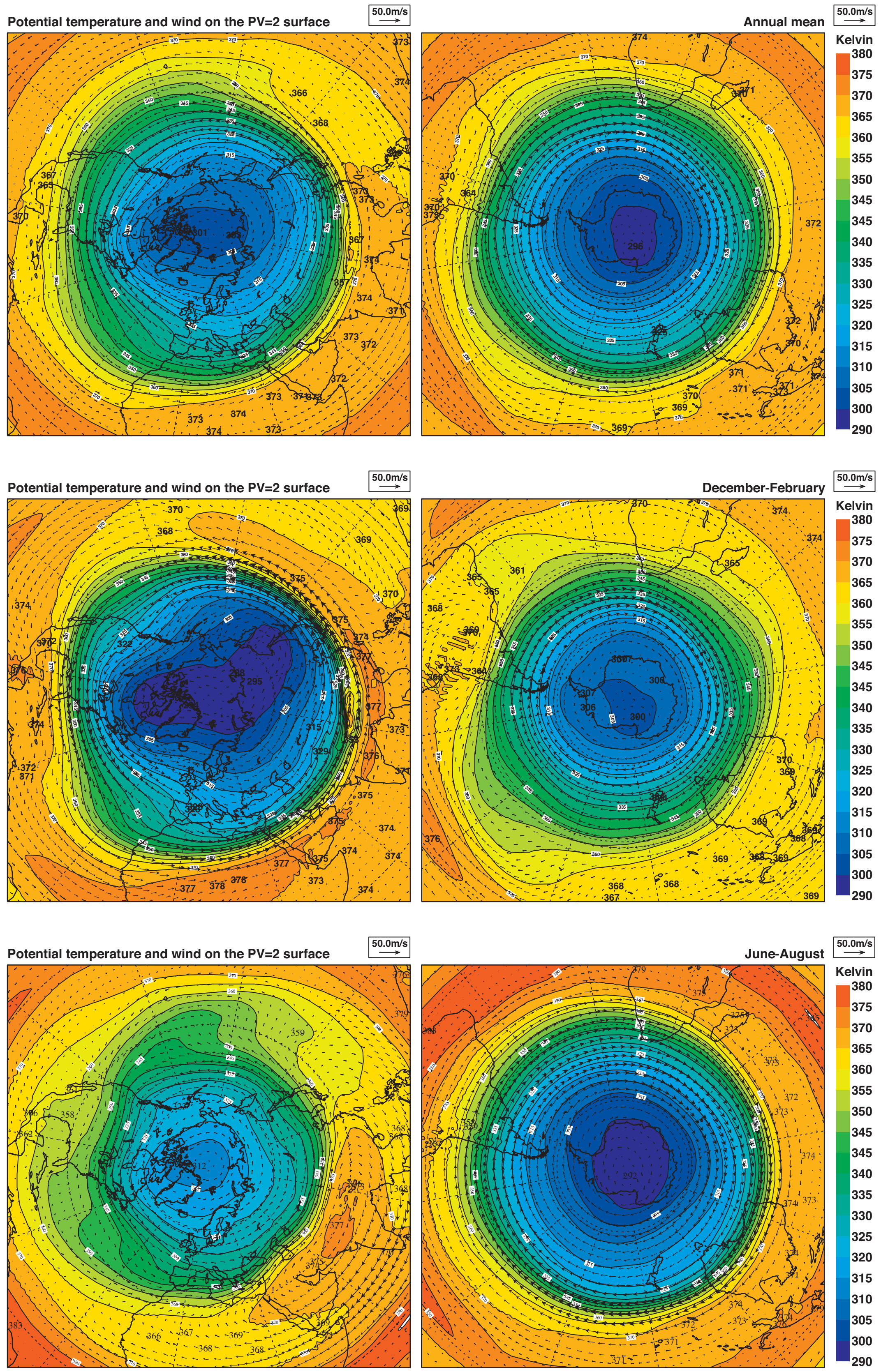

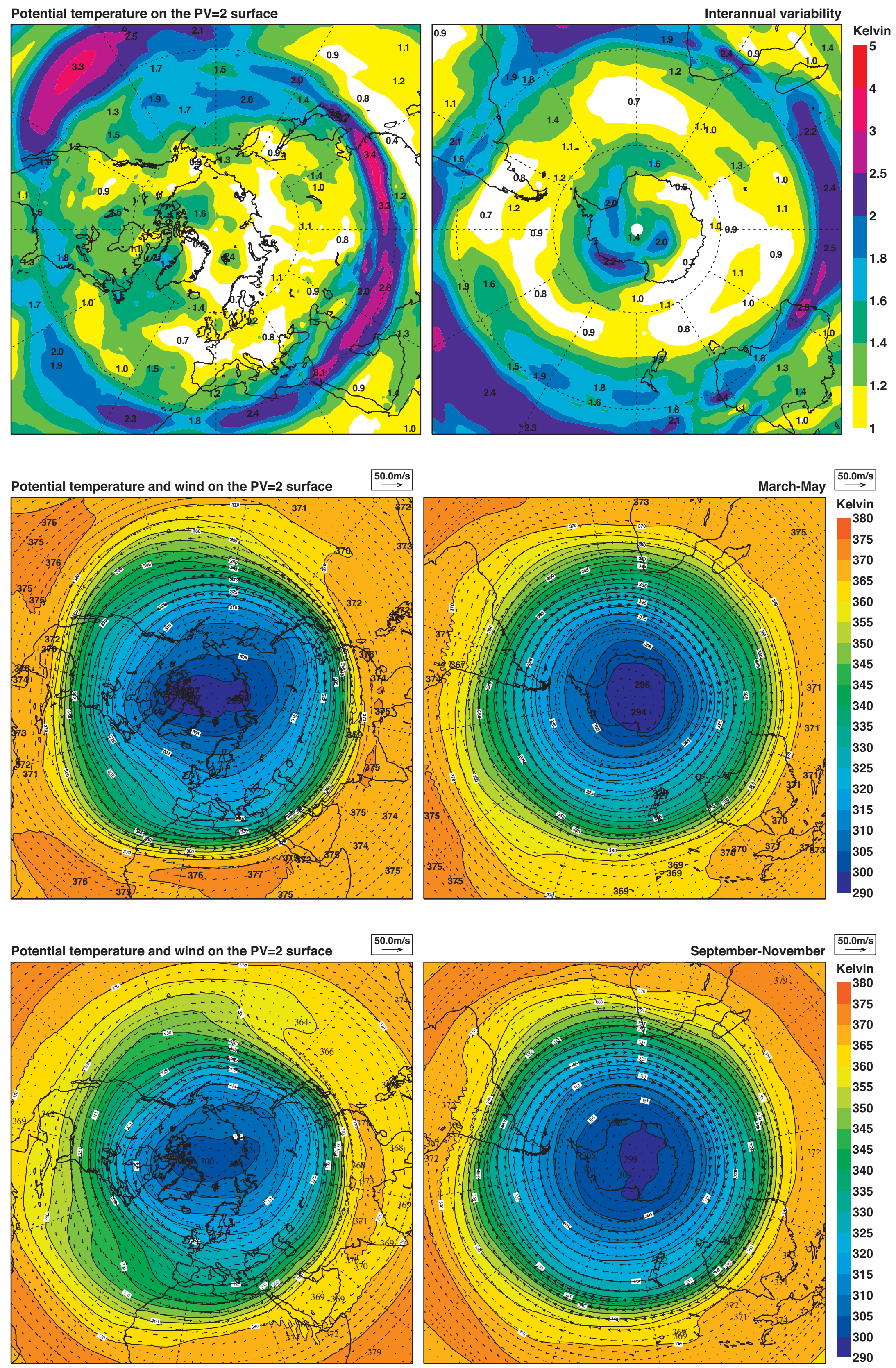

F1 Potential temperature (K) with vector wind (ms^{-1}) on the 2 pvu potential vorticity surface. For the interannual variability, the winds are omitted.

Pressure (hPa) and isotachs on the PV=2 surface — Annual mean

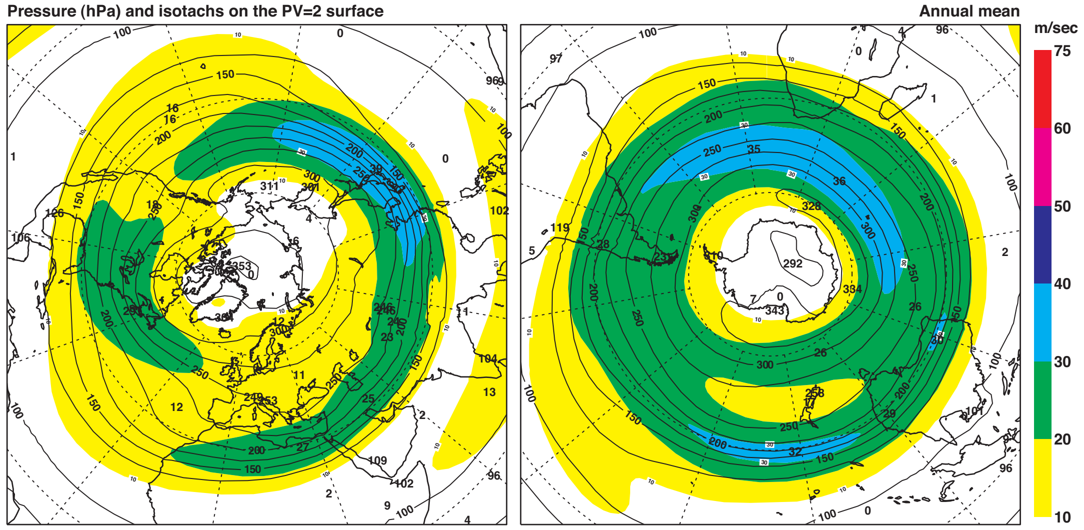

Pressure (hPa) and isotachs on the PV=2 surface — December-February

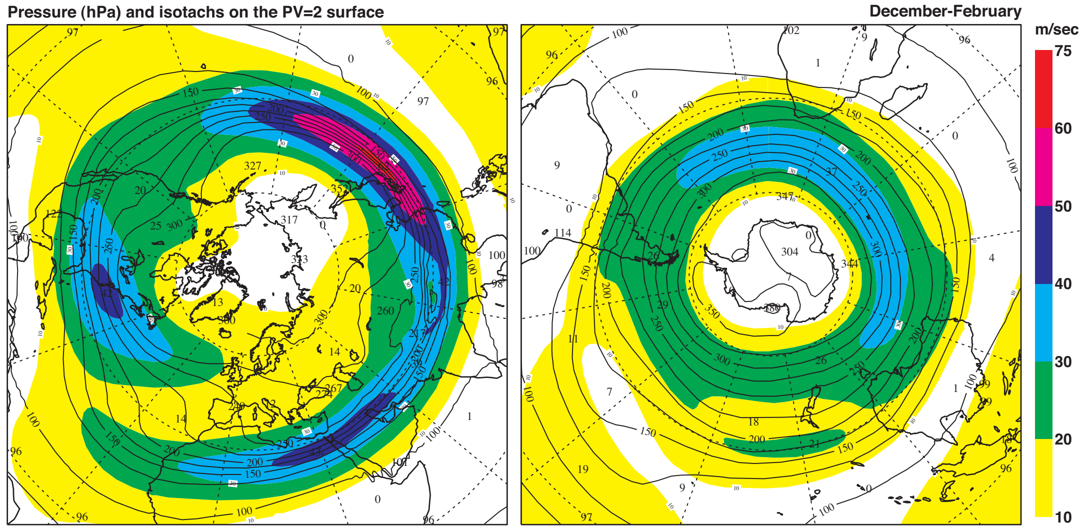

Pressure (hPa) and isotachs on the PV=2 surface — June-August

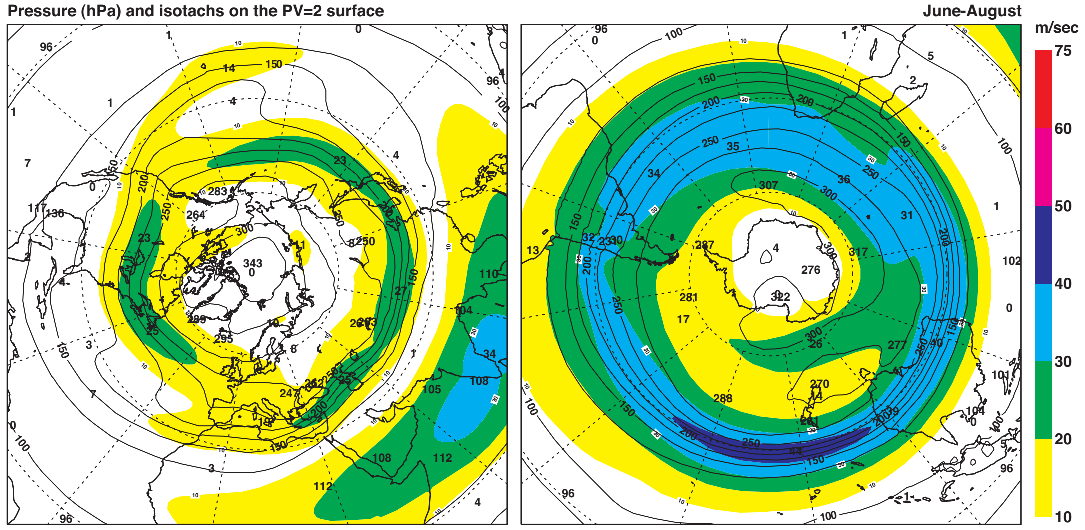

Pressure (hPa) and isotachs on the PV=2 surface — Interannual variability

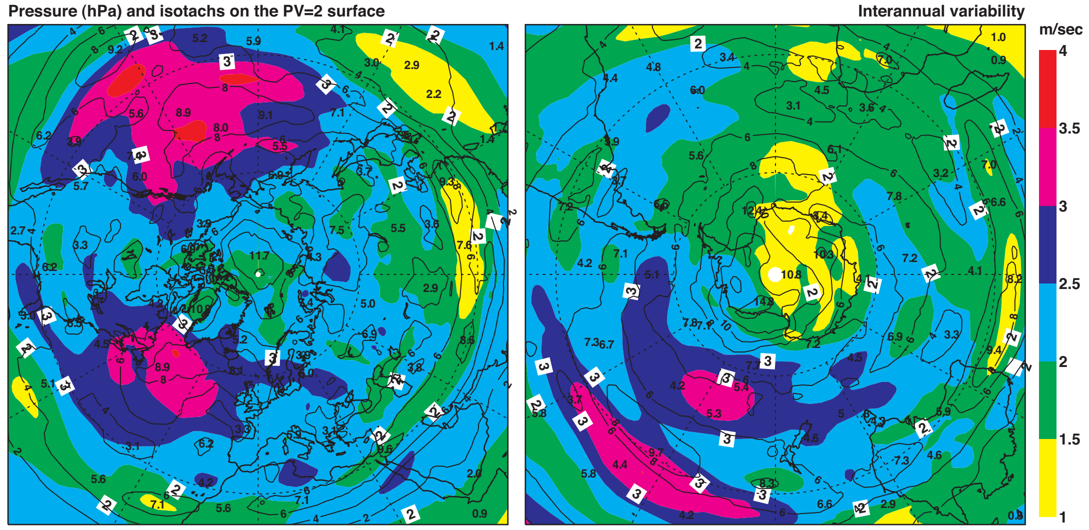

Pressure (hPa) and isotachs on the PV=2 surface — March-May

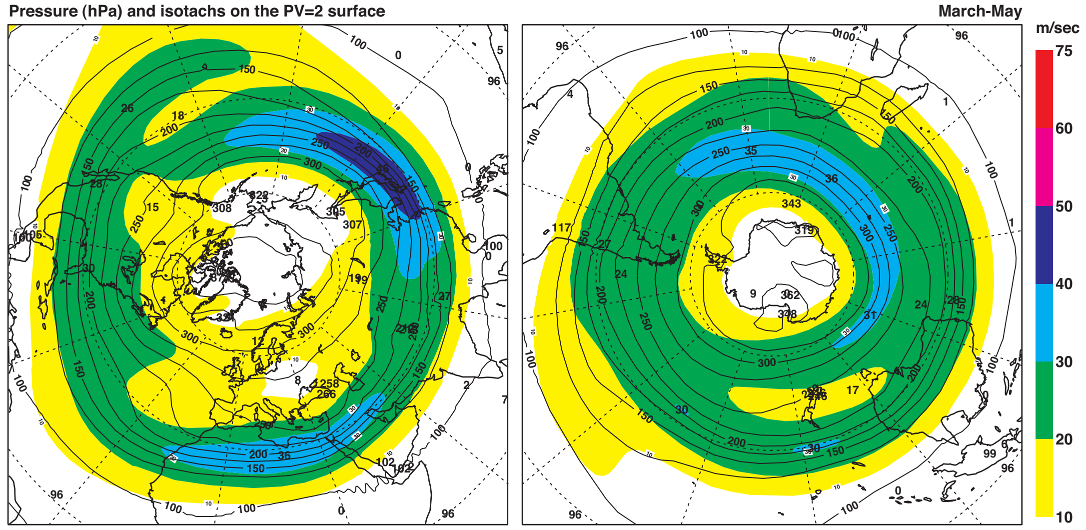

Pressure (hPa) and isotachs on the PV=2 surface — September-November

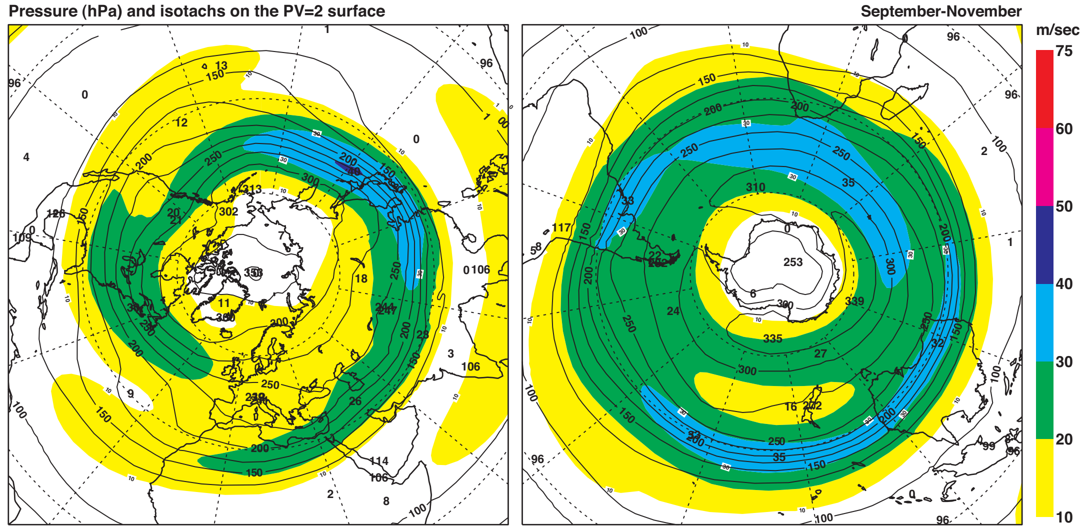

F2 Pressure (hPa) (contours) with isotachs (ms^{-1}) (colour shading) on the 2 pvu potential vorticity surface.

Section G

Time series

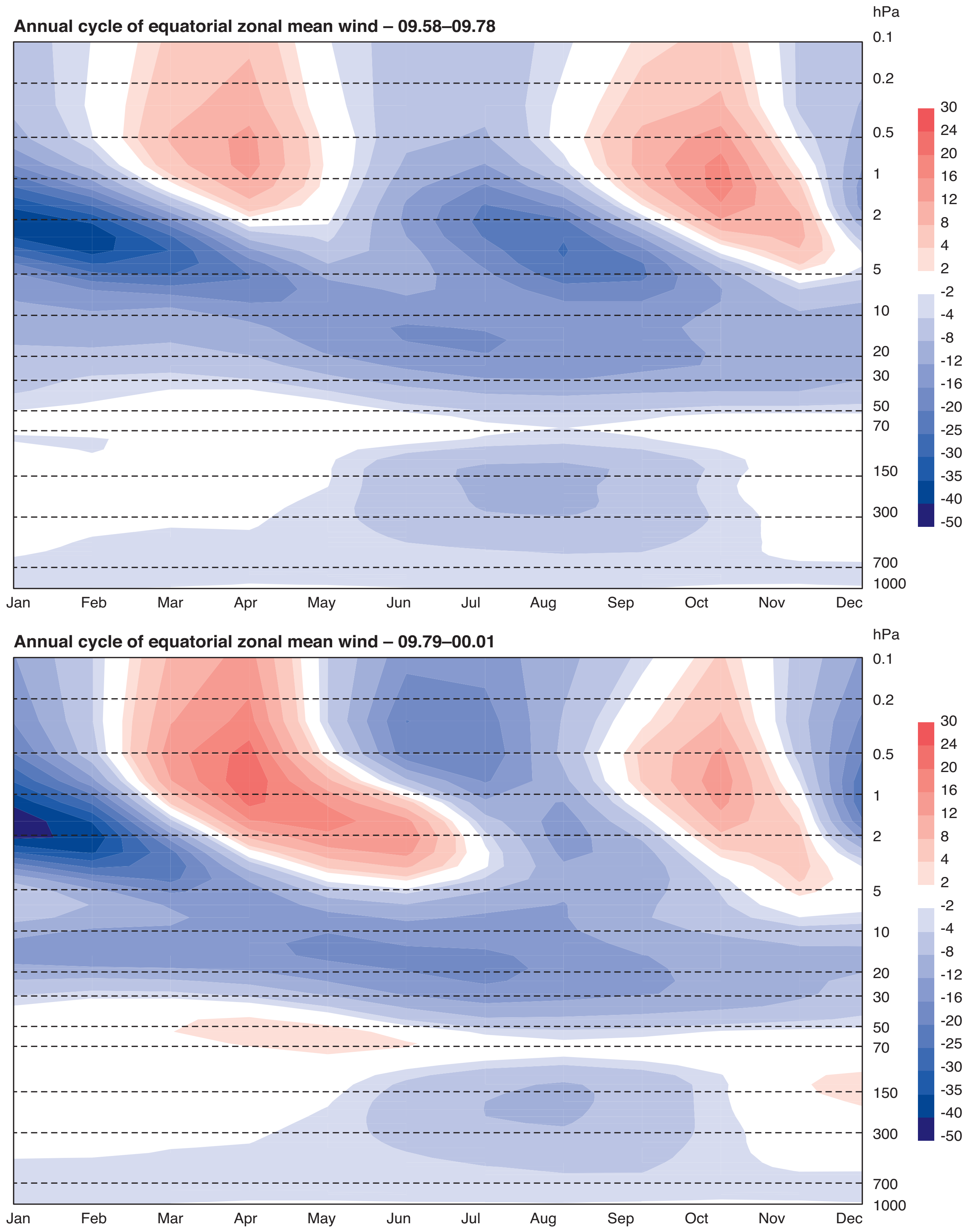

G1 The SAO. The annual cycle climatological monthly mean, zonal mean equatorial zonal wind (ms^{-1}) for 1958–1978 (upper panel) and 1979–2001 (lower panel).

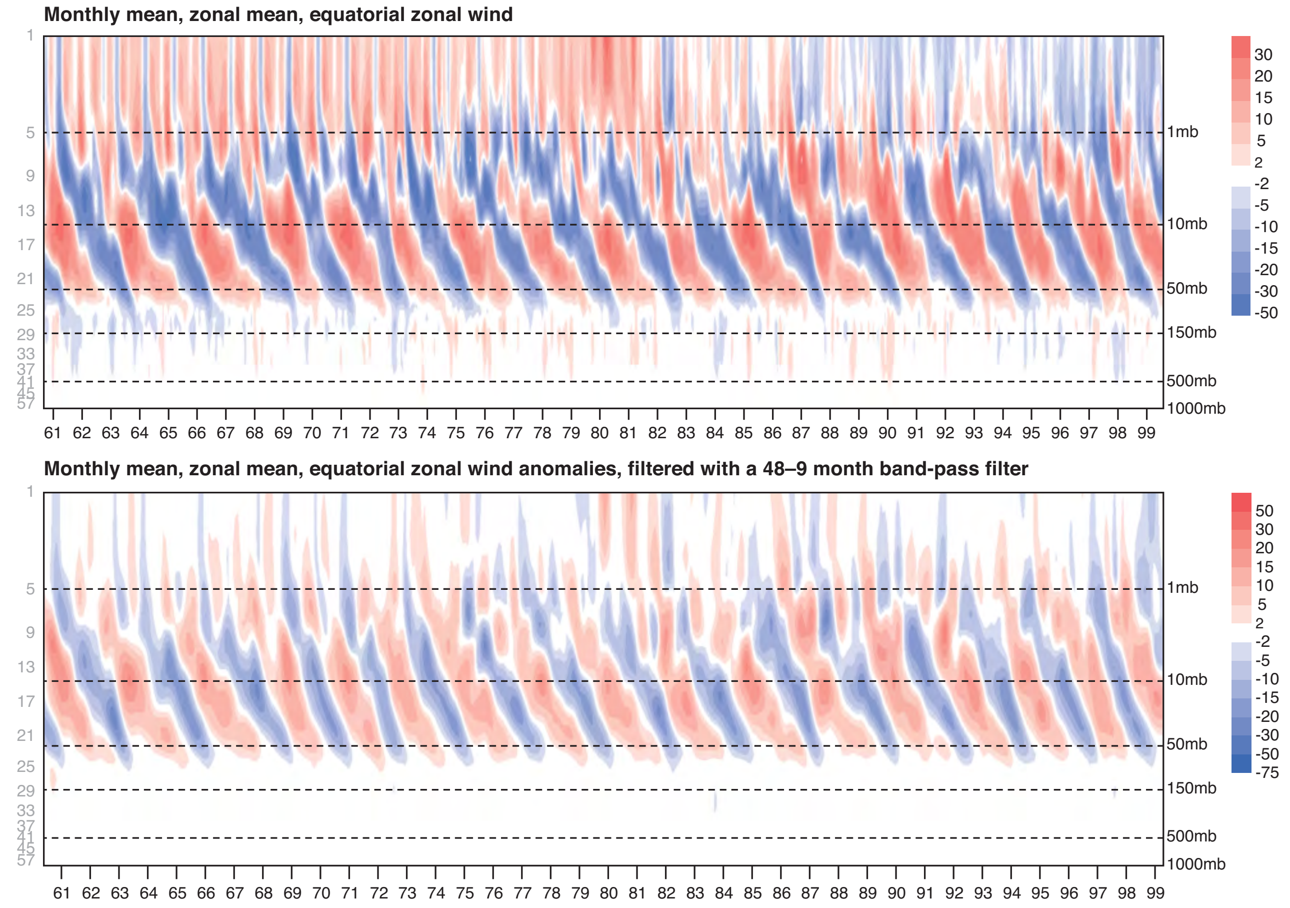

G2 The QBO. Monthly mean, zonal mean, equatorial zonal wind (ms^{-1}) (upper panel), and the anomalies (from the 45-year climatology for that calendar month) filtered with a 48–9 month band pass filter (lower panel).

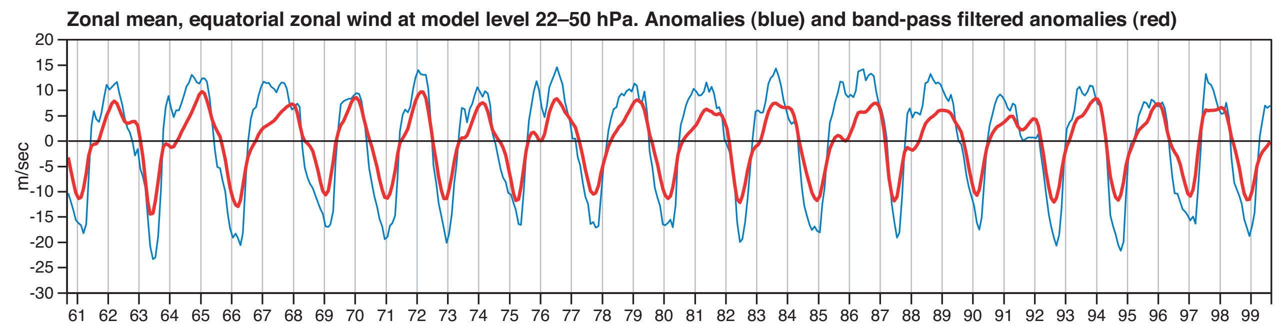

G3 The QBO at 50 hPa. Monthly mean, zonal mean 50 hPa equatorial zonal wind anomalies (from the 45-year climatology for that calendar month) (ms^{-1}) (blue line) and filtered with a 48–9 month band pass filter (red line).

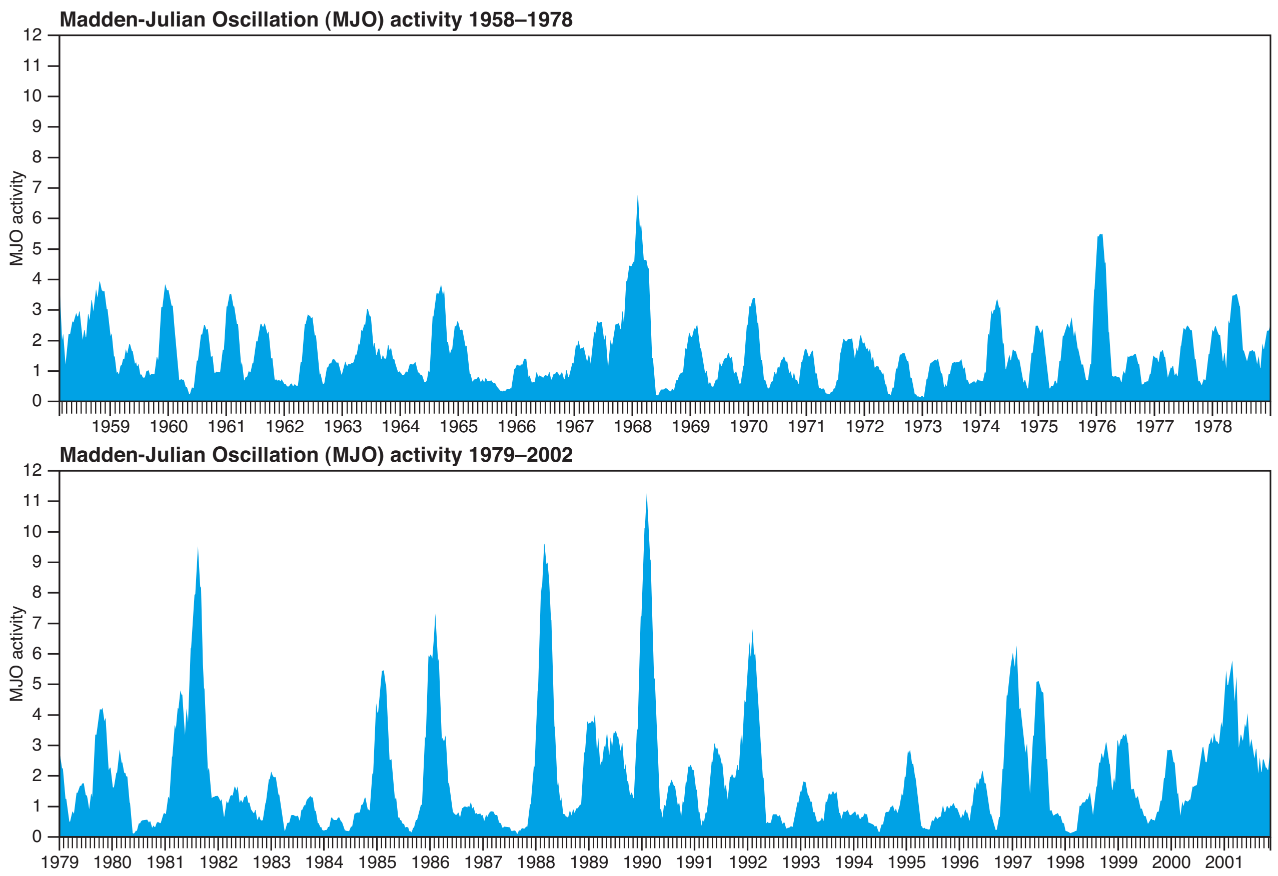

G4 The MJO Index. 10N–10S 200 hPa 6-hourly zonal mean zonal wind (ms^{-1}) filtered with a 90–30 day band pass filter, then squared and passed through a 90 day running mean.

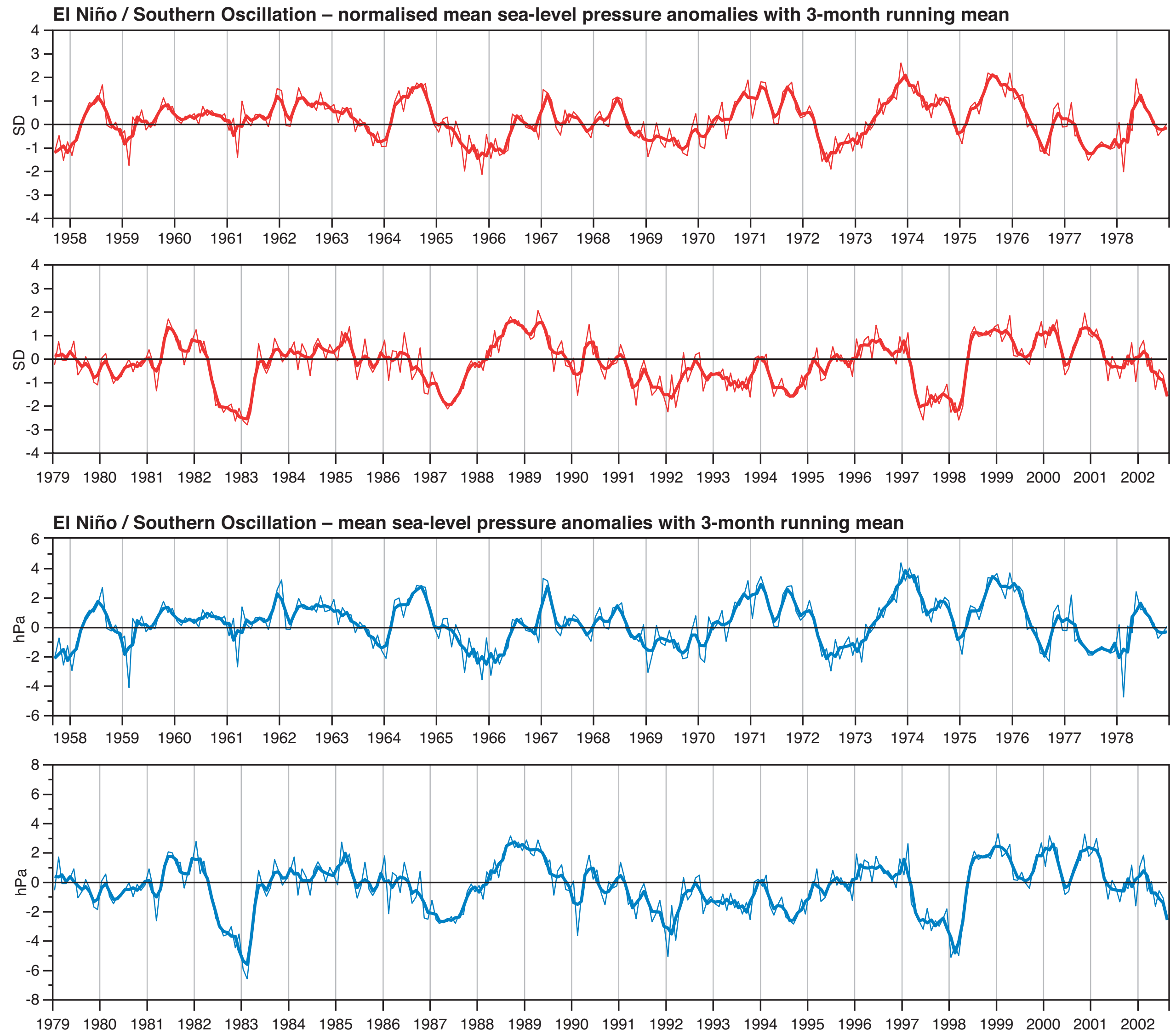

G5 The SOI. Tahiti minus Darwin monthly mean, mean sea-level pressure anomalies (hPa) (blue lines) and normalised by the 45-year climatological standard deviation for that calendar month (red lines). The thick lines represent the fields after the application of a 3-month running mean.

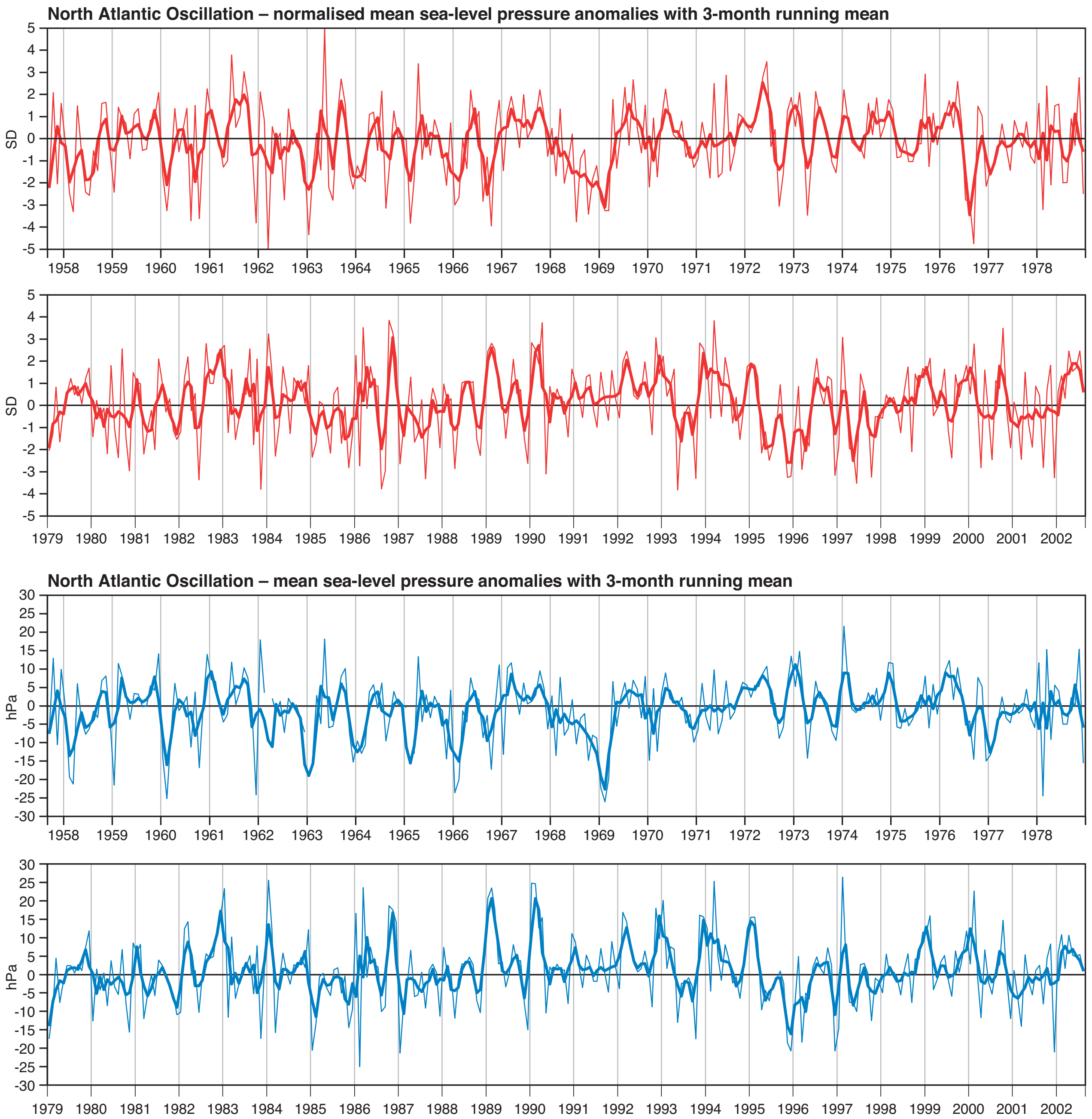

G6 The NAO Index. Azores minus Iceland monthly mean, mean sea level pressure anomalies (hPa) (blue lines) and using anomalies normalised by their 45-year climatological standard deviations for that calendar month (red lines). The thick lines represent the fields after the application of a 3-month running mean.

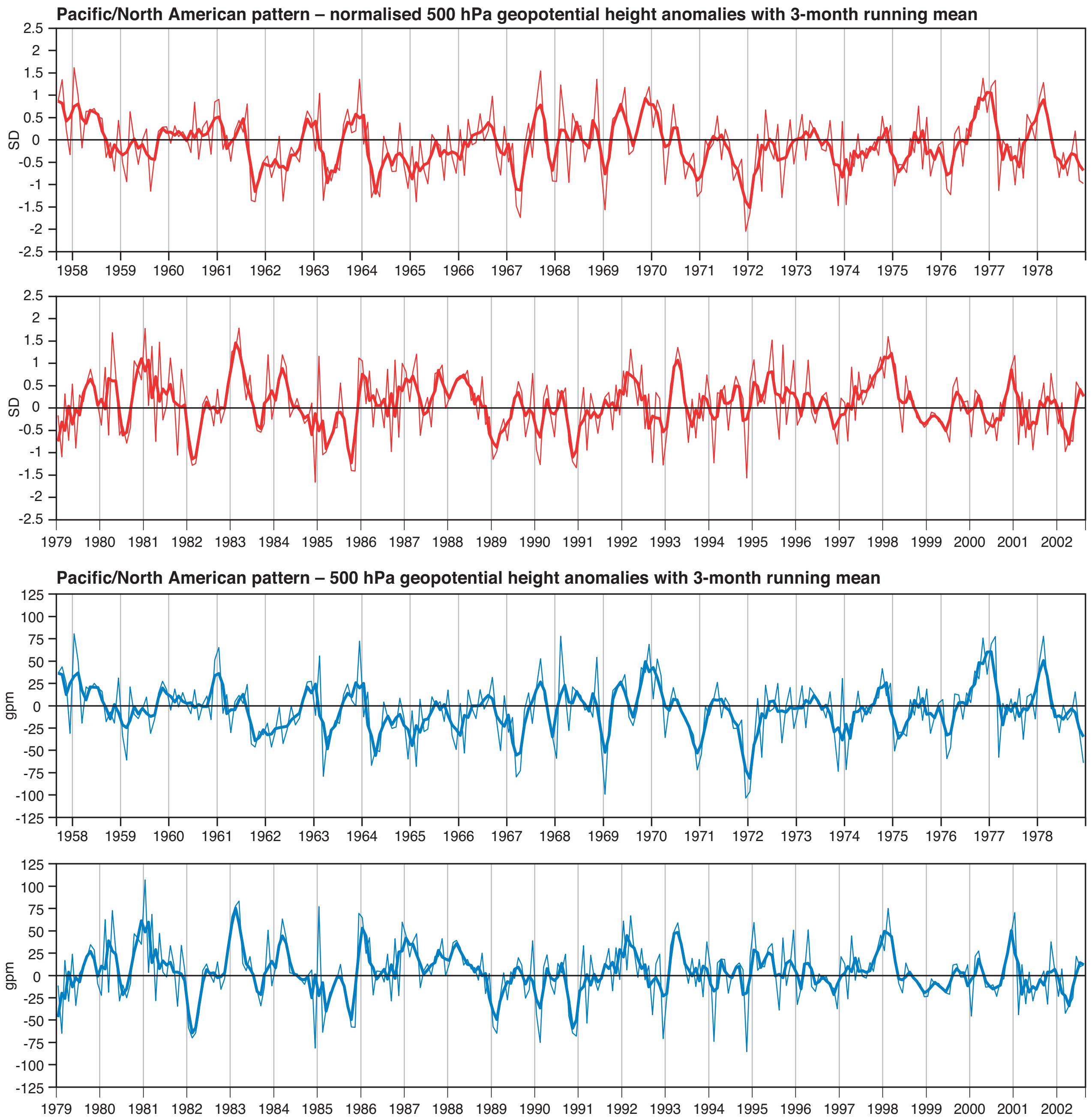

G7 The PNA Index. A linear combination of monthly mean 500 hPa geopotential height anomalies (0.25 × (z(20N,160W) – z(45N,165W) + z(55N,115W) – z(30N,85W))) (m) (blue lines) and using anomalies normalised by their 45-year climatological standard deviations for that calendar month (red lines). The thick lines represent the fields after the application of a 3-month running mean.